Transactions of the ASME®

Journal of Fluids Engineering

Published Quarterly by The American Society of Mechanical Engineers

VOLUME 117 • NUMBER 1 • MARCH 1995

(Contents continued on pg. 74)

Transactions of the ASME, Journal of Fluids Engineering (ISSN 0098-2202) is published quarterly (Mar., June, Sept., Dec.) for $150.00 per year by The American Society of Mechanical Engineers, 345 East 47th Street, New York, NY 10017. Second class postage paid at New York, NY and additional mailing offices. POSTMASTER: Send address changes to Transactions of the ASME, Journal of Fluids Engineering, c/o THE AMERICAN SOCIETY OF MECHANICAL ENGINEERS, 22 Law Drive, Box 2300, Fairfield, NJ 07007-2300.
CHANGES OF ADDRESS must be received at Society headquarters seven weeks before they are to be effective. Please send old label and new address.
PRICES: To members, $40.00, annually: to nonmembers, $150.00. Add $30.00 for postage to countries outside the United States and Canada.
STATEMENT from By-Laws. The Society shall not be responsible for statements or opinions advanced in papers or . . . printed in its publications (B7.1, Par. 3).

INDEXED by Applied Mechanics Reviews and Engineering Information, Inc.
Canadian Goods & Services Tax Registration #126148048

Contents (continued)

Journal of Fluids Engineering

Editorial

This is the annual report of the Technical Editor on the operation of this Journal. This report appears in every March issue and contains information on our efforts to disseminate more efficiently the archival material submitted by the authors and make it more accessible to our readership. This issue also contains a list of the papers published in different categories in the previous year and a list of all the reviewers who supported our effort. Authors' indices appear in a cumulative form every five years. The last author index was published in September, 1992 and was actually a ten-year index. The next will be a five-year index and will appear a year from now.

The number of submitted papers has been on a monotonic increase for the past six years. It was possible for a while to secure commensurate increases for the number of allotted pages but the past two years saw only moderate improvement. This is because many libraries have discontinued subscriptions to periodicals and the ASME Publication Committee decided to follow a uniform conservative approach by limiting to total number of pages allotted to all journals. In terms of the number of submitted papers, the *Journal of Fluids Engineering* ranks now second among all the ASME Transactions, but its net income has dropped to about the middle among the journals, even though the number of subscriptions is the third highest. Readers and authors of this Journal are kindly requested to check with their libraries and request that a library subscription be added, if not already there. The annual subscription for members of ASME is $40.00 and for nonmembers or libraries is $150.00. These are not too high, especially if compared to publications like the *International Journal of Heat and Fluid Flow, Heat and Mass Transfer*, or *Multiphase Flow* which charge $490.00, $1,841.00, and $947.00, respectively, for annual institutional subscriptions.

With continuous increases in the number of submitted papers and nearly leveling of the available space, our backlog has increased somewhat. This gave the opportunity to the Editorial Board to raise the standards of the Journal. In the process we also reconsidered and slightly adjusted the criteria for acceptance. This minor change in the guidelines was essentially based on our interpretation of the concept of originality. With today's advances in computational methods and computing hardware, as well as today's power of instrumentation and laboratory automation, it is easier to carry out complex and sophisticated research. A lot of this work is being developed independently of earlier contributions. In a sense, such work, as for example the development of a new Navier-Stokes solver, is original. But today, even though we often recognize the amount of effort involved, and the high quality of independent work required to produce the results, we are forced to apply stringent criteria to evaluate the originality of a contribution. These are essentially based on the principles that (i) a contribution to the archival literature should provide information and data on new physical phenomena or new methods of approach that further our knowledge in fluid mechanics and fluids engineering and that (ii) others should be able to employ this material in order to achieve further progress in the field.

Other factors that are now influencing the criteria for acceptance are the care in insuring good experimental accuracy and reducing numerical uncertainty as well as the proper and accurate reporting of the above. Guidelines on these issues have been outlined in the editorials of September, 1993 and September, 1991. Since the publication of the latter, a number of comments on numerical uncertainty have appeared in the Technical Forum. Many opinions and concerns, both pro and con have been expressed. Suffice it to say here that this Editorial Board will adhere as closely as possible to these guidelines but on the other hand, both the editors and the reviewer will judge each contribution on its own merits. As Dr. Freitas proposes in his editorial that appears in this issue's Technical Forum, the time has come to move on. The present guidelines can be still discussed and ideas can be exchanged through the Journals Electronic Bulletin Board as explained later in this Editorial, but the community will be served better if we start a serious discussion of guidelines that will influence and control the next generation of contributions.

Our readers must have noticed that every other issue appears now in color. Unfortunately, the cost is carried by the authors but we are happy to report that we were able to reduce it further to a small fraction of what other journals charge for this service.

Most recently, we were able to extend substantially the services offered by the *Journal of Fluids Engineering* and the Fluids Engineering Division. This was an expansion of our electronic on-line information service and was described in detail in the Editorial that appeared in the September 1994 issue. The first new development is an expansion of the scope of the JFE Data Bank to allow authors to deposit numerical data and/or program listings of codes that are available to the public. Guidelines for this procedure were formulated by a subcommittee of the FED CFD Coordinating Group. Moreover, it is now possible to deposit color figures in the Data Bank. These figures will be accessed by the readers electronically in a way similar to the access of experimental data. We have also succeeded in developing a method to store and play back short videos and this option should also be available to our readership.

We have also established a Bulletin Board and an Information Board. The electronic board allows readers to offer discussion on papers published in the Journal. Readers can log on to the Electronic JFE and open the Bulletin Board. They will then be prompted to open the file of a paper or an editorial. File names are simply the letters FN followed by the year (last two digits) and the first page of the paper. For example, a paper that appeared on page 57 in 1994 will have the file name FN94057. In each file, readers will find discussions of the paper of their interest. They can also add their own. Readers logging on to the Electronic JFE will be prompted to provide their name and e-mail address. In case a reader offers

a discussion for a paper, his or her contribution bounces back to his/her e-mail address to provide an opportunity for a final check. It is then automatically entered in the Bulletin Board. The Editor monitors the process. Readers are particularly invited to offer comments and suggestions to the editorials on experimental accuracy and numerical uncertainty as well as the comments that appeared later in the Technical Forum. Directions on how to log on to the Electronic JFE always appear on the last page of each issue.

The material added to the Bulletin Board will be retained for a few years but the contributing reader will always have the option to submit a discussion for publication in the Journal. Discussions and authors' responses contributed to the Bulletin Board will not be edited, but discussions submitted for publication in the Journal will be reviewed and edited by the Editorial Board according to a procedure established long ago.

These services will eventually be turned over to ASME-NET, a new online network offering a variety of services to ASME members. However, for the time being, this system cannot include figures or moving frames. We therefore decided to continue operating the Journal Data Bank at Va Tech for a while. We will also continue including the Bulletin Board in our Electronic JFE, to provide easier control by the Editorial Board. However, we will discontinue the listing of the FED Conference schedule in our Information Board, since this or at least a shorter version of conferences is already included in the information provided by ASME through ASMENET. For information about ASMENET the readers can contact Mark Laroche (Tel: 212-705-7177, e-mail: larochem@asme.org).

Finally we should acknowledge the valuable contribution of two of our associate editors whose tenure has expired. They are (i) Dr. Ronald L. Panton in the area of fluid mechanics and (ii) Dr. Oktay Baysal in the area of computational fluid dynamics. We sincerely appreciate their hard work. We should also acknowledge the contributions of our reviewers. The names of the individuals who helped us out this year are listed in the last pages of this issue.

Individuals have been nominated to serve three-year terms as associate editors. These and the areas they will be working on are: Dr. Promode R. Bandyopadhyay (Naval Undersea Warfare Center, Newport, RI) in the area of fluid mechanics; Professor Francesc Giralt (Universitat Rovira i Virgili, Tarragona, Spain) in the area of fluid mechanics; and Dr. Munir M. Sindir (Rocketdyne Division/Rockwell International, Canoga Park, CA) in the area of computational fluid mechanics. Dr. Michael W. Reeks was reappointed for an additional one year term and will continue to work in the area of multiphase flow. These nominations have been approved by the Executive Committee of the Fluids Engineering Division and their final approval by the ASME Board of Communications is pending.

The Technical Editor

Journal of Fluids Engineering

Technical Forum

Questions in Fluid Mechanics

Stokes' Hypothesis for a Newtonian, Isotropic Fluid

Mohamed Gad-el-Hak[1]

Is the second coefficient of viscosity equal to the negative two-third of the dynamic coefficient of viscosity?

The short answer to the above question is no, not in general. Although the issues involved remain partially open, the present brief is an attempt to clarify some of the misconceptions and misuses embroiled in the subject of bulk viscosity. Consider the genesis of the query.

To close the equations of motion for a continuum fluid, a relation between surface forces and the flow field is needed. A Newtonian fluid is that for which the stress tensor is assumed to be linearly related to the rate-of-strain tensor.[2] The constant of proportionality between these two second-order tensors is in general a fourth-rank tensor:

$$\sigma_{ij} = \sigma_{ij}^{(0)} + C_{ijkl}e_{kl} \tag{1}$$

where σ_{ij} is the stress tensor, $\sigma_{ij}^{(0)}$ is the stress distribution that can exist in a resting fluid, C_{ijkl} are the 81 coefficients of proportionality, and e_{kl} is the rate-of-strain tensor. The residual stress term must be retained for fluids, while the corresponding term is dropped when deformable, compressible solids are considered (Eringen, 1980). In the theory of linear elasticity, the displacements are measured, by convention, from a state in which the body is at rest under zero body forces, and the residual stress term has no contribution to the equations of motion. This is justified because any process which reduces the finite motion at a point to zero would not change perceptibly the thermodynamic state. For fluids, this is not necessarily the case. The *total* stress appears in the equations of motion of fluids, and it is therefore absolutely necessary to include $\sigma_{ij}^{(0)}$.

For fluids, both $\sigma_{ij}^{(0)}$ and C_{ijkl} vary with the thermodynamic state specified by, for example, the density and temperature. However, the residual stress must be the same regardless of the fluid state of motion, otherwise the assumed linear relation between σ_{ij} and e_{kl} is violated. Since the stress force exerted across any element of a surface in a resting fluid is independent of the orientation of that element (see, for example, Batchelor, 1967), it follows that:

$$\sigma_{ij}^{(0)} = -p\delta_{ij} \tag{2}$$

where p is a scalar, called hydrostatic pressure or simply pressure, and δ_{ik} is the Kronecker delta (the only isotropic second-rank tensor). The pressure is one more unknown in fluid problems,[3] but the continuity equation, which has no counterpart[4] in the theory of elasticity, provides an additional equation to close the problem.

The lack of microscopic surface moments ensures that the stress tensor is a symmetric one. If the fluid is further assumed to have no preferred directions, i.e., isotropic fluid, those 81 linear coefficients reduce to only two independent coefficients (for a proof, see, for example, Long, 1961; Aris, 1962): μ the dynamic coefficient of viscosity (shear), and λ the second coefficient of viscosity (dilatational). Thus for a Newtonian, isotropic fluid:

$$\sigma_{ik} = -p\delta_{ik} + \mu\left(\frac{\partial U_i}{\partial x_k} + \frac{\partial U_k}{\partial x_i}\right) + \lambda\left(\frac{\partial U_j}{\partial x_j}\right)\delta_{ik} \tag{3}$$

where U_i is a velocity component in the x_i-direction.

Continuum mechanics does not require any fixed relationship between the two coefficients of viscosity, and one must appeal to statistical mechanics, to macroscopic thermodynamics or, as a last resort, to experiments. The precise value of the second coefficient of viscosity is not needed for inviscid flows (both μ and λ are assumed zero), for incompressible flows ($\nabla \cdot \vec{U} = 0$), or when the boundary layer approximations are invoked (normal viscous stresses $\ll$ shear stresses). On those special cases, the thrust of the present question is muted although the conceptual issues are always important.

If we define the mean pressure $\bar{P}$ as the negative one-third of the sum of the three normal stresses (a tensor invariant), Eq. (3) yields:

$$\bar{P} \equiv -\frac{1}{3}(\sigma_{11} + \sigma_{22} + \sigma_{33}) = p - \left(\lambda + \frac{2}{3}\mu\right)(\nabla \cdot \vec{U}) \tag{4}$$

The factor $(\lambda + 2/3\mu)$ is often termed the coefficient of bulk viscosity, although some textbooks mistakenly reserve this terminology for λ itself. Physically, this factor is connected with the dissipation mechanism during a change of volume at a finite rate. In other words, the bulk viscosity provides a damp-

[1]Aerospace and Mechanical Engineering, University of Notre Dame, Notre Dame, IN 46556-5637.

[2]The present brief does not deal with nonlinear, i.e., non-Newtonian fluids.

[3]For compressible flows, if the density and internal energy, for example, are taken as the two independent intensive properties, then the intensive state of a simple thermodynamic system is fully specified. The pressure in that case is not an independent variable and follows from the appropriate equation of state. For a strictly incompressible fluid, on the other hand, the pressure does not influence the thermodynamic state and is formally an unknown mechanical force per unit area whose gradient, but not absolute value, could be determined from the equations of motion.

[4]Of course mass is conserved whether the material is solid or liquid. The simplifications of the linear elasticity theory merely eliminate the need to consider explicitly the continuity equation.

ing of volumetric vibrations such as might occur during sound absorption. Equation (4) implies that, unless either $(\lambda + 2/3\mu)$ or $(\nabla \cdot \vec{\mathbf{U}})$ is equal to zero, the mean (mechanical) pressure in a deforming viscous fluid is not equal to the thermodynamic pressure; more on this point later. The second law of thermodynamics requires that both μ and $(\lambda + 2/3\mu)$ be non-negative.

In 1845, Stokes simply assumed that $(\lambda + 2/3\mu) = 0$.[5] The resulting negative value of λ implies that the tension required to produce a specified proportional rate of stretching along one principal axis is reduced if the fluid is locally expanding. This could easily be seen if Eq. (3) is rewritten for $i = k = 1$, for example:

$$\sigma_{11} = -p + 2\mu \frac{\partial U_1}{\partial x_1} + \lambda\left(\frac{\partial U_1}{\partial x_1} + \frac{\partial U_2}{\partial x_2} + \frac{\partial U_3}{\partial x_3}\right) \qquad (5)$$

If λ is negative and $(\nabla \cdot \vec{\mathbf{U}})$ is positive, σ_{11} necessary to produce a given rate of stretching $\partial U_1/\partial x_1$ becomes smaller as the fluid dilation is intensified and/or as the absolute value of λ is increased.

Unfortunately, the above implication can neither be verified nor refuted with direct measurements. The bulk viscosity can be measured, albeit not very accurately, by the attenuation and dispersion of intense ultrasonic waves (in order to generate measurable effects). In order to satisfy the quasi-equilibrium approximation that requires the sound frequency to be small compared to the inverse of the molecular relaxation time, the high-frequency data are more often than not extrapolated to zero frequency resulting in considerable scatter. The second coefficient of viscosity may not even be a thermodynamic property, since available measurements indicate that λ is frequency dependent. Nevertheless, reasonably accurate, high-frequency acoustic absorption measurements, in conjunction with the standard low-frequency theory, do indicate that the Stokes' hypothesis is correct only for monatomic gases (Prangsma et al., 1973).

Very recently, Emanuel and Argrow (1994) have proposed an alternative, still indirect, method for measuring the bulk viscosity. Their yet-to-be-demonstrated approach is particularly suited for dense polyatomic gases, where the density-based thickness of a shock wave is typically thousands of mean free paths. Emanuel and Argrow have shown analytically that the ratio $(\lambda + 2/3\mu)/\mu$ is linear with the aforementioned thickness, which could readily be measured using the optical reflectivity method or the electron-beam absorption technique.[6]

Several controversies exist in the literature regarding the second coefficient of viscosity. First, does the kinetic theory of gases *prove* that the bulk viscosity is zero for a monatomic gas? Truesdell (1954) argues that this statement is an assumption of the theory and not a proof. On the other hand, the Chapman-Enskog expansion of the Boltzmann equation does yield a zero bulk viscosity for dilute gases without internal molecular structure (Chapman and Cowling, 1970). Furthermore, acoustic attenuation measurements for inert gases support this conclusion. Second, Karim and Rosenhead (1952) report on several sound-wave-attenuation measurements that yield a large, positive λ for most liquids. Once again, Truesdell (1954) disputes the validity of these experiments (see also the extensive discussion on the general subject of bulk viscosity provided under the leadership of Rosenhead, 1954).

Should there be any significant difference between the mechanical and thermodynamic pressures? This is an unsettling question, but the kinetic theory of gases offers some guidance (Hirschfelder et al., 1954; Vincenti and Kruger, 1965; Chapman and Cowling, 1970). The mechanical pressure is a measure of the translational energy of the molecules. The thermodynamic pressure, on the other hand, is a measure of the *total* energy, which might include additionally vibrational and rotational modes and, for liquids and dense gases, intermolecular attraction. For dilute monatomic gases, the translational energy is the only mode of molecular energy. The mechanical and thermodynamic pressures are, therefore, the same state variable and the bulk viscosity is zero as indicated earlier.

For polyatomic gases, the mechanical and thermodynamic pressures are not necessarily the same. The bulk viscosity is expected to be important if the relaxation (or adjustment) time of the molecules is not small compared to the characteristic time of the flow. Consider, for example, the passage of a polyatomic gas through a shock wave. Vibrational modes of molecular energy are excited at the expense of the translational modes, and the nonzero bulk viscosity is a measure of the corresponding transfer of energy. In this case, the gas within the shock is not in thermodynamic equilibrium, the bulk viscosity is proportional to the longer relaxation time for the relevant internal (nontranslational) modes to come to equilibrium, and the mechanical pressure is no longer equal to the thermodynamic pressure.

Classical kinetic theory is, of course, not applicable to liquids and dense gases. The bulk viscosity for those situations is determined primarily from experiment and is found, despite the considerable scatter in the data, to have a finite positive value. The dense gas theory (Chapman and Cowling, 1970) provides some support for this result.

Emanuel (1990) has recently pointed out that reliance on Stokes hypothesis may not always be warranted. He cites the example of hypersonic entry into certain planets where the atmosphere consists largely of carbon dioxide.[7] In such cases, lack of knowledge of λ might be especially detrimental to the accurate computations of relevant engineering quantities such as the skin friction or heat transfer rate.

From room temperature acoustic attenuation data, Tisza (1942) has concluded that the bulk viscosity $(\lambda + 2/3\mu)$ for CO_2 is three orders of magnitude larger than its first viscosity coefficient μ. Truesdell (1953) concurs with this result. Acoustic attenuation and other processes in gases with internal molecular structure can involve thermodynamic nonequilibrium as indicated earlier, and such effects may be modeled by a finite bulk viscosity as was done by Emanuel (1990) for a relaxing polyatomic gas.

By including a nonzero bulk viscosity as a correction term in a general, nonsimilar formulation of hypersonic laminar boundary layers, Emanuel (1992) has computed (for the class of planetary problems cited earlier) a heat transfer rate well in excess of that based on Stokes' hypothesis prediction. There is also an effect on the pressure which changed measurably across the wall layer, in contradiction to a key result of classical boundary layer theory. No significant effect on the skin friction was reported.

In summary, much confusion still remains in the literature 150 years after Stokes assumed that the bulk viscosity is zero. In general, it is not. The thermodynamic and mechanical pressures differ when the fluid undergoes nonequilibrium thermodynamic processes. Considerable scatter is present in existing data, and it is hoped that future experiments would provide more accurate estimates of the bulk viscosity for liquids and polyatomic gases.

The author would like to acknowledge the fruitful discussion with Professor George Emanuel, the University of Oklahoma, who has pointed out to me several valuable references, and to thank the three anonymous reviewers who gently showed me

[5]An alternative statement of Stokes' hypothesis is that the average normal *viscous* stress is zero.

[6]In an unpublished report (not cited by Emanuel and Argrow, 1994), Frederick S. Sherman might have been the first to use shock thickness data to estimate the second coefficient of viscosity of nitrogen (NACA TN 3298, 1955).

[7]In a boundary-layer formulation, the bulk viscosity has a third-order effect. In order to demonstrate a measurable effect, Emanuel chose the extreme example of hypersonic flow of a gas with a very large bulk viscosity.

how little I knew about this rich subject. My colleague at Notre Dame, Professor Joseph M. Powers, has read the manuscript at several stages of its development. The comments made by all five contributed significantly to the present version of my unanswered question in fluid mechanics.

References

Aris, R., 1962, *Vectors, Tensors, and the Basic Equations of Fluid Mechanics*, Prentice-Hall, Englewood Cliffs, NJ.

Batchelor, G. K., 1967, *An Introduction to Fluid Dynamics*, Cambridge University Press, London.

Chapman, S., and Cowling, T. G., 1970, *The Mathematical Theory of Non-Uniform Gases*, Third Edition, Cambridge University Press, London.

Emanuel, G., 1990, "Bulk Viscosity of a Dilute Polyatomic Gas," *Physics of Fluids A*, Vol. 2, pp. 2252–2254.

Emanuel, G., 1992, "Effect of Bulk Viscosity on a Hypersonic Boundary Layer," *Physics of Fluids A*, Vol. 4, pp. 491–495.

Emanuel, G., and Argrow, B. M., 1994, "Linear Dependence of the Bulk Viscosity on Shock Wave Thickness," *Physics of Fluids*, Vol. 6, pp. 3203–3205.

Eringen, A. C., 1980, *Mechanics of Continua*, Second Edition, Robert E. Krieger Publishing, Malabar, FL.

Hirschfelder, J. O., Curtiss, C. F., and Bird, R. B., 1954, *The Molecular Theory of Gases and Liquids*, Wiley, New York.

Karim, S. M., and Rosenhead, L., 1952, "The Second Coefficient of Viscosity of Liquids and Gases," *Review of Modern Physics*, Vol. 24, pp. 108–116.

Long, R. R., 1961, *Mechanics of Solids and Fluids*, Prentice-Hall, Englewood Cliffs, NJ.

Prangsma, G. J., Alberga, A. H., and Beenakker, J. J. M., 1973, "Ultrasonic Determination of the Volume Viscosity of N_2, CO, CH_4 and CD_4 between 77 and 300 K," *Physica*, Vol. 64, pp. 278–288.

Rosenhead, L., 1954, "A Discussion on the First and Second Viscosities of Fluids," (15 separate articles), *Proceedings of the Royal Society of London, Series A: Mathematical and Physical Sciences*, Vol. 226, pp. 1–69.

Stokes, G. G., 1845, "On the Theories of Internal Friction of Fluids in Motion," *Transactions of the Cambridge Philosophical Society*, Vol. 8, pp. 287–305.

Tisza, L., 1942, "Supersonic Absorption and Stokes' Viscosity Relation," *The Physical Reviews*, Vol. 61, pp. 531–536.

Truesdell, C., 1953, "Precise Theory of the Absorption and Dispersion of Forced Plane Infinitesimal Waves according to the Navier-Stokes Equations," *Journal of Rational Mechanics and Analysis*, Vol. 2, pp. 643–741.

Truesdell, C., 1954, "The Present Status of the Controversy Regarding the Bulk Viscosity of Fluids," *Proceedings of the Royal Society of London, Series A: Mathematical and Physical Sciences*, Vol. 226, pp. 59–65.

Vincenti, W. G., and Kruger, C. H., 1965, *Introduction to Physical Gas Dynamics*, Wiley, New York.

Comments on the Policy Statement on Numerical Accuracy

Journal of Fluids Engineering, Vol. 115, 1993, pp. 339–340

B. P. Leonard[1]

The *Journal of Fluids Engineering* Editorial Policy on numerical accuracy has sparked some lively debate, both in and out of print. This, in itself, is a positive development, as anticipated by the editors (Freitas, 1994). One of the more controversial aspects of the Policy is the effective "banning" of largely first-order-based methods. Since I was involved in the latter stages of the drafting of the Policy, and have been advocating a halt to the use of first-order methods for about twenty years, I would like to make a few comments in support of this aspect of the Policy. In an ideal world, I would agree with Professor Ferziger (1994) that we should not mandate the exclusion of any particular technique; referees should be able to filter out the "foolishness." But first-order methods are currently so wide-spread that "drastic" measures seem to be called for. (In an ideal world, one might expect automobile drivers to act wisely; in reality, rules of the road are needed to deter foolishness.)

Twenty-odd years ago, first-order methods could be of use in giving semi-quantitative results that enhanced understanding of fluid processes. My first encounter with CFD involved a simulation of a magnetic shock tube (Schneider et al., 1971). As an initial attempt at understanding this problem, we purposely made use of the inherent artificial viscosity of a first-order convection scheme to *replace* the rather complex transport processes within the shock and magnetic piston. The results were *good enough* for the experimentalists to be able to identify what they were measuring. [We jokingly referred to this as the "good-enough" method, not realizing the close relationship to an earlier (and subsequently very well-known) first-order "shock-capturing" method of a similar sounding name (Godunov, 1959).] Today, this paper would not be acceptable for publication in the *Journal of Fluids Engineering*. But a modern simulation would use a higher-order nonoscillatory method together with some simple (e.g., constant) effective viscosity (diffusivity) model. The results might be almost identical, but the philosophy is significantly different: *we* (rather than the grid-dependent differencing scheme) *are controlling the transport model.*

The problem with first-order-based methods is not just that they are somewhat less accurate than higher-order methods (actually, they are incredibly less accurate). More significant is the fact that *they are not simulating the correct physical problem*. The inherent artificial viscosity (diffusivity) of first-order upwinding (proportional to the local velocity and the mesh size) is well known and well documented. Why do people continue to use first-order-based methods? Apparently because of the philosophy that "any solution is better than none." As has been pointed out (Ferziger, 1993), this is a potentially "dangerous" attitude—one that needs to be countered with some common sense "rules of the road." First-order-based methods are typically used in high-convection flow regimes—involving *very high* grid Reynolds (Péclet) numbers—for which "classical" central-difference (or equivalent finite-element or finite-volume) schemes often blow up! The first-order simulation is equivalent to a central-difference simulation of a *nonphysical* problem in which the component grid Reynolds (Péclet) numbers are artificially manipulated and never allowed to exceed 2.0. This, of course, is (fairly) well known for schemes using first-order upwinding for convection together with central methods for diffusion. It also applies, however, to the popular Hybrid scheme (Spalding, 1972), the even more popular power-law scheme (Patankar, 1980), and the exponential-differencing scheme on which they are based (Allen and Southwell, 1955), when these methods are used out of the rather restrictive context for which they are valid (steady, quasi-one-dimensional, source-free flow, closely aligned with a grid coordinate). The most common misapplication of exponential-based schemes is to multidimensional flows oblique or skew to the grid. This introduces massive artificial "cross-wind" diffusion. Typi-

[1]Center for Computational Mechanics, The University of Akron, Akron, OH 44325-3903.

how little I knew about this rich subject. My colleague at Notre Dame, Professor Joseph M. Powers, has read the manuscript at several stages of its development. The comments made by all five contributed significantly to the present version of my unanswered question in fluid mechanics.

References

Aris, R., 1962, *Vectors, Tensors, and the Basic Equations of Fluid Mechanics*, Prentice-Hall, Englewood Cliffs, NJ.

Batchelor, G. K., 1967, *An Introduction to Fluid Dynamics*, Cambridge University Press, London.

Chapman, S., and Cowling, T. G., 1970, *The Mathematical Theory of Non-Uniform Gases*, Third Edition, Cambridge University Press, London.

Emanuel, G., 1990, "Bulk Viscosity of a Dilute Polyatomic Gas," *Physics of Fluids A*, Vol. 2, pp. 2252–2254.

Emanuel, G., 1992, "Effect of Bulk Viscosity on a Hypersonic Boundary Layer," *Physics of Fluids A*, Vol. 4, pp. 491–495.

Emanuel, G., and Argrow, B. M., 1994, "Linear Dependence of the Bulk Viscosity on Shock Wave Thickness," *Physics of Fluids*, Vol. 6, pp. 3203–3205.

Eringen, A. C., 1980, *Mechanics of Continua*, Second Edition, Robert E. Krieger Publishing, Malabar, FL.

Hirschfelder, J. O., Curtiss, C. F., and Bird, R. B., 1954, *The Molecular Theory of Gases and Liquids*, Wiley, New York.

Karim, S. M., and Rosenhead, L., 1952, "The Second Coefficient of Viscosity of Liquids and Gases," *Review of Modern Physics*, Vol. 24, pp. 108–116.

Long, R. R., 1961, *Mechanics of Solids and Fluids*, Prentice-Hall, Englewood Cliffs, NJ.

Prangsma, G. J., Alberga, A. H., and Beenakker, J. J. M., 1973, "Ultrasonic Determination of the Volume Viscosity of N_2, CO, CH_4 and CD_4 between 77 and 300 K," *Physica*, Vol. 64, pp. 278–288.

Rosenhead, L., 1954, "A Discussion on the First and Second Viscosities of Fluids," (15 separate articles), *Proceedings of the Royal Society of London, Series A: Mathematical and Physical Sciences*, Vol. 226, pp. 1–69.

Stokes, G. G., 1845, "On the Theories of Internal Friction of Fluids in Motion," *Transactions of the Cambridge Philosophical Society*, Vol. 8, pp. 287–305.

Tisza, L., 1942, "Supersonic Absorption and Stokes' Viscosity Relation," *The Physical Reviews*, Vol. 61, pp. 531–536.

Truesdell, C., 1953, "Precise Theory of the Absorption and Dispersion of Forced Plane Infinitesimal Waves according to the Navier-Stokes Equations," *Journal of Rational Mechanics and Analysis*, Vol. 2, pp. 643–741.

Truesdell, C., 1954, "The Present Status of the Controversy Regarding the Bulk Viscosity of Fluids," *Proceedings of the Royal Society of London, Series A: Mathematical and Physical Sciences*, Vol. 226, pp. 59–65.

Vincenti, W. G., and Kruger, C. H., 1965, *Introduction to Physical Gas Dynamics*, Wiley, New York.

Comments on the Policy Statement on Numerical Accuracy

Journal of Fluids Engineering, Vol. 115, 1993, pp. 339–340

B. P. Leonard[1]

The *Journal of Fluids Engineering* Editorial Policy on numerical accuracy has sparked some lively debate, both in and out of print. This, in itself, is a positive development, as anticipated by the editors (Freitas, 1994). One of the more controversial aspects of the Policy is the effective "banning" of largely first-order-based methods. Since I was involved in the latter stages of the drafting of the Policy, and have been advocating a halt to the use of first-order methods for about twenty years, I would like to make a few comments in support of this aspect of the Policy. In an ideal world, I would agree with Professor Ferziger (1994) that we should not mandate the exclusion of any particular technique; referees should be able to filter out the "foolishness." But first-order methods are currently so wide-spread that "drastic" measures seem to be called for. (In an ideal world, one might expect automobile drivers to act wisely; in reality, rules of the road are needed to deter foolishness.)

Twenty-odd years ago, first-order methods could be of use in giving semi-quantitative results that enhanced understanding of fluid processes. My first encounter with CFD involved a simulation of a magnetic shock tube (Schneider et al., 1971). As an initial attempt at understanding this problem, we purposely made use of the inherent artificial viscosity of a first-order convection scheme to *replace* the rather complex transport processes within the shock and magnetic piston. The results were *good enough* for the experimentalists to be able to identify what they were measuring. [We jokingly referred to this as the "good-enough" method, not realizing the close relationship to an earlier (and subsequently very well-known) first-order "shock-capturing" method of a similar sounding name (Godunov, 1959).] Today, this paper would not be acceptable for publication in the *Journal of Fluids Engineering*. But a modern simulation would use a higher-order nonoscillatory method together with some simple (e.g., constant) effective viscosity (diffusivity) model. The results might be almost identical, but the philosophy is significantly different: *we* (rather than the grid-dependent differencing scheme) *are controlling the transport model.*

The problem with first-order-based methods is not just that they are somewhat less accurate than higher-order methods (actually, they are incredibly less accurate). More significant is the fact that *they are not simulating the correct physical problem*. The inherent artificial viscosity (diffusivity) of first-order upwinding (proportional to the local velocity and the mesh size) is well known and well documented. Why do people continue to use first-order-based methods? Apparently because of the philosophy that "any solution is better than none." As has been pointed out (Ferziger, 1993), this is a potentially "dangerous" attitude—one that needs to be countered with some common sense "rules of the road." First-order-based methods are typically used in high-convection flow regimes—involving *very high* grid Reynolds (Péclet) numbers—for which "classical" central-difference (or equivalent finite-element or finite-volume) schemes often blow up! The first-order simulation is equivalent to a central-difference simulation of a *nonphysical* problem in which the component grid Reynolds (Péclet) numbers are artificially manipulated and never allowed to exceed 2.0. This, of course, is (fairly) well known for schemes using first-order upwinding for convection together with central methods for diffusion. It also applies, however, to the popular Hybrid scheme (Spalding, 1972), the even more popular power-law scheme (Patankar, 1980), and the exponential-differencing scheme on which they are based (Allen and Southwell, 1955), when these methods are used out of the rather restrictive context for which they are valid (steady, quasi-one-dimensional, source-free flow, closely aligned with a grid coordinate). The most common misapplication of exponential-based schemes is to multidimensional flows oblique or skew to the grid. This introduces massive artificial "cross-wind" diffusion. Typi-

[1]Center for Computational Mechanics, The University of Akron, Akron, OH 44325-3903.

cally, the (*expensively calculated*, multi-equation) turbulence transport is (actually or effectively) *switched off* above component turbulent grid Reynolds (Péclet) numbers of 2 in the case of Hybrid or about 6 for power-law or the exponential scheme itself (Leonard and Drummond, 1995), being *replaced* by the inherent artificial numerical diffusion of the first-order-upwind convection term. In such cases, expensive turbulence modelling is being used as a diagnostic to switch itself off! No wonder simulations are often rather insensitive to the turbulence model.

It appears that, under normal conditions, most people would intuitively prefer to use "central" methods (since these work perfectly well for diffusion, wave-motion, conductive heat-transfer, and solid mechanics—all involving *even*-order spatial derivatives). But when faced with the "difficulties" of high-convection problems (e.g., an obviously unphysically wiggly solution or no solution at all), there is a tendency to fall back on gratifyingly stable first-order-based methods. In the case of convection (an *odd*-order spatial derivative), there is a need for a fresh, *unbiased* attitude.

If one takes a finite-volume approach to designing algorithms, convective fluxes are seen to involve a *natural* upwind bias. It turns out that in order to construct a "central" convection scheme, one needs to assume a *downwind bias* in the subcell behavior of the transported variable (Leonard, 1994) in order to "cancel" the natural upwinding. In other words, designing centered or symmetric convection schemes requires a velocity-direction-dependent decision regarding the subcell interpolation. Velocity-direction-independent subcell interpolation corresponds to (naturally) upwinded schemes. First-order upwinding results from assuming piecewise constant subcell behavior; higher-order upwind methods result from assuming higher-order velocity-direction-independent subcell behavior. When this is realized, one sees that there is something "unnatural" about central convection schemes—no wonder they cause trouble! Natural upwind schemes for convection are (or should be) intuitively more attractive. Unfortunately, the simple first-order scheme is quite plainly too diffusive for practical use. One should then look at higher-order (natural) upwind schemes. Fromm's method, for example (Fromm, 1968), is the simplest second-order convection scheme based on velocity-direction-independent linear subcell interpolation; the shape-preserving version known as MUSCL (van Leer, 1973) is probably the most successful all-round nonoscillatory scheme using classical TVD constraints (Sweby, 1984).

The point that I think needs to be stressed is that convection is "special." Rather than being intuitively drawn toward central schemes (and then, when they don't work, being shocked into using an unsatisfactory alternative), one should be suspicious of "central" convection schemes (even before trying to use them). Then, taking a fresh look at appropriate (natural upwind) options, one can make rational choices. First-order can be quickly evaluated—and discarded because of its overwhelming inherent artificial diffusion. Higher-order (natural upwind) schemes are quite practical. My own preference is for nominally third or higher odd-order upwind schemes. For example, third-order upwinding is the lowest order convection scheme for which leading truncation error is dissipative (rather than dispersive) *but not diffusive*. Second-order upwinding, by the way, represents "upwind overkill": in addition to the natural upwinding inherent in the convective fluxes, the subcell behavior also has an upwind bias. Until the general CFD community appreciates the distinctive nature of convection, and this applies especially to the younger generation of computationalists who might be particularly susceptible to the lure of first-order-based methods, it seems prudent to take special precautions in a publishing policy. The explicit exclusion of largely first-order-based methods seems entirely appropriate (and somewhat overdue).

One final thought, in the interest of promoting further debate: in general, it seems that there is no such thing as a grid-independent solution (of a *nontrivial* CFD problem) showing first-order convergence. By its very nature, the artificial numerical diffusion is grid-dependent. The grid therefore needs to be refined until the artificial diffusion is negligible (within the prescribed tolerance) with respect to physical diffusion. With diffusion terms dominant, the convergence rate will follow a second- (or higher even-) order trend.

The Editorial Board is to be congratulated on a bold policy. This may, at first, reduce the number of submitted manuscripts—probably a good thing, judging by recent trends (Telionis, 1994). But it will certainly enhance the prestige of the journal. Note that ASME conference organizers are now requiring submitted (CFD) papers to conform to *JFE* criteria, as well. Other journals and conference organizers, whose reputations are based on "quality," cannot afford *not* to adopt similar policies.

References

Allen, D. N. deG. and Southwell, R. V., 1955, "Relaxation Methods Applied to Determine the Motion in Two Dimensions of a Viscous Fluid Past a Fixed Cylinder," *Quarterly Journal of Mechanics and Applied Mathematics*, Vol. 8, pp. 129–145.

Ferziger, J. H., 1993, "Estimation and Reduction of Numerical Error," *Symposium on Quantification of Uncertainty in Computational Fluid Dynamics*, FED Vol. 158, ASME Fluids Engineering Division, Summer Meeting, Washington, D.C., June 20–24, pp. 1–8.

Ferziger, J. H., 1994, "Comments on the Policy Statement on Numerical Accuracy," ASME JOURNAL OF FLUIDS ENGINEERING, Vol. 116, p. 396.

Freitas, C. J., "Response: To the Comments of Drs. W. Shyy and M. Sindir," ASME JOURNAL OF FLUIDS ENGINEERING, Vol. 116, p. 198.

Fromm, J. E., 1968, "A Method for Reducing Dispersion Error in Convective Difference Schemes," *Journal of Computational Physics*, Vol. 3, pp. 176–189.

Godunov, S. K., 1959, "A Difference Method for Numerical Calculation of Discontinuous Solutions of the Equations of Hydrodynamics," *Matematik Sbornik*, Vol. 47, pp. 271–306.

Leonard, B. P., 1994, "Note on the von Neumann Stability of Explicit One-Dimensional Convection Schemes," *Computer Methods in Applied Mechanics and Engineering*, Vol. 118, pp. 29–46.

Leonard, B. P., and Drummond, J. E., 1995, "Why You Should Not Use 'Hybrid', 'Power-Law', or Related Exponential Schemes for Convective Modelling—There Are Much Better Alternatives," *International Journal for Numerical Methods in Fluids*, Vol. 20, (to appear).

Patankar, S. V., 1980, *Numerical Heat Transfer and Fluid Flow*, Hemisphere Publishing Corporation, McGraw-Hill, New York.

Schneider, S. H., Chu, C. K., and Leonard, B. P., 1971, "Numerical Study of the Magnetic Shock Tube," *The Physics of Fluids*, Vol. 14, pp. 1103–1108.

Spalding, D. B., 1972, "A Novel Finite Difference Formulation for Differential Expressions Involving Both First and Second Derivatives," *International Journal for Numerical Methods in Engineering*, Vol. 4, pp. 551–559.

Sweby, P. K., 1984, "High Resolution Schemes Using Flux Limiters for Hyperbolic Conservation Laws," *SIAM Journal of Numerical Analysis*, Vol. 21, pp. 995–1011.

Telionis, D. P., 1994, Editorial, ASME JOURNAL OF FLUIDS ENGINEERING, Vol. 116, p. 1.

van Leer, B., 1973, "Towards the Ultimate Conservative Difference Scheme. I. The Quest of Monotonicity," *Proceedings of the Third International Conference on Numerical Methods in Fluid Mechanics*, Vol. 1 (*Lecture Notes in Physics*, Vol. 18), H. Cabannes and R. Temam, eds., Springer-Verlag, New York, pp. 163–168.

Toward a Numerical Error Bar in CFD

George Em Karniadakis[1]

Over the last year I have followed with great interest the discussion on the Policy Statement on the Control of Numerical Accuracy as presented by the Coordinating Group on Computational Fluid Dynamics (CGCFD), as well as the follow-up responses by several researchers involved in CFD work. The editorial authored by Dr. C. J. Freitas in the *Journal of Fluids Engineering* (JFE) (Vol. 115, p. 339) and the responses by Dr. Shy and Dr. Sindir, Dr. Vanka, and Dr. Roache in JFE, Vol. 116, focused on the issue of first versus second-order spatial accuracy and the actual obtained accuracy in a given simulation versus the formal accuracy of the numerical scheme. In general, I support the new policy and I agree with Dr. Freitas's statements. Dr. Roache, Dr. Ghia, and Dr. White boldly introduced this policy on numerical accuracy in 1986. However, such a policy has to be updated at least once every decade to accommodate software and hardware advances as well as current interest in different classes of flow simulations. Therefore, the effort of CGCFD is timely and should be supported by the entire CFD community.

This letter aims to put more emphasis on the accuracy requirements of *time-dependent* computations. The new JFE guidelines (JFE, Vol. 115, p. 340) make reference to this in item 6: "In transient calculations, phase error must be assessed and minimized." It is clear from the number of papers submitted to JFE and other journals that the number of numerical works that deal with time-dependent calculations has increased significantly in recent years. This includes papers not only on DNS and LES but also papers where the Reynolds averaged equations are used to deal with the large-scale unsteadiness of a flow. For a meaningful time-dependent simulation a *long-time integration* is required that typically extends over hundreds of time periods (e.g., vortex shedding cycles), especially if low frequencies are present. The same is true for turbulence simulations where statistics need to be computed over a very long time period.

Thus, we must ask how long-time integration relates to the formal order of accuracy of a numerical scheme, and what is the corresponding computational cost? Consider the convection of a waveform at a constant speed. Let us now assume that there are $N^{(k)}$ gridpoints required per wavelength to reduce the error to a level ϵ, where k denotes the formal order of the scheme. In addition, let us assume that we integrate for M time periods. We can neglect temporal errors $\mathcal{O}(\Delta t)^J$ (where J is the order of the time-integration) by assuming a sufficiently small time step Δt. We wish to estimate the phase error in this simulation for second-$N^{(2)}$, fourth-$N^{(4)}$, and sixth-$N^{(6)}$ order finite difference schemes. Obviously, a first-order scheme is entirely inappropriate for this application and should not be used even if the JFE guidelines were not implemented!

The following results can be obtained from this analysis following the work of Kreiss (1978). Assuming an "engineering accuracy" of $\epsilon = 10$ percent we obtain:

$$N^{(2)} \propto 20M^{1/2}; \quad N^{(4)} \propto 7M^{1/4}; \quad N^{(6)} \propto 5M^{1/6}. \qquad (1)$$

We therefore see that the required resolution depends on the number of time periods M, and that the lower the order of the scheme is the stronger that dependence. To compare the corresponding computational cost $W^{(k)}$, we have to take into account that higher-order schemes have wider stencils and thus higher operation count. For this particular example, we find that the work to achieve the 10 percent accuracy is:

$$W^{(2)} \propto 20M^{1/2}; \quad W^{(4)} \propto 14M^{1/4}; \quad W^{(6)} \propto 15M^{1/6}, \qquad (2)$$

where the superscripts on W refer to the order of the scheme. This comparison favors the fourth-order scheme for short times ($M \propto \mathcal{O}(1)$) over both the second-order as well as the sixth-order scheme. However, for long-time integration ($M \propto \mathcal{O}(100)$), even for this engineering accuracy of 10 percent, the sixth-order scheme is superior as the corresponding operation count $W^{(6)}$ is about 6 times lower than the operation count of the second-order scheme $W^{(2)}$, and half the work of the fourth-order scheme $W^{(4)}$. Of course, in practical simulations the time step restriction must be taken into account since typically the low-order scheme would correspond to fewer time steps. In that case the time differencing error should be monitored and a more elaborate analysis of break-even points would perhaps influence slightly the final the choice of the best-order scheme. Thus, the trend that we have established between resolution requirements and formal accuracy order is still valid for engineering accuracy despite, perhaps, our perception of the opposite! For an accuracy of 1 percent in the solution of this convection problem, the sixth-order scheme is superior even for short time integration. For example, for one time period (e.g., $M = 1$) the sixth-order scheme costs about 37 percent of the second-order scheme and 90 percent of the fourth-order scheme. In the limit of very high accuracy and long-time integration, spectral based algorithms are computationally more efficient.

In a multi-dimensional time-dependent computation there are, of course, many other factors that have to be taken into account, including the complexity of the geometry, the smoothness of the solution, etc. Nevertheless, a thorough analysis of a simulation problem should involve, in my opinion, using not only computations on multiple grids as suggested in the editorial of Dr. Freitas, but also an analysis of variable order stencils for a single grid. In a finite element discretization scheme, this variable order of formal accuracy can be achieved in the $(h - p)$ version through the so-called p-refinement. In other words, the mesh (consisting of a number of elements) remains unaltered but the interpolation order is increased by adjusting the Lagrangian polynomial interpolants. This p-refinement can also be achieved in finite difference schemes by using a higher-order interpolation on the same nodes used for the second-order scheme. The difficulties arising by employing long stencils can be overcome by constructing implicit differencing schemes to provide the required compactness. The use of multiple grids corresponds to an "h-refinement" (in the finite element terminology) and improves convergence at a fixed rate; however the p-refinement, that I propose here, improves convergence at a faster rate without having to generate a new mesh. The benefits of the latter approach are even more evident in simulations involving adaptive discretization. In a well planned simulation, an h-refinement will be performed first followed by a p-refinement for faster convergence.

Having established the spatial resolution requirements and corresponding temporal resolution requirements, the numerical accuracy of the scheme can be credibly established. An indirect way to check the overall accuracy of a Navier-Stokes solver that accounts collectively for discretization errors (including boundary conditions errors) may be a test for small residuals of conservation laws, which are not directly employed in the solution procedure. For example, in solutions of Navier-Stokes

[1]Center for Fluid Mechanics, Division of Applied Mathematics, Brown University, Providence, RI 02912.

equations in terms of the primitive variables (e.g., velocity and pressure), a residual test can be performed for the vorticity equation and the result should be compared to the residual in the momentum equation. This can be done globally over the entire computational domain, locally over subdomains (e.g., finite elements or collection of difference stencils) or even pointwise. Having quantified the discretization errors, a numerical error bar can be constructed even for a calculation that does not resolve all scales at a prespecified accuracy. There are many instances where a computation is performed with the required computational cost exceeding the available resources; therefore computations at marginal resolution are often performed. Having an estimate of the numerical error attached to those computations may make the corresponding results useful and time lasting.

The discussion above has focused on discretization errors; however, spatial and temporal errors are only part of a numerical error bar. Even if we assume that we know the precise constitutive laws and thus the corresponding governing equations so that modeling errors can be avoided, there are other errors that may be as significant and perhaps less controllable than discretization errors. Errors due to the limited size of the computational domain may be the most significant ones and are usually very difficult to detect, especially for external flows. The size of the computational domain is typically based on correlation lengths obtained experimentally but most often, in practice, it is dictated by the limited computational resources available to a researcher. The blockage effect in flow past a cylinder in a narrow domain or the underestimated turbulence intensities in a small channel flow cause errors of order more than 10 percent and mask the errors due to marginal resolution.

An example which demonstrates the combined effect of the size of the domain and the different type of boundary conditions is shown in Fig. 1(ab) for the two-dimensional flow past a circular cylinder at relatively low Reynolds number. Here we plot simulation results for the Strouhal number (*a*) and the base pressure coefficient (*b*) along with experimental data taken from Williamson and Roshko (1990). Data from 16 different simulations are included at Re = 100 corresponding to either uniform freestream, potential, or periodic boundary conditions as well as different sizes of the domain in all directions. Potential flow boundary conditions, for example, imposed at the truncated boundaries on a medium size computational domain give as accurate results as freestream boundary conditions at a much larger and therefore more "expensive" domain. Details of these computations can be found in Karniadakis and Triantafyllou (1992), but the point that I want to emphasize here is that the effect of resolution tests (assuming a reasonable initial discretization) is about 2 percent compared to a 20 percent effect of domain and boundary conditions. There will never, perhaps, be a sufficiently large domain to completely eliminate these errors, in the same way that there will never be a wind tunnel with a large enough test section. However, quantifying and accounting for those errors in a *composite* simulation error bar will provide confidence in the results obtained in simulations on domains of limited size or with outflow-type boundary conditions.

In summary, I support and have been a long time advocate of high-order accuracy for CFD applications. Dr. Freitas and all members of CGCFD are to be commended for following the vision of the originators of the policy, Dr. Roache, Dr. Ghia, and Dr. White, to provide a more appropriate policy for the coming decade. I hope that my comments in this article point to the need of high-order spatial accuracy especially for simulations of unsteady flows involving long-time integration, and motivate some more thinking toward the construction of a numerical error bar. Based on the discussion here, my proposed numerical error bar will then consist of spatial errors of magnitude $\mathbb{O}(\Delta x)^k$, temporal errors $\mathbb{O}(\Delta t)^l$, errors due to a size restriction in the computational domain, and errors due to boundary conditions of predominantly outflow-type. This is shown diagrammatically in Fig. 2 following the results of the simulations of Fig. 1.

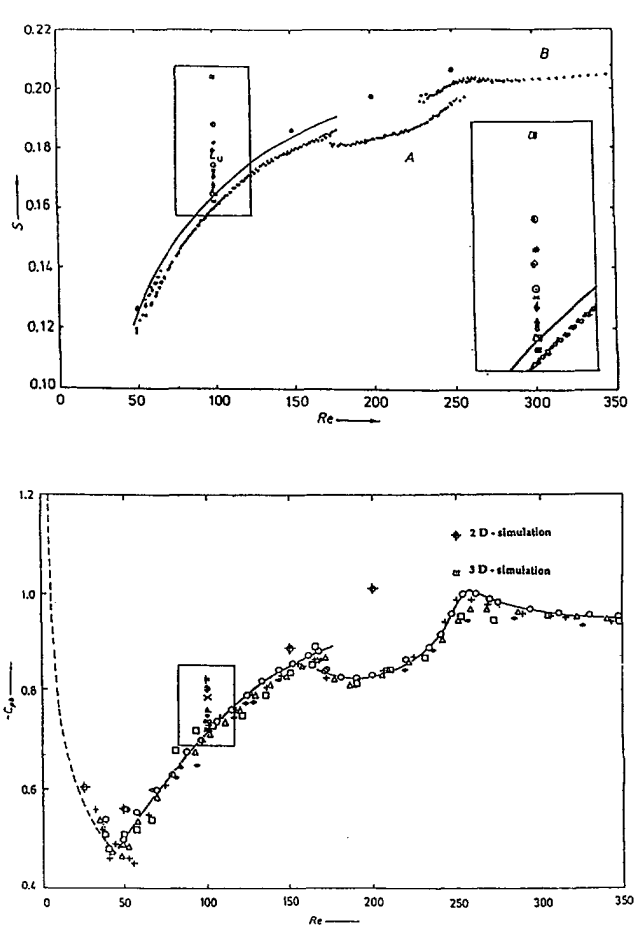

Fig. 1 Spectral element simulation of flow past a circular cylinder and comparisons with experimental results of Williamson and Roshko (1990). A large domain with fine resolution is used for the simulations denoted by • in (*a*) and ⊕ in (*b*). The boxes at Re = 100 include several simulations performed with smaller domains and different type of boundary conditions. Details of the simulation can be found in Karniadakis and Triantafyllou (1992).

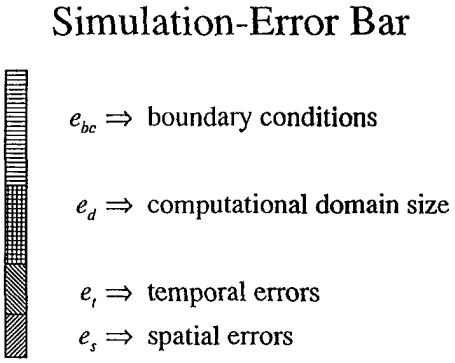

Fig. 2 The proposed numerical error bar includes resolution errors as well as errors due to boundary conditions and computational domain. This error bar is representative of simulations described in Fig. 1.

References

Freitas, C. J., 1993,"Editorial Policy Statement on the Control of Numerical Accuracy," ASME JOURNAL OF FLUIDS ENGINEERING, Vol. 115, p. 339.

Karniadakis, G. E. and Triantafyllou, G. S., 1992, "Three-Dimensional Dynamics and Transition to Turbulence in the Wake of Bluff Objects," *J. Fluid Mech.*, Vol. 238, p. 1.

Kreiss, H. O., 1978, "Numerical Methods for Solving Time-Dependent Problems for Partial Differential Equations," Technical Report, University of Uppsala, p. 74.

Roache, P. J., Ghia, K. N., and White, F. M., 1986, "Editorial Policy Statement on the Control of Numerical Accuracy," ASME JOURNAL OF FLUIDS ENGINEERING, Vol. 108, p. 2.

Williamson, C. H. K. and Roshko, A., 1990, "Measurements of Base Pressure in the Wake of a Cylinder at Low Reynolds Numbers," *Z. Flugwiss. Weltraumforsch.*, Vol. 14, p. 38.

The End of Justification, The Beginning of Implementation

Christopher J. Freitas[1]

Dr. Karniadakis has provided further technical justification for the *Journal of Fluids Engineering*'s Policy Statement on the Control of Numerical Accuracy. The concept of a Numerical Error Bar is an excellent idea. However, to support the implementation of such an error bar we must continue to define methods for the quantification of all sources of error. The policy statement identified five different sources for numerical error; i.e., one each due to spatial and temporal truncation, one due to grid resolution, one due to iterative convergence, and one due to implementation of boundary and initial conditions. These five sources of error are present, to varying degrees, in any simulation (and there may be other error generating mechanisms not covered by these five). But, what we presently lack are techniques for evaluating the magnitude of these errors and presenting them in a uniform or standard manner. The Numerical Error Bar would be a way to report the magnitude of error in a standard manner, and once a consistent set of error evaluation techniques were present, I would recommend the use of the Numerical Error Bar by the *Journal of Fluids Engineering*.

One consequence (that I had hoped for) resulting from the new policy statement on numerical accuracy has been the lively debate over the merits of such a policy for policing archival publications of CFD related papers. Now that the dust has begun to settle and the Journal has begun implementing the policy, it would be a better use of all our energies to begin to develop and refine methods for quantifying numerical accuracy. To date, two methods have been proposed to aid in the quantification of error. Both methods were proposed in papers presented at the ASME Symposium on Quantification of Uncertainty in Computational Fluid Dynamics. Ferziger (1993) proposed the use of Richardson extrapolation as a method for calculating a simulation's accuracy, while Roach (1994) developed the Grid Convergence Index. Another method for calculating simulation accuracy and eluded to in the policy statement and discussed further by Dr. Karniadakis, is the adaptation of methods employed by adaptive solution techniques for evaluating local error to the evaluation of global error, allowing for a dynamic evaluation of simulation accuracy. These are but a few of the methods that may be employed to evaluate numerical uncertainty, but all still require further development and refinement before we can implement them in the Numerical Error Bar.

Over a year has now passed since the publication of the policy statement. It is time to begin (or continue) the arduous task of formulating methods which allow for an honest evaluation of a simulation's accuracy. An ASME Forum is currently planned to focus on the Grid Convergence Index as one method for such an evaluation. Other forums should and will be organized by the Coordinating Group on CFD to examine other candidate methods. And, through the *Journal of Fluids Engineering*'s Technical Forum, the debate will continue, but perhaps now focused on the methodology for and not the concept or merit of quantification of numerical uncertainty.

[1]Computational Mechanics, Southwest Research Institute, San Antonio, TX 78228-0510.

References

Ferziger, J. H., 1993, "Estimation and Reduction of Numerical Error," *Proceedings of the Symposium on Quantification of Uncertainty in Computational Fluid Dynamics*, Celik et al., eds., ASME Fluids Engineering Conference, Washington, D.C., June 20–24.

Roache, P. J., 1994, "Perspective: A Method for Uniform Reporting of Grid Refinement Studies," ASME JOURNAL OF FLUIDS ENGINEERING, Vol. 116, No. 3, Sept., pp. 405–413.

Comment on "Toward a Numerical Error Bar in CFD" by G. Karniadakis

Pratap Vanka[1]

The idea proposed in George's note concerning an error bar in CFD is intriguing and it would be interesting to see how one can quantify such errors in a complex calculation. I am also concerned that there will again be a trend to quote incorrect values for such limits by performing inadequate tests (either discretization error tests, or boundary condition influence tests). Providing error bars can be very tricky as sometimes two errors can cancel each other. That does not remove the need for an accurate investigation of each error.

I agree with George that the preferred method of choice may be one based on spectral discretizations. However, one must realize that many ASME papers are concerned with complex geometries and in many cases only direct steady state solutions are sought. While I see the potential for spectral domain or spectral element methods to eventually come to the point of replacing current finite-difference and finite-element methods in performing practical calculations, it has not yet happened. Until then, we must insist on accurate finite-difference/finite-volume/finite-element calculations and make whatever policies that will achieve such a goal.

University of Illinois at Urbana-Champaign, Urbana, IL.

Karniadakis, G. E. and Triantafyllou, G. S., 1992, "Three-Dimensional Dynamics and Transition to Turbulence in the Wake of Bluff Objects," *J. Fluid Mech.*, Vol. 238, p. 1.

Kreiss, H. O., 1978, "Numerical Methods for Solving Time-Dependent Problems for Partial Differential Equations," Technical Report, University of Uppsala, p. 74.

Roache, P. J., Ghia, K. N., and White, F. M., 1986, "Editorial Policy Statement on the Control of Numerical Accuracy," ASME JOURNAL OF FLUIDS ENGINEERING, Vol. 108, p. 2.

Williamson, C. H. K. and Roshko, A., 1990, "Measurements of Base Pressure in the Wake of a Cylinder at Low Reynolds Numbers," *Z. Flugwiss. Weltraumforsch.*, Vol. 14, p. 38.

The End of Justification, The Beginning of Implementation

Christopher J. Freitas[1]

Dr. Karniadakis has provided further technical justification for the *Journal of Fluids Engineering*'s Policy Statement on the Control of Numerical Accuracy. The concept of a Numerical Error Bar is an excellent idea. However, to support the implementation of such an error bar we must continue to define methods for the quantification of all sources of error. The policy statement identified five different sources for numerical error; i.e., one each due to spatial and temporal truncation, one due to grid resolution, one due to iterative convergence, and one due to implementation of boundary and initial conditions. These five sources of error are present, to varying degrees, in any simulation (and there may be other error generating mechanisms not covered by these five). But, what we presently lack are techniques for evaluating the magnitude of these errors and presenting them in a uniform or standard manner. The Numerical Error Bar would be a way to report the magnitude of error in a standard manner, and once a consistent set of error evaluation techniques were present, I would recommend the use of the Numerical Error Bar by the *Journal of Fluids Engineering*.

One consequence (that I had hoped for) resulting from the new policy statement on numerical accuracy has been the lively debate over the merits of such a policy for policing archival publications of CFD related papers. Now that the dust has begun to settle and the Journal has begun implementing the policy, it would be a better use of all our energies to begin to develop and refine methods for quantifying numerical accuracy. To date, two methods have been proposed to aid in the quantification of error. Both methods were proposed in papers presented at the ASME Symposium on Quantification of Uncertainty in Computational Fluid Dynamics. Ferziger (1993) proposed the use of Richardson extrapolation as a method for calculating a simulation's accuracy, while Roach (1994) developed the Grid Convergence Index. Another method for calculating simulation accuracy and eluded to in the policy statement and discussed further by Dr. Karniadakis, is the adaptation of methods employed by adaptive solution techniques for evaluating local error to the evaluation of global error, allowing for a dynamic evaluation of simulation accuracy. These are but a few of the methods that may be employed to evaluate numerical uncertainty, but all still require further development and refinement before we can implement them in the Numerical Error Bar.

Over a year has now passed since the publication of the policy statement. It is time to begin (or continue) the arduous task of formulating methods which allow for an honest evaluation of a simulation's accuracy. An ASME Forum is currently planned to focus on the Grid Convergence Index as one method for such an evaluation. Other forums should and will be organized by the Coordinating Group on CFD to examine other candidate methods. And, through the *Journal of Fluids Engineering*'s Technical Forum, the debate will continue, but perhaps now focused on the methodology for and not the concept or merit of quantification of numerical uncertainty.

[1]Computational Mechanics, Southwest Research Institute, San Antonio, TX 78228-0510.

References

Ferziger, J. H., 1993, "Estimation and Reduction of Numerical Error," *Proceedings of the Symposium on Quantification of Uncertainty in Computational Fluid Dynamics*, Celik et al., eds., ASME Fluids Engineering Conference, Washington, D.C., June 20–24.

Roache, P. J., 1994, "Perspective: A Method for Uniform Reporting of Grid Refinement Studies," ASME JOURNAL OF FLUIDS ENGINEERING, Vol. 116, No. 3, Sept., pp. 405–413.

Comment on "Toward a Numerical Error Bar in CFD" by G. Karniadakis

Pratap Vanka[1]

The idea proposed in George's note concerning an error bar in CFD is intriguing and it would be interesting to see how one can quantify such errors in a complex calculation. I am also concerned that there will again be a trend to quote incorrect values for such limits by performing inadequate tests (either discretization error tests, or boundary condition influence tests). Providing error bars can be very tricky as sometimes two errors can cancel each other. That does not remove the need for an accurate investigation of each error.

I agree with George that the preferred method of choice may be one based on spectral discretizations. However, one must realize that many ASME papers are concerned with complex geometries and in many cases only direct steady state solutions are sought. While I see the potential for spectral domain or spectral element methods to eventually come to the point of replacing current finite-difference and finite-element methods in performing practical calculations, it has not yet happened. Until then, we must insist on accurate finite-difference/finite-volume/finite-element calculations and make whatever policies that will achieve such a goal.

University of Illinois at Urbana-Champaign, Urbana, IL.

Numerical Investigation of Unsteady Transitional Flow Over Oscillating Airfoil

S.-W. Kim
Resident Research Associate.

K. B. M. Q. Zaman

J. Panda

NASA Lewis Research Center,
Cleveland, OH 44135

A numerical investigation of unsteady transitional flow over an oscillating NACA 0012 airfoil at a Reynolds number of 44,000 and reduced frequency of 0.2 is carried out and the results are compared with experimental data. The Navier-Stokes equations defined on arbitrary Lagrangian-Eulerian coordinates are solved by a time-accurate finite volume method that incorporates an incremental pressure equation for the conservation of mass. The transitional turbulence field is described by multiple-time-scale turbulence equations. The numerical method successfully predicts the large dynamic stall vortex (DSV) and the trailing edge vortex (TEV) that are periodically generated by the oscillating airfoil. The numerical results show that the transition from laminar to turbulent state and relaminarization occur widely in time and in space. The calculated streaklines and the ensemble-averaged velocity profiles are in good agreement with the measured data.

1 Introduction

Fluid flows over lifting surfaces beyond stall angles of attack exhibit largely separated and recirculating unsteady motion. Such fluid flows can be found in helicopter rotor blades, fluttering compressor blades, and lifting devices of rapidly maneuvering aircraft. A number of experimental and numerical investigations of fluid flows over oscillating airfoils have been made in recent years to better understand the unsteady flows in such engineering applications. Compilation of all these efforts is not intended in this paper and only a few investigations relevant to or contrasted to the present numerical investigation are described below.

Measured data for high Reynolds number unsteady flows over oscillating airfoils can be found in McAlister et al. (1979, 1982) and those for a low Reynolds number case can be found in Panda and Zaman (1992). Numerical investigations of the high Reynolds number flow cases using the Baldwin-Lomax algebraic turbulence model or k-ϵ turbulence models can be found in Wu et al. (1987, 1990), Rumsey and Anderson (1988), and Cricelli et al. (1992). In these numerical investigations, either an alternating-direction-implicit scheme or a flux vector splitting scheme is used to solve the Navier-Stokes equations and the moving mesh is implicitly taken into account through the use of time-varying grid transformation Jacobians. On the other hand, in the present method, the time-varying grid is treated explicitly by solving the Navier-Stokes equations defined on arbitrary Lagrangian-Eulerian coordinates (Truesdell and Toupin, 1960; Donea et al., 1982; Belytschko et al., 1982) and the transitional turbulence field is described by the multiple-time-scale turbulence equations (Kim, 1990a, 1990b, 1991a; Kim and Benson, 1992a, 1993a). Both numerical methods can accurately take into account the moving mesh in numerical calculations, and the preference is made by the characteristics of each numerical method used. Experience obtained by many numerical analysts shows that various advanced turbulence equations can be incorporated more easily into the present class of numerical methods due to their iterative nature as compared with the other classes of numerical methods. For the high Reynolds number, unsteady flows over oscillating airfoils considered in the experimental work of McAlister et al. (1979, 1982), transition from laminar to turbulent state may exist only near the leading edge of the airfoil. However, for the low Reynolds number case considered in the experimental work of Panda and Zaman (1992), transition from laminar to turbulent state and relaminarization occur widely in space and in time. For the Baldwin-Lomax algebraic turbulence model, it is necessary to provide a cut-off ratio of the turbulent viscosity to molecular viscosity to solve transitional flows (Ameri et al., 1992). While the use of such an arbitrary cut-off ratio is not necessary for k-ϵ turbulence equations, they do not yield accurate results for transitional flows (Ameri et al., 1992). In the present work, the multiple-time-scale turbulence equations (abbreviated as M-S equations hereafter) is used to describe the transitional turbulence field occurring in the largely separated and recirculating unsteady flow around the airfoil. The numerical method and the M-S equations are introduced below.

The present numerical method is a finite volume method that incorporates a pressure-staggered mesh and an incremental pressure equation for the conservation of mass (Kim, 1990a, 1990b, 1991a; Kim and Benson, 1992b). Evolution of the fluid flow in time is obtained by solving the discrete system of equations iteratively at each time-level. Advantages and disadvan-

Contributed by the Fluids Engineering Division and presented at the ASME Fluids Engineering Conference, Symposium on Separated Flows, Washington, D.C., June 20–24, 1993. Manuscript received by the Fluids Engineering Division August 6, 1993; revised manuscript received August 30, 1994. Associate Technical Editor: W. S. Saric.

tages of the iterative time advancing scheme (ITA) as compared with the simplified Marker-and-Cell Scheme (SMAC) and the Pressure-Implicit Splitting of Operators (PISO) can be found in Kim and Benson (1992b). Calculations of a steady polar cavity flow and self-sustained oscillatory flows over a circular cylinder and a square cylinder show that the ITA is the most strongly convergent and yields the most accurate numerical results while the SMAC is the most efficient computationally and yields accurate numerical results. The PISO is unstable numerically and yields less accurate numerical results than the ITA or SMAC. Analyses of the PISO and its numerical results show that the weakly convergent nature and the inaccurate numerical results are caused by the second corrector step in which the pressure is driven by momentum imbalance. The secondly corrected velocity field largely violates the conservation of mass, and a large amount of mass imbalance can cause the numerical method to yield a divergent result. Calculations of a three-dimensional, laminar, lid-driven cavity flow and a laminar flow through a curved duct show that the present method yields more accurate results than formally third order accurate numerical methods such as the quadratic upwind interpolation scheme. The improved numerical results obtained using the present method are attributed to the use of the incremental pressure equation that can strongly enforce the conservation of mass (Kim, 1991b). Applications of the present numerical method for steady flows such as shock-separated transonic turbulent flows and circular jets in crossflows can be found in Kim (1990b) and Kim and Benson (1992a, 1993a), respectively. It can be found in these references that the present numerical method yields strongly convergent results and that the results are in good agreement with the measured data. Details of the present numerical method to solve the ensemble averaged Navier-Stokes equations defined on arbitrary Lagrangian-Eulerian coordinates is described in the "Numerical Method" section.

It has been shown that the M-S equations yield accurate numerical results for various complex turbulent flows (e.g., turbulent flows subjected to extra strains caused by streamline curvature, interaction of multiple number of shear layers, and shock wave-boundary layer interactions). The numerical results obtained using the M-S equations are in as good agreement with the measured data as those obtained using optimized k-ϵ turbulence models, algebraic Reynolds stress turbulence models (ARSM), or Reynolds stress turbulence models (RSM) for each flow case (Kim, 1990a, 1990b, 1991a, 1992; Kim and Benson, 1992a, 1993a). The capability of the M-S equations to solve widely different steady state complex turbulent flows accurately is attributed to its capability to resolve the nonequilibrium turbulence phenomena and to model the cascade of turbulent kinetic energy.

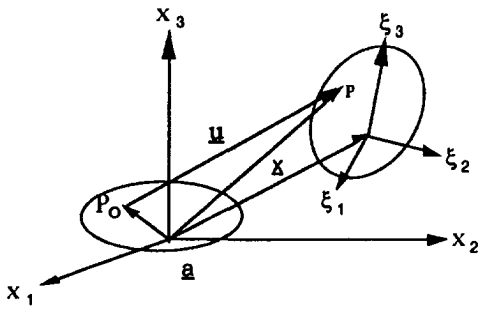

Fig. 1 Arbitrary Lagrangian-Eulerian coordinates

2 Analysis

2.1 Navier-Stokes Equations. In the arbitrary Lagrangian-Eulerian description of the equations of motion, the fluid motion is described through its material coordinates of the initial configuration of the continuum. However, the time-evolution of the fluid flow is identified through a referential frame, $\underline{\xi}$, which is independently prescribed as a function of space and time as shown in Fig. 1 (Truesdell and Toupin, 1960; Donea et al., 1982; Belytschko et al., 1982). The Navier-Stokes equations defined on the arbitrary Lagrangian-Eulerian coordinates are given as;

$$\frac{\partial}{\partial t}(\rho J) = J\frac{\partial}{\partial x_j}\{\rho(u_j^g - u_j)\} \tag{1}$$

$$\frac{\partial}{\partial t}(\rho u_i J) = J\frac{\partial}{\partial x_j}\{\rho u_i(u_j^g - u_j)\} + J\frac{\partial \tau_{ij}}{\partial x_j} - J\frac{\partial p}{\partial x_i} \tag{2}$$

where $\tau_{ij} = (\mu + \mu_t)\{\partial u_i/\partial x_j + \partial u_j/\partial x_i\}$ is the stress tensor and repeated indices imply summation over the index unless otherwise stated. The referential velocity, $u_j^g = \partial \xi_i(\underline{x}, t)/\partial t$, is the velocity of the referential frame with respect to the laboratory frame. In particular, for $u_j^g = 0$, Eqs. (1)–(2) become identical to the familiar Eulerian description of the Navier-Stokes equations, and for $u_j^g = u_j$, Eqs. (1)–(2) become identical to the Navier-Stokes equations defined on Lagrangian coordinates. Derivation of the Navier-Stokes equations in arbitrary Lagrangian-Eulerian coordinates can be found in Truesdell and Toupin (1960), Donea et al. (1982), and Belytschko et al. (1982) among many others.

Nomenclature

A_i^* = coefficient for discrete momentum equation
$\underline{a}$ = material coordinates
c = chord length of airfoil
$c_{\rho\ell}$ = model constants for ϵ_p equation (ℓ = 1,3)
$c_{t\ell}$ = model constants for ϵ_t equation (ℓ = 1,3)
$c_{\mu f}$ = constant coefficient (=0.09)
f = oscillation frequency
J = grid transformation jacobian ($=|\partial \xi_j/\partial \mathbf{a}_j|$)
k = turbulent kinetic energy ($=k_p + k_t$)
k_p = turbulent kinetic energy in production range
k_t = turbulent kinetic energy in dissipation range
P_r = production rate of turbulent kinetic energy
p = pressure
p^* = initial guess for pressure
p^{**} = corrected pressure
p' = incremental pressure
T = period of oscillation
U_0 = free-stream inertial velocity
u_j = ensemble averaged inertial velocity ($=\{u,v\}$)
u_j^* = initial guess for inertial velocity
u_j^{**} = predicted inertial velocity
u_j^{***} = corrected inertial velocity
u_j' = incremental, inertial velocity
u_j^g = referential (or grid) velocity with respect to laboratory frame ($=\{u^g, v^g\}$)
$\underline{x}$ = position vector with respect to laboratory frame ($= x_j = \{x, y\}$)
α = angle of attack
ϵ_p = energy transfer rate
ϵ_t = dissipation rate
κ = reduced frequency ($= \pi fc/U_0$)
μ = molecular viscosity
μ_t = turbulent viscosity
ρ = density
σ_ℓ = turbulent Prandtl number for ℓ-th equation, $\ell = \{k_p, \epsilon_p, k_t, \epsilon_t\}$
$\underline{\xi}$ = referential frame ($= \xi_i(\underline{x}, t) = \{\xi_1, \xi_2\}$)

Superscript

n = denotes time-level

2.2 Multiple-Time-Scale Turbulence Equations. The multiple-time-scale turbulence equations in arbitrary Lagrangian-Eulerian coordinates are described below. The turbulent kinetic energy and the energy transfer rate equations for energy containing large eddies are given as;

$$\frac{\partial}{\partial t}(J\rho k_p) = J\frac{\partial}{\partial x_j}\{\rho k_p(v_j^g - v_j)\} + J\left\{\left(\mu + \frac{\mu_t}{\sigma_{kp}}\right)\frac{\partial k_p}{\partial x_j}\right\} + J\rho(P_r - \epsilon_p) \quad (3)$$

$$\frac{\partial}{\partial t}(J\rho\epsilon_p) = J\frac{\partial}{\partial x_j}\{\rho\epsilon_p(v_j^g - v_j)\} + J\left\{\left(\mu + \frac{\mu_t}{\sigma_{\epsilon p}}\right)\frac{\partial \epsilon_p}{\partial x_j}\right\} + J\frac{\rho}{k_p}(c_{p1}P_r^2 + c_{p2}P_r\epsilon_p - c_{p3}\epsilon_p^2) \quad (4)$$

where the production rate is given as

$$P_r = \nu_t \frac{\partial u_i}{\partial x_j}\left(\frac{\partial u_i}{\partial x_j} + \frac{\partial u_j}{\partial x_i}\right)$$

The turbulent kinetic energy and the dissipation rate equations for fine scale eddies are given as:

$$\frac{\partial}{\partial t}(J\rho k_t) = J\frac{\partial}{\partial x_j}\{\rho k_t(v_j^g - v_j)\} + J\left\{\left(\mu + \frac{\mu_t}{\sigma_{kt}}\right)\frac{\partial k_t}{\partial x_j}\right\} + J\rho(\epsilon_p - \epsilon_t) \quad (5)$$

$$\frac{\partial}{\partial t}(J\rho\epsilon_t) = J\frac{\partial}{\partial x_j}\{\rho\epsilon_t(v_j^g - v_j)\} + J\left\{\left(\mu + \frac{\mu_t}{\sigma_{\epsilon t}}\right)\frac{\partial \epsilon_t}{\partial x_j}\right\} + J\frac{\rho}{k_t}(c_{t1}\epsilon_p^2 + c_{t2}\epsilon_p\epsilon_t - c_{t3}\epsilon_t^2) \quad (6)$$

The eddy viscosity is given as;

$$\mu_t = \rho c_{\mu f}\frac{k^2}{\epsilon_p} \quad (7)$$

and the turbulence model constants are given as; $\sigma_{kp} = 0.75$, $\sigma_{\epsilon p} = 1.15$, $\sigma_{kt} = 0.75$, $\sigma_{\epsilon t} = 1.15$, $c_{p\ell,\ell=1,3} = \{0.21,1.24,1.84\}$, and $c_{t\ell,\ell=1,3} = \{0.29,1.28,1.66\}$. Derivation of the turbulence model constants can be found in Kim and Benson (1992a).

In complex turbulent flows, the production and dissipation rates of the turbulent kinetic energy vary widely in space so that the shape and the frequency domain of the spectral density also vary widely in space. Such a state of turbulence is called "nonequilibrium turbulence" (Kim, 1990a, 1990b, 1991a; Kim and Benson, 1992a, 1993a). The influence of nonequilibrium turbulence on turbulent transport of mass and momentum can be observed in the eddy viscosity coefficient deduced from measured data (Tavoularis and Karnik, 1989; Rodi, 1972) and in theoretical investigations (Launder, 1982). It can be found in these references that the eddy viscosity coefficient is decreased as P_r/ϵ_t is increased, and is increased as P_r/ϵ_t is decreased. Thus, the development of the fluid flow and the turbulence fields are influenced by the spatially varying turbulent viscosity, and the spatially varying turbulent viscosity depends on the turbulence intensity and the level of nonequilibrium turbulence. The capability of the M-S equations to resolve the nonequilibrium turbulence phenomena originates from describing the turbulence length scale and the turbulent viscosity using the energy transfer rate. Rewriting the turbulent viscosity in a form compatible with that of k-ϵ turbulence models yields $\mu_t = \rho c_\mu k^2/\epsilon_t$ where $c_\mu = c_{\mu f}\epsilon_t/\epsilon_p$ is the eddy viscosity coefficient that depends on the nonequilibrium turbulence. In single-time-scale turbulence models, such as the k-ϵ turbulence models, ARSM and RSM, the turbulence length scale is defined using the dissipation rate and, hence, these turbulence models can not resolve the nonequilibrium turbulence.

In turbulent flows, the energy containing large eddies are generated by the instability of the fluid flow, the large eddies cascade to finer eddies, and the fine scale eddies are dissipated by the viscous forces. The energy containing large eddies are characterized by low frequencies and large values of k_p/k_t, and the fine scale eddies are characterized by higher frequencies and small values of k_p/k_t (Kim and Benson, 1992a). The capability to model the cascade is achieved by solving the convection-diffusion equations for the spectrum-split turbulent kinetic energies. For highly complex flows, large eddies generated in the upstream region are convected in the downstream direction. In such a downstream region, the ratios of P_r/ϵ_t and ϵ_t/ϵ_p are influenced by the convected eddies (i.e., the large value of k_p/k_t). Thus the nonequilibrium turbulence is also influenced by the cascade of turbulent kinetic energy. Again, the single-time-scale turbulence models can not resolve the cascade of turbulent kinetic energy since spectrum-split turbulence quantities are not solved for in these turbulence models. Further theoretical analysis of the M-S equations can be found in Kim and Benson (1992a).

2.3 Numerical Method. The unsteady flow equations defined on arbitrary Lagrangian-Eulerian coordinates are solved using a finite volume method that incorporates a pressure-staggered mesh and an incremental pressure equation. In the method, the inertial velocities and turbulence quantities are located at the grid points and the pressure is located at the centroid of a cell formed by the four adjacent velocity grid points (Kim and Benson, 1992b). The transient solution is obtained by solving the flow equations iteratively at each time-level, and each iteration consists of a predictor step and a corrector step. The iterative time-advancing scheme is described below.

Predictor Step. Applying the finite volume method (Kim, 1991b; Kim and Benson, 1992b) to the momentum equation yields

$$(\rho C_1 + A_i^*)u_i^{**} = \sum_{\ell=1}^{nb} A_\ell^* u_\ell^{**} + S_i^* - \frac{\partial p^*}{\partial x_i} + \left\{\int \frac{1}{\Delta t}\frac{\rho J^{n-1}}{J^n}\,d\underline{x}\right\} u_i^{n-1} \quad (8)$$

where $C_1 = \int 1/\Delta t\, d\underline{x}$, and $A_i^*(u_i^* - u_j^{g,n})$ and $A_\ell^*(u_j^* - u_j^{g,n})$ are determined from the power-law upwind differencing scheme (Patankar, 1980). The load vectors $S_i^*(u_j^*)$ and $\{\int 1/\Delta t\, \rho J^{n-1}/J^n\, dx\}u_i^{n-1}$ are contributed by the nonorthogonal mesh and the moving mesh, respectively. In deriving Eq. (8), the surface and volume integrals are carried out on the current time-level, noninertial mesh. The predicted inertial velocity, u_j^{**}, is obtained by solving Eq. (8). However, the predicted velocity field may not satisfy the conservation of mass until the solutions are fully converged.

Corrector Step for Divergence-Free Velocity Field. The corrected inertial velocity and the corrected pressure that may satisfy the conservation of mass and the linearized momentum equation can be written as

$$u_j^{***} = u_j^{**} + u_j', \quad (9)$$

$$p^{**} = p^* + p', \quad (10)$$

respectively. Then the corrected discrete momentum equation can be written as

$$(\rho C_1 + A_i^*)\,u_i^{***} = \sum_{nb} A_k^* u_k^{***} + S_i^* - \frac{\partial(p^* + p')}{\partial x_i} + \left\{\int \frac{1}{\Delta t}\frac{\rho J^{n-1}}{J^n}\,dx\right\} u_1^{n-1} \quad (11)$$

Subtracting Eq. (8) from Eq. (11) yields the relationship between the incremental, inertial velocity and the incremental

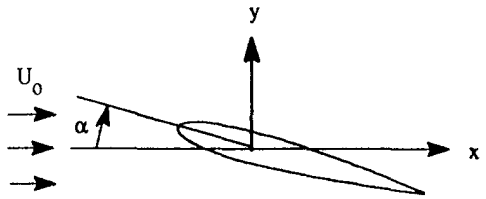

Fig. 2 Nomenclature

pressure given as

$$u_i' = -\frac{1}{(\rho C_1 + A_j^*)} \frac{\partial p'}{\partial x_i} \tag{12}$$

where the contributions from neighboring grid points have been disregarded. However, this simplification does not incur any mass imbalance in the converged solution since the incremental pressure is driven only by the mass imbalance as shown below. Substituting Eqs. (9) and (12) into the conservation of mass equation yields the incremental pressure equation given as

$$-\frac{\partial}{\partial x_j}\left\{\frac{1}{(\rho C_1 + A_j^*)} \frac{\partial p'}{\partial x_j}\right\} = -\frac{\partial\{\rho(u_j^{**} - u_j^u)\}}{\partial x_j} - \frac{1}{J}\frac{\partial(\rho J)}{\partial t} \tag{13}$$

where the right-hand side represents the mass imbalance and is identical to the original conservation of mass equation. Equations (8)–(10) and (12)–(13) are solved iteratively until the velocity and pressure satisfy the prescribed convergence criterion at each time-level. In principle, the incremental pressure equation needs to be solved iteratively until the residual term vanishes and, in such a case, the converged solution satisfies the conservation of mass and momentum equations exactly within the context of the difference approximation.

3 Numerical Results

The oscillating airfoil (Panda and Zaman, 1992) is schematically shown in Fig. 2. The free-stream inertial velocity is 6.29 m/s and the chord length of the airfoil is 0.102 m. The Reynolds number based on the chord length is 44,000 and the reduced frequency is 0.2. The angle of attack is given as

$$\alpha = \alpha_0 + \alpha_A \sin(\omega t + \alpha_\phi) \tag{14}$$

where $\omega = 2\pi f$ is the angular velocity, $f = 3.924$ Hz is the frequency of oscillation, $\alpha_0 = 15°$ is the mean angle of attack, $\alpha_A = 10$ deg is the amplitude of oscillation and $\alpha_\phi = 3\pi/2$ is the phase angle. The center of rotation is located at a quarter chord length downstream of the leading edge, and $(x, y) = (0, 0)$ refers to the center of rotation in the following discussion. The inlet boundary is located at 5 chord lengths upstream of the leading edge and the exit boundary is located at 35 chord lengths downstream of the trailing edge. The top and bottom boundaries are separated by 5 chord lengths away from the top and bottom surfaces of the airfoil, respectively. The entire domain is discretized by a 191 × 105 mesh, and the sheared moving mesh is generated algebraically at each time-level. The grid points on the solid wall are attached to the airfoil, i.e., $u_j = u_j^g$ so that the no-mass flux and no-slip boundary conditions are satisfied trivially on the solid wall. The moving meshes in the vicinity of the airfoil at $\alpha = 5$, 15, and 25 deg are shown in Fig. 3. The smallest mesh size in the direction normal to the wall is 0.4 × 10-3 m and the grid size in the direction normal to the airfoil surface is increased by a factor of approximately 1.1. It can be seen in the figure that the mesh near the airfoil is fine enough to resolve the laminar flow as well as the transitional and turbulent flow near the airfoil.

Free-stream boundary conditions are applied at the inlet, top and bottom boundaries. The measured data show that the free stream turbulence intensity is less than 0.1 percent and, hence,

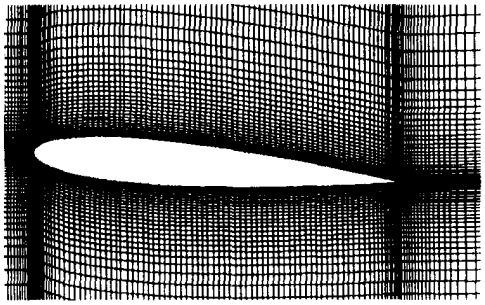

(a) $\alpha = 5^o$

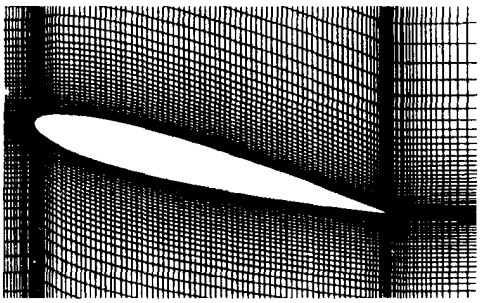

(b) $\alpha = 15^o$

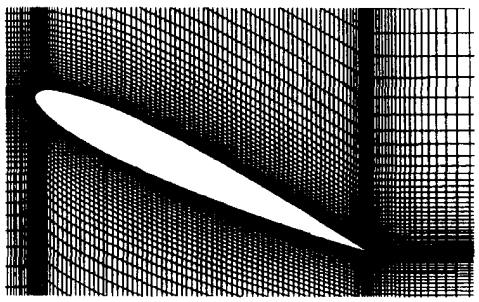

(c) $\alpha = 25^o$

Fig. 3 Moving mesh for oscillating airfoil; (*a*) α = 5 deg, (*b*) α = 15 deg, (*c*) α = 25 deg

$k = (0.001U_0)^2$ is prescribed at free-stream boundaries. The turbulence length scale for the free stream flow is not clearly known. Thus the free stream dissipation rate is obtained inversely from $\mu_t/\mu \approx 0.05$. The use of a few times different μ_t/μ still yields the same numerical results since the upstream boundary is located far away from the airfoil and the turbulence intensity and the dissipation rate are decayed as the flow approaches the airfoil. The vanishing gradient boundary condition is used for each flow variable at the exit boundary. The vanishing turbulent kinetic energy is prescribed at the solid wall boundary. The near-wall turbulence field is described by a "partially low-Reynolds number" turbulence model (Kim, 1990a). In the near-wall turbulence model, the partial differential equations for the partitioned turbulent kinetic energy equations are solved up to the wall while the energy transfer rate and the dissipation rate inside the near-wall layer are obtained from algebraic equations. It can be found in Kim (1990a, 1990b, 1991a) and Kim and Benson (1992a, 1993a) that the "partially low-Reynolds number" near-wall turbulence model (when used together with the M-S equations) yields highly improved numerical results compared with those obtained using wall functions.

The error norm used for the convergence test is given as

$$|e|_\ell = \max\left\{\text{abs}\left[\frac{A_\ell^k - A_\ell^{k-1}}{A_{\ell,0}^k}\right]_{j=1,N}\right\} < \epsilon_\ell \tag{15}$$

where A_ℓ^k is the ℓth flow variable at the kth iteration, $A_{\ell,0}^k$ is

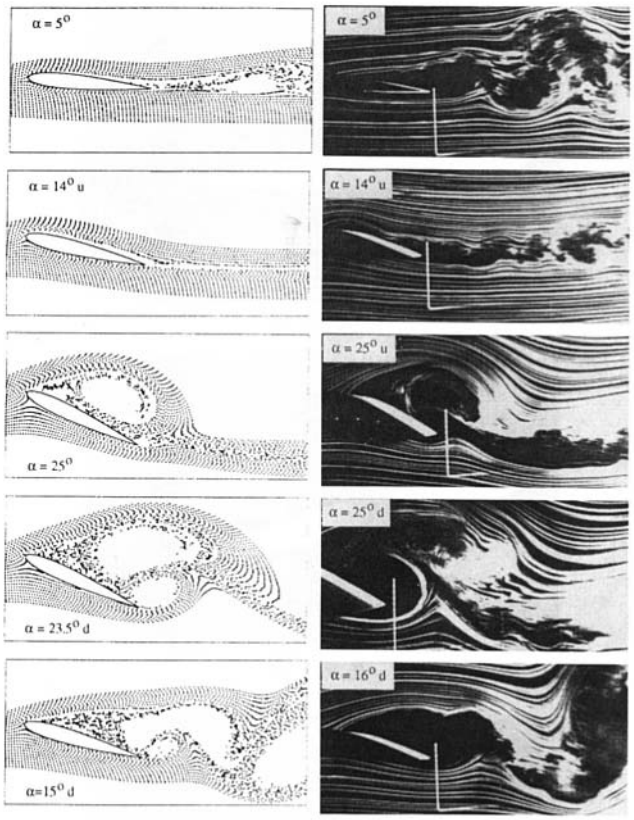

Fig. 4 Comparison of calculated streaklines with smoke picture, (u: upstroke, d: down stroke)

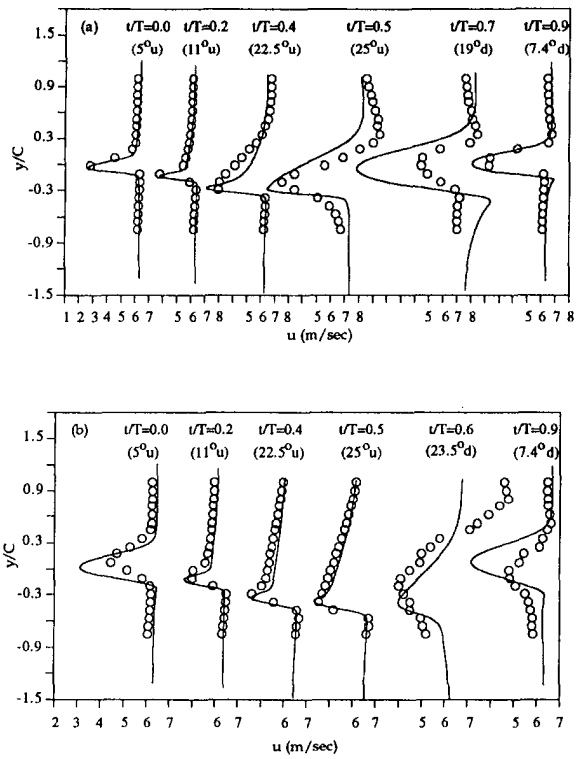

Fig. 5 Ensemble-averaged velocity profiles; (*a*) at x/c = 1.0, (*b*) at x/c = 2.1

the maximum ℓth flow variable at the kth iteration, N is the total number of grid points, and ϵ_ℓ is the convergence criterion for each flow variable. The required number of iterations to satisfy the convergence criterion depends on the angle of attack of the airfoil. For $\epsilon_\ell = 1.0 \times 10^{-4}$, the converged solutions at each time-level are obtained in approximately 25 iterations for low angles of attack and in 45 iterations for high angles of attack. The relative imbalance of the mass flow rate leaving the flow domain with respect to that entering the flow domain is less than 1.0×10^{-4} for each time-level.

The calculated streaklines at several angles of attack during a period are compared with the flow visualization pictures in Fig. 4. The flow visualization pictures were made using a "smoke-wire" method (Panda and Zaman, 1992). The accuracy of the measured angle of attack is within ±2 deg. The clean streaklines in the smoke pictures away from the airfoil indicate that the fluid flow in these regions remains in a laminar state during the entire cycle. It can be seen in the figure for $\alpha = 5$ deg that the flow exhibits a relatively wide wake in the downstream region. The wide wake is a trace of the large vortices shed into the downstream direction during the down stroke of the airfoil. In the early part of the upstroke motion, the flow is reattached and, as a result, a thin wake is developed in the downstream region as shown in $\alpha = 14$ deg u. At and near the peak angle of attack, a fully developed DSV appears on the upper surface of the airfoil and a small TEV begins to appear near the trailing edge. Shortly thereafter, the DSV is lifted by the TEV and is shed into the downstream direction. The calculated streaklines at $\alpha = 23.5$ deg d indicate that the numerical method correctly predicts the earlier development of the DSV and the TEV. Subsequently, the DSV-TEV pair is convected into the wake region and forms a "mushroom-like" structure as shown in the smoke picture for $\alpha = 25$ deg. However, the calculated results show that the DSV loses its strength as it travels in the downstream direction and that the TEV does not completely lift the DSV. The discrepancy between the calculated results and the experimental data at and near the peak angle of attack may be caused by the relatively coarse mesh in the right upper corner of the airfoil that cannot fully resolve the interaction between the DSV and the TEV. At a later time during the down stroke, the DSV-TEV pair and the small vortices located near the leading edge are cascaded and shed into the downstream direction as shown in calculated streaklines for $\alpha = 15$ deg d. The small vortices located near the leading edge at $a = 23.5$o are not clearly observed in the calculated streaklines, but these can be observed clearly in the velocity vector plots (Kim et al., 1993b). It can be found in Fig. 4 that the calculated streaklines are in very good agreement with the smoke pictures for most of period.

The calculated ensemble-averaged velocity profiles are compared with the measured data in Fig. 5. The measured velocity profiles are obtained by ensemble averaging the instantaneous velocity data for 80 cycles. It can be seen in the figures that the fluid flow originating from the lower surface exhibits a strong velocity gradient. The steep velocity gradient in the region indicates that the lower part of the airfoil remains in a laminar state during most of a cycle. The transitional turbulence field is discussed later in this section. At $x/c = 1.0$, the calculated velocity profiles are in good agreement with the measured data during a large part of a period. The deteriorated comparison for $\alpha = 25$ through $\alpha = 19$ deg is caused mostly by two reasons. First, hot wire anemometers cannot measure velocity components accurately when flow is misaligned more than approximately 30 deg from the hot wire axis. The calculated velocity vectors show that the inclination angles of the fluid particles are increased when large vortices are passing through the wake region (Kim et al., 1993b). Second, the interaction between the DSV and the TEV occurs in the region where the mesh is relatively coarse and the numerical method yields somewhat deteriorated results. At a farther downstream location ($x/c = 2.1$), the numerical results may suffer coarse grid inaccuracy more compared with the upstream trailing edge

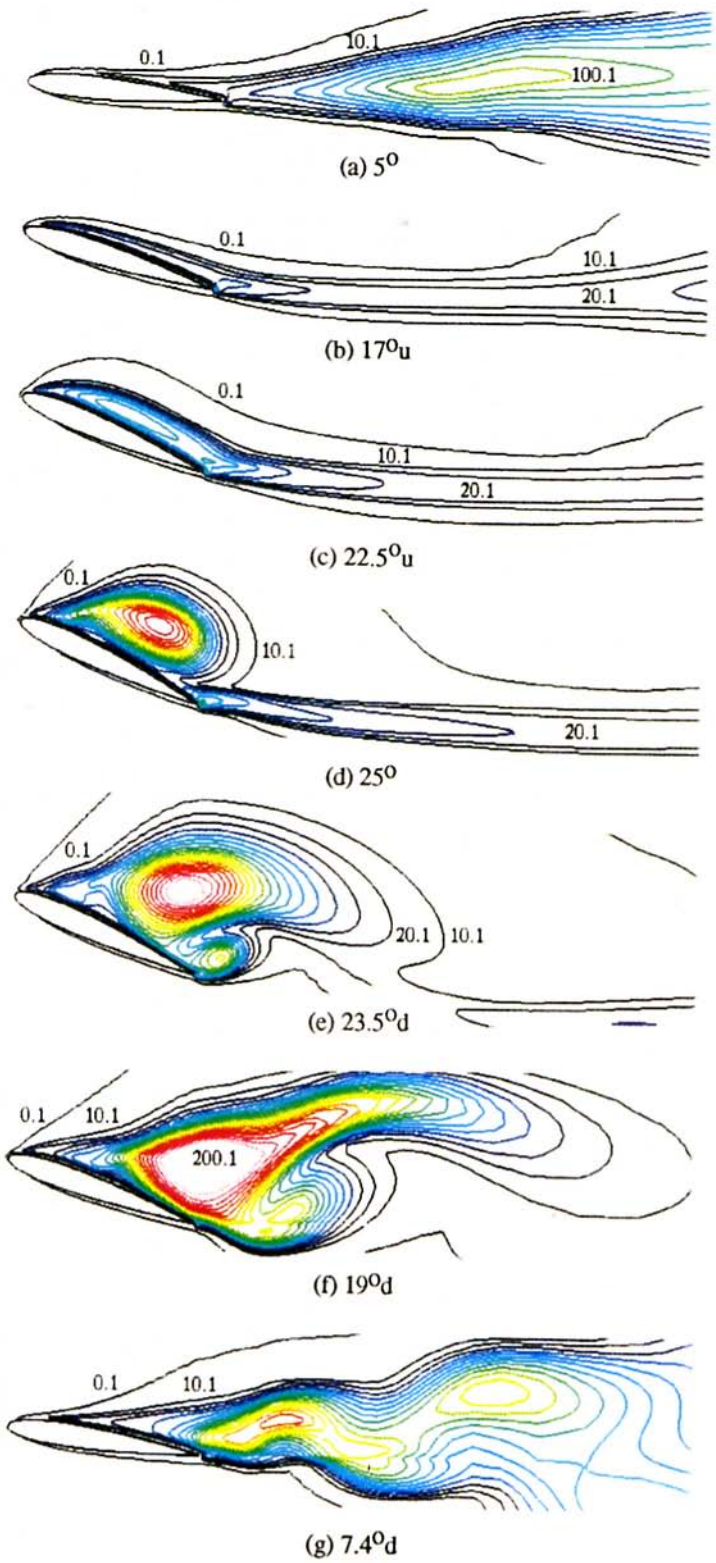

Fig. 6 Turbulent viscosity contour ($\Delta\mu_t/\mu$ = 10)

region where the mesh is very fine. Nevertheless, the calculated and the measured velocity profiles exhibit almost the same level of agreement as those in the upstream region. Comparison of the calculated vorticity contours with the measured data is given in Kim et al. (1993b). It can be found in the reference that the calculated and the measured vorticity contours are also in good agreement.

The calculated turbulent viscosity contours are shown in Fig. 6, where the increment between the contour lines is uniform. Recall that usually $\mu_t/\mu \approx 10$ is used as a cut-off value in numerical calculations of transitional flows using algebraic turbulence models (Ameri et al., 1992). In the present case using the M-S equations, the numerical calculation successfully predicts the transition and the relaminarization without using such a cut-off value. It can be seen in the figure that the trend of turbulent viscosity distribution is almost the same as that of the streaklines. The turbulent viscosity contours show that the fluid flow in the far field and in the lower part of the airfoil remains in a laminar state for the entire cycle. Due to the low free-stream velocity and the low free-stream turbulence intensity, a strong turbulence field is formed only along the separated and recirculating flow region. It can be seen in the figure that the transition and relaminarization occur widely in space and in time.

4 Conclusions and Discussion

Numerical investigation of unsteady transitional flow over a periodically oscillating airfoil is presented. The ensemble-averaged Navier-Stokes equations defined on arbitrary Lagrangian-Eulerian coordinates are used to describe the unsteady transitional flow with moving boundaries. The numerical method is based on a finite volume method that incorporates a pressure-staggered mesh and an incremental pressure equation for the conservation of mass. The calculated and the experimentally observed streaklines show that the flow is fully attached at low angles of attack. The calculated turbulence field shows that an almost laminar state prevails around the entire surface of the airfoil at small angles of attack during the upstroke motion. As the angle of attack is increased close to the stall angle of attack, the flow on the top surface of the airfoil separates, and the separated flow forms the clockwise rotating dynamic stall vortex (DSV) as the angle of attack is further increased. As the oscillating airfoil approaches the peak angle of attack, the fluid particles near the trailing edge are forced to flow upward by the strong pressure on the pressure side of the airfoil, and these fluid particles forms the clockwise rotating trailing edge vortex (TEV). The length scales of the DSV and the TEV are almost the same as the chord length of the airfoil. The two counter-rotating large vortices generate an intense turbulence field on the upper surface of the airfoil. As the angle of attack is decreased, the intense turbulence field is convected into the wake region together with the cascading vortices. The calculated turbulent viscosity contours show that the transition from laminar to turbulent state and the relaminarization occur widely in space as well as in time. The calculated streaklines, the ensemble-averaged velocity profiles and the vorticity contours are in good agreement with the measured data.

It is shown that the numerical method successfully predicts the large DSV and the TEV that are periodically generated by the oscillating airfoil. The successful calculation of the complex transitional flow, in which transition from laminar to turbulent state and relaminarization occur widely in space and in time, is attributed to the capability of the multiple-time-scale turbulence equations to simulate the cascade of energy-containing eddies and to resolve the nonequilibrium turbulence.

References

Ameri, A. A., Sockol, P. M., and Gorla, R. S. R., 1992, "Navier-Stokes Analysis of Turbomachinery Blade External Heat Transfer," *Journal of Propulsion and Power*, Vol. 8, No. 2, pp. 374–381.

Belytschko, T., Flanagan, D. P., and Kennedy, J. M., 1982, "Finite Element Methods with User-Controlled Meshes for Fluid-Structure Interaction," *Computer Methods in Applied Mechanics and Engineering*, Vol. 33, pp. 669–688.

Cricelli, A. S., Ekaterinaris, J. A., and Platzer, M. F., 1992, "Unsteady Airfoil Flow Solutions on Moving Zonal Grids," AIAA paper 92-0543.

Donea, J., Giuliani, S., and Halleux, J. P., 1982, "An arbitrary Lagrangian-Eulerian Finite Element Method of Transient Dynamic Fluid-Structure Inter-

actions," *Computer Methods in Applied Mechanics and Engineering*, Vol. 33, pp. 689–723.

Kim, S.-W., 1990a, "A Near-Wall Turbulence Model and Its Application to Fully Developed Turbulent Channel and Pipe Flows," *Numerical Heat Transfer*, Part B, Vol. 17, pp. 101–122.

Kim, S.-W., 1990b, "Numerical Investigation of Separated Transonic Turbulent Flows with a Multiple-Time-Scale Turbulence Model," *Numerical Heat Transfer*, Part A, Vol. 18, pp. 149–171.

Kim, S.-W., 1991a, "Calculation of Reattaching Shear Layers in Divergent Channel with a Multiple-Time-Scale Turbulence Model," *AIAA Journal*, Vol. 29, pp. 547–554.

Kim, S.-W., 1991b, "Calculations of Separated 3-D Flows with a Pressure-Staggered Navier-Stokes Equations Solver," NASA CR-187065.

Kim, S.-W., and Benson, T. J., 1992a, "Calculation of a Circular Jet in Crossflow with a Multiple-Time-Scale Turbulence Model," *International Journal of Heat and Mass Transfer*, Vol. 35, pp. 2357–2365.

Kim, S.-W., and Benson T. J., 1992b, "Comparison of the SMAC, PISO and Iterative Time-Advancing Schemes for Unsteady Flows," *Computers and Fluids*, Vol. 21, No. 3, pp. 435–454.

Kim, S.-W., and Benson, T. J., 1993a, "Fluid Flow of a Row of Circular Jets in Crossflow-A Numerical Study," *AIAA Journal*, vol. 31, pp. 806–811.

Kim, S.-W., Zaman, K. B. M. Q., and Panda, J., 1993b, "Calculation of Unsteady Transitional Flow over Oscillating Airfoil" *Separated Flows*, J. C. Dutton and L. P. Purtell, eds., ASME FED-Vol. 149, pp. 165–176, The Fluid Engineering Conference, Washington, DC, June 20–24, 1993.

Launder, B. E., 1982, "A Generalized Algebraic Stress Transport Hypothesis," *AIAA Journal*, Vol. 20, pp. 436–437.

McAlister, K. W., and Carr, L. W., 1979, "Water tunnel visualization of dynamic stall," ASME JOURNAL OF FLUIDS ENGINEERING, Vol. 106, pp. 376–380.

McAlister, K. W., Pucci, S. L., McCroskey, W. L., and Carr, L. W., 1982, "An experimental study of dynamic stall in advanced airfoil sections," NASA TM-84245.

Panda, J., and Zaman, K. B. M. Q., 1992, "Experimental investigation of the flow field of an oscillating airfoil," AIAA Paper 92-2622.

Patankar, S. V., 1980, *Numerical Heat Transfer and Fluid Flow*, McGraw-Hill, New York.

Rodi, W., 1972, "The Prediction of Free Boundary Layers by Use of a Two-Equation Model of Turbulence," Ph.D. Thesis, University of London, London.

Rumsey, C. L., and Anderson, W. K., 1988, "Some Numerical and Physical Aspects of Unsteady Navier-Stokes Computations over Airfoils Using Dynamic Mesh," AIAA Paper 88-0329.

Tavoularis, S., and Karnik, U., 1989, "Further Experiments on the Evolution of Turbulent Stresses and Scales in Uniformly Sheared Turbulence," *Journal of Fluid Mechanics*, Vol. 204, pp. 457–478.

Truesdell, C., and Toupin, R., 1960, "The Classical Field Theory" *Encyclopedia of Physics*, Vol. 3, Springer, Berlin.

Wu, J.-C., Kaza, K. R. V., and Sankar, L. N., 1987, "A Technique for the Prediction of Airfoil Flutter Characteristics in Separated Flow," AIAA Paper 87-0910.

Wu, J.-C., Huff, D. L., and Sankar, L. N., 1990, "Evaluation of Three Turbulence Models in Static Airloads and Dynamic Stall Predictions," *Journal of Aircraft*, Vol. 27, pp. 382–384.

Separating and Reattaching Flow Structure in a Suddenly Expanding Rectangular Duct

G. Papadopoulos[1]
Graduate Research Assistant.

M. V. Ötügen
Assistant Professor of Aerospace Engineering.

Turbulent Fluid Mechanics Laboratory,
Polytechnic University,
Brooklyn, NY 11201

The incompressible turbulent flow over a backward-facing step in a rectangular duct was investigated experimentally. The side wall effects on the core flow were determined by varying the aspect ratio (defined as the step span-to-height ratio) from 1 to 28. The Reynolds number, based on the step height and the oncoming free-stream velocity, was 26,500. Detailed velocity measurements were made, including the turbulent stresses, in a region which extended past the flow reattachment zone. Wall static pressure was also measured on both the step and flat walls. In addition, surface visualizations were obtained on all four walls surrounding the separated flow to supplement near-wall velocity measurements. The results show that the aspect ratio has an influence on both the velocity and wall pressure even for relatively large aspect ratios. For example, in the redevelopment region downstream of reattachment, the recovery pressure decreases with smaller aspect ratios. The three-dimensional side wall effects tend to slow down the relaxation downstream of reattachment for smaller aspect ratios as evidenced by the evolution of the velocity field. For the two smallest aspect ratios investigated, higher centerplane streamwise and transverse velocities were obtained which indicate a three-dimensional mean flow structure along the full span of the duct.

Introduction

Reattaching separated flows have applications in many engineering problems. Such flows are encountered in heat exchangers, ducts, flows around buildings, microelectronic circuit boards, and many combustor configurations. The flow past a backward-facing step is one of the simplest geometries to produce separation and reattachment of turbulent shear layers. The separation point is fixed by a sharp corner and thus, no additional complexities arise due to the motion of this point. Nevertheless, the flow downstream of the step is still very complex and numerous investigations have been aimed at developing a better understanding of these flows. Despite the considerable attention it has received due to its importance, the internal flow downstream of a backward-facing step has not been fully understood. Most previous investigators have utilized external flow configurations with small step heights compared to the upstream channel height ($ER \approx 1$). Furthermore, large aspect ratios were utilized so that the flow may be considered two-dimensional along the centerplane. Consequently, the additional complexities in the flow structure due to the proximity of the flat and side walls have not been fully investigated. This is unfortunate since a large number of fluidic applications involve rectangular sudden expansions where, externally-imposed three-dimensional effects can be severe.

de Brederode and Bradshaw (1972) studied the effects of small aspect ratios on the general features of the "external" flow ($ER \approx 1$) downstream of the backward-facing step. They concluded that side wall effects on the flow along the centerplane were negligible for aspect ratios greater than 10. In addition, smaller aspect ratios yielded longer centerplane reattachment lengths if the boundary layer was laminar at separation, and shorter reattachment lengths if the oncoming boundary layer was turbulent. More recently, in the investigations of the internal flow separating over a backward-facing step, Armaly et al. (1983) and Ötügen (1991) employed laser Doppler anemometry to determine a number of flow characteristics, the former as a function of the Reynolds number in the laminar and transitional regimes and the latter as a function of the expansion ratio in the turbulent regime. Although both studies concentrated on the flow characteristics mostly along the centerplane, in similar types of measurements of reattachment length along the span of the tunnel, they both observed a significant decrease in this length near the side walls where the flow could no longer be considered two-dimensional.

Apart from the early work of de Brederode and Bradshaw (1972), there have been only a small number of investigations addressing this type of geometry-imposed three-dimensionality in turbulent flow separation. Stevenson et al. (1984), Berbee and Ellzey (1989) and Lim et al. (1990) performed limited studies focusing on arbitrarily chosen aspect ratios. In the former and the latter studies, aspect ratios of 2 and 3.3 were used, respectively. In Berbee and Ellzey experiments, aspect ratios of 10 and 4, were studied. Ötügen et al. (1992) explored the side wall effects on the spanwise uniformity of the time-mean

[1]Present Address: University of Erlangen, Erlangen, Germany.

Contributed by the Fluids Engineering Division for publication in the JOURNAL OF FLUIDS ENGINEERING. Manuscript received by the Fluids Engineering Division March 21, 1994; revised manuscript received October 27, 1994. Associate Technical Editor: M. Gharib.

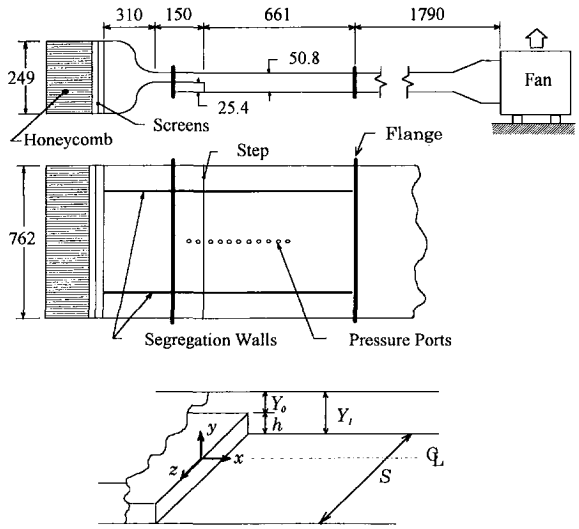

Fig. 1 Experimental setup and flow geometry (dimensions in millimeters)

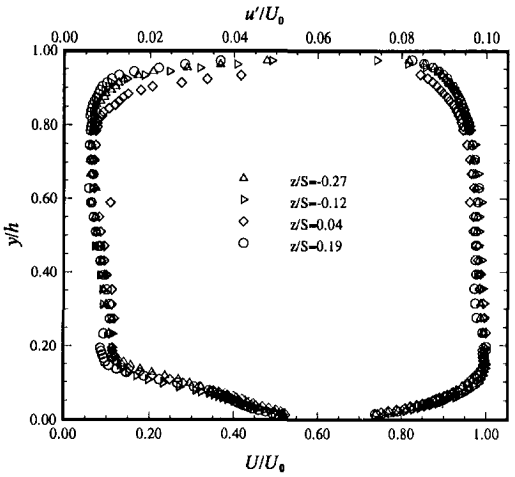

Fig. 2 Mean and turbulent velocity profiles at step edge for AR = 27. (Uncertainty in U and u' are 2 and 3 percent, respectively.)

flow for a fixed aspect ratio of AR = 10. Some insight into the structure of the flow field along the step wall as a function of step height was given by the surface visualizations of Jesek and Reznicek (1987), and Badawy et al. (1989).

The present study was undertaken in order to gain a more comprehensive understanding of the three-dimensional side wall effects on the separated flow structure. Experiments were conducted in a facility featuring a fixed expansion ratio (ER = 2) and a variable aspect ratio capability. Throughout the experiments, all inlet parameters such as the Reynolds number, freestream velocity, boundary layer type and thickness, and the turbulence intensity were kept constant in order to isolate the aspect ratio effects on the flow structure.

Experimental Setup and Procedure

A schematic representation of the open-circuit wind tunnel and the flow geometry is shown in Fig. 1. The step height, h, was fixed at 25.4 mm and the upstream channel height leading to the step (Y_0) was also 25.4 mm, hence yielding an expansion ratio of ER = 2. The span of the step was 762 mm, rendering a maximum aspect ratio of AR = 30. Smaller aspect ratios were obtained by using a pair of segregation walls. These walls ran along the full length of the tunnel to minimize inlet and exit effects. The leading edge of the walls was contoured to prevent vortex shedding in the inlet section. Once in place, these segregation walls prevented pressure leakage across compartments.

The wall static pressure was measured using variable reluctance pressure transducers and through a 48-port computer-controlled pressure switching system. Constant temperature anemometry was used for the velocity measurements. The 10 μm tungsten x-wire sensors with various sensor orientations were built in-house and tangential cooling effects were taken into account in the calibration procedure. Since the hot-wire probe is not capable of resolving reversed flow, the measurements were performed outside of the recirculation zone, the extent of which was determined from previous flow visualizations (Papadopoulos, 1994). The x-wire probe was mounted on a computer-controlled dual-axis traverse system having a resolution of 0.6 μm and 0.32 mm in the transverse and streamwise directions, respectively. The x-wire probe was inserted into the flow field through a 4 mm slot located on the flat wall, and to minimize leakage effects while at the same time enabling probe motion in both directions, the entire probe assembly including the positioning system was enclosed within a sealed rectangular container, isolating it from the laboratory environment. Repositioning of the x-wire probe sensor relative to the step wall was performed at each streamwise location, with an accuracy of ±0.05 mm, using the technique of Papadopoulos and Ötügen (1993). Both the hot-wire and the pressure signals were digitized on-line using a 12-bit A/D converter and processed on a personal computer.

Results and Discussion

All flow conditions at the step edge were kept constant to insure uniform initial conditions throughout the experiments. The free stream velocity was U_0 = 16 m/s yielding a Reynolds number of 26,500. Figure 2 shows velocity profiles at the step

Nomenclature

AR = aspect ratio ($=S/h$)
C_p = mean pressure coefficient ($=(P-P_0)/q$)
ER = expansion ratio ($=Y_1/Y_0$)
h = step height
P = mean wall static pressure
P_0 = reference mean wall static pressure
P' = rms of wall static pressure
p_0' = rms of wall static pressure at reference location
q = freestream dynamic pressure ($=1/2(\rho U_\infty^2)$)
Re = Reynolds number ($=(U_0h)/\nu$)
S = channel width
U_0 = freestream mean velocity
U = mean streamwise velocity
u' = rms of streamwise velocity
$u'v'$ = Reynolds shear stress
V = mean transverse velocity
v' = rms of transverse velocity
W = mean spanwise velocity
x = streamwise distance from the step edge
x_R = reattachment length
y = transverse distance from the step edge
Y_0 = upstream channel height
Y_1 = downstream channel height
z = spanwise distance from channel centerline
δ = boundary layer thickness
δ^* = boundary layer displacement thickness
ν = dynamic viscosity
ρ = density

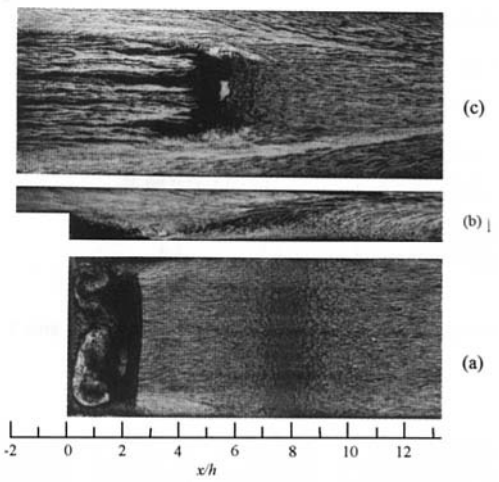

Fig. 3 Surface visualization on (*a*) step wall; (*b*) side wall; (*c*) flat wall for *AR* = 6

edge for the aspect ratio of 27. Both the mean and the turbulence profiles, obtained at various z/S locations show good agreement indicating a spanwise uniform inlet flow. The boundary layer at separation is turbulent and its thickness is uniform along the span direction. The average boundary layer thickness is $\delta = 4$ mm ($\delta/h = 0.16$) with a variation of less than 10 percent across the span. The corresponding displacement thickness is $\delta^* = 0.46$ mm ($\delta^*/h = 0.018$). The slightly higher free stream velocity near the boundary layer is due to the flow's local acceleration shortly before the streamline curvature downstream of the step.

Surface Visualizations Oil-based surface flow visualizations were obtained on all four walls surrounding the flow for various AR. The results for $AR = 6$ are shown in Fig. 3. For the complete set of visualizations for various aspect ratios, the reader is referred to Papadopoulos (1994).

On the step wall (Fig. 3(*a*)), four flow zones are evident along the streamwise direction: (*i*) a three-dimensional zone of slow moving fluid immediately downstream of the step, made up of a pair of counter rotating eddies situated adjacent to the side walls and other secondary flow structures between these two eddies; (*ii*) a flow reversal zone where the flow direction near the step wall is negative throughout, and where the wall mean shear stress becomes larger with smaller streamwise distances, abruptly reaching zero at the edge of the initial dead zone; (*iii*) a flow reattachment zone where the free shear layer created by the step edge impinges on the step wall in an unsteady fashion; and (*iv*) a redeveloping flow zone where the velocity of the flow along the step wall is always positive. Two "dead" zones in the separating-reattaching flow are evident in Fig. 3(*b*). The first is essentially the extension in the z direction of zone (*i*) seen in Fig. 3(*a*). The second dead zone is a divider between a strong reversed flow and the redeveloping flow further downstream. It is essentially the side wall extension of the reattachment zone (or the zone of zero mean shear). Near the side walls, the dead zone is lifted up away from the step wall. A surprising result is the existence of flow separation on the flat wall approximately five step heights downstream of the step (Fig. 3(*c*)). This strip of separated flow, which is observed in most of the *AR* cases studied, does not extend across the full span of the tunnel. Downstream of this strip, the flow moves in the streamwise direction with streamlines near the side walls moving towards the centerplane.

The dependence of x_R on the aspect ratio is summarized in Fig. 4. The reattachment length values are obtained from the surface visualizations. As the aspect ratio decreases, so do the x_R values. This trend agrees with the results of de Brederode

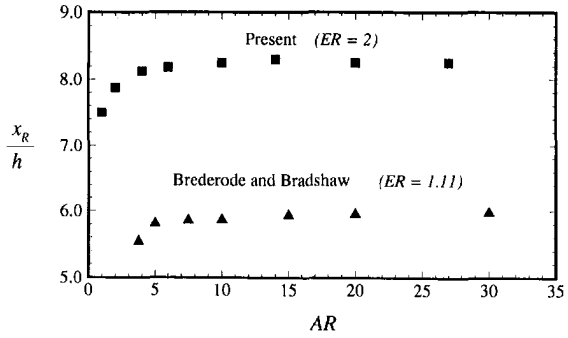

Fig. 4 The effect of aspect ratio on reattachment length

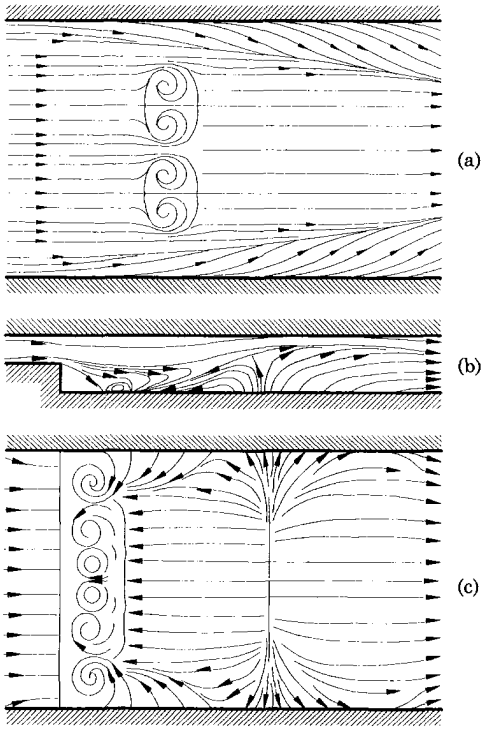

Fig. 5 Near-wall flow model based on surface visualization results

and Bradshaw (1972) in the case of turbulent boundary layer at separation. As the aspect ratio becomes smaller, the side walls effects penetrate the core flow and this results in an overall reduction of the reattachment length. The present reattachment lengths for large aspect ratios are around 8.2 step heights. This value is within, but closer to the high end of the x_R/h values reported in the literature. For example, the results of De Brederode and Bradshaw (1972) indicate $x_R/h \approx 6$ while Ötügen (1991) and Westphal and Johnston (1984) reported $x_R/h = 6.7$ and 8.6, respectively (all for $AR \geq 12$). Several factors influence the value of the reattachment length. These include the method of inference, and flow conditions at separation. The initial conditions of Westphal and Johnston (1984) match fairly well with those of the present study.

From the surface flow patterns, a model of the complex, separating and reattaching flow structure is constructed as shown in Fig. 5. The nearly dead zone on the step wall immediately downstream of the step is dominated by a pair of primary eddies whose axes are normal to the step wall. In between these primary eddies is yet another set of counter rotating eddies of even number which are induced by the motion of the primary eddies. The streamwise extent of the dead zone is approximately three step heights, and since the eddies scale with this length, the number of the secondary eddies depends on the

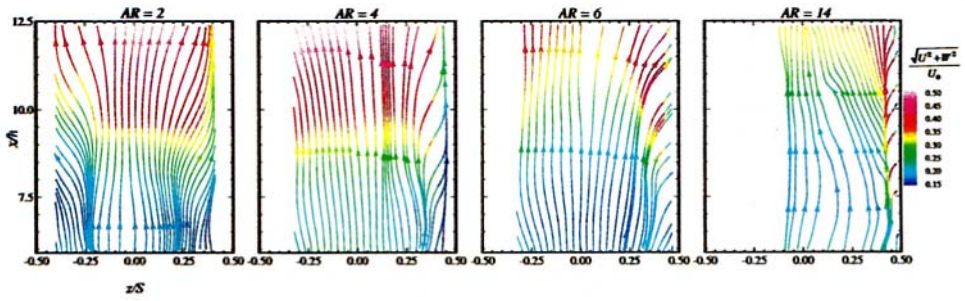

Fig. 6 Time-averaged streamline patterns near step wall ($y/h = -0.97$). (Uncertainty in the measurement of U and W are 4 and 7 percent, respectively.)

aspect ratio. An interesting feature of the flow is the disappearance of the reattachment zone adjacent to the side walls (Fig. 3(a)). On the step wall, the zone of no-shear is replace by a flow toward the side walls. Some of this flow impinges on the side wall and moves upwards (Fig. 3(b)). In effect, near the side walls, the reattachment zone is lifted up from the step wall and the zero mean shear region is located away from this wall.

It is postuled that the structure of the flow near the side walls is dominated by two streamwise vortices each originating at the junction of the step edge and side wall (Ötügen et al., 1992). Although the present time-mean surface visualizations cannot identify the exact extent and dynamic behavior of the vortices, they do confirm their existence. These vortices are located underneath the separated shear layer and grow rapidly under the influence of the adverse pressure gradient. For a turbulent boundary layer at separation, the sense of rotation of the vortices is such that they bring fluid upwards near the side walls, and downwards near the center of the tunnel as seen in Fig. 3. Therefore, the vortices push the separated shear layer downward near the centerplane hence reducing the reattachment length for smaller aspect ratios as Fig. 4 indicates. Their effect near the side walls is to lift the reattachment zone away from the step wall (Fig. 3). The boundary layer developing on the flat wall experiences an adverse pressure gradient downstream of the step due to the expansion into the larger duct. As a result, in some instances it separates forming a strip inhabited by a set of weak counter rotating eddies. Near the side walls, no separation can be sustained due to the increased momentum near the flat wall as a consequence of the lifting of the reattachment zone from the step wall.

Near-Wall Velocity. The streamwise and spanwise velocities were measured near the step wall at fixed planes parallel to this wall using an x-wire arrangement. The purpose of these measurements was to obtain a complete three-dimensional picture of the near-wall flow development downstream of reattachment. Figure 6 shows the streamline patterns for the plane 0.7 mm away from the wall ($y/h = -0.97$). The flow patterns are generally symmetric about the tunnel centerplane, with best symmetry belonging to the $AR = 2$ case.

Downstream of reattachment, the flow starts a slow redevelopment process. The development of the flow near the surface is unlike that of an ordinary boundary layer. High momentum fluid is constantly brought into the near-wall layer by the downward motion of the outer flow, thereby continuously increasing the streamwise velocity in this layer extending to $x/h = 13$. (The transverse motion of the outer flow towards the step wall is evident in the centerplane profiles of V which will be discussed later). Interestingly, a uniform flow region exists in the central portion of the channel only for the two smallest AR cases. For these aspect ratios, the streamwise velocity is highest in the central portion of the tunnel and it decreases towards the side walls. The opposite trend is seen for $AR = 6$ and 14 where, a tongue of low streamwise velocity

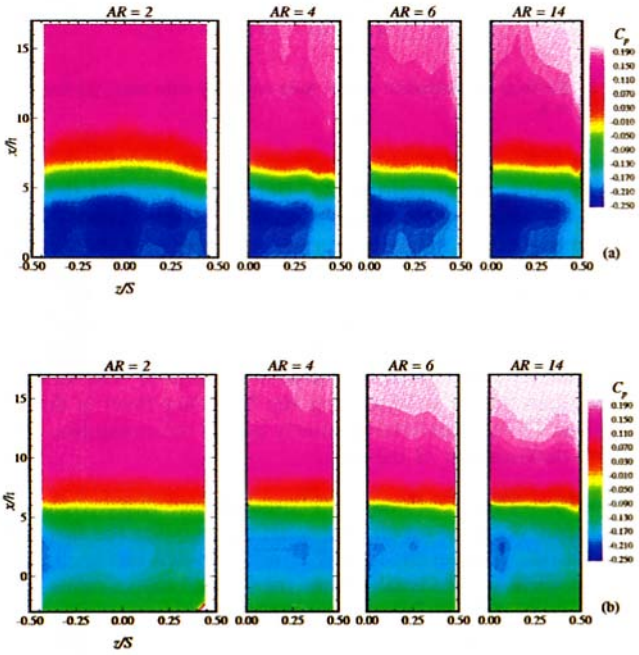

Fig. 7 Contours of wall pressure coefficient on (a) step wall; (b) flat wall. (Uncertainty of C_p is 9 percent.)

extends in the central portion of the tunnel, and maximum streamwise velocities occur on the two sides, away from the centerplane. The secondary flow pattern persists downstream of reattachment. Its spanwise location and extent depend on the aspect ratio. Naturally, the relative extent of the secondary flow is larger for smaller aspect ratios. It is believed that this secondary flow is the cause of the maximum streamwise velocities occurring away from the centerplane for larger aspect ratios. It creates an upwash adjacent to the side walls and a downwash near the centerplane thereby bringing higher velocity fluid closer to the step wall. For larger aspect ratios, the spanwise extent of the secondary flow is smaller than the half-span of the tunnel and thus, the region of high streamwise velocity forms away from the centerplane.

Wall Static Pressure. Figure 7 shows contours of the mean static pressure coefficient on both the step and the flat walls for several aspect ratios. Full span contours are shown for $AR = 2$, while these pressure distributions are shown for only half-span of the tunnel for all other aspect ratios due to symmetry of the flow. The reference static pressure, P_0, was obtained at the centerplane of the duct at a location, $x/h = -3.14$, upstream of the step. Ahead of the step, a small favorable pressure gradient exists to drive the flow through the upstream duct. Downstream of the expansion, the bulk velocity drops leading to an increase in the mean static pressure. The recovery pres-

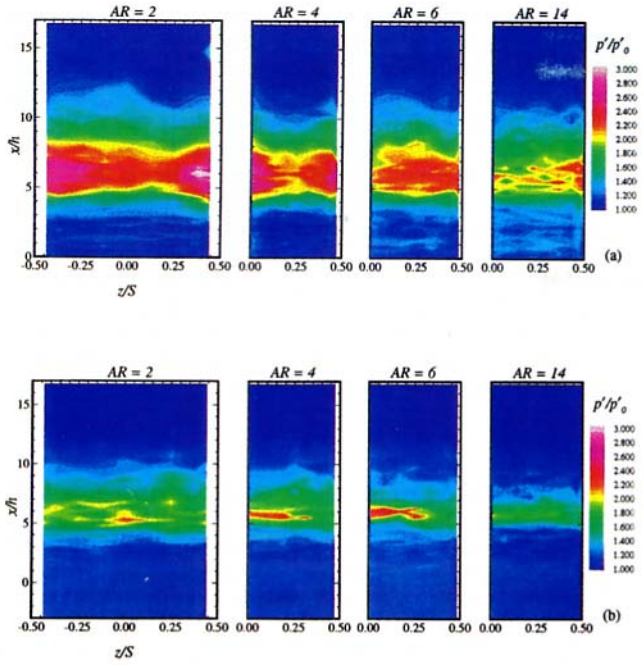

Fig. 8 Contours of fluctuating wall pressure on (*a*) step wall; (*b*) flat wall. (Uncertainty of (p'/p'_0) is under 20 percent.)

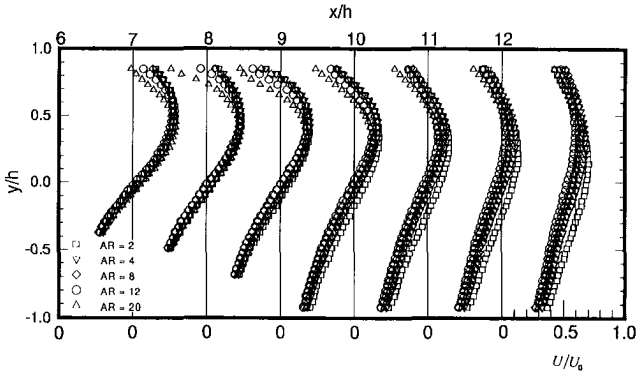

Fig. 9 Profiles of centerplane mean streamwise velocity. (Uncertainty of *U* is 2 percent.)

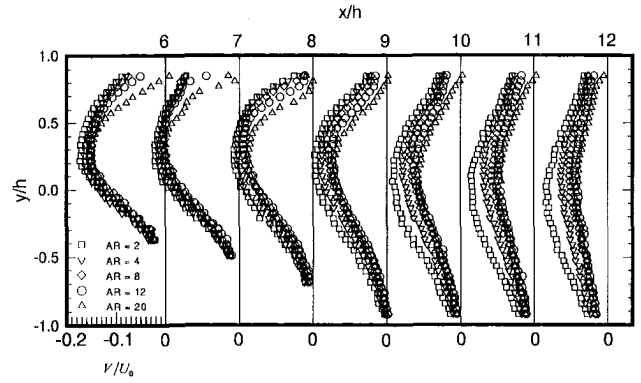

Fig. 10 Profiles of centerplane mean transverse velocity. (Uncertainty in *V* is 3 percent.)

sure downstream of the reattachment region reaches a maximum at a streamwise location of $x/h \approx 17$. Further downstream, the mean static pressure decreases monotonically as the recovery from the sudden expansion is completed. In the region of separation, the static pressure on the step wall is slightly smaller than that on the flat wall. This is due to the local flow acceleration around the step edge (Fig. 2). The effect of the aspect ratio on C_p is apparent especially with respect to the recovery pressure downstream of reattachment. As *AR* becomes smaller, the recovery pressure decreases as a result of the viscous effects. In Fig. 7, the spanwise alternating high and low pressure zones in the region $0 \leq x/h \leq 4$ on the step wall is caused by the counter rotating eddies observed in the surface visualizations (see Fig. 5).

The fluctuating wall pressure within the separated flow region immediately downstream of the step ($x/h < 3$) remains constant and its level is comparable to that upstream of the step (Fig. 8). Further downstream, the separated shear layer impinges on the step wall creating a region of high pressure fluctuations. The location of maximum pressure fluctuations is slightly upstream of the mean reattachment line. The unsteady nature of the reattachment process, and the large roll-up structures embedded in the separated shear layer contribute to the fluctuating pressure levels in this region. The impact due to reattachment is also felt by the flat wall, albeit with reduced intensity. For $AR = 14$, maximum pressure fluctuations are observed near the side wall. Away from the wall, however, maximum levels of p'/p'_0 are approximately uniform over the span of the tunnel. As the aspect ratio decreases, both the level and the zone of the large pressure fluctuations increase. For $AR = 4$, maximum levels of p/p'_0 are observed at the centerplane. A further reduction in the aspect ratio leads to a decrease in the maximum centerplane fluctuating pressure.

Centerplane Velocity. The evolution of the mean streamwise velocity downstream of reattachment is shown in Fig. 9. The effect of the aspect ratio on the centerplane profiles is moderate. Two features stand out in Fig. 9: (i) reduced velocities near the top flat wall for the two largest aspect ratios in the region $x/h < 10$, and (ii) increased velocities in the lower half of the tunnel for the smaller aspect ratios in the region $x/h > 9$. The reduced velocity near the flat wall for $AR = 20$ and 12 may be attributed to the recovery from the flat wall recirculating bubble. The recirculation zones tend to occur around $x/h \approx 5$. They are strong, continuous strips for large aspect ratios, while for small aspect ratios, they tend to be made up of multiples of weak isolated strips eventually vanishing for $AR < 4$. In the case of $AR = 20$, the velocity recovery is relatively slow and extends to about $x/h = 10$. For $x/h > 10$, the velocity profiles are quite similar for all aspect ratios except for $AR = 2$ and 4. For these aspect ratios, the mean streamwise velocity is fuller, especially in the lower half of the tunnel. This is an indication of the three-dimensionality of the flow for the smallest aspect ratios. It is noted that for all aspect ratios larger than four, the deviation from the two-dimensional profiles is quite small, indicating only a minor side wall effect on the centerplane mean velocity. The present hot-wire results of mean streamwise velocity compare well, both qualitatively and quantitatively, with the LDV results of Stevenson et al. (1984) for $AR = 2$. Figure 10 shows the profiles of the mean transverse velocity. The trend in the transverse velocity distributions is similar to that observed in the streamwise velocity profiles. For larger aspect ratios, the downward mean motion of the fluid near the flat wall is reduced due to the recovery from the flat wall recirculating bubble. On the other hand, the shorter reattachment lengths associated with the smaller aspect ratios (Fig. 4) may also have a role on the comparatively large negative transverse velocities observed near the flat wall for the smaller aspect ratios. The large transverse mean velocity magnitude seen in $AR = 2$ and 4 further downstream is possibly due to the still persistent secondary flow pattern. This is consistent with the near-wall velocity and step wall fluctuating pressure results presented earlier (Figs. 6 and 8, respectively). For the larger aspect ratios ($AR > 4$) on the other hand, the centerplane mean velocities

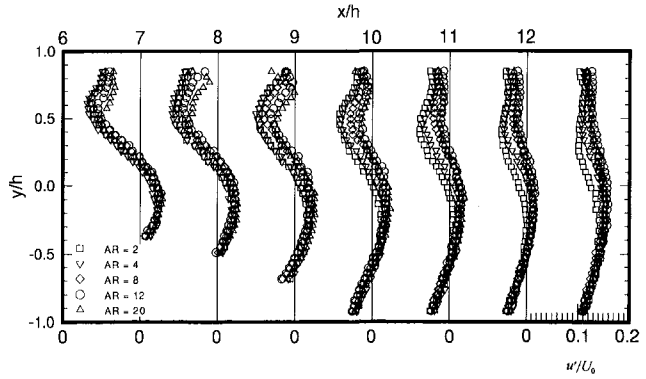

Fig. 11 Profiles of centerplane turbulent streamwise velocity. (Uncertainty of u' is 3 percent.)

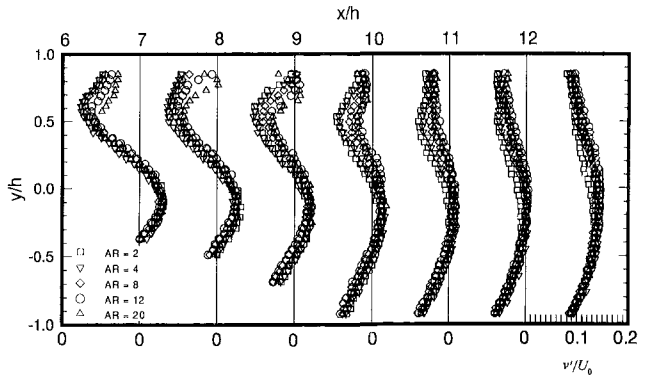

Fig. 12 Profiles of centerplane turbulent transverse velocity. (Uncertainty of v' is 3.5 percent.)

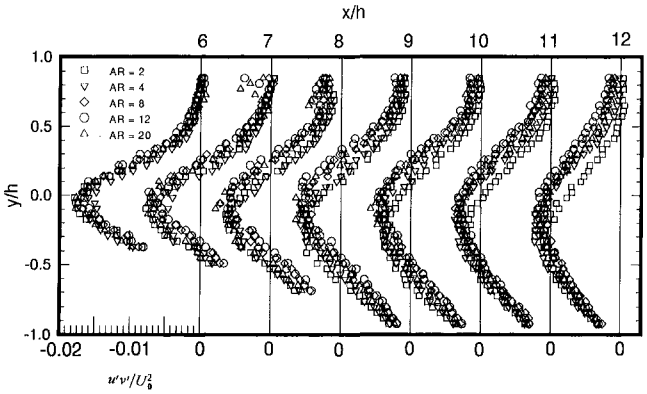

Fig. 13 Centerplane profiles of the Reynolds shear stress. (Uncertainty of $u'v'$ is 5 percent.)

are not influenced by the side wall effects and thus, the decay of the transverse velocity is fairly rapid.

The distributions of the turbulent velocities u' and v' are shown in Figs. 11 and 12, respectively. The trends in the two distributions are nearly identical. Turbulence intensities exhibit maxima around the locations of maximum mean strain rate and assume their minimum values where the mean streamwise velocity gradient is zero. In addition to the trends, the quantitative levels of u' and v' are also nearly identical throughout the reattachment and redevelopment regions. Overall, the influence of AR on the centerplane turbulence intensities is quite small.

The Reynolds shear stress, $u'v'$, distributions are shown in Fig. 13. Again, the profiles of the Reynolds shear stress show maxima around the locations of maximum $\partial U/\partial y$ in Fig. 9. The profiles for all aspect ratios collapse very well at $x/h = 6$. However, the agreement between these profiles are not as strong further downstream. It is interesting to note that smaller aspect ratios do not lead to higher turbulent shear stress levels on the centerplane as one would expect simply due to the presumed increase in turbulence activity fueled by the secondary flow. Another interesting feature of the profiles is that $u'v'$ is negative even in the upper portion of the tunnel where the mean streamwise velocity gradients are negative. This trend goes counter to the gradient transport concept of turbulent momentum, at least in this region of the flow. Clearly, in this recovery region, the turbulence is far from being in a state of equilibrium. This may have significance since it puts into question the ability of computational models of turbulence which are based on the gradient transport relation.

Conclusions

From the surface visualizations obtained on all four walls surrounding the flow, a model of this complex flow is constructed as shown in Fig. 5. At the tunnel centerplane, the separated shear layer reattaches to the step wall approximately 8.2 step heights downstream from the step for aspect ratios larger than 10. For $AR < 10$, however, the reattachment length becomes shorter with smaller aspect ratios. Adjacent to the side walls, the nearly dead flow zone defining reattachment is lifted away from the step wall. The flow downstream of reattachment can be characterized as three-dimensional. A lack of uniformity in the spanwise distributions of velocity and wall pressure is observed in the region of reattachment and further downstream even for large aspect ratios ($AR > 10$). It is believed that the stream-aligned vortex which forms at the corner of the step edge and side wall is the principal mechanism which causes the nonuniform spanwise flow structure. The vortex creates a secondary flow pattern which grows spatially with downstream distance. It moves fluid upwards near the side walls and downwards (towards the step wall) near the tunnel centerplane. As a result of this motion, the spanwise location of the maximum fluctuating wall pressure moves towards the tunnel centerplane as the aspect ratio decreases. At $AR \approx 4$, the maximum pressure fluctuations occur at the centerplane. For this aspect ratio, it appears that the two vortices coincide at the centerplane and constructively impinge on the step wall. However, a further reduction in the aspect ratio forces the two vortices closer together thus resulting in the destructive interference of the two. This causes a reduction in the fluctuating pressure levels, as observed in Fig. 8 (a). The secondary flow also affects the mean streamwise and spanwise velocities near the step wall. While the high near-wall streamwise velocities occur at the centerplane for $AR < 6$, the zone of high streamwise velocity moves towards the side walls for larger aspect ratios. The recovery pressure downstream of flow reattachment decreases with decreasing aspect ratios, again due to the three-dimensional side wall effects. These side wall effects are also evident in the evolution of the mean centerplane profiles of streamwise and transverse velocities. Finally, the centerplane profile of the Reynolds shear stress $u'v'$ indicates that the gradient transport concept of turbulent momentum is not valid in the redevelopment region.

References

Armaly, B. F., Durst, F., Pereira, J. C. F., and Schonung, B., 1983, "Experimental and Theoretical Investigation of Backward-Facing Step Flow," *Journal of Fluid Mechanics*, Vol. 127, pp. 473–496.

Badawy, M. T., El, S., Jesek, J., and Topinka, P., 1989, "Visualization of a Backward-Facing Step Flow," *Proceedings of the Fifth International Symposium on Flow Visualization, Prague*, Chechoslovakia, p. 436.

Berbee, J. B., and Ellzey, J. L., 1989, "The Effect of Aspect Ratio on the Flow over a Rearward-Facing Step," *Experiments in Fluids*, Vol. 7, pp. 447–452.

Brederode, V. de, and Bradshaw, P., 1972, "Three-Dimensional Flow in

Nominally Two-Dimensional Separation Bubbles; I. Flow Behind a Rearward-Facing Step," Imperial College of Science and Technology, Aero Report 72–19.

Jesek, J., and Reznicek, R., 1987, "Visualization of a Backward-Facing Step Flow," *Flow Visualization IV*, C. Veret, ed., Hemisphere, Washington D.C., pp. 365–370.

Lim, K. S., Park, S. O., and Shim, H. S., 1990, "A Low Aspect Ratio Backward-Facing Step Flow," *Experimental Thermal Fluid Science*, Vol. 3, pp. 508–514.

Ötügen, M. V., 1991, "Expansion Ratio Effects on the Separated Shear Layer and Reattachment Downstream of a Backward-Facing Step," *Experiments in Fluids*, Vol. 10, pp. 273–280.

Ötügen, M. V., Papadopoulos, G., Vradis, G. C., and Muchenthaler, G., 1992, "Spanwise Characteristics of the Separated Flow in a Suddenly Expanding Duct," *Experiments in Fluids*, Vol. 14, pp. 213–216.

Papadopoulos, G., 1994, "The Three-Dimensional Turbulent Flow Past a Backward-Facing Step," Ph.D. Dissertation, Polytechnic University, Aerospace Engineering Department.

Papadopoulos, G., and Ötügen, M. V., 1993, "A Simple Automated Hot-Wire Repositioning Technique for Near-Wall Measurement," *Experiments in Fluids*, Vol. 15, pp. 459–461.

Stevenson, W. H., Thompson, H. D., and Craig, R. R., 1984, "Laser Velocimeter Measurements in Highly Turbulent Recirculating Flows," ASME JOURNAL OF FLUIDS ENGINEERING, Vol. 106, pp. 173–180.

Westphal, R. V., and Johnston, J. P., 1984, "Effect of Initial Conditions on Turbulent Reattachment Downstream of a Backward-Facing Step," *AIAA Journal*, Vol. 22, pp. 1727–1732.

Relationship Between Unsteady Flow, Pressure Fluctuations, and Noise in a Centrifugal Pump—Part A: Use of PDV Data to Compute the Pressure Field

S. Chu

R. Dong

J. Katz

Department of Mechanical Engineering,
The Johns Hopkins University,
Baltimore, MD 21218

Velocity distributions determined by using Particle Displacement Velocimetry are used for computing the pressure field within the volute of a centrifugal pump. It is shown that blade-tongue interactions and nonuniform outflux from the impeller are primary contributors to local pressure fluctuations and far field noise. Consequently, a slight increase in the space between the impeller and the tongue causes significant changes in flow structure and reductions in the resulting noise. The impact is significant as long as the tongue-impeller gap is less than 20 percent of the impeller radius. It is also shown that the vorticity distributions, particularly the large vortex trains associated with the jet/wake phenomenon, dominate variations in the total pressure. Thus, it is unlikely that a potential flow model can provide any realistic description of the flow structure.

Introduction

Background. The present paper is the first of a series of publications dealing with the relationship between unsteady flow structure, pressure fluctuations, and noise generation within centrifugal pumps. It follows earlier observations (Dong et al., 1992 and Chu et al., 1993) that characterized the flow in different sections of the volute. Based on the results, the present study focuses on blade-tongue interactions. The available literature on this subject is scarce, and to the best of our knowledge there isn't even a single source that provides data in sufficient detail to determine the impact of the flow structure on the pressure field. The few available LDV measurements (Miner et al., 1989, 1992, Cader et al., 1992, for example) demonstrate some of the characteristics of the flow, but do not deal with the pressure. Conversely, detailed surface pressure measurements, performed for example by Tourret et al. (1991), do not provide information on the flow structure. Sources that include combined measurements, such as Yuasa and Hinata's (1979) are limited to a few points, and cannot really explain the measured spectra. Consequently, our present understanding of the impact of the flow structure on unsteady forces, vibrations, and noise is limited at best.

Even with detailed maps of the velocity distribution available, results of surface pressure measurements, performed in the same pump, are quite puzzling and difficult to explain. Figure 1(*a*), for example, contains a series of signals measured by neighboring flush-mounted transducers (description of the overall setup and the location of measurements are discussed in Dong et al., 1992a and in Part B). In spite of their proximity and similar spectra (Fig. 1(*b*)), the wave forms are considerably different. Temporal correlations between signals (see a sample in Fig. 1(*c*)) show some dependence on blade orientation, but the correlations are much higher at different times. Furthermore, the relationship to the local velocity is unclear, and it is apparent that to understand the pressure distribution one needs an overall, detailed description of the entire flow structure. When such information is available, by using PDV for example, it is possible to compute the pressure distribution from the velocity field if the pressure at a single point is known. The results enable identification of specific flow phenomena that dominate the pressure field and far field noise. The present study describes such a process. It is divided to two parts. In the first we describe the process of computing the pressure field, and compare the results to measurements in selected points. The second part focuses on the results, namely, on the impact of the flow structure on the pressure field. Once dominating phenomena have been identified, a following paper deals with modifications to the geometry of the tongue, and their impact on flow structure, pressure fluctuations, and noise.

Computing the Pressure Field From the Velocity. The phase averaged pressure can be computed by using the Reyn-

Contributed by the Fluids Engineering Division for publication in the JOURNAL OF FLUIDS ENGINEERING. Manuscript received by the Fluids Engineering Division November 8, 1993; revised manuscript received May 11, 1994. Associate Technical Editor: L. Nelik.

olds equation:

$$\frac{\partial p}{\partial x_i} = -\rho\left[\frac{\partial u_i}{\partial t} + u_j\frac{\partial u_i}{\partial x_j} + \frac{\partial}{\partial x_j}(\overline{u_i' u_j'})\right] \quad (1)$$

The viscous stresses are neglected here due to the high Reynolds number, and in part also due to the large error associated with use of second-order derivatives of a measured quantity (accuracy will be discussed later). Turbulence is defined here as deviations of the instantaneous velocity at a certain impeller orientation from the phase averaged results. The value of u_i represents phase averaged velocity. Then, if the pressure is known at one point (x_0, y_0, z_0), it can be estimated at any other point by integrating Eq. (1). Nondimensionalizing this using the impeller radius, R_T, and the tip speed, U_T, as reference length and velocity scales, respectively, results in the following dimensionless equation:

$$\frac{p(x_i, t) - p(x_{0i}, t)}{\rho U_T^2} = -\frac{1}{U_T^2}\int_{(x_{0i},t)}^{(x_i,t)}\left[\frac{\partial u_i}{\partial t} + u_j\frac{\partial u_i}{\partial x_j} + \frac{\partial}{\partial x_j}(\overline{u_i' u_j'})\right]dx_i \quad (2)$$

An exact solution requires knowledge of all three velocity components along the path of integration. Two-dimensional distributions can be obtained by using conventional PDV, but the third component has to be measured separately. In the present study we investigate the flow within a two-dimensional volute of a centrifugal pump. This geometry does not insure, of course, that the flow is two dimensional. However, as the results show, in most cases the dominating terms of Eq. (2) can be computed from the velocity distribution in a plane normal to the axis of the pump (in selected sections we measured all three components). In fact even the turbulent terms are small as long as the integration is performed along a short path.

Without the turbulent and "out-of-plane" terms, Eq. (1) can be rewritten as:

$$\frac{\partial u}{\partial t} - \nu\xi_z = -\frac{\partial}{\partial x}\left[\frac{p}{\rho} + (u^2 + v^2)/2\right]$$

$$\frac{\partial v}{\partial t} + u\xi_z = -\frac{\partial}{\partial y}\left[\frac{p}{\rho} + (u^2 + v^2)/2\right] \quad (3)$$

where $\xi_z = \partial v/\partial x - \partial u/\partial y$ is the vorticity. This expression is useful for distinguishing between vorticity and unsteady effects on the total pressure of the fluid, and should serve as a guideline as to whether potential flow models can describe the flow structure in the volute. As will be shown shortly, in most cases the vorticity term is dominant along a path which is approximately normal to the streamlines. Thus, potential flow models cannot be used for describing this flow without significant errors.

Experimental Setup

Test Facility. The experiments were performed in a pump flow visualization facility, which is described in detail by Dong et al. (1992). The test model was a centrifugal pump operating at 890 rpm. The impeller was 9.95 inches in diameter, and had 7 blades, all of them with an exit angle of 15 deg. The original casing of this pump was replaced with a transparent casing on its perimeter and bottom (shroud) side. The volute had constant thickness (H = 0.975 in.) which was equal to the thickness of the impeller. Thus, an attempt was made to create a two-dimensional flow, at least as far as boundary conditions were concerned.

Techniques and Procedures. Velocity measurements were performed by utilizing PDV, following procedures described in detail by Dong et al. (1992a, b). Briefly, this method consists of recording multiple exposure images of a flow field illuminated by a laser sheet and seeded with microscopic neutrally buoyant particles. The analysis consists of dividing the image into a large number of small windows, and determining the mean shift of all the particles within each window by computing the auto-correlation function of the intensity distribution. Calibration experiments have shown that the uncertainty level can be kept at about 1 percent, provided certain conditions associated with particle density and magnification are satisfied. The region sampled during the present study is outlined in Fig. 2(b), and a schematic illustration of the optical setup in the pump facility is presented in Fig. 2(a). The thickness of the laser sheet is 1 mm, and it can illuminate any section of the volute through the transparent perimeter or bottom. The images are recorded by a 35 mm camera. Three laser pulses, typically delayed by 160 μs, were used for recording a single image. The timing of each laser pulse was synchronized with orientation of the impeller by installing an encoder on the shaft of the pump.

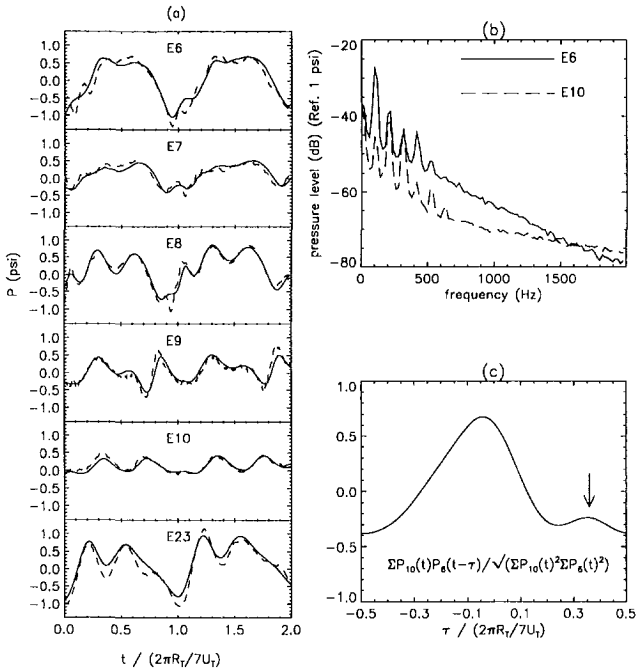

Fig. 1 (*a*) Measured pressure fluctuations at different locations (indicated in Fig. 2). Dashed line: instantaneous; continuous line: phase averaged. (*b*) Power spectra of pressure fluctuations at E6 and E10. (*c*) Their temporal correlation; the arrow marks the peak associated with blade passage

Pressure fluctuation measurements were performed on the upper (hub side) surface, mostly with flush-mounted, 2.5 mm diameter, piezo-electric transducers (PCB model 105B02). In order to increase the spatial resolution, at one point (r/R_T = 1.07, θ = 356.9 deg) the transducer was actually installed inside a small chamber (2.5 mm diameter, and 1 mm long) located below the surface and connected to it through a 1mm diameter tap. The noise was measured with flush mounted hydrophones (PCB model 106M12) located 1 m upstream and downstream of the pump. The signal was amplified and recorded by a PC based data acquisition system. FFT was used for computing the spectra. Mean pressure measurements were performed using 0.5 mm pressure taps. The transducers were regularly calibrated, and the error level of the absolute pressure (mean + fluctuations) should be about 1 percent. In order to perform both measurements at the same point, part of the upper surface was replaced with an insert that could accommodate either the transducer or the taps. The sites of measurements are indicated in Fig. 2(b). Only part of the data is included in this paper.

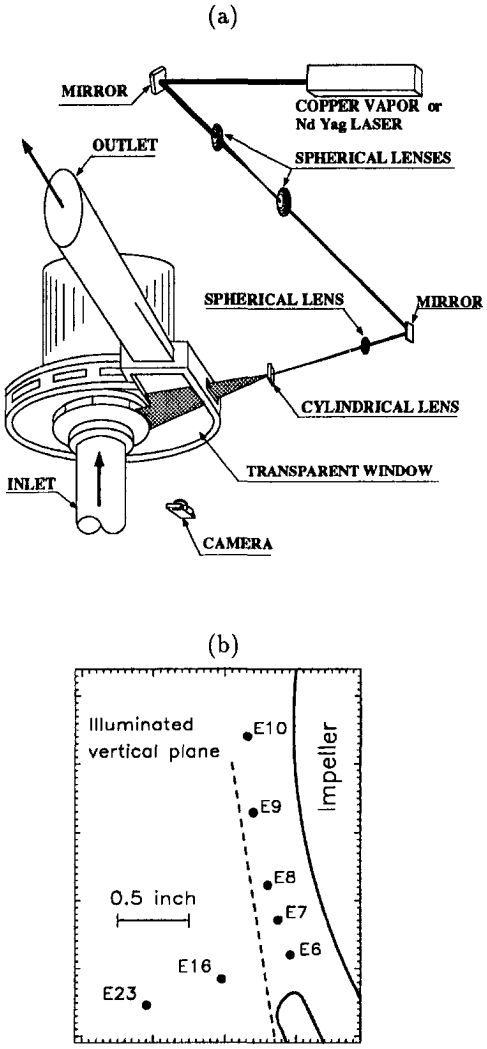

Fig. 2 Schematic description of: (*a*) the optical setup; (*b*) the location of pressure transducers and the illuminated vertical plane discussed in this paper

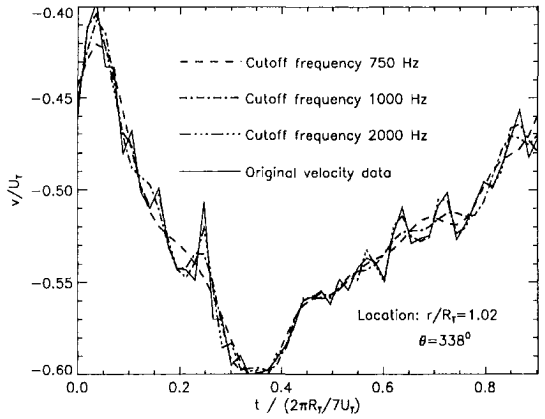

Fig. 3 Samples of original and filtered velocity at a single point

Data Required for Computing the Pressure. A careful analysis involving computations of gradients requires us to keep the dimensionless time and spatial increments comparable. Based on previous experience, the spatial increment, Δx, has been selected as 1.35 mm ($\Delta x/R_T = 0.0107$). Consequently, the time increment Δt is selected as 0.19 ms ($\Delta t U_T/R_T = 0.0177$), which is the time required for the impeller to rotate by 1.01 deg. Since most of the spectrum (Fig. 1) is concentrated well below 5 KHz, this time scale should be short enough to cover all the significant spatial and temporal variations. Thus, 51 sets of images were recorded every 1 deg of impeller orientation, covering an entire blade passage. At least 12 images were analyzed at each angle in order to calculate the phase averaged velocity distribution. This number was selected by estimating the number of measurements required to keep the variation resulting from an additional measurement at about 1 percent, the error level of the velocity measurements. Velocity fluctuations and Reynolds stresses were then estimated as the mean deviation of the instantaneous data from the phase averaged results.

PDV measurements provide only two velocity components in the center plane of the volute (u and v in cartesian coordinates and v_r, v_θ in cylindrical coordinates). Values of w, the axial velocity, are known only in selected sections (Dong et al., 1992 and Chu et al., 1993). The results (not shown here) show that in regions located away from the immediate vicinity of the tongue w is an order of magnitude smaller than v_θ, and is also smaller than v_r. Near the tongue v_r and w are comparable, but still v_θ is considerably higher. Thus, the terms that we cannot determine in Eq. (2) $w\partial v/\partial z$ and $w\partial u/\partial z$, are much smaller than $v\partial v/\partial y$, and $v\partial u/\partial y$. For the most part they are also considerably smaller than $u\partial v/\partial x$ and $u\partial u/\partial x$. However, we computed the values of $w\partial v/\partial z$ and $\partial(w'v')/\partial z$ along one line of integration, for which we had all the 3-D data. The results were used for evaluating the error introduced by omitting terms that include the axial derivatives.

Procedures for Computing the Pressure. A simple approach to estimate the time derivatives in Eq. (2) is to compute $[v(t + \Delta t) - v(t - \Delta t)]/2\Delta t$. However, derivatives computed in this fashion (by comparing the velocity in different vector maps) introduce "jitters", caused by subtraction of numbers of similar magnitudes. Consequently, a smoothing scheme is necessary. Since significant pressure fluctuations extend up to about 700–800 Hz, and the velocity is sampled essentially at 5.3 KHz (the blade rate frequency is 104 Hz), one can still utilize a low pass filter without eliminating significant phenomena. The process involves computation of the Fourier transform, using FFT, for all the 51 data points at a specific location. Then, a cutoff frequency, ranging between 500–2000 Hz is selected, the spectrum is filtered (we selected a simple, top-hat filter) and converted back to the time domain. The derivative is also estimated first in the frequency domain. Examples of original and filtered data are provided in Fig. 3. Based on such results we somewhat arbitrarily selected a cutoff frequency of 750 Hz for estimating the time derivatives. At this frequency the filtered signal seems to be sufficiently smooth, but does not sacrifice relevant information. The spatial derivatives are much less jittery, due to the overlap of windows during analysis, and due to the velocity computation routines that involve comparison and matching of data in neighboring windows (Dong et al., 1992a). However, we still utilized the same filtering procedures, in order to prevent any bias in the results. The process consisted of computing the FFT using 51 points along the path of integration, and filtering the results.

Sample characteristic distributions of the terms in Eq. (2), for integration along vertical (y) and horizontal (x) pathes are presented in Figs. 4(a–e) and 5(a–e), respectively. Of the terms involved with integration along a vertical path, $\partial v/\partial t$ and $v\partial v/\partial y$ are dominant, except for a small region located near the tongue, where $u\partial v/\partial x$ is also significant. In other words, phase averaged pressure gradients occur as a result of an imbalance between the unsteady and vertical convective terms in the Reynolds equation. Similarly, in integrations along a horizontal path $\partial u/\partial t$ and $v\partial u/\partial y$ are dominant, and $u\partial u/\partial x$ is small. The turbulent terms are for the most part insignificant.

A comparison between the measured phase-averaged surface pressure and the computed values, at two selected points, are

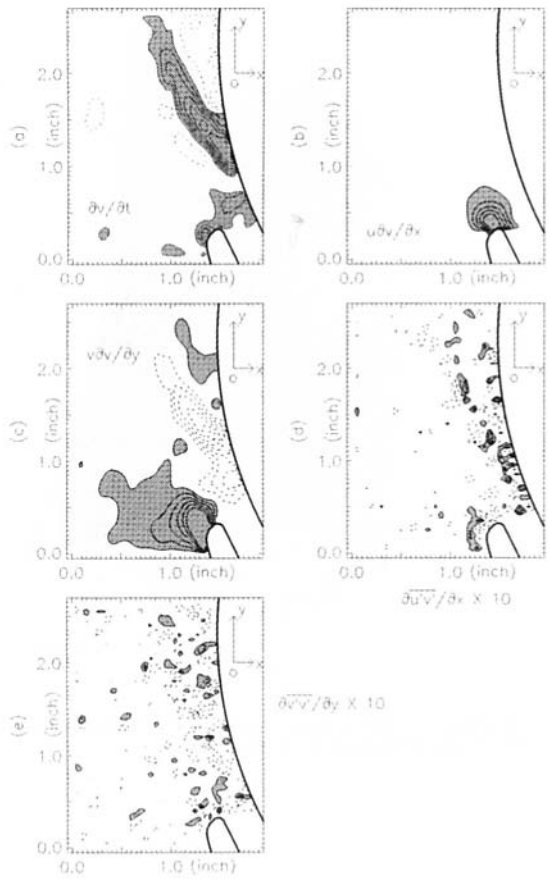

Fig. 4 Terms involved in vertical integration of the Reynolds equation when the blade is at 10 deg. (Dark shade: negative; light shade: positive. Increment between lines is 0.2 U_T^2/R_T.)

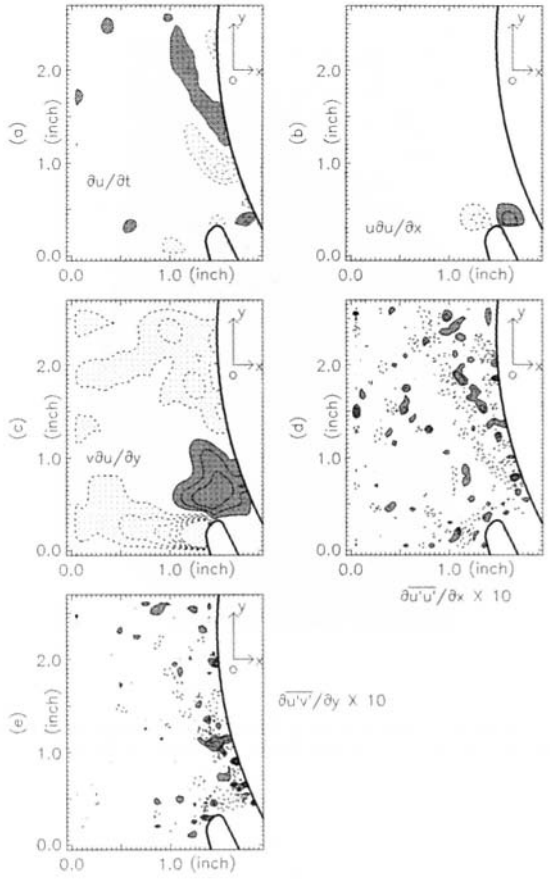

Fig. 5 Terms involved in horizontal integration of the Reynolds equation when the blade is at 10 deg. (Dark shade: negative; light shade: positive. Increment between lines is 0.2 U_T^2/R_T.)

presented in Fig. 6. In both cases (and for the rest of our analysis), the starting point is E10 (r/R_T = 1.07 and θ = 341.2 deg), and the two selected examples represent the largest distance from the starting point within the sampled section, in which the pressure is measured. In both cases the agreement is quite good, especially in view of the assumptions made, and since we compare surface pressure measurements to computations determined from data recorded at the center plane of the volute. A contour map of the pressure distribution, determined from the data presented in Figs. 4 and 5, is presented in Fig. 7. Other pressure distributions, and detailed explanation on how they are related to the flow field, are presented in Part B of this paper.

As noted before, in order to demonstrate the impact of neglecting the terms involving the axial velocity we calculated the pressure distribution along a path for which we had all three velocity component. This path is marked with a dashed line in Fig. 2(*b*). For most of the flow field the values of w, the axial velocity, vary between 1–2 percent of U_T. Only at the intersection of the tongue with the shroud w increases to 6–8 percent. At the center plane w/U_T never exceeds 2 percent. Values of $w\partial v/\partial z$ and $\partial(w'v')/\partial z$ were computed from the axial distributions, and the impact of these terms on the pressure field is demonstrated in Fig. 8. At least along the path of integration this effect is negligible. However, around the tongue, particularly near the impeller, there are regions where $w\partial v/\partial z$ is significant (data not shown here, some axial distributions are presented by Dong et al., 1992b and Chu et al., 1993). Consequently, in computations involving points located near the tongue, we always choose a path that minimizes the use of data in this region.

It is also interesting to demonstrate the impact of the vorticity on the pressure field. For this purpose, Eq. 3 is used for computing the total pressure ($p/\rho + (u^2 + v^2)/2$) and a sample result presented in Fig. 9. The relevant temporal derivatives can be found in Figs. 4 and 5, and the dimensionless values of $v\xi_z$ and $u\xi_z$ are presented in Fig. 10. As expected, along a

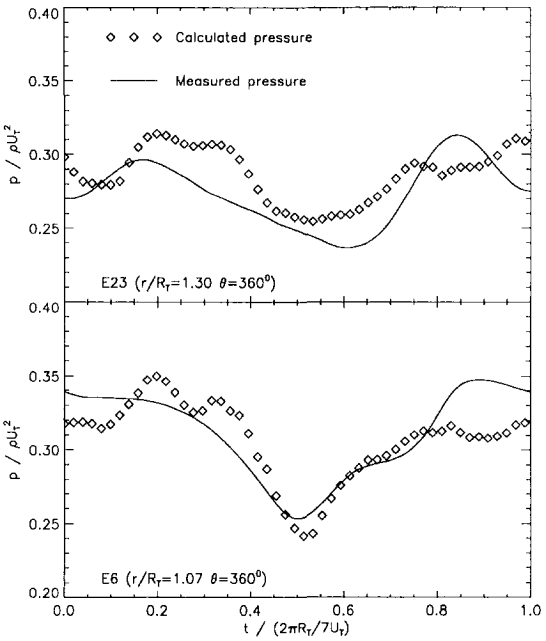

Fig. 6 Comparison of measured and calculated pressure at two locations

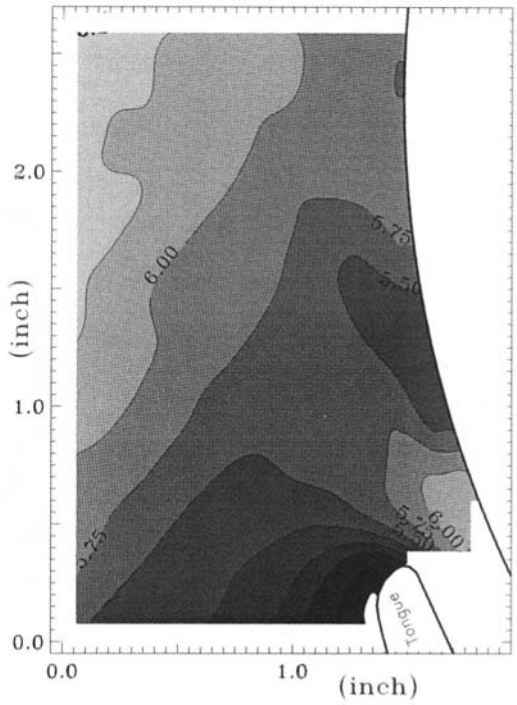

Fig. 7 A sample contour map of the calculated pressure distribution (in psi) at Q/Q_{DESIGN} = 1.35 and blade orientation of 10 deg

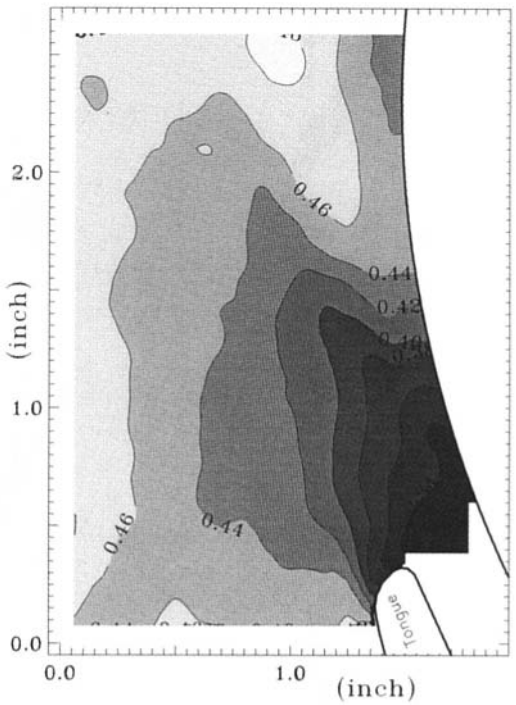

Fig. 9 A sample contour map of $\{p/\rho + (u^2 + v^2)/2\}/U_T^2$ at Q/Q_{DESIGN} = 1.35 and blade orientation of 10 deg

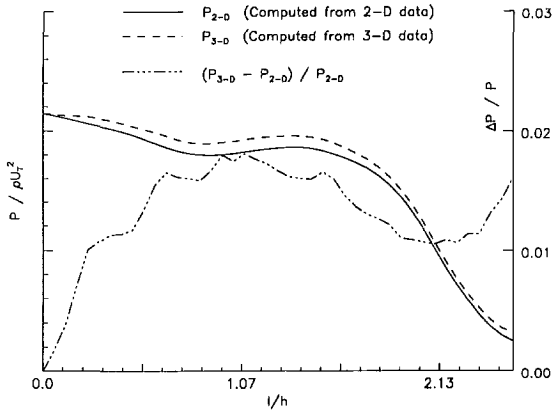

Fig. 8 Comparison of the pressure calculated along the path defined in Fig. 2(*b*) with and without the terms involving the axial velocity

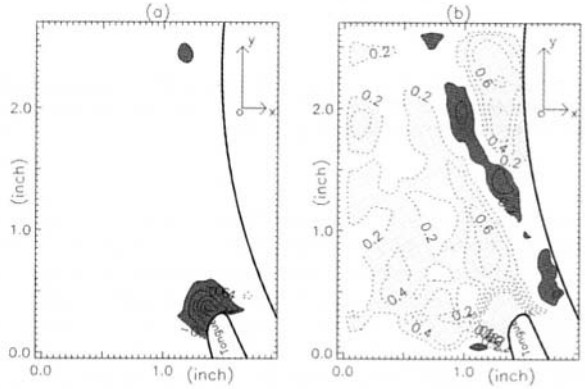

Fig. 10 (*a*) $u\xi_z$ and (*b*) $-v\xi_z$ distributions at Q/Q_{DESIGN} = 1.35 and blade orientation of 10 deg

vertical path, which is almost parallel to the streamlines in most of the flow field, $\partial v/\partial t$ is much larger than $u\xi_z$. However, along a horizontal path $\partial u/\partial t$ is comparable to $v\xi_z$ only near the impeller and the tongue. In any other region $v\xi_z$ is much larger. For example, when the blade is at 11^0 and 21^0 the vorticity field, particularly the vortex trains (see Part B), dominates the variations in total pressure. Thus, it is unlikely that a potential flow model can provide any realistic description of the flow structure.

Error Analysis. As noted before, we have to use Fourier transform and filtering at 750 Hz to reduce the "jitter" in the time derivatives. This smoothing routine actually reduces our error as explained in this section. The Fourier series expansion of the measured velocity, $U(t_i)$, is:

$$U(t_i) = \frac{a_0}{2} + \sum_{n=1}^{25}\left[a_n \cos\left(2n\pi\frac{t_i}{T}\right) + b_n \sin\left(2n\pi\frac{t_i}{T}\right)\right] \quad (4)$$

where $i = 0, \ldots, 50$; $T = 9.6308 \times 10^{-3}$ s; $t_i = iT/50.0$. Using FFT the uncertainties in the values of a_n and b_n are:

$$\Delta a_n = \left[\left(\frac{\Delta t}{\pi}\right)^2 \sum_{i=0}^{50} \cos^2\left(2n\frac{t_i}{T}\right)\Delta U(t_i)\right]^{1/2} \quad (5)$$

$$\Delta b_n = \left[\left(\frac{\Delta t}{\pi}\right)^2 \sum_{i=0}^{50} \sin^2\left(2n\frac{t_i}{T}\right)\Delta U(t_i)\right]^{1/2} \quad (6)$$

where $\Delta U(T_i)$, the uncertainty in velocity measurements is about 1 percent, and $\Delta t = T/50.0$. The error in $\partial U(t_i)/\partial t$ is:

$$\Delta\left[\frac{\partial U(t_i)}{\partial t}\right] = \left(\sum_{n=1}^{25}\left[-\frac{2n\pi}{T}\sin\left(2n\pi\frac{t_i}{T}\right)\Delta a_n\right]^2 + \sum_{n=1}^{25}\left[\frac{2n\pi}{T}\cos\left(2n\pi\frac{t_i}{T}\right)\Delta b_n\right]^2\right)^{1/2} \quad (7)$$

Since n now is a coefficient of each term, higher order terms have increasing impact on the uncertainty for similar values of Δan and Δbn. Filtering the signal at 750 Hz that, as Fig. 3 shows, does not affect trends in the velocity, reduces the max-

imum value of n form 25 to 7. A characteristic value for $(r_T/U_T^2)\Delta(\partial U(t_i)/\partial t)$, calculated with n varying between 1 and 7, is 0.016. If all the higher order terms are kept, the error is 10–20 times larger, which means that the calculated derivatives are meaningless. Similar results are obtained for all the other spatial and temporal derivatives.

The Reynolds stresses, $\overline{u_i' u_j'}$, which are estimated from:

$$u_i' = \left(U_i - \frac{1}{N} \sum U_i \right); \quad N = 12 \tag{8}$$

result in uncertainties of $\Delta u' = 0.014\ \bar{U}$ and $\Delta \overline{u_i' u_j'} = 0.017\ \bar{U}^2$. Dimensionless gradients of stress, computed using Fourier transform and filtering, are typically about 0.0066.

During a single integration step (δy) the pressure changes by δp, and the associated uncertainty can be estimated from:

$$\left(\Delta \frac{\delta p}{\delta y}\right)^2 = \left(\Delta \frac{\partial V}{\partial t}\right)^2 + \left(U\Delta \frac{\partial V}{\partial x}\right)^2 + \left(\frac{\partial V}{\partial x}\Delta U\right)^2 + \left(V\Delta \frac{\partial V}{\partial y}\right)^2 + \left(\frac{\Delta V}{\partial y}\Delta V\right)^2 + \left(\Delta \frac{\partial \overline{u'v'}}{\partial x}\right)^2 + \left(\Delta \frac{\partial \overline{v'v'}}{\partial y}\right)^2 \tag{9}$$

Typical values vary between 3 to 20 percent. In sites with relative error above 10 percent, the primary cause is a very small $\delta p/\delta y$. In regions with significant pressure change, the relative error is well below 10 percent.

Summary and Conclusions

Velocity distributions obtained using PDV have been used successfully for computing the pressure field within the volute of a centrifugal pump. This procedure enables direct comparison between the flow structure and the pressure field. For the flow conditions relevant to the present study, two-dimensional data is for the most part sufficient for obtaining correct results. In regions located away from the tongue pressure gradients occur as a result of imbalance between the unsteady terms ($\partial v/\partial t$ and $\partial u/\partial t$) and convection in the vertical direction ($v\partial v/\partial y$ and $v\partial u/\partial y$, respectively). This trend is a result of differences in the magnitudes of v ($\sim -v_\theta$) and u ($\sim -v_r$). The turbulent terms are insignificant. Distributions of total energy and the terms affecting them show that in a direction normal to the stream line, one cannot neglect the effect of the vorticity. Thus, potential flow model cannot provide an acceptable description of the flow. The paper includes also a detailed error analysis, that shows that the uncertainty in the computed pressure is for the most part less than 10 percent.

Acknowledgment

This research is sponsored by the Office of Naval Research, under contract number N00014-89-J-1672.

References

Cader, T., Masbernat, O., and Roco, M. C., 1992, "LDV Measurements in a Centrifugal Slurry Pump: Water And Dilute Slurry Flows," ASME JOURNAL OF FLUIDS ENGINEERING, Vol. 114, pp. 606–615.

Chu, S., Dong, R., and Katz, J., 1993, "The Effect of Blade-Tongue Interactions on The Flow Structure, Pressure Fluctuations and Noise Within a Centrifugal Pump," *1st International Symposium on Pump Noise and Vibrations*, Paris, France, July 7–9.

Dong, R., Chu, S., and Katz, J., 1992, "Quantitative Visualization of The Flow Structure Within The Volute of a Centrifugal Pump," Part A: Technique, ASME JOURNAL OF FLUIDS ENGINEERING, Vol. 114, No. 3, pp. 390–395.

Dong, R., Chu, S., and Katz, J., 1992, "Quantitative Visualization of The Flow Structure Within The Volute of a Centrifugal Pump, Part B: Results," ASME JOURNAL OF FLUIDS ENGINEERING, Vol. 114, No. 3, pp. 396–403.

Miner, S. M., Beaudoin, R. J. and Flack, R. D., 1989, "Laser Velocimeter Measurements in a Centrifugal Flow Pump," *Journal of Turbomachinery*, Vol. 111, pp. 205–212.

Miner, S. M., Flack, R. D., and Allaire, P. E., 1992, "Two Dimensional Flow Analysis of A Laboratory Centrifugal Pump," ASME *Journal of Turbomachinery*, Vol. 114, pp. 333–339.

Tourret, J., Kamga, M., Godefroi, B., Kermarec, J., Pluviose, M., and Bertinier, M., 1991, "Hydraulic Noise Generation Studies in Centrifugal Turbomachine Through Visualization of The Non Stationary Pressure Field in The Volute and in the Impeller," *Experimental and Numerical Flow Visualization*, ASME FED- Vol. 128 pp. 239–246.

Yuasa, T., and Hinata, T., 1974, "Fluctuating Flow Behind The Impeller of Centrifugal Pump," *Bulletin of JSME*, Vol. 22, pp. 1746–1753.

Relationship Between Unsteady Flow, Pressure Fluctuations, and Noise in a Centrifugal Pump—Part B: Effects of Blade-Tongue Interactions

S. Chu

R. Dong

J. Katz

Department of Mechanical Engineering,
The Johns Hopkins University,
Baltimore, MD 21218

Maps of pressure distributions computed using PDV data, combined with noise and local pressure measurements, are used for identifying primary sources of noise in a centrifugal pump. In the vicinity of the impeller pressure minima occur around the blade and near a vortex train generated as a result of non-uniform outflux from the impeller. The pressure everywhere also varies depending on the orientation of the impeller relative to the tongue. Noise peaks are generated when the pressure difference across the tongue is maximum, probably due to tongue oscillations, and when the wake impinges on the tip of the tongue.

Introduction

There are numerous possible sources of unsteady loading, vibrations and noise within a pump. As shown in Dong et al., (1992a and b), the entire flow within the volute and the leakage between the tongue and the impeller are "pulsating" and depend on the location of the blade relative to the tongue. Blade effects are particularly evident near the impeller (at $r/R_T < 1.2$, R_T being the impeller radius), where the flow is dominated by the jet/wake phenomenon, observed before by Dean and Senoo (1960) and Eckardt (1975 and 1976). Unsteady phenomena are also associated with Blade-tongue interactions. For example, tongue induced blockage to the space between blades causes an increase in the radial velocity in the unobstructed section. The stagnation point on the tip of the tongue also fluctuates, as demonstrated also by Miner et al. (1992).

The periodic unsteady flow phenomena are also accompanied by turbulence (Dong et al., 1992b). It is particularly high at the interface between the "jet" and the "wake" and behind the blade. Angular momentum balances show that torques caused by estimated turbulent $\tau_{r\theta}$ and $\tau_{\theta\theta}$ (tangential and circumferential stresses, respectively) can be as high as 2 and 5 percent of the overall change in angular momentum flux, respectively. Turbulence production is also significant, and a considerable portion of energy losses occur within the volute.

Determining the impact of these unsteady phenomena on the pressure field and far field noise is not an easy task, as discussed in part A of this paper. The wave-form measured by the pressure transducer contains several peaks, whose origins and how they are related to the flow field are unclear. In order to remedy this problem we use PDV data to compute the pressure field. After verifying in Part A that the results are acceptable, we end up with a map of the entire pressure distribution, as well as a map of the velocity and vorticity fields causing it. As the present paper shows, this data base can be instrumental in identifying primary causes for pressure fluctuations and far field noise. Specific dominating phenomena are direct blade-tongue interactions and unsteady flow associated with the jet/wake phenomenon. Consequently, as a following paper shows, relatively small changes to the gap between the tongue and the impeller cause major changes to the entire flow structure, pressure fluctuations and "far field" noise.

Setup and Procedures

The test model was a vertical centrifugal pump operating at 890 rpm. The impeller was 9.95 in. in diameter, and had 7 blades, all of them with an exit angle of 15 deg. The configuration of the volute perimeter (in inches) was $r_v = R_T + 0.34 + 4(\theta/360 \text{ deg})$ where $\theta = 0$ deg was located 3 deg upstream of the tip of the tongue. The volute had constant thickness ($H = 0.975$ in.) which was equal to the thickness of the impeller. The 4 in. × 0.975 in. exit gradually expanded to a 4 in. pipe by using a fiberglass diffuser with maximum expansion angle of 7 deg. The design flux of this volute was 200 gpm (specific speed of 1250), but the maximum efficiency occurred at a slightly lower flux (about 190 gpm). Further detail can be found in Dong et al. (1992). Measurements were performed 35 percent above design flow rate in order to highlight nonuniformities and unsteady phenomena. Velocity measurement was performed using PDV. Data was recorded at the center plane of the volute every 1 deg of impeller orientation for the entire 51 deg of a blade passage (Fig. 1). At least 12 data sets were

Contributed by the Fluids Engineering Division for publication in the JOURNAL OF FLUIDS ENGINEERING. Manuscript received by the Fluids Engineering Division November 8, 1993; revised manuscript received May 11, 1994. Associate Technical Editor: L. Nelik.

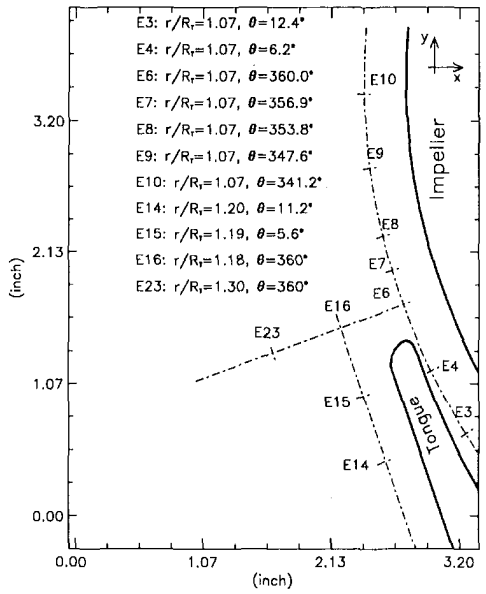

Fig. 1 A schematic description of the sample area and location of pressure transducers

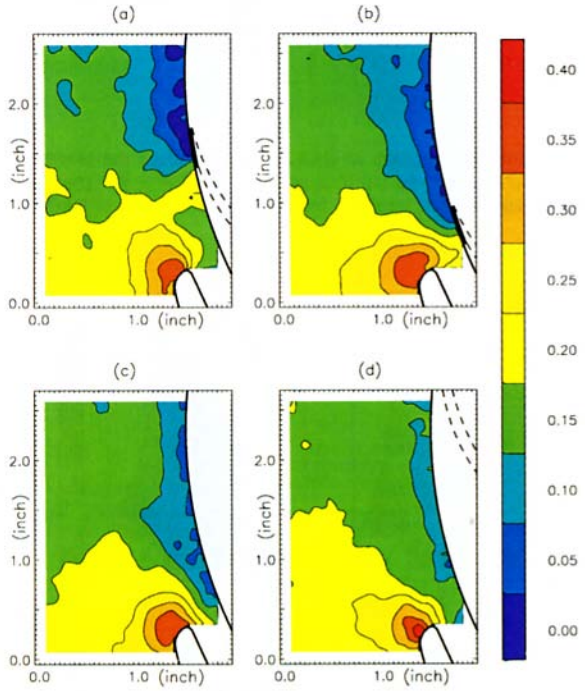

Fig. 2 V_r/U_T distributions at Q/Q_{design} = 1.35 with blade at: (*a*) 351 deg; (*b*) 1 deg; (*c*) 11 deg; and (*d*) 21 deg

used for generating a single phase averaged distribution. The pressure was computed using Reynolds Equations following procedures described in Part A. Vorticity ($\xi_z = \partial v/dx - du/dy$) was determined by computing $\Delta v/\Delta x - \Delta u/\Delta y$.

Results

Sample Velocity Distributions. Four characteristic samples of phase-averaged radial (V_r) and tangential (V_θ) velocity distributions are presented in Figs. 2–3, respectively. They are selected to illustrate characteristic blade-tongue interactions, and the impact of non-uniform outflux from the impeller. The jet/wake phenomenon is clearly evident. V_r peaks in the pressure side of the impeller (Fig. 2(*a*)), where V_θ is minimum

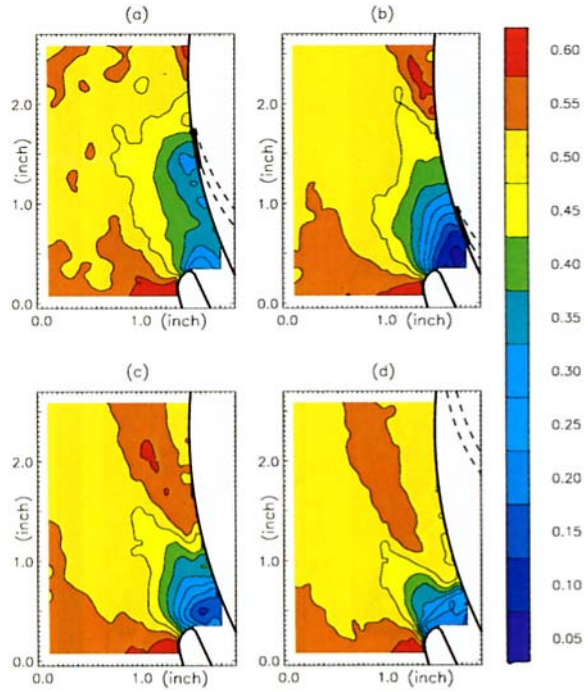

Fig. 3 V_θ/U_T distributions at Q/Q_{design} = 1.35 with blade at: (*a*) 351 deg; (*b*) 1 deg; (*c*) 11 deg; and (*d*) 21 deg

(Fig. 3(*a*)), and V_θ peaks at about 20 percent of the blade passage behind the suction side (Figs. 3(*a*) and (*b*)), where V_r is minimum (Figs. 2(*a*) and (*b*)). As the blade moves closer to the tongue, the induced blockage to the outflux first increases the radial velocity in the unobstructed portion. When the blade is located near the tongue V_θ between the blade and the tongue is at a minimum level, indicating that the leakage is minimal. In fact, high speed movies of this flow (data not shown here) shows that the leakage drops almost to zero at a certain angle. As the blade moves behind the tongue, the bulk of fluid with high V_θ is convected away from the impeller, and as demonstrated in Fig. 3(*d*), creates what appears to be an "impinging jet" on the tip of the tongue. The impact of this phenomenon on the pressure will be discussed later.

Vorticity and Turbulence From Fig. 3, it is clear that there is a considerable mismatch between V_θ leaving the impeller and the local tangential velocity in the volute, particularly within the "wake." Consequently, as the vorticity distributions show (Fig. 4), a powerful vortex train with negative vorticity is generated at the wake "front", namely when V_θ starts increasing. High positive vorticity peaks exist on the other side of this region, namely when V_θ starts decreasing (it is harder to identify them since most of the flow has some positive vorticity). Thus, the region with high V_θ is bounded by the appropriate shear layers on both sides. Traces of the same phenomenon have been visible in other locations and flow conditions, but they are particularly evident when the outflux is high and the local V_θ in the volute is low, such as upstream of the tongue above design conditions. Another pair of counter rotating vorticity peaks develops in the pressure side of the impeller, especially when the blockage increases V_r (Fig. 2(*b*) and 4(*b*)). Since the convection velocity between the tongue and the impeller is low under these conditions (i.e., when the blade is located near the tongue), the negative vorticity peak remains "stuck" in the corner and eventually coincides with the larger vorticity train (Fig. 4(*c*)). With increasing velocity in this region, the combined vortex train is convected around the tongue. As we have realized, this phenomenon depends on the impeller-tongue spacing, and in experiments with a slightly larger spacing (11 percent of the radius, instead of 7 percent),

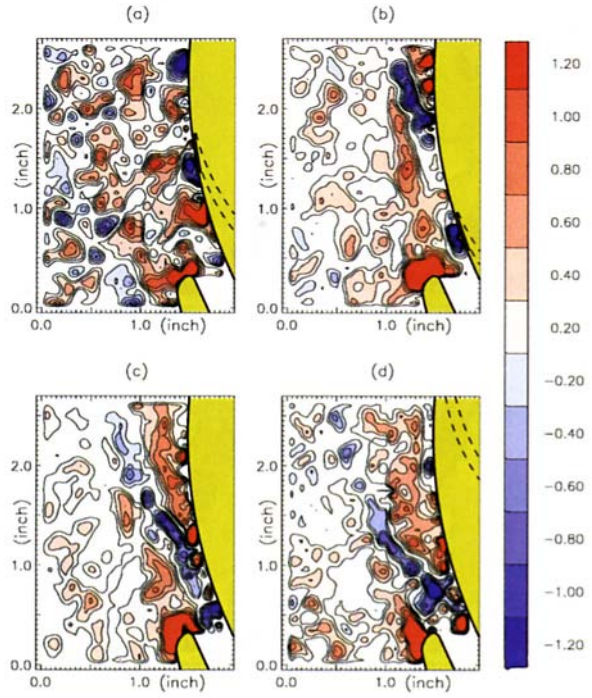

Fig. 4 Vorticity distributions at Q/Q_{design} = 1.35 with blade at: (*a*) 351 deg; (*b*) 1 deg; (*c*) 11 deg; and (*d*) 21 deg. (Data was scaled with U_T/R_T.)

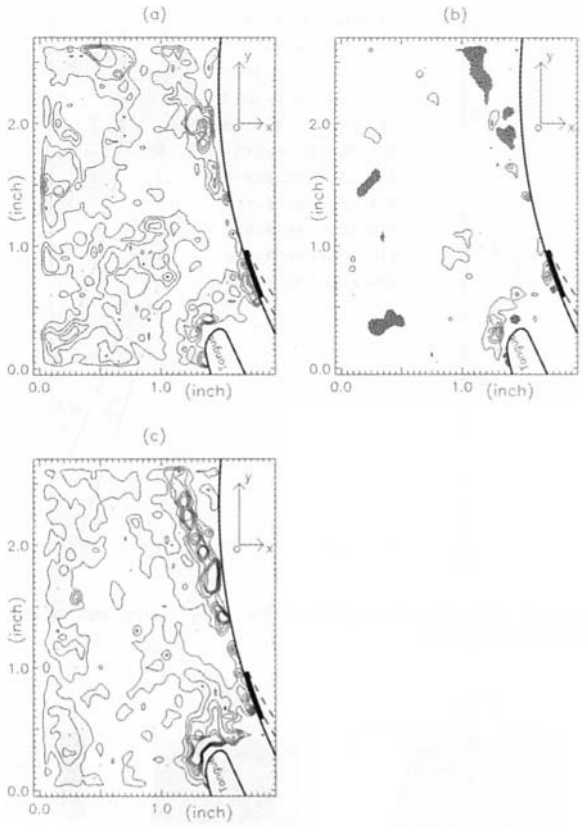

Fig. 5 Turbulent stresses at Q/Q_{Design} = 1.35 when the blade is at 1 deg: (*a*) $-\overline{u'u'} \times 10^3$; (*b*) $-\overline{u'v'} \times 10^3$ and (*c*) $-\overline{v'v'} \times 10^3$. (Dark shade: negative; light shade: positive. Increment between line is $0.5U_T^2$.)

the vortex train is mostly convected with the leakage into the beginning of the volute.

Generation of the large vortex train causes formation of a thin layer with relatively high turbulence levels (defined as mean deviation of the instantaneous data from the phase averaged velocity), as shown in Fig. 5. This layer exactly coincides with the high vorticity peaks. Increased levels of turbulence can be seen also near the tip of the blade, especially when it is located near the tongue. As discussed by Dong et al. (1992), as the overall flow rate of the pump decreases, the turbulence level near the blade increases. At 50 percent of design conditions there is very little outflux near the tongue and the blade becomes a major turbulence generator.

Pressure. Four contour maps of the instantaneous, phase-averaged pressure are presented in Fig. 6. The corresponding velocities and vorticity are presented in Figs. 2–4. There are some readily observed phenomena, such as a pressure minimum near the blade. The finite thickness of the blade (equivalent to 5 deg), which prevents outflux and causes formation of a separated region at the tip is responsible for this phenomenon. A second pressure minimum is located at the originating point the negative vortex train (the latter is particularly evident when the blade is at 1 deg and 11 deg). Pressure maxima occur between the blade and the vortex train, and within the wake, but slightly behind the point of maximum V_θ. There is also an overall decrease in pressure everywhere when the blade is located near the tongue, consistent with the previously observed increase in the overall flow rate (Dong et al. 1992). When the blade is located relatively far from the tongue, at 351 deg and 21 deg for example, the pressure is higher everywhere. In the latter case, the pressure gradients between the tongue and the impeller are minimal, and as Dong et al. (1992) observed, the leakage is maximum. This trend occurs since the measurements are performed above design conditions, namely the mean pressure at the beginning of the volute is higher than the pressure at the exit. When there is least obstruction between these regions, that is when the blade is far from the tongue, the pressure in the exit region reaches its maximum.

Other less obvious phenomena require careful examination.

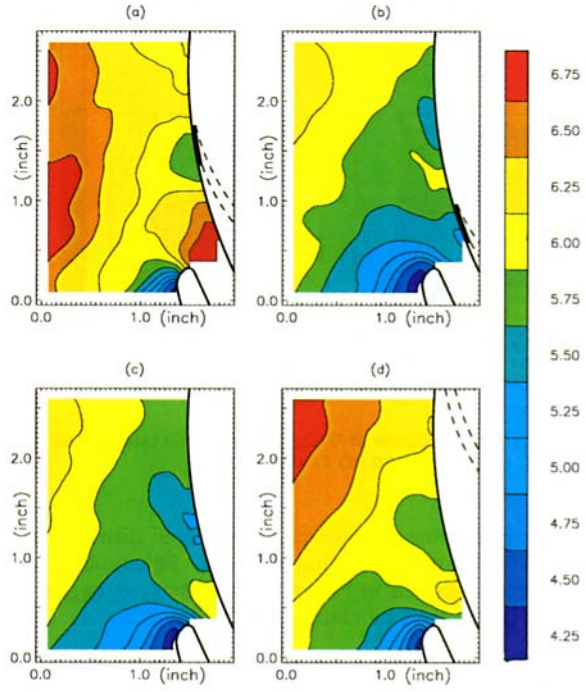

Fig. 6 Pressure distributions (in psi) at Q/Q_{design} = 1.35 with blade at: (*a*) 351 deg; (*b*) 1 deg; (*c*) 11 deg; and (*d*) 21 deg

For example, the low velocity between the tongue and the impeller creates conditions similar to a flow around an upstream (foreward) facing step, including a high pressure in the "stagnation region" (between the tongue and the impeller), and a

Fig. 7 Distributions of $\partial v/\partial t$ and $v\partial v/\partial y$ when the blade is at: (*a*) 340 deg; (*b*) 346 deg; (*c*) 353 deg; (*d*) 355 deg; (*e*) 3 deg; (*f*) 11 deg; (*g*) 16 deg; and (*h*) 21 deg. (Dark shade: negative; light shade: positive. Increment between lines is $0.2U_T^2/R_T$.)

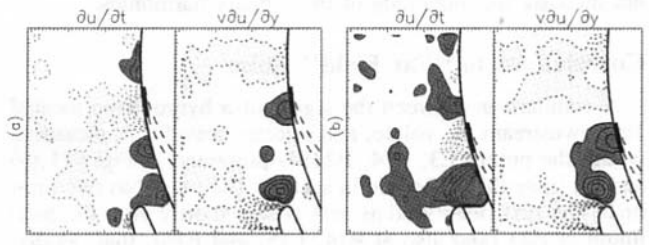

Fig. 8 Distributions of $\partial u/\partial t$ and $v\partial u/\partial y$ when the blade is at: (*a*) 349 deg and (*b*) 355 deg (Dark shade: negative; light shade: positive. Increment between lines is $0.2U_T^2/R_T$.)

low pressure as the flow circumvents the tongue. This phenomenon is clearer when the blade is located far from the tongue, but is evident in all the data. The distributions of $v\partial v/\partial y$, (Figs. 7(*a*)–(*b*) and Part A, for example) provide the clearest demonstration with positive and negative peaks on both sides of the tongue.

As noted in Part A, in most cases, pressure gradients result from an imbalance between the vertical convective terms, $v\partial/\partial y$, and temporal changes, $\partial/\partial t$ (samples are provided in Figs. 7 and 8). In the immediate vicinity of the impeller, the temporal changes and the origin of unsteady phenomena are closely as-

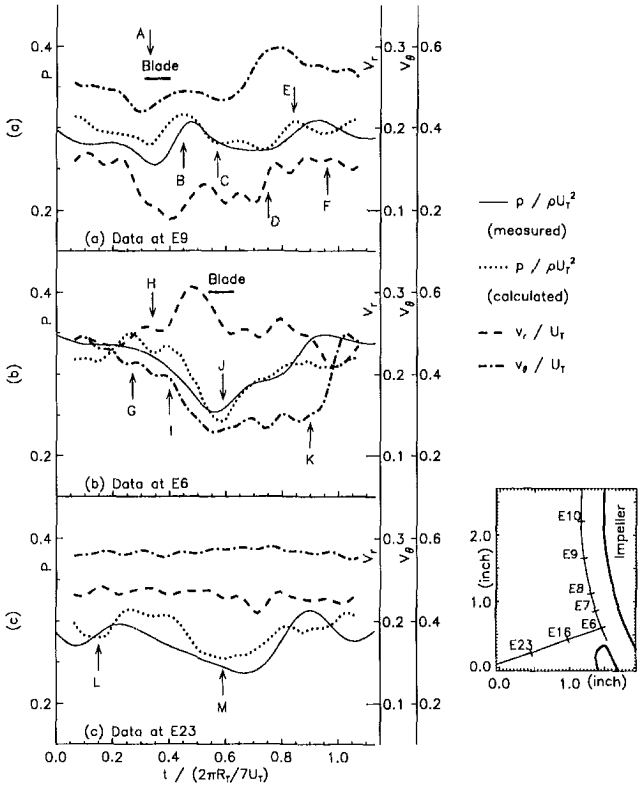

Fig. 9 Comparison of measured and calculated pressures (with E10 as the starting point) at three locations. V_r and V_θ are also shown for reference

sociated with the motion of the blade. Convection into the volute, however, is controlled by the local velocity, which is considerably lower (see Fig. 3). This lag causes several phenomena, the most obvious being the diagonal structure, which is clearly evident in Figs. 7(*e*)–(*h*) (all are associated with the shear layer/vortex train). Anytime that the temporal structure lags or leads the convected structure, it results in local pressure gradients. Consequently, a series of pressure peaks appear at different times on both sides of the vortex train. For example, the pressure minimum near the impeller at 21 deg (Fig. 6(*d*)) occurs since convection ($v\partial v/\partial y$) lags behind the temporal ($\partial v/\partial t$) structure, as is evident from Fig. 7(*h*). It has no relationship to a pressure minimum at the same location at 11 deg (Fig. 6(*c*)), which is located under the vortex train, and results from differences in the magnitudes of $\partial v/\partial t$ and $v\partial v/\partial y$ (Fig. 7(*f*)).

The few examples provided do not cover all the details of this flow, but they should demonstrate its complexity. We can now return to the starting point, namely the pressure signal at selected sites, and explain the occurrence of specific peaks. This exercise is useful for identifying dominating phenomena. Several peaks at points E9, E6 and E23 are identified in Fig. 9(*a*)–(*c*), respectively. For comparison purposes, each plot contains also distributions of V_r and V_θ. The corresponding relevant convective and temporal terms are included in Figs. 7 and 8. At E9, there are minima when the blade (point A) and the wake (between *C* and *D*) are passing by. The latter also coincides with the arrival of the blade to the tip of the tongue. The maximum at point B occurs in part since both $\partial v/\partial t$ and $v\partial v/\partial y$ are positive (Fig. 7(*d*)) a short distance behind the blade. Just after the wake clears E9 V_θ decreases rapidly ($\partial v/\partial t$ increases in Fig. 7(*g*)), causing an increase in pressure at (point E). A short time later (Fig. 7(*h*)) $\partial v/\partial t$ is smaller, and the pressure decreases again (point F). In summary, the wave-form at E9 is created by the blade and the jet/wake phenomenon.

At E6, there is a major pressure dip when the blade is pass-

ing by (point J in Fig. 9(*b*), and Fig. 7(*e*)). This dip always involves a difference between magnitudes of $\partial v/\partial t$ and $v\partial v/\partial y$ (the former is negative and larger). At E6 this minimum is augmented since the blade lines up with the tip of the tongue at the same time. Maxima at points G and I and the minimum at point H are all a result of variations in the magnitude of $\partial v/\partial t$ as the blade is approaching. The measured surface pressure does not contain these small peaks, but it is still relatively high, indicating that the deceleration of V_θ ($\sim -V$) still dominates the flow. Another significant phenomenon is the increase in v_r ($\sim -u$) as the gap between the blade and the tongue decreases (see Fig. 2). It results in high negative values of $\partial u/\partial t$ (compare Fig. 8(*a*) to 8(*b*)), namely positive $\partial p/\partial x$ ($v\partial u/\partial y$ is almost always negative above the tongue). The outcome is a further increase in the pressure between the impeller and the tongue, that contributes to the peak at point I.

As noted before, the vortex train remains in the vicinity of the tongue for quite a while due to the low convection velocity there (the arrival of the train to E6 is marked with *K* in Fig. 9(*b*)). At this phase trends in the computed and measured pressures do not agree. The computed distribution has a "plateau," with a small minimum when the vortex train arrives, whereas the measured pressure reaches a maximum value. Note that a positive peak appears in E9 and E23 almost at the same time, and that in all the examples presented there is a discrepancy between the measured and computed pressures. We cannot explain this discrepancy since the present study does not include computations of pressure in the third dimension. However, the available data in vertical planes (Chu et al., 1991) indicate that the values of $v\partial w/\partial y$ are sufficient to create axial pressure gradients ($\partial p/\partial z$) of this magnitude. It is also possible that there is a discrepancy between the surface and center-plane pressures at the starting point (E10), which is carried through the entire integration.

Although the absolute values differ, the waveforms in points E14, E15, E16, and E23 are quite similar, and only one sample (E23) is presented in Fig. 9(*c*). There are two main pressure dips, the first (point M in the computed data) occurs when the blade lines up with the tip of the tongue and there is an overall drop in pressure everywhere. The second minimum occurs when the wake climbes around the tongue and reaches point E16 (point L). Its leading front can be identified by the negative vorticity train (Fig. 4(*a*)), and its bulk can be recognized by the elongated regions with negative $v\partial v/\partial y$ and positive $\partial v/\partial t$ (Fig. 7(*a*)). Since $v\partial v/\partial y$ is almost always negative to the left of the tongue (overcoming the wake traces) $\partial p/\partial y$ is high in the vicinity of E16, resulting in a decrease in pressure below this point. Although it is possible to identify weak traces of the same wake in the distributions of $\partial v/\partial t$ at 346 deg and 353 deg (Figs. 7(*b*) and (*c*)), as well as from the vorticity distribution at 351 deg and 1 deg, its impact becomes weaker and overshadowed by other phenomena. Pressure gradients to the left and below E16 show weak dependence on time, and consequently, the waveforms are quite similar in shape (the absolute pressures are not the same, but the differences are weakly dependent on time). Part of the waveform at E23, such as the pressure minimum when the blade is lined up with the tip of the tongue, is related to the local flow dynamics. The other part, which is a result of interaction of the wake with the tip of the tongue, is not associated with changes in the local flow. Thus, the unsteady pressure at E23 "qualifies" in part as noise. The same conclusion applies to most points located at $r/R_T \geq 1.2$. The origin (flow structures causing them) of pressure fluctuations within the volute is limited to the immediate vicinity of the impeller ($r/R_T \leq 1.2$).

Spectra of pressure waveforms, for a single blade passage, as well as for the entire impeller cycle are presented in Fig. 10. The single passage spectra show the amplitude of Fourier coefficients of the phase averaged waveform (the waveform of single blade passage can only be decomposed to coefficients

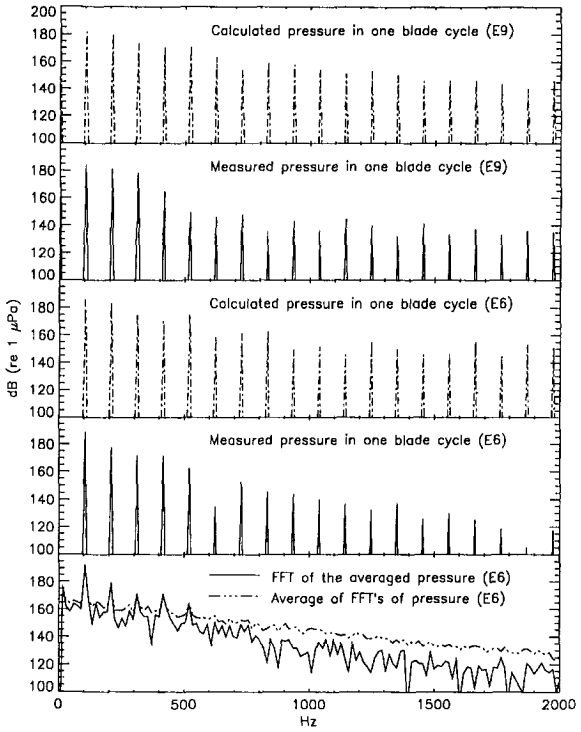

Fig. 10 Spectra of pressure waveforms at two locations for a single blade passage as well as for the entire impeller cycle

at discrete frequencies nf_0, where f_0 is the fundamental frequency). In some cases the computed and measured spectra are similar (E9), and in others there is a discrepancy, that increases with increasing frequency (E6). We do not have an explanation for this difference. Some may be related to the size of the transducer ($\approx 0.02R_T$), which causes attenuation of signal occurring due to convected phenomena at frequencies exceeding 2328Hz ($\approx V_\theta/0.02R_T \approx 0.5U_T/0.02R_T \approx 2328$ Hz). The phase averaged spectrum of the entire impeller contains already "broad band" component, both due to variations between blades, as well as the complex flow discussed in this paper. Turbulence adds energy to the broad band portion of the spectrum, that increases with increasing frequency, but does not increase the amplitude of the primary harmonics.

Correlations to "Far Field" Noise

A comparison between the signal of a hydrophone located 1m downstream the volute, and selected waveforms measured within the pump (E3, E14, E23) is presented in Figs. 11 (*a*) and (*b*) (note the difference in scales). The noise has two minima. The first (identified as m1) occurs shortly after the minimum at E23 (and also at E14, E15, and E16), that, as discussed before, is a result of impingement of the wake on the tip of the tongue. The maximum that follows (m2) occurs a short time after the maximum at E23. The delay between them, ~0.5 ms, is comparable to the travel time of sound between these points.

The second and larger minimum, as well as the maximum that follows, do not appear to have the same relationship to E23. To identify their origin Fig. 11 includes also the pressures at E3 and E14 as well as the pressure difference across the tongue, p(E3)-p(E14). It is evident that the pressure at E3 is maximum when p(E14) is close to its minimum. Thus, the overall force on the tongue is maximum. Peak *m*4 in the noise signal occurs a short time (0.5 to 1 msec) later, which suggests that it is caused by tongue oscillations, induced by the pressure difference across it. This delay is comparable to the time required for sound to travel between the tongue and the hydro-

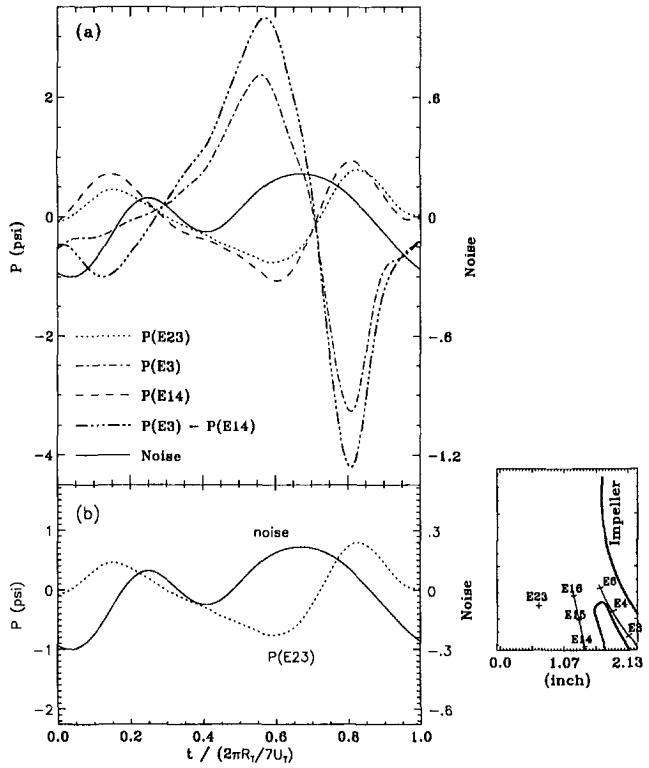

Fig. 11 Comparison between the (hydrophone) noise and local pressure fluctuations

phone (~0.7 ms). This peak does not exist in the signal of E23 since the local flow dynamics are sufficient to overcome the momentum pulse induced by tongue oscillations. In fact the pressure in the entire exit region is minimum at the same time (the blade is lined up with the tip of the tongue). It is important to explain how can the pressure at E23 have a minimum and the hydrophone reading, 1 m downstream, does not. Since the velocity at E23 is weakly dependent on time, the convective terms of the momentum equation are small. Thus, the pressure difference between E23 and the hydrophone is approximately equal to the mass of fluid between them times its mean acceleration. Even when the acceleration is small, the mass is sufficiently large to create substantial pressure difference. This explanation was confirmed using $\partial v/\partial t$ at E23 and the present pump geometry.

Conclusions

Maps of the phase averaged pressure distributions, computed using PDV data, have been used for explaining the effect of blade-tongue interactions on pressure fluctuations and far field noise within a centrifugal pump. Near the impeller pressure minima occur when the blade passes by a point and when the blade lines up with the tip of the tongue. An additional minimum occurs below a vortex train, which is generated as a result of non uniform outflux from the impeller (jet/wake phenomenon). Pressure maxima occur within the wake, behind the blade, and when the blade is located far from the tongue. The latter is a result of performing the tests above design conditions. Maxima in the far field noise are generated due to tongue oscillations, forced by local pressure fluctuations, as well as a result of impingement of the wake on the tip of the tongue. All the sources of pressure fluctuations and noise are located within $r/R_T \leq 1.2$. Dominating phenomena are associated with interaction of the tongue with the blade, and nonuniform outflux from the impeller. Thus, it seems that by increasing the gap between the tongue and the impeller, and as a result reducing the nonuniformities near the tongue, it is possible to reduce the far field noise. This issue is the primary subject of the next paper.

Acknowledgment

This research is sponsored by the Office of Naval Research, under contract number N00014-89-J-1672.

References

Dean, R. C. and Senoo, Y., 1960, "Rotating Wake in Vaneless Diffusers," ASME *Journal of Basic Engineering*, Vol. 82, No. 3, pp. 563–574.

Eckardt, D., 1975, "Instantaneous Measurements in the Jet/Wake Discharge Flow of a Centrifugal Compressor Impeller," ASME *Journal of Engineering For Power*, Vol, 97, No. 3, pp. 337–346.

Eckardt, D., 1976, "Detailed Flow Investigation Within a High Speed Centrifugal Impeller," ASME JOURNAL OF FLUIDS ENGINEERING, Vol. 98, pp. 390–402.

Miner, S. M., Flack, R. D., Allaire, P. E., 1992, "Two Dimensional Flow Analysis of A Laboratory Centrifugal Pump," ASME *Journal of Turbomachinery*, Vol. 114, pp. 333–339.

Fluid Flow Structures in Staggered Banks of Cylinders Located in a Channel

M. J. Braun
Department of Mechanical Engineering,
The University of Akron,
Akron, OH 44325

V. V. Kudriavtsev
Department of Mechanical Engineering,
The University of Akron/
Moscow Aviation Institute,
School of Engine Technology, Russia

This paper contains numerical experiments that model fluid flow through a staggered array of cylinders and represents a continuation of work previously performed by the authors (Braun et al., 1993; Kudriavstsev et al., 1993). The results shown here concentrate on the analysis of the physics of flow and pressure distribution in (i) one row of cylinders, and (ii) seven rows of cylinders. The test section is the same square channel described by Braun et al. (1993). The numerical experiments were run in transient mode at Reynolds numbers ($Re = u_{max}d/\nu$) ranging from 86 to 869. The primary purpose of this paper is to report qualitative results regarding the attached near-wall jet phenomenon and to discuss its flow mechanics. The authors compare various stages of the transient evolution of the flow structures for geometric configurations that contain one, and seven rows of pins respectively. The associated pressure distributions in the arrays of pins are also discussed.

I Introduction

The literature reviewed by the authors presents information limited to flow visualization studies (Weaver et al., 1985), flow instabilities (Paidoussis et al., 1985; Moretti et al., 1987), and flow interference between two cylinders (Zdravkovich, 1977 and Li et al., 1991). While there is a considerable amount of theoretical and experimental work devoted to studies of different aspects of flow around a single cylinder, tandem of cylinders, or flow in sparse arrays, information about the flow within *densely* packed cylinder arrays is very limited. However, in spite of its significant practical importance (heat exchangers, nuclear reactors, continuous type chemical reactors, screens within the aerodynamic tubes, cooling of turbine blades passages), this latter problem has been treated mostly experimentally, while analytical and numerical modeling efforts providing design and predictive capabilities have been largely neglected. This is perhaps not surprising since the complexity of the flow and geometry configurations imposed serious computational obstacles. Stansby (1981) performed an investigation with the potential flow assumption and Chen (1986) obtained unsteady solutions without vortex shedding. Fornberg (1991) performed a numerical study of the flow through one row of cylinders limiting it to the steady state flow and symmetric periodic conditions. Zdravkovich et al. (1988) showed the existence of a nonuniform flow across a single row of equidistantly spaced tubes, thus proving that the basic periodicity assumptions of Fronberg's model were somewhat inadequate.

The material to be presented in this paper concentrates on the numerical simulation of transient and steady-state flow in densely packed rows of cylinders. The authors use the conservative, incompressible, transient form of the two dimensional Navier-Stokes equations.

II Mathematical Model

If one considers a uniform external flow with zero angle of incidence past an array of two-dimensional round cylinders, the two-dimensional Navier-Stokes equations can be written in dimensionless conservative form as

$$\frac{\partial U}{\partial t} + \frac{\partial (UU)}{\partial X} + \frac{\partial (UV)}{\partial Y} = -\frac{\partial P}{\partial X} + \frac{1}{\mathrm{Re}}\left(\frac{\partial^2 U}{\partial X^2} + \frac{\partial^2 U}{\partial Y^2}\right) \quad (1)$$

$$\frac{\partial V}{\partial t} + \frac{\partial (VV)}{\partial Y} + \frac{\partial (UV)}{\partial X} = -\frac{\partial P}{\partial Y} + \frac{1}{\mathrm{Re}}\left(\frac{\partial^2 V}{\partial X^2} + \frac{\partial^2 V}{\partial Y^2}\right) \quad (2)$$

The corresponding pressure Poisson equation is

$$\nabla^2 P = -\frac{\partial^2 (U^2)}{\partial X^2} - 2\frac{\partial^2 (UV)}{\partial X \partial Y} - \frac{\partial^2 (V^2)}{\partial Y^2} + \left\{-\frac{\partial \mathcal{D}}{\partial t} + \frac{1}{\mathrm{Re}}\left(\frac{\partial^2 \mathcal{D}}{\partial X^2} + \frac{\partial^2 \mathcal{D}}{\partial Y^2}\right)\right\} \quad (3)$$

$$\mathcal{D} = \frac{\partial U}{\partial X} + \frac{\partial V}{\partial Y} \quad (4)$$

One should note that the characteristic length used in this study is the horizontal dimension of the physical domain (L_0 and L_x (Fig. 1(*a*))), while the time scale is determined by the division of this length by the free stream velocity (U_0). During calculations, the dilation term $\mathcal{D}$ represents the residual that has to shrink to zero if continuity is to be satisfied. This is a necessary but not sufficient condition for the convergence of pressure in Eq. (3), since the joint solution of the pressure and

Contributed by the Fluids Engineering Division for publication in the JOURNAL OF FLUIDS ENGINEERING. Manuscript received by the Fluids Engineering Division August 22, 1993; revised manuscript received August 9, 1994. Associate Technical Editor: D. P. Telionis.

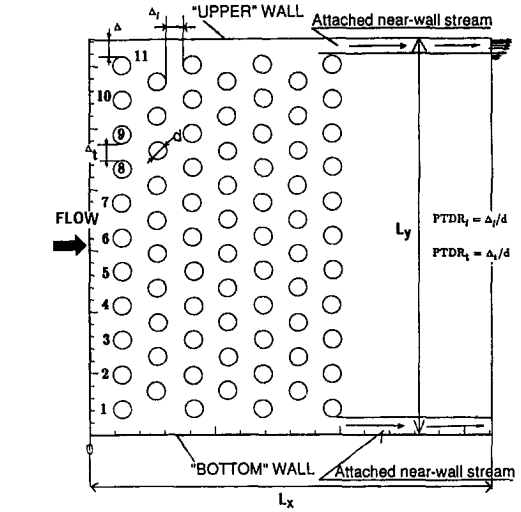

a) Geometry sketch

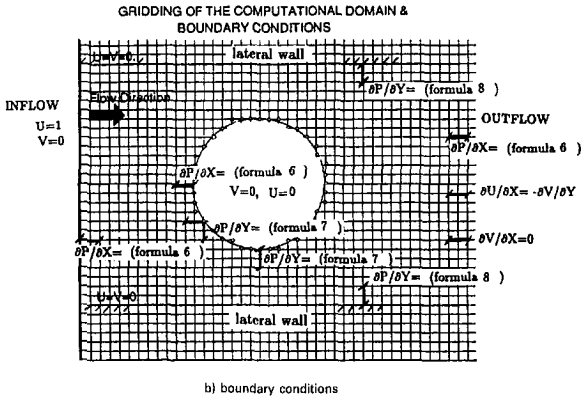

b) boundary conditions

Fig. 1(*a*, *b*) Characteristic geometry and boundary conditions

momentum equations does not necessarily imply the satisfaction of the continuity equation.

Boundary and Initial Conditions for the Momentum Equation. The boundary conditions (Fig. 1(*b*)) on the lateral solid walls assume non-slip conditions and non-porous walls. The inflow velocity is uniform with $U = 1$, and $V = 0$ (zero angle of incidence). A reference pressure is assigned to one point on the inflow boundary, and the exit flow is allowed to develop naturally, Eqs. (5a), (5b) and (6). The velocity boundary conditions imposed at the exit are derived from (i) the satisfaction of the continuity equation (specifically in the direction of the U velocity),

$$\frac{\partial U}{\partial X} = -\frac{\partial V}{\partial Y} \tag{5a}$$

and (ii) the condition for constant vertical velocity gradient in X-direction

$$\frac{\partial V}{\partial X} = 0 \tag{5b}$$

Boundary Conditions for the Poisson Equation. The dynamic pressure P, is allowed to float freely on the inflow and outflow boundaries, and is determined from the balance of the normal forces with the inertia and viscous forces. The effects of the terms $\partial U/\partial T$ and $\partial V/\partial T$, both at inflow and outflow boundaries, have been considered negligible. The following formulation of Eqs. (6) and (7) is totally independent of the internal boundary configuration, and thus applicable with no restrictions

$$\frac{\partial P}{\partial X} = -\left[\frac{\partial (UU)}{\partial X} + \frac{\partial (UV)}{\partial Y}\right] + \frac{1}{\mathrm{Re}}\left(\frac{\partial^2 U}{\partial X^2} + \frac{\partial^2 U}{\partial Y^2}\right);$$

$$\text{at } x = 0, X = 1; 0 < Y < L_y \tag{6}$$

On the noncontiguous internal boundaries of the pins, in addition to Eq. (6) one needs to add a boundary condition expression for $\partial P/\partial Y$

$$\frac{\partial P}{\partial Y} = -\left[\frac{\partial (UV)}{\partial X} + \frac{\partial (VV)}{\partial Y}\right] + \frac{1}{\mathrm{Re}}\left(\frac{\partial^2 V}{\partial X^2} + \frac{\partial^2 V}{\partial Y^2}\right) \tag{7}$$

At the channel's upper and lower walls the pressure boundary condition takes a simplified form due to the fact that $U = V = 0$

$$\frac{\partial P}{\partial Y} = \frac{1}{\mathrm{Re}}\left(\frac{\partial^2 V}{\partial Y^2}\right) \tag{8}$$

Initial Conditions ($t = 0$). The input velocities are given as $U = 1$, $V = 0$. The pressures are set initially to an arbitrary, operator-chosen $P = P_{\mathrm{ref}} = \text{const}$.

Solution Procedure. The discretization of the system of governing equations introduced above, uses the Alternative Direction Implicit (ADI) method as applied to a collocated grid. The procedure uses the full direct approximation of each term within the differential equation on every half time step. The computational domain is inclusive, 74 irregularly shaped internal islands (cylinders), thus allowing performance of the calculations without the need of introducing periodic type boundary conditions. The spatial derivatives, with the exception of the convection terms, and cross-derivatives, are approximated by a second-order central finite difference. For the convection terms the authors used the first-order conservative scheme as proposed by Torrance (1968). This scheme con-

Nomenclature

d = cylinder diameter
H = nondimensional height $L_y = h/L_0$
h = physical height
l = physical length
L_x = nondimensional characteristic length $L_x = l/L_0$
L_0 = length scale, also dimensional horizontal length, $L_0 = l$
PTDR = pitch to diameter ratio
U_0 = free-stream velocity, velocity scale
$U_{\max}$ = mean flow velocity in the pitch, $U_{\max} = 2U_0$
U = nondimensional horizontal speed $U = u/U_0$
V = nondimensional vertical speed $V = v/U_0$
t = nondimensional time, $t = T/T_0$, $T_0 = L_0/U_0$
P = nondimensional pressure, $P = p/\rho U_0^2$
ΔP = nondimensional pressure drop ($\Delta P = \Delta p/\rho U_0^2$)
Re = Reynolds number, $\mathrm{Re}_d = (U_{\max} - d)/\nu$, $\mathrm{Re}_L = (U_0 L_0)/\nu$

Subscripts

l = longitudinal
t = transversal
ν = kinematic viscosity
ρ = density

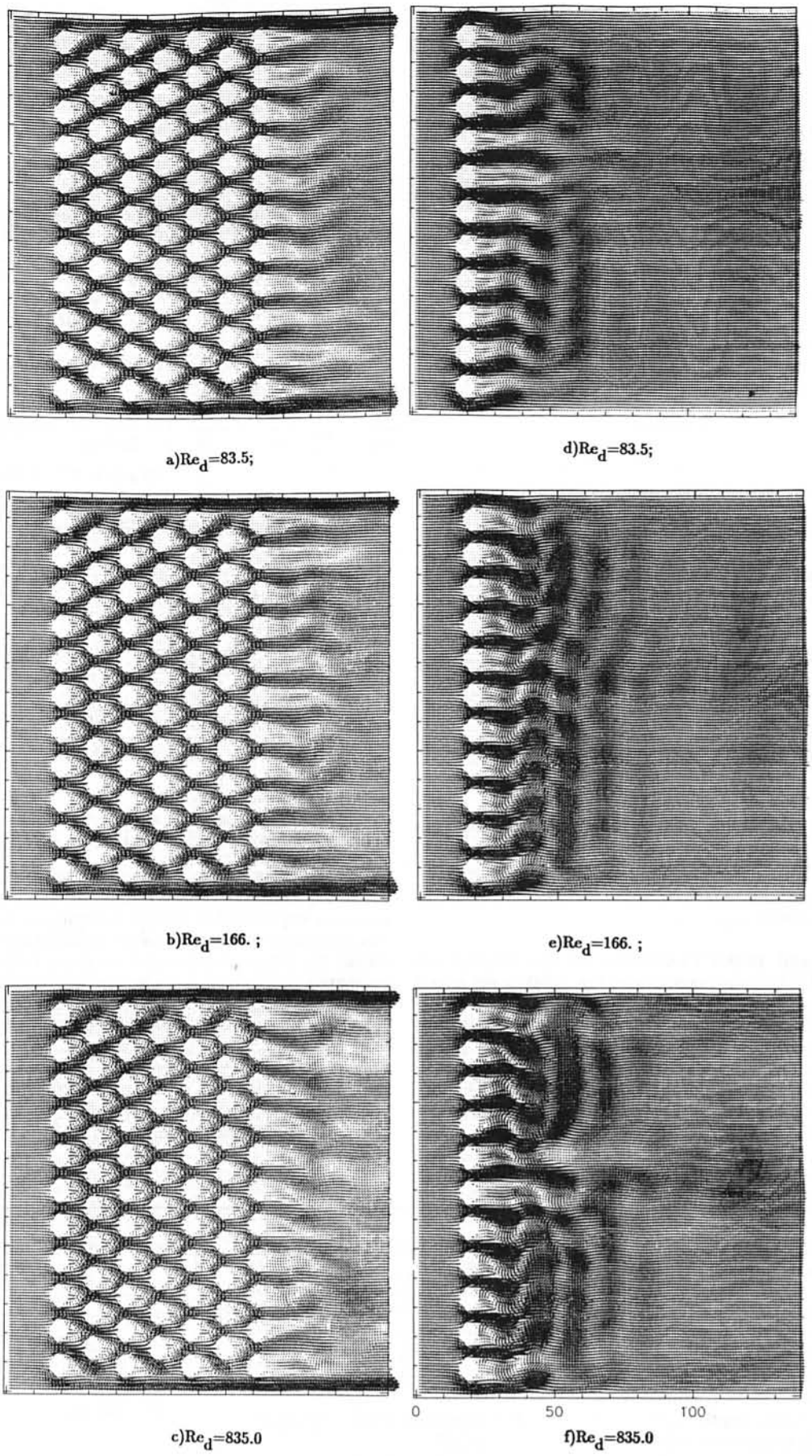

Fig. 2 Flow through the cylinders bundle at the different Reynolds numbers on the quasi-steady regime (t = 0.7)

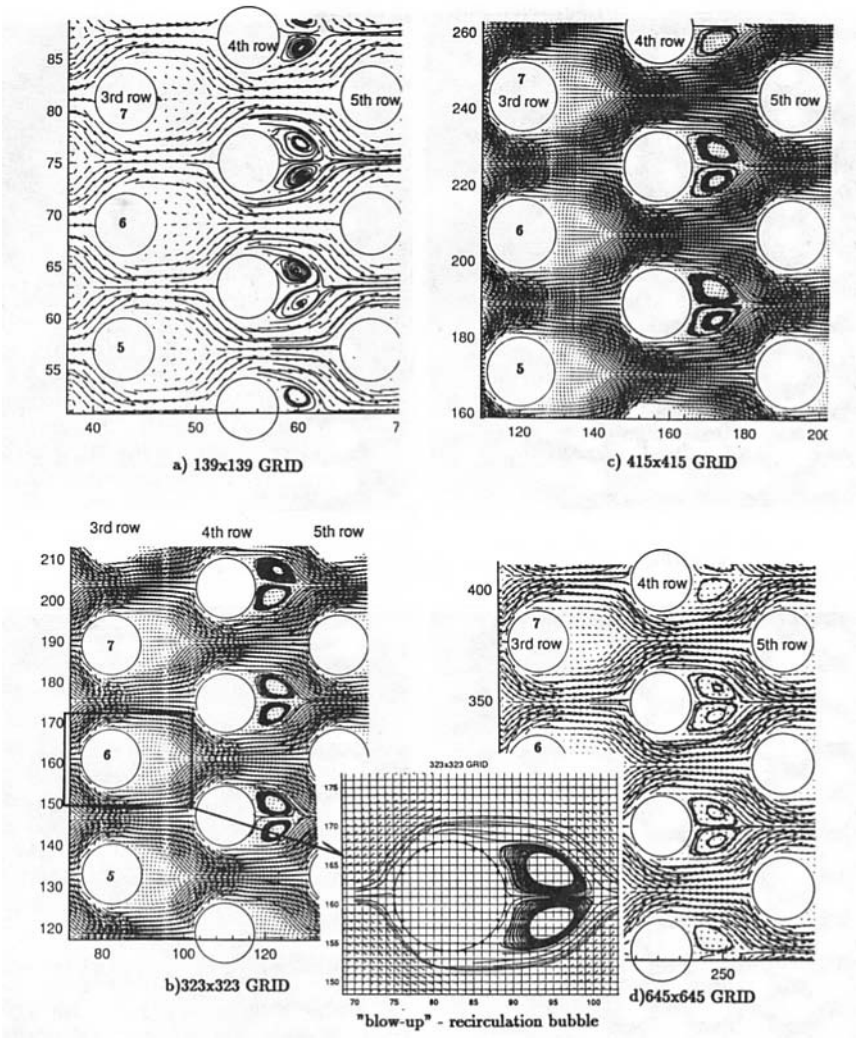

Fig. 3(*a*, *b*, *c*, *d*) Fluid flow in the central segment of the cylinders array. Grid convergence study.

tributes to the stability of the whole computational process, and proved to be well suited to the conditions of intermediate and high convection flow (Roache, 1981).

The solution follows according to the time-dependent ADI method using a tridiagonal matrix elimination. The details of the solution procedure, as well as the iterative convergence and accuracy of the algorithm have been discussed by the authors in other recent publications (Kudriavtsev et al., 1993 and Braun et al., 1992, 1993).

III Results and Discussion

The geometry of the channel as well as boundary conditions considered in this paper are shown in Figs. 1(*a*), and 1(*b*). The channel has a square cross section with a characteristic length L_x, and contains a multi-row array configuration of staggered cylinders. The pitch to diameter ratio, both transversal and longitudinal, are $PTDR_l = PTDR_t = 1$. The numerical calculations were generally performed on 139 × 139 grid.

The flow patterns presented in Figs. 2(*a*), 2(*b*), and 2(*c*), emphasize the existence of strong, near wall jet-type flow streams, that are attached to the lateral walls. These jets represent an intrinsic feature of the flow through staggered arrays of cylinders situated in channels like the one shown in Fig. 1. One can notice that the phenomenon is present within a wide range of Reynolds numbers, $Re_d = 86–869$. If however, the array is replaced by a single row configuration, the near-wall attached streams do not form anymore for the range of Re_d numbers considered in Figs. 2(*d*), 2(*e*), 2(*f*).

In Figs. 3(*a*), 3(*b*), 3(*c*), and 3(*d*) one can study the flow visualization of the central part of the cylinders array. The results were obtained on computational grids of different resolutions (139 × 139, 323 × 323, 415 × 415, and 645 × 645, respectively.). Based on these data one may conclude that vortex structures as well as the size of the recirculation bubble obtained on 139 × 139 mesh are grid independent.

The mechanics of this near-wall stream phenomenon seems to be principally due to a lower resistance to flow along the walls, when compared to the resistance to flow in the tube bundle. We believe that this feature is a *principal* characteristic of the intermediately dense, and dense arrays of cylinders. One can observe that the stream of fluid entering between the wall and the first column of pins remains confined to this path, while vigorous rivulets are merging into it from behind the 1st, the 3rd, and 5th rows, Figs. 2(*a*), 2(*b*), and 2(*c*). This situation appears to (i) continuously stimulate the acceleration, and increase the velocity of the near-wall stream as it traverses the length of the array, (ii) engender the appearance of considerable transversal flow components that direct the fluid from the center of the array toward the lateral walls, and finally (iii) contribute to the formation of a lower pressure region near the wall that is attracting the fluid from the central zone towards the wall regions.

In Figs. 4 and 5 the reader can find an illustration of the transient flow development within the array structure, and be-

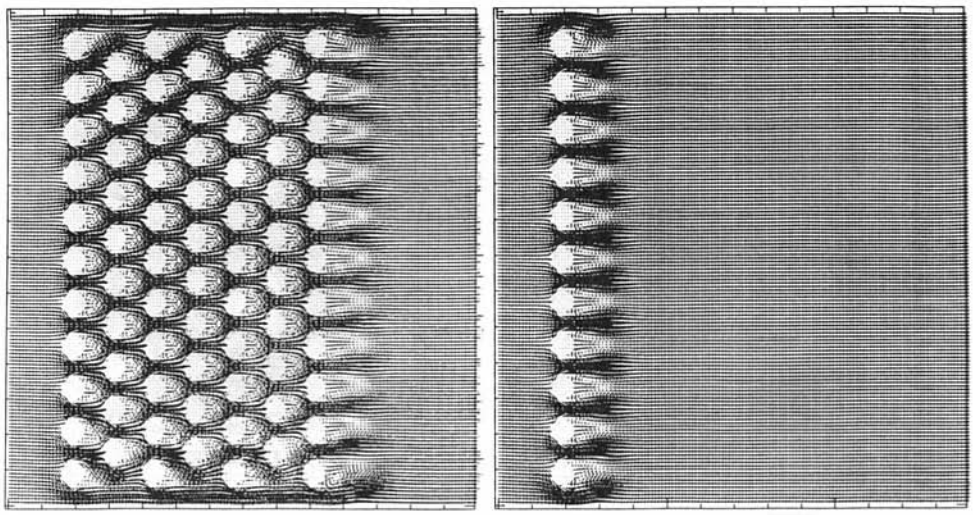

a)t=0.07;

d)t=0.07;

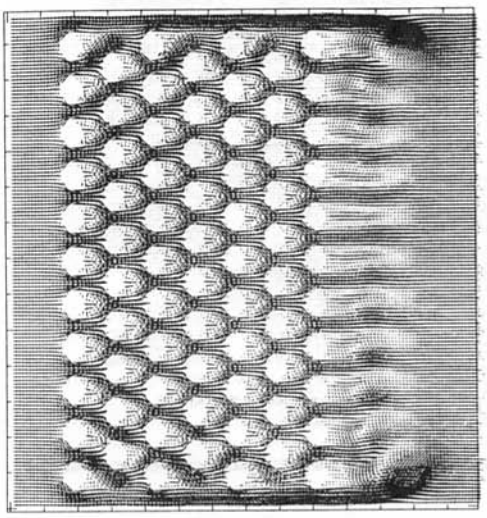

b)t=0.14;

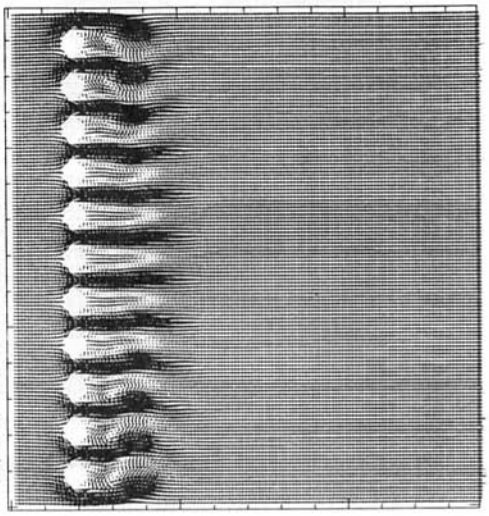

e)t=0.14;

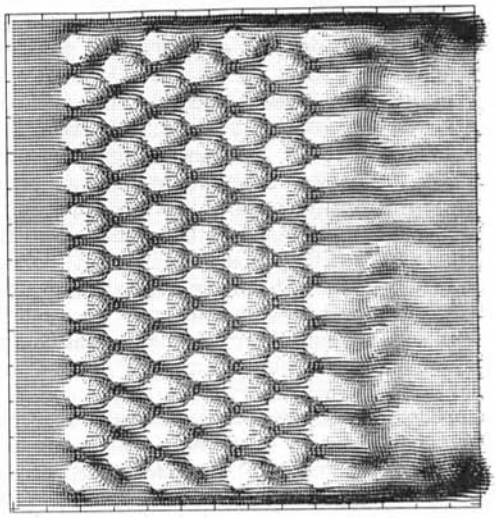

c)t=0.21

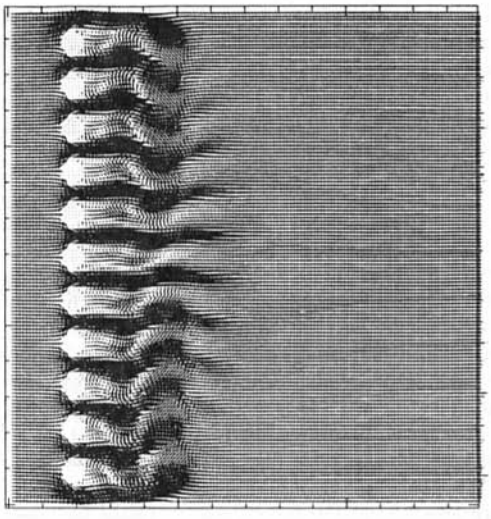

f)t=0.21

Fig. 4 Transient evolution of fluid flow through the cylinder arrays for Re_d = 835.0, (a) t = 0.07; (b) t = 0.14; (c) t = 0.21 (7 rows of pins); (d) t = 0.07; (e)t = 0.14; (f)t = 0.21 (1 row of pins)

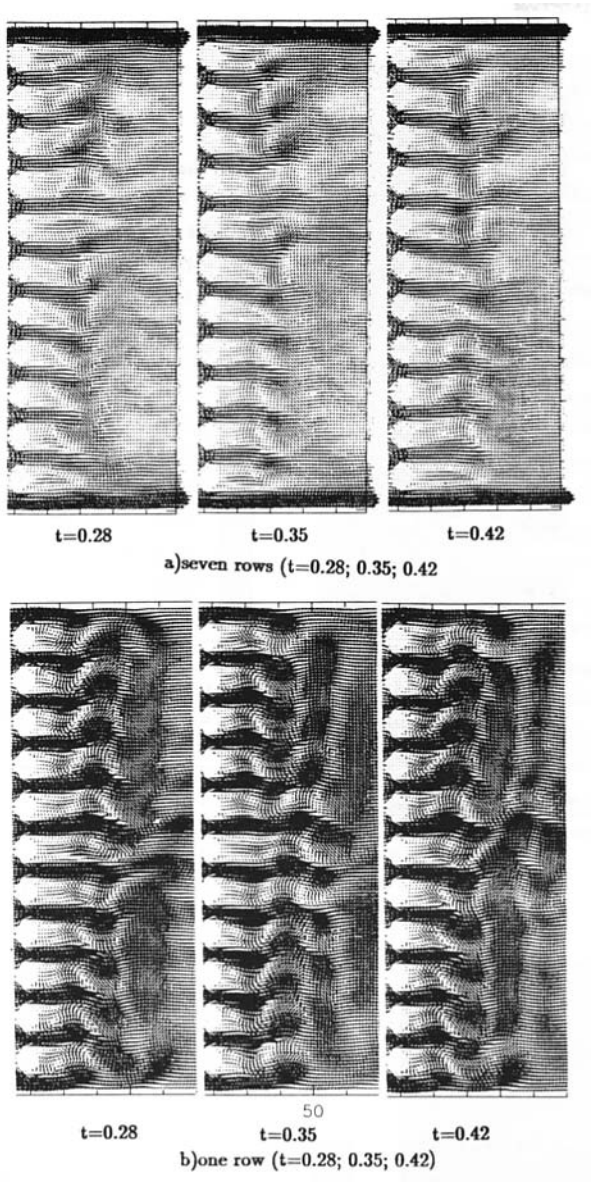

Fig. 5 Transient evolution of fluid flow behind the last row of the cylinder arrays Re_d = 835

hind the last row of cylinders. One can notice that the form and size of the recirculation eddies behind the cylinders, *within* the array, is not changing considerably with time. The vortical formations *behind* the pin array show, however, an ever-changing structure that is similar in its evolution to the ones found in the case of the flow around one cylinder (Bouard et al., 1990 and Kudriavtsev et al., 1993). This proves that the flow is intrinsically transient in nature. During the early stages $t = 0.07$ (Fig. 4(a), and 4(d)), the flow development behind the multi-row array seven rows, Fig. 4(a), is similar to the flow behind the single row case, Fig. 4(b). However, later on, ($t > 0.14$) one can see a considerable difference in the development of the structure of the recirculation and jetting zones. Thus, for the one row case the central jets are stronger, and penetrate deeper than the near wall streams (Figs. 4(d), 4(e), and 4(f)). In the seven-row array, in the early stages of flow development ($t < 0.28$), the exiting, near-wall jets are trying to penetrate the main central flow causing "hugging"-like effects (Figs. 4(b) and 4(c)). Later on, they are getting reattached to the walls, and do not change their shape with time anymore (Fig. 5). In Fig. 4(c) and Fig. 5(a) ($0.21 < t < 0.42$) one can notice in the area behind the last row of cylinders a considerable transversal flow directed from the center line of the channel to the walls. The trend of these formations is due to the already formed, strong, near-wall streams that create near-wall associated lower pressure zones that attract the fluid from the center of the channel. The opposite phenomenon can be found for the single-row configuration, (Figs. 4(f) and 5(b)). The central jets are much stronger around the centerline and one can find lateral flow streams directed from the walls to the center. The numerical results presented in Fig. 5(a) (for seven-rows array) are strongly supported by the conclusions of Zdravkovich and Stonebanks (1988) regarding the intrinsically nonuniform nature of the flow behind tube rows. One can find that flow has lost its symmetry, and the jet-merging phenomenon described by Moretti (1987) and Zdravkovich et al. (1988) is clearly apparent.

Flow images that are shown in Figs. 6(a), 6(b), and 6(c) are associated with the distribution of the horizontal velocity U in, and behind the cylinder's array. The red and white regions are indicative of maximum horizontal U-velocities, Fig. 6(a). One can see that for the multi-row array the largest velocities are right behind the last row, in the near-wall area. The jet strength decays as we move from the wall toward the centerline. Along the centerline, the jets also decrease in strength as we move from the first to the last row, Fig. 6(a).

As was mentioned before, this is not true for the single row configuration. It can be clearly seen from Fig. 6(b) that the central jets penetrate deeper. To support our comments about the factors that trigger the near wall stream development we provide a horizontal U-velocity image for one row of pins with the three additional cylinders attached (in a staggered arrangement) near the "bottom" wall, Fig. 6(c). These added cylinders create lower near-wall hydraulic resistance and partial flow blockage in the "lower" part of the channel. One can see, by comparison, the appearance of a strong stream flow near the lower wall, versus the lower jet penetration at the upper end of the channel. The reader can also inspect the horizontal velocity profiles at different cross-sections, Fig. 7, and the associated pressure distributions in the transversal direction, Fig. 8. For the multi-row array, the results presented in these figures completely support our previous conclusions that flow is accelerating in the near-wall regions, and has a decreased velocity in the central zone. Further, the nondimensional pressure shows higher pressure drops ΔP near the walls, and lower ΔP in the central area. This creates pressures distributions with lower absolute pressures near the walls, and higher pressures in the center of the channel. This situation causes the appearance of the strong lateral flow streams that were mentioned and discussed earlier.

Finally, one can look at Fig. 9 and consider it as a corollary of the phenomena described in this paper. Using the method of particle streaks, the figure shows the particle traces emerging from the center and moving towards the lateral walls *within* the cylinder array ("flow expansion"). The small side jets behind the 1st, 3rd, and 5th row also merge into the strong near-wall jet. Similar qualitative conclusions follow from the analysis of the experimental flow visualization picture (Fig. 9(d)) presented by Sarapkaya (1988).

To ensure that the existence of the lateral flow and near wall jet phenomena reported in this paper are grid independent we performed calculations on a variety of computational grids (139 × 139, 278 × 279, 323 × 323, 415 × 415, 645 × 645). In Figs. 9(a), 9(b), and 9(c) and Figs. 2–3 we present results of the calculations that employed different grid resolution. Based on these figures we can conclude that the findings presented in this paper are grid independent.

IV Conclusions

This paper has presented a numerical visualization of the flow inside and in the wake of an array of densely packed

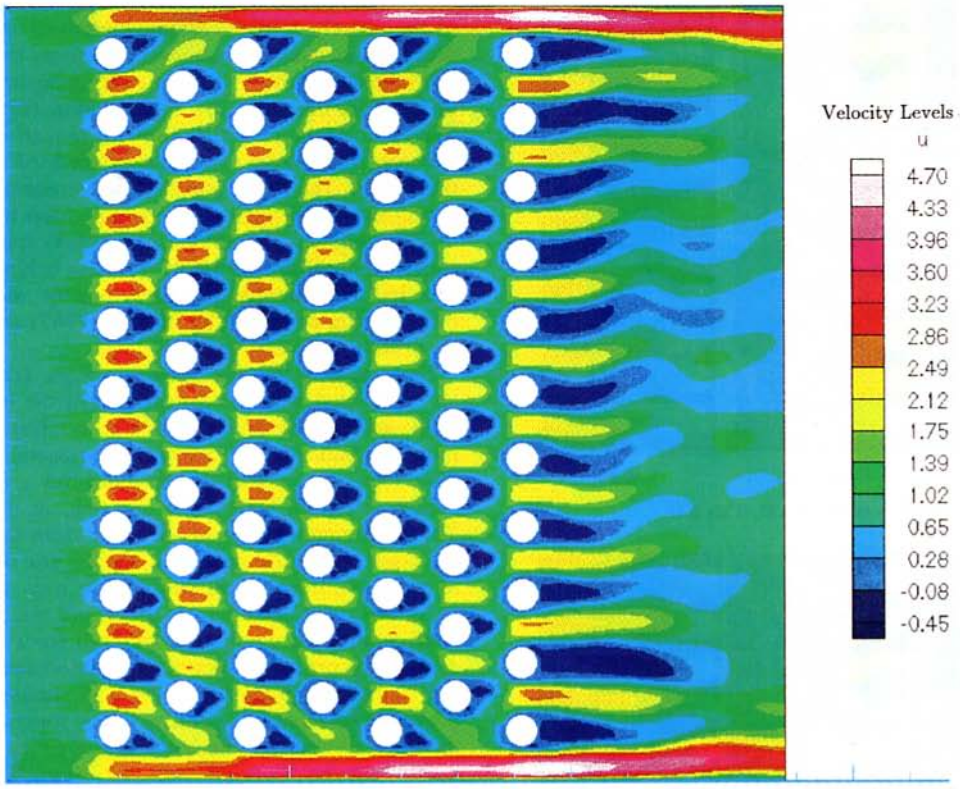

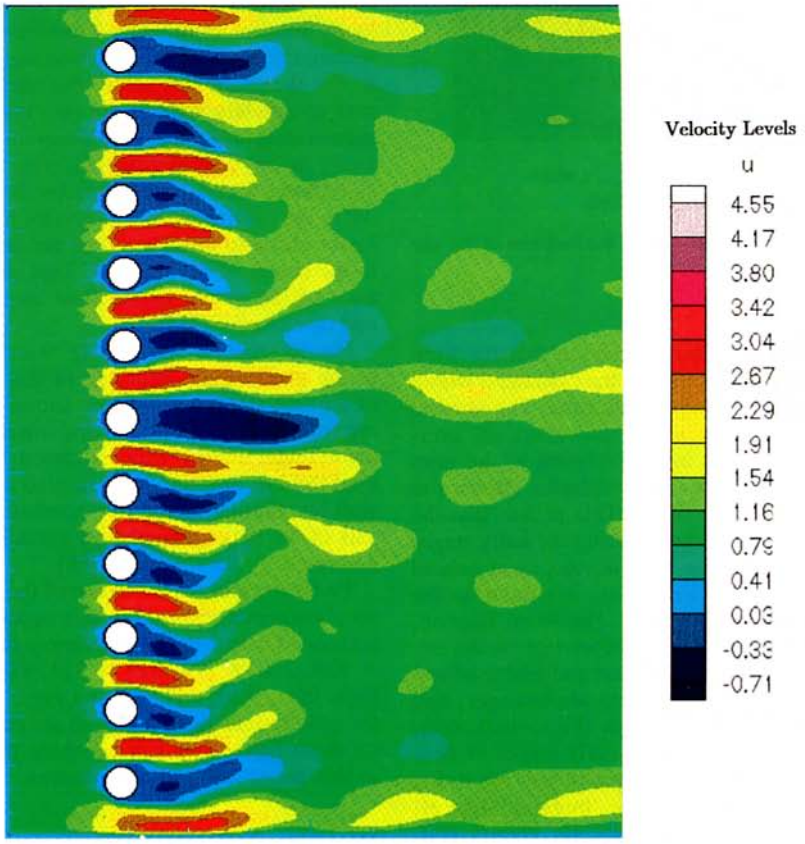

Fig. 6 Image of the *U*-velocity distribution for Re_d = 835. (*a*) seven rows of cylinders; (*b*) one row; (*c*) one row with partial flow blockage

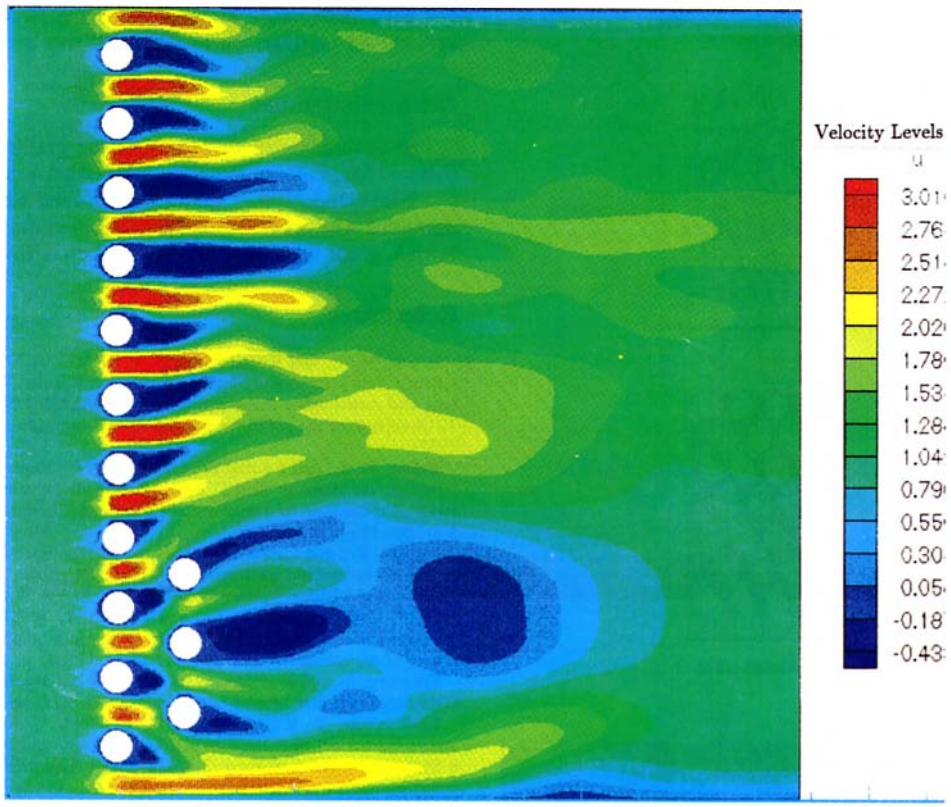

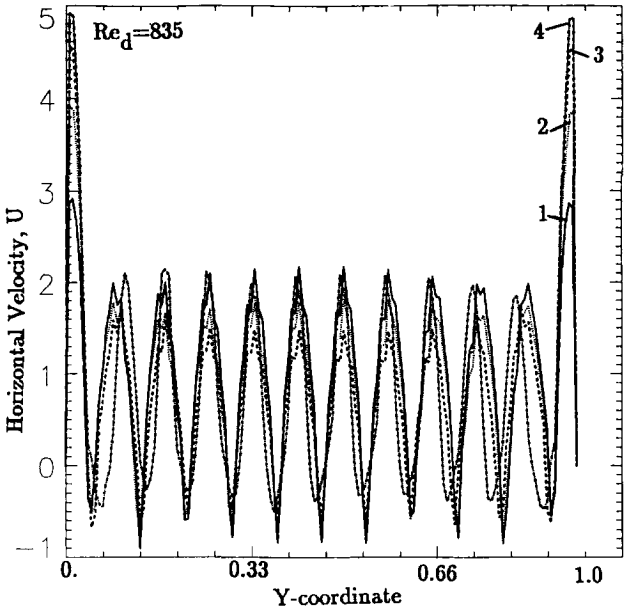

Fig. 7 Horizontal *U*-velocity profiles in transversal *Y*-direction in a different cross section 1—behind the first row; 2—third row; 3—fifth row 4—seventh row

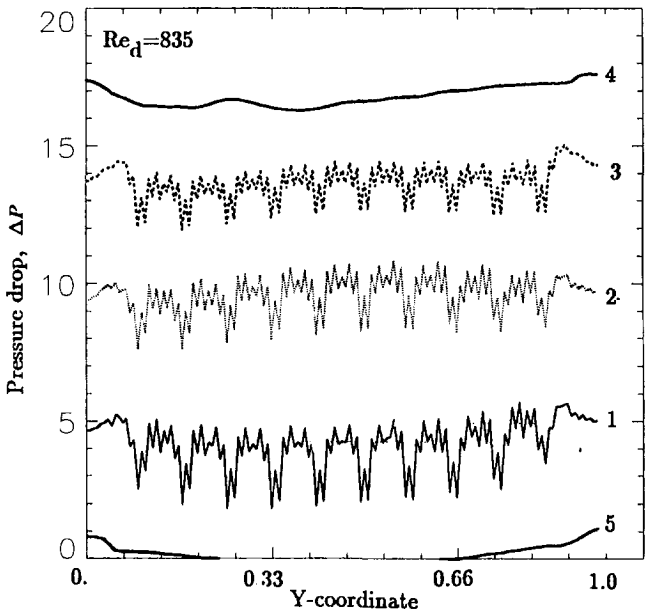

Fig. 8 Dynamic pressure profiles in transversal *Y*-direction in a different cross section (corresponding with Fig. 6); 1-behind the first row; 2-third row; 3-fifth row; 4-seventh row; 5-inflow

cylinders located in a channel of cross square section. The major thrust concentrated toward the visualization and physical explanation of the near-wall jets which generate lower pressure environments along their flow path. It was found that these jets, as they form, influence totally the flow structure inside the array by attracting the flow from the center regions toward the walls. The pressure charts confirmed the existence of these flow patterns and helped explain both the generation of the strong lateral flows, and the strong and confined stream like behavior of the jets in the near-wall areas. It was also shown that the near wall jet phenomenon appears only in the case of multi-row arrays. In the case of one row, the near wall jets do

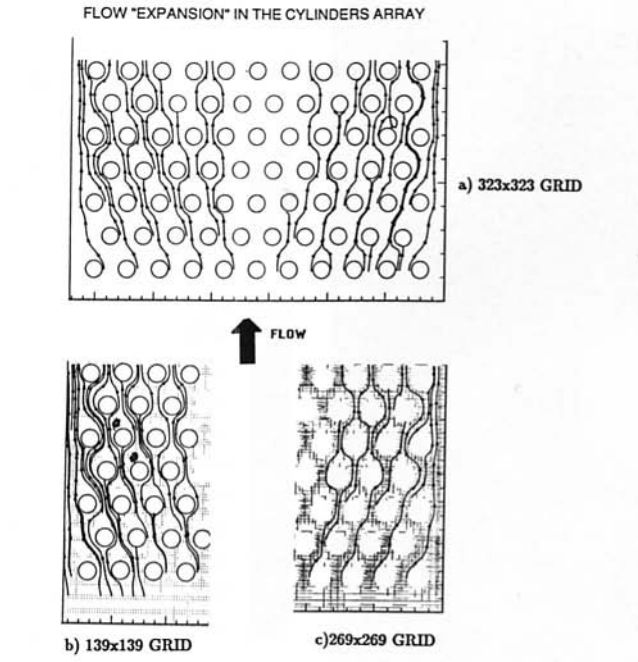

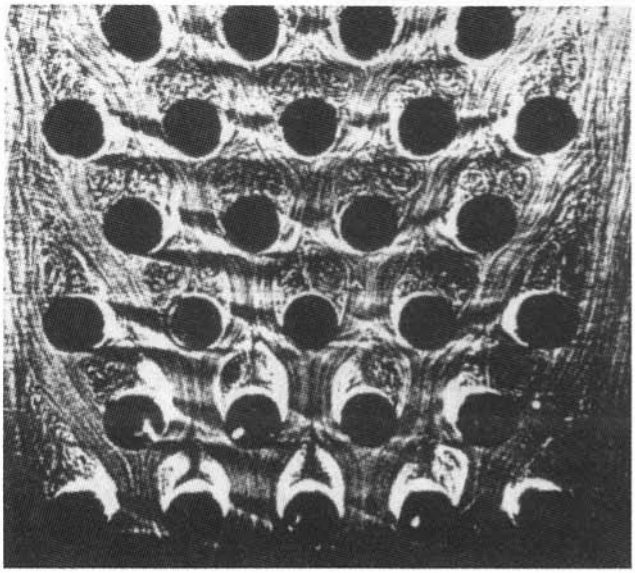

d) EXPERIMENTAL FLOW VISUALIZATION, Sarapkaya(1989)

Fig. 9(*a, b, c, d*) Particle traces in the cylinders array (seven rows) for the Reynolds number $Re_d = 125$

not have the chance to form since the flow structure is "reversed" on comparison to the multi-row array.

Acknowledgment

The authors wish to express their gratitude to Dr. Robert Bill and Mr. George Bobula from NASA Lewis Research Center, Cleveland, Ohio, for their continued support and encouragement. The work has been performed under the auspices of NASA grant NAG 3-969, NASA Lewis Research Center.

References

Braun, M. J., and Kudriavtsev, V. V., 1993, "A Numerical Simulation of a Brush Seal Section and Some Experimental Results," International Gas Turbine and AeroEngine Congress, Cincinnati, ASME Paper 93-GT-387, pp. 1–12 (accepted for the publication in the ASME *Journal of Turbomachinery*, Feb. 1995).

Braun, M. J., and Kudriavtsev, V. V., 1992, "Experimental and Analytical Investigation of Brush Seals," Seals Flow Code Development-92, NASA CP-10124, Proceedings of a workshop held at NASA Lewis Research Center, Aug. 5–6, pp. 181–195.

Bouard, R., and Coutanceau, M., 1980, "The Early Stage of Development of the Wake Behind an Impulsively Started Cylinder for $40 < Re < 10^4$," *Journal of Fluid Mechanics*, Vol. 101, Part 3, pp. 583.

Chen, C. K., Wong, K. L., and Cleaver, J. W., 1986, "Finite Element Solution of Laminar and Heat Transfer of Air in a Staggered and In-Line Tube Bank," *International Heat and Fluid Flow*, No. 4, p. 291.

Fornberg, B., 1991, "Steady Incompressible Flow Past a Row of Circular Cylinders," *Journal of Fluid Mechanics*, Vol. 225, pp. 655–671.

Kudriavtsev, V. V., and Braun, M. J., 1993, "A Reynolds Number Parametric Numerical Investigation of Flow Structure and Pressure Distribution in a System of Cylinders Array," ASME Fluids Engineering Conference, *Separated Flows*, M. Purtell and C. Dutton, eds., FED—Vol. 149, pp. 75–83, Washington, D.C. June 20–24.

Kudriavtsev, V. V., and Braun, M. J., 1994, "Advances in Brush Seal Numerical Modeling," SAE TP-941208, 1994 SAE Aerospace Atlantic Conference and Exposition, Dayton, Ohio, Apr. 18–22.

Li, J., Chambarel, A., Donneaud, M., and Martin, R., 1991, "Numerical Study of Laminar Flow Past One and Two Circular Cylinders," *Computers and Fluids*, Vol. 19, No. 2, pp. 155–170.

Moretti, P. M., and Cheng, M., 1987, "Instability of Flow Through Tube Rows," ASME JOURNAL OF FLUIDS ENGINEERING, Vol. 109, p. 197.

Paidoussis, M. P., Price, S. J., and Mavriplis, D., 1985, "A Semipotential Flow Theory for the Dynamics of Cylinder Arrays in Cross Flow," ASME JOURNAL OF FLUIDS ENGINEERING, Vol. 107, pp. 500–506.

Roache, P. L., 1985, *Computational Fluid Mechanics*, Hermosa Publishers.

Stansby, P. K., 1981, "A Numerical Study of Vortex Shedding from One and Two Circular Cylinders," *Aeronautical Quaterly*, pp. 48–71.

Sarapkaya, T., 1989, "Computational Methods with Vortices—the 1988 Freeman Scholar Lecture," ASME JOURNAL OF FLUIDS ENGINEERING, Vol. 111, No. 5, pp. 23–26.

Torrance, K. E., 1968, "Comparison of Finite-Difference Computations of Natural Convection," *Journal Research NBS: Mathematical Sciences*, N72B, 281.

Weaver, D. S., and Abd-Rabbo, A., 1985, "A Flow Visualization Study of a Square Array of Tubes in Water Crossflow," ASME JOURNAL OF FLUIDS ENGINEERING, Vol. 107, pp. 354–363.

Zdravkovich, M. M., and Stonebanks, K. L., 1988, "Intrinsically Non-Uniform and Metastable Flow in and Behind Tube Arrays," *ASME International Symposium on Flow-Induced Vibrations and Noise*, M. P. Paidoussis, O. M. Griffin, and C. Dalton, eds., Vol. 1, pp. 61–73.

Zdravkovich, M. M., 1977, "Review of Flow Interference Between Two Circular Cylinders in Various Arrangements," ASME JOURNAL OF FLUIDS ENGINEERING, Vol. 99, No. 4, pp. 618–633.

Effects of Initial Acceleration on the Flow Field Development Around Rapidly Pitching Airfoils

(Data Bank Contribution)*

C. P. Gendrich

M. M. Koochesfahani

Department of Mechanical Engineering,
Michigan State University,
E. Lansing, MI 48824

M. R. Visbal

CFD Research Branch,
Aeromechanics Division,
Wright Laboratory,
Wright-Patterson AFB,
Dayton, OH 45433

Computational results are presented to show how the acceleration period at the start of nominally constant pitch rate trajectories affects the dynamic stall process. Large amplitude motions of an NACA 0012 airfoil pitching about the quarter-chord axis were studied using constant (ON/OFF) acceleration profiles with nondimensional acceleration periods ranging between 0.039 to 0.6, and large pitch rates ($0.1 \leq \Omega^* \equiv \dot{\alpha}\, c/2U_\infty \leq 0.4$). The initial acceleration is observed to affect the integrated loads, surface pressure distribution, and the evolution of reversed flow regions just above the surface of the airfoil only during the acceleration period and for a relatively short time $\Delta\tau \leq 0.25$ afterwards; $\tau \equiv tU_\infty/c$. After that time, all of these quantities only depend on the instantaneous angle of attack for a given pitch rate. These results are consistent with and explain previous experimental flow visualization observations. The onset of leading edge separation at high and low pitch rates is shown to be characterized by different processes. At low pitch rates leading edge separation occurs after the reversed flow front originating at the trailing edge has reached the leading edge. At higher pitch rates leading edge separation and the upstream progression of the (trailing edge) reversed flow front develop independently.

1 Introduction

The dynamic stall process has been under investigation for over two decades now, and significant progress has been made toward understanding the physical processes associated with rapidly pitching an airfoil beyond its static stall angle of attack. The reviews of McCroskey (1982), Carr (1988), and Visbal (1990) provide good descriptions of the dynamic stall process as it is currently understood.

Constant pitch rate motions have received a great deal of attention recently for their potential application to supermaneuverable aircraft. For these motions a nondimensional pitch rate, $\Omega^* \equiv \dot{\alpha}c/2U_\infty$, has been introduced as one of the governing parameters; $\dot{\alpha}$ refers to the pitch rate, c the airfoil chord, and U_∞ the free-stream speed. It is clear that the initial part of the motion trajectory has to be distinguished by a nonconstant pitch rate motion due to the finite acceleration period which is characteristic of a real device. Very little is known about the influence of this initial acceleration period on the subsequent flow development around airfoils pitching to high angles of attack, α.

In an experimental flow visualization study by Koochesfahani and Smiljanovski (1993), the initial acceleration was systematically varied in order to document its effects on flow development for constant, relatively high pitch rate motions. The motion trajectory consisted of a constant acceleration period followed by a constant pitch rate segment and finally a constant deceleration portion. The airfoil pitched from 0 to 60 deg; see Fig. 1. The acceleration effects were described in terms of a non-dimensional acceleration period, $e \equiv T_a/T_c$, where T_a is the acceleration period and T_c refers to the time to pitch from 0 to 60 deg for the ideal (i.e., $T_a \rightarrow 0$) constant pitch rate motion. It was found that the angle of attack at the onset of leading edge separation was practically independent of the acceleration period. Furthermore, the subsequent flow developments after leading edge separation, such as the evolution of the dynamic stall vortex and its convection over the airfoil, were similarly insensitive to the details of the start of the motion. In all the cases studied, leading edge separation occurred after the initial acceleration period had ended. That investigation, which was qualitative and based entirely on flow visualization, only addressed the timing of the various events in the flow field development. The effects of initial acceleration on other important features of the flow, such as the integrated loads on the airfoil and the surface pressure gradient, have not yet been quantified.

All computational studies of nominally constant pitch rate motions also contain an initial acceleration phase. However, except for one preliminary investigation (Visbal, 1986), none

*Data have been deposited to the JFE Data Bank. To access the file for this paper, see instructions on p. 204 of this issue.

Contributed by the Fluids Engineering Division for publication in the JOURNAL OF FLUIDS ENGINEERING. Manuscript received by the Fluids Engineering Division July 23, 1993; revised manuscript received June 10, 1994. Associate Technical Editor: O. Baysal.

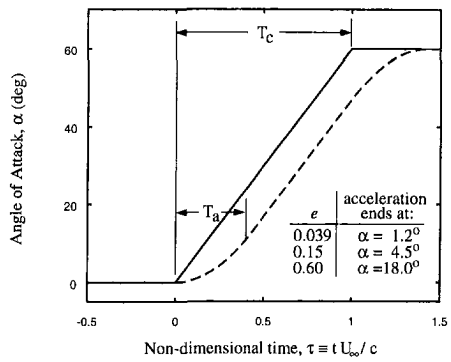

Fig. 1 Ideal and typical motion profiles. $e = = T_a/T_c$

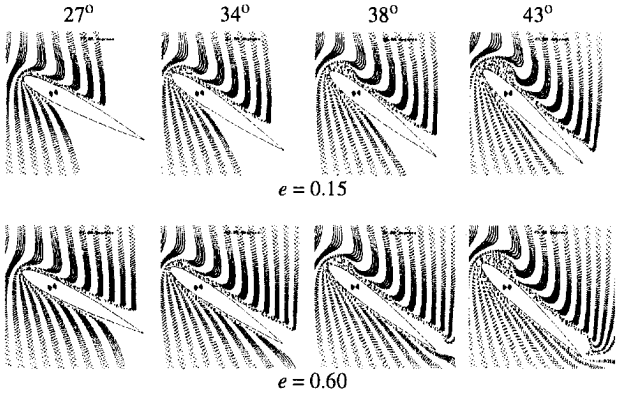

Fig. 2 Computational flow visualizations for $\Omega^* = 0.4$ and two different accelerations

of the previous studies has specifically addressed the effects of initial acceleration on the flow evolution. The current work, which is the computational counterpart of the flow visualization study of Koochesfahani and Smiljanovski (1993), aims to provide a quantitative basis for explaining the previous flow visualization results using two-dimensional full Navier-Stokes computations. The initial acceleration effects are characterized here in terms of the computed flow visualizations, the integrated load on the airfoil, the surface pressure distributions, and the evolution of reversed flow fronts just above the airfoil surface.

2 Computational Procedure

The current computations are based on the Navier-Stokes solver of Visbal and Shang (1989); see also Visbal (1986). This code uses the implicit approximately-factored algorithm of Beam and Warming (1978). This scheme is formulated using Euler implicit time differencing and second-order centered approximations for all spatial derivatives. In order to control numerical stability, implicit and explicit nonlinear dissipation as described by Jameson et al. (1981) is employed. The O-grid topology was used with 203 × 101 points along and normal to the airfoil boundary, respectively. The minimum grid spacings in these directions were $6 \times 10^{-4}c$ and $8 \times 10^{-5}c$, and the grid extended 30 chords away from the airfoil.

The effects of grid resolution, time step, and numerical damping on the accuracy of the computations have been described in previous studies. The grid used for our work is directly comparable to the medium resolution grid discussed in Visbal (1986) and Visbal and Shang (1989). In the latter study, differences in lift and drag coefficients computed using the medium and fine grids for the case $\Omega^* = 0.3$ were less than 1 percent for $\alpha \leq 40$ deg. In the former study, the worst case occurred for the lowest pitch rate considered, $\Omega^* = 0.1$, yet the lift and drag coefficients changed less than 3 percent for $\alpha \leq 30$ deg between the medium and coarse grid computations. The principal results presented in this paper address the flow behavior up to the onset of leading edge separation and the subsequent initial stages of dynamic stall vortex evolution. These phenomena occur over ranges of α below those referred to above (for each pitch rate mentioned). The present computations, therefore, provide accurate simulations for the portions of the flow field in which we are interested.

Results of Visbal (1986) for $\Omega^* = 0.1$ indicated that if the time step, $\Delta t U_\infty/c \leq 10^{-3}$, the numerical solution was independent of time step (e.g., lift and drag coefficient profiles remained unchanged upon halving the time step). This criterion was satisfied in all of the current computations; the maximum time steps were 10^{-3}, 5×10^{-4}, and 3×10^{-4} for $\Omega^* = 0.1$, 0.2, and 0.4, respectively. During the initial acceleration period, the time step was reduced even further to values which ranged between 5×10^{-5} and 2×10^{-4}.

Finally, the influence of damping in our computations was assessed by systematically increasing the damping coefficient. It was found that increasing the damping coefficient by a factor of two resulted in only small changes. For example, the lift and drag coefficients for $\Omega^* = 0.4$ changed by less than 0.6 percent throughout the entire motion trajectory; the angle of attack at the onset of leading edge separation, and the angles of attack characterizing the occurrence and evolution of the primary zones of reversed flow on the suction surface, varied by less than one degree for all the cases presented in this paper.

Particle tracking was added to the code for this study in order to visualize the flow field; 30,000 "particles" were introduced into the computational domain, and their positions were advanced using a first-order marching scheme. The initial spatial locations of these particles were selected to give the appearance of hydrogen bubbles from a pulsed wire used in previous water visualization experiments. Gendrich et al. (1992) have shown a very good correspondence between these computed "flow visualizations" and those obtained experimentally. For example, the angle of attack marking the first visual appearance of a "bulge" near the nose of the airfoil as the flow separates there agrees to about 2.5 degrees between the experiment and computations.

3 Results and Discussion

The flow parameters were selected to allow comparison with the range of experimental conditions in the water tunnel studies of Koochesfahani and Smiljanovski (1993) and Brown (1992). The computed flow field was that of an NACA 0012 airfoil pitching about the quarter-chord axis from zero to 60 deg angle of attack. The chord Reynolds number, Re_c, was varied between 8000 and 20,000, but results are discussed here only for a Reynolds number of 12,000. Since the boundary layer is laminar over the Reynolds number range considered here, the use of a turbulence model was not required. The freestream Mach number was maintained at 0.1, and the maximum density variation was less than 3 percent for all cases, which should enable acceptable comparisons to be made with previous water tunnel studies. Pitch rates were computed in the range $0.1 \leq \Omega^* \leq 0.4$, with acceleration values in the range $0.001 \leq e \leq 0.6$. In this paper, results will be presented only for $\Omega^* = 0.1$, 0.2, and 0.4 with $e = 0.6$, 0.15, and 0.039. The entire computational domain was stored every half degree from 0 through 50 deg.

In Fig. 2 we present computed flow visualizations for $\Omega^* = 0.4$ at various angles of attack, illustrating the onset of leading edge separation for two different accelerations. At $\alpha = 27$ deg the flow near the leading edge is seen to follow the contour of the airfoil, and to that extent it exhibits the behavior of an

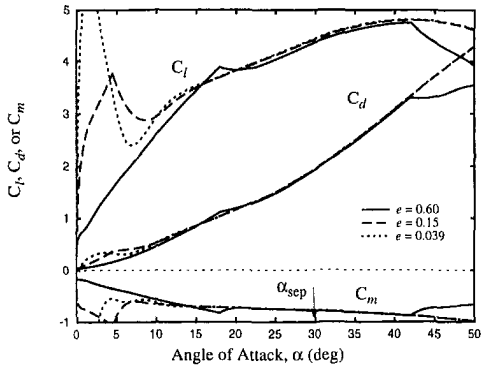

Fig. 3 Lift, drag, and moment coefficients for $\Omega^* = 0.4$. α_{sep} is based on the appearance of curve (2) in Fig. 9(*c*)

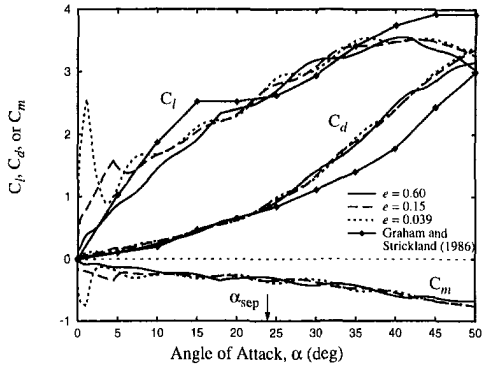

Fig. 4 Lift, drag, and moment coefficients for $\Omega^* = 0.2$. α_{sep} is based on the appearance of curve (2) in Fig. 9(*b*)

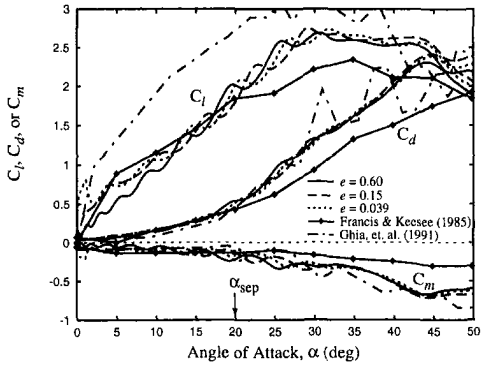

Fig. 5 Lift, drag, and moment coefficients for $\Omega^* = 0.1$. α_{sep} is based on the appearance of curve (2) in Fig. 9(*a*)

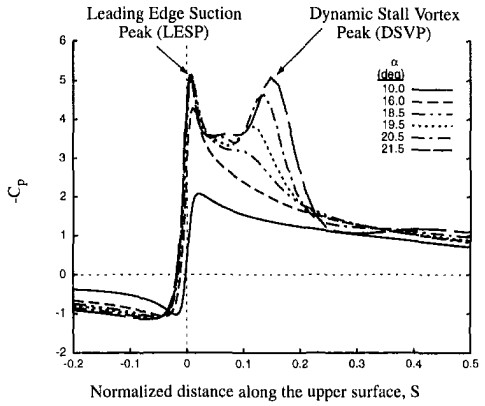

Fig. 6 Surface pressure development during a dynamic stall event. $\Omega^* = 0.1$, and $e = 0.15$

attached flow. By 34 deg a "bulge" has formed near the leading edge, and visually we can identify the onset of leading edge separation to have occurred already at an angle, α_{sep}, somewhere between 27 and 34 deg. As the airfoil continues pitching to higher angles of attack, the bulge develops into the dynamic stall vortex (DSV). It should be noted that the term "separation" is used here to refer to the condition where the outer inviscid flow no longer follows the airfoil contour; it does not refer to occurrence of reverse flow in the boundary layer. The computational results shown in Fig. 2 indicate that the visual appearance of the flow separation from the leading edge is not influenced by the initial acceleration, in agreement with the experimental observations of Koochesfahani and Smiljanovski (1993).

To quantify the initial acceleration effects, we first discuss the behavior of the integrated loads on the airfoil. The computed lift, drag, and moment curves for $\Omega^* = 0.4$ are shown in Fig. 3. The spiky overshoots near the beginning of each curve are believed to be due to apparent mass effects. The α_{sep} estimates indicated in Figs. 3–5 are based on the development of closed recirculation zones near the leading edge (to be discussed later) and not the visual appearance of the DSV "bulge," which typically lags behind. The important result from Fig. 3 is that each force coefficient approaches a curve which depends only on the instantaneous angle of attack (i.e., is independent of e) within a time scale of $\Delta\tau \cong 0.25$ after the end of the acceleration period (see the table in Fig. 1); τ is the nondimensional time defined by $\tau \equiv tU_\infty/c$. For the particular pitch rate shown in Fig. 3, this time scale corresponds to a maximum change in α of approximately 10 deg beyond the end of acceleration. Note that the sudden change in the behavior of the force coefficients at 42 deg for $e = 0.6$ is due to the beginning of the deceleration phase for that case.

Figures 4 and 5 show the lift, drag, and moment coefficients versus angle of attack for $\Omega^* = 0.2$ and 0.1, respectively. The same acceleration effects are observed as for the higher pitch rate, namely, that within $\Delta\tau \cong 0.25$ after the end of the acceleration period, the force coefficients have become independent of acceleration history. Results available from the experiments of Graham and Strickland (1986), Francis and Keesee (1985), and the computations of Ghia et al. (1991) are included in Figs. 4 and 5 for comparison. These studies were selected because they used sets of parameters closest to those of the current computations. While the overall agreement between the lift, drag, and moment profiles is good, it is difficult to assess the sources of any discrepancies in these figures, since the flow conditions and the airfoil types in the studies cited above are not identical to those used here. The primary differences are: Graham and Strickland used an NACA 0015 airfoil and $Re_c = 10^5$; Francis and Keesee used $\Omega^* = 0.13$, $Re_c = 1.4 \times 10^5$, and a pitch axis at 0.317 chord; Ghia et al. used an NACA 0015 airfoil and $Re_c = 10^4$. Additionally the level of experimental and computational uncertainties are not available from the above references.

Since leading edge separation is connected to the surface pressure gradient, the effects of acceleration history on the development of the surface pressure coefficient (C_p) and pressure gradient ($\partial C_p/\partial s$) profiles are presented next. The typical evolution of the C_p profile at a fixed value of initial acceleration is first illustrated in Fig. 6. Note the formation of the leading edge suction peak (LESP) followed by the formation of a second suction peak due to the vorticity concentration that ultimately becomes the dynamic stall vortex. Following the nomenclature used by Acharya and Metwally (1992), we will refer to this second peak as the dynamic stall vortex peak (DSVP). The DSVP magnitude is initially less than that of the LESP, but it grows in strength and finally exceeds the leading edge suction peak. While the LESP remains practically fixed

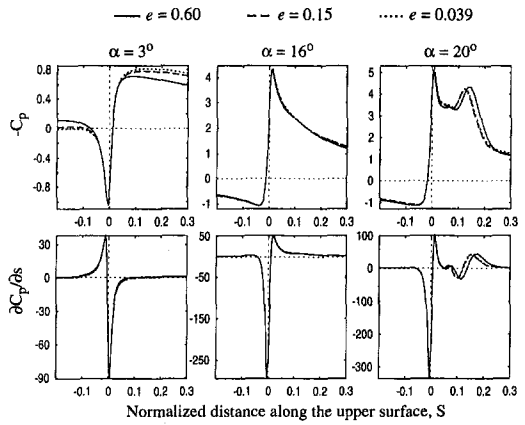

Fig. 7 Surface pressure and pressure gradient profiles for $\Omega^* = 0.1$

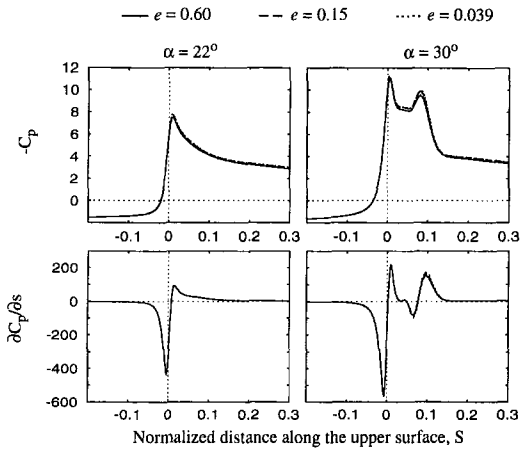

Fig. 8 Surface pressure and pressure gradient profiles for $\Omega^* = 0.4$

at a location near the leading edge, the DSVP moves toward the trailing edge at a fairly constant rate. The development of the pressure field displayed in Fig. 6 agrees very well with that presented by Acharya and Metwally (1992) and Visbal (1991), among others.

The effects of varying the initial acceleration on the development of the surface pressure and pressure gradient distributions are illustrated in Figs. 7 and 8. Results are shown for two pitch rates at selected angles before and at the onset of leading edge separation. The evolution for the lower pitch rate ($\Omega^* = 0.1$) is presented in Fig. 7 for $\alpha = 3$ and 16 deg (before α_{sep}) and $\alpha = 20$ deg (at α_{sep}). At 3 deg the acceleration has already ended for $e = 0.039$, while it continues for the other two e values. The pressure over practically the entire surface is different for each value of e, with the exception of the stagnation region. Note, however, that the pressure gradient shows much less sensitivity to variations in e. Similar behavior of the surface pressure gradient is exhibited at $\alpha = 16$ deg, just before α_{sep}; note that by this angle of attack the surface pressure profile has also relaxed to a single curve nearly independent of the variations in e. The similarity among the different acceleration cases for both surface pressure and pressure gradient persists even at a higher angle corresponding to α_{sep} (see Fig. 7, $\alpha = 20$ deg). Since the initial acceleration history has little effect on the surface pressure gradient, this explains the corresponding insensitivity of the leading edge separation angle and the subsequent flow development observed in both the current computations and the previous flow visualization experiments.

Figure 8 showing the pressure field before and at α_{sep} for the higher pitch rate of $\Omega^* = 0.4$ supports all the assertions made earlier. For this pitch rate the pressure field exhibits even less dependence on initial motion history as compared to the $\Omega^* = 0.1$ case. It should be emphasized that the discussion presented here refers to the behavior of the surface pressure field over the first 30 percent of the chord (see Figs. 7–8). There are differences in the pressure field in the aft region of the airfoil which are responsible for the variation in the loads among the different cases (see Figs. 3–5); however, those differences do not have a significant impact on the development of separation near the leading edge.

The discussion above addresses the flow behavior for only selected angles of attack. The evolution of the surface pressure field for the entire motion has been analyzed in terms of the magnitude and location of the various surface pressure minima and pressure gradient maxima corresponding to the LESP and DSVP evolution. The main conclusion from these results (not shown here) is that the effects of initial acceleration are limited to a short period (no more than $\Delta\tau \cong 0.25$) after the end of acceleration. After a certain angle of attack ($\alpha \cong 6$ deg for $\Omega^* = 0.1$, $\alpha \cong 8$ deg for $\Omega^* = 0.2$, and $\alpha \cong 10$ deg for $\Omega^* = 0.4$) the magnitudes and locations for both the pressure minima and pressure gradient maxima become independent of initial motion history and depend, for each pitch rate, only on the instantaneous angle of attack.

One of the prominent features of the unsteady separation process on a pitching airfoil is the existence of a thin region of reversed flow over the suction surface of the airfoil. The evolution of this reversed flow is believed to be intimately connected with the leading edge separation process. The effect of the initial acceleration on the development of various regions of tangential flow reversals in the rotating frame of the airfoil and just above its surface is characterized in Fig. 9 for three different pitch rates. Figure 9(a) illustrates that the front of the reversed flow region which originates near the trailing edge, i.e., the curve labeled (1), continuously moves upstream during pitch up for the case $\Omega^* = 0.1$. When this front nears the leading edge ($\alpha \cong 20$ deg), a new region of forward flow labeled (2) forms, which corresponds to the formation of a counterclockwise recirculation zone above the airfoil surface. Based on the evolution of the vorticity field near the leading edge and flow visualizations similar to those in Fig. 2, Gendrich et al. (1992) determined that the occurrence of this forward flow region marks the initial stages of flow separation from the leading edge. Recent computations of Choudhuri et al. (1994) have reached similar conclusions.

It is very important to note that this behavior is different at higher pitch rates; see Fig. 9(c) for $\Omega^* = 0.4$. In this case the progression of the reversed flow front originating at the trailing edge never nears the leading edge before separation is observed there. Instead, an independent region of reversed flow labeled (3) develops near the leading edge at approximately 20 deg, and the forward flow region (curve 2) forms within it at $\alpha_{sep} = 30$ deg, signalling the onset of leading edge separation. Experimental evidence for the occurrence of leading-edge reverse flow independent of the trailing-edge reverse flow has also recently been provided by Acharya (private communication).

The important result from Fig. 9 is that, regardless of which of the two processes described above is characteristic of the flow (i.e., leading edge stall versus trailing edge stall), the initial acceleration does not significantly influence that process.

4 Conclusions

The unsteady flow field around an NACA 0012 airfoil pitching to large angles of attack has been computed for three different pitch rates, $\Omega^* = 0.1$, 0.2, and 0.4, and three different initial constant acceleration periods, $e = 0.039$, 0.15, and 0.6. For all of these cases, leading edge separation begins after the

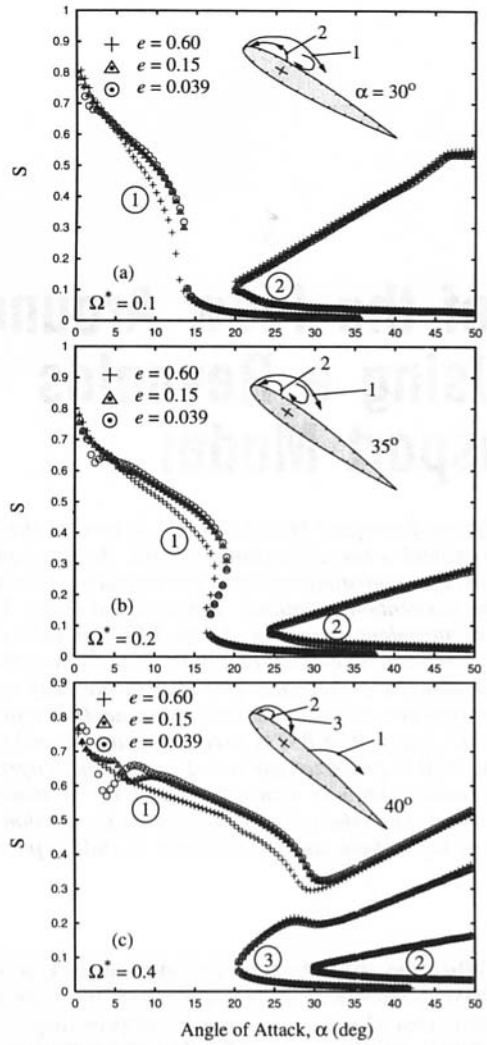

Fig. 9 Tangential velocity flow reversal locations just above the airfoil surface. The sketches approximate the flow reversal topology for the indicated angles of attack

acceleration has ended; no cases have been presented for which the airfoil was still accelerating at the onset of leading edge separation.

The present computations provide detailed quantitative information, which was not available from previous experiments, about the effects of initial acceleration on the integrated loads, surface pressure distributions, and the evolution of reversed flow regions just above the surface of the airfoil. Our results show that the initial acceleration influences these quantities only during the acceleration period and for a relatively short time ($\Delta\tau \leq 0.25$) afterwards. After that time, all of these quantities only depend on the instantaneous angle of attack for a given pitch rate. The value of $\Delta\tau$ determined here applies to the specific range of flow parameters presented; its dependence on parameters such as Reynolds number and Mach number has not been investigated.

These findings not only support the conclusions reached from the experimental observations of Koochesfahani and Smiljanovski (1993), they also provide a physical explanation for those observations. The findings reported here are in qualitative agreement with the inviscid flow lift-curve slope results of Jumper et al. (1987) which indicate that at high enough pitch rates motion history effects will saturate.

We would like to draw attention to the important implication of our results that a convenient acceleration profile can be selected for experimental and computational studies without seriously impacting the dynamics of the unsteady stall process, as long as acceleration ends before leading edge separation begins.

The results presented also demonstrate that two different processes characterize the onset of laminar leading edge separation at high and low pitch rates. At low pitch rates the onset of leading edge separation occurs after the reversed flow front originating at the trailing edge has reached the leading edge. At higher pitch rates, these two features develop independently, and leading edge separation occurs without the reversed flow front from the trailing edge having ever reached the leading edge region.

JFE Data Bank Contribution

Some of the data from these computations are deposited in the form of a video tape.

Acknowledgments

The first two authors would like to acknowledge the support of the U.S. Air Force which provided computational resources and funding through grants AFOSR-89-0417 and F49620-86-C-0127.

References

Acharya, M. and Metwally, M. H., 1992, "Unsteady Pressure Field and Vorticity Production Over a Pitching Airfoil," *AIAA Journal*, Vol. 30, No. 2.

Beam, R. M. and Warming, R. F., 1978, "An Implicit Factored Scheme for the Compressible Navier-Stokes Equations," *AIAA Journal*, Vol. 16, No. 4.

Brown, T. A., "Effects of Motion History on Leading Edge Separation for an Airfoil Pitching to Large Angles of Attack," M.S. thesis, Michigan State University, 1992.

Carr, L. W., 1988, "Progress in Analysis and Prediction of Dynamic Stall," *Journal of Aircraft*, Vol. 25, No. 1.

Choudhuri, P. G., Knight, D. D., and Visbal, M. R., 1994, "Two-Dimensional Unsteady Leading-Edge Separation on a Pitching Airfoil," *AIAA Journal*, Vol. 32, No. 4.

Francis, M. S. and Keesee, J. S., 1985, "Airfoil Dynamic Stall Performance with Large-Amplitude Motions," *AIAA Journal*, Vol. 23, No. 11.

Gendrich, C. P., Koochesfahani, M. M., and Visbal, M. R., 1992, "The Visual and Vortical Signature of Leading Edge Separation," *Bulletin of the American Physical Society*, Vol. 37, No. 8.

Ghia, K. N., Yang, J., Osswald, G. A., and Ghia, U., 1991, "Study of Dynamic Stall Mechanism Using Simulation of Two-Dimensional Unsteady Navier-Stokes Equations," AIAA Paper 91-0546.

Graham, G. M. and Strickland, J. H., 1986, "An Experimental Investigation of an Airfoil Pitching at Moderate to High Rates to Large Angles of Attack," AIAA Paper 86-0008.

Jameson, A., Schmidt, W., and Turkel, E., 1981, "Numerical Solutions of the Euler Equations by Finite Volume Methods Using Runge-Kutta Time Stepping Schemes," AIAA Paper 81-1259.

Jumper, E. J., Shreck, S. J., and Dimmick, R. L., 1987, "Lift-Curve Characteristics for an Airfoil Pitching at Constant Rate," *Journal of Aircraft*, Vol. 24, No. 10.

Koochesfahani, M. M. and Smiljanovski, V., 1993, "Initial Acceleration Effects on Flow Evolution Around Airfoils Pitching to High Angles of Attack," *AIAA Journal*, Vol. 31, No. 8.

McCroskey, W. J., 1982, "Unsteady Airfoils," *Annual Review of Fluid Mechanics*, Vol. 14.

Visbal, M. R., "Evaluation of an Implicit Navier-Stokes Solver for some Unsteady Separated Flows," AIAA Paper 86-1053, May, 1986.

Visbal, M. R., 1990, "On Some Physical Aspects of Airfoil Dynamic Stall," *Proceedings of the ASME Symposium on Non-Steady Fluid Dynamics*, June 4–7.

Visbal, M. R., 1991, "On the Formation and Control of the Dynamic Stall Vortex on a Pitching Airfoil," AIAA Paper 91-0006.

Visbal, M. R. and Shang, J. S., 1989, "Investigation of the Flow Structures around a Rapidly Pitching Airfoil," *AIAA Journal*, Vol. 27, No. 8. See also AIAA Paper 87-1424, June, 1987.

Prediction of the Flow Around an Airfoil Using a Reynolds Stress Transport Model

Lars Davidson
Thermo and Fluid Dynamics,
Chalmers University of Technology,
S-412 96 Gothenburg, Sweden

A second-moment Reynolds Stress Transport Model (RSTM) is used in the present work for computing the flow around a two-dimensional airfoil. An incompressible SIMPLEC code is used, employing a non-staggered grid arrangement. A third-order QUICK scheme is used for the momentum equations, and a second-order, bounded MUSCL scheme is used for the turbulent quantities. As the RSTM is valid only for fully turbulent flow, an eddy viscosity, one-equation model is used near the wall. The two models are matched along a preselected grid line in the fully turbulent region. Detailed comparisons between calculations and experiments are presented for an angle of attack of $\alpha = 13.3$ deg. The RSTM predictions agree well with the experiments, and approaching stall is predicted for $\alpha = 17$ deg, which agrees well with experimental data. The results obtained with a two-layer $k - \epsilon$ model show poor agreement with experimental data; the velocity profiles on the suction side of the airfoil show no tendency of separation, and no tendency of stall is predicted.

Introduction

Flow around airfoils is an interesting turbulent flow configuration involving a number of fundamental physical flow phenomena such as transition, curvature-induced production of turbulence, separation and wake flow. Transition is usually not predicted but is prescribed from experimental data. Some work has been presented in which transition is predicted using the e^n-method based on the linearized stability theory (Cebeci, 1989). In real (industrial) configurations, it is of utmost importance to be able to predict the locations of transition; in the present study, however, the locations of transition are prescribed from experimental data.

Curvature effects, related either to curvature of the wall or streamline curvature, are known to have significant effects on the turbulence (Bradshaw, 1973). Both types of curvature are present in airfoil flows, the former on the suction side and the latter in and near the separation region. The entire Reynolds tensor is active in the interaction process between shear stresses, normal stresses and mean velocity strains. When predicting flows where curvature effects are important, it is thus necessary to use turbulence models that accurately predict all Reynolds stresses, not only the shear stresses.

Second-moment closures such as RSTM are superior to simpler turbulence models such as the $k - \epsilon$ or the Baldwin-Lomax models. The main reasons for their superiority are their ability to account for (i) streamline curvature, (ii) strong nonlocal effects and history effects for the individual stresses, and (iii) irrotational strains, phenomena which all are present in airfoil flow.

(i) When the streamlines in boundary layer type of flow have a convex (concave) curvature, the turbulence is stabilised (destabilized), which dampens (augments) the turbulence (Bradshaw, 1973; Rodi and Scheuerer, 1983), especially the shear stress and the Reynolds stress normal to the wall. Bradshaw demonstrates that even small amounts of convex curvature can have a significant effect on the turbulence. In the present configuration, both wall curvature and streamline curvature are present.

(ii) The adverse pressure gradient on the suction side of the airfoil with a subsequent separation produces strong anisotropy in the Reynolds stresses, which is transported downstream.

(iii) In boundary layer flow, the only term which contributes to the production term in the k equation is $-\rho\overline{uv}\partial U/\partial y$ (x denotes streamwise direction). Thompson and Whitelaw (1985) found that, near the separation point as well as in the separation zone, the production term $-\rho(\overline{u^2} - \overline{v^2})\partial U/\partial x$ is of equal importance. This is also the case for airfoil flow, where large irrotational strains ($\partial U/\partial x$, $\partial V/\partial y$) prevail, for example, near the point of separation.

In a previous paper (Davidson and Rizzi, 1992), an Algebraic Stress Model was applied on the same configuration as in the present study. In the ASM, which is a truncated form of the RSTM, the transport terms (convection and diffusion) are approximated as being proportional to the transport of turbulent kinetic energy. This is maybe a sound approximation for the normal stresses, but not for the shear stresses. The RSTM is superior to ASM, mainly because the more accurate treatment of convection and diffusion, where in the RSTM the individual stresses are transported independently of each other.

The paper is organized as follows: the mean flow equations are presented first, together with some details on the compu-

Contributed by the Fluids Engineering Division for publication in the JOURNAL OF FLUIDS ENGINEERING. Manuscript received by the Fluids Engineering Division March 23, 1993; revised manuscript received April 25, 1994. Associate Technical Editor: O. Baysal.

tational method. The turbulence model is described in the section that follows. A discussion is then presented of the way in which the turbulence is affected by streamline curvature and how the RSTM accounts for these effects. The subsequent section presents the results, and in the final section conclusions are drawn.

Mean Flow Equations

We have the incompressible form of the continuity equation

$$\frac{\partial}{\partial x_i}(U_i) = 0 \tag{1}$$

and momentum equation

$$\rho \frac{\partial}{\partial x_j}(U_i U_j) = -\frac{\partial p}{\partial x_i} + \frac{\partial}{\partial x_j}\left(\mu \frac{\partial U_i}{\partial x_j} - \rho \overline{u_i u_j}\right) \tag{2}$$

Numerical Method. The finite volume computer program CALC-BFC (Boundary Fitted Coordinates) for three-dimensional complex geometries (Davidson and Farhanieh, 1992; Johansson et al., 1993) is used in this study. The program uses Cartesian velocity components, and the pressure-velocity coupling is handled with the SIMPLEC procedure. Staggered grids for the velocities have been used (Patankar, 1980) in most finite volume programs. In the present work, however, a collocated grid arrangement is used, which means that velocities are stored together with the other variables (p, k, ϵ, $\overline{u_i u_j}$) at the center of the control volume. This concept was suggested by Rhie and Chow (1984), and has also been used by, e.g., Burns and Wilkes (1986), Perić et al. (1988), and Majumdar et al. (1992).

The convective terms in the mean flow equations are discretized using QUICK, a third-order scheme by Leonard (1979). For turbulent quantities ($\overline{u^2}$, $\overline{v^2}$, $\overline{uv}$, k, and ϵ) MUSCL, a second-order, bounded scheme of van Leer (1979), is used.

Boundary Conditions. All variables are set to zero at the walls except for pressure, for which $\partial^2 p/\partial n^2 = 0$ is used. At the farfield the velocity components are set from experimental data, i.e.,

$$U = \cos\alpha, \quad V = \sin\alpha, \tag{3}$$

where α denotes angle of attack. The pressure is set from $\partial^2 p/\partial n^2 = 0$. All turbulent quantities are either set to zero or are extrapolated, depending on whether the case is inflow or outflow.

The Reynolds Stress Transport Model

The Reynolds Stress Transport Model has the form (Gibson and Younis, 1986):

$$\underbrace{\frac{\partial}{\partial x_k}(\rho U_k \overline{u_i u_j})}_{\text{convection}} = \underbrace{-\rho\overline{u_i u_k}\frac{\partial U_j}{\partial x_k} - \rho\overline{u_j u_k}\frac{\partial U_i}{\partial x_k}}_{\text{production } P_{ij}} + \Phi_{ij} + D_{ij} - \rho\epsilon_{ij} \tag{4}$$

The convection and production terms are exact and do not require any modelling assumptions. The pressure strain Φ_{ij} and the dissipation ϵ_{ij} are modeled in a standard manner (Gibson and Younis, 1986).

The diffusion term D_{ij} can be modelled using the Generalized Gradient Diffusion Hypothesis GGDH (Daly and Harlow, 1970)

$$D_{ij} = \frac{\partial}{\partial x_m}\left(c_s \rho \overline{u_k u_m}\frac{k}{\epsilon}\frac{\partial \overline{u_i u_j}}{\partial x_k}\right) \tag{5}$$

However, as severe convergence problems were experienced using the GGDH owing to the destabilising cross-derivatives, the diffusion term D_{ij} is modelled using the eddy viscosity assumption

$$D_{ij} = \frac{\partial}{\partial x_m}\left(\frac{\mu_t}{\sigma_t}\frac{\partial \overline{u_i u_j}}{\partial x_m}\right). \tag{6}$$

Following a suggestion by Lien (1992), the turbulent Prandtl number σ_t has been modified. The diffusion in the normal direction is usually much more important than in the streamwise direction. The diffusion coefficient using the eddy viscosity formulation in Eq. (6) is μ_t/σ_t and can be compared with the one in the GGDH-expression in Eq. 5, so that

$$\frac{\nu_t}{\sigma_t} \equiv \frac{c_\mu k^2}{\epsilon \sigma_t} = c_s \frac{k\overline{v^2}}{\epsilon} \tag{7}$$

With $c_s = 0.22$ and $\overline{v^2}/k \simeq 0.5$, we get $\sigma_t = 0.82$. Thus the viscosity in the diffusion term in Eq. (6) is computed as

$$\frac{\mu_t}{\sigma_t} = \frac{\rho}{0.82}\frac{c_\mu k^2}{\epsilon} \tag{8}$$

For ϵ, we obtain the Prandtl number $\sigma_\epsilon = 1$ with $c_\epsilon = 0.18$.

The one-equation eddy viscosity model by Wolfshtein (1969), modified by Chen and Patel (1988), is used near the walls. In this model, the standard k equation is solved and the turbulent length scale is taken from an algebraic expression; for more details see Davidson (1993b).

The k and ϵ-Equations In an RSTM, there are two equivalent sets of equations which can be solved, either $\overline{u^2}$, $\overline{v^2}$, $\overline{w^2}$, $\overline{uv}$, and ϵ or $\overline{u^2}$, $\overline{v^2}$, k, $\overline{uv}$, and ϵ. The latter set has been chosen in the present study. The primary reason for this choice is that the k equation must in any case be solved in the one-equation region.

The standard k and ϵ equations in the RSTM have the form:

$$\frac{\partial}{\partial x_j}(\rho U_j k) = D^k + P^k - \rho\epsilon \tag{9}$$

$$\frac{\partial}{\partial x_j}(\rho U_j \epsilon) = D^\epsilon + \frac{\epsilon}{k}(c_{1\epsilon}P^k - c_{2\epsilon}\rho\epsilon) \tag{10}$$

As for the Reynolds stresses, the diffusion terms D^k, D^ϵ are calculated using the eddy viscosity assumption with $\sigma_k = 0.82$ and $\sigma_\epsilon = 1$, see Eqs. (6)–(8).

Two Variants of RSTM. Two different Reynolds stress models are compared. One is the standard model of Gibson and Launder (1978) (hereafter denoted GL), which has been used extensively in the literature. The other model is that proposed by Gibson and Younis (1986) (hereafter denoted GY). The two models differ only in the choice of constants. When modelling the pressure strain term $\Phi_{ij,1} + \Phi_{ij,2}$, there are three chief physical processes used to determine the constants: (*a*) return-to-isotropy when all mean strains are zero, (*b*) rapid-distortion theory, and (*c*) experimental stress levels in simple shear flows. In the GL model, (*b*) and (*c*) have been favoured at the expense of (*a*). Lumley (1978) argues that (*b*) is not relevant since it is assumed in rapid-distortion theory that the mean strain (the rapid part of the pressure-strain term, $\Phi_{ij,2}$) acts on the entire turbulence spectra. In reality, it acts only on the low-wave number part of the spectra, i.e., the large scales, whose energy is spread to the smaller scales through the cascade effect. In the GY model, the criteria dictated by rapid distortion is relaxed, and the return-to-isotropy criterion is taken fully into account. The constants for the two models are:

Model GY (c_1, c_2, c_1', c'_2, $c_{1\epsilon}$, $c_{2\epsilon}$) = (3.0, 0.3, 0.75, 0.15, 1.4, 1.8)

Model GL (c_1, c_2, c_1', c_2', $c_{1\epsilon}$, $c_{2\epsilon}$) = (1.8, 0.6, 0.5, 0.3, 1.44, 1.9)

The two models are compared in Fig. 1. Model GY is otherwise used throughout this study.

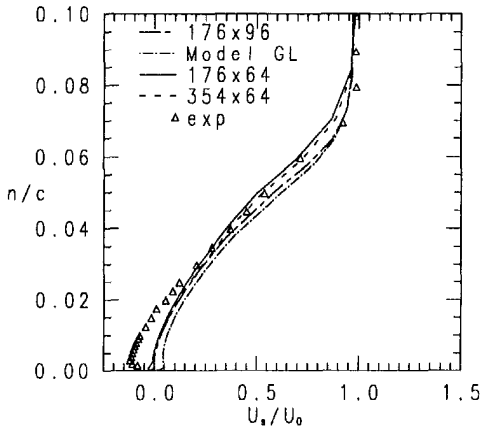

Fig. 1 U_s **profiles predicted with RSTM (Model GY) using different meshes. The** U_s **profile computed with Model GL is also included (mesh 176 × 96)**

Streamline Curvature

When the streamlines in boundary layer flow have a convex curvature, the turbulence is stabilised. This dampens the turbulence (Bradshaw, 1973; Rodi and Scheuerer, 1983), especially the shear stress and the Reynolds stress normal to the wall. Concave curvature destabilises the turbulence. The ratio of boundary layer thickness δ to curvature radius R is a common parameter for quantifying the curvature effects on the turbulence. The work reviewed by Bradshaw demonstrates that even such small amounts of convex curvature as $\delta/R = 0.01$ can have a significant effect on the turbulence. Thompson and Whitelaw (1985) carried out an experimental investigation on a configuration simulating the flow near a trailing edge of an airfoil, where they measured $\delta/R \simeq 0.03$. They reported a 50 percent decrease of $\rho\overline{v^2}$ (Reynolds stress in the normal direction to the wall) owing to curvature. The reduction of $\rho\overline{v^2}$ and $-\rho\overline{uv}$ was also substantial. In addition, they reported significant damping of the turbulence in the shear layer in the outer part of the separation region.

An illustrative model case is curved boundary layer flow. A polar coordinate system $r - \theta$ with θ locally aligned with the streamline is introduced. As $U_\theta = U_\theta(r)$ (with $\partial U_\theta/\partial r > 0$ and $U_r = 0$), the radial inviscid momentum equation degenerates to

$$\frac{\rho U_\theta^2}{r} - \frac{\partial p}{\partial r} = 0 \tag{11}$$

Here the variables are instantaneous or laminar. The centrifugal force exerts a force in the normal direction (outward) on a fluid following the streamline, which is balanced by the pressure gradient. If the fluid is displaced by some disturbance (e.g., turbulent fluctuation) outwards to level A, it encounters a pressure gradient larger than that to which it was accustomed at $r = r_0$, as $(U_\theta)_A > (U_\theta)_0$, which from Eq. (11) gives $(\partial p/\partial r)_A > (\partial p/\partial r)_0$. Hence the fluid is forced back to $r = r_0$. Similarly, if the fluid is displaced inwards to level B, the pressure gradient is smaller here than at $r = r_0$ and cannot keep the fluid at level B. Instead the centrifugal force drives it back to its original level.

It is clear from the model problem above that convex curvature, when $\partial U_\theta/\partial r > 0$, has a stabilizing effect on (turbulent) fluctuations, at least in the radial direction. It is discussed below how the Reynolds stress model responds to streamline curvature.

Assume that there is a flat-plate boundary layer flow. The ratio of the normal stresses $\rho\overline{u^2}$ and $\rho\overline{v^2}$ is typically 5. At one x station, the flow is deflected upwards. How will this affect the turbulence? Let us study the effect of concave streamline curvature. The production terms P_{ij} in Eq. (4) owing to rotational strains can be written as

Table 1 Effect of streamline curvature on turbulence

	$\partial U_\theta/\partial r > 0$	$\partial U_\theta/\partial r < 0$
Convex curvature	stabilizing	destabilizing
Concave curvature	destabilizing	stabilizing

$$\text{RSTM, } \overline{u^2}\text{ - eq. : } \quad P_{11} = -2\rho\overline{uv}\frac{\partial U}{\partial y} \tag{12}$$

$$\text{RSTM, } \overline{uv}\text{ - eq. : } \quad P_{12} = -\rho\overline{u^2}\frac{\partial V}{\partial x} - \rho\overline{v^2}\frac{\partial U}{\partial y} \tag{13}$$

$$\text{RSTM, } \overline{v^2}\text{ - eq. : } \quad P_{22} = -2\rho\overline{uv}\frac{\partial V}{\partial x} \tag{14}$$

$$k - \epsilon : P^k = \mu_t\left(\frac{\partial U}{\partial y} + \frac{\partial V}{\partial x}\right)^2 \tag{15}$$

As long as the streamlines are parallel to the wall, all production is a result of $\partial U/\partial y$. However as soon as the streamlines are deflected, there are more terms resulting from $\partial V/\partial x$. Even if $\partial V/\partial x$ is much smaller than $\partial U/\partial y$ it will still contribute non-negligibly to P_{12} as $\rho\overline{u^2}$ is much larger than $\rho\overline{v^2}$. Thus the magnitude of P_{12} will increase (P_{12} is negative) as $\partial V/\partial x > 0$. An increase in the magnitude of P_{12} will increase $-\overline{uv}$, which in turn will increase P_{11} and P_{22}. This means that $\rho\overline{u^2}$ and $\rho\overline{v^2}$ will be larger and the magnitude of P_{12} will be further increased, and so on. It is seen that there is a positive feedback, which continuously increases the Reynolds stresses. It can be said that the turbulence is destabilised owing to concave curvature of the streamlines.

However, the $k - \epsilon$ model is not very sensitive to streamline curvature (neither convex nor concave), as the two rotational strains are multiplied by the same coefficient (the turbulent viscosity).

If the flow (concave curvature) is a wall jet flow where $\partial U/\partial y < 0$, the situation will be reversed: the turbulence will be stabilised. If the streamline (and the wall) is deflected downwards, the situation will be as follows: the turbulence is stabilizing when $\partial U/\partial y > 0$, and destabilizing for $\partial U/\partial y < 0$.

The stabilising or destabilising effect of streamline curvature is thus dependent on the type of curvature (convex or concave), and whether there is an increase or decrease in momentum in the tangential direction with radial distance from its origin (i.e., the sign of $\partial U_\theta/\partial r$). For convenience, these cases are summarized in Table 1.

Results

The results calculated are compared with experimental data taken from Capbern and Bonnet (1989) and Gleyzes (1989). The experimental airfoil is the A-profile, which also was used in the CFD validation EUROVAL project (1993). The Reynolds number and the Mach number are 2.1×10^6 and 0.15, respectively. In the calculations, the flow is assumed to be incompressible. Measurements have been carried out in two wind tunnels, F1 and F2, the F1 wind tunnel being larger than F2. Global characteristics such as friction coefficients and surface pressures were measured in the F1 wind tunnel, whereas the flow field was studied in more detail in the F2 wind tunnel where mean velocity profiles and Reynolds stresses were measured using a three-component LDV system. The blockage effect in the F2 tunnel was more important than in the F1 tunnel, leading to three-dimensional effects for $\alpha \geq 13$ deg.

The Mesh. A C-mesh with 353 × 65, generated by Chanez and Palicot (1990), was used. The near-wall nodes are located at $y^+ \simeq 1$, and 7 to 10 nodes—in the normal direc-

tion—are situated in the region $0 \leq y^+ \leq 20$. Two modifications of this mesh have been tested. In the first modification the number of nodes in the tangential direction to the airfoil was divided by two (178 × 65). In these two meshes a constant stretching factor in the normal direction was used. In the second modification of the 353 × 65 mesh, the stretching factor was decreased from 1.12 to 1.07 between $n/c \simeq 0.0029$ and $n/c \simeq 0.12$, adding 32 extra nodes in the boundary layer so that a 178 × 96 node mesh was obtained.

The thickness of the experimental (real) airfoil is finite at the trailing edge, whereas it is preferable in the calculations that it is zero. Following the procedure chosen in EUROVAL, the lower surface near the trailing edge is displaced slightly upwards so that it joins the upper surface at $x/c = 1.0$, thus giving the same airfoil length as in the experiments.

Transition. Transition was initially imposed by setting k, ϵ, $\overline{u^2}$, $\overline{v^2}$, $\overline{uv}$ to zero before the transition point. After the transition point the turbulence quantities grow naturally without any sort of triggering. The reason why no triggering is needed is because of the one-equation model, which does not damp the turbulent as much as other low-Re models. In an earlier work (Davidson, 1990), where the low-Re model of Chien (1982) was used, is was found necessary to introduce some turbulence after the transition point.

Setting the turbulent quantities to zero before the transition point, created some problems on the 353 × 65, which resulted in separation on the suction side of the airfoil where the transition was imposed, probably because it caused too abrupt an increase in the viscosity. Thus the transition is imposed more smoothly, which is probably also more physically correct. If the transition is to be imposed at x_{tr}, the turbulent viscosity is made to vary linearly in the x direction between its calculated values at $x_{tr} - \Delta x$ and x_{tr}; for $\alpha = 13.3$ deg, on the upper side, $x_{tr}/c = 0.12$, $\Delta x/c = 0.05$ were used, and on the lower side $x_{tr}/c = 0.3$, $\Delta x/c = 0$ were used.

Mean Flow Quantities. The velocity profiles at $x/c = 0.96$ are presented in Fig. 1 using the three different meshes. It can be seen that the doubling of the number of mesh points in the tangential direction to the airfoil does not have any great effect on the calculated results. Included in Fig. 1 is also the velocity profile predicted with the Model GL, a profile which is more smeared out compared with Model GY, which means that the former model predicts a more diffusive (turbulent) flow field with larger Reynolds stresses. It is instructive to study the truncated ASM (Rodi, 1980) form of the stress tensor

$$\overline{u_i u_j} = \frac{2}{3}\delta_{ij}k + \frac{k}{\epsilon}\frac{(1-c_2)\left(P_{ij} - \frac{2}{3}\delta_{ij}P^k\right) + \Phi'_{ij,1} + \Phi'_{ij,2}}{c_1 - 1 + P^k/\epsilon} \tag{16}$$

On the curved part of the airfoil (close to the wall) up to approximately mid-chord, as well as close to the wall in the separation region, the dissipation is larger than P^k, i.e., $P^k/\epsilon < 1$ (see Fig. 10). The denominator in Eq. (16) is reduced as its last term decreases, which augments $\overline{u_i u_j}$. As the coefficient c_1 has the value 1.8 in Model GL compared with 3.0 in Model GY, the relative importance of P^k/ϵ is larger for Model GL; the resulting increase in $\overline{u_i u_j}$ with Model GL gives a more smeared out velocity profile and counteracts the streamline curvature-induced reduction resulting from convex curvature. All results presented below have been obtained using the 178 × 96 mesh and Model GY.

In Fig. 2 the RSTM-predicted lift-coefficients C_L are compared with two-layer $k - \epsilon$ predictions and experimental data. It can be seen that the RSTM agrees well with experiments predicting decreasing C_L at $\alpha = 17$ deg, which agrees well with experimental data. However, the $k - \epsilon$ model shows no tendency to predict stall. It should be noted that there is a considerable difference between the experimental results in the two wind tunnels F1 and F2. The results obtained in the larger wind tunnel F1, are considered to be more reliable than those obtained in F2. This should be kept in mind when making detailed comparisons between experimental profiles taken in F2 and calculated results.

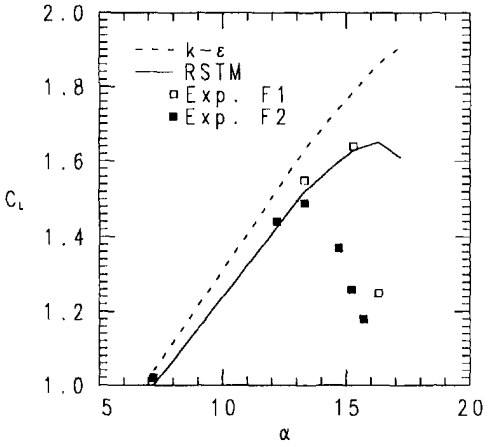

Fig. 2 Lift-coefficients C_L versus angle of attack α

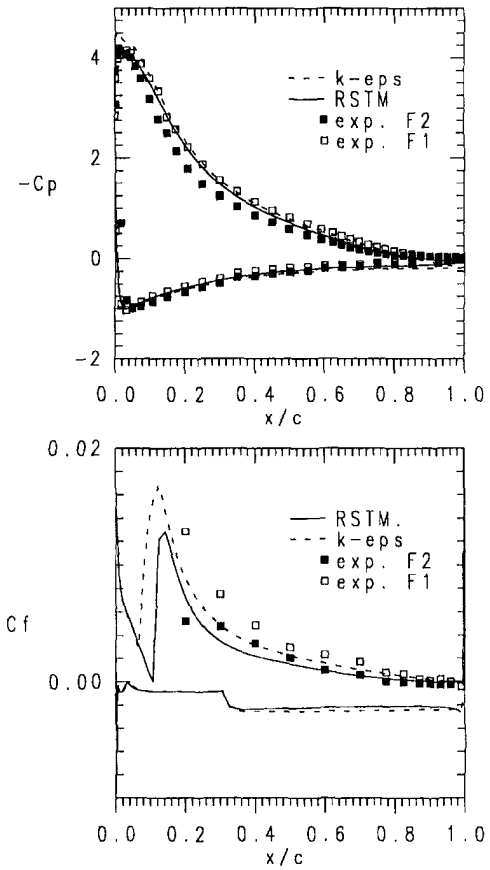

Fig. 3 Wall pressure $c_p = (p - p_0)/0.5\rho U_0^2$ and skin friction $\tau_\omega/1/2\rho U_0^2$

The wall pressure and the skin friction are presented in Fig. 3. It can be seen that, with the $k - \epsilon$ model, the (negative) pressure peak at the suction side is overpredicted as compared with experiments, and that the RSTM predictions agree well with experiments. The skin friction predicted with $k - \epsilon$ is higher than that predicted with RSTM. This is probably partly due to how the models react to the imposed transition, but it

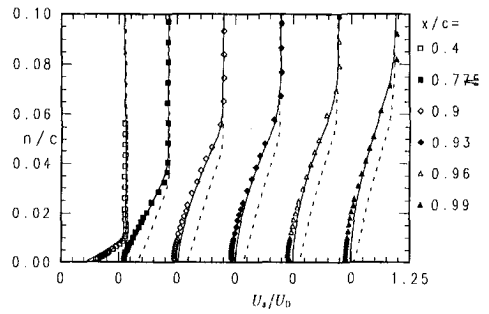

Fig. 4 U_s profiles on the suction side of the airfoil. Solid lines: RSTM; dashed lines: $k - \epsilon$

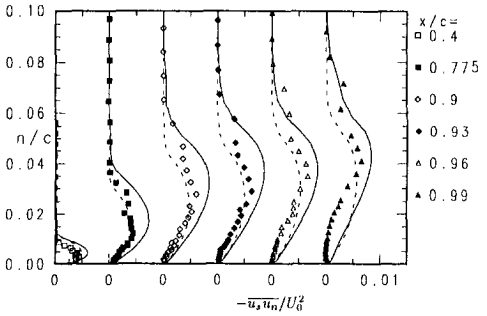

Fig. 6 $\overline{u_s u_n}$ profiles on the suction side of the airfoil. Solid lines: RSTM; dashed lines: $k - \epsilon$

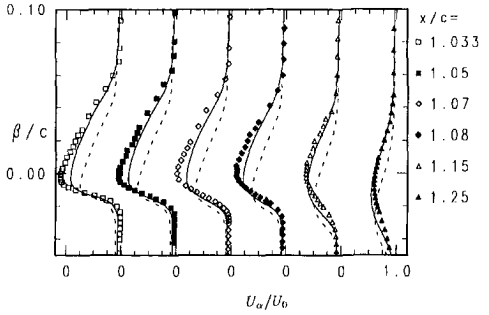

Fig. 5 U_α profiles in the wake after the airfoil. Solid lines: RSTM; dashed lines: $k - \epsilon$

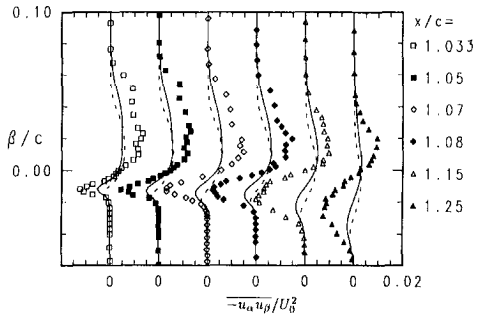

Fig. 7 $\overline{u_\alpha u_\beta}$ profiles in the wake after the airfoil. Solid lines: RSTM; dashed lines: $k - \epsilon$

is also logical since the velocity profiles (see below) predicted with the RSTM show more tendency to separate than do the $k - \epsilon$ profiles. But it was also found in a previous work on testing different low-Re variants of $k - \epsilon$ models (Davidson, 1993a), that predicted skin-frictions are not a very reliable indicator of the global flow characteristics, not even the velocity profiles.

The velocity profiles on the suction side of the airfoil are presented in Fig. 4. Note that an orthogonal $s - n$ coordinate system is used, with origin on the surface. The s coordinate is tangential to the airfoil. The U_s-velocities on the airfoil are well predicted when using the RSTM. A small separation is predicted, occurring at $x/c \simeq 0.90$. This type of separation can be termed *incipient detachment* (Simpson, 1989). As separation is approached, it is seen that the predicted U_s profiles follow the experimental ones, that the profiles become progressively less full and that an inflexion point appears in the profiles. The separation region in the experiments is considerably larger than that in the RSTM-predictions. This may perhaps be attributed to experimental uncertainty in the F2 wind tunnel, because the lift-coefficient in Fig. 2 and the surface pressure data in Fig. 3 indicate that the separation zone in the more reliable measurements in the F1 wind tunnel is smaller. The velocity profiles predicted with the $k - \epsilon$ model do not agree very well with experiments: no tendency toward separation is observed, which implies that the $k - \epsilon$ predicts excessively large shear stresses, giving too high a turbulent diffusion and thus smearing out the U_s profiles.

The wake velocity profiles U_α/U_0 are compared with experiments in Fig. 5. Note that an $\alpha - \beta$ coordinate system is used in the wake with origin at the trailing edge; the α axis is parallel to the free-stream velocity, and β is orthogonal to $\hat{\alpha}$. From Fig. 5 it can be seen that the RSTM shows better performance than the $k - \epsilon$ model.

Turbulent Quantities. The stresses on the airfoil and the wake are presented in Figs. 6–7. Using RSTM, the shear stresses are in fairly good agreement with experimental data, whereas the shear stresses are overpredicted, especially near the trailing edge. In the wake, the predicted shear stresses are much smaller than in the experiments, which is probably related to the larger experimental separation zone.

The shear stresses predicted with the $k - \epsilon$ model are smaller than those predicted with the RSTM. The reason why the shear stresses are higher with RSTM than with $k - \epsilon$ is that the turbulent quantities were computed with different velocity fields. The velocity gradients in the $k - \epsilon$ predictions are smaller than in the RSTM predictions, leading to lower production of turbulence in the former case.

When presenting turbulent quantities such as Reynolds stresses, it may be overlooked that it is not the stresses that enter the momentum equations but their gradients, where the Reynolds stresses constitute net (vectorial) forces/area, i.e., net stress vectors. The force resulting from shear stresses, $\mathbf{F}_s$ can be written

$$\mathbf{F}_s = \rho\left(-\frac{\partial \overline{uv}}{\partial x}, \quad -\frac{\partial \overline{uv}}{\partial y}\right), \tag{17}$$

and from the normal stresses:

$$\mathbf{F}_n = \rho\left(-\frac{\partial \overline{u^2}}{\partial x}, \quad -\frac{\partial \overline{v^2}}{\partial y}\right), \tag{18}$$

which should be compared to the force resulting from pressure

$$\mathbf{F}_p = \left(-\frac{\partial p}{\partial x}, \quad -\frac{\partial p}{\partial y}\right) \tag{19}$$

In Fig. 8, the force-fields near the trailing edge are presented as vector plots. It can be seen from the pressure force F_p that the flow goes against an adverse pressure gradient, both on the suction side of the airfoil and in the wake. It is interesting to see how the forces (net stress vectors) resulting from the Reynolds stresses are fairly important in the wake region, especially along the centre line, where the very thin boundary layer from the pressure side mixes with the separated boundary layer from the suction side. Large gradients are formed that give strong

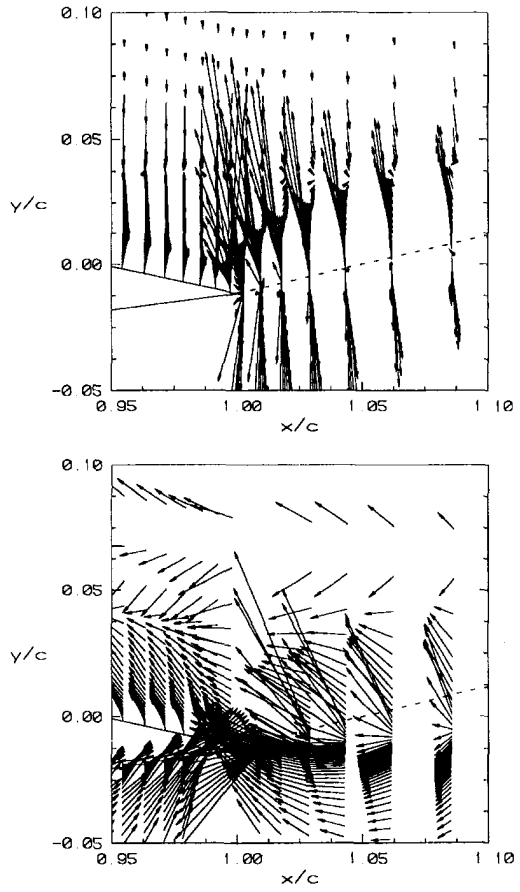

Fig. 8 Vector plots of turbulent stresses and pressure vectors near the trailing edge. The same scaling of vectors is used in all plots. The dashed line has the same direction as the far-field flow (α = 13.3). (*a*) $\rho(-\partial\overline{uv}/\partial x, -\partial\overline{uv}/\partial y)$, (*b*) $(-\partial p/\partial x, -\partial p/\partial y)$

downward forces owing to both shear and normal stresses (the normal stresses are not shown here due to space constraints; see Davidson, 1993c), which are even larger than the forces resulting from the pressure gradient.

As Cartesian velocity components have been used in the calculations, no explicit curvature terms appear in the Reynolds stress equations (see Eq. (4)). Of course, the Reynolds stresses formulated in Cartesian coordinates are also affected by curvature, but are affected *implicitly*. To investigate the curvature effects, let us—in the post-processing—study the equations in polar coordinates $r - \theta$, with the flow in the circumferential θ direction (i.e., $U_\theta = U_\theta(r)$, $U_r = 0$). The θ axis is thus chosen so that the flow is locally aligned with this axis. Curvature terms now appear because the r = const. coordinate lines are curved. The Reynolds stress equation can, in symbolic form, be written

$$C_{ij} - D_{ij} = P_{ij} + \Phi_{ij} - \epsilon_{ij} + P^c_{ij} + C^c_{ij} \qquad (20)$$

where superscript c on P_{ij} and C_{ij} denotes curvature terms originating from production and convection, respectively, see Table 1. The larger these terms, the more important the curvature effects.

The flux Richardson number

$$R_f = \frac{2U_\theta/r}{U_\theta/r + \partial U_\theta/\partial r} \qquad (21)$$

is a convenient parameter for studying curvature effects. Its physical meaning is (minus) the ratio of the production of $\overline{u_r^2}$ owing to curvature to the total production of $\overline{u_\theta^2}$ (see Table 2). The ratio δ/R and the flux Richardson number are shown in Fig. 9 at three different x stations: at x/c = 0.2 where the wall

Table 2 Source terms in the Reynolds stress equations (see Eq. (20)) due to production and convection in a polar coordinate system

	P_{ij}	P^c_{ij}	C^c_{ij}
$\overline{u_r^2}$	—	$2\overline{u_r u_\theta}\dfrac{U_\theta}{r}$	$2\overline{u_r u_\theta}\dfrac{U_\theta}{r}$
$\overline{u_\theta^2}$	$-2\overline{u_r u_\theta}\dfrac{\partial U_\theta}{\partial r}$	—	$-2\overline{u_r u_\theta}\dfrac{U_\theta}{r}$
$\overline{u_r u_\theta}$	$-\overline{u_r^2}\dfrac{\partial U_\theta}{\partial r}$	$\overline{u_\theta^2}\dfrac{U_\theta}{r}$	$(\overline{u_\theta^2} - \overline{u_r^2})\dfrac{U_\theta}{r}$

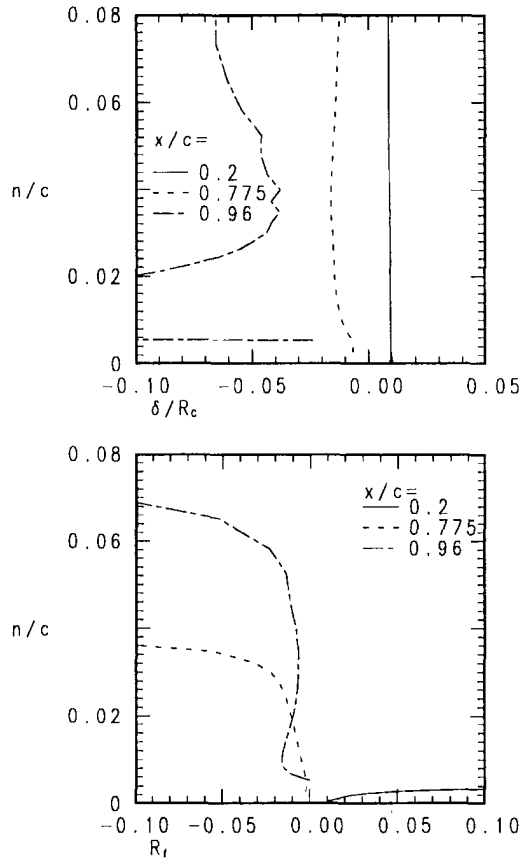

Fig. 9 Parameters describing streamline curvature effects on the turbulence. (*a*) Boundary layer thickness over streamline curvature radius δ/R_c. (*b*) Flux Richardson number R_f

curvature is most important, near the separation point (x/c = 0.775) and in the separation zone (x/c = 0.96). As can be seen, the streamline curvature is positive at x/c = 0.2, which in the outer part of the boundary layer gives an increasing flux Richardson number. The flow here is parallel to the curved wall, which gives constant $\delta/R_c \simeq 0.01$, i.e. boundary thickness over wall curvature. The boundary layer is very thin ($\delta/c \simeq 0.005$), which explains the strong increase in the flux Richardson number at $n/c \simeq 0.004$, close to the outer edge of the boundary layer. As separation is approached, the streamlines become concave, which destabilises the turbulence. It is seen in Fig. 9 that δ/R and R_f become negative. The flux Richardson number reaches values of ± 0.1 in the outer region of the boundary layer. These values should be compared with reported values on the critical flux Richardson number (the R_f value at which the turbulence collapse, suppressed by dissipation and buoyancy/curvature effects) in buoyant flows, ranging between 0.15 (Ellison, 1957) and 0.5 (Townsend, 1958). The curvature effects are largest in the outer boundary layer, where the curvature term U_θ/R becomes comparable with

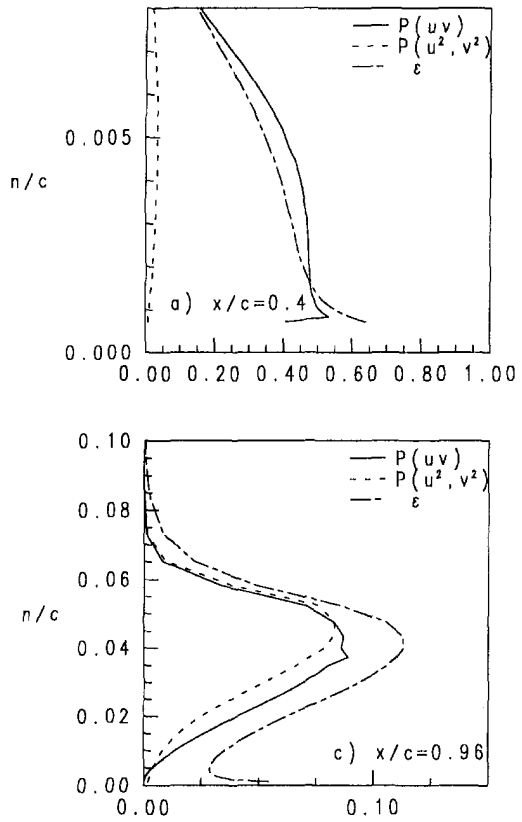

Fig. 10 Calculated productions terms in the k equation. Solid lines: $-\overline{u_s u_n}\,\partial U_s/\partial n$; dashed lines: $(\overline{u_n^2}-\overline{u_s^2})\partial U_s/\partial s$; dashed-dotted lines: ϵ. (a) x/c = 0.4, (b) x/c = 0.96

the velocity gradient $\partial U_\theta/\partial r$. The direct influence of the curvature effects are thus largest in the outer part of the boundary layer, but they will also have indirect influence via convective and diffusive transport. The Reynolds stresses, augmented or dampened by curvature, increase or decrease the production terms in the equations and, through convection and diffusion, also affect the surroundings.

The streamlines bounding the separation region in separated flows are usually convex. It may be noted that, in the present case, the turbulence in the shear layer bounding the separation zone on the suction side is mostly destabilised as a result of the concave curvature of the streamlines. This is because the flow is forced upwards when it reaches the wake, giving concave streamline curvature in the region of the trailing edge.

The production contribution to the k-equation from the shear stress $-\overline{u_s u_n}\partial U_s/\partial n$ and the normal stresses $-(\overline{u_s^2}-\overline{u_n^2})\partial U_s/\partial s$ are presented in Fig. 10. The production resulting from the normal stresses is not very large at x/c = 0.4 (at most, ten percent of that resulting from the shear stress). Near the separation point (the conditions near the separation point are not shown here due to space constraints; see Davidson, 1993c) and in the separation region, the two terms are of equal importance. The dissipation is also presented in Fig. 10, and it is seen that production and dissipation balance each other at x/c = 0.4, but that this is not the case near the separation point or in the separation region.

Conclusions

The flow around a low-speed airfoil has been computed. The code used is based on SIMPLEC, which employs collocated grid arrangement and solves for the Cartesian velocities. A third-order differencing scheme (QUICK) for the mean flow equations has been used together with a second-order, bounded scheme (MUSCL) for the turbulent quantities. Two turbulence models are compared: a Reynolds Stress Transport Model (RSTM) and a $k-\epsilon$ model. As neither model is valid in the viscous-dominated near-wal region, they are matched with a one-equation eddy-viscosity model.

The most important global feature of a low-speed airfoil is to determine at which angle of attack stall occurs. In the present work, it has been shown that an adequate turbulence model should be used, capable of accounting for important physical phenomena such as transport of individual stresses, streamline curvature effects and irrotational strains. In order to account for these effects, the turbulence model must properly respond to irrotational strains and the interaction process between strains and all Reynolds stresses. The only model that fulfills these requirements is a Reynolds Stress Transport Model (or perhaps its algebraic variant, ASM).

The following conclusions can be drawn.

- The RSTM predicts the flow in good agreement with experimental data, and a small separation zone is predicted at α = 13.3 deg which could be described as incipient detachment. The computed lift coefficient C_L has a maximum at an angle of attack of 17 deg, indicating approaching stall, which is in good agreement with experimental data.
- The $k-\epsilon$ model predictions are in poor agreement with experiments, the computed flow showing no tendency toward separation at α = 13.3 deg. No stall is predicted and the lift coefficient continues to increase at α = 17 deg.
- Curvature effects resulting from wall curvature and streamline curvature are important. Computed curvature radii show that the boundary layer thickness over curvature radius is approximately 0.01 ($\delta/R_C \simeq 0.01$) at the suction side close to the pressure minimum. In the region in which the flow approaches the separation region, it is forced further away from the wall. This results in streamlines with a concave curvature; values of δ/R_C close to -0.05 are found.
- When comparing Reynolds stresses one may overlook it is not the Reynolds stresses that appear in the momentum equations but their gradients. The (net) stress vectors resulting from shear stresses $\rho(-\partial\overline{uv}/\partial x, -\partial uv/\partial y)$ and normal stresses $\rho(-\partial\overline{u^2}/\partial x, -\partial\overline{v^2}/\partial y)$ are compared with the forces (per unit volume) resulting from the pressure gradient $(-\partial p/\partial x, -\partial p/\partial y)$ in the region of the trailing edge. It is found that the forces that results from both normal stresses and shear stresses are comparable to the forces resulting from the pressure gradient.
- Two variants of RSTM have been tested: the model of Gibson and Launder (1978) (GL), which is the "standard" one, and the model of Gibson and Younis (1986) (GY). The difference between the models lies in the choice of constants. It was found that the Model GL is more diffusive than Model GY, the reason being that the ratio P^k/ϵ is smaller than one, which has a greater effect in the former model in which the c_1-coefficient has a smaller value (c_1 = 1.8) than in Model GY (c_1 = 3.0). In the present work, Model GY has been used throughout the study, as this model gave better agreement with experiments than Model GL.

References

Bradshaw, P., 1973, "Effects of Streamline Curvature on Turbulent Flow," AGARDograph, no. 169.

Burns, A. D., and Wilkes, N. S., 1986, "A Finite Difference Method for the Computation of Fluid Flow in Complex Three-Dimensional Geometries," Report AERE R 12342, Harwell Laboratory, U.K..

Capbern, C., and Bonnet, C., 1989, "Opération décrochage: Rapport Final de Synthèse," Report Aerospatiale 443.535./89, Toulouse.

Cebeci, T., 1989, "Essential Ingredients of a Method for Low Reynolds-Number Airfoils," *AIAA Journal*, Vol. 27, pp. 1680–1688.

Chanez, Ph. and Palicot, L., 1990, "Évaluation d'un code Navier-Stokes

bidimensionnel pour le calcul de l'écoulement autour d'un profil d'aile," Report Aerospatiale, 443.548/90, Toulouse.

Chen, H. C. and Patel, V. C., 1987, "Practical Near-Wall Turbulence Models for Complex Flows Including Separation," *AIAA J.*, Vol. 26, pp. 641–648.

Chien, K. Y., 1982, "Predictions of Channel and Boundary Layer Flows with a Low-Reynolds Number Turbulence Model," *AIAA Journal*, Vol. 20, pp. 33–38.

Daly, B. J. and Harlow, F. H., 1970, "Transport Equations of Turbulence," *Physics of Fluids*, Vol. 13, pp. 2634–2649.

Davidson, L., 1990, "Implementation of a Semi-Implicit $\kappa - \epsilon$ Turbulence Model in a Explicit Runge-Kutta Navier-Strokes Code," Report TR/RF/90/25, CERFACS, Toulouse.

Davidson, L. and Farhanieh, B., 1992, "CALC-BFC: A Finite-Volume Code Employing Collocated Variable Arrangement and Cartesian Velocity Components for Computation of Fluid Flow and Heat Transfer in Complex Three-Dimensional Geometries," Report 92/4, Thermo and Fluid Dynamics, Chalmers University of Technology, Gothenburg.

Davidson, L. and Rizzi, A., 1992, "Navier-Stokes Stall Predictions Using an Algebraic Stress Model," *Journal of Spacecraft and Rockets*, Vol. 29, pp. 794–800 (see also AIAA-paper 92–0195, Reno, Jan. 1992).

Davidson, L., 1993a, "CERFACS' contribution in Task 3.2 to EUROVAL: A European Initiative on Validation of CFD-codes," W. Haase, F. Brandsma, E. Elsholz, M. Leschziner and D. Schwamborn, (eds.), Notes on Numerical Fluid Mechanics, Vol. 42, Vieweg Verlag.

Davidson, L., 1993b, "Reynolds Stress Transport Modelling of Shock/Boundary-Layer Interaction," AIAA-paper 93–2936, AIAA 24th Fluid Dynamics Conference, Orlando, July.

Davidson, L., 1993c, "High-Lift Airfoil Flow Simulations Using a Two-Layer Reynolds Stress Transport Model," Proc *5th International Symposium on Refined Flow Modelling and Turbulence Measurements*, pp. 777–784, Paris, Sept. 7–10.

Ellison, T. H., 1957, "Turbulent Transport of Heat and Momentum From an Infinite Rough Plane," *Journal of Fluid Mechanics*, Vol. 2, pp. 456–466.

Euroval, 1993, "A European Initiative on Validation of CFD-codes," W. Haase, F. Brandsma, E. Elsholz, M. Leschziner and D. Schwamborn, (eds.), *Notes on Numerical Fluid Mechanics*, Vol. 42, Vieweg Verlag.

Gibson, M. M. and Launder, B. E., 1978, "Ground Effects on Pressure Fluctuations in the Atmospheric Boundary Layer," *Journal of Fluid Mechanics*, Vol. 86, pp. 491–512.

Gibson, M. M. and Younis, B. A., 1986, "Calculation of Swirling Jets With a Reynolds Stress Closure," *Physics of Fluids*, Vol. 29, pp. 38–48.

Gleyzes, C., 1989, "Opération décrochage: Résultats de la deuxième campagne d'essais à F2 (mesures de pression et vélocimetrie laser)," Report ONERA/CERT 57/5004.22, Toulouse.

Johansson, S., Davidson, L. and Olsson, E., 1993, "Numerical Simulation of Vortex Shedding Past Triangular Cylinders at High Reynolds Number," *International Journal for Numerical Methods in Fluids*, Vol. 16, pp. 859–878.

Leonard, B. P., 1979, "A Stable and Accurate Convective Modelling Based on Quadratic Upstream Interpolation," *Computational Methods in Applied Mechanical Engineering*, Vol. 19, pp. 59–98.

Lien, F. S., 1992, "Computational Modelling of 3D Flow in Complex Ducts and Passages," PhD thesis, University of Manchester, Manchester.

Lumley, J. L., 1978, "Computational Modelling of Turbulent Flows," *Advances in Applied Mechanics*, Vol. 18, pp. 123–176.

Majumdar, S., Rodi, W. and Zhu, J., 1992, "Three-Dimensional Finite-Volume Method for Incompressible Flows With Complex Boundaries," ASME JOURNAL OF FLUIDS ENGINEERING, Vol. 114, pp. 496–503.

Patankar, S. V., 1980, Numerical Heat *Transfer and Fluid Flow*, McGraw-Hill, New York.

Rhie, C. M. and Chow, W. L., 1984, "Numerical Study of the Turbulent Flow Past an Airfoil with Trailing Edge Separation," *AIAA Journal*, Vol. 21, pp. 1527–1532.

Perić, M., Kessler, K. and Scheuerer, G., 1988, "Comparison of Finite-Volume Numerical Methods with Staggered and Collocated GRIDS," *Computer & Fluids*, Vol. 16, pp. 389–403.

Rodi, W., 1980, *Turbulence Models and Their Application in Hydraulics*, International Association of Hydraulic Research, Monograph, Delft.

Rodi, W. and Scheuerer, G., 1983, "Calculation of Curved Shear Layers With Two-Equation Turbulence Models," *Physics of Fluids*, Vol. 26, pp. 1422–1435.

Simpson, R. L., 1989, "Turbulent Boundary-Layer Separation," *Annual Review in Fluid Mechanics*, Vol. 21, pp. 205–234.

Thompson, B. E. and Whitelaw, J. H., 1985, "Characteristics of a Trailing-Edge Flow With Turbulent Boundary-Layer Separation," *Journal of Fluid Mechanics*, Vol. 157, pp. 305–326.

Townsend, A. A., 1958, "Turbulent Flow in Stably Stratified Atmosphere," *Journal of Fluid Mechanics*, Vol. 3, pp. 361–372.

Van Leer, B., 1979, "Towards the Ultimate Conservative Difference Scheme. V. A. Second-Order Sequel to Godonov's Method," *Journal of Computational Physics*, Vol. 32, pp. 101–136.

Wolfshtein, M., 1969, "The Velocity and Temperature Distribution in One-Dimensional Flow with Turbulence Augmentation and Pressure Gradient," *International Journal Heat and Mass Transfer*, Vol. 12, pp. 301–318.

Propagation of the Velocity Shear Front in Spin-up From Rest in a Cut-Cone

Jae Won Kim
Division of Home Appliance,
Dae Woo Electronics Corporation,
316-3, Hyosung-dong, Buk-ku, Incheon,
South Korea

Jae Min Hyun
Department of Mechanical Engineering
Korea Advanced Institute of Science and Technology
Yusong-ku, Taejon 305-701,
South Korea.
Mem. ASME

The behavior of the dominant azimuthal velocity field during spin-up from rest of a homogeneous fluid in a cut-cone is investigated. The fundamental mechanism of spin-up process is recapitulated. In line with the classical flow model of Wedemeyer, the importance of the meridional circulation, driven by the Ekman layers, is stressed. The experimental apparatus, together with the image processing technique of the visualized flow data, is described. The reliability and accuracy of this experimental method are validated by performing parallel measurements using an LDV system. The experimental results clearly indicate that the azimuthal velocity shear front propagates faster as the incline angle of the side wall decreases. In the rotating zone of the interior, the azimuthal velocities are larger in magnitude in a cut-cone than in a circular cylinder of comparable size. Plausible physical explanations are offered, and the experimental observations are supportive of these physical arguments.

1 Introduction

Let us consider an incompressible viscous fluid of kinetic viscosity ν, filling an axisymmetric closed container. Initially, the entire system is at rest. At $t = 0$, the container impulsively starts rotating about its central axis with rotation rate Ω. The subsequent motion of the fluid, in response to the spinning solid boundary walls of the container, is termed spin-up from rest (Wedemeyer, 1964): this transient rotating flow has posed a prominent classical problem. Here, concern is with the situations in which the Ekman number E $[=\nu/\Omega L^2]$, where L is the characteristic length of the flow system, is much smaller than unity. These are of great interest in practical industrial applications as well as in fundamental fluid dynamics.

Wedemeyer (1964), by resorting to physically insightful arguments and judicious approximations, derived a theoretical flow model for a right circular cylindrical container of radius R and height h, $R/h \sim 0(1)$. Figure 1 shows a schema of flow configuration (for a circular cylinder, $\alpha = 90$ deg) and coordinate system. It has been recognized that, when $E \ll 1$, the main flow characteristics can be divided into the essentially inviscid interior core and boundary layers adjacent to the solid walls of the container. The most significant dynamic ingredient is the fluid pumping mechanism by the Ekman layers which form on the endwall disks ($z = 0$, $z = h$) perpendicular to the rotating central axis. The fluid is propelled radially outward in the Ekman layers, moves vertically in the sidewall ($r = R$) boundary layer, and subsequently enters radially in the interior region. This constitutes the internal meridional flows; the velocities of this internal circulation are small in magnitude, being $0(E^{1/2})$ of the primary azimuthal velocity. However, owing to this meridional circulation, the bulk of the fluid acquires much of the angular momentum in a time scale $0(E^{-1/2}\Omega^{-1})$, which is an order of magnitude smaller than the purely diffusive time scale $0(E^{-1}\Omega^{-1})$. The effectiveness of the Ekman layer pumping mechanism and the associated meridional circulation in achieving spin-up was established earlier by Greenspan and Howard (1963) for the linearized counterpart of this problem.

The objective of the present investigation is to portray the velocity fields in spin-up from rest of a homogeneous fluid in a cut cone. As ascertained earlier, due to the inclination of the conical sidewall, the meridional interior circulation exhibits features which are different from those of a much-studied right circular cylinder. In this paper, extensive experimental observations are made to delineate the impact of the sidewall incline angle α on the propagation speed of azimuthal velocity shear front. The experimental results produce a global picture of the meridional circulation, and they show how this is affected by the constraints imposed by the geometrical configuration of the container. Once again, the crucial role played by the meridional circulation in accomplishing the spin-up process is brought into focus by inspecting the azimuthal velocity field, as compared with the case of a circular cylinder. The present research will be of interest to several types of modern technological devices such as spin-stabilized liquid-carrying projectiles.

2 The Experiments

A carefully controlled experimental program has been carried out. The experimental apparatus consists of a rotating turntable, a container filled with a fluid, photographic image recording devices, and a computer.

Contributed by the Fluids Engineering Division for publication in the JOURNAL OF FLUIDS ENGINEERING. Manuscript received by the Fluids Engineering Division July 7, 1993; revised manuscript received October 11, 1994. Associate Technical Editor: W. S. Saric.

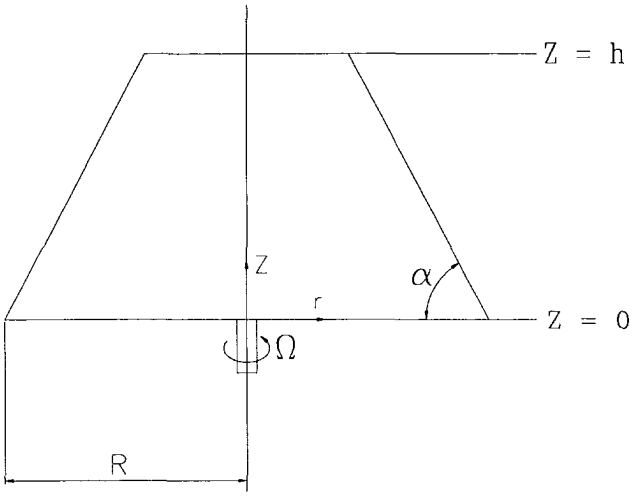

Fig. 1 Schematic diagram of the flow system

The turntable is made of a precision controlled AC servo motor (0.4 kw rating). The rotational speed of the motor is continuously checked by monitoring the signal from the servo-unit of the motor. The turntable is capable of maintaining the rotational speed within ±0.1 percent of the set value. The response time of the turntable to achieve the set value of the rotation rate by an impulsive start is less than 0.012 second (i.e., less than 0.1 revolution at a typical rotational speed of 400 rpm). The turntable is equipped with a fixture to mount the container. The fixture secures the container, and sloshing and vibration are minimized. The container preserves the upright configuration to a high degree of accuracy.

The axisymmetric containers were fabricated with plexiglass. A numerically-controlled lathe was used to produce wooden molds to form the inclined side wall. Four different containers, with incline angles α = 30, 45, 60, and 90 deg (a right circular cylinder), were prepared. The diameter of the bottom end wall disk, $2R$, was the same for these containers [R = 10 cm in the experiment]. The height of the container, h, was adjusted such that the fluid volume Q remained the same for the entire set of these cut-cone containers [Q = 604.6 cm^3, h = 2.0 cm for α = 90 deg, h = 2.2 cm for α = 60 deg, h = 2.5 cm for α = 45 deg, h = 5.77 cm for α = 30 deg, respectively, corresponding to the above four incline angles]. This geometrical condition allows a thorough and systematic comparison of the experimental results.

In order to determine the radial location of the azimuthal velocity shear front, a digitized image processing technique was utilized. A classical flow visualization method using aluminum particles was adopted. Disk-like aluminum particles suspended in the working fluid are randomly oriented in the region where the fluid is nonrotating; however, a shearing motion tends to align the particles in the primary direction of shear front. The container is illuminated from the side by a slit-beam generator. The randomly oriented particles in the fluid reflect the illuminating light in the perpendicular direction. Otherwise, the scattering particles within the rotating region shut the light. Therefore, the rotating region is displayed as a dark area in the image. The demarcation between the dark (rotating region) and white (nonrotating region) areas in the image indicates the position of the velocity shear front [see, e.g., Fig. I.4 of Greenspan, 1968]. The identification of the exact location of this demarcation line is accomplished by choosing a reference gray level in the digitized image. A photo depicting a typical visualized flow pattern is demonstrated in Fig. 2(*a*). The corresponding digitally-processed image is illustrated in Fig. 2(*b*). For more specifics, the reader is referred to Choi et al. (1990, 1991).

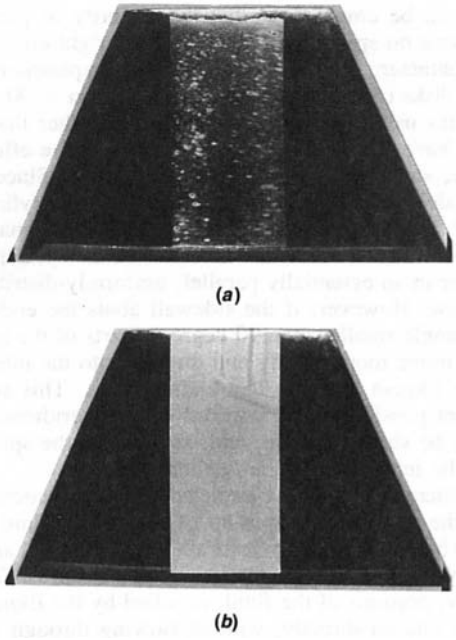

Fig. 2 Exemplary photographs displaying the visualized velocity shear front. Fig. 2(*a*) Flow visualization, Fig. 2(*b*) Image-enhanced picture.

In order to verify the image-processed data, parallel efforts were undertaken to measure the azimuthal velocity field by an LDV system. The LDV was oriented such that the laser beam passed through the bottom endwall disk of the container. Passing the laser beam through the side wall was avoided, since the beam could be distorted by the inclined sidewall. The optical arrangement of the LDV was similar to the system reported by Kawashima and Yang (1988).

3 Results and Discussion

A set of the present experiment is characterized by the Reynolds number Re [$\equiv \Omega R^2/\nu$] and the incline angle α. For all runs, the Reynolds number was Re = 10^5. This procedure singled out α as the variable parameter.

One striking feature of the Wedemeyer model for a right cylinder [α = 90 deg] is the depiction of the velocity shear front, which propagates radially inward from the cylindrical sidewall. Noting that, for E $\ll$ 1, the azimuthal and radial velocities in the interior are substantially uniform in the axial direction. Wedemeyer gave analytical predictions for the dominant azimuthal velocities V:

$$\frac{V}{R\Omega} \simeq \frac{re^{2T}/R - R/r}{e^{2T} - 1.0} \quad \text{for } r/R > e^{-T},$$

$$\frac{V}{R\Omega} = 0 \quad \text{for } r/R < e^{-T}, \tag{1}$$

where T denotes time normalized by the spin-up time scale, i.e., $T = \mathrm{E}^{1/2}t(R/h)\Omega$, where t the dimensional time. In the above, (r, θ, z) represents the cylindrical coordinates (see Fig. 1). Clearly, $R_s = R\exp(-T)$ describes the radial location R_s of the radially-propagating velocity shear front. The major physical implication of the velocity shear front is that it is the demarcation surface which separates the region of non-rotating fluid [$r/R < \exp(-T)$] and the rotating region [$r/R > \exp(-T)$].

The presence of the velocity shear front described in Eq. (1) is a salient feature of the Wedemeyer model. Verifications and refinements of this model, both experimental and numerical, have ensued, and these efforts have been qualitatively supportive of the basic Wedemeyer model (see, e.g., Weidman, 1976; Watkins and Hussey, 1977; Hyun et al., 1983).

It should be emphasized that the majority of previous investigations on spin-up have dealt with a right circular cylindrical container, i.e., sidewalls ($r = R$) perpendicular to the endwall disks ($z = 0$, and $z = h$), rendering $\alpha = 90$ deg (Fig. 1). Studies using axisymmetric containers other than a right cylinder have not been numerous. However, the effect of the geometric shape of the container is not trivial. Since the previous models were concerned mostly with a right cylinder, they assumed that, in the return circuit of the meridional circulation, the fluid enters the interior core from the cylindrical sidewall layer in an essentially parallel, uniformly-distributed, radial inflow. However, if the sidewall abuts the endwall disk with an angle smaller than 90 degrees, parts of the return circuit can move more readily and directly into the interior core from the Ekman layer on that endwall disk. This suggests a significant possibility that portions of the meridional circulation may be short-circuited, and, as a result, the spin-up process of the interior could be facilitated.

The patterns of the above-depicted meridional circulation are akin to the situations in spin-up of a stratified fluid. As emphasized by Walin (1969), Sakurai (1969), Hyun et al. (1982), buoyancy suppresses vertical motions of a stratified fluid; consequently, portions of the fluid, expelled by the Ekman layer, enter the interior directly, without flowing through vertically in the sidewall layer. The important conclusion is that spin-up proceeds at different rates in the flow field in the case of a stratified fluid: the fluid spins up faster in the regions close to the endwall disks. In summary, the above considerations clearly point to the possibility of enhancement of spin-up. This is principally caused by the particular behavior of local meridional circulation in the corner regions between the endwall disk and the sidewall. In these regions, the fluid, after having travelled horizontally in the Ekman layers and, thus, having acquired higher angular momentum, is expelled from the Ekman layers. Spin-up in the interior is enhanced if significant portions of the expelled fluid enter directly the interior core, without having to move vertically in the sidewall layer. In summary, this pattern of meridional circulation is achieved under the aforestated conditions. One example is the introduction of buoyancy effect, as observed in the stratified spin-up in a vertically mounted circular cylinder. Another possibility is the use of geometrical constraint of a noncylindrical container, and this aspect is addressed in the present paper.

Before undergoing the analysis of processed image data, the reliability and accuracy of the imaging technique were assessed by cross-comparisons of the data with the corresponding LDV measurements. Elaborate data verifications were conducted, and these two sets of data were found to be mutually consistent. Figure 3 shows an exemplary data-validation plot of azimuthal velocity profile. In this display, the identification of the velocity shear front can be readily made by tagging the almost discontinuous change in the brightness of image over an extremely small radial interval. As remarked previously, of particular importance in this experimental method is the presence of such a well-defined demarcation separating the dark and bright areas in the image-enhanced flow field. It is evident in Fig. 3 that such a sharp contrast of the brightness indicates the location of the velocity shear front.

Figure 4 presents the systematically-organized results of the propagating velocity shear front location R_s. The fluid in the region $r > R_s$ has finite angular velocity, but the fluid in $0 < r < R_s$ remains nonrotating. For the sake of comparison, the analytical prediction by Wedemeyer, $R_s = R \exp(-T)$, expressed in (1) for a right circular cylinder ($\alpha = 90$ deg), is also included in Fig. 4. The definite trend discernible in Fig. 4 is that the propagation speed increases as α decreases. The increase of the propagation speed is more pronounced at earlier times. In the case of a right circular cylinder ($\alpha = 90$ deg), the present results indicate that the analytical solution, Eq. (1), underpredicts the front propagation. This is due to the neglect

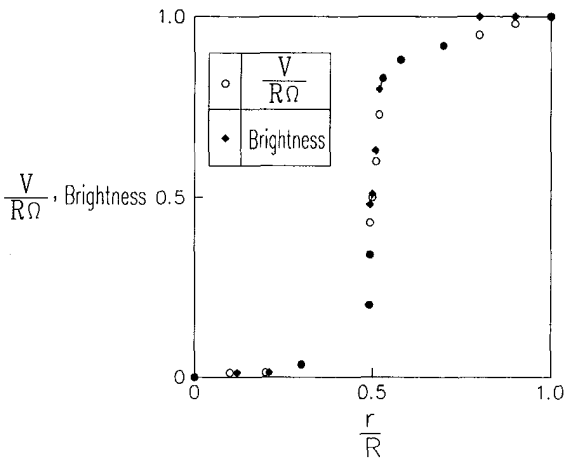

Fig. 3 Typical plots of the azimuthal velocity profile. ○ denotes the LDV measurements, and ◆ visualization data. The height is at z/h = 0.5. (Uncertainty in r/R = ±0.025, in $V/R\Omega$ = ±0.05, in brightness is ±0.07)

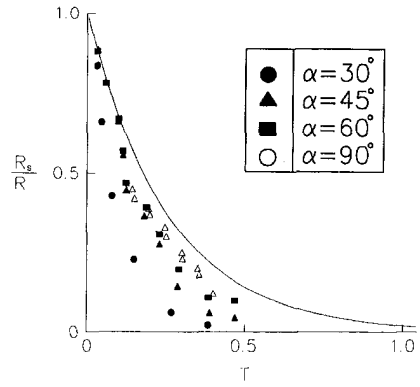

Fig. 4 Radial location, R_s, of the azimuthal velocity shear front. The solid line denotes the analytic solution by Wedemeyer for a right circular cylinder. The experimental results are: ●, α = 30 deg; ▲, α = 45 deg; ■, α = 60 deg: △, α = 90 deg. (Uncertainty in T = ±0.01, in R_s/R = ±0.07)

of the viscous effects in the Wedemeyer solution of Eq. (1). This point has been amply demonstrated by earlier studies (Weidman, 1976: Watkins and Hussey, 1977: Hyun et al., 1983), and the present results reconfirm the trend illustrated in Fig. 4.

As envisioned by the classical model of Wedemeyer for a right circular cylinder, the propagation of the velocity front may be described by the following mechanisms. After the impulsive start of the turntable rotation, the Ekman layers form on both end wall disks ($z = 0$ and $z = h$) within the dimensional time $0(\Omega^{-1})$. The interior fluid, initially non-rotating, is sucked into these Ekman layers (the Ekman pumping), and the fluid particles acquire angular momentum while traveling horizontally in the Ekman layers and in the sidewall layer in the direction of the sidewall inclination. The angular momentum at a given location in the interior core remains zero until the arrival of the fluid particles that have traveled through these boundary layers. These constitute the well-documented interior meridional circulation. Now, for a cut-cone, the travel paths of fluid particles are shorter than those of a right circular cylinder. The inclined side wall ($\alpha < 90$ deg) forces the meridional circulation to travel in the direction oblique to the endwall disks. Consequently, in the vicinity of the corner region between the bottom end wall disk ($z = 0$) and the inclined sidewall, as the fluid is propelled upward along the sidewall, the fluid that carries higher angular momentum enters the in-

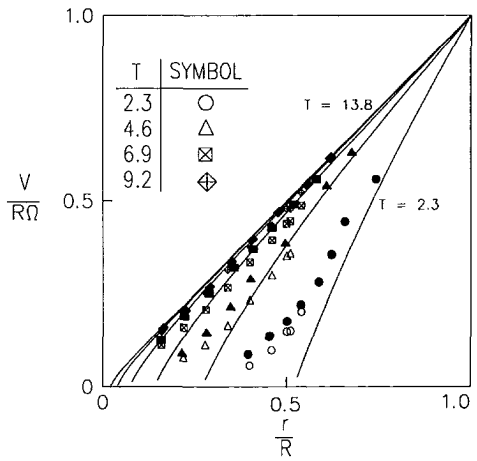

Fig. 5 Transient azimuthal velocity fields. The Wedemeyer solution for a right circular cylinder is shown by solid line. Open symbols refer to the experimental results for α = 90 deg and closed symbols denote the experimental results for α = 45 deg. (Uncertainty in r/R = ±0.025, in $V/R\Omega$ = ±0.05)

terior region more effectively than for a right circular cylinder. On the contrary, in the vicinity of the corner region between the top end wall disk ($z = h$) and the sidewall, the fluid is propelled from the top Ekman layer and travels away from the interior region. Therefore, in comparison to the case of a right cylinder, the meridional circulation cell in the bottom speeds up the spin-up in the interior: however, the cell in the top retards the interior spin-up. However, the combined effect is an overall enhancement of the interior spin-up, since the effect of the bottom end wall disk outweighs that of the top disk. The bottom disk is larger than the top disk, and, accordingly, the Ekman layer-induced meridional circulation cell is stronger near the bottom end wall disk than near the top disk. These physical pictures are consistent with the experimental observation depicted in Fig. 4, i.e., the global spin-up process in the interior is enhanced as α decreases.

In passing, it is worth noting that the meridional circulation in the bottom part of a cut-cone resembles the corner-jet phenomenon, which was suggested by Sakurai (1969) and Hyun et al. (1982) in stratified spin-up in a right circular cylinder. In that case, buoyancy inhibits the vertical motion: consequently, the fluid ejected by the Ekman layer in the corner region tends to be suppressed in travelling in the straight vertical direction. The meridional flow in this region, therefore, enters directly the interior in a jet-like fashion: the direction of this jet makes an acute angle (<90 deg) from the horizontal end wall disks. In the present case, the geometrical shape of the inclined side wall acts like a guide to induce an inclined meridional flow in the bottom region, which is akin to the above-mentioned corner-jet.

Further physical insight is extracted by scrutinizing the evolution of the azimuthal velocity field in the entire flow domain. Figure 5 exemplifies explicit comparisons between a circular cylinder (α = 90 deg, shown in open symbols) and a cut-cone (α = 45 deg, shown in closed symbols) at z/h = 0.5. It is clear in Fig. 5 that the azimuthal velocity at a given location in the rotating region of the interior is larger in a cut-cone than in a circular cylinder. These illustrations of the dominant azimuthal velocity field are compatible with the overall physical explanations asserted earlier.

It is mentioned here that the data for a smaller incline angle (say α = 30 deg) were not possible to be included for explicit comparison. For a very small incline angle, the usable surface area of the top endwall disk in the present experimental setup is substantially reduced. This posed practical difficulties in inserting the laser beam through this restricted opening in the top endwall disk.

4 Conclusions

Experimental observations of the azimuthal velocity field reveal that the velocity shear front propagates faster as α decreases. Also, the azimuthal velocities in the rotating region of the interior increase as α decreases. These flow characteristics are in line with the physical descriptions inferred from the behavior of the meridional interior circulation, which is strongly influenced by the presence of the inclined side wall in a cut-cone. The fluids ejected from the Ekman layers near the corner area, between the inclined side wall with an acute angle and the endwall disk, can enter the interior in a more effective manner than for the case of a right circular cylinder. This gives rise to enhancement of spin-up.

References

Choi, S., Kim, J. W., and Hyun, J. M., 1990, "Transient Free Surface Shape in an Abruptly-Rotating, Partially-Filled Cylinder," ASME JOURNAL OF FLUIDS ENGINEERING, Vol. 111, pp. 431–439.

Choi, S., Kim, J. W., and Hyun, J. M., 1991, "Experimental Investigation of the Flow With a Free Surface in an Impulsively Rotating Cylinder," ASME JOURNAL OF FLUIDS ENGINEERING, Vol. 113, pp. 245–249.

Greenspan, H. P., and Howard, L. N., 1963, "On a Time Dependent Motion of a Rotating Fluid," *Journal of Fluid Mechanics*, Vol. 17, pp. 385–404.

Greenspan, H. P., 1968, *The Theory of Rotating Fluids*, Cambridge University Press, Cambridge.

Hyun, J. M., Fowlis, W. W., and Warn-Varnas, A., 1982, "Numerical Solutions for the Spin-Up of a Stratified Fluid," *Journal of Fluid Mechanics*, Vol. 117, pp. 71–90.

Hyun, J. M., Leslie, F., Fowlis, W. W., and Warn-Varnas, A., 1983, "Numerical Solutions for Spin-Up From Rest in a Cylinder," *Journal of Fluid Mechanics*, Vol. 127, pp. 263–281.

Kawashima, G., and Yang, W. J., 1988, "Unsteady Flow in Rotating Drums Using Laser Doppler Velocimetry," *Experiments in Fluids*, Vol. 6, pp. 165–171.

Sakurai, T., 1969, "Spin-Down Problem of Rotating Stratified Fluid in Thermally Insulated Circular Containers," *Journal of Fluid Mechanics*, Vol. 37, pp. 689–699.

Walin, G., 1969, "Stratified Rotating Fluid Mechanics," *Journal of Fluid Mechanics*, Vol. 36, pp. 289.

Watkins, W. B., and Hussey, R. G., 1977, "Spin-Up From Rest in a Cylinder," *Physics of Fluids*, Vol. 20, pp. 1596–1604.

Wedemeyer, E. H., 1964, "The Unsteady Flow Within a Spinning Cylinder," *Journal of Fluid Mechanics*, Vol. 20, pp. 383–399.

Weidman, P. D., 1976, "On the Spin-Up and Spin-Down of a Rotating Fluid. Part I: Extending the Wedemeyer Model. Part II: Measurements and Stability," *Journal of Fluid Mechanics*, Vol. 77, pp. 685–735.

Experimental Study of Uniform-Shear Flow Past a Rotating Cylinder

Hyung Jin Sung
Professor.
Mem. ASME

Chong Kuk Chun
Graduate Student.

Jae Min Hyun
Professor.
Mem. ASME

Department of Mechanical Engineering,
Korea Advanced Institute of Science and Technology,
373-1 Kusong-dong, Yusung-ku,
Taejon, Korea
305-701

An experimental study is made of two-dimensional uniform-shear flow ($U = U_c + Gy$) past a rotating cylinder of diameter D. A water-tunnel, equipped with a shear generator, was constructed. Laser-Doppler velocity measurements were undertaken to describe the wake characteristics. Data are compiled over the ranges of $600 \le Re \le 1,200$, the shear parameter $K[\equiv GD/U_c]$ up to 0.15, and the value of the cylinder rotation parameter $\alpha[\equiv \omega D/2U_c]$, $-2.0 \le \alpha \le 2.0$. The power spectra of velocity measurements at downstream locations were analyzed to examine the vortex shedding patterns. In general, the dominant shedding frequency is shifted to a higher value as $|\alpha|$ and K increase. When $|\alpha|$ increases beyond a certain threshold value, the dominant frequency becomes less distinct. If $|\alpha|$ takes a value larger than around 1.5, the velocity field becomes randomized and diffuse, and the organized Karman vortex street activity weakens. The variations of the Strouhal number with K and α are described. The evolution of mean velocity profiles in the wake field is depicted. Characterizations of the velocity profiles, as K and α vary, are made based on the measurement data.

1 Introduction

Much work has ben reported on the flow characteristics around a circular cylinder which is placed in an oncoming crossflow. The principal issues of this classical flow configuration are wake patterns, boundary-layer separation, vortex shedding, and external forces acting on the body, to name a few. In light of the complexities of the problem, the prior studies have been mostly experimental, utilizing a wind tunnel or a water channel. It is to be noted that the majority of past investigations dealt with the cases when the cylinder is placed in a uniform, constant-velocity approaching crossflow. Obviously, this poses the most fundamental flow setup and a large body of relevant information has been compiled for this situation (see e.g., Roshko, 1954; Friehe, 1980; Williamson, 1989).

An important variation of the above basic flow is the case when the oncoming free-stream is uniform-shear flow. Clearly, it is implied that a constant vorticity is embedded in the free-stream, and this gives rise to complicated interactions associated with the boundary-layer separations. In particular, the subject of vortex shedding has been examined extensively by several researchers (Kiya et al., 1980; Yoshino and Hayashi, 1984; Kwon et al., 1992). These investigations revealed, among others, the changes in the Reynolds number-Strouhal number diagram as well as in the drag coefficient, as the shear in the approach flow increases.These findings lead to an improved understanding of the impact of the free-stream vorticity on the gross characteristics of flow patterns around the body. The study of the behavior of a body in approaching uniform-shear flow is useful from the standpoint of practical applications as well.

In the present paper, the preceding work is extended to consider uniform-shear flow past a circular cylinder which rotates steadily about its longitudinal axis. As remarked earlier, the major dynamic ingredient of the uniform-shear stream is the existence of a constant vorticity carried in the oncoming flow. This velocity shear interacts with the boundary layer in the close vicinity of the cylinder. These bring forth the changes in the vortex shedding pattern, compared to the case of a constant-velocity approach free stream. Now, the rotation of the cylinder produces strong velocity shear in the immediate neighborhood of the body surface. This is another significant dynamic element that affects the boundary-layer separation and the resulting vortex shedding patterns. The objective of the present endeavor is to explore the salient features which are generated by a rotating cylinder in uniform-shear flow. As stressed, both the free-stream vorticity and the generation of velocity shear by the cylinder rotation are simultaneously present in the flow geometry under study.

The vortex shedding from a rotating cylinder, placed in uniform-velocity free-stream, has been addressed by several authors (see, e.g., Moore, 1957; Swanson, 1961; Coutanceau and Menard, 1985; Badr and Dennis 1985; Badr et al. 1990; Diaz et al., 1983, 1985; Massons et al., 1989; Kimura et al., 1992). In particular, Diaz et al. (1983, 1985) performed an extensive experimental program in a relatively high Reynolds number range (Re = 9,000) using a wind tunnel. Spectral analyses were made of the velocity data in the near wake of a rotating cylinder. The results indicated that the Karman vortex activity deteriorates rapidly when the cylinder rotation param-

Contributed by the Fluids Engineering Division for publication in the JOURNAL OF FLUIDS ENGINEERING. Manuscript received by the Fluids Engineering Division September 28, 1993; revised manuscript received February 22, 1994. Associate Technical Editor: M. Gharib.

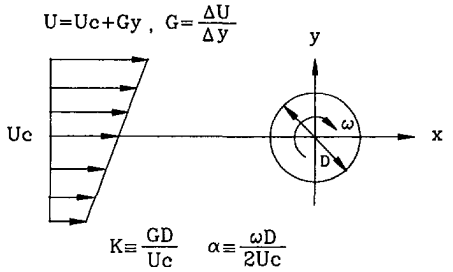

Fig. 1 Definition sketch of uniform-shear flow approaching a rotating circular cylinder

eter α exceeds a certain critical value α_c. On a related subject, Coutanceau and Menard (1985) presented an extensive treatise on the influence of rotation on the development of near-wake behind an impulsively started circular cylinder. Ranges of moderate Reynolds number ($\mathrm{Re} \leq 1{,}000$) were considered. The increase of flow asymmetry with increase in rotation was discussed. On a similar theme, Badr and Dennis (1985) and Badr et al. (1990) presented numerical and experimental studies on the unsteady flow about an impulsively rotating and translating cylinder in the Reynolds number range $10^3 \leq \mathrm{Re} \leq 10^4$.

A thorough literature survey reveals, however, that no published accounts are available which illustrate the wake patterns behind a rotating cylinder in approaching shear flow. As a sequel to the previous efforts using water-channel experiments (Kwon et al., 1992), an expanded experimental research was undertaken in the present work. The wake field was measured by using the laser-Doppler velocimeter, and the data were digitally processed. As anticipated, the character of flow is significantly influenced by the introduction of the free-stream shear and the generation of strong velocity gradients in the vicinity of the rotating cylinder.

2 The Problem Statement

As sketched in Fig. 1, a two-dimensional cylinder of diameter D is placed in the approaching free stream U,

$$U = U_c + Gy$$

where G is the velocity gradient in the y-direction.

The cylinder rotates steadily with angular velocity ω. Accordingly, three relevant nondimensional parameters emerge: the Reynolds number $\mathrm{Re} \equiv U_c D/\nu$, where ν denotes the kinematic viscosity of the fluid; the shear parameter of the free-stream $K \equiv GD/U_c$; and the cylinder rotation parameter $\alpha \equiv \omega D/2U_c$, which is the ratio of the peripheral linear speed of cylinder to the centerline free stream speed U_c. The value of α is positive (negative) when the cylinder rotates in the clockwise (counterclockwise) direction in Fig. 1.

The specific mission of the present study is to monitor the vortex shedding frequency (characterized by the Strouhal number St) over extended ranges of K ($0 \leq K \leq 0.15$) and α ($-2.0 \leq \alpha \leq 2.0$) at moderate Reynolds numbers ($600 \leq \mathrm{Re} \leq 1{,}200$). Furthermore, by carrying out detailed wake surveys, the variations in the velocity profiles in the entire flow field are depicted. The effect of K and α on the behavior of the Karman vortices are described. The combined role of K and α on the reduction of the velocity defect in the downstream is scrutinized.

3 Experimental Apparatus and Procedure

A special-purpose circulating water tunnel was constructed. The dimensions of the rectangular test section were: spanwise width $W = 260$ mm, height $H = 300$ mm, and the length in the streamwise direction was 3700 mm. In order to provide the free-stream shear, a shear generator was fabricated. It was composed of twenty equally-spaced channels, each channel wall of which was 0.7 mm in thickness. The flow passing through each channel was individually regulated by twenty separate valves. The streamwise length of the shear generator was 700 mm. A detailed description of the water tunnel and shear generator was given previously in Kwon et al. (1992).

The rotation rate of the cylinder was controlled by using a DC motor (25W), fitted with a gear head of reduction ratio 12.5 to 1. The rotation rate of the cylinder was typically in the range of 7 rpm to 136 rpm. The shear parameter K of the oncoming stream, $K \equiv GD/U_c$, was determined by varying the value of G by means of the shear generator valve controls. In the experiments, both D ($D = 30$ mm) and U_c ($U_c = 30$ mm/s) were fixed for each setting, and G was adjusted to achieve the desired value of K.

The tunnel blockage ratio, D/H was 0.10. In order to assess the influence of the blockage ratio, the empirical formula of Roshko (1954) for uniform flow was utilized. By this method, the impact of the present blockage ratio was estimated to be less than 6 percent. The aspect ratio of the cylinder, D/W, was 0.115. For the present experimental rig, the two-dimensional flow assumption is applicable to a reasonable degree of accuracy, at least for much of the central portions of the cylinder (see Kiya et al., 1980; Richter and Naudascher, 1976).

The velocity fields were measured by using the laser-Doppler velocimeter (TSI 1990), together with the frequency shifter (TSI 1980). The velocity at a spatial location was secured by averaging five data sets, which represented a total of 2048 data points with a 0.06 s sampling interval. The frequency shift was implemented in 50 kHz, which was capable of depicting the reverse flow in the wake. The upstream velocity data were generally within the range of ± 1.5 percent deviation from the mean shear profile.

The vortex shedding frequency was monitored by the LDV signal processor (TSI 1991), in conjunction with a D/A converter. These devices generated a continuous analog signal by holding the last measurement value until a new measurement was acquired. When the particle validation rate is sufficiently high, the magnitude of instantaneous velocity can be taken to be inversely proportional to the time interval between two successive particle arrivals (Lee and Sung, 1994). In the present experiments, the sampling rate is approximately 2000 s^{-1}.

4 Results and Discussion

The global velocity profile in the immediate neighborhood of the rotating cylinder displays qualitative changes as K and α vary. At the cylinder surface, the no-slip condition is enforced. Naturally, the overall flow patterns will be directly

Nomenclature

D = cylinder diameter
E_u = power spectrum of velocity fluctuations
f = shedding frequency
G = velocity gradient ($\equiv \Delta U/\Delta y$)
H = height of test section
K = shear parameter ($\equiv GD/U_c$)
Re = Reynolds number ($\equiv UD/\nu$)
St = Strouhal number ($\equiv fD/U_c$)
U = streamwise velocity
U_c = centerline velocity
x = streamwise coordinate from center of the cylinder
y = transverse coordinate from center of the cylinder
α = rotation parameter ($\equiv \omega D/U_c$)
ν = kinematic viscosity of fluid
ω = angular velocity of rotating cylinder

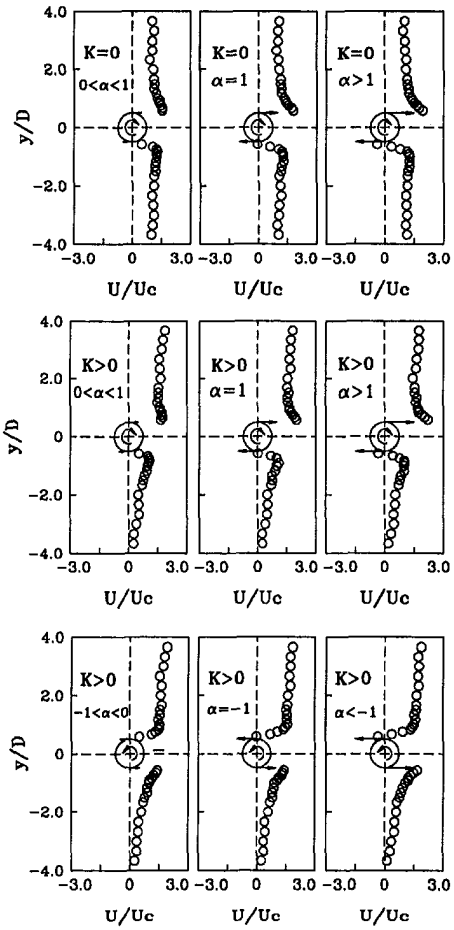

Fig. 2 Measurements of the streamwise velocity profiles along $x=0$. (Uncertainty in $U=\pm 2.2$ percent)

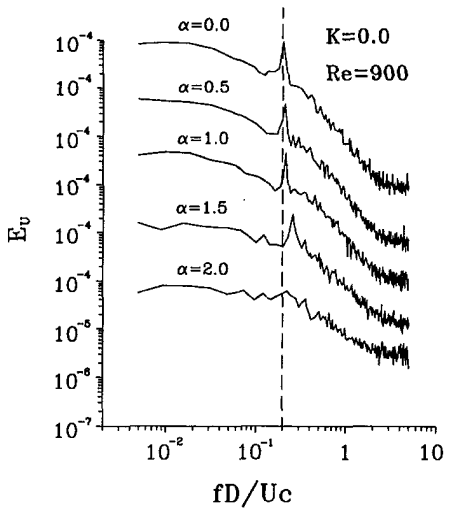

Fig. 3 Power spectra E_u of velocity fluctuations. The location is $x/D=3.0$, $y/D=-0.6$. $K=0.0$, Re = 900.

affected by the free-stream shear and the magnitude and sense of the cylinder rotation. The velocity data were procured over a range of Re ($600 \le Re \le 1{,}200$), where the changes in Re were accomplished by using two different cylinders ($D=20.0$ mm and $D=30.0$ mm) and by adjusting the free stream speed (30 mm/s $\le U_c \le$ 40 mm/s). The qualitative essentials of the data remain unchanged with the variation of Re in this Reynolds number range. Consequently, the results for Re = 900 will be displayed for detailed analysis to typify the flow character.

Figure 2 exhibits the measured streamwise velocity profiles

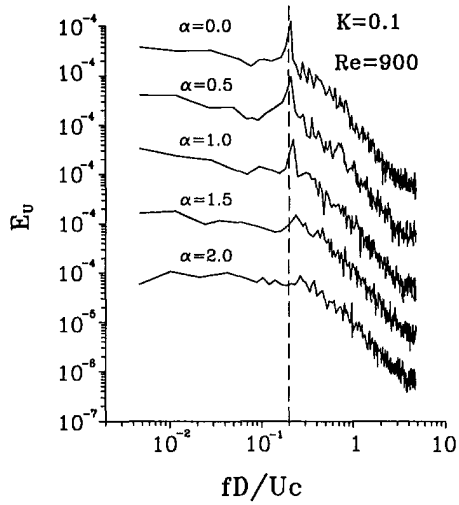

Fig. 4 Power spectra E_u of velocity fluctuations. The location is $x/D=3.0$, $y/D=-0.6$. $K=0.1$, Re = 900.

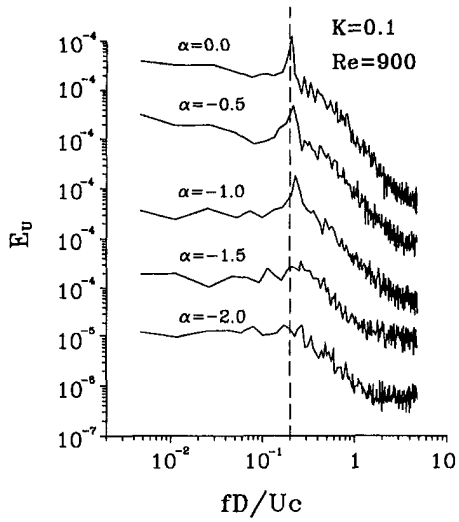

Fig. 5 Power spectra E_u of velocity fluctuations. The location is $x/D=3.0$, $y/D=-0.6$. $K=0.1$, Re = 900.

along the y-axis. In the top frame, characterizations are made of a uniform free-stream ($U=U_c, K=0$) approaching a rotating cylinder ($\alpha \neq 0$). Obviously, $\alpha=1.0$ corresponds to the case when the velocity at the cylinder periphery equals the uniform oncoming speed. Note that, when the rotating effect is substantial ($\alpha>1$), a zone of reverse flow is seen near the bottom of the cylinder. The present velocity measurement data for $K=0$ in Fig. 2 clearly demonstrate consistency with the experimental findings shown in Fig. 9 (*a*, *b*) of Badr et al. (1990). The fundamental aspects of the basic mechanism of the near-wake formation and flow separation were discussed in a highly mathematical account of Coutanceau and Menard (1985) as well as in Badr and Dennis (1985). As emphasized earlier, the primary mission of the present work is to provide experimental descriptions of the gross characteristics of wake at moderate and far downstream locations. The reader is referred to the above-cited publications for more in-depth mathematical delineations of separation phenomena in the close vicinity of the cylinder surface for the case of $K=0$. When the free-stream contains shear ($K>0$), the velocity profiles show marked changes depending on the sense of the cylinder rotation ($\alpha>0$ or $\alpha<0$). The extent and strength of the reverse-flow zone tend to increase as $|\alpha|$ increases. In the case of $K>0$ and $\alpha<0$, the reverse-flow region is narrow, and it is characterized by strong velocity gradients in the vertical direction.

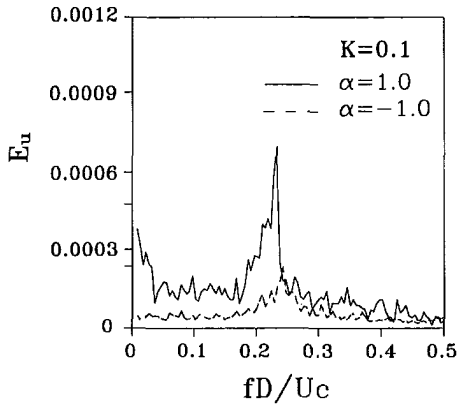

Fig. 6 Power spectra E_u of velocity fluctuations. The location is $x/D = 3.0$, $y/D = -0.6$. $K = 0.1$, $\alpha = -1.0$ and $\alpha = 1.0$.

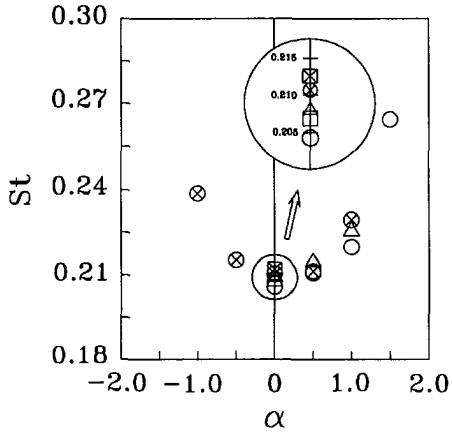

Fig. 7 Diagram of St versus α. (Uncertainty in St = ±6.7 percent, in $\alpha = \pm 1.0$ percent). (○: present results ($K = 0.0$), ⊗: present results ($K = 0.1$), △: Diaz et al., □: Kwon et al. ($K = 0.0$), ⊠: Kwon et al. ($K = 0.1$)).

Quantitative measurements of the shedding frequency are displayed in Figs. 3–5. For this purpose, the power spectra of velocity fluctuation at a downstream location ($x/D = 3.0$, $y/D = -0.6$) were assembled for specific comparisons. The shedding frequency f is represented in the non-dimensional parameter, the Strouhal number, $St = fD/U_c$. Figure 3 is for the case of uniform flow ($K = 0$). For a non-rotating cylinder ($\alpha = 0$), St takes the well-known value $St \approx 0.21$. The peak frequency exhibited in Fig. 3 corresponds to this Strouhal number. As the cylinder rotation rate increases, it is conspicuous in Fig. 3 that the dominant shedding frequency is shifted to higher values. For the case of an impulsively translating and rotating cylinder, Coutanceau and Menard (1985) noted that, as α increases, the detachment of eddies behind the cylinder tends to be accelerated. However, as α takes a large value, the peak frequency itself becomes less distinctly identifiable. The power spectrum shows a tendency of spreading out toward broad ranges of frequency. As is evident in Fig. 3, for the case of $\alpha = 2.0$, a single dominant shedding frequency is not discernible. These trends are consistent with the earlier findings of Diaz et al. (1983), Massons et al. (1989), and Badr et al. (1990).

The results of a clockwise-rotating cylinder ($\alpha > 0$) placed in positive-shear flow ($K > 0$) are illustrated in Fig. 4. It is seen that, as α increases, St takes higher values. Also, at large α, the dominant shedding frequency becomes less distinct, as was noticed for uniform flow ($K = 0$). However, a perusal of Fig. 3 and Fig. 4 indicates that the above-cited blurring of the dominant frequency at large α is more pronounced for shear flow than for uniform flow. Referring to the velocity profile characterizations of Fig. 2, when $K > 0$ and $\alpha > 0$, the flow at the top (bottom) surface of the cylinder is aided (retarded) by the cylinder rotation. This tends to amplify the imbalance due to mean shear between the momentum carried by the fluids in these two regions.

When the cylinder rotation is in the counter-clockwise direction (see Fig. 5 for $\alpha < 0$, $K = 0.1$), the flow at the top (bottom) surface of the cylinder is retarded (aided) by the approaching shear flow. Due to this interaction, the velocity gradient in the y-direction is intensified, which results in the thinning of the boundary layer in the close neighborhood of the top surface. In general, the loss of sufficient forward-moving momentum in the boundary layer contributes to the flow separation from the body. This causes the general shift of the peak frequency toward higher values as $|\alpha|$ increases, which turns up in the form of an increase in St. In addition, as seen in Figs. 3, 4 and 5, there is a tendency toward randomization of velocity components of high frequencies. This is in conformity with the flow visualization of Masson et al. (1989).

In order to signify the difference between the cases of positive and negative α, enlarged views of the power spectra, plotted in linear-linear scales, are shown in Fig. 6. For $\alpha > 0$, since $K > 0$, the faster (slower) moving fluid near the top (bottom) surface of the cylinder is accelerated (decelerated) by the approaching shear flow. For $\alpha < 0$, the opposite situation prevails. Figure 6 suggests that small-scale high-frequency flow fluctuations in the wake region are more diffuse and randomized for $\alpha < 0$. The peak frequency of spectra is more distinct for $\alpha > 0$. For the exemplary cases of $K = 0.1$ and $\alpha = -1.0$ in Fig. 6, the dominant frequency in the spectra is not readily identifiable, pointing to vigorous randomization of velocity oscillations.

The overall findings of the vortex shedding patterns are compiled in the plot of St-α in Fig. 7. The well-documented value of $St = 0.205$ for a uniform stream and a non-rotating cylinder ($K = 0$, $\alpha = 0$) serves as a reference point. For a non-rotating cylinder ($\alpha = 0$), St increases as K increases, and this was established in Kiya et al. (1980) and Kwon et al. (1992). Also, for a uniform stream ($K = 0$), Diaz et al. (1983, 1985) observed that St increases as α increases from zero. However, it should be emphasized that, as the measurements of Diaz et al. indicate, no clearly definable St exists when α increases beyond a threshold value α_c. This reflects the fact that the wake is becoming diffuse and randomized, and a conspicuous peak frequency is not discernible in the power spectra (Massons et al., 1989; Kimura et al., 1992).

The results of the present experiments ($K \neq 0$, $\alpha \neq 0$) are overlayed in Fig. 7. As remarked earlier, for shear flow, St increases as $|\alpha|$ increases from zero. However, the dominant shedding frequency tends to be higher for a negative α than for a positive α for the same absolute value of rotation parameter $|\alpha|$. The present measurements for $K = 0.1$ suggest that the organized Karman street activity becomes weak when $|\alpha|$ reaches beyond around 1.0.

The evolution of the mean velocity profile in the wake is described by the detailed laser-Doppler measurements. Figure 8 is for uniform flow ($K = 0$). The results for this case were illustrated previously by means of a wind-tunnel experiment by Diaz et al. (1985), and the present data are in qualitative consistency with those of Diaz et al. As α increases, the velocity profile becomes nonsymmetrical, especially in the near-wake region, with respect to the center line $y = 0$. As pointed out by Diaz et al. (1985), the location of y_m, at which the maximum velocity defect is detected, is shifted to below the centerline ($y = 0$). The measurement data of Fig. 8 are in support of the earlier observations of Diaz et al. (see Fig. 2).

The velocity profiles for shear flow ($K = 0.1$) are exhibited in Fig. 9. For a non-rotating cylinder ($\alpha = 0$), the numerical simulation of laminar flow by Jordon and Fromm (1972) demonstrated that, due to the nonsymmetry of the approach stream,

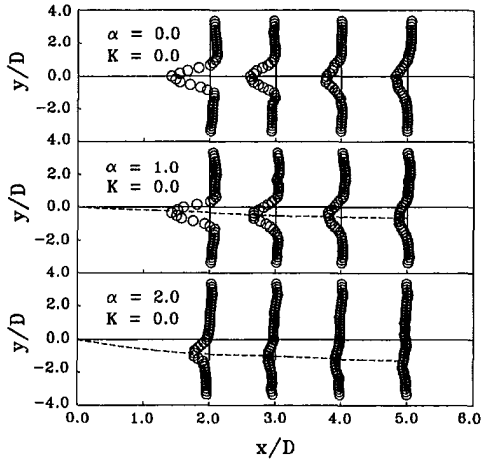

Fig. 8 Exemplary velocity profiles. at $x/D = 2.0$, 3.0, 4.0 and 5.0. $K = 0$. (Uncertainty in $U = \pm 2.2$ percent)

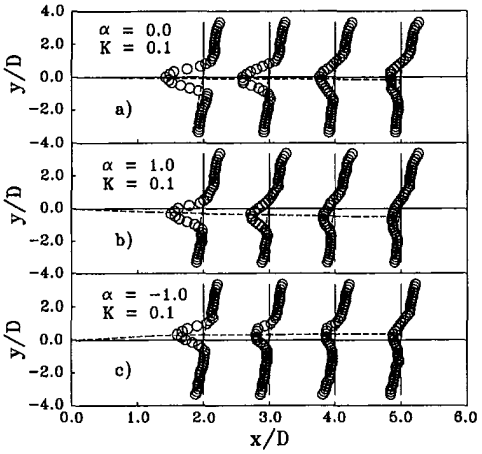

Fig. 9 Exemplary velocity profiles. at $x/D = 2.0$, 3.0, 4.0 and 5.0. $K = 0.1$. (Uncertainty in $U = \pm 2.2$ percent)

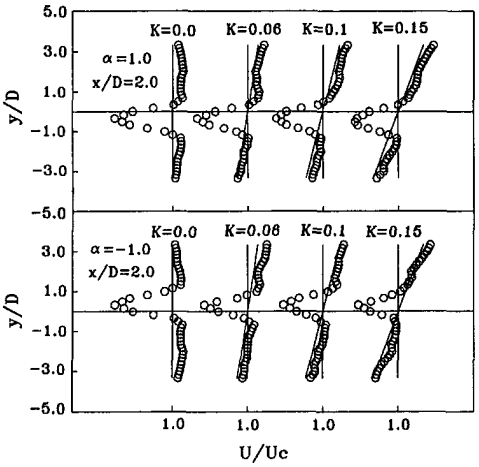

Fig. 10 Exemplary velocity profiles at $x/D = 2.0$. (Uncertainty in $U = \pm 2.2$ percent)

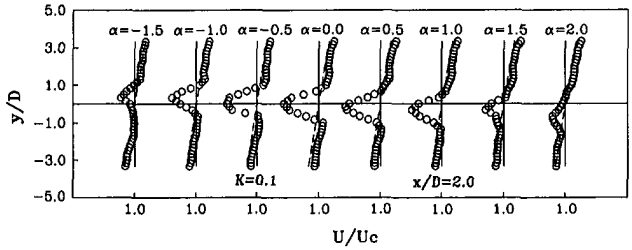

Fig. 11 Velocity profiles at $x/D = 2.0$ for $K = 0.1$ and $-1.5 \le \alpha \le 2.0$. (Uncertainty in $U = \pm 2.2$ percent)

the forward stagnation point is shifted toward the fast side of the free stream ($y > 0$). Owing to this asymmetry, a slight displacement of y_m toward the $y < 0$ region is seen in Fig. 9(*a*). For $\alpha > 0$, in the bottom region of the cylinder, a thick layer of reduced forward-velocities or of reverse-flows is formed. This causes higher rates of diffusion of momentum than for $\alpha = 0$. Therefore, as seen in Fig. 9(*b*), the deviation of the velocity profiles in the wake from the original free-stream profile tends to be smaller than for $\alpha = 0$. The locations of y_m are below the center line. For $\alpha < 0$, the fluid in the bottom region of the cylinder is energized, but the flow in the top region of the cylinder is retarded. Consequently, the velocity defect is pronounced in the region above the centerline $y = 0$. These trends are manifested in the present data of Fig. 9(*c*). In the downstream locations, the diffusion of momentum is more vigorous for $\alpha < 0$. As portrayed in Fig. 9(*c*), the evolution of the velocity profile in the wake toward the original free-stream profile tends to be facilitated in the case of $\alpha < 0$.

In connection with the portrayals of velocity profiles, it is noted that, in the present experiment, the effect of free-stream shear is relatively mild ($K \le 0.1$) in comparison to the effect of cylinder rotation $|\alpha| \le 2.0$. Therefore, some of the classical descriptions of a uniform flow about a rotating cylinder ($K = 0$, $\alpha \ne 0$) exhibit qualitative consistency with the present depictions (see Swanson, 1960; Coutanceau and Menard, 1985; Badr et al., 1990).

The explicit influence of K on the velocity profiles is exemplified in Fig. 10. It is clear that the magnitude of velocity defect is reduced as K increases, for both $\alpha > 0$ and $\alpha < 0$. This indicates that, as the free stream shear is strengthened, the overall diffusion of momentum tends to increase, yielding a faster recovery in the wake of the approach free-stream velocity profile. This trend is more pronounced for $\alpha < 0$ than $\alpha > 0$, as was discussed in Fig. 9.

Characterizations of the velocity profiles at the same location of $x/D = 2.0$, as α varies over the ranges of $-1.5 \le \alpha \le 2.0$, are displayed in Fig. 11. It is also evident that the magnitude of velocity defect is reduced as $|\alpha|$ increases. A closer inspection of the wake profiles reveals that sudden changes in the wake profiles can be seen in the regions of $-1.5 \le \alpha \le -1.0$ and $1.0 \le \alpha \le 1.5$. These ranges are coincident with the ranges of earlier findings of vortex shedding in the wake in Figs. 3–5.

5 Conclusion

The velocity field measurements provided depictions of the gross flow characteristics in the wake.

For a uniform oncoming stream ($K = 0$), the dominant vortex-shedding frequency shifts to a higher value, as the rotation effect (α) increases. For a shear flow ($K > 0$), a similar trend is seen. However, if $|\alpha|$ exceeds a certain threshold value, velocity fluctuations are randomized and diffuse. For large $|\alpha|$, the distinct organized Karman-street activity diminishes. The Strouhal number-rotation parameter plot is constructed, which clearly demonstrates the above findings.

The mean velocity profiles in the wake are illustrated to identify the explicit effects of K and α. When $K = 0$, the cylinder rotation ($\alpha > 0$) causes the zone of velocity defect to be located below the centerline $y = 0$.

For a shear flow ($K > 0$), the forward stagnation streamline is displaced upward to the fast-side of the flow ($y > 0$). For $\alpha < 0$, the lateral location y_m for the maximum velocity defect is shifted upward.

The randomization of velocity field owing to enhanced diffusive activities is more pronounced for the case of $\alpha<0$. Consequently, the overall velocity defect in the wake tends to be milder for $\alpha<0$.

Acknowledgment

Appreciation is extended to the referee whose comments led to improvements of the paper.

References

Badr, H. M., and Dennis, S. C. R., 1985, "Time-Dependent Viscous Flow Past an Impulsively Started Rotating and Translating Circular Cylinder," *Journal of Fluid Mechanics*, Vol. 158, pp. 447–488.

Badr, H. M., Coutanceau, M., Dennis, S. C. R., and Menard, C. 1990, "Unsteady Flow Past a Rotating Circular Cylinder at Reynolds Numbers 10^3 and 10^4," *Journal of Fluid Mechanics*, Vol. 220, pp. 459–484.

Coutanceau, M., and Menard, C., 1985, "Influence of Rotation on the Near-Wake Development Behind an Impulsively Started Circular Cylinder," *Journal of Fluid Mechanics*, Vol. 158, pp. 399–446.

Diaz, F., Gavalda, J., Kawall, J. G., Keffer, J. F., and Giralt, F., 1983, "Vortex Shedding from a Spinning Cylinder," *Physics of Fluids*, Vol. 26, No. 12, pp. 3454–3460.

Diaz, F., Gavalda, J., Kawall, J. G., Keffer, J. F., and Giralt, F., 1985, "Asymmetrical Wake Generated by a Spinning Cylinder," *AIAA Journal*, Vol. 23, pp. 49–54.

Friehe, C. A., 1980, "Vortex Shedding from Cylinders at Low Reynolds Number," *Journal of Fluid Mechanics*, Vol. 100, pp. 237–241.

Jordan, S. K., and Fromm, J. E., 1972, "Laminar Flow Past a Circle in a Shear Flow," *Physics of Fluids*, Vol. 15, pp. 972–976.

Kimura, T., Tsutahara, M., and Wang, Z. Y., 1992, "Wake of a Rotating Circular Cylinder," *AIAA Journal*, Vol. 30, No. 2, pp. 555–556.

Kiya, M., Tamura, H., and Arie, M., 1980, "Vortex Shedding from a Circular Cylinder in Moderate-Reynolds Number Shear Flow," *Journal of Fluid Mechanics*, Vol. 101, part 4, pp. 721–735.

Kwon, T. S., Sung, H. J., and Hyun, J. M., 1992, "Experimental Investigation of a Uniform-Shear Flow Past a Circular Cylinder," *Trans. ASME*, Vol. 114, pp. 457–460.

Lee, D. H., and Sung, H. J., 1994, "Assessment of Turbulent Spectral Bias in LDV," *Experiments in Fluids*, Vol. 16, pp. 223–235.

Massons, J., Ruiz, X., and Diaz, F., 1989, "Image Processing of the Near Wakes of Stationary and Rotating Cylinders," *Journal of Fluid Mechanics*, Vol. 204, pp. 167–184.

Moore, D. W., 1957, "The Flow Past a Rapidly Rotating Circular Cylinder in a Uniform Stream," *Journal of Fluid Mechanics*, Vol. 2, pp. 541–550.

Richter, A., and Naudascher, E., 1976, "Fluctuating on a Rigid Circular Cylinder in Confined Flow," *Journal of Fluid Mechanics*, Vol. 78, part 3, pp. 561–576.

Roshko, A., 1954, "On the Development of Turbulent Wakes from Vortex Streets," NACA Report 1191.

Swanson, W. M., 1961, "The Magnus Effect: A Summary of Investigations to Date," ASME *Journal of Basic Engineering*, pp. 461–470.

Wiliamson, C. H. K., 1989, "Oblique and Parallel Modes of Vortex Shedding in the Wake of a Circular Cylinder at Low Reynolds Numbers," *Journal of Fluid Mechanics*, Vol. 26, pp. 576–626.

Yoshino, F., and Hayashi, T., 1984, "The Numerical Solution of Flow Around a Rotating Circular Cylinder in Uniform Shear Flow," *Bulletin of JSME*, Vol. 27, No. 231, pp. 1850–1857.

Experimental and Numerical Investigation of Flow Oscillations in a Rectangular Cavity

J. C. F. Pereira
Associate Professor.
Mem. ASME

J. M. M. Sousa

Instituto Superior Técnico/Technical University of Lisbon,
Mechanical Engineering Department,
Av. Rovisco Pais, 1096 Lisbon Codex,
Portugal

The unsteady, incompressible, moderate Reynolds number flow past a rectangular cavity is experimentally and numerically investigated. Laser-Doppler anemometry, flow visualization and unsteady numerical simulation using fully second-order accuracy in time and space, were the tools employed to meet this purpose. Large-amplitude organized oscillations are reported to occur in the investigated geometry due to fluid-dynamic instability. Detailed flow visualization and unsteady predictions clearly show that the instability process involves a complex coupling of shear layer and recirculating flowfield dynamics. The paper also demonstrates the accuracy of the present calculations.

1 Introduction

It is well known that oscillations develop in the shear layer of a cavity when a critical value of the Reynolds number is exceeded. These flow oscillations are associated with the presence of organized structures evolving in the cavity shear layer, generated by the selective amplification of extraneous disturbances. However, the process is still much more complex, since it has also been observed that the aforementioned oscillations may be self-sustained, implying the existence of a feedback mechanism. Although this subject is not free of some controversy, it is generally accepted that the impingement of the vortical structures at the downstream cavity edge, leading to large-amplitude variations of pressure and velocity, originate pressure waves, which propagating upstream, provide the necessary feedback to sustain the oscillations.

A wide variety of engineering flow applications and systems can be modeled as single or as a series of cavities. As examples, we mention the slotted walls of wind tunnels (King et al., 1958), where the oscillations are undesirable due to the inherent structural vibrations and noise, and the cooling of electronic chip carriers (Sparrow et al., 1983), where, in contradistinction, the enhanced rate of heat transfer is a direct benefit of the unsteady character displayed by the flow. The problem of self-sustained oscillations in impinging flows has been the subject of endeavored research for many years (see Rockwell and Naudascher (1979) for a review). Simplified models, based solely in shear layer considerations, were formulated (King et al., 1958; Rockwell, 1977; Sarohia, 1977), aiming to describe the behavior of the oscillations. Recent numerical investigations (Ghaddar et al., 1986; Najm and Ghoniem, 1991; Pereira and Sousa, 1993) have allowed more thorough studies of these flows, now taken as dynamical systems where other agents than the shear layer coexist, namely the recirculating flowfield and the interaction with the main flow. As these mechanisms have been neglected in most previous analyses, a few lacunae still subsist in the description of the process of formation of the large-scale structures in cavity flows. On the other hand, and notwithstanding several methodical experimental investigations carried out by different authors, experimental data on the overall cavity flowfield, are still scant. For the stationary case Sinha et al. (1982) have reported experimental data, obtained using a hot-wire anemometer, characterizing a few aspects of the separated flow over two-dimensional rectangular cavities, whilst for the unsteady case very accurate flow measurements are available (Rockwell and Knisely, 1979) but these only concern the cavity shear layer. This picture encourages the accomplishment of detailed measurements of the whole flowfield in and near a cavity wherein oscillations occur.

The overall characteristics of the flow structure inside the cavity are known to be strongly influenced by the cavity aspect ratio and, to a certain extent, by the Reynolds number (Durão et al., 1992). Cavities may, on account of this (Sarohia, 1977), be classified as "open," when the flow over the cavity separates at the upstream edge, reattaching subsequently near the downstream edge; and, conversely, as "closed," when the separated flow reattaches at the cavity floor. Furthermore, open cavities are commonly classed into "shallow" or "deep," according as the depth-to-length ratio is smaller or greater than unity, respectively. It is relevant to accent that the mechanisms behind the phenomenon of flow oscillations in shallow open cavities, briefly described above, are distinct of those associated to deep, except when the ratio of the cavity length to the acoustic wavelength of standing waves is small, as pointed out by Rockwell and Naudascher (1978).

Contributed by the Fluids Engineering Division for publication in the JOURNAL OF FLUIDS ENGINEERING. Manuscript received by the Fluids Engineering Division January 2, 1993; revised manuscript received May 3, 1994. Associate Technical Editor: A. F. Ghoniem.

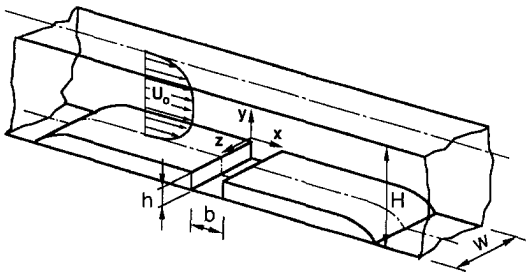

Fig. 1 Geometrical flow configuration

In the present investigation the problem of incompressible, moderate Reynolds number flow ($Re_h = 3360$) over a shallow, open cavity (length-to-depth ratio $b/h = 2$) will be considered. Thus, the subsequent analysis will be restricted to fluid dynamic oscillations and, therefore, the subject of acoustic resonance will not be dealt with. A detailed study comprising flow visualization, laser-Doppler anemometry measurements and unsteady numerical predictions is presented. An explicit quadratic Leith-type of discretization (Leonard, 1979), known as QUICKEST, will be used for the numerical calculations. Its fully second-order accuracy in time and space allows capturing the details of self-sustained oscillations, in order to reveal the complexity of the interaction between the recirculating flowfield and the shear layer.

In the following section of this paper, the experimental apparatus and techniques utilized are briefly described. The third section summarizes the method used to obtain the numerical predictions for the present flow problem. Afterwards, the results of both experimental and numerical procedures are presented and discussed. The last section provides the main conclusions of this work.

2 Experimental Procedure

2.1 Flow Configuration. The experimental setup, illustrated in Fig. 1, consisted of a rectangular cavity model formed on the floor of a PERSPEX water tunnel, 0.170 m in depth, 0.200 m in width, and 7 m in length. The water was drawn from a constant-head discharge tank and pumped, in a closed-circuit, into a pressurized tank. Further details concerning the water tunnel were given by Durão et al. (1989). The cavity model spanned the width of the test section by the combination of appropriate upstream and downstream PERSPEX plates, yielding a depth-to-cavity length ratio $h/b = 0.5$ and depth-to-width ratio $h/w = 0.12$, where $h/H = 0.141$ (see Fig. 1).

The present results were obtained for a fully developed channel flow, characterized by a Reynolds number $Re_H = U_0H/\nu = 23{,}800$. The corresponding characteristic parameter for the cavity flow under study was $Re_h = 3360$. Concerning the boundary layer at separation, the characteristic dimensionless groups based on the momentum thickness and layer thickness were $\theta_0/\delta_0 = 0.097$ and $\delta_0/h = 2.48$, which undoubtedly influenced the mechanisms later described in this paper as found by Sarohia (1977).

2.2 Instrumentation and Measurement Uncertainty. Laser-Doppler anemometry (LDA) was employed to obtain accurate measurements of the time averaged flowfield. A 15 mW (nominal) He-Ne laser (Nippon Electronic Corporation—GL G5600) was used as laser source for the velocimeter, which was operated in the dual-beam forward-scatter mode. The sensitivity to the flow direction was provided by acousto-optic modulation, from a Bragg cell unit Opto-Elektronische Instruments (OEI) LD-OE-402. The frequency shift was set to 0.2 MHz and the velocimeter transfer constant was 3.34 (ms^{-1})/MHz.

The light scattered by naturally-occurring centers in the water was collected by a lens (focal length of 200 mm) and focused into the pinhole aperture (0.3 mm) of an OEI photomultiplier. The photomultiplier output signal was monitored in an oscilloscope, band-pass filtered and processed by a TSI 1980B frequency counter. The validated data was, then, read into a 386SX computer. Time averaged velocities and velocity statistics (not shown) were evaluated by ensemble averaging, calculated from 20 to 60 thousand samples. The large number of samples was indispensable in order to provide a correct statistical characterization of a flow, known apriori to be intrinsically unsteady. The transmitting and receiving optics were both mounted in a traversing table, while the test section was held stationary.

Errors incurred in the measurement of velocity by displacement and distortion of the measuring volume, due to refraction on the duct walls and to the change in refractive index, were found to be negligibly small and within the accuracy of the measuring equipment, as investigated by Durão et al. (1989). Nonturbulent Doppler broadening errors due to gradients of mean velocity across the measuring volume (see, e.g., Durst et al., 1981) affect essentially the variance of the velocity fluctuations. In the experiments, the number of individual velocity values used to form the averages, always above 20 thousand as mentioned before, led to a statistical (random) error below 0.5 percent for the time averaged values, according to the analysis referred by Yanta and Smith (1978) for a 95 percent confidence interval. No corrections were made for sampling bias, and the systematic errors that could have arisen were minimized by using high seed rates in relation to the fundamental velocity fluctuation rate, as suggested for example by Dimotakis (1978), Erdmann and Tropea (1981) and Erdmann et al. (1984) for both random and periodic flows. It is also noted that the zone of the flow characterized by the highest amplitude of the flow oscillations (which were essentially non-turbulent and occurred for the vertical velocity component, as discussed below) was also that where the time averaged velocity was close to zero and the probability density distributions were near bimodal, such that the bias of the negative velocities offset that of the positive velocities, as shown by Erdmann et al. (1984). Thus, the various sources of errors and bias suggested an uncertainty of less than 1 percent for the time averaged velocities. Moreover, the condition under which the output of the counter yields a satisfactory spectral analysis, discussed by, e.g., Dimotakis (1978), Edwards and Jensen (1983), Adrian and Yao (1985) and Srikantaiah and Coleman (1985), was satisfied in the present experiments.

The measurements reported in the present paper regard the time averaged longitudinal component in the channel centerplane, as well as power spectra of the vertical velocity component in the shear layer region.

2.3 Flow Visualization. The recirculating fluid motion was made visible by light reflecting the particles in the water. A laser light (Spectra-Physics 2540 Ar-Kr laser) from above illuminated the water tunnel centerplane and still photographs were taken at right angle to the sheet of light. A 3200 ASA film was employed, using time exposures of order 1/2 sec. The cavity shear layer was visualized by injection of a solution of Rhodamin 6 G particles, from inside the cavity, which was found to be an adequate fluid tracer for the intended purpose. The above mentioned light source was, once again, used. Worthy of note is the fact that the long residence time of the particles inside the cavity, due to the presence of a recirculating flowfield, allowed to record the motion of the shear layer vortices some time after seeding the flow. This enabled us to ensure that the injection of the tracer solution was not disturbing the flow. Motion pictures were taken using a CCD camera and the images were later processed and digitized.

3 Numerical Solution

The governing equations for the fluid flow problem under consideration are the unsteady Navier-Stokes and continuity

equations. The flow is assumed to be two-dimensional and the fluid is treated as incompressible. The former assumption has proved to be reasonable by inspection of the flow visualization results. In fact, for the present Reynolds number $Re_h = 3360$, the flow displayed a quasi-two-dimensional behavior at the channel centerplane, despite the relatively large value of the geometrical ratio h/w.

The above referred equations can be expressed, written in a Cartesian reference frame, as

$$\nabla \cdot \mathbf{v} = 0 \tag{1}$$

$$\frac{\partial \mathbf{v}}{\partial t} + (\mathbf{v} \cdot \nabla)\mathbf{v} = -\frac{1}{\rho}\nabla p + \nu \nabla^2 \mathbf{v} \tag{2}$$

where $\mathbf{v} = (u, v)$ is the velocity, p is the pressure, ν is the kinematic viscosity, and ρ stands for the fluid density. The integration of Eqs. (1) and (2) was obtained by a finite volume method, using an explicit quadratic Leith-type of temporal discretization (Leonard, 1979). For the sake of simplicity, the resulting finite differences equation is presented here assuming the case of one-dimensional flow with $u > 0$, i.e.,

$$\hat{u}_i = u_i^n - \frac{1}{2}\mathrm{C}(u_{i+1}^n - u_{i-1}^n) + \left(\alpha + \frac{1}{2}\mathrm{C}^2\right)(u_{i+1}^n - 2u_i^n + u_{i-1}^n) + \mathrm{C}\left(\frac{1}{6} - \alpha - \frac{1}{6}\mathrm{C}^2\right)(u_{i+1}^n - 3u_i^n + 3u_{i-1}^n - u_{i-2}^n) + \frac{\Delta t}{\rho \Delta x}(p_i^n - p_{i-1}^n). \tag{3}$$

Thus, the dependent variable $\hat{u}$ at an intermediate time step, for each control "volume," can be obtained explicitly from the above equation, where C is the Courant number and α denotes the non-dimensional diffusion coefficient. The continuity equation is driven approximately to zero by adjusting the control volume pressure, amounting to solving a Poisson equation for the pressure correction, which produces a corresponding velocity adjustment. Combining these two equations

$$\frac{u_i^{n+1} - \hat{u}_i}{\Delta t} = -\nabla \phi_i^{n+1} \tag{4}$$

and

$$\nabla \cdot u_i^{n+1} = 0, \tag{5}$$

results the Poisson equation for the pressure correction ϕ_i,

$$\nabla^2 \phi_i^{n+1} = \frac{1}{\Delta t}\nabla \cdot \hat{u}_i. \tag{6}$$

So, the velocity at the $(n + 1)$ time step is obtained by taking into account the velocity correction

$$u_i^{n+1} = \hat{u}_i + \frac{\Delta t}{\rho \Delta x}(\phi_i^{n+1} - \phi_{i-1}^{n+1}). \tag{7}$$

Details concerning two-dimensional calculations using this method were recently presented by Pereira and Sousa (1993). The numerical method is fully second-order accurate in space and in time.

The numerical predictions were performed in a computational domain of length $5h$. The inlet was located at $h/10$ upstream of the cavity separating edge, while the outlet was placed at $29h/10$ downstream of the impingement edge. As mentioned in Section 1, the physical process under investigation involves the interaction between vortical structures in the cavity shear layer and the downstream corner, so that the presence of convective waves was expected. It was, therefore, important to ensure that the location of the outlet boundary did not incur significant wave reflections into domain regions where the relevant phenomena take place. At the open boundary, a monochromatic traveling wave was implemented, i.e., a Sommerfeld-type of radiation condition, which is credited to be a good compromise in the presence of convective waves (Orlanski, 1976; Kobayashi et al., 1993), ensuring nonreflectivity and, consequently, negligible influence on the interior solution. On the walls, no-slip conditions were applied and, as initial condition, the measured time averaged velocity profile was used.

In the laboratory there existed disturbances from various sources. These can be classified into two main categories: irrotational (e.g., resonance from pumping devices) and vortical disturbances (e.g., turbulence). So, in the present computations, small-amplitude random disturbances were superimposed to the mean flow velocity field (both components) at the beginning of simulation. These were obtained from a random-number generator, tapering to zero at the walls and channel centerline. The idiosyncrasy of the employed disturbances does not imply a tacit acknowledgment of that the irrotational perturbations play the main role in the process. Rather, it reflects the difficulties to model the disturbances in the numerical simulations. The perturbations in the laboratory are probably continuous in both space and time, still the model has the merit of allowing the "natural selection" of most amplified modes (Ghoniem and Ng, 1987). Besides, the outcome of the numerical model was found not to be significatively affected, in terms of fluid dynamic behavior, neither by the character of the disturbances nor by their strength, as long as contained within reasonable limits.

The computational mesh used for the numerical simulation comprised 160 × 205 control volumes in the longitudinal and normal directions respectively, and the time step was chosen so that the maximum Courant number did not exceed 0.25. According to Pereira and Sousa (1993), these parameters meet the necessary requirements to asseverate a numerically accurate solution of cavity flow at a moderate Reynolds number, using the present method. The comparison of these results with those obtained using a coarser grid, comprising 81 × 103 control volumes, implied a change in the computed Strouhal number of less than 3 percent. No further error estimation analysis was conducted due to the excellent agreement obtained between time averaged predictions and experimental results, which is attributed to the very fine computational grid as well as to the high accuracy of the employed temporal and spatial discretizations.

4 Results

The extensive experimental information compiled by Rockwell (1977), on the spectral distribution of fluctuations for flows past rectangular cavities, evidenced the existence of different modes of oscillation. Furthermore, it was shown that the preferred (or predominant) mode of oscillation was influenced by the cavity aspect ratio b/h. However, for each mode, it was possible to identify clear trends of the Strouhal number $\mathrm{St} = fh/U_0$, for a wide range of values of b/h. Based on the above referred information, for the cavity geometry under consideration $b/h = 2$, the so-called second mode ($n = 2$) of oscillation was expected to be found as the most persistent one. In fact, spectral information provided by LDA measurements of the vertical velocity component in the cavity shear layer indicated a Strouhal number of St = 0.56 (uncertainty estimate: 0.02), which is in excellent agreement with the aforementioned investigation results, for $b/h = 2$ and $n = 2$. The dynamical behavior of the corresponding flow structure, usually denoted as a two-eddy system, is then characterized by the presence of two eddies evolving simultaneously within the impingement length. Experimental evidence of this fact can be achieved by inspection of Fig. 2(a), obtained by means of the flow visualization procedure formerly described. Both snapshots in this figure show the shear layer vortices, allowing the clear observation of two eddies with different degrees of maturity. The roll-up of the separating shear layer is not a sur-

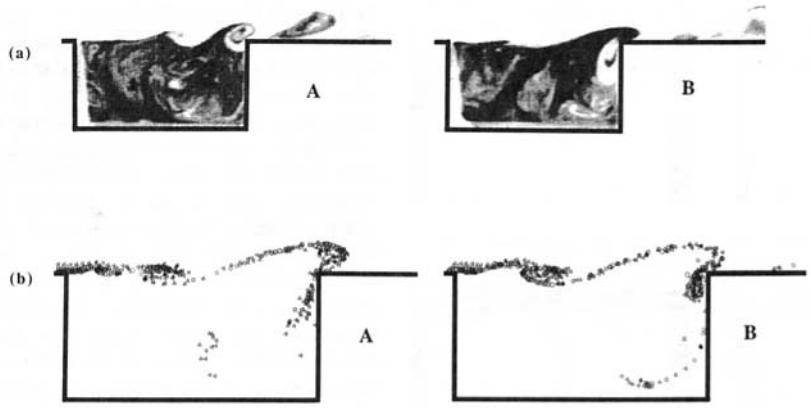

Fig. 2 Cavity shear layer (*a*) Experimental flow visualization; (*b*) numerical simulation using passive particles (streaklines)

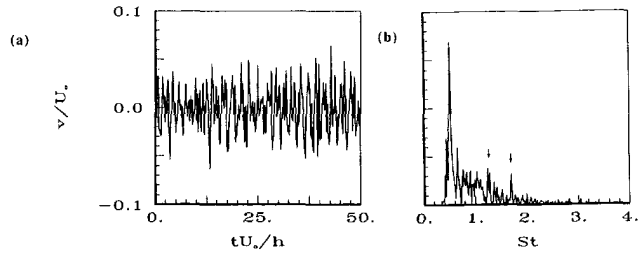

Fig. 3 Calculated vertical velocity component at (x/h, y/h) = (0.51, 1.09). (*a*) Time trace; (*b*) power spectrum

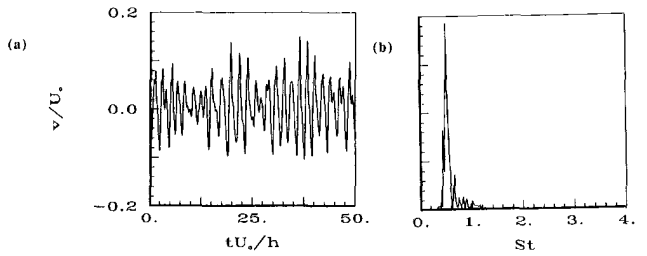

Fig. 4 Calculated vertical velocity component at (x/h, y/h) = (1.15, 1.09). (*a*) Time trace; (*b*) power spectrum

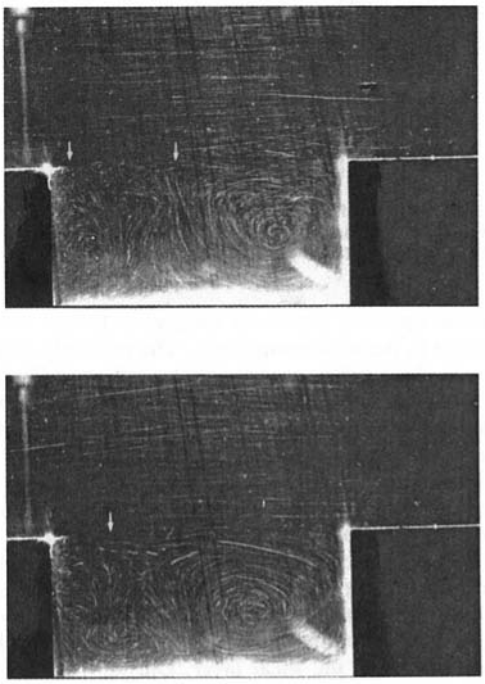

Fig. 5 Flow visualization of the recirculating flowfield. The arrows indicate the recirculation eddies as they are shed within the cavity

prising event, since Kelvin-Helmholtz instability is known to play an important role in the process. Nevertheless, the remarkable organization of the shear layer structures is indeed an interesting feature. As a result of the inevitable interaction with the impingement edge, a former eddy was deformed and shed, as can also be observed in both snapshots of Fig. 2(*a*). Numerical flow visualization of the shear layer, picturing the unsteady flow at two different time steps, obtained using passive tagged particles, is presented in Fig. 2(*b*). This figure, in conjunction with Fig. 2(*a*), illustrates the phenomenon reported by Rockwell and Knisely (1979) termed as "jitter." They have found that, in the complex process of interaction between the vortical structures and the impingement corner, a vortex can experience one of several possible fates. It may suffer clipping by the impingement edge in a complete or in a partial way, or else escape from being clipped. Referring again to Fig. 2, it is clear that, while the snapshots on the left (A) correspond to partial vortex escape, the snapshots on the right (B) display partial vortex clipping. The variability of events for the present flow is observable in Figs. 3(*a*) and 4(*a*), which display computed time traces of the vertical velocity component in the shear layer region, at (x/h, y/h) = (0.51, 1.09) and (x/h, y/h) = (1.15, 1.09), respectively. In this figure, the lack of determinism associated to the phenomenon under study is patent, despite the quasi-periodic behavior exhibited by the flow. The corresponding power spectral analysis yielded a very well defined dominant frequency in both stations (see Figs. 3(*b*) and 4(*b*)), but less energized higher harmonics were also discernable at the foregoing upstream location. The resulting Strouhal numbers, based on the momentum thickness at separation, were $St_\theta = f\theta_0/U_0 = 0.13$, 0.29, and 0.40, far from the usual range for natural instability frequencies in a shear layer (see Husain and Hussain, 1983). However, the computed value of Strouhal number for the highest peak, based on the cavity depth, was St = 0.54, in very good agreement with reported measurements. Equivalent good agreement is also observed with respect to the time averaged velocity profiles of the unsteady calculations, as will be discussed at the end of the present section.

The recirculating flowfield inside the cavity also displays very interesting dynamical characteristics, actively partaking in the process of instability. Figure 5 shows the recirculation eddies at two different time instants. The visualized flow patterns infer the quasi-two-dimensional nature of the flow, which governs the oscillation process (Rockwell and Naudascher, 1978). However, the main insight extracted from Fig. 5 is related to the dynamics of the recirculation eddies. The cavity

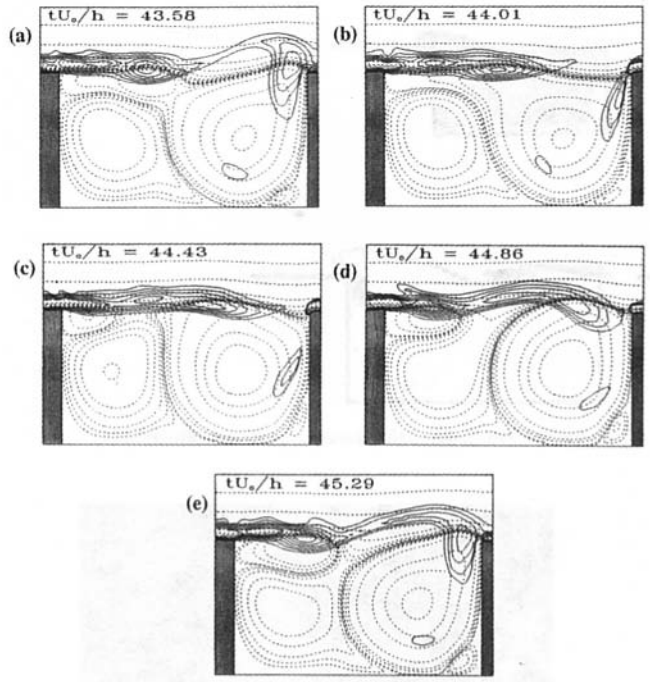

Fig. 6 Series of time frames obtained by unsteady numerical simulation. (*a*) tU_0/h = 43.58; (*b*) tU_0/h = 44.01; (*c*) tU_0/h = 44.43; (*d*) tU_0/h = 44.86; (*e*) tU_0/h = 45.29

space is occupied by a primary (larger) eddy and a secondary eddy (close to the separating edge). The unsteady character of the flow is also visible, seeming that a tertiary eddy is ejected from the separating edge, traveling over the secondary eddy and leading to coalescence with the main eddy. The numerical simulation has confirmed the above described behavior. In Fig. 6 the dynamics of the flow can clearly be observed since we have superimposed the instantaneous vorticity contours (solid lines) to the corresponding flow streamlines (dotted lines). It should be mentioned that, for the sake of the figure clearness, the vorticity contour levels have been selected in order to evidence only the shear layer vortices. The figure demonstrates the significant coupling which takes place between the recirculation region and the shear layer. During the depicted time instants, one of the shear layer vortices accompanies the shedding of the tertiary recirculation eddy (see, for example, Fig. 6(*a*)). In sequence, another shear layer vortex travels over the cavity (see Fig. 6(*b*)), but this vortex cannot maintain its identity because it is not associated to the shedding of a large-scale eddy. The flapping imposed by the recirculation region originates the lateral displacement of the vortex cores and subsequent amalgamation of the structures (see Figs. 6(*c*) and 6(*d*)), giving rise to the large-scale vortex that later impinges on the downstream cavity edge (see Fig. 6(e)). This is in agreement with the power spectra shown in Figs. 3(*b*) and 4(*b*), where the former (upstream) spectrum reveals two additional peaks corresponding to the fast shear layer vortex shedding from the step, while the latter (past middle cavity) displays only one peak reflecting the accomplishment of the merging process between the shed vortices. The merging interaction above described, known as "pairing," is therefore induced or, in a more precise way, catalyzed by excitation due to eddy-shedding in the recirculating flowfield by which it strongly modulates the shear layer dynamics. These observations suggest that the shear layer is forced to adapt to the flow organization imposed by the shedding of recirculation eddies within the cavity, although the process has been initiated through destabilization of the recirculating flowfield by Kelvin-Helmholtz instability. To substantiate this assertion we refer to the investigation of the dynamical response of forced shear layers, both experimental, by Ho and Huang (1982) and numerical, by Ghoniem and Ng (1987). The behavior of the shear layer under consideration in the present work is clearly similar to that exhibited by a forced one, when the forcing frequency is below the natural roll-up frequency. The low-frequency displacement of the vortex cores and the merging of roll-up eddies, in order to form a resultant eddy which is in tune with the forcing frequency (the so-called "resonant eddy"), are mechanisms observed in shear layers when subjected to the mentioned forcing technique that can also be recognized in the present simulations. Moreover, the application of forcing is here attributed to the large-scale recirculation zone shedding. Nevertheless, reported studies on shear layer oscillations, namely by Ziada and Rockwell (1982), demonstrated that most of the features discussed here were displayed even in the absence of recirculating flow, but not to what concerns "pairing." Also, if we deem the work of Rockwell and Knisely (1979), once again pairing was not noticeable, regardless of the fact that in this case there existed a recirculation zone. While for the first reference it can be argued that this was due to the absence of the recirculating flow, for the second reference the explanation can only be found based on the employment of a cavity geometry which was different from the present one, therefore directing to an equally distinct dynamical behavior of the separated region, as already pointed out by Najm and Ghoniem (1991). In any case, the variability of events (the so-called "jitter") reported to occur in cavity flows displaying flow oscillations can be attributed to the variety of possible nonlinear interactions in an excited shear layer, either mainly by virtue of forcing provided by the recirculation region (present case), or solely as a result of the upstream influence caused by vortex-edge interaction.

On the other hand, in the present case, the above-mentioned oscillations do not seem to affect the channel flow. In fact, measured and computed power spectra at the channel centerline do not reveal significant energizing of any frequency. This is at odds with previously reported investigations on the presence of self-sustained oscillations in grooved channels (see, e.g., Ghaddar et al., 1986; Pereira and Sousa, 1993), where the authors have obtained a matching of the flow oscillations with the least stable Tollmien-Schlichting channel mode frequency. One of the findings of these investigations was that the Tollmien-Schlichting modes conform to the new geometry, in terms of wavenumber (imposed by the grooves' periodicity) and cross-stream amplitude distribution, although retaining their main feature, i.e. the related frequency and, hence, ruling the system dynamics. The whole process is facilitated if the characteristic lengths associated to the channel and to the cavity are close. If this is not the case, as for the presently studied geometry (Cf. Section 2), the frequency matching will not take place and, therefore, the cavity flow dynamics can be considered independently of the channel flow.

At this stage, a plausible physical mechanism describing the observed flow oscillations may be summarized as follows. The instability process can be interpreted as shear layer destabilization of the recirculating flowfield. As the shear layer instability is known to be broadband (e.g., Husain and Hussain, 1983), it seems reasonable to conclude that the "stable" part of the flow, i.e., the recirculation eddies, due to their larger characteristic energy, determine the nature and consequently the frequency of the oscillations, while the "unstable" portion of the flow, i.e., the shear layer, locks onto it, providing that the disturbance is within the unstable band of the shear layer. Otherwise, the separating shear layer will itself dictate the frequency of the oscillations and the role of the remainder flowfield will be probably restricted to a secondary modulation of the shear layer, as concluded by Knisely and Rockwell (1982).

Extensive LDA measurements of the mean flowfield were also performed in order to provide a more complete characterization of the time averaged cavity flow at a moderate Reynolds number. The data further allowed to assess the perfor-

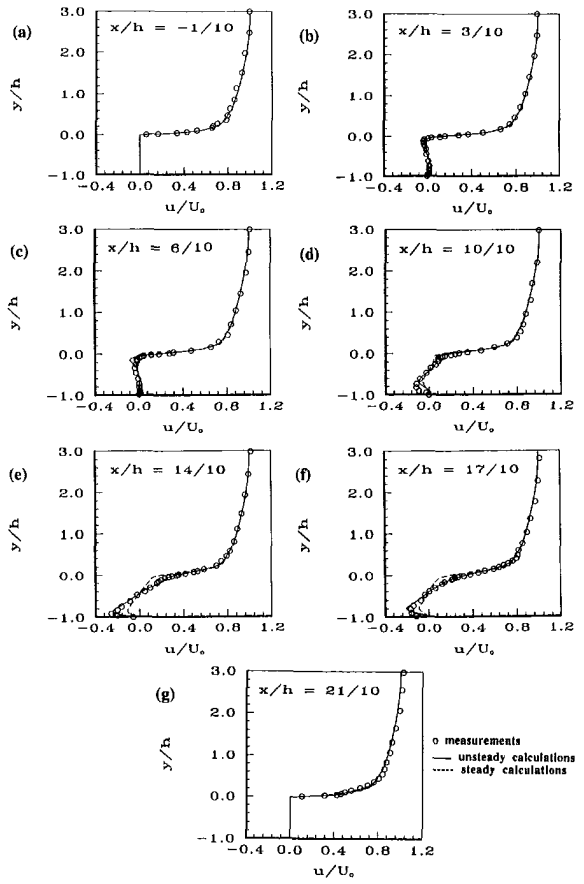

Fig. 7 Longitudinal time averaged velocity profiles at various locations across the cavity. Uncertainty estimate for measurements: 0.01. (*a*) $x/h = -1/10$; (*b*) $x/h = 3/10$; (*c*) $x/h = 6/10$; (*d*) $x/h = 10/10$; (*e*) $x/h = 14/10$; (*f*) $x/h = 17/10$; (*g*) $x/h = 21/10$.

mance of the present numerical method. Figure 7 shows the comparison between experimental measurements and numerical simulation results at several stations across the cavity. The time averaged longitudinal velocity component was evaluated from data acquired for 40,000 time steps, covering more than 50 oscillation periods. Open symbols represent the measurements and lines were used for numerical predictions. In this figure, we have also included the results of a steady calculation of the same flow geometry (dashed lines), obtained using the elliptic form of the Navier-Stokes equations and keeping unchanged the numerical grid. Although the differences between steady and unsteady predictions are not very large, the physical interpretation reported in this paper clearly shows that steady calculations cannot be used to characterize cavity flows at a moderate Reynolds number. These predictions enlighten the action of the main recirculation eddy, in the unsteady case, increasing the mean velocity of the recirculating fluid. This fact is also responsible by the augmented drag experimentally encountered whenever flow oscillations are present. Finally, we emphasize the good agreement between the unsteady predictions (solid lines) and measurements.

5 Conclusions

The present experimental and numerical investigation was concentrated on the unsteady character of the flow past a shallow, open rectangular cavity. The flow is at a moderate Reynolds number, $Re_h = 3360$, where cavity oscillations have been observed. Flow visualization, LDA measurements and unsteady flow predictions allowed to improve the understanding of the dynamics of such flows.

The detailed time-resolved information provided by the experimental and numerical data demonstrated the existence of mechanisms that have been disregarded in most previous investigations. The coexistence of the unstable shear layer with the recirculating flowfield results in the destabilization of the latter. As a consequence, eddy shedding from the recirculation zone can be observed. The shear layer thereby reconciles its dynamics with the formed disturbance, imposed by the "stable" (in the sense of more energetic) part of the flow (the recirculating flowfield). However, if the shear layer cannot adapt to this disturbance, the shear layer itself will presumably rule over the remainder flow, as shown in Rockwell and Knisely (1979) experiments. In any case, it is unquestionable that the forcing/modulation of the shear layer imposed either by the recirculation region, or by the upstream influence resultant of the impingement of flow structures on the downstream edge, is responsible for the variability of events (jitter) in unsteady cavity flows.

The results provided by the numerical simulation further allowed to conclude about the indispensability of using an unsteady formulation for predicting the time averaged characteristics of cavity flows displaying self-sustained oscillations. Very good agreement (within experimental uncertainty) was obtained between experimental and unsteady calculation results, embracing time averaged longitudinal velocity profiles and Strouhal number of the oscillations.

Acknowledgments

The authors gratefully acknowledge to "Fundação para o Desenvolvimento dos Meios Nacionais de Cálculo Científico" for computing facilities. The reviewers' suggestions are also acknowledged.

References

Adrian, R. J., and Yao, C. S., 1985, "Power Spectra of Fluid Velocities Measured by Laser-Doppler Velocimetry," *ASME Winter Annual Meeting*, Miami Beach, FL.

Dimotakis, F., 1978, "Single Scattering Particle Laser Doppler Measurements of Turbulence," AGARD CP 193, paper 10.7.

Durão D. F. G., Heitor, M. V., and Pereira, J. C. F., 1989, "A Laser Anemometry Study of Separated Flow Over a Model Three-Dimensional Hill," *Applications of Laser Anemometry to Fluid Mechanics*, Adrian et al., eds., Springer-Verlag, pp. 93–118.

Durão, D. F. G., Pereira, J. C. F., and Sousa, J. M. M., 1992, "LDV Measurements of Turbulent Separated Flow Over a Cavity," *Proceedings of the Sixth International Symposium on Applications of Laser Techniques to Fluid Mechanics*, Lisbon, Portugal, paper 7.2.

Durst, F., Melling, A., and Whitelaw, J. H., 1981, *Principles and Practice of Laser-Doppler Anemometry*, 2nd ed., Academic Press, New York.

Edwards, R. V., and Jensen, A. S., 1983, "Particle-Sampling Statistics in Laser Anemometers: Sample-and-Hold and Saturable Systems," *Journal of Fluid Mechanics*, Vol. 133, pp. 397–411.

Erdmann, J. C., and Tropea, C. D., 1981, "Turbulence-Induced Statistical Bias in Laser Anemometry," *Proceedings of the Seventh Biennal Symposium on Turbulence*, Rolla, Missouri.

Erdmann, J. C., Lehmann, B., and Tropea, C. D., 1984, "The Statistical Bias of Laser Anemometry Applied in Sinusoidal Flowfields," *Proceedings of the Second International Symposium on Applications of Laser Anemometry to Fluid Mechanics*, Lisbon, Portugal, paper 2.4.

Ghaddar, N. K., Korezak, K. Z., Mikic, B. B., and Patera, A. T., 1986, "Numerical Investigation of Incompressible Flow in Grooved Channels. Part 1. Stability and Self-Sustained Oscillations," *Journal of Fluid Mechanics*, Vol. 163, pp. 99–127.

Ghoniem, A. F., and Ng, K. K., 1987, "Numerical Study of the Dynamics of a Forced Shear Layer," *Physics of Fluids*, Vol. 30, No. 3, pp. 706–721.

Ho, C. M., and Huang, L. S., 1982, "Subharmonics and Vortex Merging in Mixing Layers," *Journal of Fluid Mechanics*, Vol. 119, pp. 443–473.

Husain, Z. D., and Hussain, K. M. F., 1983, "Natural Instability of Free Shear Layers," *AIAA Journal*, Vol. 21, No. 11, pp. 1512–1517.

King, J. L., Boyle, P., and Ogle, J. B., 1958, "Instability in Slotted Wall Tunnels," *Journal of Fluid Mechanics*, Vol. 4, pp. 283–305.

Knisely, C., and Rockwell, D., 1982, "Self-Sustained Low-Frequency Components in an Impinging Shear Layer," *Journal of Fluid Mechanics*, Vol. 116, pp. 157–186.

Kobayashi, M. H., Pereira, J. C. F., and Sousa, J. M. M., 1993, "Comparison of Several Open Boundary Numerical Treatments for Laminar Recir-

culating Flows," *International Journal of Numerical Methods in Fluids*, Vol. 16, pp. 403–419.

Leonard, B. P., 1979, "A Stable and Accurate Convective Modelling Procedure Based on Quadratic Upstream Interpolation," *Computer Methods in Applied Mechanical Engineering*, Vol. 19, pp. 59–98.

Najm, H. N., and Ghoniem, A. F., 1991, "Numerical Simulation of the Convective Instability in a Dump Combustor," *AIAA Journal*, Vol. 29, No. 6, pp. 911–919.

Orlanski, I., 1976, "A Simple Boundary Condition for Unbounded Hyperbolic Flows," *Journal of Computational Physics*, Vol. 21, pp. 251–269.

Pereira, J. C. F., and Sousa, J. M. M., 1993, "Finite Volume Calculations of Self-Sustained Oscillations in a Grooved Channel," *Journal of Computational Physics*, Vol. 106, No. 1, pp. 19–29.

Rockwell, D., 1977, "Prediction of Oscillation Frequencies for Unstable Flow Past Cavities," ASME JOURNAL OF FLUIDS ENGINEERING, Vol. 99, pp. 294–300.

Rockwell, D., and Knisely, C., 1979, "The Organized Nature of Flow Impingement Upon a Corner," *Journal of Fluid Mechanics*, Vol. 93, pp. 413–432.

Rockwell, D., and Naudascher, E., 1978, "Review—Self-Sustaining Oscillations of Flow Past Cavities," ASME JOURNAL OF FLUIDS ENGINEERING, Vol. 100, pp. 152–165.

Rockwell, D., and Naudascher, E., 1979, "Self-Sustained Oscillations of Impinging Free Shear Layers," *Annual Revue of Fluid Mechanics*, Vol. 11, pp. 67–94.

Sarohia, V., 1977, "Experimental Investigation of Oscillations in Flows Over Shallow Cavities," *AIAA Journal*, Vol. 15, No. 7, pp. 984–991.

Sinha, S. N., Gupta, A. K., and Oberai, M. M., 1982, "Laminar Separating Flow Over Backsteps and Cavities Part II: Cavities," *AIAA Journal*, Vol. 20, No. 3, pp. 370–375.

Sparrow, E. M., Vemuri, S. B., and Kadle, D. S., 1983, "Enhanced and Local Heat Transfer, Pressure Drop, and Flow Visualization for Arrays of Block-Like Electronic Components," *International Journal of Heat and Mass Transfer*, Vol. 26, pp. 689–699.

Srikantaiah, D. V., and Coleman, H. W., 1985, "Turbulence Spectra from Individual Realization in Laser Velocimetry Data," *Experiments in Fluids*, Vol. 3, pp. 35–44.

Yanta, W. J., and Smith, R. A., 1978, "Measurements of Turbulent-Transport Properties with a Laser Doppler Velocimeter," AIAA paper 73–169, *Eleventh Aerospace Science Meeting*, Washington.

Ziada, S., and Rockwell, D., 1982, "Oscillations of an Unstable Mixing Layer Impinging Upon an Edge," *Journal of Fluid Mechanics*, Vol. 124, pp. 307–334.

F. H. Ling*
Research Associate Professor.
Mem. ASME

X. Zhang
Graduate Student.

The Polymer Processing Institute and
Department of Chemistry and
Chemical Engineering,
Stevens Institute of Technology,
Hoboken, NJ 07030

Mixing of a Generalized Newtonian Fluid in a Cavity

Mixing of a generalized Newtonian fluid in a corotating discontinuous cavity flow is studied. The flow period and the rheological coefficients are used as parameters. Using geometrical construction of periodic orbits and bifurcation analysis we find mixing windows in the parameter space. A system within a mixing window is capable of producing uniform mixtures. Some bifurcation values have also been determined. A system whose parameters are in the neighborhood of these values will mostly not produce a uniform mixture. The main conclusion is that shear thinning degrades mixing in the cavity flow.

1 Introduction

Mixing of fluids takes place in a variety of natural and engineering processes. It is assisted by turbulent flows at high Reynolds number, such as in the interior of stars, in combustion, and in the atmosphere. It is also facilitated by laminar flow at low Reynolds numbers, such as in food and polymer processing and in the mantle of the earth; see e.g., Ottino (1990). Mixing in the laminar flow is now better understood using chaos theory introduced by Aref (1984). A monograph (Ottino, 1989) and an IUTAM Symposium (Acrivos, 1991) have been devoted to this topic.

From a practical point of view, one of the most important objectives of the study of mixing is to find systems which rapidly produce uniform mixtures. A brute force method can be used for this purpose, i.e., to follow deformation of a minor component to be mixed in a base fluid computationally. The uniformity of a mixture during mixing can be measured with statistical techniques, e.g., the standard deviation and Kolmogorov test used by Ling and Gogos (1992) and Ling (1993). The rate of mixing can be evaluated from the time history of the uniformity of a mixture. This kind of brute force method is useful but tedious. If the rate of mixing is not the main concern, the Poincaré section method can be used to determine the ultimate uniformity of the mixture, i.e., whether a system can produce a uniform mixture given sufficiently long time. The Poincaré section method should be used prior the evaluation of the rate of mixing. This will guarantee that the rate of mixing analysis is only performed to those systems which potentially will produce good mixtures. From the Poincaré sections one can see that low-periodic orbits with their surrounding islands are the main obstacle to uniform mixing, hence, nearly global chaos is a necessary condition for producing a uniform mixture.

Based on this observation, Ling and Schmidt (1992, 1993) proposed the concept of *mixing windows*. The mixing windows are defined as regions in the parameter space where mixing systems are nearly globally chaotic. On the other hand, systems with stable periodic orbits are found in the neighborhood of bifurcation values. Therefore, to produce a uniform mixture one should use mixing systems within a mixing window and avoid the systems in the neighborhood of bifurcation values. Ling and Schmidt (1992, 1993) studied bifurcation and mixing windows in cavity flows with a Newtonian fluid; a good agreement with the available simulation and experimental results was observed. It is very convenient to find mixing windows using bifurcation analysis, complemented by generating several Poincaré sections to examine whether all major periodic orbits with measurable islands have been considered.

Many fluids in nature and industrial processes are non-Newtonian. A non-Newtonian fluid maybe shear thinning (decreasing viscosity with increasing shear rate), be viscoelastic (having memory of the deformation history) of be both. The mixing of non-Newtonian fluids has been studied by several researchers; see, e.g., Kiani et al. (1989) and Sastrohartono and Kwon (1990). However, we are not aware of an investigation showing the effects on non-Newtonian properties on mixing. The purpose of this paper is to study the effect of shear thinning on the mixing in a cavity flow.

2 Velocity Field

Viscosity of a Newtonian fluid is constant. Many fluids, in particular polymers, often do not behave that simple during processing. A number of such fluids are classified as the generalized Newtonian fluids, whose viscosity, μ, is merely a function of the shear rate, $\dot{\gamma}$,

$$\mu = \mu(\dot{\gamma}) = \mu(\dot{\gamma}(x,y,z)). \tag{1}$$

Theoretical considerations lead to various formulas of the function $\mu(\dot{\gamma})$; coefficients in these formulas are determined from experimental data. The simplest formula is the well-known power law

$$\mu = \mu_0 \dot{\gamma}^{1-n}, \tag{2}$$

*Current address: High-Technology Corporation, 144 South Street, Hackensack, NJ 07601.

Contributed by the Fluids Engineering Division and presented at the Winter Annual Meeting, Anaheim, CA, November 8–13, 1992 of THE AMERICAN SOCIETY OF MECHANICAL ENGINEERS. Manuscript received by the Fluids Engineering Division July 27, 1992; revised manuscript received February 15, 1994. Associate Technical Editor: R. H. Panton

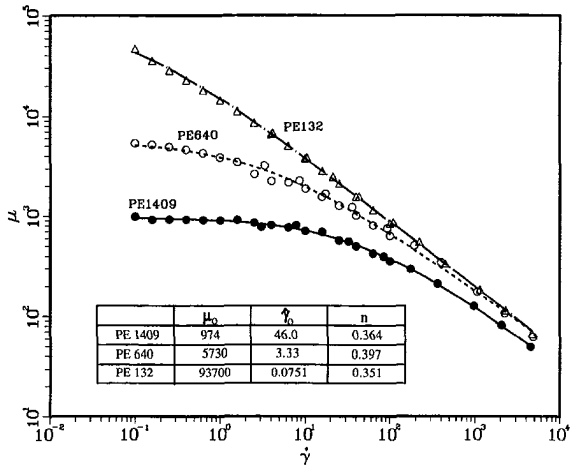

Fig. 1 Dependence of viscosity on shear rate for three polyethylene solutions fitted with the Powell model

where μ_0 is the viscosity at zero shear rate and n is the power law index. The smaller the index, n, the lower the viscosity in high shear rate regions, i.e., the greater the degree of shear thinning. While μ_0 varies in a wide range, n varies between 0.2 and 0.6 for most fluids at high shear rate. For a number of polymers at a typical processing temperature, $n \approx 0.35$.

More sophisticated formulas have more parameters and fit viscosity in wider shear rate and temperature range, such as the Cross model (Cross, 1973). Ignoring the temperature effects, the Cross model is reduced to the Powell model (Powell, 1966),

$$\mu = \frac{\mu_0}{1 + (\dot{\gamma}/\dot{\gamma}_0)^{1-n}}, \tag{3}$$

which is used in this paper. Taking the logarithm of Eq. (3) gives

$$\ln \mu = \ln \mu_0 - \ln (1 + e^{(1-n)\ln(\dot{\gamma}/\dot{\gamma}_0)}), \tag{4}$$

Equation (4) suggests that $\mu \to \mu_0$ when $\dot{\gamma} \to 0$, and $d(\ln \mu)/d(\ln \dot{\gamma}) \to (n-1)$ when $\dot{\gamma} \to \infty$. Furthermore, $d^3(\ln \mu)/d(\ln \dot{\gamma})^3 = 0$ at $\dot{\gamma} = \dot{\gamma}_0$. Hence, the $\ln \mu$ versus $\ln \dot{\gamma}$ curve is composed of a horizontal line for small $\dot{\gamma}$ (often called the Newtonian plateau) and an inclined line with slope $n - 1$ for large $\dot{\gamma}$ (the power law region) connected with a curve whose maximum curvature is at $\dot{\gamma} = \dot{\gamma}_0$. We fitted a set of experimental data of three polymer (polyethylene) melts at 200°C with the Powell model using a least square algorithm. The experimental data were measured by an experimental group in the Polymer Processing Institute. The fit, as shown in Fig. 1, is very good, therefore, we adopt the Powell model in this study.

For laminar mixing, the following assumptions are usually made: the flow is creeping, the fluid is incompressible, and the process is isothermal. The last assumption may not be appropriate under certain polymer processing conditions and will be discussed elsewhere. The governing equations of the velocity field are derived from the mass conservation and momentum balance and are solved using a finite difference method. Introducing a stream function Ψ defined by

$$u = \frac{\partial \Psi}{\partial y}, \quad v = -\frac{\partial \Psi}{\partial x} \tag{5}$$

the shear rate, $\dot{\gamma}$, can be expressed as

$$\dot{\gamma} = \sqrt{\left(\frac{\partial^2 \Psi}{\partial x \partial y}\right)^2 + \frac{1}{4}\left(\frac{\partial^2 \Psi}{\partial y^2} - \frac{\partial^2 \Psi}{\partial x^2}\right)^2}. \tag{6}$$

With the assumptions made above, the governing equation of $\Psi(x,y)$ for a Newtonian fluid is

$$\nabla^4 \Psi = 0 \tag{7}$$

and that for a generalized Newtonian fluid is

$$\mu \nabla^4 \Psi + 2\frac{\partial \mu}{\partial x}\left(\frac{\partial^3 \Psi}{\partial x \partial^2 y} + \frac{\partial^3 \Psi}{\partial x^3}\right) + 2\frac{\partial \mu}{\partial y}\left(\frac{\partial^3 \Psi}{\partial x^2 \partial y} + \frac{\partial^3 \Psi}{\partial y^3}\right) + 4\frac{\partial^2 \mu}{\partial x \partial y}\frac{\partial^2 \Psi}{\partial x \partial y} + \left(\frac{\partial^2 \mu}{\partial y^2} - \frac{\partial^2 \mu}{\partial x^2}\right)\left(-\frac{\partial^2 \Psi}{\partial y^2} - \frac{\partial^2 \Psi}{\partial x^2}\right) = 0. \tag{8}$$

The velocity field is independent of the viscosity of a Newtonian fluid, since μ does not appear in Eq. (7), though shearing stresses are higher for fluid with higher viscosity. Furthermore, Eq. (8) is linear with respect to viscosity and its derivatives, so its solution remains unchanged when the viscosity of a generalized Newtonian fluid is scaled up or down. On the other hand, Eq. (8) is nonlinear with respect to Ψ and its derivatives (the viscosity is a function of the second derivatives of Ψ as seen from Eqs. (2), (3), and (6)) and has to be solved iteratively. If a simple iteration procedure converges, 5 to 10 iterations are typically required, so that the calculation work can be one order more than that to calculate the velocity field of a Newtonian fluid. Frequently, a Newton-Raphson method has to be used, and the calculation work is even more, since the Jacobian of the discretized form of Eq. (8) has to be calculated as well.

Traditionally, the velocity field of the matrix fluid and the related quantities, such as pressure, shear rate, shearing stress, etc., are calculated in a study of mixing. But they are insufficient, since one cannot judge mixing performance from these quantities straightforwardly. In fact, calculation of the velocity field is only the first step of the study of mixing based on chaos theory.

3 Mixing Windows in the Corotating Discontinuous Cavity Flow

Mixing of a Newtonian fluid in a cavity flow has been studied by Chien et al. (1986) and Leong and Ottino (1989) experimentally. Some simulation results are given in Leong (1989). Ling and Schmidt (1992, 1993) studied bifurcation and mixing windows in cavity flows for a Newtonian fluid. We will briefly review the approach of finding bifurcation values and mixing windows, together with some results for mixing of a Newtonian fluid in a cavity flow in this section.

The corotating discontinuous cavity flow studied in this paper is produced by periodic and alternative motion of the top and bottom walls in the opposite directions. The cavity is rectangular with an aspect ratio $h/w = 0.6$. We use $v_{top} = v_{bottom} = v = 0.2612$w/second in this paper. The period of the alternating wall motion, T, is taken as one of the parameters. Other parameters are the power law index, n, and the turning point, $\dot{\gamma}_0$, in the Powell model.

The velocity field is calculated by solving a boundary value problem of the nonlinear equation (8). The only nonzero boundary condition is $\partial \Psi/\partial y = 1$ on the top wall corresponding to its motion in the first half period. The velocity field in the second half period, caused by the motion of the bottom wall, is a 180 degree rotation of that in the first half period.

Mixing of fluids is characterized by the motion of a particle in a given velocity field $\mathbf{v}(\mathbf{x}, t)$. Assuming that the mass of the particle is negligible, its passive motion is governed by

$$\frac{d\mathbf{x}}{dt} = \mathbf{v}(\mathbf{x}, t). \tag{9}$$

Because the system (9) is time-periodic, instead of studying a continuous trajectory, one may study its Poincaré map, i.e., the relationship between successive points on the trajectory with time spacing T,

$$\mathbf{x}_{m+1} = \Phi(\mathbf{x}_m). \tag{10}$$

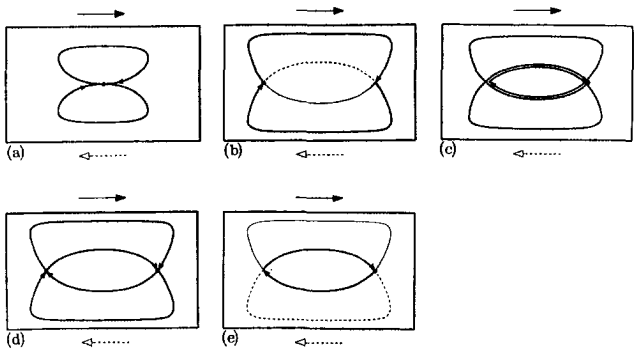

Fig. 2 Geometrical construction of basic P-1 orbits, (*a*) a critical case, (*b*) large loop, P-1L_1, (*c*) small loop, P-1S_2, (*d*) double loop, P-1D_1, (*e*) small loop, P-1S_1

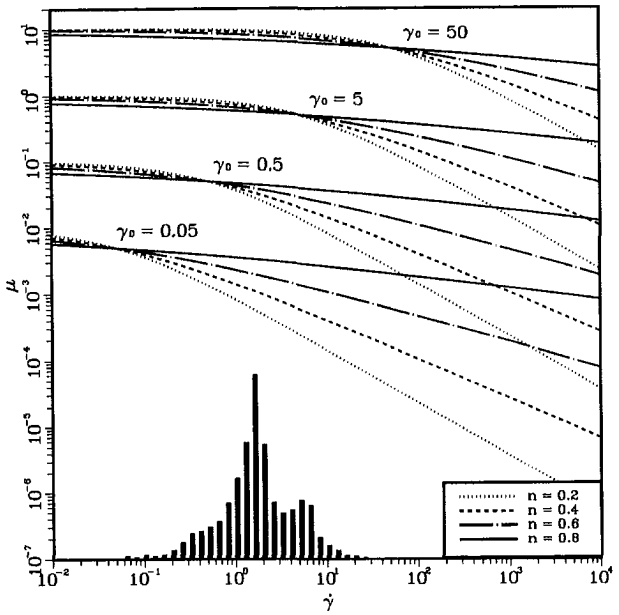

Fig. 3 Dependence of viscosity on shear rate for the generalized Newtonian fluids studied and distribution of the shear rate in a Newtonian Fluid

When a particle can reach almost everywhere in a Poincaré section, its motion state is nearly globally chaotic and hence, a uniform mixing is expected. As analyzed by Franjione et al. (1989) and Ling and Schmidt (1993), the Poincaré map (10) has S_y symmetry when sampled at every other switching point. That is, the x-axis is the axis of symmetry, and all periodic points are either on the x-axis or symmetric about the x-axis. In fact, P-1 (period one) points with large islands are all on the axis of symmetry as observed in the Poincaré sections for various T.

Let us consider a particle in the center of the cavity. It will complete a cycle along the streamline and will return to the center in a time of $T_0/2$. The value of T_0 can be calculated by integrating Eq. (9); it is a function of $\dot{\gamma}_0$ and n. If the motion of the walls switches exactly at the time $T_0/2$, i.e., $T_0/2 = T/2$, then the particle will complete another cycle on the lower part of the cavity at the end of the period, T; see Fig. 2(*a*). A possible periodic orbit whose period is greater than T_0 is shown in Fig. 2(*b*). This orbit is called P-1L_1, since it has a large loop. Two possible periodic orbits whose period is greater than T_0 are shown in Figs. 2(*c*) and (*d*), respectively. The orbit in Fig. 2(*c*) has two small loops and is called P-1S_2, and another orbit in Fig. 2(*d*) is called P-1D_1, implying one double loop. There is also a periodic orbit with a small single loop, which is called P-1S_1 as shown in Fig. 2(*e*). Thus, the orbit shown in Fig. 2(*a*)

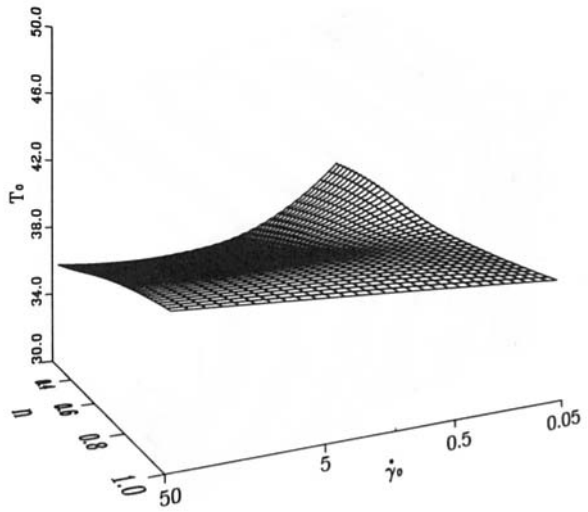

Fig. 4 Period of a class of bifurcation values of the corotating discontinuous cavity flow with generalized Newtonian fluids, $h/w = 0.6$, $v = 0.2612$ w/second

changes its topological class when perturbed and hence, it is not structurally stable. The corresponding period, T_0, is the bifurcation value (Guckenheimer and Holmes, 1983). Periodic orbits with more loops can be similarly constructed and are classified to three families, P-1S_k, P-1L_k and P-1D_k, $k = 1, 2, \ldots$. It is clear that these periodic orbits originate from one of the following bifurcation values: $T = kT_0(\dot{\gamma}_0, n)$, $k = 0,1,2, \ldots$. Stability of these orbits is determined using the Floquet theory; see Ling and Schmidt (1992) for details. The P-1S_1 orbit emanates from the stagnation point in the $T \to 0$ limit. This orbit loses its stability through a pitchfork bifurcation, and the two new-born stable P-1 orbits subsequently undergo infinite period-doubling bifurcations, which lead to chaos. The P-1L_2 orbit is born at a larger T through a tangent bifurcation and turns into P-1S_2 and P-1D_1 at the bifurcation value, $T = T_0$. The P-1D_1 orbit is marginally stable and is surrounded by an island within a small interval of T. This scenario repeats itself for an increasing T, but the stable region of P-1S_k becomes smaller and smaller and finally disappears for $k \geq 6$. Within the gaps between these stable regions, all P-1 orbits are unstable. Although there might be stable higher periodic orbits, no measurable islands are visible in the Poincaré sections we have plotted. Therefore, these gaps are the mixing windows we are looking for.

4 Mixing Windows for a Generalized Newtonian Fluid

Bifurcation values and mixing windows in the corotating discontinuous cavity flow with a generalized Newtonian fluid have been calculated using the method described in the previous section. The parameters in the Powell model, Eq. (3), are varied in a wide range, $0.2 \leq n \leq 1$ and $0.05 \leq \dot{\gamma}_0 \leq 50$. Note that $n = 1$ or $\dot{\gamma}_0 = \infty$ corresponds to a Newtonian fluid. Viscosity of several generalized Newtonian fluids and the distribution of shear rates in a Newtonian fluid are shown in Fig. 3. The distribution of shear rates in a generalized Newtonian fluid is not very different from that in a Newtonian fluid. Because the value of μ_0 has no influence on the velocity field, we have chosen different μ_0 for different n, so that the viscosity curves are not overlapping. From Fig. 3, one can determine whether a generalized Newtonian fluid with a given n and $\dot{\gamma}_0$ is mostly in the Newtonian plateau region or in the power law region.

For a generalized Newtonian fluid with a given $\dot{\gamma}_0$ and n, its bifurcation values are periodic in T with a period of T_0 as shown in Fig. 4. The T_0 surface goes up with decreasing $\dot{\gamma}_0$

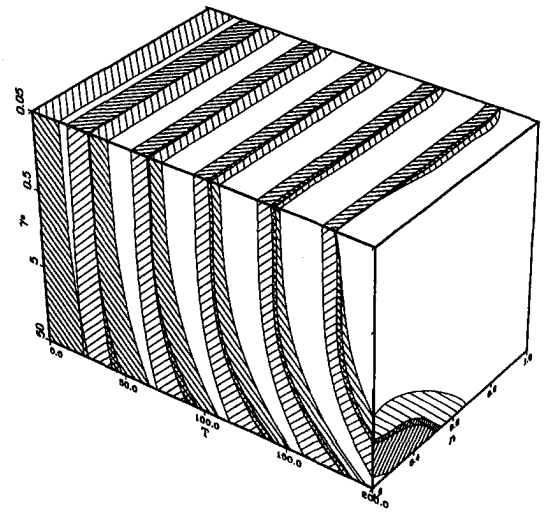

Fig. 5 Mixing windows in the parameter space ($\dot{\gamma}_0, n, T$) of the corotating discontinuous cavity flow with generalized Newtonian fluids, h/w = 0.6, v = 0.2612 w/second, ▭ mixing windows, \\\\\\ stable regions of P-1P$_k$ orbits, ////// stable regions of P-1L$_k$ orbits, XXXXXX stable regions of P-1D$_k$ and other P-1 orbits

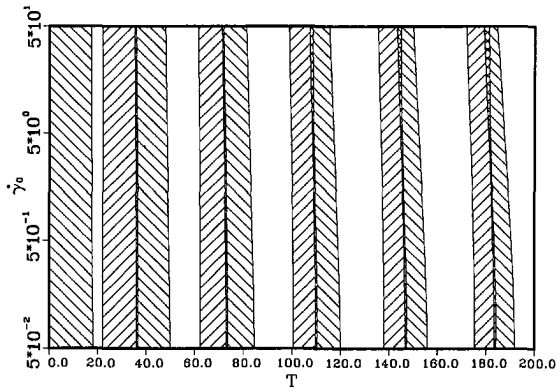

Fig. 6(*a*)

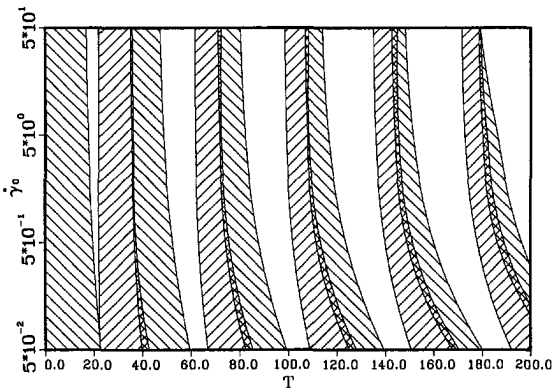

Fig. 6(*b*)

and n, implying that the greater the degree of shear thinning the longer the period. Figure 5 shows stable P-1 regions (shaded) and mixing windows (not shaded) in the parameter space ($\dot{\gamma}$, n, T). Note that, for the sake of simplicity, we did not consider stable regions of the P-1 orbits bifurcated from P-1L$_k$, since they only occupy a small T-interval. Moreover, their surrounding islands are very small as in the case of a Newtonian fluid described by Ling and Schmidt (1992). Several cross-sections with constant n or $\dot{\gamma}_0$ are shown in Fig. 6; n = 0.8 in Fig. 6(*a*), n = 0.4 in Fig. 6(*b*), $\dot{\gamma}_0$ = 5 in Fig. 6(*c*), and $\dot{\gamma}_0$

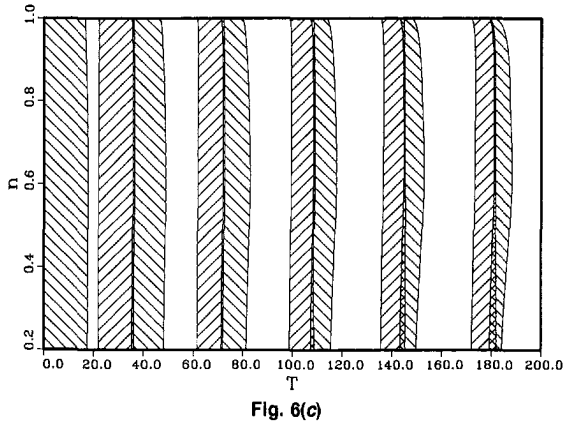

Fig. 6(*c*)

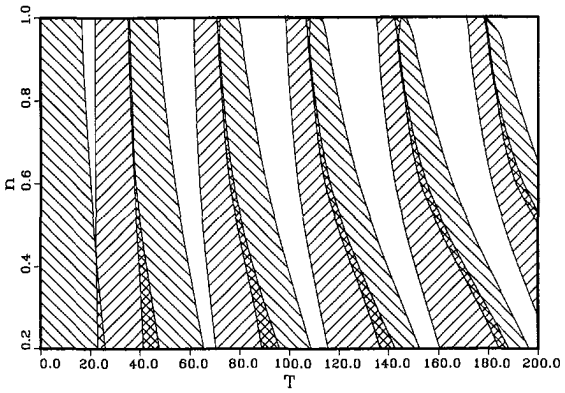

Fig. 6(*d*)

Fig. 6 Cross section of mixing windows in the parameter space ($\dot{\gamma}_0, n, T$) of the corotating discontinuous cavity flow with generalized Newtonian fluids, h/w = 0.6, v = 0.2612 w/second, ▭ mixing windows, \\\\\\ stable regions of P-1S$_k$ orbits, ////// stable regions of P-1L$_k$ orbits, XXXXXX stable regions of the P-1D$_k$ and other P-1 orbits, (*a*) n = 0.8, (*b*) n = 0.4, (*c*) $\dot{\gamma}_0$ = 5, (*d*) $\dot{\gamma}_0$ = 0.05

= 0.05 in Fig. 6(*d*). Since n = 1 corresponds to a Newtonian fluid, the uppermost part of the mixing windows in Fig. 6(*c*) and (*d*) for various $\dot{\gamma}_0$ are exactly the same. For a Newtonian fluid, the stable regions of different P-1 orbits never overlap, so that there are gaps in between forming mixing windows. As the degree of shear thinning increases, i.e., n decreases and $\dot{\gamma}_0$ is sufficiently small to keep the shear rate mostly beyond the Newtonian plateau, the stable regions of P-1 orbits become larger, and eventually, the first one or two mixing windows disappear due to overlapping of the adjacent stable P-1 regions. Thus, the greater the degree of shear thinning the worse the mixing in the co-rotating discontinuous cavity flow.

Poincaré sections for $\dot{\gamma}_0$ = 5, n = 0.6 and different T are shown in Fig. 7 to visualize different mixing behavior within and outside the mixing windows. The mixing system is integrable in the $T \to 0$ limit, as can be observed in Fig. 7(*a*). As T increases, a chaotic region appears, however, a large island remains as illustrated in Fig. 7(*b*) for T = 8. A further increase of T results in alternate occurrence of nearly global chaos (Figs. 7(*c*), (*e*), and (*g*) for T = 20, 60 and 90, respectively) or islands in chaotic seas (Figs. 7(*d*), (*f*), and (*h*) for T = 35, 70, and 100, respectively), which verifies the existence of the mixing windows.

5 Concluding Remarks

To study the influence of the degree of shear thinning on mixing, one has to consider different fluids. Our results show that shear thinning degrades mixing in the corotating discontinuous cavity flow. The corotating discontinuous cavity flow

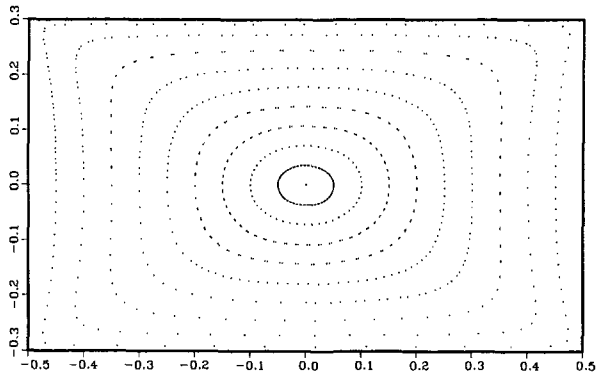

Fig. 7(*a*)

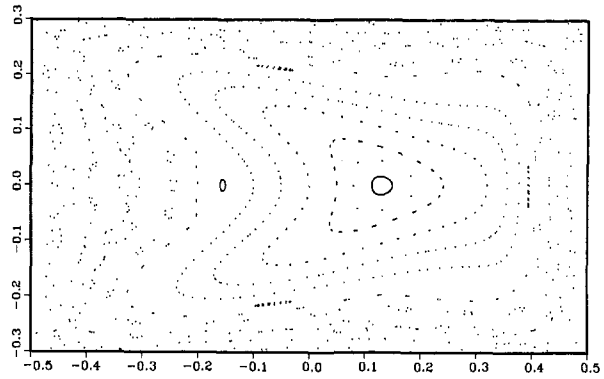

Fig. 7(*b*)

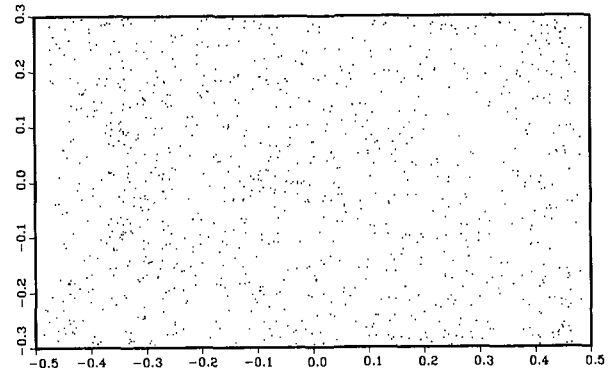

Fig. 7(*c*)

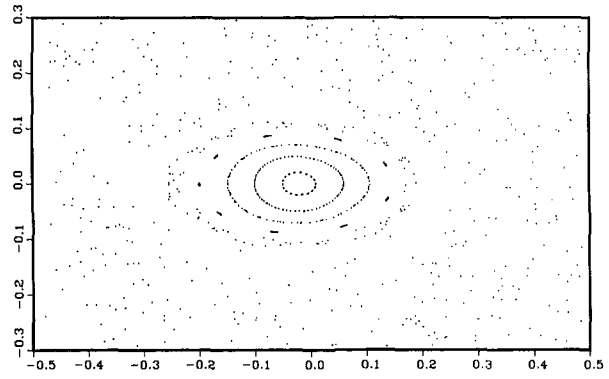

Fig. 7(*d*)

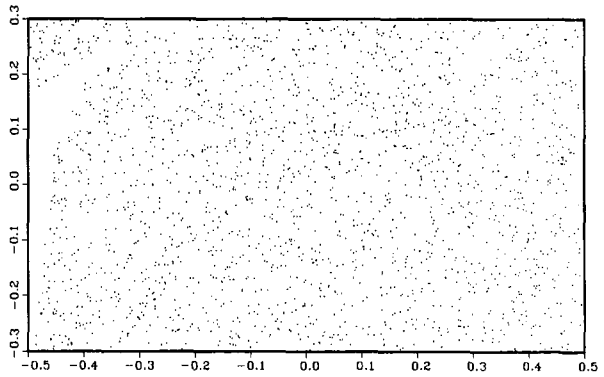

Fig. 7(*e*)

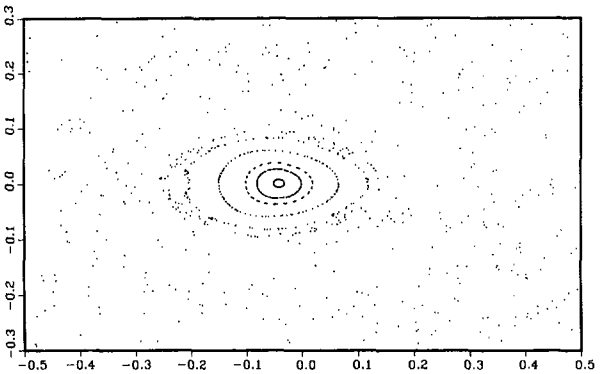

Fig 7(*f*)

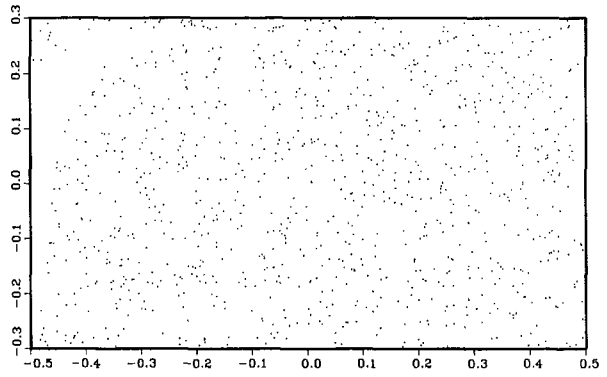

Fig. 7(*g*)

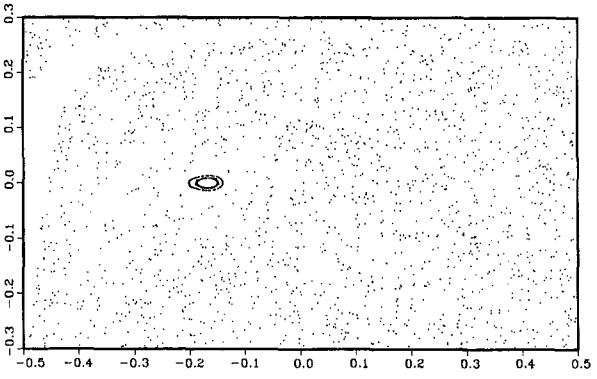

Fig. 7(*h*)

is piecewise steady, and each steady branch contains a vortex in the upper and lower half of the cavity, as if the vortex jumps up and down periodically. It is expected that this conclusion is also valid for other piecewise flows with vortices in each

Fig. 7 Poincaré sections of the corotating discontinuous cavity flow mixing systems with a generalized Newtonian fluid, h/w = 0.6, v = 0.2612 w/second, γ_0 = 5, n = 0.6, (*a*) $T \to 0$, (*b*) T = 8, (*c*) T = 20, (*d*) T = 35, (*e*) T = 58, (*f*) T = 70, (*g*) T = 90, (*h*) T = 100

steady branch as in the case of the Aref blinking vortex (Aref, 1984) and the discontinuous journal bearing flow. Shear thinning reduces strength of the vortices and weakens the link between the high and low shear rate regions and hence, degrades the mixing performance. It is of interest to examine whether this conclusion is also valid for mixing in different types of flows; further studies will be conducted.

A related issue is the effect of visco-elasticity on mixing. It is worthwhile to mention the experimental results on mixing of the Boger fluids in a cavity flow by Leong and Ottino (1990). Their experimental results suggest that there are two major differences between Newtonian and visco-elastic fluids. First, the mixing process of the visco-elastic fluid is slower, and second, their islands are larger. The strategy described in this paper can also be used to study the visco-elastic fluid, if the mixing time is sufficiently longer than the relaxation time of the fluid, so that a periodic state is established. This strategy can also be used for other periodic systems, including spatially periodic systems, such as the Kenics Mixer.

Acknowledgments

This work is part of the ongoing Polymer Mixing Study, which is conducted at the Polymer Processing Institute and is industrially cosponsored. A discussion with S. Widagdo and M. Avgousti is acknowledged.

References

Acrivos, A., ed., 1991, *Proceedings of the IUTAM Symposium of Fluid Mechanics of Stirring and Mixing*, La Jolla, CA, 20–24 Aug. 1990, *Physics of Fluids A*, Vol. 3, pp. 1009–1469.

Aref, H., 1984, "Stirring by Chaotic Advection," *Journal of Fluid Mechanics*, Vol. 143, pp. 1–21.

Chien, W.-L., Rising, H., and Ottino, J. M., 1986, "Laminar Mixing and Chaotic Mixing in Several Cavity Flows," *Journal of Fluid Mechanics*, Vol. 170, pp. 355–377.

Cross, M. M., 1973, "Rheology of Synthetic Latices: Influence of Shear Rate and Temperature," *Journal of Colloid Interface Science*, Vol. 44, pp. 175–176.

Franjione, J. G., Leong, C. W., and Ottino, J. M., 1989, "Symmetries Within Chaos: A Route to Effective Mixing," *Physics of Fluid A*, Vol. 1, pp. 1772–1783.

Greene, J. M., MacKay, R. S., Vivaldi, F., and Feigenbaum, M. J., 1981, "Universal Behaviour in Families of Area Preserving Maps," *Physica D*, Vol. 3, pp. 468–486.

Guckenheimer, J., and Holmes, P., 1983, *Nonlinear Oscillations, Dynamical Systems, and Bifurcations of Vector Fields*, Springer-Verlag, New York, p. 119.

Kiani, A., Rakos, R., and Sebastian, D. H., 1989, "Three-Dimensional Computational Analysis of Fluted Mixing Devices," *Proceedings of the ANTEC 89*, pp. 62–65.

Leong, C. W., 1989, "A Detailed Analysis of Chaotic Mixing of Viscous Fluids in Time-Periodic Cavity Flows," Ph.D. thesis, University of Massachusetts, Amherst.

Leong, C. W., and Ottino, J. M., 1989, "Experiments on Mixing Due to Chaotic Advection in a Cavity," *Journal of Fluid Mechanics*, Vol. 209, pp. 463–499.

Leong, C. W., and Ottino, J. M., 1990, "Increase in Regularity by Polymer Addition During Chaotic Mixing in Two-Dimensional Flows," *Physical Reviews Letters*, Vol. 64, pp. 874–877.

Ling, F. H., 1993, "The Effect of Mixing Protocol on Mixing in Discontinuous Cavity Flows," *Physics Letters A*, Vol. 177, pp. 331–337.

Ling, F. H., and Gogos, C., 1992, "Statistical Evaluation of Uniformity of Simulated Mixtures," *Proceedings of the ANTEC 92*, pp. 2476–2479.

Ling, F. H., and Schmidt, G., 1992, "Mixing Windows in Discontinuous Cavity Flows," *Physics Letters A*, Vol. 165, pp. 221–230.

Ling, F. H., and Schmidt, G., 1993, "Bifurcations and Mixing Windows in Sinusoidal Cavity Flow Mixing Systems," *International Journal of Bifurcation and Chaos*, Vol. 3, pp. 1457–1476.

Ottino, J. M., 1989, *The Kinematics of Mixing: Stretching, Chaos, and Transport*, Cambridge University Press, Cambridge.

Ottino, J. M., 1990, "Mixing, Chaotic Advection, and Turbulence," *Annual Review of Fluid Mechanics*, Vol. 22, pp. 207–253.

Powell, A., 1966, "The Influence of the Molecular Size Distribution within a Liquid on the Viscous Flow of the Liquid," *Polymer*, Vol. 7, pp. 91–97.

Sastrohartono, T., and Kwon, T. H., 1990, "Finite Element Analysis of Mixing Phenomena in Tangential Twin-Screw Extruders for Non-Newtonian Fluids," *International Journal of Numerical Methods in Engineering*, Vol. 30, pp. 1369–1383.

The Axisymmetric Motion of a Liquid Film on an Unsteady Stretching Surface

R. Usha
Department of Mathematics,
Indian Institute of Technology,
Madras, Tamil Nadu,
India

Rukmani Sridharan
Department of Mathematics,
Stella Maris College,
Madras, Tamil Nadu,
India

The axisymmetric motion of a fluid caused by an unsteady stretching surface that has relevance in extrusion process and bioengineering has been investigated. It has been shown that if the unsteady stretching velocity is prescribed by $rb/(1-\alpha t)$, then the problem admits a similarity solution which gives much insight to the character of solutions. The asymptotic and numerical solutions are obtained and they could be used in the testing of computer codes or analytical models of more realistic engineering systems. The results are governed by a nondimensional unsteady parameter S and it has been observed that no similarity solutions exist for $S > 4$.

Introduction

In extrusion processes, it is important to study the motion of fluid caused by a stretching surface. Such a study is also applicable to the elongation of bubbles, pseudopods and in bioengineering, where the flexible surfaces of the biological conduits, cells and membranes in living systems are typically lined/surrounded with fluid and constantly being stretched. Crane (1970) investigated the steady two-dimensional flow induced by a stretching boundary. Brady and Acrivos (1981) and Wang (1984, 1988) have obtained the exact similarity solutions of the Navier-Stokes equations for the steady stretching boundaries in three dimensions. Wang (1990) has investigated the similarity solution for the liquid film on an unsteady stretching surface for the two-dimensional Cartesian case.

In this paper, we present an exact similarity solution of the unsteady axisymmetric Navier-Stokes equations for the motion of a liquid film on a stretching surface. The problem considered is unsteady since the liquid film stretches with the boundary and its thickness decreases in response. Recently, Usha and Uma (1991) have shown that the unsteady, axisymmetric flow of a viscous incompressible fluid admits the following four parameter Lie group of transformations, written in an infinitesimal manner

$$\begin{aligned}\bar{r} &= r + \sigma\zeta(r, z, t, \psi) + o(\sigma^2)\\ \bar{z} &= z + \sigma\beta(r, z, t, \psi) + o(\sigma^2)\\ \bar{t} &= t + \sigma\gamma(r, z, t, \psi) + o(\sigma^2)\\ \bar{\psi} &= \psi + \sigma\Lambda(r, z, t, \psi) + o(\sigma^2)\end{aligned} \tag{1}$$

where r, z, t are space-time coordinates, ψ is the stream function and ζ, β, γ, Λ are given by (Usha and Uma, 1991)

$$\begin{aligned}\zeta &= Cr\\ \beta &= Cz + h(t)\\ \gamma &= 2Ct + D\\ \Lambda &= C\psi - (r^2/2)\dot{h}(t) + k(t)\end{aligned} \tag{2}$$

where dot denotes a time derivative. This group has two explicit parameters C and D and two implicit parameters contained in $h(t)$ and $k(t)$.

We use Eqs. (1) and (2) to show that the flow of a liquid film caused by a stretching surface admits a similarity solution if the unsteady stretching velocity is proportional to $r(2Ct + D)^{-1}$ and that the liquid film thickness is proportional to $(2Ct + D)^{1/2}$. The flow is described by the nondimensional unsteady parameter S, which governs the thickness of the liquid film and the other fluid dynamic properties. For some values of the parameter S, the flows that arise models certain industrial processes and engineering systems although the motivation for the present work sprang from the authors' interest in finding exact similarity solutions of the unsteady, axisymmetric Navier-Stokes equations. The asymptotic and numerical solutions are obtained for the resulting nonlinear ordinary differential equation which could be used for testing of computer codes and for validating analytical models of more realistic engineering systems.

Mathematical Formulation

We consider the surface at $z = 0$ to be stretched with velocity $rg(t)$ (Fig. 1). We assume, the end effects and gravity are negligible and the liquid film of thickness $H(t)$ is uniform and stable. Let (u, w) denote the velocity components in the r and z increasing directions where (r, θ, z) correspond to cylindrical polar coordinates. The boundary conditions are

$$z = 0: \quad u = rg(t) \tag{3}$$

$$z = 0: \quad w = 0 \tag{4}$$

$$z = H(t): \; w = \dot{H}(t) \tag{5}$$

$$z = H(t): \; \frac{\partial u}{\partial z} + \frac{\partial w}{\partial r} = 0 \tag{6}$$

Contributed by the Fluids Engineering Division for publication in the JOURNAL OF FLUIDS ENGINEERING. Manuscript received by the Fluids Engineering Division April 15, 1993; revised manuscript received September 6, 1994. Associate Technical Editor: R. L. Panton.

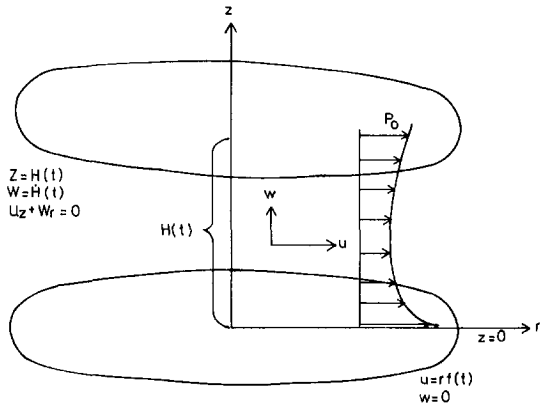

Fig. 1 Liquid film on a stretching surface

We select a subgroup of (2) that leaves invariant the boundary curves and the boundary conditions (3)–(6). Invariance of the boundary curve $z = 0$ implies that $h(t) = 0$ and the invariance of the boundary $z = H(t)$ implies that

$$\bar{z} = H(\bar{t})$$

which yields

$$H(t) = (C_1/C)(2Ct + D)^{1/2} \tag{7}$$

Invariance of the boundary condition (3) suggests that

$$\bar{u} = \bar{r}g(\bar{t}) \text{ on } z = 0 \tag{8}$$

which requires that (Bluman and Cole, 1974)

$$\frac{1}{(r + \sigma\zeta)}[\Psi_z + \sigma\{\Lambda_z + \Psi_z(\Lambda_\Psi - \beta_z) - \zeta_z\Psi_r - \gamma_z\Psi_t - \zeta_\Psi\Psi_r\Psi_z - \beta_\Psi\Psi_z^2 - \gamma_\Psi\Psi_z\Psi_t\}] = (r + \sigma\zeta)[g(t) + \sigma\gamma\dot{g}(t)] \quad \text{on} \quad z = 0 \tag{9}$$

which yields

$$-2Cg(t) = (2Ct + D)\dot{g}(t)$$

so that

$$g(t) = C_2/(2Ct + D) \tag{10}$$

Also, the invariance of the boundary condition (5) yields the same expression for $H(t)$ as given in (7). The invariance of the boundary conditions (4) and (6) are automatically satisfied. Thus, if the liquid film thickness is given by $H(t) = (C_1/C)(2Ct + D)^{1/2}$ and if the stretching velocity of the surface $z = 0$ is given by $rg(t) = C_2r(2Ct + D)^{-1}$, then the flow of liquid film caused by the stretching surface admits a similarity solution described by the following σ parameter Lie group of transformations

$$\begin{aligned} \zeta &= Cr \\ \beta &= Cz \\ \gamma &= 2Ct + D \\ \Lambda &= C\Psi + k(t) \end{aligned} \tag{11}$$

The case when $k(t) = 0$ admits the following similarity solution

$$\frac{dr}{Cr} = \frac{dz}{Cz} = \frac{dt}{2Ct + D} = \frac{d\Psi}{C\Psi} \tag{12}$$

The first two equalities yield the similarity variables

$$\epsilon = r/(2Ct + D)^{1/2}, \quad \eta = z/(2Ct + D)^{1/2} \tag{13}$$

from which the stream function $\Psi(r, z)$ is obtained as

$$\Psi(r, z) = rF(\epsilon, \eta) \tag{14}$$

To construct a similarity solution, we take $C_1 = C = -\nu\alpha/2b$, $C_2 = \nu$, $D = \nu/b$ so that

$$H(t) = \frac{\sqrt{\nu}}{\sqrt{b}}\sqrt{1 - \alpha t}, \quad g(t) = b/(1 - \alpha t) \tag{15}$$

where b and α are constants with dimensions [time^{-1}] and ν is the kinematic viscosity. The similarity variables are

$$\epsilon = \frac{\sqrt{b}}{\sqrt{\nu}}\frac{r}{\sqrt{1 - \alpha t}}, \quad \eta = \frac{\sqrt{b}}{\sqrt{\nu}}\frac{z}{\sqrt{1 - \alpha t}} \tag{16}$$

A similarity solution can be constructed when $F(\epsilon, \eta) = \nu\epsilon f(\eta)$ so that the stream function and the velocity components are given by

$$\begin{aligned} \Psi(r, z) &= \frac{\sqrt{\nu b}\, r^2}{\sqrt{1 - \alpha t}} f(\eta) \\ u &= \frac{br}{(1 - \alpha t)} f'(\eta) \\ w &= \frac{-2\sqrt{\nu b}}{\sqrt{1 - \alpha t}} f(\eta) \end{aligned} \tag{17}$$

where a prime denotes the derivative with respect to η. It must be mentioned that the equation of continuity yields the expressions for C and D interms of α and b. The stretching is accelerated if α is positive and decelerated if α is negative ($t < 1/\alpha$). The r-momentum equation of the unsteady Navier-Stokes equation reduces to

$$S[f' + \eta f''/2] + f'^2 - 2ff'' - f''' = 0 \tag{18}$$

where $S = \alpha/b$ is a nondimensional parameter signifying the relative importance of unsteadiness to the stretching rate and it has been assumed that $\partial p/\partial r = 0$. The z-momentum equation gives the pressure $p(z, t)$ as

$$p(z, t) = \frac{\rho\nu b}{1 - \alpha t}[S\eta f - 2f^2 - 2f'] + Q(t) \tag{19}$$

The boundary conditions on the stretching boundary are

$$f'(0) = 1 \tag{20}$$

$$f(0) = 0 \tag{21}$$

On the free surface $z = H(t)$ or $\eta = \delta$, where δ defines the unknown thickness of the liquid film, we require that $w = \dot{H}(t)$ which gives

$$f(\delta) = S\delta/4 \tag{22}$$

The tangential stress on the free surface is zero which yields

$$f''(\delta) = 0 \tag{23}$$

The ambient pressure p_0 balances the normal stress and Eq. (19) gives

$$Q(t) = p_0 - \frac{\rho\nu b}{(1 - \alpha t)}\left[\frac{S^2\delta^2}{8} - 2f'(\delta)\right] \tag{24}$$

The shear stress on the stretching sheet is given by

$$\tau = \mu\left.\frac{\partial u}{\partial z}\right|_{(z=0)} = \frac{\rho b\sqrt{b\nu}}{(1 - \alpha t)^{3/2}} rf''(0) \tag{25}$$

Thus, the problem of investigating the behavior of a liquid film on a stretching surface reduces to solving the differential Eq. (18) subject to the conditions (20)–(23) with the thickness δ as an unknown.

Asymptotic Solution for Thin Film The tangential velocity u closely follows that of the stretching surface when the

film is thin so that $f(\eta) \simeq \eta$. Let $\eta = \delta\xi$, since η is small. Here $\xi = 0(1)$ and the free surface is at $\xi = 1$. We take

$$f(\eta) = \delta\xi + \delta^3 F_1(\xi) + \delta^5 F_2(\xi) + 0(\delta^7) \quad (26)$$

and

$$S = S_0 + \delta^2 S_1 + \delta^4 S_2 + 0(\delta^6) \quad (27)$$

Equation (22) gives

$$S_0 = 4, \quad F_1(1) = S_1/4, \quad F_2(1) = S_2/4 \quad (28)$$

Substituting (26) and (27) in (18), (20)–(23), we obtain the successive equations

$$F_1''' = 5, \quad F_1(0) = 0, \quad F_1'(0) = 0, \quad F_1''(1) = 0 \quad (29)$$

$$F_2''' = S_1 + 6F_1', \quad F_2(0) = 0, \quad F_2'(0) = 0, \quad F_2''(1) = 0 \quad (30)$$

The solutions are

$$F_1 = (5/6)(\xi^3 - 3\xi^2) \quad (31)$$

$$F_2 = (9\xi^5 - 45\xi^4 - 40\xi^3 + 300\xi^2)/36 \quad (32)$$

Thus

$$S = 4 - \frac{20}{3}\delta^2 + \frac{224}{9}\delta^4 + 0(\delta^6) \quad (33)$$

Inversion gives

$$\delta = \frac{\sqrt{3}}{\sqrt{5}}(1 - S/4)^{1/2}[1 + (28/25)(1 - S/4) + 0(1 - S/4)^2] \quad (34)$$

The third initial condition yields

$$f''(0) = \delta F_1''(0) + \delta^3 F_2''(0) + \ldots = -5\delta + \frac{50}{3}\delta^3 + 0(\delta^5) \quad (35)$$

where δ is given by (34). When δ approaches infinity and $f(\eta)$ is bounded, Eq. (22) shows that S approaches zero. In that limit, the solution approaches Wang's (1984) steady solution for the axisymmetric flow due to a stretching flat surface. Unfortunately, a closed form solution does not exist and hence, a perturbation solution cannot be found for the case of a thick film.

Numerical Integration

If δ is not small, then numerical integration of Eqs. (18), (20)–(23) is necessary. Integration of the Eq. (18) from $\eta = 0$ to $\eta = \delta$ gives

$$S\left[\frac{f}{2} + \frac{\eta f'}{2}\right]\Bigg|_0^\delta + 3\int_0^\delta f'^2\, d\eta - 2ff'\Big|_0^\delta = f''\Big|_0^\delta \quad (36)$$

Using the boundary conditions, Eq. (35) simplifies to

$$f''(0) = -3\int_0^\delta f'^2\, d\eta - \frac{S^2\delta}{8} \quad (37)$$

which shows that the initial value $f''(0)$ is negative. For a given S, we guess $f''(0)$ and integrate Eqs. (18), (20)–(23) as an initial value problem by Runge-Kutta Gill method. The integration continues until f' becomes zero and we check whether Eq. (22) is satisfied there. If not, the value of $f''(0)$ is adjusted.

Figure 2 shows the computed thickness δ as a function of unsteady parameter S. The approximate solution given in (34) agrees well with numerical integration in the valid range. The solutions exist for $0 \le S \le 4$ for positive value of S. We observe that the faster the stretching rate S, the smaller the thickness δ.

In Fig. 2, the initial value $f''(0)$ is shown as a function of S. It is observed that $f''(0)$ is -1.329 when $S = 0$. The shear stress on the stretching surface $z = 0$ can be obtained with the computed value of $f''(0)$ using Eq. (25). The value of $|f''(0)|$ attains a maximum of 1.54 near $S = 1.8$.

Figure 3 shows the velocity profiles for values of $S = 2.2$, 3.2, and 3.7.

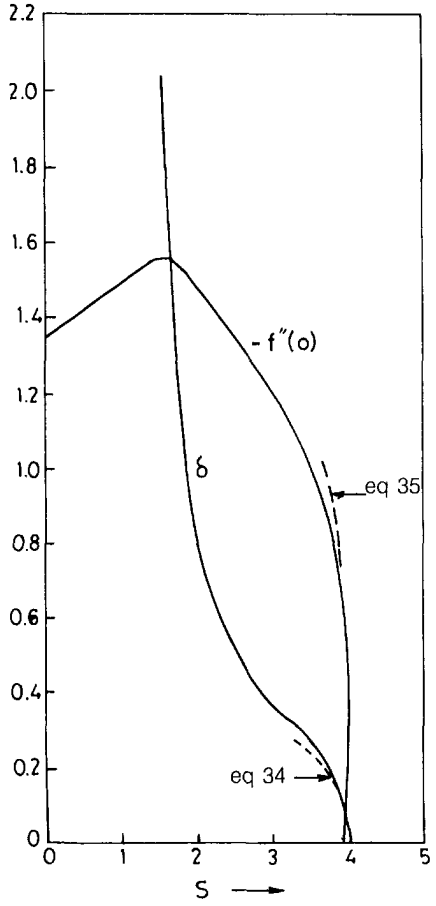

Fig. 2 Thickness δ and the initial value $-f''(0)$ as a function of S-dashed lines are approximations

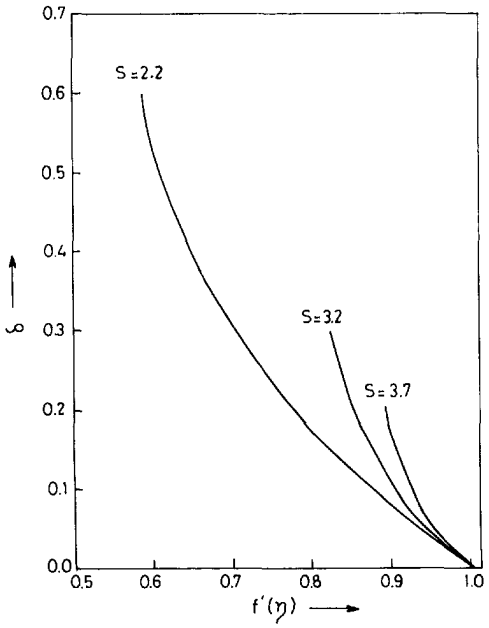

Fig. 3 Lateral velocities

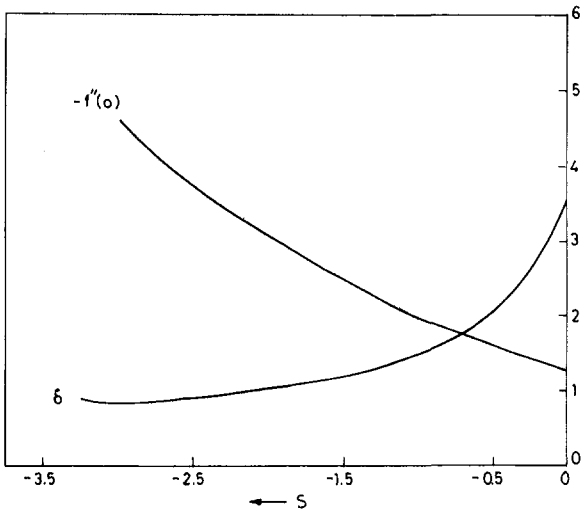

Fig. 4 Decelerated stretching surface, $S < 0$

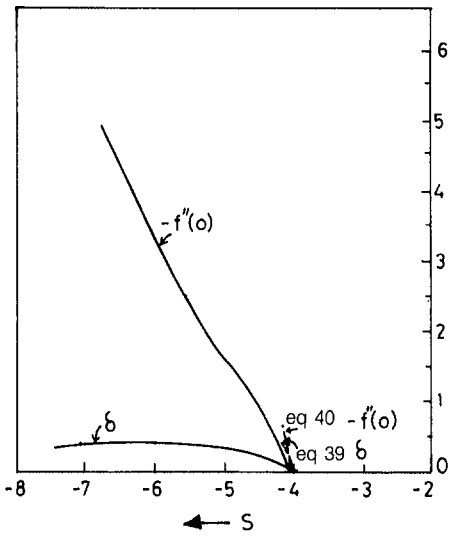

Fig. 6 Decelerated contracting surface $S < 0$ initial value $-f''(0)$ and thickness δ as a function of S

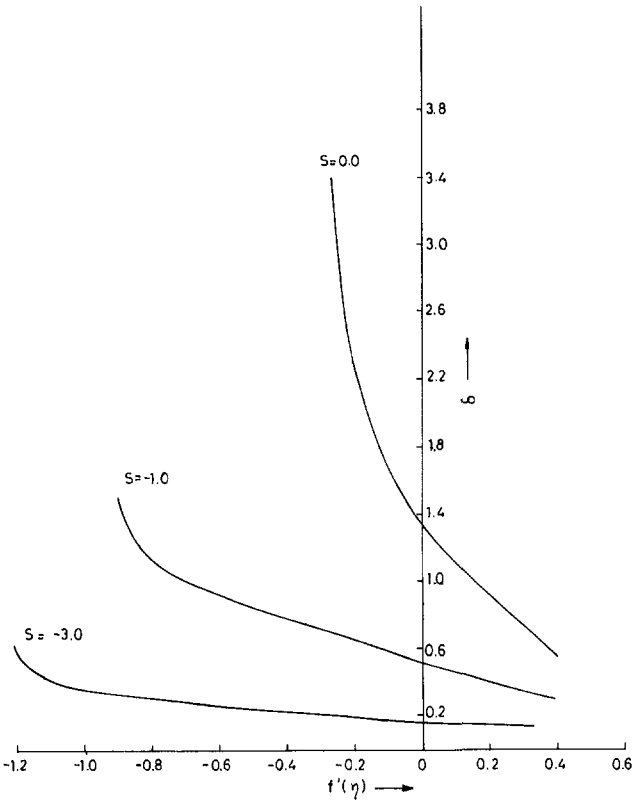

Fig. 5 Lateral velocities for decelerated stretching

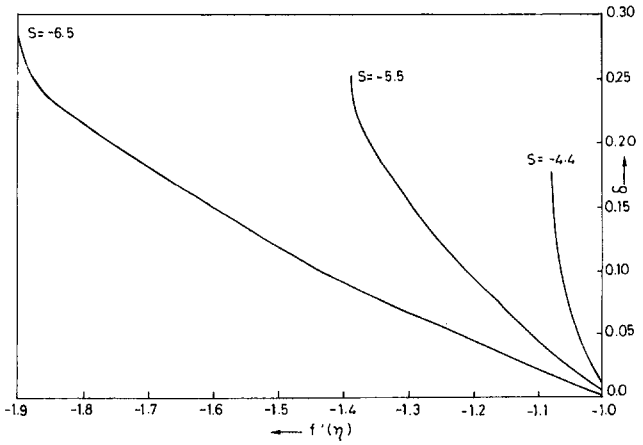

Fig. 7 Lateral velocities for decelerated contracting surface

The Stretching Decelerating Surface. This case corresponds to both α and S assuming negative values. Equation shows that $f(\delta)$ must be negative. It follows from Eqs. (20) and (21) that f' is zero somewhere inside the film and thus there are both negative and positive velocities. The numerical results are plotted in Fig. 4. Of interest is the steady solution $S = 0$, $f''(0) = -1.298$, $\delta = 3.55$. Figure 5 shows some of the velocity profiles for $S = 0.0, -1.0, -3.0$.

The Contracting Decelerating Surface. The velocity u is negative for a contracting surface which leads to $f'(0) = -1$ and for this case Eq. (18) has to be integrated subject to the conditions $f'(0) = -1$ and (21)–(23). A similar asymptotic perturbation for thin film yields

$$S = -4 - \frac{20}{3}\delta^2 - \frac{224}{9}\delta^4 + 0(\delta^6) \tag{38}$$

which shows that $S < -4$.

Therefore,

$$\delta = \frac{\sqrt{3}}{\sqrt{5}}\left(-1 - \frac{S}{4}\right)^{1/2}\left[1 + \frac{28}{25}\left(1 + \frac{S}{4}\right) + 0\left(1 + \frac{S}{4}\right)^2\right] \tag{39}$$

The initial value is

$$f''(0) = -5\delta - \frac{50}{3}\delta^3 + 0(\delta)^5 \tag{40}$$

The results of the numerical integration are presented in Fig. 6 and Fig. 7. The thickness δ attains a maximum value of 0.358 when $S = -6.5$. The lateral velocity profiles are presented for values of $S = -4.4$, -5.5 and -6.5 in Fig. 7.

Conclusions

A rare exact similarity solution of the unsteady axisymmetric Navier-Stokes equations governing the motion of the liquid

film on a moving surface with prescribed velocity has been obtained and the importance of such a solution is that it has been possible to give interpretation of the fluid motion on a stretching accelerating or decelerating surface and thereby more physical insight to the nature and character of the solution has been obtained. A steady solution with finite thickness and reverse flow (Fig. 5, $S = 0.0$) has been found in the steady case $S = 0.0$. Also, no solutions are found for $S > 4.0$ which only means that no similarity solutions exist and does not pertain to non similar solution. The present solution scores over the numerical results in the sense that it is an exact solution of the unsteady Navier-Stokes equations governing the problem and that it could be used in validating the computer or analytical models of more realistic engineering systems.

Acknowledgment

The authors are grateful to the referees for their valuable suggestions and useful and encouraging comments.

References

Bluman, G. W., and Cole, J. D., 1974, *Similarity Methods for Differential Equations*, Springer-Verlag, New York.

Brady, J. F., and Acrivos, A., 1981, "Steady Flow in a Channel or Tube with an Accelerating Surface Velocity. An Exact Solution to the Navier-Stokes Equations with Reverse Flow," *Journal of Fluid Mechanics*, Vol. 112, pp. 127–150.

Crane, L. J., 1970, "Flow Past a Stretching Plane," *Zeitschrift fuer Angewandte Mathematik und Physik*, Vol. 21, pp. 645–652.

Usha, R., and Uma, M., 1991, "Similarity Transformations for the Unsteady, Axisymmetric, Squeeze Flow Problems," *Indian Journal of Technology*, Vol. 29, pp. 493–497.

Wang, C. Y., 1984, "The Three-Dimensional Flow Due to a Stretching Flat Surface," *Physics of Fluids*, Vol. 27, pp. 1915–1917.

Wang, C. Y., 1988, "Fluid Flow due to a Stretching Cylinder," *Physics of Fluids*, Vol. 31, pp. 466–468.

Wang, C. Y., 1990, "Liquid Film on an Unsteady Stretching Surface," *Quarterly of Applied Mathematics*, Vol. XLVIII, pp. 601–610.

Numerical Analysis of a Vortex Controlled Diffuser

R. E. Spall
Department of Mechanical Engineering,
University of South Alabama,
Mobile, AL 36688

A numerical study of a prototypical vortex controlled diffuser is performed. The basic diffuser geometry consists of a step expansion in a pipe of area ratio 2.25:1. The incompressible Reynolds averaged Navier-Stokes equations, employing the RNG based $K-\epsilon$ turbulence model, are solved. Results are presented for bleed rates ranging from 1 to 7 percent. Diffuser efficiencies in excess of 80 percent were obtained. These results are in good qualitative agreement with previous experimental work. The results do not confirm previous suggestions that the increases in effectiveness of the VCD over a step expansion result from an inhibition of flow separation due to the generation and downstream convection of extremely high levels of turbulence generated in the region of the bleed gap. The results do indicate that the effectiveness of the diffuser is a consequence of the turning of the flow toward the outer wall due to the influence of the low pressure vortex chamber. Calculations employing the RNG based turbulence model were able to capture the abrupt increase in diffuser effectiveness that has been shown experimentally to occur at low bleed rates. Calculations employing the standard $K-\epsilon$ model were unable to predict this occurrence.

Introduction

The central idea behind the vortex controlled diffuser (VCD) is that highly efficient diffusion may be achieved by bleeding off fluid through a small gap located at a region of rapid expansion. This concept appears to have been first introduced by Heskestad (1965). In that work, edge suction was applied through a slot situated at the edge of a convex corner. It was found that the flow turned the corner in a manner that significantly decreased the extent of the recirculation region. Heskestad (1968) later experimented with edge suction at the step expansion of a circular pipe, evaluating the effectiveness of the configuration as a short diffuser. That study employed a uniform inlet profile with a thin boundary layer. Heskestad (1970) also considered the effectiveness of edge suction in producing a short diffuser when the inlet profiles were fully developed. High static pressure recoveries were produced in both cases.

The desirability of a short diffuser between the compressor and combustor in gas turbine applications provided the incentive for further development of the VCD concept. Adkins (1975) obtained data for a series of research diffusers with area ratios ranging from 1.9:1 to 3.2:1. He found that for moderate bleed rates, efficiencies in excess of 80 percent could be achieved with diffuser lengths 1/3 that required with conventional conical diffusers. A hybrid diffuser (a combination VCD and conventional diffuser) was later studied by Adkins et al. (1981). Results showed that bleed rates were reduced from those required for the previously studied step VCD configurations. Most recently, Sullerey et al. (1992) have investigated the effect of inlet flow distortion on a VCD. Results revealed that as inlet distortions were increased, so too were the levels of bleed required to maintain diffuser efficiency.

It appears that the only previous numerical work concerning the VCD was performed by Busnaina and Lilley (1982). In that work, the incompressible Navier-Stokes equations were solved for the flow in a two-dimensional VCD geometry. Although the effects of turbulence were not modeled, and the grid employed was quite coarse, the general trends followed those observed experimentally.

The mechanism by which the VCD operates is still unclear. One explanation is that a region of high shear is produced at the bleed gap, resulting in a layer of intense turbulence that is convected downstream, inhibiting flow separation along the outer wall (Adkins, 1975). Others have suggested that the primary result of suction is to simply deflect or turn the mean flow around the sharp corner, thus diminishing the length of the recirculation zone (c.f. Heskestad, 1970).

In the present work the performance of a prototypical VCD is investigated numerically. The incompressible, axisymmetric Reynolds averaged Navier-Stokes equations are solved for the flow through a pipe containing a step expansion of area ratio 2.25:1. The vortex chamber and bleed gap height-to-length ratio are representative of those employed in previous experimental works. The effect of turbulence was modeled using the renormalization group (RNG) based $K-\epsilon$ model (Yakhot et al., 1992). (For a complete discussion of turbulence models applied to internal flows see Nallasamy (1987)). Calculations were performed to bleed rates ranging from 1 to 7 percent. For comparative purposes, results for a step expansion without bleed are also presented. Details of the flow structure are presented and studied using contour plots of velocity, pressure and turbulence kinetic energy. One goal of this work is to shed

Contributed by the Fluids Engineering Division for publication in the JOURNAL OF FLUIDS ENGINEERING. Manuscript received by the Fluids Engineering Division August 3, 1993; revised manuscript received June 2, 1994. Associate Technical Editor: O. Baysal.

additional light onto the physical mechanisms responsible for efficiencies achieved by the VCD. An additional purpose of this work is to document the improved performance of the RNG based $K-\epsilon$ model over the standard $K-\epsilon$ model in predicting complex recirculating flows of this type.

Numerical Approach

The incompressible Reynolds-averaged Navier-Stokes equations are appropriate to describe the motion within a prototypical axisymmetric VCD configuration. Although the governing equations are solved in cylindrical polar coordinate form, for purposes of brevity they are presented below in cartesian tensor form. The continuity and momentum equations are given as:

$$\frac{\partial u_i}{\partial x_i}=0 \tag{1}$$

$$\frac{\partial u_i}{\partial t}+u_j\frac{\partial u_i}{\partial x_j}=-\frac{1}{\rho}\frac{\partial p}{\partial x_i}+\frac{\mu}{\rho}\nabla^2 u_i-\frac{\partial \tau_{ij}}{\partial x_j} \tag{2}$$

respectively, where u_i is the mean velocity, ρ is the density, μ is the viscosity, p is the mean pressure and $\tau_{ij}=\overline{u_i'u_j'}$ are the Reynolds stresses.

When the standard or RNG based $K-\epsilon$ models are employed, the Boussinesq hypothesis provides an expression for the Reynolds stresses in terms of the gradients of the mean flow as:

$$-\tau_{ij}=-\frac{2}{3}\delta_{ij}K+2\nu_t S_{ij} \tag{3}$$

where ν_t is the turbulent viscosity, K is the turbulent kinetic energy and S_{ij} is the strain rate.

The RNG based models have been shown to produce results superior to the standard $K-\epsilon$ model for separated flows and flows with high streamline curvature and strain rate (Yakhot et al., 1992). The RNG model is similar in form to the standard $K-\epsilon$ model except for the addition of a rapid strain term in the dissipation equation. The transport equations for K and ϵ, respectively, are given as:

$$\frac{DK}{Dt}=\frac{\partial}{\partial x_i}\left(\frac{\nu_t}{\sigma_k}\frac{\partial K}{\partial x_i}\right)+2\nu_t S_{ij}^2-\epsilon \tag{4}$$

$$\frac{D\epsilon}{Dt}=\frac{\partial}{\partial x_j}\left(\frac{\nu_t}{\sigma_\epsilon}\frac{\partial \epsilon}{\partial x_j}\right)+2\nu_t C_{\epsilon 1}\frac{\epsilon}{K}S_{ij}^2-C_{\epsilon 2}\frac{\epsilon^2}{K}-\overline{R} \tag{5}$$

where

$$\overline{R}=\frac{C_\mu\eta^3(1-\eta/\eta_0)}{1+\beta\eta^3}\frac{\epsilon^2}{K} \tag{6}$$

In addition, $\nu_t=C_\mu K^2/\epsilon$, $\eta=SK/\epsilon$ and $S=(2S_{ij}S_{ij})^{1/2}$. For the standard $K-\epsilon$ model, $\overline{R}=0$. An additional feature of the RNG model is that no empirical constants appear in the equations. Theoretical analysis yields $_\mu=0.084$, $C_{\epsilon_1}=1.42$, $C_{\epsilon 2}=1.68$, $\sigma_k=\sigma_\epsilon=0.72$, $\beta=0.012$ and $\eta_0=4.38$ (c.f. Yakhot et al., 1992).

The governing equations were solved using the commerical code FLUENT (Fluent Inc., Hanover, HN). FLUENT employs a pressure-based control volume technique. Third-order QUICK interpolation is used to provide values of the variables on cell faces (Leonard, 1979). Pressure-velocity coupling is implemented using the SIMPLE algorithm (Patankar, 1980). Convergence of the solution was assumed when the sum of the normalized residuals for each conservation equations was decreased to 10^{-3}. Residuals were further decreased to 5.0×10^{-4}, and no significant changes in the solutions resulted. (The residual for a given equations consists of the summation of the unbalance in the equation for each cell in the domain.) Since the above solution techniques are well known and widely discussed in the literature, they will not be elaborated upon here.

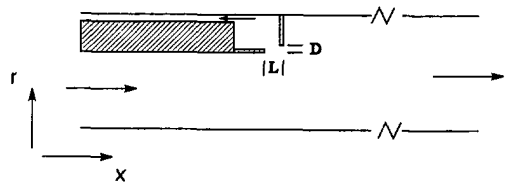

Fig. 1 Vortex controlled diffuser geometry

Geometry and Boundary Conditions

A prototypical axisymmetric VCD of expansion area ratio 2.25:1 is considered (see Fig. 1). The diffuser geometry is typical of that employed in dump combustors. The essence of the diffuser is the suction slot at the expansion corner. Small quantities of fluid (typically 5 percent of the mass flow) are bled off through the suction slot into a vortex chamber. Fluid exits the chamber through a channel (as shown in Fig. 1). In the present study, the axial extent of the slot (L) is taken as 0.1 units, and the radial depth (D), 0.05 units providing a fence subtend angle (atan (D/L)) of 26.6 deg. Thus, the slot length-to-depth ratio is 2.0, typical of those employed in experimental works appearing in the literature. The radius of the diffuser upstream of the step is 1 unit; downstream, 1.5 units. The total length of the VCD configuration is 25 units, with the gap beginning 2.4 units downstream from the inflow plane. A length of 25 was chosen so that outflow boundary conditions could be specified with reasonable accuracy. Two different grid densities were employed—one consisting of 85 cells in the axial direction and 45 cells in the radial direction, and another with double the number of cells in each coordinate direction. As will be shown in the Results section, the 85×45 grid is deemed sufficient. For each grid, cells were clustered toward the vortex fence (the aft wall of the vortex chamber) and the lateral diffuser walls.

For all cases, a uniform inflow axial velocity profile was specified. Previous experimental studies (Heskestad, 1968, 1970) reveal that thin inlet boundary layers result in higher pressure recoveries than fully developed turbulent profiles, and thus it is expected that pressure recoveries in the present study would be somewhat decreased if fully developed turbulent inlet profiles were used. The Reynolds number, based on inflow pipe diameter and velocity is 200,000. This is representative of Reynolds numbers employed in most experimental investigations, which range from 100,000 to 840,000 (c.f. Adkins, 1975 and Adkins et al., 1981). The inlet turbulence intensity was set to 10 percent (a reasonable value for dump combustor geometries). Given the turbulence intensity, the turbulence kinetic energy and dissipation rates are calculated from:

$$K=3/2\ (u')^2 \tag{7}$$

$$\epsilon=C_\mu^{3/4}\frac{K^{3/2}}{l} \tag{8}$$

where l is a turbulence length scale given as $0.07R$, (R is the inlet pipe radius). At the outlet, fully developed flow conditions are assumed; that is, streamwise gradients of the flow properties are set to zero.

Results

Results have been obtained for the VCD with bleed rates ranging from 1 to 7 percent, and for a step expansion (without the vortex chamber). However, before delving into a description of the flow-field, it is first desirable to provide some means of quantifying improvements in diffuser effectiveness as a function of bleed rate. Toward this end, a one dimensional correction may be applied to the usual definition of diffuser effectiveness, which results in the expression (Adkins, 1975):

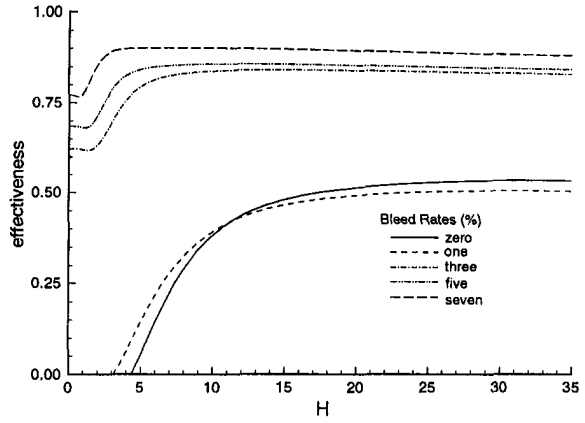

Fig. 2 Diffuser effectiveness as a function of the downstream distance from the vortex fence

$$\eta = \frac{p_2 - p_1}{1/2\ \rho \bar{v}_1^2 \left(\alpha_1 - \left(\frac{1-B}{AR}\right)^2\right)} \tag{9}$$

where B is the bleed rate, AR is the area ratio and α is a kinetic energy coefficient. For the case of uniform inflow profiles, α equals unity. (For fully developed turbulent flows in circular pipes, $\alpha \cong 1.05$.) In Fig. 2, diffuser effectiveness as determined by the numerical calculations is plotted as a function of distance downstream from the step expansion. The pressure p_1 in Eq. (9) is taken as the value at the wall downstream from the inflow boundary, and p_2 is taken along the wall downstream of the expansion. In the case of the step expansion, the maximum effectiveness reaches approximately 50 percent, and is not achieved until 20 step heights (H) downstream from the expansion. Maximum effectiveness increases to 83, 86, and 90 percent, for VCD bleed rates of 3, 5, and 7 percent, respectively. In addition, the distance required for maximum diffusion to take place decreases from approximately 20 H for the step expansion to 3 H for 7 percent bleed. For the 3, 5, and 7 percent bleed rates, losses to friction cause the effectiveness of the diffuser to diminish slowly beyond about 10 H. These results are in good qualitative agreement with experimental results for both tubular and annular VCD's presented by Adkins (1975). There, it was revealed that maximum pressure recoveries in excess of 80 percent could be obtained with bleed rates of 3 percent. In addition, recovery lengths were reduced by a factor of two compared to conventional conical diffusers.

Adkins (1975) indicates that at low bleed rates, diffuser effectiveness increases slowly with increases in bleed rate. Then, at some critical rate, diffuser effectiveness increases rapidly with slight additional increases in bleed. Thereafter, increases in effectiveness with increases in bleed rate become minimal. Adkins suggests that this critical bleed rate corresponds to the point at which fluid enters the slot from the freestream only, as opposed to entering over the vortex fence. The calculations performed using the RNG based $K-\epsilon$ model have captured these features. That is, an abrupt increase in diffuser effectiveness was realized as the bleed rate increased from 1 to 3 percent. In addition, at 1 percent bleed rate, the numerical results show that the fluid enters the vortex chamber from the lee of the fence; however at rates of 3 percent and greater fluid enters only from the freestream. This will be further discussed when contours of axial velocity and turbulence kinetic energy are presented. It is noted that when the standard $K-\epsilon$ model was employed, a considerable increase in effectiveness at 1 percent bleed was found, and no sudden jump between 1 percent bleed and 3 percent bleed occurred. However, at higher bleed rates the standard $K-\epsilon$ and RNG results were quite similar. (For purposes of brevity, the standard $K-\epsilon$ based results are not shown). Thus, at low bleed rates, the RNG based model appears to better model the physics of the flow than the standard $K-\epsilon$ model. This improvement was achieved at the expense of an approximate 20 percent increase in cpu time. It is also noted that for the 5 percent bleed case, results were also computed using an inlet turbulence intensity of 2.5 percent. In terms of diffuser effectiveness, the results were within 1 percent of those presented above.

One benefit of numerical solutions is that detailed flow patterns are obtained which may be valuable in determining the physical mechanisms responsible for the high efficiency of the VCD. In the remainder of this section contour plots for the 1 and 5 percent bleed rates are examined with an emphasis on revealing information concerning the physical processes involved.

Contours of constant axial velocity for the VCD with 5 percent bleed for both the fine (170×90) and coarse (85×45) grids are shown in Figs. 3(a,b) respectively (dimensionless with respect to the inflow velocity). For the purposes of the present study, the two solutions are deemed sufficiently close, and thus the 85×45 grid was considered sufficient for the step expansion and the VCD 1, 3, and 7 percent bleed rate calculations. Thus, the contour plots for the 5 percent bleed VCD are from calculations computed using the 170×90 grid; results for all other figures were computed on the 85×45 grid.

The effect of bleed in reducing the extent of the recirculation region is clearly revealed in Fig. 3(a) decreasing from approximately 8.5H for the step expansion (not shown) to approximately 2.5H for the 5 percent bleed case. (Note that the results for the step expansion, both experimentally (8.5H-9H) and numerically with several different turbulence models, are well known, c.f. Nallasamy (1987).) A stable vortical structure within the vortex chamber is also indicated. However, most important is the rapid directional change and acceleration of the fluid toward the bleed slot. Of course for the step expansion, a clean separation from the corner without rapid directional change is obtained. In Figs. 3(c,d) contours of constant axial velocity in the immediate region of the bleed gap are shown for 5 and 1 percent bleed rates, respectively. From Fig. 3(c) it is quite clear that for 5 percent bleed, fluid enters the slot only from the freestream (no negative contours in the slot region). However, for the 1 percent bleed case, negative contour values in the region of the slot indicate that fluid enters from the lee side of the fence. Fluid entering from the lee side has the effect of decreasing the effective fence subtend angle and hence significantly increases the length of the recirculation zone. In agreement with Adkins (1975) observations, this result suggests that in order to achieve high VCD effectiveness, the fluid should not enter the vortex chamber from the lee side. Perhaps then, a short fence perpendicular to the lee fence could accomplish this task and minimized the bleed requirements.

Figure 3(c) also reveals an acceleration of the fluid in the near wall region just upstream of the expansion due to the presence of the low pressure vortex chamber. This is followed by a region in which a rapid decrease in the axial velocity of the fluid occurs as it passes over the gap and, due to the expansion, encounters a strong adverse pressure gradient. The net result is the creation of regions of high localized normal and shear stresses (above that which would be present in the absence of the bleed slot). For the 1 percent bleed case, the region of strong normal stresses is absent.

Contours of constant pressure (normalized with respect to the dynamic pressure at the inlet boundary) area shown in Fig. 4 for the 5 percent bleed rate configuration. The pressure variations presented are with respect to a reference pressure located adjacent to the duct inlet. The figure reveals that away from the wall, a significant adverse pressure gradient has begun to form upstream of the suction slot. This is due, of course, to continuity requirements. A local minimum in the pressure

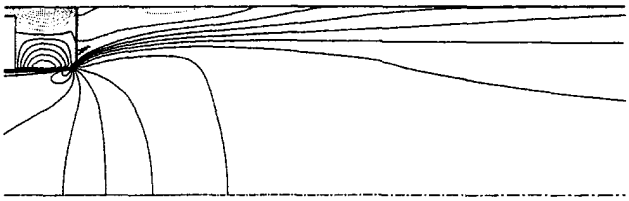

Fig. 3(*a*) VCD with 5 percent bleed, 170 × 90 grid (contours from −0.8 to 1.2 in intervals of 0.1)

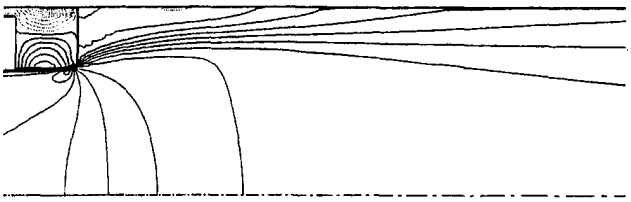

Fig. 3(*b*) VCD with 5 percent bleed, 85 × 45 grid (contours from −0.8 to 1.2 in intervals of 0.1)

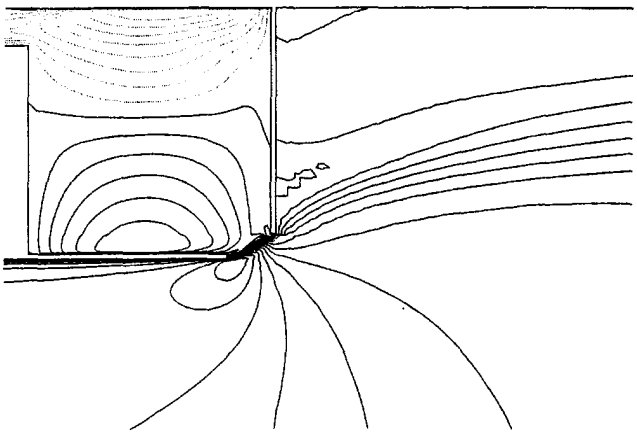

Fig. 3(*c*) VCD with 5 percent bleed, in the region of the vortex chamber (contours from −0.8 to 1.2 in intervals of 0.1)

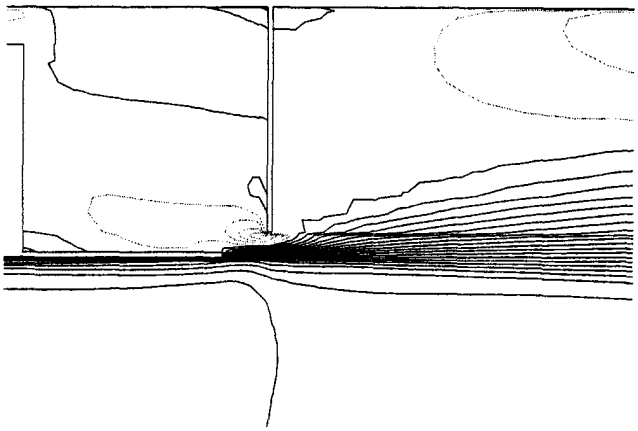

Fig. 3(*d*) VCD with 1 percen bleed, in the region of the vortex chamber (contours from −0.8 to 1.0 in intervals of 0.1)

Fig. 3 Contours of constant axial velocity (negative values in grey)

also occurs at the slot entrance, and thus serves to deflect the oncoming fluid around the slot toward the outer wall. The figure also illustrates the rapid completion of the diffusion process, essentially complete at a distance of only a few step heights downstream of the fence.

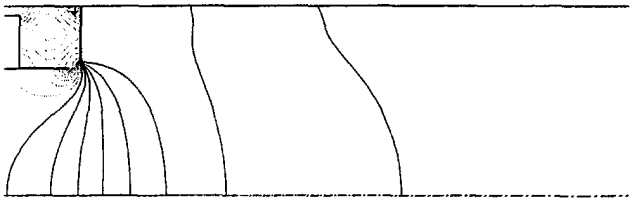

Fig. 4 Contours of constant pressure for the VCD with 5 percent bleed (contours from −1.9 to 0.8 in intervals of 0.1, negative values in grey)

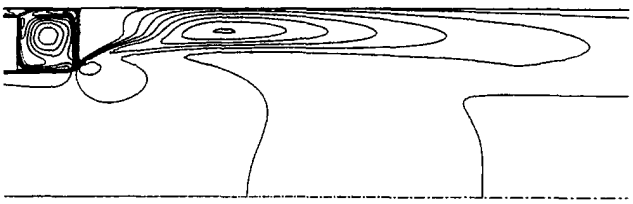

Fig. 5 Contours of turbulence kinetic energy for the VCD with 5 percent bleed (contours from 0.0025 to 0.045 in intervals of 0.0025)

Contours of turbulence kinetic energy are shown in Fig. 5 for the 5 percent bleed rate. As previously mentioned, the region near the slot is one of high shear, and is thus responsible for the generation of considerable turbulence kinetic energy. However, these increased levels are quite localized, and rather than being convected downstream, much of this turbulence kinetic energy is convected into the vortex chamber. An additional local maximum appears further downstream, near the central to aft portion of the recirculation region. The maximum levels at this point are below those at the bleed slot. However, the general distribution of turbulence kinetic energy downstream of the fence is quite similar to that of the step expansion (not shown). Hence, it appears that the increased levels of turbulence generated at the slot are not critical toward achieving the high efficiencies of the VCD.

Conclusions

The numerical results shed light on the mechanism by which VCD operates. The results do not appear to support the hypothesis proposed by Adkins (1975)—that the increased turbulence generated at the suction slot inhibits flow separation along the wall downstream of the fence. That high levels of turbulence are formed near the suction slot is borne out in the present study. However, much of this energy is convected into the vortex chamber, and thus levels of turbulence downstream are similar to those for the step expansion. The numerical results do support the proposal put forth by Heskestad (1970)—that the primary contributions of the suction slot and low pressure vortex chamber are to simply deflect the fluid toward the outer wall, effectively decreasing the extent of the recirculation zone. The results are also consistent with the suggestion by Adkins (1975) that for maximum diffuser efficiencies, the fluid should not enter the vortex chamber from the lee side of the fence. Also born out in this study was the superiority of the RNG based $K-\epsilon$ model over the standard $K-\epsilon$ model for predicting complex recirculating flows of this type.

Acknowledgements

The author would like to acknowledge the NASA JOVE program for providing partial support for this work.

References

Adkins, R. C., 1975, "A Short Diffuser With Low Pressure Loss," JOURNAL OF FLUIDS ENGINEERING, Vol. 97, pp. 297–302.

Adkins, R. C., Martharu, D. S., and Yost, J. O., 1981, "The Hybrid Diffuser," ASME *Journal of Engineering Power*, Vol. 103, pp. 229–236.

Busnaina, A. A., and Lilley, D. G., 1982, "A Simple Finite Difference Procedure for the Vortex Controlled Diffuser," AIAA-82-0109, AIAA 20th Aerospace Sciences Meeting, Jan. 11–14, Orlando, FL.

Heskestad, G., 1965, "An Edge Suction Effect," *AIAA Journal*, Vol. 3, pp. 1958–1961.

Heskestad, G., 1968, "A Suction Scheme Applied to Flow Through a Sudden Enlargement," ASME *Journal of Basic Engineering*, Vol. 90, pp. 541–544.

Heskestad, G., 1970, "Further Experiments with Suction at a Sudden Enlargement in a Pipe," ASME *Journal of Basic Engineering*, Vol. XX, pp. 437–449.

Leonard, B. P., 1979, "A Stable and Accurate Convective Modeling Procedure Based on Quadratic Upstream Interpolation," *Methods in Applied Mechanical Engineering*, Vol. 19, pp. 59–98.

Nallasamy, M., 1987, "Turbulence Models and Their Applications to the Prediction of Internal Flows: A Review," Computers & Fluids, Vol. 15, pp. 151–194.

Patankar, S. V., 1980, *Numerical Heat Transfer and Fluid Flow*, Hemisphere Publishing Corp., Washington, D.C.

Sullerey, R. K., Ashok, V., and Shantharam, K. V., 1992, "Effect of Inlet Flow Distortion on Performance of Vortex Controlled Diffusers," ASME JOURNAL OF FLUIDS ENGINEERING, Vol. 114, pp. 191–197.

Yakhot, V., Orzag, S. A., Thangam, S., Gatski, T. B., and Speziale, T. B., 1992, "Development of Turbulence Models for Shear Flows by a Double Expansion Technique," *Physics of Fluids A*, Vol. 4, pp. 1510–1520.

Deguan Wang

E. Benjamin Wylie

Department of Civil and Environmental Engineering,
University of Michigan,
Ann Arbor, MI 48109

Unsteady 2-D Compressible Flow in Unbounded Domain

An unsteady isentropic flow model is presented to calculate the two-dimensional flow field in an arbitrarily closed region or in an open fluid domain. In the open domain, a unique boundary condition is implemented to simulate the infinite character of the open space. The characteristics-like method presented herein is shown to be robust over the entire subsonic flow range and, with the implementation of the infinite boundary, provides numerical results in agreement with analytic solutions and experimental data.

Introduction

An isentropic model has been developed for the simulation of unsteady plane, two-dimensional nonviscous compressible gas flow involving Mach numbers up to about one. During the process of unsteady subsonic compressible flow at high Mach number the variation of pressure and gas density may be large. If the duration of the process is short, enthalpy may be taken as constant (Shapiro, 1954). A detailed comparison of various isentropic models has been given by Sullivan (1981). For the sake of simplicity and accuracy for gaseous flow, the present model assumes the closed-form polytropic process.

The method of characteristics is widely used in unsteady flow computations (Shin and Valentin, 1978). This paper utilizes the characteristics-like method (Henke and Wylie, 1982; Wylie and Streeter, 1993), as it is simple, efficient, and numerically accurate. A staggered grid, which avoids singularities at corners in the physical domain, is used in implementing the numerical process.

When the receiving domain is open a large computational domain, with large core storage and excessive computational time, may be necessary. To avoid this situation an appropriate boundary condition was sought which could make the computational domain appear as it were infinite. A simple but effective boundary treatment, named the "infinite boundary," is proposed and used to represent the response from the region beyond the boundary.

Basic Equations and Numerical Integration

Two-dimensional, unsteady, nonviscous, compressible gas flow is governed by the following set of nonlinear equations:

$$L_0 = u\frac{\partial p}{\partial x} + v\frac{\partial p}{\partial y} + \frac{\partial p}{\partial t} + \rho c^2\frac{\partial u}{\partial x} + \rho c^2\frac{\partial v}{\partial y} = 0 \quad (1)$$

$$L_1 = \frac{\partial p}{\partial x} + \rho u\frac{\partial u}{\partial x} + \rho v\frac{\partial u}{\partial y} + \rho\frac{\partial u}{\partial t} = 0 \quad (2)$$

$$L_2 = \frac{\partial p}{\partial y} + \rho u\frac{\partial v}{\partial x} + \rho v\frac{\partial v}{\partial y} + \rho\frac{\partial v}{\partial t} = 0 \quad (3)$$

Contributed by the Fluids Engineering Division for publication in the JOURNAL OF FLUIDS ENGINEERING. Manuscript received by the Fluids Engineering Division July 1, 1993; revised manuscript received June 3, 1994. Associate Technical Editor: O. Baysal.

In these equations, p, u, and v are pressure and velocity components in the x- and y-directions, respectively; t = time; ρ = the density of the fluid; and c = acoustic velocity. Equation (1) represents the conservation of mass condition including the sound speed definition $dp = c^2 d\rho$. Equations (2) and (3) are the momentum equations in x- and y-directions. An additional equation, which merely states an identity, completes the set of equations for the treatment herein.

$$L_3 = \frac{\partial u}{\partial y} + \frac{\partial v}{\partial x} - \left(\frac{\partial u}{\partial y} + \frac{\partial v}{\partial x}\right) = 0 \quad (4)$$

This identity statement is necessary as a fourth equation to permit the transformation that follows (Henke and Wylie, 1982, Wylie and Streeter, 1993). Without Eq. (4) the transformation of Eqs. (1) to (3) leads to the standard method of characteristics.

A combination of these four equations (Wang and Wylie, 1993), using linear multipliers λ_1, λ_2, and λ_3, is carried out in the following manner: $L_0 + \lambda_1 L_1 + \lambda_2 L_2 + \lambda_3 L_3 = 0$, which leads to a set of ordinary equations. By defining

$$q = \frac{1}{2}\left(\frac{\partial u}{\partial y} + \frac{\partial v}{\partial x}\right) \quad (5)$$

and taking into account the variation of density through the isentropic relation

$$\frac{p}{\rho^\kappa} = C_a \quad (6)$$

in which κ is the specific heat ratio, and C_a is a constant, the sets of equations, ready for numerical integration, are obtained.

$$\frac{dx}{dt} = u + c \qquad \frac{dy}{dt} = v + c \quad (7a)$$

$$C_{a1}p^{-\kappa+1/2\kappa}\frac{dp}{dt} + \frac{du}{dt} + \frac{dv}{dt} - 2qc = 0 \quad (7b)$$

A new constant has been substituted, $C_{a1} = \sqrt{C_a^{1/\kappa}/\kappa}$. Equations (7*a*) define the path of line AP in x-y-t space shown in Fig. 1. Eq. (7*b*) is valid along this path. Three other equation pairs define specific lines in the x-y-t space, and a correspond-

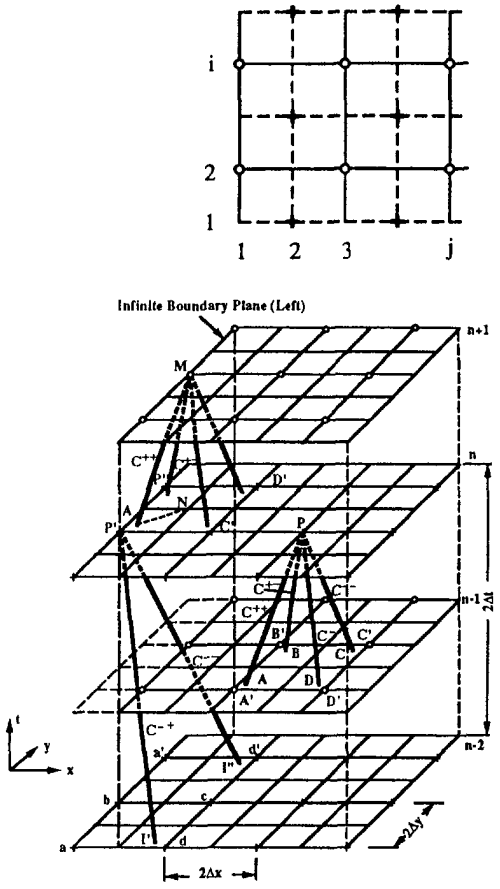

Fig. 1 Path lines in *x-y-t* space, interior point and infinite left boundary

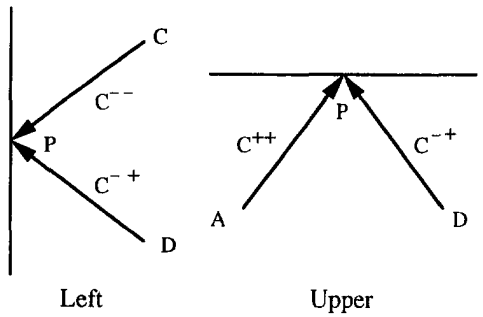

Fig. 2 Boundary points at left and upper edges

ing equation is valid along each line. At point P, four equations are valid, providing the opportunity to solve for the four primary variables p, u, v, and q in the problem, which are assumed to be known initially in the x-y plane, in particular at grid intersection points. The lines of integration along the path lines shown in Fig. 1 are distinct and unique, unlike the characteristics lines in the more traditional two-dimensional method of characteristics. The compatibility conditions, Eq. (7*b*) and its counterparts, must be applied only along these lines to assure stability of the method. There have been no mathematical approximations, beyond those that already exist in Eqs. (1)–(4) and (6), in the transformation.

The stability condition for implementing the method is the same as the method of characteristics, i.e.,

$$\Delta t \le \frac{\Delta x}{|u| + c} \quad \Delta t \le \frac{\Delta y}{|v| + c} \tag{8}$$

In Fig. 1, points A, B, C, and D should remain as close as possible to points A', B', C', and D', respectively, during the computation to reduce numerical damping due to interpolations. The time-step size may be adjusted during the transient to accomplish this, i.e., to satisfy the equality in Eq. (8) for the maximum current values of $|u| + c$ or $|v| + c$. In the limiting case of low Mach number flows with constant wave propagation velocity, the equations may be linearized, which leads to

$$\Delta t = \frac{\Delta x}{c} = \frac{\Delta y}{c} \tag{9}$$

Under these conditions, there is no interpolation and the numerical solution is precise, as long as the parameter q remains small during the transient (Wylie and Streeter, 1993).

With a square computational grid $\Delta x = \Delta y$, and selected time step, Δt, integration of the compatibility equations along the path lines leads to the following set of equations

$$C_{a2}p_P^{\kappa-1/2\kappa} + u_P + v_P - q_P c\Delta t = e_1 \tag{10}$$

$$C_{a2}p_P^{\kappa-1/2\kappa} + u_P - v_P + q_P c\Delta t = e_2 \tag{11}$$

$$C_{a2}p_P^{\kappa-1/2\kappa} - u_P - v_P - q_P c\Delta t = e_3 \tag{12}$$

$$C_{a2}p_P^{\kappa-1/2\kappa} - u_P + v_P + q_P c\Delta t = e_4 \tag{13}$$

in which $C_{a2} = C_{a1}2\kappa/(\kappa - 1)$. The wave speed in the last term is assumed constant during the integration. An average local pressure from the previous time step, points A', B', C', and D', is used in calculating the wave speed c. The terms on the right side, e_1 to e_4, are evaluated based on the known transient conditions at the previous time step. To evaluate e_1 to e_4, conditions at each point of A, B, C, and D are determined by a bi-interpolation method based on the known values at points A', B', C', and D', Fig. 1. With a square mesh, a common time step must be utilized throughout the computational domain, and the time step-distance interval required by the four equation pairs, like Eqs. (7*a*), must be met. However, the size of the time step can vary as the velocity and wave speed change to keep A, B, C, and D near the corner nodes, at least in some portion of the domain.

The simultaneous solution of Eqs. (10)–(13) provides variables p_P, u_P, v_P, and q_P at each interior point.

$$p_P = [(e_1 + e_2 + e_3 + e_4)/(4C_{a2})]^{2\kappa/\kappa-1} \tag{14}$$

$$u_P = (e_1 + e_2 - e_3 - e_4)/4 \tag{15}$$

$$v_P = (e_1 - e_2 - e_3 + e_4)/4 \tag{16}$$

$$q_P = (-e_1 + e_2 - e_3 + e_4)/(4c\Delta t) \tag{17}$$

In order to save computer time and to avoid specification of conditions at singular points, the staggered grid, Fig. 1, is used in the model to discretize the computational domain. When a general domain is covered by a square mesh with i rows, j columns and ij grid intersection points (nodes), computations are made only at 50 percent or less of the nodes, Fig. 1(a), with about 25 percent of the nodes used at each time step, Fig. 1(b). That is, computations are made at the same node only at every other time step (i.e., at every two Δt). This staggered grid is fundamental to the satisfactory use of the model in a flow domain of any general shape. It provides considerable flexibility, and it enables the selection of a grid size that places singular points in the computational domain at non-computational nodes, thus simplifying the specification of boundary conditions. Square grids only have been utilized in the examples presented herein. A nonuniform grid could be used, with a dense grid in the active transient domain and a sparse grid away from the active region. However, in regions where high frequency transients exist it is highly recommended to utilize a square grid with the maximum Δt, while still satisfying Eqs. (8).

At each boundary, only two of equations in Eqs. (10) to (13) apply, Fig. 2. Thus, two boundary relations have to be specified to solve for the four variables. In addition, a vorticity

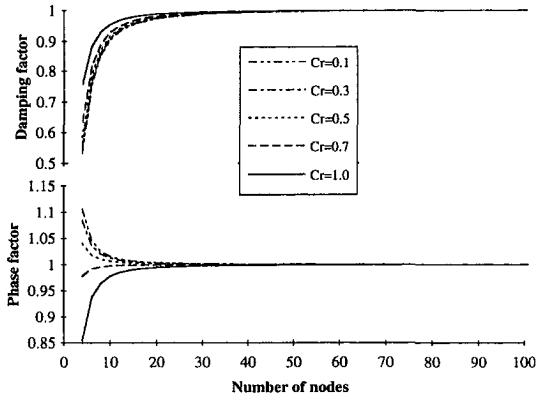

Fig. 3 Damping and phase factor versus number of nodes

statement is needed:

$$\frac{\partial u}{\partial y} - \frac{\partial v}{\partial x} = 0 \tag{18}$$

The variable $q = (u_y + v_x)/2$ becomes

$$q = \frac{\partial u}{\partial y} = \frac{\partial v}{\partial x} \tag{19}$$

In calculation of e_1 to e_4, p, u, v, and q at two points among A, B, C, and D are extrapolated from adjacent square grids. A non-flow boundary condition is given as an example. This condition would be used to represent an impermeable condition, or to represent grid points along a line of symmetry in the physical domain. The additional boundary conditions, along with the appropriate pair from Eqs. (10) to (13), are

$$\begin{cases} u_p = 0, & q_p = 0, \quad \text{right and left;} \\ v_p = 0, & q_p = 0, \quad \text{lower and upper.} \end{cases} \tag{20}$$

Error Study

A formal analysis of damping and phase error of this model was performed with the von Neumann method. In the analysis, the density and convective velocity are assumed constants, as commonly done, to avoid mathematical difficulty. Analytical results show that this model has damping and leading or lagging phase error when the Courant number, which is defined as $(u + c)\Delta t/\Delta x$, is less than one and the Mach number, which is defined as $(\sqrt{u^2 + v^2})/c$, is apart from zero. There is no damping or phase error when the Courant number equals one and the Mach number equals zero. The typical behavior of the dependency of the damping factor and the phase factor on the Mach number, Courant number, and the number of grid points per wave length, are shown in Fig. 3. The damping factor is defined as the modulus of the eigenvalue of the amplification matrix of the scheme, and the phase factor is defined as the ratio of numerical phase speed and true phase speed. Quantitively, the damping factor varies from 0.9767 to 1.0, and the phase factor varies from 1.0017 to 1.0 when the Courant number is in the range of 0.3 to 1.0, and the number of grid points per wave length equals 20. The results show that the damping and phase errors of the present model are quite small when the number of grid points per wave length is larger than 20.

Infinite Boundary Condition

An infinite boundary, located at an intermediate position in an open system, would provide, ideally, the same response to a transient event in the active domain as the open system would provide. Such a numerical boundary is possible, without difficulty, for inviscid, low Mach number (linearized) unsteady one-dimensional flow by use of a characteristic impedance termination with the traditional method of characteristics (Wylie and Streeter, 1993). This is a nonreflective boundary with complete energy transmission, and is numerically precise. Examples of the implementation of successful infinite terminal conditions also exist (Poinsot and Lele, 1992; Ramahi et al., 1991; Rudy and Strikwerda, 1980; and Thompson, 1987) for nonlinear multi-dimensional unsteady flows, although the procedures are less obvious. The nonlinearity, which is likely to cause partial reflection of the wave energy back to the source, may be the result of viscosity, frequency-dependent material properties, large variations in Mach number, etc.

Since the infinite boundary condition must account for reflections generated by the nonlinear distributed properties of the infinite space, and for attenuation due to the geometric properties of the multi-dimensional field, it is likely to be an approximation at best. The goal is a boundary that will permit wave energy from the source to transmit through the boundary, while reflecting only that portion of the energy returned naturally by the distributed parameters of infinite space. There is unlikely to be a unique solution to handle all of the possible conditions. This study addresses only the geometric response, and the special sub-set of nonlinearity caused by the inclusion of the transport terms in the two-dimensional compressible flow equations.

Experience to date has led to the use of two different types of infinite boundary conditions. Type A is an Interpolation and Projection procedure, with two implementation methods A-1 and A-2, and Type B is an Extended Exterior Characteristics-Like Line. Each possesses attributes that are attractive in a particular application.

Type A, Interpolation and Projection. Visualizing the physical nature of characteristics, a characteristic line in mathematical space represents, conceptually, a locus in a physical system along which disturbances travel without losing their properties. Therefore, the values of p, u, v, and q at a node, which are the properties of a disturbance, can be considered coming from the position where the disturbance was situated at an earlier time through a corresponding characteristic. Based on this concept, considering a left boundary node M at time level $n + 1$, Fig. 1, two imaginary nodes P', P'' may be set up outside the boundary. They are one Δx away from the actual boundary of the computational domain and at time level n. Two different methods may be implemented to project variables p, u, v, and q from inside the domain to outside the infinite boundary, i.e., to points P' and P''. The first (A-1) projects the information along appropriate characteristics-like lines, such as C^{--} and C^{-+} in Fig. 1. The second (A-2) projects directly along either the x- or y-coordinate axis, as appropriate. For the left boundary, the projection would be along the x-axis. Details of the procedure are described in Wang and Wylie (1993).

Procedures A-1 and A-2 both require interpolations at time level $n - 2$. Procedure A-1 averages the values interpolated from the surface variables at time level $n - 2$. Procedure A-2 assumes the values along the x-axis to be a suitable average, interpolates along this axis, then projects to time level n.

Computational results show that this infinite boundary procedure is most effective when the disturbance, internal to the domain, creates a flow pattern in which the velocity and pressure waves are moving directly out of or into the domain; that is, for a disturbance propagating normal to the boundary. At the extreme opposite end of the scale for flow direction, is one in which the incident wave is parallel to the infinite boundary. For this extreme situation, procedure A-2 outperforms procedure A-1 significantly. The reason for this is that procedure A-1 averages the projected values at time level n. When the wave parallels the infinite boundary, one projected value is reliable, and one is not. If the projected value is inaccurate

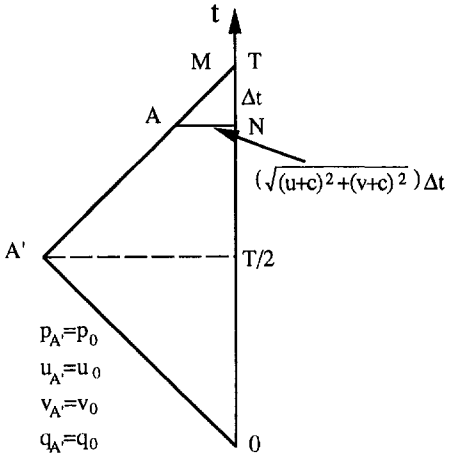

Fig. 4 Extended exterior characteristics-like line at the infinite left boundary, type B

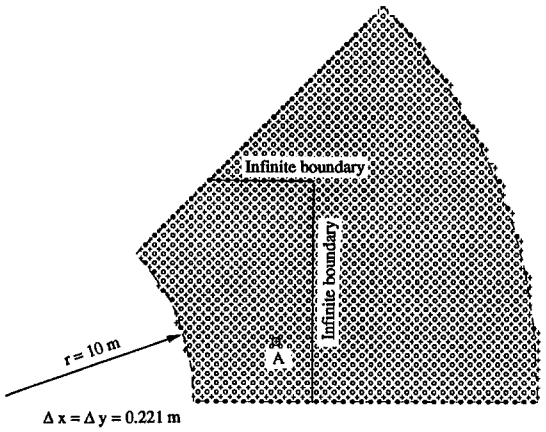

Fig. 5 The mesh for 45 deg sector

then the calculated value at the infinite boundary is as well. Procedure A-2 does not suffer this malady and, thus, produces better results. This is illustrated in the second example, which follows.

One negative aspect in the use of the Type A procedure is that there may be a tendency for the pressure to gradually drift in one direction or the other, since there is no direct relationship to the reference pressure level in the unbounded domain. The Extended Exterior Characteristic-Like Line, which follows, avoids this problem.

Type B, Extended Exterior Characteristic-Like Line. This procedure is best suited in a region of small change, low velocity gradients, and minimal vorticity. It can be used at relatively high Mach number as long as the gradients are low. To visualize this treatment it is necessary to refer to the ordinary differential equations, prior to integration to place them in finite difference form. The concept is one of extending the characteristics-like lines, that exist outside the computational domain (i.e., those beyond the infinite boundary), back in time to the initial undisturbed conditions. The characteristics-like lines inside the domain are treated in the standard manner.

As an example, for the left infinite boundary plane shown in Fig. 1, the C^{++} and C^{+-} characteristics-like lines, initiating at point M would not terminate in the xy-plane at time n, but would extend back in time as far as is necessary to reach undisturbed conditions in infinite space. To illustrate, Fig. 4 shows a view in the plane of the C^{++} characteristics-like line (MNA, Fig. 1). Line $A'M$ is defined by Eq. (7a) along which Eq. (7b) is valid. Equation (7b) is integrated from point A' to M, rather than A to M. The first three terms are integrated exactly, regardless of the length of the line. The final term containing q requires an approximation in the integration. If the value of q is not large, and if it is not changing rapidly along the infinite boundary, the following integration of Eq. (7b) is recommended:

$$C_{a2}(p_M^{\kappa-1/2\kappa} - p_{A'}^{\kappa-1/2\kappa}) + u_M - u_{A'} + v_M - v_{A'} - 2c(q'_A + q_M)/2(t_M - t_{A'}) = 0 \quad (21)$$

In the last term, $q_{A'} = 0$, since A′ is always located in initial conditions, $t_M = T$, and $t_{A'} = T/2$. Thus, the last term becomes $cq_MT/2$, in which T is the total computational time, beginning at the initiation of the transient. The trapezoidal rule has been used. It is recognized that this approximation is poor if q varies dramatically, or if q is large, at the infinite boundary during the transient. The same type of integration is used along the C^{+-} characteristics-like line for the left infinite boundary. The other two lines, which extended into the computational domain, are treated like any other lines in the domain, and the compatibility equations are integrated over the current time step Δt.

Applications

The two-dimensional model and the two types of proposed infinite boundary treatments have been validated by comparisons with analytical, and experimental examples, plus one example from the literature that is only intuitive.

Line Source Disturbance. The transient pressure and velocities that develop in a continuum as a result of a line source can be calculated analytically (Lamb, 1945). The theory assumes compressible potential flow with low Mach numbers. The strength of the source at the origin is described as a function of time by the equation,

$$f(t) = \frac{\tau}{t^2 + r^2} \quad (22)$$

in which τ is a constant. The dimensionless velocity as a function of time, t, and distance, r, is given by:

$$v = \frac{1}{4V_0}\left(\frac{c\cos\eta}{2r\tau}\right)^{1/2}\left[\frac{1}{r}\cos\psi + \frac{c\tau}{c^2r^2 + (ct - r)^2}(\sin\psi - \cos\psi\tan\eta)\right] \quad (23)$$

in which η is defined in the equation $t = r/t + r\tan\eta$; $\psi = \pi/4 - \eta/2$; V_0 is an arbitrary velocity used in nondimensionalizing the problem, $v = V/V_0$. Eq. (23) is valid if $r \gg c\tau$ and $t \ll 2r/c$. The mesh for modeling a 45 deg sector of the two-dimensional space is shown in Fig. 5. Two domains are used in two separate computations, the large domain shown by the grid in Fig. 5, and the smaller domain on the left side, bounded on the right and the top by the dashed line where the infinite boundary was placed. Infinite boundary Type A-1 is chosen here since the disturbance is propagating radially. The two radial lines are represented by the no-flow (impermeable) condition since they represent lines of symmetry, and the inner boundary is the excitation source, which is a specified velocity history. The mesh size is 0.221 m, $\tau = 0.01$, $c = 342.0$ m/s, $V_0 = 1.0$ m/s. The total computational time is chosen as 0.045 s, long enough so the velocity pulse can pass completely through node A. Figure 6(a) shows a graph of velocity versus time at node A. Figure 6(b) shows a graph of velocity versus distance along a line parallel to the x-axis through point A at $t = 0.0391$ s. In both graphs the solid and dashed lines show agreement between analytical and numerical results to be excellent. The Courant number in this example varies from 0.985 to 1.0. With the mesh size of 0.221 m the damping factor varies from 0.9996 to 1.0, and the phase factor varies from 0.9981 to 1.0, so it

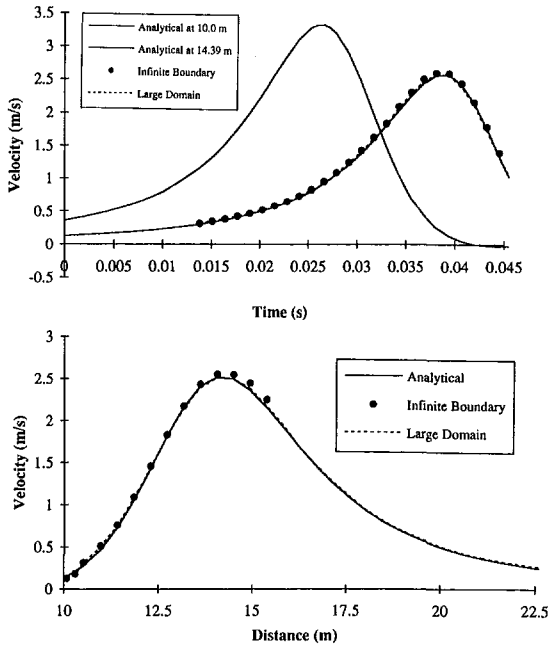

Fig. 6 The comparison of velocity response; (*a*) response at A, (*b*) response along a line

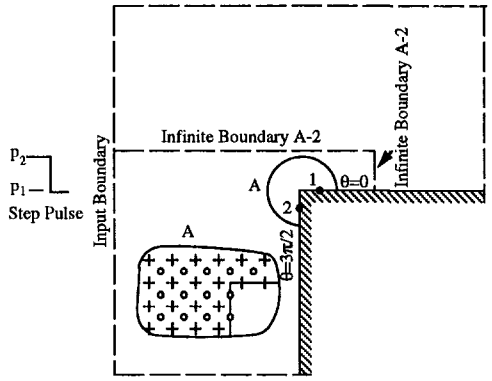

Fig. 7 The schematized computational domain for corner diffraction problems

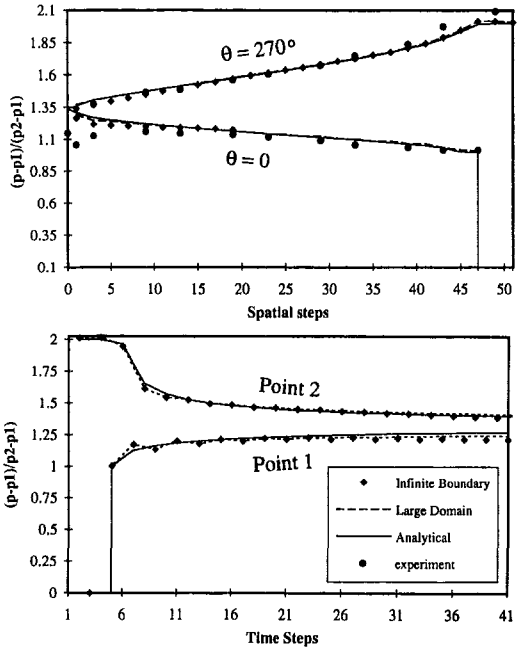

Fig. 8 (*a*) Pressure-distance profile at 90 deg wedge; (*b*) pressure-time history profile at points on face of wedge

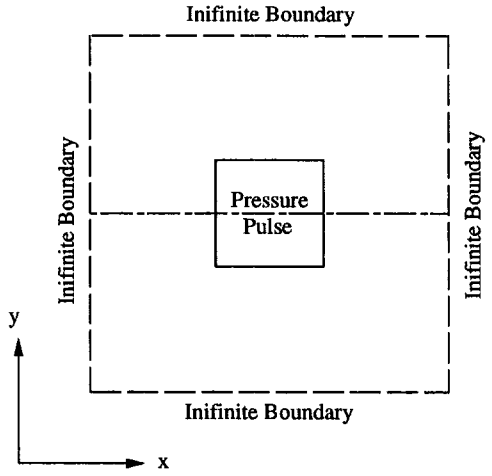

Fig. 9 The schematized computational domain for pressure perturbation

should be anticipated that the numerical results show excellent agreement with the analytics. The circles on the graphs show the response when the infinite boundary is used, and they show that the infinite boundary has not seriously contaminated the numerical results.

Transient Response at 90 Deg Wedge. The two-dimensional transient pressure response is studied for validation when a pressure discontinuity strikes a right-angled wedge. The positive pressure pulse approaches the corner with its front parallel to one face (270 deg face) of the wedge, Fig. 7. Again, two domains are used in simulating this problem. The small domain shown in dashed lines in Fig. 7 has two sides with infinite boundaries of Type A-2. The mesh size $\Delta x = \Delta y = 0.0382$ m, $c = 340.0$ m/s, $p_1 = 1$ atm, and $p_2 = 1.2p_1$. The total computing time is also chosen long enough so the diffraction waves can penetrate the infinite boundaries of the small domain, but short enough to avoid reflecting waves from the outer boundaries of the large domain to interact with flow patterns on the two faces of the wedge. Two comparisons are presented: pressure profiles along the edges of the wedge at a particular instant, and the pressure time history at two points located on the wedge faces at some distances from the corner. Figure 8(*a*) presents the analytical solution and experimental data (Keller, 1952), and numerical results from both large and small domains along the edges of the wedge within the diffracted wave front and in front of it. Figure 8(*b*) presents the pressure-time history at point 1, four distance intervals from the corner along the face $\theta = 0$ deg, and at point 2, three distance intervals from the corner along the face $\theta = 270$ deg. All numerical results compare quite well with the analytical solution.

Pressure Perturbation Mid-Point of the Domain. A unique problem was presented by Rudy and Strikwerda (1980) to demonstrate the use of their model. A similar problem is presented here to illustrate the use of infinite boundary, Type B. Figure 9 shows a domain with a pressure pulse imposed in a central region. A horizontal centerline defines a line of symmetry, so the lower domain was modeled by a grid 101 × 51. The central region pressure pulse covered a region 30 × 15. A negative pressure pulse is simulated at two free stream Mach numbers in the x-direction, $M_\infty = 0$ and $M_\infty = 0.6$. The free stream velocity in the y-direction is zero, and the pressure is

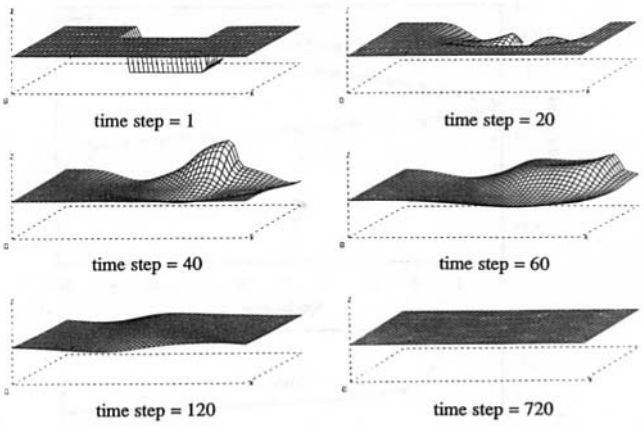

Fig. 10 Pressure profiles at different instants of time

Table 1 Pressure pulse Δp is negative

Boundary treatment	Time steps	$D\%$ ($M_\infty = 0.0$)	$D\%$ ($M_\infty = 0.6$)
A-2, I&P	240	0.25	1.68
	360	0.20	1.52
	720	0.11	1.32
B, EECLL	240	0.045	0.96
	360	0.003	0.66
	720	0.000	0.17

uniform throughout the domain initially, except in the central region of the imposed pressure pulse where it differs by $\Delta p = 0.476 p_\infty$.

A total of four sets of computations were carried out, in order to exercise infinite boundary Type A-2 and B for each different problem. Graphical displays are shown for only one problem, while tabulated data are summarized for each case. The response from the negative pulse is illustrated in Fig. 10 where sequential three-dimensional pressure profiles are shown at specific time steps, that is, at specific instants of time. Steady flow with $M_\infty = 0.6$ and a uniform pressure is achieved in approximately 720 time steps when infinite boundary Type B is used.

Table 1 provides an index D which represents the deviation from the final steady state. It is defined as

$$D = \sqrt{\frac{\Sigma(p/p_\infty - 1)^2}{N}} \tag{24}$$

in which N is the number of nodes where computations are being made. It may be viewed as a dimensionless error averaged over the domain. Table 1 presents D*100, or a percentage error.

Table 1 shows the computations to approach final steady conditions in a realistic manner. It may be observed that computations with infinite boundary Type B reach steady state faster than with Type A-2. The no-flow case, $M_\infty = 0$, reaches steady conditions faster than the case $M_\infty = 0.6$, as might be anticipated. The true time to steady state is unknown for each case. However, since it takes 50 time steps for a pulse at the center of the domain to reach the edge of the domain, these times appear quite appropriate. A negative result from computations with procedure A-2 is that there is a drift from the final steady conditions, however, the deviation is less than 2 percent. Even with this boundary type the solution is convergent and stable. The results merely show the amount of drift during the indicated time frame, and that the pressure pattern is recovering slowly back to p_∞.

Conclusion

This paper presents an unsteady, isentropic, two-dimensional model to calculate nonviscous compressible gas flow in an arbitrarily closed region or in an open fluid domain. Computational results show that the characteristic-like model is reliable in simulating a number of different flow situations. Several dynamic flow cases provide the opportunity for comparisons between computational results, analytic solutions, and experimental data. Although not demonstrated herein, the model has application in the nuclear industry, space technology, and in various automotive industry applications such as air-bag studies for vehicle occupant protection (Nucholtz et al. 1993) and head-impact studies. The gas jet dynamics may be useful in a number of different practical linear momentum applications, such as deflector mechanisms, air-bag deployment, etc.

An infinite boundary has also been introduced to limit the computational domain when the flow field physically discharges into a semi-infinite space. Computational experiences show that as long as appropriate dimensions are selected for positioning the infinite boundary in the receiving domain it performs extremely well and has little impact on the near-flow field around the flow source.

References

Henke, R., and Wylie, E. B., 1982, "Tortional Dynamic Response of Solid Media," *Journal of Engineering Mechanics Division*, ASCE, Vol. 108.

Keller, J., 1952, "Diffraction of a Shock or an Electromagnetic Pulse by Right-Angled Wedge," *Journal of Applied Physics*, Vol. 23, pp. 1267–1268.

Lamb, H., 1945, *Hydrodynamics*, Dover Publications.

Nucholtz, G., Wang, D. G., and Wylie, E. B., 1993, "Simulation Model of Air-bag Deployment Gas Flow," ASME Winter Annual Meeting, AMD-Vol. 169/BED-Vol. 25, New Orleans, pp. 243–253.

Poinsot, T. J., and Lele, S. K., 1992, "Boundary Conditions for Direct Simulations of Compressible Viscous Flows," *Journal of Computational Physics*, Vol. 101, pp. 104–129.

Ramahi, O. M., Khebir, A., and Mittra, R., 1991, "Numerically Derived Absorbing Boundary Condition for the Solution of Open Region Scattering Problem," *IEEE Transactions on Antennas and Propagation*, Vol. 39, No. 3, pp. 350–353.

Rudy, D. H., and Strikwerda, J. C., 1980, "A Nonreflecting Outflow Boundary Condition for Subsonic Navier-Stokes Calculations," *Journal of Computational Physics*, Vol. 36, pp. 55–70.

Shapiro, A. H., 1954, *Compressible Fluid Flow*, Vol. I, Ronald Press, New York, pp. 454–455.

Shin, Y. W., and Valentin, R. A., 1978, "A Numerical Method Based on the Method of Characteristics for Two-Dimensional Fluid Transients," ASME Paper 78-PVP-57, 7 pp.

Sullivan, D. A., 1981, "Historical Review of Real-Fluid Isentroic Flow Models," ASME JOURNAL OF FLUIDS ENGINEERING, Vol. 103, pp. 258–267.

Thompson, K. W., 1987, "Time Dependent Boundary Conditions for Hyperbolic Systems," *Journal of Computational Physics*, Vol. 68, pp. 1–24.

Wang, D. G., and Wylie, E. B., 1993, "Two-Dimensional Unsteady Compressible Flow Model," ASME, *Forum on Unsteady Flows*, FED-Vol. 157, Washington, DC, pp. 119–127.

Wylie, E. B., and Streeter, V. L., 1993, *Fluid Transients in Systems*, Prentice-Hall.

Molecular Dynamics Simulations on Internal Structures of Normal Shock Waves in Lennard-Jones Liquids

Akira Satoh
Department of Mechanical Engineering,
Faculty of Engineering,
Chiba University,
1-33, Yayoi-cho, Inage-ku,
Chiba 263, Japan

The present paper describes a highly efficient method for simulating the generation of shock waves in liquids by using the periodic-shell boundary condition, which is an outer boundary condition for molecular dynamics simulations. This method is used to simulate normal shock waves in Lennard-Jones liquids, clarifying the internal structures of shock fronts and the dependence of shock thicknesses on the shock Mach number. The present method significantly decreases computation times because it enables us to simulate only the shock fronts. Some of the main results derived by these simulations of molecular dynamics are that an overshoot in the profile of longitudinal temperature arises in liquid shock waves as well as in gas shock waves, that the thickness of shock front decreases with increasing Mach number, and that this thickness is about two times the diameter of molecules when the Mach number is 4.

1 Introduction

The internal structures of shock waves in gases have been widely studied by applying Monte Carlo direct simulation methods to the Boltzmann equation (Bird, 1970; Nanbu and Watanabe, 1984; Erwin et al., 1991; Boyd, 1990; Muntz, 1989) instead of by taking classical approaches to the Navier-Stokes equations (for example, Schwartz and Hornig, 1963). The internal structures of liquid shock waves, in contrast, have not been extensively studied, in part because the applications of liquid shock waves in engineering fields were not clear. Liquid shock waves have recently been applied in medical engineering, however (for example, Takayama, 1987), and the shock structures in liquids and solids have thus become important subjects.

The Monte Carlo direct simulation method (Bird, 1976) cannot be applied to liquid problems because it is a solution to the Boltzmann equation. Molecular dynamics (MD) methods, though, are extremely useful for investigating liquids and solids from a microscopic point of view. They have therefore been widely used along with variant of the Monte Carlo technique (Ciccotti and Hoover, 1986). Tsai and Trevino (1981) and Holian and his co-workers (1980, 1988), for example, have used MD methods to investigate the internal structures of normal shock waves for weak and for very strong shock waves in Lennard-Jones liquids (corresponding to liquid argon).

In ordinary MD simulations, liquid shock waves are generated by compressing a cylinder in which molecules are initially enclosed in a liquid state. Since the shock wave travels in the direction of piston motion, this method requires a long simulation region in order to obtain averaged values of reasonable accuracy. This means that a very high percentage of the molecules are outside the shock front, and therefore irrelevant in the averaging procedure. This makes the conventional shock-gathering method inefficient and computationally expensive. Studies have therefore been carried out only for a few shock Mach numbers and many questions remain unanswered. If we want to simulate shock fronts alone, then the relations between upstream and downstream quantities (i.e., the Rankine-Hugoniot relations) need to be known before the simulations. The Rankine-Hugoniot relations for Lennard-Jones liquids have already been clarified (Satoh, 1994a), it is now possible to use MD methods to simulate only the shock fronts.

The present paper first describes a highly efficient shock-generating method for simulating shock fronts alone by applying the periodic-shell boundary condition developed as an outer boundary condition for MD simulations (Satoh, 1994b). Then by simulating normal shock waves for Lennard-Jones liquids, it shows how internal structures such as densities, temperatures, and pressures depend on the shock Mach number.

2 Model System and Assumptions

The present shock-generating method, which differs significantly from the conventional piston-moving method, generates steady normal shock waves of desired shock strength by

Contributed by the Fluids Engineering Division for publication in the JOURNAL OF FLUIDS ENGINEERING. Manuscript received by the Fluids Engineering Division November 10, 1993; revised manuscript received April 15, 1994. Associate Technical Editor: O. Baysal.

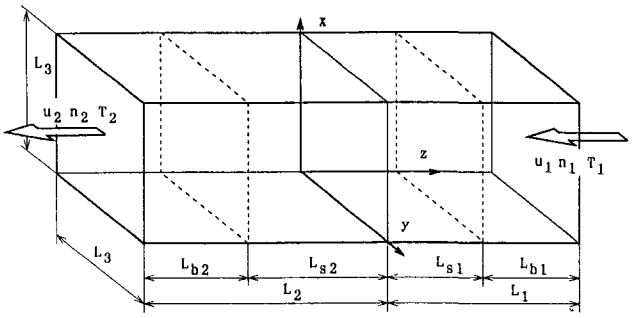

Fig. 1 Molecular dynamics simulations of steady normal shock waves

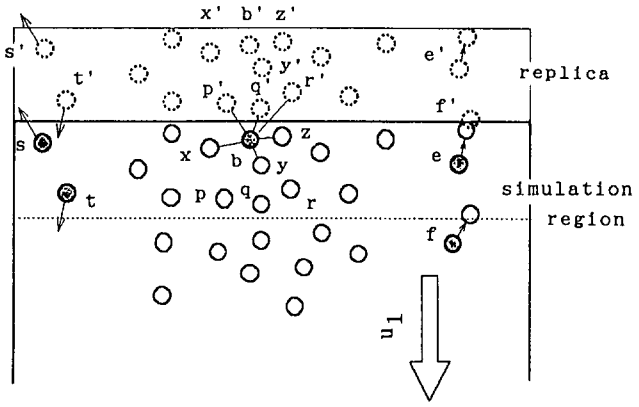

Fig. 2 Periodic-shell boundary condition

restricting upstream and downstream quantities to prescribed values. The model system used here is shown in Fig. 1. The molecules are initially on the sites of face-centered-cubic lattices, and the initial lengths L_1, L_2, and L_3 of the sides of the simulation box are adjusted so that the number densities at $z > 0$ and $z < 0$ are the prescribed values n_1 and n_2, respectively. The initial velocities of the molecules are also given in such a way that temperatures and average velocities are prescribed values: T_1 and u_1 for $z > 0$, and T_2 and u_2 for $z < 0$. The shell areas (described in the following sections) have an upstream length L_{b1} and downstream length L_{b2}. The conventional periodic boundary condition is used for the boundary surfaces perpendicular to the x and y axes.

The present shock-generating method requires that the Rankine-Hugoniot relations for the fluid of interest should be known before the simulations. Although these relations are unknown for general liquids, they have been numerically clarified for Lennard-Jones liquids (Satoh, 1994a). Thus, if the number densities, average velocities, and temperatures of the upstream and downstream shells are taken in such a way that they satisfy the Rankine-Hugoniot relations, we can obtain the normal shock waves around the origin of the z axis. The techniques restricting the quantities to desired values are given in Section 3.3.

3 Molecular Dynamics Methods

3.1 Velocity Verlet Algorithm. Many computational algorithms for soft molecular systems have already been presented, but because we deal here with flow problems it is better to use an algorithm in which molecular velocities are explicitly appeared in the determination of molecular positions. We therefore adopt the velocity Verlet algorithm (Allen and Tildesley, 1987), which is easy to handle and relatively accurate. That is,

$$\mathbf{r}_i^{n+1} = \mathbf{r}_i^n + h\mathbf{v}_i^n + \frac{h^2}{2m}\mathbf{f}_i^n, \tag{1}$$

$$\mathbf{v}_i^{n+1} = \mathbf{v}_i^n + \frac{h}{2m}(\mathbf{f}_i^{n+1} + \mathbf{f}_i^n), \tag{2}$$

in which m is the molecular mass, $\mathbf{r}_i$ is the molecular position vector, $\mathbf{v}_i$ is the molecular velocity vector, $\mathbf{f}_i$ is the force acting a molecule i, and h is the time interval. And for simplicity the time step is denoted by the superscript n.

3.2 Periodic-Shell Boundary Condition. The periodic-shell boundary condition is an outer boundary condition for MD simulations that diminishes the influence of limited size of the simulation regions, and the application of this boundary condition to the upstream and downstream boundary surfaces enables us to simulate shock fronts alone. This boundary condition is described in detail in another paper (Satoh, 1994b), so here it is just summarized. Since there is no essential difference of the treatment between upstream and downstream, the following shows only the upstream treatment.

The particles near the upstream and downstream boundary surfaces have to be made to interact with imaginary particles outside the region; otherwise, the limitedness of the simulation regions significantly distorts a flow field. The thin layer (shell) near the boundary is replicated next to the region itself so that the particles in the shell also act as imaginary particles. As shown in Fig. 2, the particle b interacts not only with the real particles x, y, z, etc., but also with the imaginary particles p', q', r', etc. The particle s in Fig. 2 is completely removed if it goes out of the simulation region. Incoming particles, on the other hand, are generated as follows: if the particle t in Fig. 2 moves from the shell area to the inner region, the imaginary particle t' naturally comes into the shell area; this particle t' is regarded as a new incoming particle independent of the particle t. Some problems may result from the particle f, which crosses the broken line to enter the shell area. Suppose that at the next time step the particles e and f move to the heads of the arrows. In this case, the particle f moves to the upper region across the broken line and, at the same time, the imaginary particle f' suddenly appears in front of the particle e. Such sudden appearances of imaginary particles may cause

Nomenclature

$\mathbf{f}$ = force vector
h = time interval
k = Boltzmann's constant
L, L_s = lengths of simulation box
L_b = length of shell region
M_1 = shock Mach number
m = mass of molecule
n = number density of molecules
p = pressure
$\mathbf{r}$ = molecular position vector
r_{ij} = distance between molecules i and j
r_c = cut-off radius for computation
T = temperature
u = flow velocity
v = Lennard-Jones potential
$\mathbf{v}$ = molecular velocity vector
W = internal virial
ϵ, σ = constants of Lennard-Jones potential

Subscripts

1 = upstream quantity
2 = downstream quantity
i = ith molecule

Superscripts

* = normalized quantity
n = time step

unreasonable overlapping with real particles, so special attention has to be paid to those particles. In actual simulations, such unreasonable overlapping may be relieved by shifting real particles an infinitesimal distance. Monte Carlo methods are used to do this. We have to note, however (from presimulations), that such procedures are important in equilibration, but that the overlapping of particles very seldom occurs after equilibration.

3.3 Techniques for Maintaining Quantities at Desired Values. Steady normal shock waves can be generated by compelling the upstream and downstream quantities to be desired values, which satisfy the Rankine-Hugoniot relations, throughout the simulation process. This can be done by adjusting the lengths of shells and the velocities of the molecules in the shells. For shock wave problems, conducting such operations at every time step greatly influences the formations of shock waves, so these lengths and velocities are adjusted at intervals of a certain number of time steps in order to make the correction per operation small.

The density can be maintained at a prescribed value by first evaluating the average density in the shell for a certain number of time steps and then adjusting the shell length L_{b1} to give the desired shell density n_1. At the same time, the positions of the molecules in the shell are also adjusted similarly.

The temperature and average velocity must also be maintained at prescribed values, and this can be done as follows. If the average velocity in the shell, evaluated for a certain number of time steps, is denoted by $(\bar{v}_x, \bar{v}_y, \bar{v}_z)$, then the desired average velocity $(0, 0, u_1)$ is obtained by replacing the velocity (v_x, v_y, v_z) of an arbitrary molecule in the shell by the following velocity (v_x', v_y', v_z'):

$$(v_x', v_y', v_z') = (v_x - \bar{v}_x, v_y - \bar{v}_y, v_z - \bar{v}_z + \mathbf{u}_1). \tag{3}$$

Further replacement of the velocity (v_x', v_y', v_z') by (v_x'', v_y'', v_z'') gives the desired temperature T_1 in the shell:

$$(v_x'', v_y'', v_z'') = (c_0 v_x', c_0 v_y', c_0(v_z' - u_1) + u_1). \tag{4}$$

The coefficient c_0 is written as

$$c_0 = \left[\frac{3N_s k T_1/m}{\sum_{i=1}^{N_s} \{v_x'^2 + v_y'^2 + (v_z' + u_1)^2\}} \right]^{1/2}, \tag{5}$$

where k is Boltzmann's constant and N_s is the number of the molecules for which the average velocity $(\bar{v}_x, \bar{v}_y, \bar{v}_z)$ is calculated. In short, the desired average velocity u_1 and temperature T_1 can be obtained by replacing the velocity (v_x, v_y, v_z) of each molecule in the shell by (v_x'', v_y'', v_z'').

3.4 Evaluation of State Quantities. State quantities such as pressures and internal energies are obtained by taking the time averages of the corresponding quantities at a microscopic level.

Consider the infinitesimal volume ΔV in a shock front. If the local number density and temperature in this volume are n and T, then from the virial theorem the pressure p is written in the following form:

$$p = nkT + \overline{W}/\Delta V, \tag{6}$$

in which the upper bar means the time average, n and T are the time-averaged quantities, and W is given by

$$W = -\frac{1}{3} \sum_i \sum_{j(>i)} w(r_{ij}), \tag{7}$$

with

$$w(r_{ij}) = r_{ij} \frac{dv(r_{ij})}{dr_{ij}}, \tag{8}$$

Table 1 Rankine-Hugoniot values and prescribed parameters. Note that uncertainty of (M_1, u_1^*, u_2^*, n_2^*, T_2^*, p_2^*) ≈ (2, 1, 2, 1, 2, 8) percent for M_1 = 1.25, and (1, 1, 1, 0.5, 1.5, 3) percent for the other cases of M_1

Shock Mach Number, M_1	u_1^*	u_2^*	n_2^*	T_2^*	p_2^*	h*	L_3^*	L_{s1}^*	L_{b1}^*	L_{s2}^*	L_{b2}^*
1.25	-5.6	-5.08	0.772	1.50	2.71	0.00027	6.8	3.3	6.6	10.2	8.5
1.69	-7.6	-6.08	0.875	2.16	8.74	0.0002	6.5	3.6	7.0	9.8	8.2
2.12	-9.5	-7.02	0.947	3.00	17.2	0.00016	6.4	3.7	7.6	7.2	8.0
2.56	-11.5	-8.00	1.006	4.19	28.9	0.00014	6.3	3.9	7.9	6.3	7.8
3.21	-14.4	-9.39	1.073	6.62	51.2	0.00011	6.1	6.1	8.0	3.6	7.7
4.01	-18.0	-11.1	1.136	11.0	87.8	0.00009	6.0	6.2	5.7	3.0	7.6

where r_{ij} is the distance between molecules i and j, and v is the Lennard-Jones 12-6 potential written as

$$v(r_{ij}) = 4\epsilon \left\{ \left(\frac{\sigma}{r_{ij}}\right)^{12} - \left(\frac{\sigma}{r_{ij}}\right)^{6} \right\}. \tag{9}$$

In this equation, ϵ and σ are constants, and for argon, $\epsilon/k = 119.8\ K$ and $\sigma = 3.405 \times 10^{-10}$ m.

A cut-off radius r_c is usually used for the evaluation of interaction energies between molecules, and if a sufficiently large value of r_c cannot be taken in simulations the computed values (such as pressures and energies) have to be corrected. A correction term $\langle W_{\mathrm{LRC}} \rangle$ is written as

$$\langle W_{\mathrm{LRC}} \rangle = -\frac{2\pi n^2 \Delta V}{3} \int_{r_c}^{\infty} w(r) r^2 dr = 16\, \pi n^2 \Delta V \left\{ \frac{2\sigma^{12}}{9 r_c^9} - \frac{\sigma^6}{3 r_c^3} \right\}. \tag{10}$$

The internal virial $\overline{W}$ is therefore obtained as the sum of the correction term $\langle W_{\mathrm{LRC}} \rangle$ and the value $\overline{W}_c$ computed from the simulations with a cut-off radius. The temperature T in the infinitesimal volume is obtained from the sum of temperatures in each direction: that is, $T = (T_x + T_y + T_z)/3$. The temperatures in each direction are defined as

$$T_x = \frac{m}{kN_s} \sum_{i=1}^{N_s} v_x^2,$$

$$T_y = \frac{m}{kN_s} \sum_{i=1}^{N_s} v_y^2,$$

$$T_z = \frac{m}{k} \left\{ \frac{1}{N_s} \sum_{i=1}^{N_s} v_z^2 - \left(\frac{1}{N_s} \sum_{i=1}^{N_s} v_z \right)^2 \right\}, \tag{11}$$

where N_s is the number of molecules for objects.

3.5 Normalization. For Lennard-Jones systems, it is very convenient for each quantity to be normalized by representative values made up of ϵ, σ, and m. Therefore the following representative values are used: the length of σ, the time is $\sigma(m/\epsilon)^{1/2}$, the temperature is ϵ/k, the number density is $1/\sigma^3$, the force is ϵ/σ, the pressure is ϵ/σ^3, the energy is ϵ, the velocity is $(\epsilon/m)^{1/2}$, etc. From this point on, the normalized quantities are indicated by a superscript *.

4 Parameters for Simulations

The present study deals with Lennard-Jones liquids under the upstream conditions of $n_1^* = 0.7$, $T_1^* = 1.2$, and $p_1^* = 0.657$. MD simulations have been carried out for the six cases of the shock Mach number M_1 ranging from 1.25 to 4.01. The parameters used here are listed in Table 1, where the velocities and state quantities are taken from previous results (Satoh, 1994a). The uncertainty of the data is also indicated in the table, and these uncertainties arise from the fact that shock waves may travel very slowly along the z axis in real simulation processes. There is thus some uncertainty in determining the actual shock Mach number (which is a little different from the

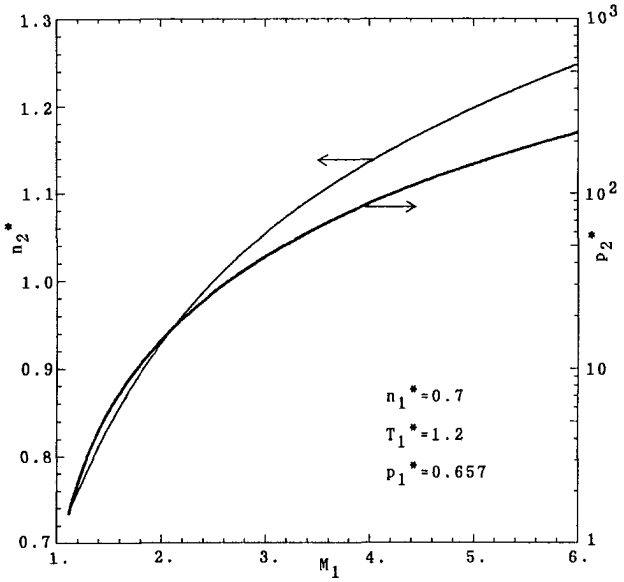

Fig. 3(*a*) Number density and pressure

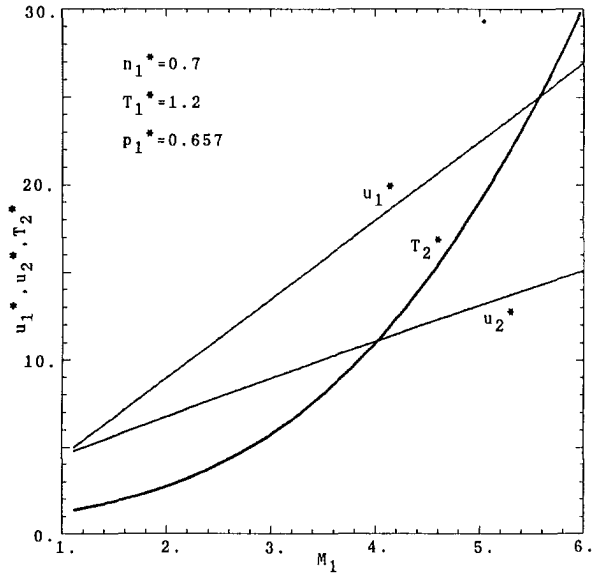

Fig. 3(*b*) Velocity and temperature

Fig. 3 Rankine-Hugoniot relations for Lennard-Jones liquids

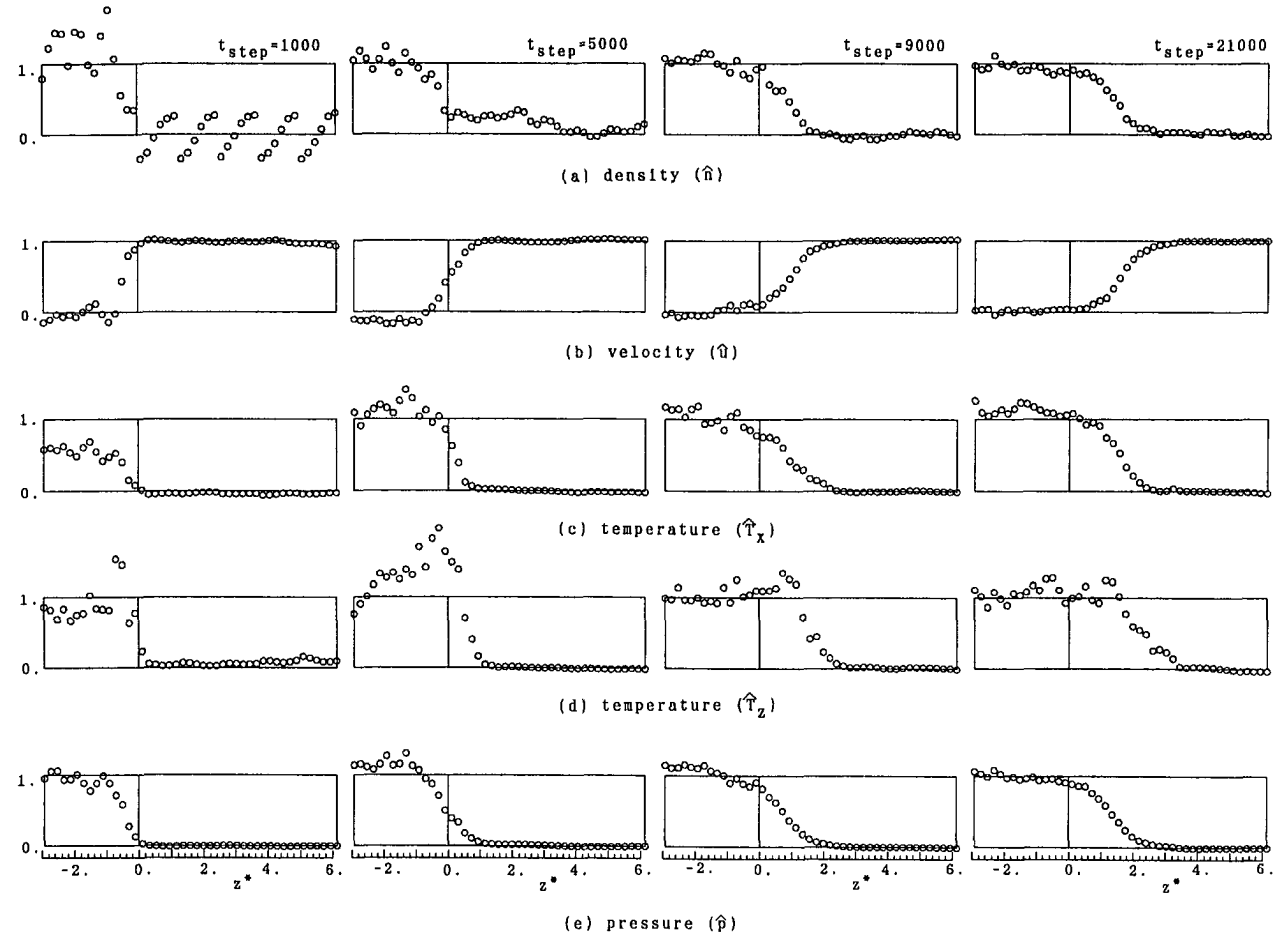

Fig. 4 Formation processes of shock waves (M_1 = 4.01)

ideal shock Mach number). The Rankine-Hugoniot relations are shown in Fig. 3 as a function of Mach number. Since the value of L_{b1}^* fluctuates in simulation process, the average values are listed in Table 1. The shell lengths are taken so that each length is greater than $2r_c^*$, where the cut-off radius r_c^* is set to be 3.0. We have to pay special attention to the determination of the values of time interval h^*. If h^* is too large, the unreasonable overlapping of molecules arises and causes the ve-

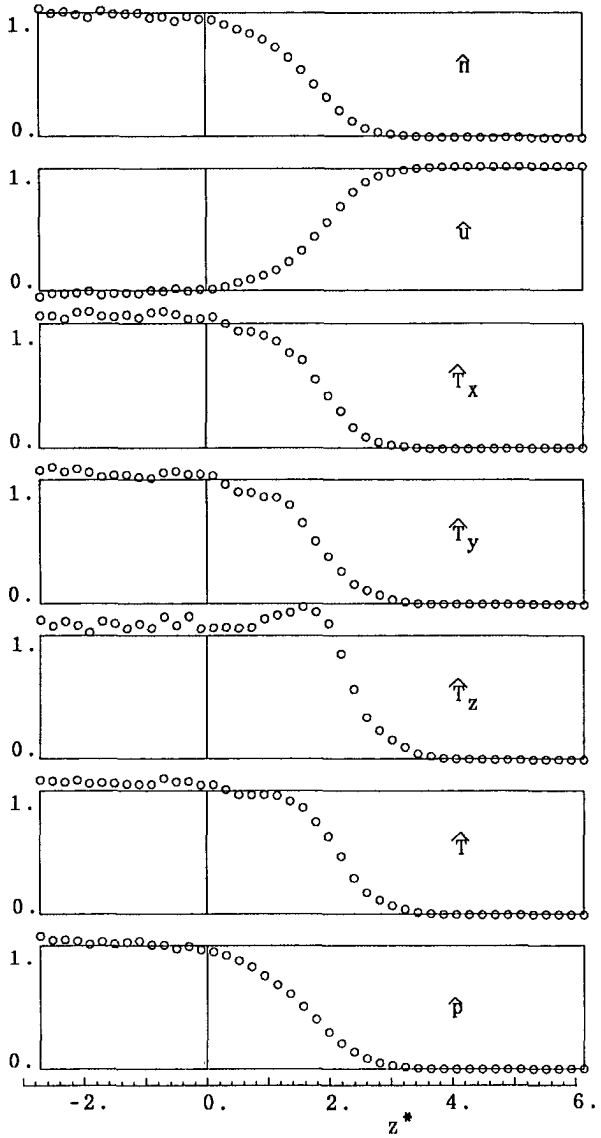

Fig. 5 Internal structures of shock waves (M_1 = 4.01)

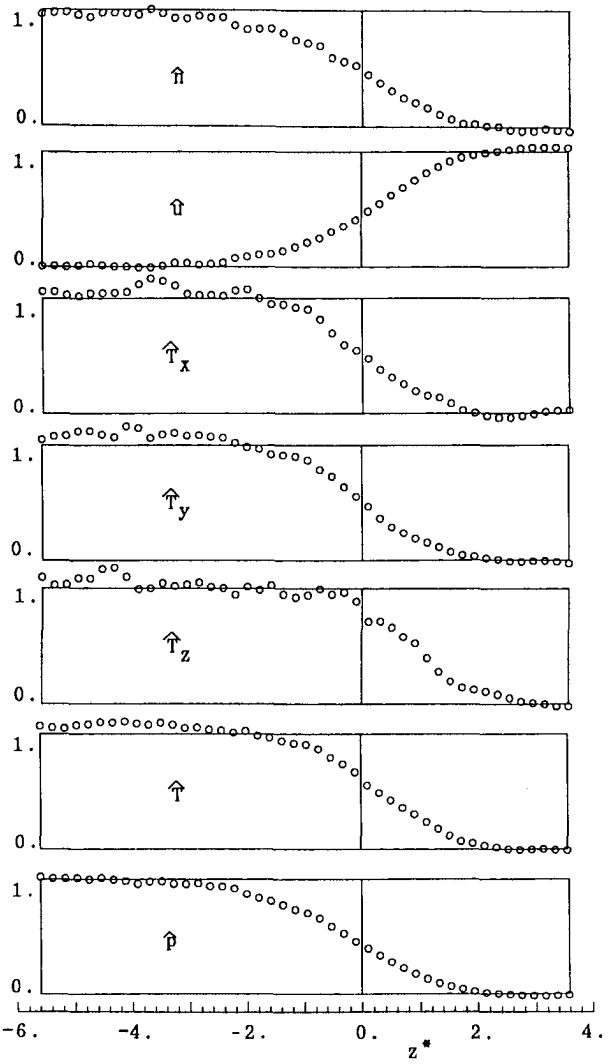

Fig. 6 Internal structures of shock waves (M_1 = 2.12)

locities, pressures, etc. to diverge. The values of h^* in Table 1 were obtained from pre-simulations for a small system: they are not intended to indicate the most appropriate values.

In actual simulations, some seeding-up techniques are usually used for the computations of interaction energies: the one used here is the cell index method (Allen and Tildesley, 1987).

Each simulation was carried out to 40,000 time steps, and three different initial molecular velocities were used for each Mach number. The internal structures were evaluated using the data generated between 10,000 and 40,000 time steps (the data for the first 10,000 time steps were excluded because it included the influence of the initial conditions). The averaged profiles of state quantities, which were evaluated every 2000 time steps, are used here for discussing the processes forming shock waves.

The molecular velocities were scaled and the upstream shell length adjusted every 2000 time steps to keep the density, pressure, and temperature at the desired values. Note that the downstream shell length was not adjusted in the present study and that the following results show that steady normal shock waves can be obtained even without such adjustment.

As mentioned in Section 3.2, Monte Carlo methods are used for relieving the unreasonable overlapping between real and imaginary molecules. In such cases, ten relieving procedures per corresponding molecule were performed.

The large computer used here for these simulations was the M-680H (not a supercomputer, but a standard mainframe produced by Hitachi, Japan) at the computer center of Chiba University. For the shock Mach number of M_1 = 4.01, the CPU time needed for 40,000 time steps (and about 780 molecules) was about 330 minutes. The CPU times for other Mach numbers were similar and roughly proportional to the number of molecules in the system.

5 Results and Discussion

5.1 Formation of Shock Waves. The processes forming shock fronts are shown for M_1 = 4.01 in Fig. 4, where the more time-advanced results are shown more to the right and where t_{step} = 5,000, for example, means that the data from 4000 to 6000 time steps was used to evaluate the profiles. This figure also uses the following symbols: $\hat{n} = (n - n_1)/(n_2 - n_1)$, $\hat{u} = (u - u_2)/(u_1 - u_2)$, $\hat{T}_x = (T_x - T_1)/(T_2 - T_1)$ (similar definition for $\hat{T}_z$), and $\hat{p} = (p - p_1)/(p_2 - p_1)$. Note that the profiles for $t_{step} \geq 21{,}000$ are in agreement with that for t_{step} = 21,000 within the range of statistical errors.

We can clearly see from Fig. 4 that the steady normal shock waves are gradually formed from the initially discontinuous profiles. The density profile for t_{step} = 1,000 has a periodic shape on the upstream side, which means that the initial mo-

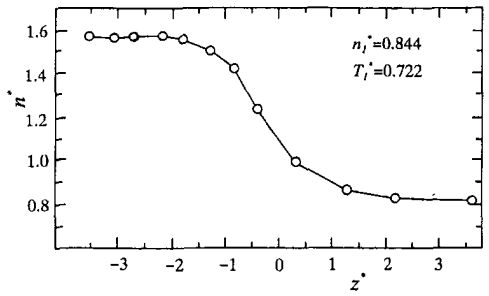

Fig. 7(*a*) Number density

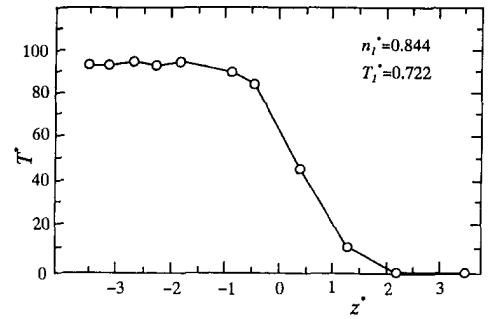

Fig. 7(*b*) Temperature

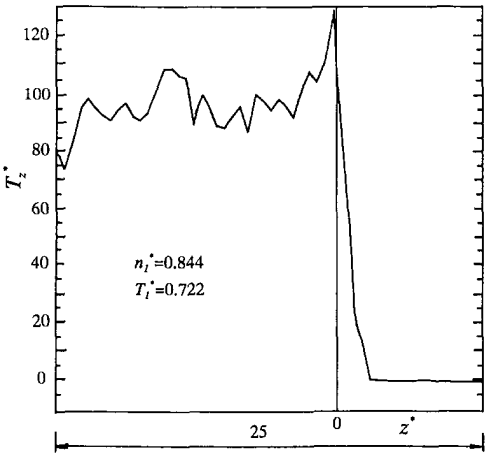

Fig. 7(*c*) Longitudinal temperature

Fig. 7 Internal structures of highly strong shock waves obtained by Holian et al. (1980)

lecular positions still have a great influence even at this time step: the wavelength is about half the lattice constant of the initial molecular positions. Despite the initial temperatures having been set at the Rankine-Hugoniot values, the downstream temperature for t_{step} = 1,000 is considerably lower than the Rankine-Hugoniot value, especially for $\hat{T}_x$. This means that, at the initial stage of simulation, the transmission of the information about the discontinuity profile leads to the suppression of thermal molecular motion. Then the quantity converges to the Rankine-Hugoniot value as time advances. The profiles for t_{step} = 9,000 are similar to steady profiles (i.e., sufficiently developed profiles) and the profiles for t_{step} = 21,000 have already attained to steady states. These characteristics were similar in simulations of the other Mach numbers.

It might be surprising that information evidently travels in the upstream direction in supersonic flow problems, but such transmission at the starting stage is not unreasonable because the initial molecular positions are solid-like positions.

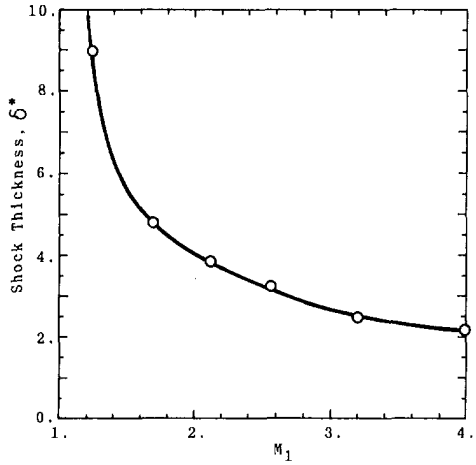

Fig. 8 Dependence of shock thickness on Mach number (each value has an uncertainty of about 7 percent)

5.2 Internal Structures of Shock Waves. The internal structures of shock waves are shown in Fig. 5 for M_1 = 4.01 and in Fig. 6 for M_1 = 2.12. Although the profiles obtained by Holian et al. (1980) are shown for reference in Fig. 7, those profiles cannot be compared quantitatively because the shock waves in those results were extremely strong (note that T_2^* is about 100 times T_1^*). The present profiles are much smoother than those obtained by the ordinary simulation methods (Fig. 7). This is seen most clearly for the temperature profiles. The quality of the present shock-generating method is indicated by the number density, velocity, and pressure downstream agreeing well with the Rankine-Hugoniot values. The downstream values of temperature are 3 to 7 percent greater than the Rankine-Hugoniot values, and the reason for this is not clear. The most interesting profile in Fig. 5 is that for the longitudinal temperature $\hat{T}_z$. Monte Carlo direct simulations (Nanbu and Watanabe, 1984) showed that for gas shock waves an overshoot of the longitudinal temperature appears even at M_1 = 2.5, whereas it has not been completely clear until the present time whether or not liquid shock waves also have such an overshoot profile. The results of Holian et al. (1980) and of Klimenko and Dremin (1979) suggested the overshoot feature of the longitudinal temperature, but those data were not accurate enough to be certain. It is clear from Fig. 5, however, that the overshoot of temperature $\hat{T}_z$ does occur even for liquids. The distribution of $\hat{T}_z$ for M_1 = 2.12 does not have such an overshoot, and the overshoot profile was not obtained at the shock Mach numbers below M_1 = 3.21. Figure 5 and 6 also show the significant discrepancy between the $\hat{T}_z$ and $\hat{T}_x$ (or $\hat{T}_y$) profiles: that is, the nonequilibrium of translational temperatures arises in the shock front, which is in agreement with the results obtained for gas shock waves.

5.3 Dependence of Shock Thickness on Shock Mach Number. The relationship between the shock Mach number and the thickness of shock front is shown in Fig. 8 (where each of the values plotted has an uncertainty of about 7 percent, which arises mainly in determining the maximum slope values of density profiles). The shock thickness δ^*, defined in a usual way based on density profile, is

$$\delta^* = \frac{n_2^* - n_1^*}{|dn^*/dz^*|_{max}}, \tag{12}$$

where the denominator is the maximum absolute value of the slope of the tangent to the density profile.

Figure 8 clearly shows that the shock front becomes thin with increasing the shock Mach number, which is similar to what is observed with gas shock waves. For example, if we use the argon data of T_2 = 1320 K and p_2 = 3.68 × 10^9 Pa

for $M_1 = 4.01$, the dimensional shock thickness δ is 7.47 Å. This is about two times the molecular diameter for $M_1 = 4.01$, which is in relatively good agreement with the other data in Fig. 7(*a*)—obtained for a very strong shock wave. Since liquid shock waves are much thinner than gas shock waves ($\delta^* \approx 9$ even for $M_1 = 1.25$), extremely accurate measuring techniques will have to be devised to experimentally clarify the internal structures of liquid shock waves.

6 Conclusions

We have discussed a highly efficient method for simulating the generation of shock fronts alone by applying the periodic-shell boundary condition, and we have investigated the internal structures of the liquid shock waves by simulating the normal shock waves for Lennard-Jones liquids. The present shock-generating method is expected to significantly decrease computation times. An overshoot in the longitudinal temperature profile arises in liquid shock waves, just as it does in gas shock waves. The method has also shown that thickness of shock front decreases with increasing shock Mach number and is about two times the molecular diameter when the Mach number is 4.

References

Allen, M. P., and Tildesley, D. J., 1987, *Computer Simulation of Liquids*, Clarendon Press, Oxford.

Bird, G. A., 1970, "Aspects of the Structure of Strong Shock Waves," *Physics of Fluids*, Vol. 13, pp. 1172–1177.

Bird, G. A., 1976, *Molecular Gas Dynamics*, Clarendon Press, Oxford.

Boyd, I. D., 1970, "Rotational-Translational Energy Transfer in Rarefied Nonequilibrium Flows," *Physics of Fluids A*, Vol. 2, pp. 447–452.

Ciccotti, G., and Hoover, W. G., (eds), 1986, *Molecular-Dynamics Simulation of Statistical-Mechanical Systems*, North-Holland Physics Publishing, Amsterdam.

Erwin, D. A., Pham-Van-Diep, G. C., and Muntz, E. P., 1991, "Nonequilibrium Gas Flows. I: A Detailed Validation of Monte Carlo Direct Simulation for Monatomic Gases," *Physics of Fluids A*, Vol. 3, pp. 697–705.

Holian, B. L., Hoover, W. G., Moran, B., and Straub, G. K., 1980, "Shock-Wave Structure via Nonequilibrium Molecular Dynamics and Navier-Stokes Continuum Mechanics," *Physical Review A*, Vol. 22, pp. 2798–2808.

Holian, B. L., 1988, "Modeling Shock-Wave Deformation via Molecular Dynamics," *Physical Review A*, Vol. 37, pp. 2562–2568.

Klimenko, V. Yu., and Dremin, A. N., 1979, "Structure of a Shock-Wave Front in a Liquid," *Soviet Physics*, Doklady, Vol. 24, pp. 984–985.

Muntz, E. P., Weaver, D. P., and Campbell, D. H., (eds.), 1989, "Rarefied Gas Dynamics: Theoretical and Computational Techniques," AIAA, Washington, D.C.

Nanbu, K., and Watanabe, Y., 1984, "Analysis of the Internal Structure of Shock Waves by Means of the Exact Direct-Simulation Method," *Rarefied Gas Dynamics*, H. Oguchi, ed., University of Tokyo Press, Tokyo, pp. 183–190.

Satoh, A., 1994a, "Rankine-Hugoniot Relations for Lennard-Jones Liquids," ASME Journal of Fluids Engineering, [to be published].

Satoh, A., 1994b, "A New Outer Boundary Condition for Molecular Dynamics Simulations and Its Application to a Rarefied Gas Flow Past a Cylinder (Periodic-Shell Boundary Condition)," *Advanced Powder Technology*, Vol. 5, pp. 105–117.

Schwartz, L. M., and Hornig, D. F., 1963, "Navier-Stokes Calculations of Argon Shock Waves Structure," *Physics of Fluids*, Vol. 6, pp. 1669–1675.

Takayama, K., 1987, *Shock Waves*, Maruzen, Tokyo (in Japanese).

Tsai, D. H., and Trevino, S. F., 1981, "Thermal Relaxation in a Dense Liquid under Shock Compression," *Physical Review A*, Vol. 24, pp. 2743–2757.

The Influence of Swirl Brakes on the Rotordynamic Forces Generated by Discharge-to-Suction Leakage Flows in Centrifugal Pumps

J. M. Sivo

A. J. Acosta

C. E. Brennen

T. K. Caughey

Division of Engineering
and Applied Science,
California Institute of Technology,
Pasadena, CA 91125

Increasing interest has been given to swirl brakes as a means of reducing destabilizing rotordynamic forces due to leakage flows in new high speed rocket turbopumps. Although swirl brakes have been used successfully in practice (such as with the Space Shuttle HPOTP), no experimental tests until now have been performed to demonstrate their beneficial effect over a range of leakage flow rates. The present study investigates the effect of swirl brakes on rotordynamic forces generated by discharge-to-suction leakage flows in the annulus of shrouded centrifugal pumps over a range of subsynchronous whirl ratios and various leakage flow rates. In addition, the effectiveness of swirl brakes in the presence of leakage inlet (pump discharge) swirl is also demonstrated. The experimental data demonstrates that with the addition of swirl brakes a significant reduction in the destabilizing tangential force for lower flow rates is achieved. At higher flow rates, the brakes are detrimental. In the presence of leakage inlet swirl, brakes were effective over all leakage flow rates tested in reducing the range of whirl frequency ratio for which the tangential force is destabilizing.

Introduction

Previous experimental and analytical results have shown that discharge-to-suction leakage flows in the annulus of a shrouded centrifugal pump contribute substantially to the fluid induced rotordynamic forces (Adkins, 1988). Experiments conducted in the Rotor Force Test Facility (RFTF) at Caltech on an impeller undergoing a prescribed whirl have indicated that the leakage flow contribution to the normal and tangential forces can be as much as 70 and 30 percent of the total, respectively (Jery, 1986). Recent experiments at Caltech have examined the rotordynamic consequences of leakage flows and have shown that the rotordynamic forces are functions not only of the whirl ratio but also of the leakage flow rate and the impeller shroud to pump housing clearance. The forces were found to be inversely proportional to the clearance and a region of forward subsynchronous whirl was found for which the average tangential force was destabilizing. This region decreased with flow coefficient (Guinzburg, 1992a).

The motivation for the present research is that the previous experiments have shown that leakage inlet (pump discharge) swirl can increase the cross-coupled stiffness coefficient (in some tests by over 100 percent) and hence increase the range of positive whirl for which the tangential force is destabilizing. One might therefore surmise that if the swirl velocity within the leakage path were reduced, then the destabilizing tangential force might be reduced. One way of reducing the leakage flow swirl is with the use of ribs or swirl brakes on the housing. In fact, swirl brakes installed upstream of the interstage seal on the Space Shuttle Main Engine High Pressure Oxygen Turbopump completely eliminated the subsynchronous whirl motion over the steady state operating range of the unit (Childs, 1990). The present study investigates the influence of swirl brakes on the rotordynamic forces generated by discharge-to-suction leakage flows in shrouded centrifugal pumps over a range of subsynchronous whirl ratios and various leakage flow rates typical of present rocket turbopump designs. In addition, the effectiveness of swirl brakes in the presence of leakage inlet (pump discharge) swirl is also demonstrated.

Rotordynamic Forces

Figure 1 shows a schematic of the hydrodynamic forces that act on a rotating impeller whirling in a circular orbit. F_x^* and F_y^* are the instantaneous lateral forces in the laboratory frame. Ω is the whirl radian frequency and ω is the main shaft radian frequency. The eccentricity of the orbit is given by ϵ. The

Contributed by the Fluids Engineering Division for publication in the JOURNAL OF FLUIDS ENGINEERING. Manuscript received by the Fluids Engineering Division December 16, 1993; revised manuscript received May 11, 1994. Associate Technical Editor: L. Nelik.

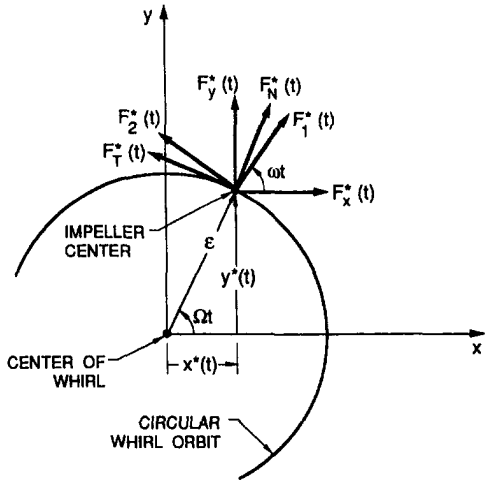

Fig. 1 Schematic of the fluid-induced forces acting on an impeller whirling in a circular orbit

lateral forces are given in linear form as:

$$\begin{pmatrix} F_x^*(t) \\ F_y^*(t) \end{pmatrix} = \begin{pmatrix} F_{ox}^* \\ F_{oy}^* \end{pmatrix} + [A^*] \begin{pmatrix} x^*(t) \\ y^*(t) \end{pmatrix} \tag{1}$$

F_{ox}^* and F_{oy}^* are the steady forces which result from flow asymmetries in the volute. $[A^*]$ is the rotordynamic force matrix. It is a function of the mean flow conditions, pump geometry, whirl frequency ratio Ω/ω and if outside the linear range it may also be a function of the eccentricity ϵ. In the case of a circular whirl orbit:

$$x^*(t) = \epsilon \cos(\Omega t) \tag{2}$$

$$y^*(t) = \epsilon \sin(\Omega t) \tag{3}$$

The normal and tangential forces for a circular whirl orbit are given by (Jery, 1986 and Franz 1989):

$$F_n^*(t) = \frac{1}{2}(A_{xx}^* + A_{yy}^*)\epsilon \tag{4}$$

$$F_t^*(t) = \frac{1}{2}(-A_{xy}^* + A_{yx}^*)\epsilon \tag{5}$$

Rotordynamic Coefficients and Stability

To study the stability of an impeller, it is convenient for rotordynamicists to fit the dimensionless normal force F_n to a quadratic function of the whirl ratio and to fit the dimensionless tangential force F_t to a linear function of the whirl ratio. The expressions are given by:

$$F_n = M\left(\frac{\Omega}{\omega}\right)^2 - c\left(\frac{\Omega}{\omega}\right) - K \tag{6}$$

$$F_t = -C\left(\frac{\Omega}{\omega}\right) + k \tag{7}$$

where the dimensionless coefficients are the direct added mass (M), direct damping (C), cross-coupled damping (c), direct stiffness (K), and cross-coupled stiffness (k). As can be seen from (7), a positive cross-coupled stiffness is destabilizing because it starts the forward whirl of the impeller since it is equal to the tangential force at zero whirl ratio. Also, from (6), a large negative direct stiffness is destabilizing because it promotes a positive normal force which increases the eccentricity of the whirl orbit.

A convenient measure of the rotordynamic stability is the ratio of the cross-coupled stiffness to the direct damping (i.e., k/C) termed the whirl ratio. This is just a measure of the range of positive whirl frequency ratios for which the tangential force is destabilizing.

Test Apparatus

The present experiments were conducted in the Rotor Force Test Facility (RFTF) at Caltech. The leakage flow test section of the facility is shown in Fig. 2.

The working fluid is water. The main components of the test section apparatus consist of a solid or dummy impeller (or rotating shroud), a housing (or stationary shroud) instrumented for pressure measurements, a rotating dynamometer (or internal force balance), an eccentric whirl mechanism (not shown), a leakage exit seal ring and a leakage inlet swirl vane (shown installed in Fig. 3). The solid impeller is used so that leakage flow contributions to the forces are measured but the main through flow contributions are not experienced. The inner surface of the housing has been modified to accommodate meridional ribs or swirl brakes along the entire length of the leakage annulus. The ribs are each 3/16 of an inch wide and 2 mm high. Up to 8 equally spaced ribs can be installed. The leakage flow annulus between the impeller and housing is inclined at 45 deg to the axis of rotation. The nominal clearance between the solid impeller and the housing can be varied by axial adjustment of the housing. The flow through the leakage path is generated by an auxiliary pump. The solid impeller is

Nomenclature

- $[A^*]$ = rotordynamic force matrix
- B = depth of logarithmic spiral channel on swirl vane
- c = cross-coupled damping coefficient, normalized by $\rho\pi\omega^2R_2^2L\epsilon$
- C = direct damping coefficient, normalized by $\rho\pi\omega^2R_2^2L\epsilon$
- $F_x^*(t)$ = lateral horizontal force in the laboratory frame
- $F_y^*(t)$ = lateral vertical force in the laboratory frame
- F_{ox}^* = steady horizontal force
- F_{oy}^* = steady vertical force
- F_n^* = force normal to whirl orbit
- F_n = force normal to whirl orbit normalized by $\rho\pi\omega^2R_2^2L\epsilon$
- F_t^* = force tangent to whirl orbit
- F_t = force tangent to whirl orbit normalized by $\rho\pi\omega^2R_2^2L\epsilon$
- F_1, F_2 = lateral forces in rotating frame
- H = clearance between impeller shroud and housing
- k = cross-coupled stiffness coefficient normalized by $\rho\pi\omega^2R_2^2L\epsilon$
- K = direct stiffness coefficient normalized by $\rho\pi\omega^2R_2^2L\epsilon$
- L = axial length of impeller
- M = direct added mass coefficient normalized by $\rho\pi\omega^2R_2^2L\epsilon$
- Q = volumetric leakage flow rate
- R_2 = radius of impeller at leakage inlet
- u_s = mean leakage inlet path velocity of fluid
- u_θ = mean leakage inlet swirl velocity of fluid
- $x^*(t)$ = horizontal displacement of impeller on its orbit
- $y^*(t)$ = vertical displacement of impeller on its orbit
- α = turning angle of logarithmic spiral channel on swirl vane
- Γ = leakage inlet swirl ratio, $u_\theta/\omega R_2$
- ϵ = eccentricity of impeller's circular whirl orbit
- ρ = density of leakage fluid
- ϕ = leakage flow coefficient, $u_s/\omega R_2$
- ω = main shaft radian frequency
- Ω = whirl radian frequency

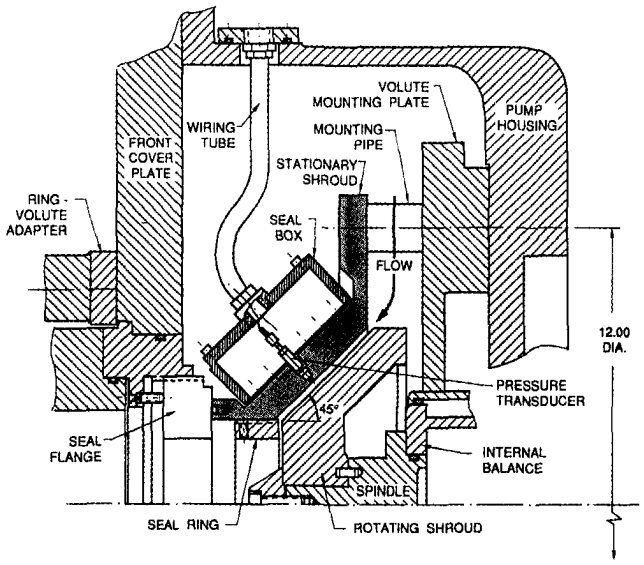

Fig. 2 Leakage flow test section (Zhuang, 1989)

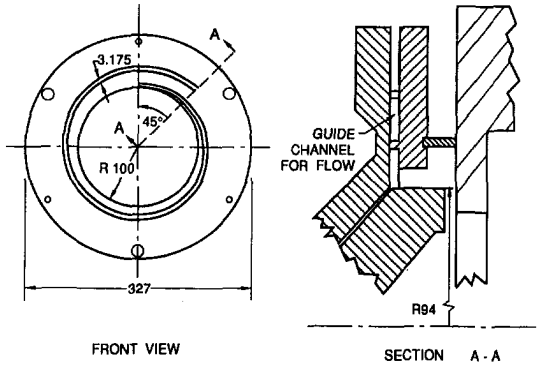

Fig. 3 Installation of leakage inlet swirl vane. Dimensions in mm (Guinzburg, 1992b)

mounted on a spindel attached to the rotating dynamometer connected to a data acquisition system which permits measurements of the rotordynamic force matrix. Jery (1986) and Franz (1989) describe the operation of the dynamometer. The eccentric drive mechanism imposes a circular whirl orbit on the basic main shaft rotation. The radius of the circular whirl orbit (or eccentricity) can be varied. The seal ring at the leakage exit models a wear ring. The clearance between the seal ring and impeller face is adjustable. The effect of swirl was investigated by installing a swirl vane at the leakage inlet to introduce prerotated fluid in the direction of shaft rotation. Figure 3 shows that the vane consists of a logarithmic spiral channel with a turning angle of 2 deg. The swirl ratio Γ (the ratio of the leakage flow circumferential velocity to the impeller tip velocity) is varied by changing the leakage flow rate. The swirl ratio depends on the flow coefficient according to:

$$\frac{\Gamma}{\phi} = \frac{H}{B\,\mathrm{Tan}(\alpha)} \tag{8}$$

B is the depth of the logarithmic spiral channel equal to 0.125 in. A derivation of Eq. (8) can be found in Guinzburg (1992a).

Test Matrix

This experiment is designed to measure the rotordynamic forces due to simulated leakage flows for different parameters

Table 1 Tests without swirl

rpm	Ω/ω	Brakes	Q (GPM)	ϕ
1000	−0.9 to +0.9	0	0	0.0
			10	0.026
			20	0.052
			30	0.077
		4	0	0.0
			10	0.026
			20	0.052
			30	0.077
		8	0	0.0
			10	0.026
			20	0.052
			30	0.077
2000	−0.6 to +0.7	0	0	0.0
			10	0.013
			20	0.026
			30	0.039
		4	0	0.0
			10	0.013
			20	0.026
			30	0.039
		8	0	0.0
			10	0.013
			20	0.026
			30	0.039

Table 2 Tests with swirl

rpm	Ω/ω	Brakes	Q (GPM)	ϕ	Γ
2000	−0.6 to +0.7	0	0	0.0	0.0
			10	0.013	0.5
			20	0.026	1.0
			30	0.039	1.5
		4	0	0.0	0.0
			10	0.013	0.5
			20	0.026	1.0
			30	0.039	1.5
		8	0	0.0	0.0
			10	0.013	0.5
			20	0.026	1.0
			30	0.039	1.5

such as whirl frequency ratio, shaft speed, leakage flow coefficient, number of swirl brake ribs and leakage inlet swirl ratio. For all tests a nominal annulus clearance H of 0.167 in, a whirl eccentricity ϵ of 0.0465 in and a leakage exit face seal clearance of 0.04 in were maintained. Tests without leakage inlet swirl were conducted at shaft speeds ω of 1000 and 2000 rpm, leakage flow rates Q of 0, 10, 20, and 30 GPM and 0, 4, and 8 brake ribs. For the 1000 rpm runs, the above flow rates correspond to flow coefficients ϕ of 0.0, 0.026, 0.052 and 0.077, respectively. For the 2000 rpm runs, the above flow rates correspond to flow coefficients ϕ of 0.0, 0.013, 0.026, and 0.039, respectively. The above flow coefficients cover the range of typical leakage rates for the new Space Shuttle Alternate Turbopump (ATP) presently being developed. For the 1000 rpm runs, tests are performed for whirl frequency ratios in the range $-0.9 \le \Omega/\omega \le +0.9$ at 0.1 increments. For the 2000 rpm runs, tests are performed for whirl frequency ratios in the range $-0.6 \le \Omega/\omega \le +0.7$ at 0.1 increments. Tests with the swirl vane installed are conducted at a shaft speed of 2000 rpm and the same flow rates as above. With the swirl vane, the above leakage flow rates yield swirl ratios Γ of 0.0, 0.5, 1.0, and 1.5, respectively. The above test matrix is summarized in Tables 1 and 2.

Results for Tests Without Leakage Inlet Swirl

Figures 4 and 5 show plots of the dimensionless rotordynamic coefficients for 2000 and 1000 rpm, respectively for the three different number of brake ribs. Figures 6 and 7 show the whirl ratio. Tests are done at two different rotor speeds to access the Reynolds number effects. The 2000 rpm runs are shown first since they give the results at a lower flow coefficient range.

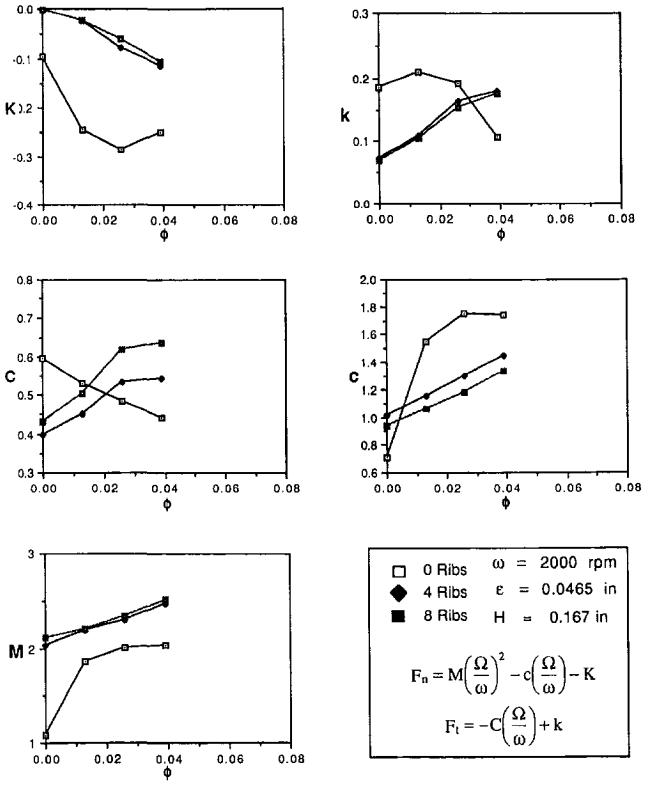

Fig. 4 Rotordynamic coefficients at 2000 rpm, no swirl

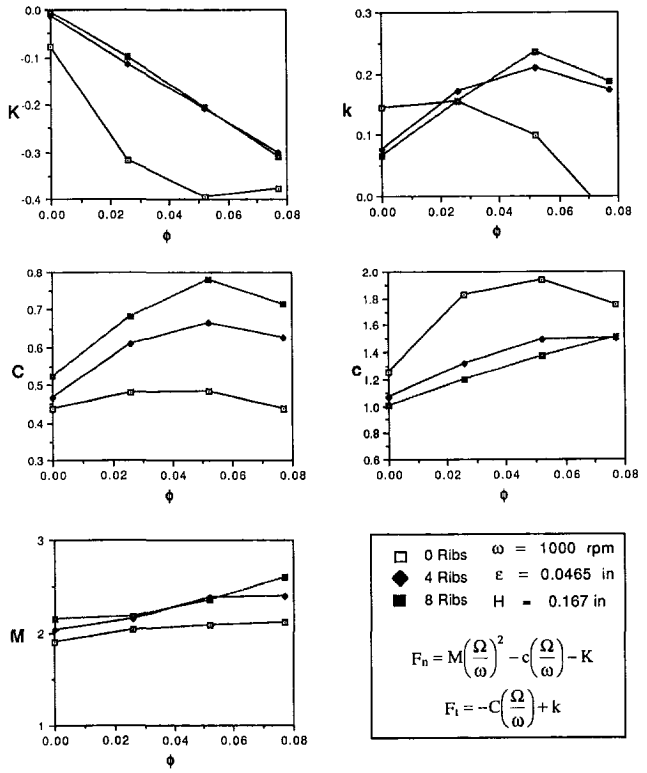

Fig. 5 Rotordynamic coefficients at 1000 rpm, no swirl

A comparison of Figs. 4 and 5 show differences between corresponding coefficient plots at the lower flow coefficients indicating that Reynolds number effects are important at low flow rates. At flow coefficients above about 0.03 there seems to be little difference between corresponding coefficient plots at 1000 and 2000 rpm. Reynolds number effects are stronger with no brake ribs installed. C and k seem to have the greatest discrepancies between the 1000 and 2000 rpm runs.

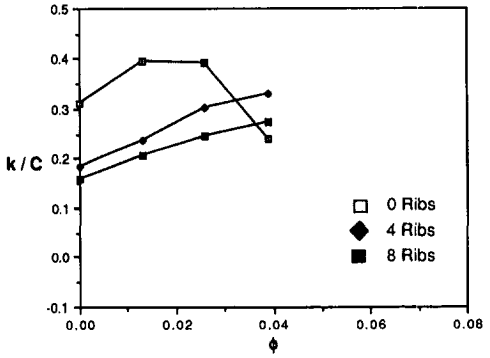

Fig. 6 Whirl ratio at 2000 rpm, no swirl

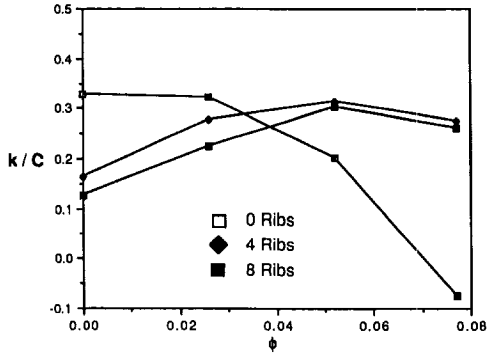

Fig. 7 Whirl ratio at 1000 rpm, no swirl

Focusing on the coefficients corresponding to the tangential force, we can see that with no brakes the tangential force decreases with increasing leakage flow rate, as was found previously by Guinzburg (1992a). The cross-coupled stiffness coefficient, k, is decreased by increasing the flow from 0 to 30 GPM, and for the 1000 rpm case, C remains essentially constant. Hence the range for which the tangential force is destabilizing, k/C, decreases with increasing flow rate. This can be seen in Fig. 7. However, looking at k for the case with 4 or 8 brake ribs, the opposite trend with flow rate is observed. The cross-coupled stiffness increases as the flow rate increases from 0 to 30 GPM in both the 1000 and 2000 rpm runs. The above may appear to indicate that brakes are not beneficial. On the contrary, although the destabilizing tangential force with brakes increases with flow rate, there is a flow rate below which the tangential force with brakes is less than the tangential force without brakes. From the k plots in Fig. 4 and 5 we can see that below $\phi = 0.025$ the cross-coupled stiffness coefficient is reduced by the addition of 4 or 8 brakes. 8 brakes are only marginally more effective than 4. The beneficial effect of brakes is better exemplified by looking at the whirl ratio plots in Figs. 6 and 7. Below about $\phi = 0.03$, the range of destabilizing tangential force is much less with the addition of brakes.

Focusing on the coefficients corresponding to the normal force, we can see that with no brakes, the normal force increases with increasing leakage flow rate. K becomes more negative with increasing flow, hence increasing the normal force at zero whirl frequency and therefore is destabilizing. The same is true with 4 or 8 brakes, but we can also see from K that the destabilizing normal force is significantly reduced by the addition of brakes throughout the range of flow rates tested.

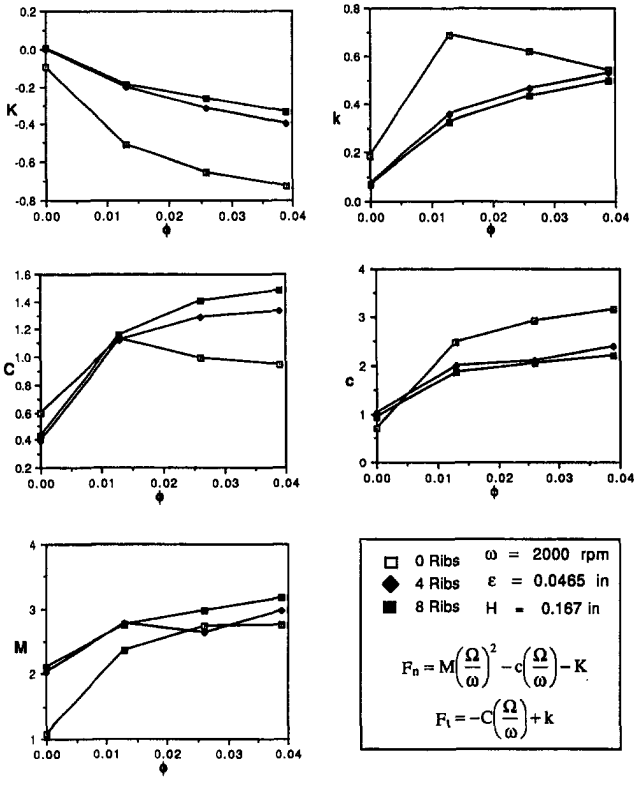

Fig. 8 Rotordynamic coefficients at 2000 rpm with swirl

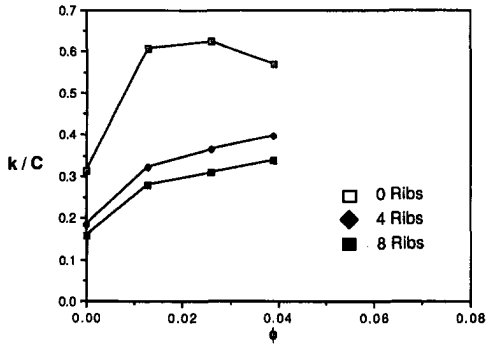

Fig. 9 Whirl ratio at 2000 rpm with swirl

Results for Tests With Leakage Inlet Swirl

Figure 8 shows plots of the dimensionless rotordynamic coefficients for the 2000 rpm runs with leakage inlet swirl for the three different number of ribs. Figure 9 shows the whirl ratio. As was previously found by Guinzburg (1992b), swirl dramatically increases the tangential force. This is evident by comparing the plot of k without swirl from Fig. 4 with the plot of k with swirl from Fig. 8. Once again, with no brakes, it can be seen that as the leakage rate increases, the tangential forces decrease, even though in the process the swirl ratio is increased. The stabilizing effect of an increase in flow rate dominates the destabilizing effect of an increase in swirl ratio. When 4 or 8 brake ribs are used, the opposite trend with flow rate is observed, as shown with the results without swirl. With brakes, the tangential force increases with flow rate and swirl ratio. But, for the entire flow range tested, the cross-coupled stiffness is decreased by the addition of brakes.

Focusing on the coefficient K corresponding to the normal force, K is much large in the presence of swirl. We can see that with no brakes the normal force increases with increasing leakage flow rate. The same is true with 4 or 8 brakes, although from K, the destabilizing normal force is significantly reduced by the addition of brakes throughout the range of flow rates tested.

The most dramatic beneficial effect of brakes is found by comparing the whirl ratio plots for 4 or 8 brakes without and with swirl, Figs. 6 and 9, respectively. The 4 or 8 brake runs with and without swirl are almost identical. This indicates that the brakes almost completely eliminated the effect of swirl. With brakes present, swirl produces only a slight increase in the range for which the tangential force is destabilizing. Also, looking at Fig. 9, for all flow rates tested, the addition of brakes reduces the range for which the tangential force is destabilizing.

Conclusions

The influence of swirl brakes on the rotordynamic forces generated by discharge-to-suction leakage flows in centrifugal pumps with and without leakage inlet swirl has been investigated. The destabilizing normal force at zero whirl is reduced by the addition of brakes. The tangential force and the range of whirl frequency ratios for which the tangential force is destabilizing is reduced by the addition of brakes for low leakage flow rates. Brakes are beneficial in reducing the tangential force up to a higher leakage flow rate in the presence of leakage inlet swirl. Finally, the increase in the range of whirl frequency ratios for which the tangential force is destabilizing due to an increase in the leakage inlet swirl is nearly eliminated by the addition of swirl brakes.

Acknowledgments

The assistance provided by Asif Khalak and Kyle Roof with the experimental program is greatly appreciated. We would also like to thank the NASA George Marshall Space Flight Center for support under Grant NAG8-118 and technical monitor Henry Stinson.

References

Adkins, D. R. and Brennen, C. E., 1988, "Analysis of Hydrodynamic Radial Forces on Centrifugal Pump Impellers," ASME JOURNAL OF FLUIDS ENGINEERING, Vol. 110, No. 1, pp. 20–28.

Childs, D. W., Baskharone, E., and Ramsey, C., 1990, "Test Results for Rotordynamic Coefficients of the SSME HPOTP Turbine Interstage Seal with Two Swirl Brakes," ASME, *Journal of Tribology*, 90-Trib-45.

Franz, R. J., 1989, "Experimental Investigation of the Effect of Cavitation on the Rotordynamic Forces on a Whirling Centrifugal Pump Impeller," Ph.D. thesis, California Institute of Technology.

Guinzburg, A., 1992a, "Rotordynamic Forces Generated By Discharge-To-Suction Leakage Flows in Centrifugal Pumps," Ph.D. thesis, California Institute of Technology.

Guinzburg, A., 1992b, "The Effect of Inlet Swirl on the Rotordynamic Shroud Forces in a Centrifugal Pump," ASME Paper 92-GT-126.

Jery, B., 1986, "Experimental Study of Unsteady Hydrodynamic Force Matrices on Whirling Centrifugal Pump Impellers," Ph.D. thesis, California Institute of Technology.

Zhuang, F., 1989, "Experimental Investigation of the Hydrodynamic Forces on the Shroud of a Centrifugal Pump Impeller," E249.9, Division of Engineering and Applied Science, California Institute of Technology.

Measurement and Analysis of Static Pressure Field in a Torque Converter Pump

R. R. By*
NAO Engineering Center,
General Motors Corporation,
Warren, MI 48090

B. Lakshminarayana
Aerospace Engineering Department,
The Pennsylvania State University,
University Park, PA

In this paper, the static pressure field and performance parameters of a torque converter pump are measured, analyzed, and interpreted under three turbine/pump speed ratio conditions (0, 0.6, and 0.8). A potential flow code is used to predict the static pressure distribution. Results show that: 1) centrifugal force has a dominant effect on the static pressure rise in the pump; 2) the static pressure field is generally poor at the core section; and 3) the potential flow code can fairly well predict the static pressure distribution at the blade mid-span, but not at the core and shell sections.

Introduction

The automotive torque converter, as shown in Fig. 1, is a complex turbomachine used to transfer power from an engine to a transmission. It consists of a mixed-flow pump connected to the engine crankshaft, a mixed-flow turbine attached directly to the transmission, and either a mixed-flow or an axial-flow stator attached to a stationary housing through a one-way clutch. Torque converter flow fields are difficult to measure and to visualize. The geometry of the elements is highly three-dimensional with a high angle of blade turning. Unlike other turbomachines, the torque converter is a closed-loop machine with the same oil circulating through its elements. In addition, the torque converter elements operate under an extremely wide range of incidence angle. These physical features give rise to complex three-dimensional flow fields with three-dimensional through-flow distribution, strong secondary-flow phenomena, large flow separation regions, and highly unsteady characteristics that lead to large losses in the performance of the torque converter.

There are three main motives for studying torque converter flow fields. First, converter axial length is an important parameter in the powertrain packaging of front-wheel-drive vehicles. Its effects on performance characteristics must be quantified. Second, since the lock-up clutch has a small effect in the EPA urban driving cycle, significant improvement in vehicle fuel economy and performance can be obtained by optimizing converter flow paths. Third, the lead-time required to design and build new torque converters can be significantly reduced if the physics of the flow fields are understood.

Kubo et al. (1991) used a steady-state five hole probe to measure the three velocity components, static pressure and total pressure in the gap regions of a torque converter under a speed ratio range of 0 to 0.8. The measured deviation angles were used to improve the performance prediction of torque converters.

By and Lakshminarayana (1991) measured steady-state static pressures in a torque converter stator. Results show that the static pressure distribution is poor at the core section and the potential flow theory can fairly well predict the static pressure distribution at the mid-span, but not at the core and shell sections.

Experimental Facility, Instrumentation, and Measurement Technique

An experimental facility was designed and built to measure static pressures in a torque converter pump. The experimental facility consists of: 1) an experimental torque converter unit, 2) an input dynamometer to drive the torque converter pump, 3) an eddy-current dynamometer to absorb the output power of the torque converter, 4) a hydraulic system to cool, pressurize and lubricate the torque converter, and 5) a control system to control rotational speeds and torque's.

The experimental torque converter has an outer diameter of 230 mm and a peak efficiency of about 82 percent. The pump has 27 blades with 1 mm constant blade thickness; an inlet blade angle of −25 degrees at core and −40 degrees at shell; and, an outlet blade angle of zero degrees at both blade sections. The meridional blade length of the pump at the core is about 3 times shorter than that at the shell. The turbine has 29 blades with 1 mm of constant thickness; an inlet blade angle of 55 degrees at core and 49 degrees at shell; and, an outlet blade angle of −64 degrees at core and −57 degrees at shell. The meridional blade length of the turbine at the core is about 2.5 times shorter than that at the shell. The stator has 19 airfoil blades with an inlet blade angle of about 7 degrees at both core and shell and an outlet blade angle of 63 degrees.

Steady-state performance characteristics of the experimental torque converter are shown in Fig. 2. It is important to measure static pressures under constant turbine/pump speed ratio conditions, since it is the key independent performance param-

*Presently, President, Fluid Machinery Consulting, New Baltimore, MI.

Contributed by the Fluids Engineering Division for publication in the JOURNAL OF FLUIDS ENGINEERING. Manuscript received by the Fluids Engineering Division March 25, 1993; revised manuscript received October 26, 1994. Associate Technical Editor: L. Nelik.

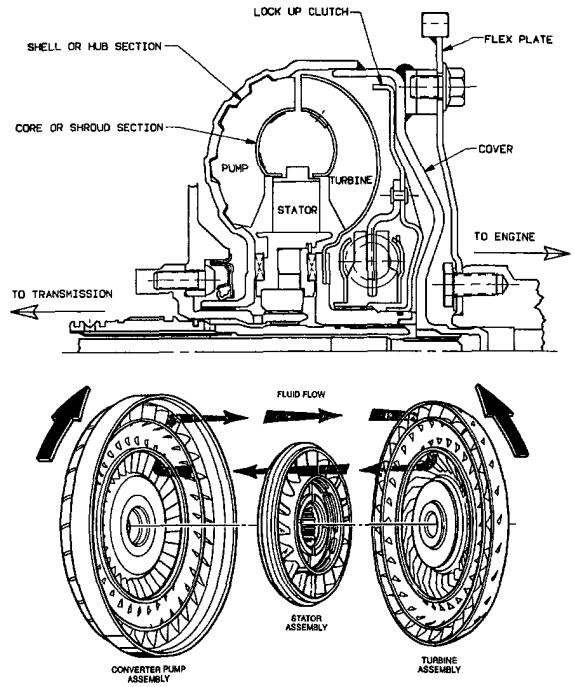

Fig. 1 Components of the automotive torque converter

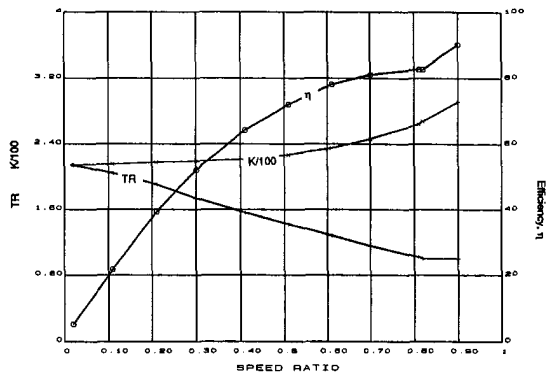

Fig. 2 Steady-state performance characteristics of the experimental torque converter at Tq = 24 Nt-m

Table 1 Test conditions for static pressure measurement

	Condition #1	Condition #2	Condition #3
SR	0	0.6	0.8
N_P, rpm	1050	1160	1300
i_P, degrees	−43	+3	+22
N_T, rpm	0	696	1040
i_T, degrees	+18	+11	0
N_S, rpm	0	0	0
i_S, degrees	+67	−2	−47
$\mathrm{Re}_{L,P}$	44,000	27,000	23,000

eter. Static pressure measurement was conducted under three speed ratio conditions: 0, 0.6, and 0.8. The three test conditions are shown in Table 1. The incidence angles were obtained from a one-dimensional performance analysis. Figure 3 shows the range of the inlet flow angle entering the pump, the turbine, and the stator. The oil temperature inside the torque converter was kept at 60 degrees C during the experiments.

The measurement of static pressures in a rotating pump is a challenging and difficult task. A schematic diagram of the measurement process is shown in Fig. 4. The torque converter arrangement for the measurement of static pressures is shown in Fig. 5. A multi-channel data transmission device is required to transmit pressure signals from the pump rotating frame to a stationary frame. Tubes were routed from the tap locations to the shell housing where they were connected to eight pressure manifolds. A miniature pressure transducer was mounted to the outlet of each manifold. Eight static pressures were measured simultaneously. Electrical output signals from the eight pressure transducers were connected to a slip ring.

A piezoresistive transducer was the only commercial type that satisfied the packaging requirement. Endevco model 8530C-50 was chosen, since it was a high precision type with thermal compensation from −18 to 93°C. Several transducer units were custom-made and the combined linearity, hysteresis, and repeatability was less than ± 0.1 percent.

The slip ring is a brush type with 37 gold alloy rings built by the Quality Aero Technology Corporation. Its outer housing is stationary and carries 3 brushes per ring. The brushes transfer analog pressure signals from the rotating rings to terminals on the stationary housing. A separate hydraulic system was built to lubricate and cool the ring/brush assembly. The

Nomenclature

C_p = static pressure coefficient, $C_p = (p - p_{\mathrm{ref}})/(0.5\rho U_{\mathrm{tip}}^2)$
C_T = blade torque coefficient as defined in Eq. (1)
H = blade span or height
i = incidence angle, $i = \beta_1' - \beta_1$
K = pump speed parameter, $K = N/(Tq)^{0.5}$
L = meridional blade length
N = number of blades/rotational speed in rpm
p = static pressure
$P^* = p + 0.5\,\rho(W^2 - U^2)$
R = radius from the center of machine axis
Re_L = Reynolds number based on meridional blade length, $\mathrm{Re}_L = W_m L_{\mathrm{mid}}/\nu$
SR = ratio of turbine to pump speed
T = blade torque at a blade section
Tq = torque of all pump blades or pump torque
TR = ratio of turbine to pump torque
U, V, W = blade, absolute flow, relative flow velocity
x, y, z = coordinates in the streamwise, pitchwise, and spanwise directions ($x = 0$ at the leading edge)
η = power efficiency, $\eta = SR * TR$
ρ = density in kg/m^3
ν = kinematic viscosity in m^2/s
Ω = angular velocity in rad/s
β, β' = flow, blade angle
ϕ = potential function

Subscripts

m, θ = meridional or through-flow, tangential component shell, core shell, core blade section (see Fig. 1)
P, T, S = pump, turbine, stator
p, s = pressure, suction surface
le, te = leading, trailing edge
centr = centrifugal
ref = reference
tip = tip location of the pump blade
tap = location of a static pressure tap
∞, 1 = upstream, inlet of a blade row

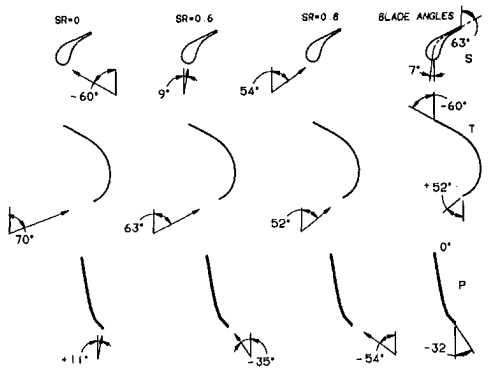

Fig. 3 Range of flow angle entering pump, turbine and stator

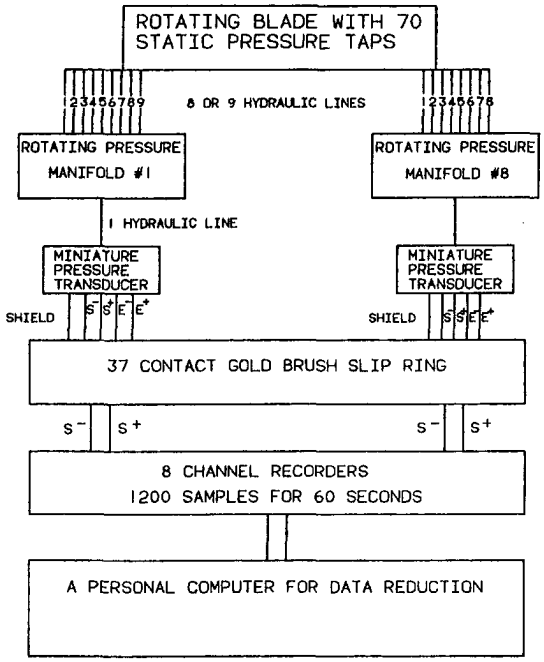

Fig. 4 Schematic diagram of the measurement process

oil temperature of the slip ring was also kept at 60°C. The noise was less than 80 micro volts with 20 micro amps (0.14 kPa based on the sensitivity of 0.57 mV/kPa at 10 V excitation). The noise to signal ratio was typically less than 0.1 percent.

Two electronic recorders were used to collect and store output signals from the slip ring. Each recorder is a four-channel strip chart recorder that is capable of storing up to 32 K of data per channel and reads data at a frequency range of 20 Hz to 250 kHz. The accuracy is ±0.5 percent.

The pressure transducers were mounted to the manifolds at a radius of 105.64 mm from the machine axis--this was the radius where the centrifugal pressure developed during the measurement process. Therefore, a correction must be used to correct for the difference in centrifugal pressure due to the difference in radius. The correction can be obtained from the radial momentum equation and is of the form

$$\Delta p_{\text{centr}} = \frac{1}{2000}\rho\Omega_p^2(R_{\text{tap}}^2 - 0.10564^2) \tag{1}$$

the correction is −42.73 to +10.25 kPa kPa at $SR = 0$, −52.15 to +12.64 kPa at $SR = 0.6$, and −65.50 to +15.88 kPa at $SR = 0.8$.

Results and Discussion

The C_p distributions at the shell, mid-span and core sections are shown in Figs. 6, 7, and 8 for $SR = 0$, $SR = 0.6$, and $SR = 0.8$, respectively. Results are plotted as a function of meridional blade length, so that the area enclosed between the curves can be related directly to the torque exerted by the fluid on the blade. Meridional blade length is normalized by meridional blade length at the shell, since it is the longest length.

Blade Torque. Blade torque is the torque exerted by each pump blade on the fluid. Blade torque is an important parameter in the energy transfer between the fluid and blades of the pump. Since the meridional length of the pump blade is about 3 times longer at the shell than at the core, it is more appropriate to calculate the blade-torque-per-unit meridional length. At any blade section, the blade torque coefficient is

$$C_T = \frac{T}{0.5\rho U_{\text{tip}}^2 H_2 R_{\text{tip}} L} = \int_{x_{le}/L}^{x_{te}/L} \frac{H}{H_2}\frac{R}{R_{\text{tip}}}(C_{p,p} - C_{p,s})d\left(\frac{x}{L}\right) \tag{2}$$

In addition to the dynamic pressure based on pump tip speed, two other parameters are used to normalize the blade torque coefficient. The two parameters are pump blade height or span

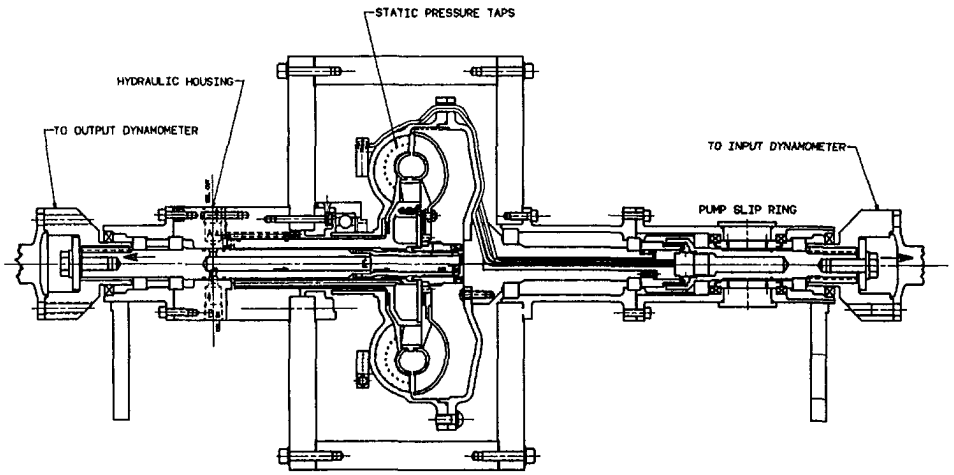

Fig. 5 Torque converter arrangement for the measurement of static pressures in the pump

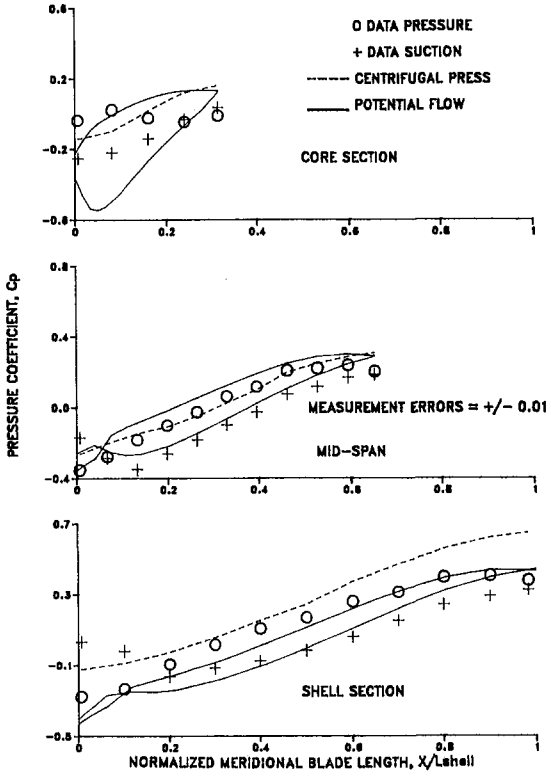

Fig. 6 C_p distribution at $SR = 0$

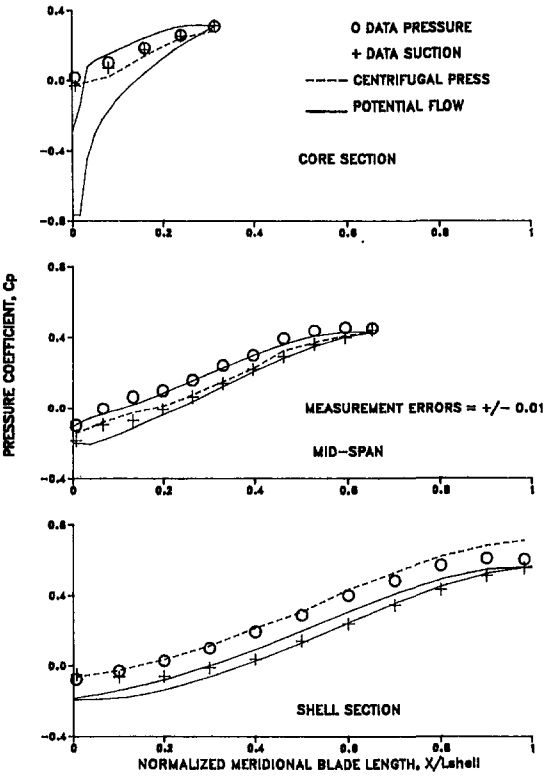

Fig. 7 C_p distribution at $SR = 0.6$

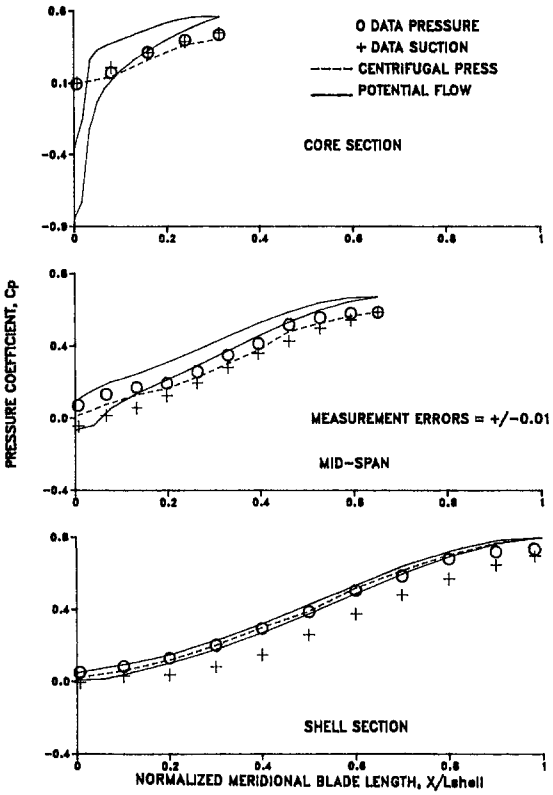

Fig. 8 C_p distribution at $SR = 0.8$

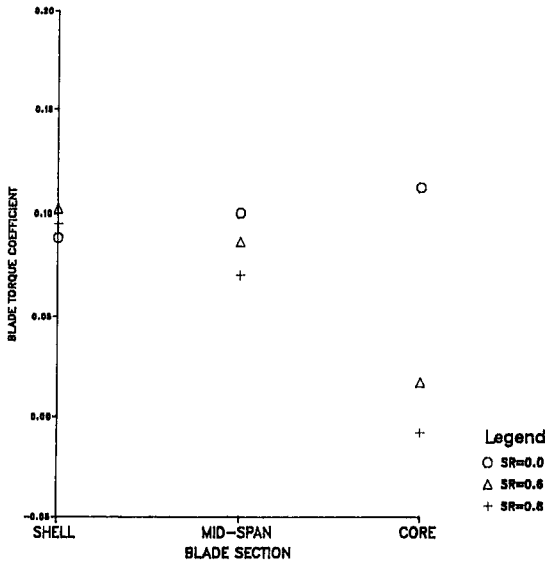

Fig. 9 Distribution of blade torque coefficient (C_T)

at the pump exit, H_2, and pump tip radius, R_{tip}. Equation (2) is used to calculate the blade torque coefficient at the shell, mid-span and core sections under the three speed ratio conditions. Results are shown in Fig. 9.

Under the zero speed ratio condition, the blade torque coefficient is 0.088, 0.100 and 0.112 at the shell, mid-span and core sections, respectively. The blade torque coefficient is almost constant at the three blade sections. The C_T is a maximum at the core section, since the incidence there is a minimum of -36 degrees (vs -43 and -51 degrees at the mid-span and shell, respectively). If the incidence effect is the same at the three blade sections, the blade torque coefficient is expected to be a maximum at the mid-span section (since the effect of the annulus wall boundary layer is a minimum there).

Under the 0.6 speed ratio condition, the C_T is maximum at the shell and minimum at the core. It is 0.103, 0.086 and 0.017 at the shell, mid-span and core sections, respectively. The C_T distribution is good at the mid-span and shell sections, since

the incidence angle is only a few degrees and the flow is well behaved.

Under the 0.8 speed ratio condition, the C_T distribution is good at the mid-span and shell sections and is poor at the core. It is 0.095, 0.070, and −0.010 at the shell, mid-span and core sections, respectively. The C_T is even negative at the core section; this result is evident from the static pressure distribution of Fig. 8. The C_T is higher at the shell than at the mid-span, since the incidence at the shell is smaller (+14 versus +22 degrees).

Static Pressure Rise. The static pressure rise along a streamline is

$$\frac{p - p_1}{0.5\rho U_{tip}^2} = (C_p - C_{p,1}) = \left(\frac{U^2 - U_1^2}{U_{tip}^2}\right) + \left(\frac{W_1^2 - W^2}{U_{tip}^2}\right) - \frac{\Delta P^*}{0.5\rho U_{tip}^2} \quad (3)$$

The static pressure rise consists of three terms. The first term is the pressure rise due to centrifugal pressure. The second term is the contribution due to the diffusion of relative velocity. The third term is the total pressure loss due to viscous effects.

The static pressure rise due to centrifugal pressure (the first term in the above equation) is calculated at the shell, mid-span and core sections. The calculated pressure rise is compared with the measured static pressure distribution. From the pump inlet to the pump exit of any blade section, the difference between the two results represents: 1) the loss of static pressure due to viscous effects and 2) the change in static pressure due to the diffusion of relative velocity. The comparison is shown in Figs. 6, 7, and 8 for the speed ratios of 0, 0.6 and 0.8, respectively. It is evident that centrifugal force has the dominant effect on the static pressure rise in the pump.

Under the zero speed ratio condition, the static pressure rise due to centrifugal pressure is significantly higher than the measured static pressure data at the three blade sections. This is due to the effect of a large negative incidence angle ($i = -43$ degrees) and the third term in Eq. (3) becomes large.

Under the 0.6 and 0.8 speed ratio conditions, the static pressure rise due to centrifugal pressure is about the same as the measured data at the mid-span and core sections, but it is about 10 percent higher at the shell. The discrepancy at the shell is probably caused by the diffusion of through-flow velocity from the core to the shell section.

Interpretation of the C_p Distribution at $SR = 0$. At the blade mid-span section, the C_p distribution shows that the flow at $SR = 0$ is poorly behaved in the first 7 percent of the shell meridional length and is fairly well-behaved beyond this point to the trailing edge. As a result of a large negative incidence angle of about −43 degrees (see Table 1), the role of the pressure and suction surfaces is reversed from the leading edge to about 7 percent of the shell meridional length. The incidence effect is most pronounced in the pump, since the blade was constructed from sheet metal with a very sharp leading edge. This incidence effect leads to a significant loss in total pressure; the pump pressure rise is only 46 percent of the dynamic pressure based on tip speed. The pump pressure rise would have been significantly higher if the blade leading edge was round and blunt (in a similar fashion to the leading edge of the stator).

At the core section, the C_p distribution shows that the flow is poorer than that at the mid-span and the last 25 percent of the blade is not effective. As a result of a large negative incidence angle of about −36 degrees, the C_p is expected to be higher on the blade suction surface near the leading edge. The fact that the C_p is actually lower there indicates that the flow is poorly behaved and the through-flow velocity is small. On the pressure surface, the flat C_p distribution also indicates that the through-flow velocity is small. Flow separation may exist near the core section.

At the shell section, the C_p distribution shows that the flow is also worse than that at the mid-span. The flow is especially poor in the first 17 percent of the shell meridional length. In this region, the role of the pressure and suction surfaces are reversed. This is due to the combined effect of a large negative incidence angle and the shell annulus boundary layer. The incidence angle at the shell section is a maximum of about −51 degrees; the inlet blade angle is −40, −32, and −25 degrees at the shell, mid-span and core sections, respectively. As a result, the pump pressure rise at the shell is very poor; it is only 48 percent of the dynamic pressure which is about the same as that at the mid-span.

Interpretation of the C_p Distribution at $SR = 0.6$. At the mid-span section, the C_p distribution of Fig. 7 shows that the flow is fairly well-behaved under the speed ratio of 0.6. The pressure rise is significantly higher than that at $SR = 0$ (59 versus 46 percent of the dynamic pressure), since the incidence angle is only about 3 degrees (see Table 1). Therefore, the incidence angle has a major effect on the static pressure rise. The blade loading is also significantly higher than that at $SR = 0$. There is no evidence of flow separation at the mid-span under the 0.6 speed ratio condition.

At the core section, the static pressure distribution shows that the pressure rise at $SR = 0.6$ is significantly higher than that at $SR = 0$ (32 versus 16 percent of the dynamic pressure). The flow at the core section is, however, still poorly behaved in spite of the large pressure rise. The blade loading is very poor, the C_T is only 0.017. This is probably due to combined effects of the positive incidence angle of +10 degrees, the core annulus boundary layer, and flow blockage effects at the inner housing of the stator. Again, flow separation may occur near the core section.

At the shell section, the C_p distribution shows that the flow is poorer than that at the mid-span, but is better than that at the core. The static pressure rise is significantly higher than that at $SR = 0$ (64 versus 48 percent of the dynamic pressure), since the incidence angle is only about −5 degrees. It is again evident that the incidence angle has a profound effect on the static pressure rise. The blade loading is also significantly higher than that at $SR = 0$.

Interpretation of the C_p Distribution at $SR = 0.8$. At the mid-span section, the C_p distribution of Fig. 8 shows that the pressure rise at $SR = 0.8$ is significantly higher than that at $SR = 0$, but slightly lower than that at $SR = 0.6$ (57 at $SR = 0.8$ versus 59 percent at $SR = 0.6$ versus 46 percent at $SR = 0$ of the dynamic pressure). This is again caused by the incidence effect. The incidence is a minimum of +3 degrees at $SR = 0.6$, a maximum of −43 degrees at $SR = 0$, and +22 degrees at $SR = 0.8$ (see Table 1). It is also seen from Fig. 8 that the C_p distribution on the pressure surface is poor between 7 and 46 percent of the shell meridional length. This phenomenon may be caused by the diffusion of the through-flow velocity from the suction to pressure surface as the fluid flows from the pump inlet to exit.

At the core section, the C_p distribution shows that the pressure rise at $SR = 0.8$ is about the same as that at $SR = 0.6$ (35 versus 32 percent versus 16 percent of the dynamic pressure). The flow at the core section is, however, still poorly behaved in spite of the large pressure rise. The blade loading is very poor; the C_T is even negative. This is also due to combined effects of a positive incidence angle of +29 degrees, the core annulus boundary layer and flow blockage effects at the inner housing of the stator. Again, flow separation may occur near the core section.

At the shell section, the C_p distribution shows that the pressure rise at $SR = 0.8$ is higher than that at $SR = 0.6$ and $SR = 0$ (69 percent vs 64 percent vs 48 percent of the dynamic

pressure). The incidence angle at the shell is about +14 degrees. The flow is better behaved at the shell than at the mid-span and core sections, since the incidence angle is a minimum there (+14, +22, and +29 degrees at the shell, mid-span, and core sections, respectively).

A Navier-Stokes analysis conducted by By et al. (1995) in the same torque converter pump shows that: 1) the flow near the core section is indeed separated, 2) there is a strong secondary flow field in the pump, and 3) there is a strong diffusion of the through-flow velocity from core to shell and from the suction to pressure surface as the fluid flows from the pump inlet to exit.

Potential Flow Analysis. Although the pump flow field is not irrotational, an assessment is made using the potential flow equation. If the flow is irrotational, a scalar potential function ϕ exists such that

$$\bar{\nabla}\phi = \bar{V} \tag{4}$$

where $\bar{V} = \bar{W} + \bar{U}$ is the absolute flow velocity. The substitution of Eq. (4) into the continuity equation yields

$$\nabla^2\phi - \bar{\nabla}(\bar{i}_\theta \Omega R) = 0 \tag{5}$$

The condition of constant total energy at the upstream of the pump requires that the flow there must be free vortex, $(RV_\theta)_\infty$ = constant. The requirement of free-vortex flow at the upstream of the pump is also physically unrealistic, since the radius ratio from shell to core is large.

Ecer et al. (1983) developed a three-dimensional potential flow code name TFLOW using the finite element method. Equation (5) is solved by sub-dividing the computational domain into eight noded isoparametric finite elements. A pseudo-time integration scheme is used to iteratively solve the discretized system of equations. To enhance numerical stability and convergence, a relaxation parameter is employed. The TFLOW code is used to analyze the pump blade under the three speed ratio conditions. The meridional and plan views of the 30 × 9 × 9 computational grid are shown in Fig. 10. Required input flow parameters are rotational speed, mass flow rate, density, and pre rotation RV_θ. Mass flow rate and pre-rotation are estimated from a one-dimensional performance model. The comparison between the static pressure distribution predicted by the potential flow code and the measured data is shown in Figs. 6, 7, and 8 for the speed ratios of 0, 0.6, and 0.8, respectively.

Under the zero speed ratio condition, the comparison between the predicted and measured C_p distributions is shown in Fig. 6. As a result of the free-vortex requirement, the inlet flow angle was about 49, 16, and −12 degrees at the shell, midspan, and core sections, respectively. The inlet flow angle obtained from a one-dimensional performance analysis is about 11 degrees (see Fig. 3). At the mid-span, the agreement between the predicted and measured static pressure distribution is fairly good. The pressure rise predicted by the code is slightly higher than the measured data. The reversal in the static pressure distribution near the leading edge is well predicted. The blade loading is also well predicted. At the core section, the agreement is poor. This is due to the effect of the wrong incidence angle imposed by the free-vortex requirement and the fact that the flow is not irrotational at the blade core section. The pressure rise predicted by the code is fairly good, since it is due mainly to the effect of rotation. The blade loading is, however, poorly predicted. At the shell section, the agreement is also poor for the same reasons. The same type of results are obtained for $SR = 0.6$ and $SR = 0.8$ and is not repeated to keep the number of pages to a minimum.

There are two important conclusions about the ability of a potential flow code in predicting the static pressure distribution in a pump. First, a potential flow code can fairly well predict the static pressure distribution at the blade mid-span section, since the pressure field is nearly irrotational there and the inlet flow angle imposed by the free vortex condition is realistic.

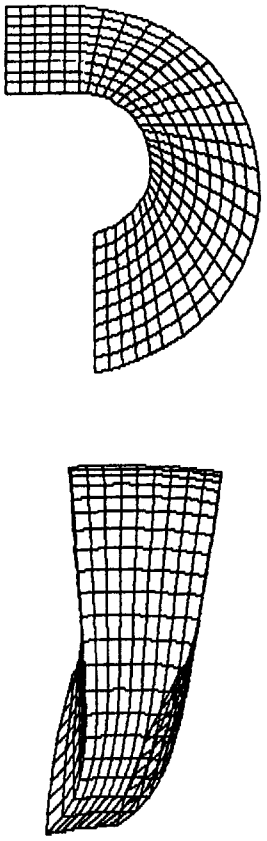

Fig. 10 Meridional and plan views of the 30 × 9 × 9 pump grid

Second, a potential flow code predicts very poorly the static pressure distribution at the shell and core sections, since the inlet flow angle imposed by the free-vortex condition is unrealistic there and the pressure field is not irrotational at the two annulus-wall sections.

Conclusions

Important conclusions drawn from this investigation are:

1) The static pressure distribution is poor at the core section under all speed ratio conditions; the flow may be separated near the core at all speed ratio conditions.

1) The pump static pressure field changes drastically from the shell to the core section. Hence, the one-dimensional flow theory cannot accurately predict the spanwise distribution of the blade torque coefficient. Centrifugal force is found to have a dominant effect on the static pressure rise in the pump.

2) Under the zero speed ratio condition, the static pressure distribution is reversed in the first 7 and 17 percent of the shell meridional blade length at the mid-span and shell sections, respectively. The incidence effect is most pronounced in the pump, since the blade is constructed from sheet metal with a very sharp leading edge. The blade torque coefficient is almost constant at the three blade sections.

3) The static pressure distribution under $SR = 0.6$ condition is significantly better than that under $SR = 0$. The pressure rise is significantly higher at the three blade sections. The flow at the core section is still poorly behaved in spite of the large pressure rise, since the blade loading is very small. The C_T distribution is good at the shell and mid-span sections, but it is poor at the core.

4) The static pressure distribution under $SR = 0.8$ condition is significantly better than that under $SR = 0$, but slightly poorer than that under $SR = 0.6$. The C_T distribution is good at the shell and mid-span sections, but it is poor at the core.

5) A three-dimensional potential flow code can fairly well predict the static pressure distribution at the blade mid-span section under all speed ratio conditions, since the static pressure field there is nearly potential. At the core and shell sections, however, the predicted C_p distribution is poor.

Acknowledgments

This work was a portion of the first author's dissertation and it was partially supported by the General Motors Corporation. The authors would like to express their gratitude to John Cicerone, Ted Hojna, and Roy Harvey for their assistance and contributions in designing, constructing, and testing the experimental facility; and to John Mahoney for his continuous support.

References

By, R. R., and Lakshminarayana, B. 1991, "Static Pressure Measurement in a Torque Converter Stator," SAE Paper #911934 and also in the 1992 SAE Journal of Passenger C.

By, R. R., Kunz, R. F., and Lakshminarayana, B., (1995), "Navier-Stokes Analysis of the Pump Flow Field of an Automotive Torque Converter," ASME JOURNAL OF FLUIDS ENGINEERING, Vol. 117, March, pp. 116–122.

Ecer, A., Akay, H. U., and Mattai, S. (1983), "Finite Element Analysis of Three-Dimensional Flow Through a Turbocharger Compressor Wheel," ASME Paper No. 83-GT-92.

Kubo, M., Ejiri, E., Okada, K., and Ishii, Y., (1991), "Improvement of Accuracy in Torque Converter Performance Prediction by Internal Flow Measurement," JSAE Academic Preprint #912279.

APPENDIX

Analysis of Measurement Errors.

The total measurement error (E_T) is the sum of the bias error (E_B) and the precision error (E_P). The bias and precision errors are the fixed and random components of the total error, respectively. If the bias and precision errors are known, the total measurement error can be calculated as follows

$$E_T = \sqrt{(E_B)^2 + (E_P)^2} \tag{6}$$

The bias error consists of errors of the pressure transducers, errors of the slip ring, errors of the data acquisition system, and others. It was the same in every reading and it was reduced to a minimum by calibration. Since 1200 sample outputs were recorded for each reading during a measurement span of 60 seconds, it was possible to place 95 percent confidence limit on the true mean population (p_{avg}). The standard deviation (σ) was less than 2 percent of the mean value. The maximum bias error is about ± 0.04 kPa based on 95 percent confidence level using the t distribution.

The precision error is the error associated with the repeatability of the measurement. It consists of errors associated with the trapped air in the hydraulic pressure lines, errors associated with induced-flow disturbances, and others. The maximum precision error is about ± 0.80 kPa based on 95 percent confidence level using the t distribution. As expected, the precision error is significantly larger than the bias error.

The total measurement error is found from Eq. (6) to be about ± 0.80 kPa or ± 1 percent of the dynamic pressure based on blade tip speed.

R. R. By[1]

R. Kunz[2]

NAO Engineering Center,
General Motors Corporation,
Warren, MI 48090

B. Lakshminarayana
Aerospace Engineering Department,
The Pennsylvania State University,
University Park, PA 16802

Navier-Stokes Analysis of the Pump Flow Field of an Automotive Torque Converter

A three-dimensional, incompressible, viscous flow code, developed by NASA AMES (INS3D) using the pseudo-compressibility method, is modified for torque converter flow field computations. The code is used to predict the velocity and pressure fields in the pump of an automotive torque converter. Numerical results are compared to measured static pressure and velocity distributions. Results show that: 1) the code can fairly well predict the C_p distribution, the distribution of the through-flow velocity, and the secondary flow field, 2) pump rotation has a major effect on the secondary flow field and on the mass-averaged total pressure loss, and 3) inlet velocity profiles have a profound effect on the mass-averaged total pressure loss.

Introduction

The numerical simulation of three-dimensional incompressible viscous flows is a difficult and challenging task, because the governing system of time-dependent equations is elliptic-parabolic. Therefore, time-marching methods for the hyperbolic type of equations can not be directly applied. To resolve this problem, Chorin (1967) proposed the concept of pseudo-compressibility. In the pseudo-compressibility method, an artificial compressibility is introduced by adding a time-derivative of pressure to the continuity equation. Together with the momentum equations, the resulting system of equations becomes hyperbolic-parabolic. Therefore, efficient numerical implicit schemes developed for compressible flows can be implemented.

Kwak et al. (1986) and Rogers et al. (1987 developed a three-dimensional, incompressible, viscous flow code named INS3D using the pseudo-compressibility method. The code has the following features: 1) the coordinates are transformed for general three-dimensional applications, 2) a central differencing scheme for spatial discretization and an implicit factorization scheme for temporal discretization are used, 3) a second-order implicit artificial dissipation and a fourth-order explicit artificial dissipation are employed to enhance numerical stability, and 4) the flow is assumed to be laminar. There are two basic versions of the code that have been made available to the public. In the first version of INS3D, an approximate factorization scheme is used to perform the inversion of three block tridiagonal matrices. In the second version of INS3D, a diagonal scheme is used to perform the inversion of four scalar tridiagonal systems. The diagonal scheme was reported to be 2.5 to 3 times faster than the block approximate factorization scheme. This code was validated and tested for numerous applications, including flow in a 90 degree curved duct, flow in a rocket pump, and flow in the Penn State artificial heart.

The objective of this study is to assess the role of computational fluid dynamics on the analysis of the pump flow field of a torque converter. The second version of the INS3D code was modified for the computation of the pump flow field. The following features were implemented to the INS3D code: 1) periodic boundary conditions, 2) system rotation, 3) low Reynolds number two-equation turbulence models, and 4) local time stepping.

Pseudo-Compressibility Method and Modeling Procedure

Governing Equations. The governing equations for incompressible flow in a rotating coordinate system are

$$\frac{\partial Q}{\partial t} + \frac{\partial}{\partial x}(E - E_v) + \frac{\partial}{\partial y}(F - F_v) + \frac{\partial}{\partial z}(G - G_v) = S \quad (1)$$

The vectors Q, E, F, G, E_v, F_v, G_v, and S are defined as follows

$$Q = \begin{bmatrix} p/\rho \\ u \\ v \\ w \end{bmatrix},$$

$$S = \begin{bmatrix} 0 \\ -(\partial\overline{u'u'}/\partial x + \partial\overline{u'v'}/\partial y + \partial\overline{u'w'}/\partial z) \\ \Omega^2 y + 2\Omega w - (\partial\overline{v'u'}/\partial x + \partial\overline{v'v'}/\partial y + \partial\overline{v'w'}/\partial z) \\ \Omega^2 z - 2\Omega v - (\partial\overline{w'u'}/\partial x + \partial\overline{w'v'}/\partial y + \partial\overline{w'w'}/\partial z) \end{bmatrix},$$

$$E = \begin{bmatrix} \beta u \\ u^2 + p/\rho \\ uv \\ uw \end{bmatrix}, \quad E_v = \frac{1}{\rho}\begin{bmatrix} 0 \\ 2\mu\, \partial u/\partial x \\ \mu(\partial u/\partial y + \partial v/\partial x) \\ \mu(\partial u/\partial z + \partial w/\partial x) \end{bmatrix},$$

[1]Presently President, Fluid Machinery Consulting, New Baltimore, MI.
[2]Presently Senior Engineer, Martin Marietta, Schenectady, NY.

Contributed by the Fluids Engineering Division for publication in the JOURNAL OF FLUIDS ENGINEERING. Manuscript received by the Fluids Engineering Division March 25, 1993; revised manuscript received April 26, 1994. Associate Technical Editor: R. W. Metcalfe.

$$F = \begin{bmatrix} \beta v \\ uv \\ v^2 + p/\rho \\ vw \end{bmatrix}, \quad F_v = \frac{1}{\rho}\begin{bmatrix} 0 \\ \mu(\partial v/\partial x + \partial u/\partial y) \\ 2\mu\, \partial v/\partial y \\ \mu(\partial v/\partial z + \partial w/\partial y) \end{bmatrix},$$

$$G = \begin{bmatrix} \beta w \\ uw \\ vw \\ w^2 + p/\rho \end{bmatrix}, \quad G_v = \frac{1}{\rho}\begin{bmatrix} 0 \\ \mu(\partial w/\partial x + \partial u/\partial z) \\ \mu(\partial w/\partial y + \partial v/\partial z) \\ 2\mu\, \partial w/\partial z \end{bmatrix} \quad (2)$$

where β is the pseudo-compressibility constant, Ω is the angular velocity, and rotation is clockwise about the x-axis. Turbulence Reynolds stresses, Coriolis force and centrifugal force appear in the source term of Eq. (2). The resulting system of equations is hyperbolic and can be solved efficiently using an implicit time-marching scheme. When the flow variables converge to steady-state values, the modified continuity equation satisfies the divergence-free velocity field condition.

Turbulence Modeling. To solve Eq. (1), additional equations must be provided to evaluate the turbulence Reynolds stresses, $\overline{u_i' u_j'}$. From the Boussinesq approximation, a turbulent or an eddy viscosity, μ_t, is defined as

$$-\rho\overline{u_i' u_j'} = \mu_t\left(\frac{\partial u_i}{\partial x_j} + \frac{\partial u_j}{\partial x_i}\right) - \frac{2}{3}k\delta_{ij} \quad (3)$$

where δ_{ij} is the Kronecker delta and k is the turbulent kinetic energy. Equation (1) can be solved if μ_t and k are known. The role of an eddy viscosity turbulence model is to determine μ_t and k. The q-ω model as proposed by Coakley (1983) was incorporated and used in this investigation. The velocity scale (q) and the specific dissipation rate of turbulent kinetic energy (ω) are

$$q = \sqrt{k}, \quad \omega = \epsilon/k \quad (4)$$

where k is the turbulent kinetic energy and ϵ is the dissipation rate of turbulent kinetic energy; and they are defined as

$$k = \frac{1}{2}\overline{u_i' u_i'}, \quad \epsilon = \nu\frac{\overline{\partial u_i'}}{\partial x_j}\frac{\overline{\partial u_i'}}{\partial x_j} \quad (5)$$

The transport equations for q and ω are in the form

$$\frac{\partial Q'}{\partial t} + \frac{\partial}{\partial x}(E' - E_v') + \frac{\partial}{\partial y}(F' - F_v') + \frac{\partial}{\partial z}(G' - G_v') = S' \quad (6)$$

where the vectors Q', E', F', G', E_v', F_v', G_v', S' are

$$Q' = \begin{bmatrix} q \\ \omega \end{bmatrix}, \quad E' = \begin{bmatrix} uq \\ u\omega \end{bmatrix}, \quad F' = \begin{bmatrix} vq \\ v\omega \end{bmatrix}, \quad G' = \begin{bmatrix} wq \\ w\omega \end{bmatrix},$$

$$E_v' = \frac{1}{\rho}\begin{bmatrix} \left(\mu + \dfrac{\mu_t}{\mathrm{Pr}_q}\right)\dfrac{\partial q}{\partial x} \\ \left(\mu + \dfrac{\mu_t}{\mathrm{Pr}_\omega}\right)\dfrac{\partial \omega}{\partial x} \end{bmatrix}, \quad F_v' = \frac{1}{\rho}\begin{bmatrix} \left(\mu + \dfrac{\mu_t}{\mathrm{Pr}_q}\right)\dfrac{\partial q}{\partial y} \\ \left(\mu + \dfrac{\mu_t}{\mathrm{Pr}_\omega}\right)\dfrac{\partial \omega}{\partial y} \end{bmatrix},$$

$$G_v' = \frac{1}{\rho}\begin{bmatrix} \left(\mu + \dfrac{\mu_t}{\mathrm{Pr}_q}\right)\dfrac{\partial q}{\partial z} \\ \left(\mu + \dfrac{\mu_t}{\mathrm{Pr}_\omega}\right)\dfrac{\partial \omega}{\partial z} \end{bmatrix},$$

$$S' = \begin{bmatrix} \dfrac{q}{2}\left(\dfrac{C_\mu D}{\omega}\left(\dfrac{\partial u_i}{\partial x_j} + \dfrac{\partial u_j}{\partial x_i}\right)\dfrac{\partial u_i}{\partial x_j} - \omega\right)\right) \\ \left(C_1 C_\mu\left(\dfrac{\partial u_i}{\partial x_j} + \dfrac{\partial u_j}{\partial x_i}\right)\dfrac{\partial u_i}{\partial x_j} - C_2\omega^2\right) \end{bmatrix} \quad (7)$$

The coefficients and functions are given in Coakley (1983).

The turbulent transport equations of Eq. (6) are in the same vector form as the mean flow equations of Eq. (1). Therefore, the same numerical technique can be used to solve the two sets of equations. That is, the transport equations are solved in a similar fashion to the mean flow equations, but they are uncoupled from the mean flow equations. Specifically, at each iteration, the four mean flow equations are solved by using the value of eddy viscosity, μ_t, calculated from the previous iteration. Then the turbulent transport equations for q and ω are solved sequentially.

Equations (1) and (6) are transformed from physical space to computational space by the following relations: $\xi = \xi(x, y, z, t)$, $\eta = \eta(x, y, z, t)$, $\zeta = \zeta(x, y, z, t)$. The transformed equations are given in Rogers et al. (1987) for laminar flows.

Numerical Technique. The numerical procedure consists of the following:

Nomenclature

A = area
C_p = static pressure coefficient, $C_p = (p - p_{\mathrm{ref}})/(0.5\rho U_{\mathrm{tip}}^2)$
H = blade span or height (see Fig. 3)
k = turbulent kinetic energy (TKE) as defined in Eq. (5)
L = meridional blade length (see Fig. 3)
p = static pressure
p^* = $p + 0.5\rho(W^2 - U^2)$
q = turbulent velocity scale as defined in Eq. (4)
$\dot{Q}$ = volume flow rate ($\dot{Q}$), m^3/s
S = blade spacing or pitch
Re_L = Reynolds number based on meridional length, $W_m L/\nu$
SR = ratio of turbine to pump speed
t = time
$\overline{u_i' u_j'}$ = turbulence Reynolds stresses
u, v, w = velocity components in the Cartesian coordinates
U, V, W = blade, absolute flow, relative flow velocity
x, y, z = Cartesian coordinates
X, Y, Z = coordinate in the meridional, blade-to-blade, spanwise direction (see Fig. 3)
ρ = density in kg/m^3
ν = kinematic viscosity in m^2/s
Ω = angular velocity in rad/s
β = pseudo-compressibility constant
ξ, η, ζ = curvilinear coordinates
ϵ = dissipation rate of TKE as defined in Eq. (5)
ω = specific dissipation rate of TKE as defined in Eq. (4)
μ, μ_t = molecular, turbulent viscosity in kg/m.s
$\bar{\zeta}$ = mass-averaged total pressure loss coefficient as defined by Eq. (9)

Subscripts

r, a, θ = radial, axial, tangential direction
s, m, θ = spanwise, meridional, tangential direction
i, j, k = index in the streamwise, pitchwise, spanwise direction shell, core blade shell, core section (see Fig. 1)
ref = reference
tip = tip location of the pump blade
$1\infty, 2\infty$ = at the inlet, exit of the computational grid

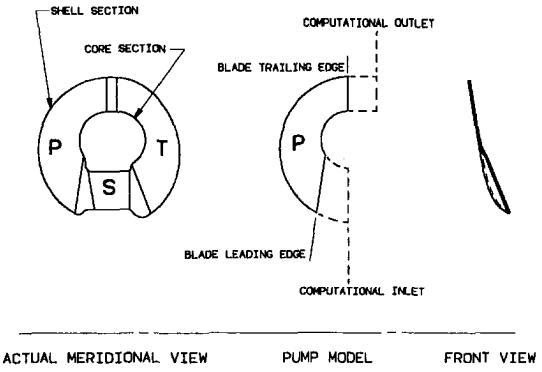

Fig. 1 Geometry of the actual and modeled pumps

1) The numerical algorithm used to advance the transformed equations in time is an implicit, time marching, approximately-factored, finite-difference scheme.

2) A second order accurate central differencing scheme is used for spatial discretization.

3) The four mean-flow equations are solved in coupled form using the diagonalized approximate factorization scheme. The use of the diagonal scheme requires the inversion of four scalar tri-diagonal systems three successive times at each iteration. The two turbulent transport equations are solved in uncoupled form using the standard approximate factorization scheme (ADI).

4) A small amount of 4th difference artificial dissipation, scaled by the spectral radius of the inviscid flux Jacobian, is added explicitly to the RHS of Eq. (1) to stabilize the central difference scheme. Additionally, 2nd difference artificial dissipation operators are included implicitly.

Modeling Assumptions and Errors. It would be desirable to simultaneously simulate the flow fields in the pump, in the turbine, and in the stator. Since it is not practical to perform such a task, the pump element is modeled as a single unit in steady-state mode. There are several key assumptions associated with this approach. First, the flow is assumed to be steady. Second, interaction effects between pump/turbine are assumed to be negligible (the interaction effects between stator/pump is partially accounted for in the inlet boundary conditions). Third, the flow is assumed to be periodic. Fourth, the inlet profile of the mean velocity components, the inlet turbulence intensity, and the inlet turbulent length scale must be assumed for the specification of inlet boundary conditions. Fifth, the time-averaged Navier-Stokes equations and the low Reynolds number two-equation model are assumed to be valid for the computation of the pump flow field. It is hoped that the assumptions made here are realistic enough to provide important insights into the pump flow field.

There are two types of errors. First, the above assumptions lead to some physical errors, since: 1) the actual pump flow field is unsteady and the interaction effects between the elements are significant, 2) inlet boundary conditions are not generally known and vary from one torque converter to another, and 3) eddy viscosity models are known to be inadequate for the prediction of complex shear layers such as those in the pump flow field. Second, the modeling procedure introduces some numerical errors, since the geometry of the upstream of the pump inlet, as shown in Fig. 1, is poorly modeled. In addition, implicit and explicit artificial dissipations may have some effects on the accuracy of the numerical solution.

Grid. The IGB grid code, developed by Beach (1989), was used to generate a structured H grid for the pump blade passage. It contains a combination of algebraic and elliptic techniques coded for use on a Silicon Graphics workstation. IGB generates a 3-D grid in a blade row by stacking a series of surfaces between the hub and the tip. Smoothing of the grids within these surfaces is performed by interactively invoking an elliptic smoother.

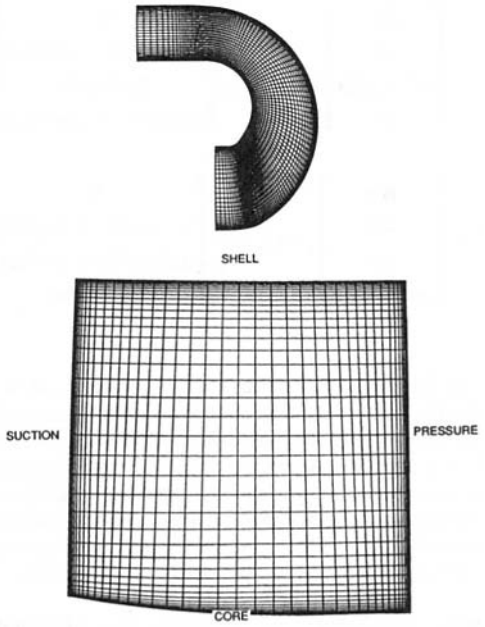

Fig. 2 Meridional and streamwise views of 125 × 41 × 41 grid

Figure 2 shows the meridional view of the 125 × 41 × 41 pump grid along the mid-channel of the blade passage. The grid consists of 125, 41, and 41 grid stations in the streamwise (inlet to exit), pitchwise (suction to pressure), and spanwise (shell to core) directions, respectively. There are 20 grid stations upstream of the blade leading edge and 20 grid stations downstream of the blade trailing edge. A streamwise view of the grid at the mid-chord plane is also shown in Fig. 2. To effectively capture viscous effects, grids are clustered near blade and wall surfaces. The 41 × 41 cross-stream grid provides good resolution; the value of y^+ is about 3 at grid point adjacent to the blade surfaces and along the core and shell housings. The authors performed grid resolution studies using a 125 × 81 × 41 and 125 × 41 × 81 meshes. Because the flow Reynolds number is rather small (Re_L = 5,100), it was found that solutions obtained with the 125 × 41 × 41 mesh were nearly identical to those with finer meshes (the difference in the total pressure loss was less than 2 percent at mid-span).

Results and Discussion

The inlet flow boundary conditions were obtained from a laser velocimetry measurement (LDV) of an identical torque converter at SR = 0.8. The LDV measurement was conducted by Gruver (1992) at three planes (inlet, mid-chord, and exit planes). The coordinate system and the velocity components are defined in Fig. 3. At the inlet of the computational plane, the spanwise velocity component is assumed to be negligible. The spanwise distribution of the through-flow velocity (V_m) and the relative tangential velocity (W_θ) is shown in Fig. 4.

The code was run on the GMR Cray Y-MP. Input parameters used to run the code are summarized in Table 1. For turbulent flow computations, the code executes at approximately 2.8 × 10^{-5} CPU seconds/(grid point * iteration). For the pump case with 210,125 grid points, it takes about 60 CPU minutes.

Comparison With the Measured C_p Distribution. The comparison of the C_p distribution is shown in Fig. 5. The data was measured by By and Lakshminarayana (1995).

At the shell section, the agreement is very good between numerical and experimental results. The pressure rise and the

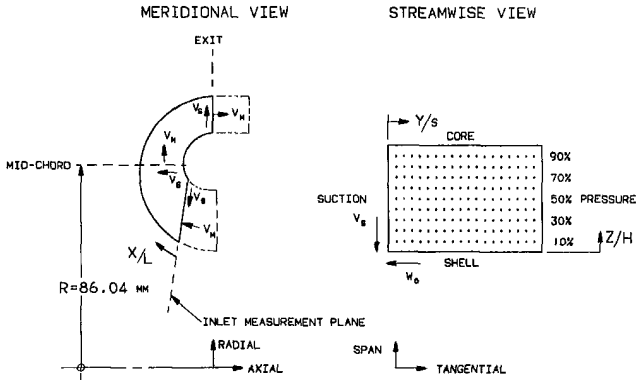

Fig. 3 Coordinate system and velocity components

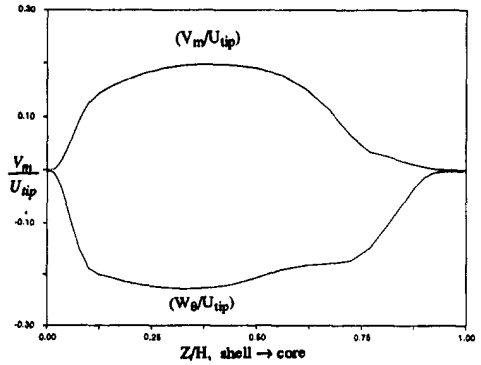

Fig. 4 Measured spanwise distribution of (V_m/U_{tip}) and (W_θ/U_{tip}) at the inlet computational plane

Table 1 Input parameters used to run the code @ 0.8SR

$\beta/V^2_{m,1\infty}$	5
Inlet free-stream turbulence intensity, percent	5
Inlet free-stream turbulence length scale, mm	0.8
Total volume flow rate ($\dot{Q}$), m^3/s	0.014
Inlet flow angle, degrees	−54
Incidence angle, degrees	+22
Re_L	5,100
Pump rotation (Ω_P), rad/s	115.2

blade loading are well predicted. Near the blade leading edge, the code under predicts the effect of a large positive incidence angle of 22 degrees. As a result, the pressure rise predicted by the code is slightly higher than the measured C_p distribution.

At the mid-span section, the agreement is good, but it is slightly poorer than that at the shell. The pressure rise is well predicted by the code. On the suction surface, the agreement is very good except near the blade trailing edge. On the pressure surface, the agreement is poorer. The code predicts a lower C_p distribution in the first 18 percent of the shell meridional length. From 18 to 54 percent of the shell meridional length, the predicted C_p distribution is significantly higher. The data shows that the C_p on the pressure surface is poorly distributed between 7 and 46 percent of the shell meridional length; the code does not predict this phenomenon accurately.

At the core section, the agreement is good, but it is also poorer than that at the shell. The pressure rise is well predicted by the code. The predicted blade loading, however, is significantly higher than the measured data. The discrepancy between the two results may be largely due to the incorrect specification of the inlet velocity profiles near the core section.

Comparison with the LDV Velocity Data. The meridional velocity predicted by the INS3D code is compared to the

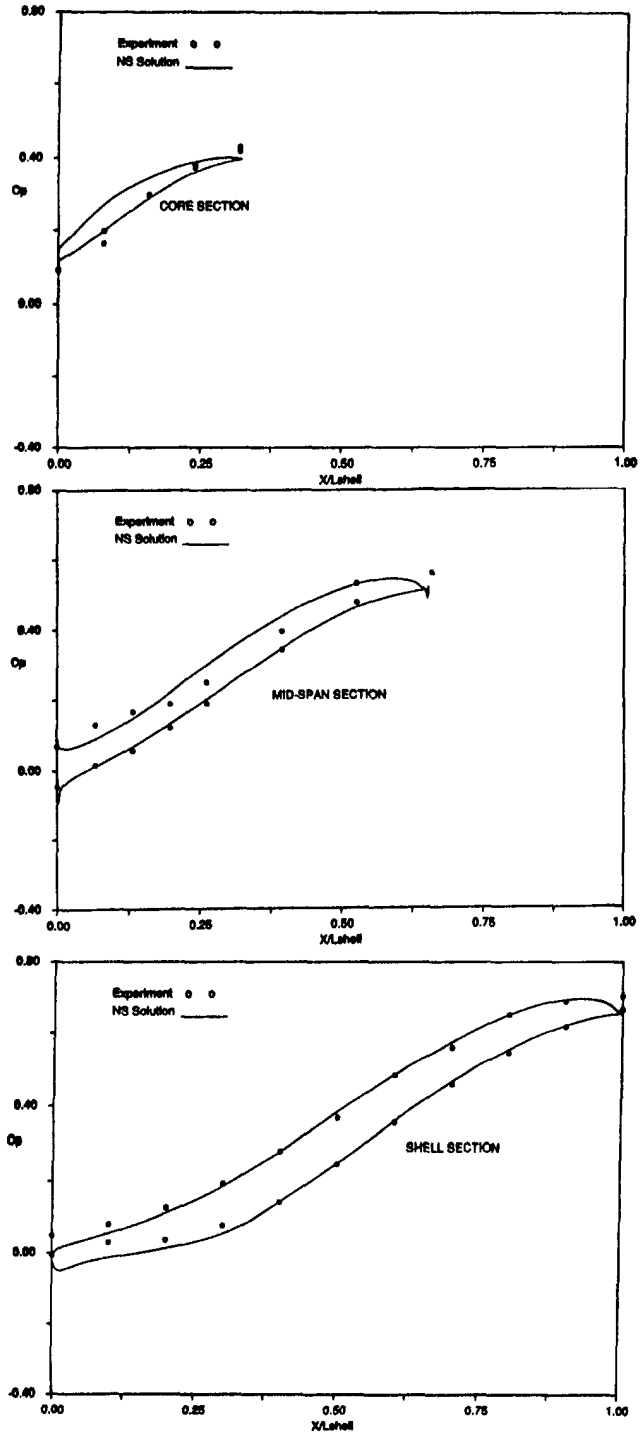

Fig. 5 Comparison of measured and predicted C_p distribution

LDV velocity data measured by Gruver (1992). The comparison is shown in Fig. 6 at the exit plane; it is made at 5 spanwise locations (10, 30, 50, 70, and 90 percent, starting from the shell). At each spanwise location, there are 18 measurement points from the suction to pressure surface. The meridional velocity is normalized by blade tip speed.

Considering the complexity of the pump flow field and the assumptions associated with the numerical simulation, the overall agreement between the numerical results and the velocity data is very good. The agreement is good at all spanwise locations. It is, however, slightly poorer at 90 percent of the blade span. The discrepancy may be largely due to the incorrect specifi-

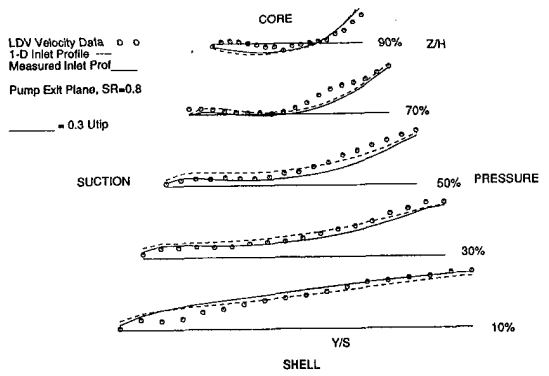

Fig. 6 Distribution of (V_m/U_{tip}) at the exit plane

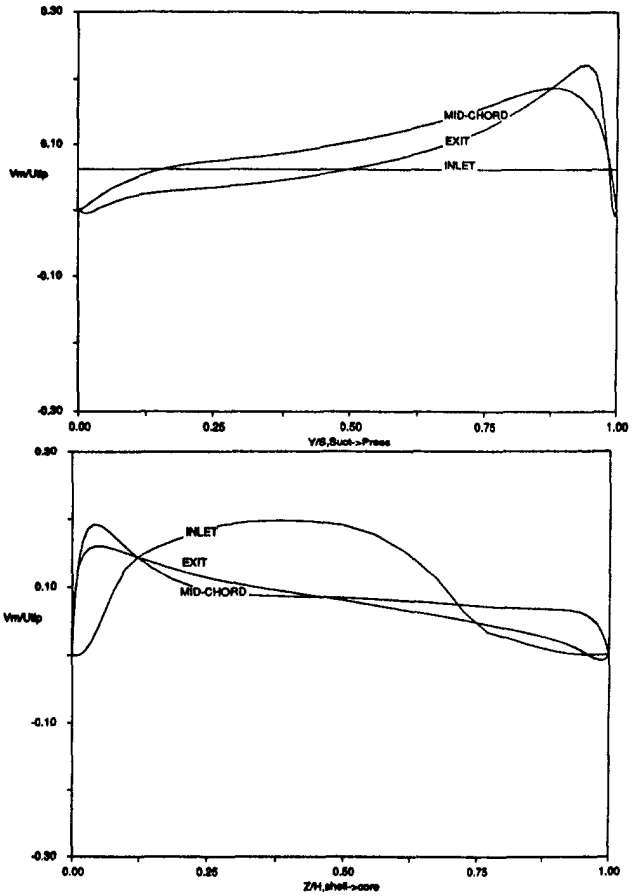

Fig. 7 Spanwise and pitchwise distributions of (V_m/U_{tip})

cation of the inlet velocity profiles near the core section. At all spanwise locations, V_m is maximum near the pressure surface and minimum near the suction surface. As expected, the meridional velocity near the shell section is significantly higher than that near the core section.

Interpretation of the Pump Flow Field

Diffusion of the Meridional Velocity. The spanwise and pitchwise distributions of V_m are shown in Fig. 7. In the spanwise distribution, V_m at each spanwise location is obtained by averaging velocities in the pitchwise direction. Similarly, in the pitchwise distribution, V_m at each pitchwise location is obtained by averaging velocities in the spanwise direction.

In the spanwise distribution, there is a strong diffusion of the meridional velocity from the core to the shell section as

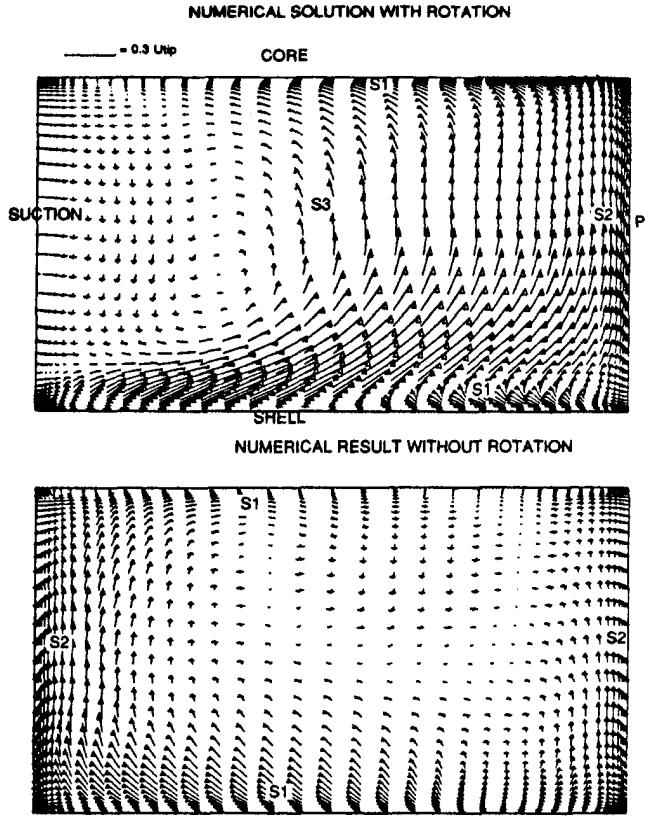

Fig. 8 Predicted secondary flow field at the mid-chord plane with and without pump rotation

the fluid flows from the pump inlet to exit. In the pitchwise distribution, there is a strong diffusion of the meridional velocity from the suction to pressure surface. At the mid-chord and exit planes, the meridional velocity is maximum near the corner of the shell and the pressure surface and is minimum near the corner of the core and suction surface.

Secondary Flow Field. A strong secondary flow field exists at the mid-chord and exit planes. It can be visualized by plotting the relative tangential and relative spanwise velocity components in vector form. The numerical results are shown in Figs. 8 and 9 for the mid-chord and exit planes, respectively. The most striking feature of this secondary flow field is that it circulates counter clockwise at the mid-chord plane, but it switches to clockwise circulation at the exit plane.

To determine the causes of this secondary flow field, an analysis is made for the case without pump rotation. In this case ($\Omega_P = 0$), the flow in the blade passage is reduced to the flow in a curved duct, since the pressure rise due to centrifugal pressure is zero. The grid and all input parameters are identical except that $\Omega_P = 0$. The predicted secondary flow field is shown in Figs. 8 and 9 for the mid-chord and exit planes, respectively. At both planes, the secondary flow velocity components are much smaller for the $\Omega_P = 0$ case. It is clear that rotation has a major effect on the development of secondary flow in the pump.

The expression for secondary vorticity in a rotating coordinate system for inviscid, incompressible flow is given in Lakshminarayana and Horlock (1973). It is expressed as follows

$$\frac{\partial}{\partial s}\left(\frac{\omega_s}{\rho W}\right) = \frac{2\omega_n}{2\rho WR} - \frac{2\bar{\Omega} \times \bar{\omega}}{\rho W^2} \cdot \bar{s} \tag{8}$$

where ω is the vorticity in absolute flow, ω_s and ω_n are its components in the relative streamline (s) and principle normal

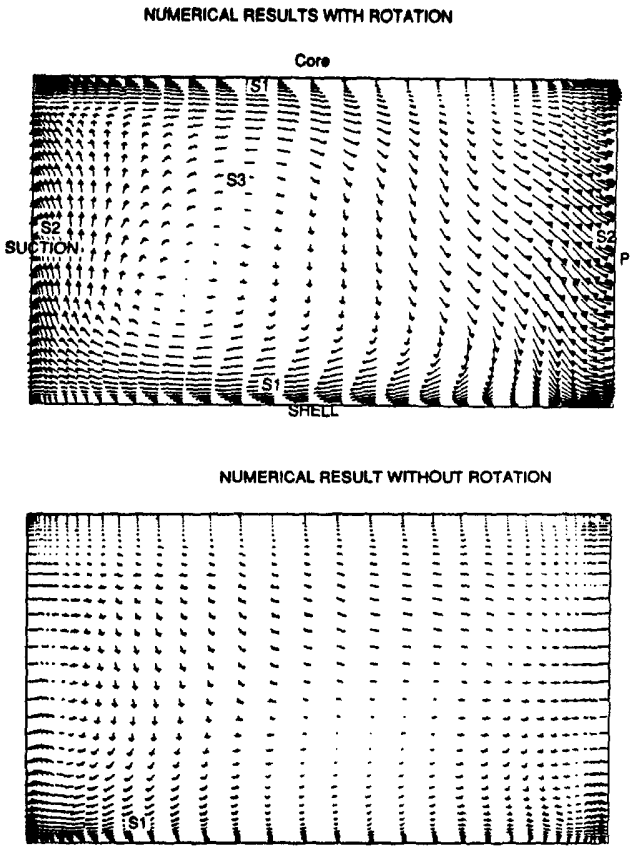

Fig. 9 Predicted secondary flow field at the exit plane with and without pump rotation

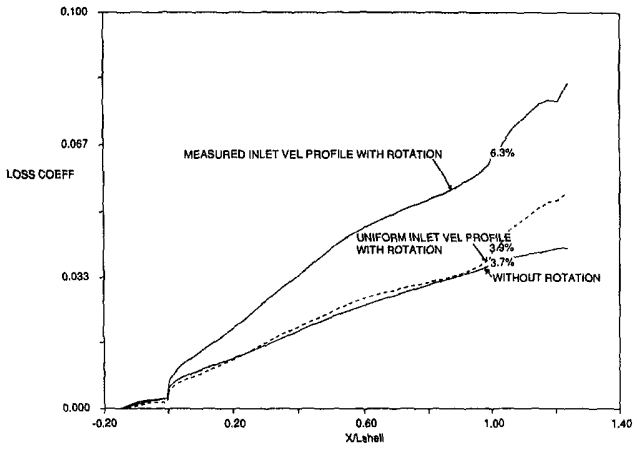

Fig. 10 Comparison of mass-average total pressure loss ($\bar{\zeta}$)

(n) directions, respectively, W is the relative velocity, and R is the radius of curvature. There are three kinds of secondary flows in the torque converter pump. The secondary flow of the first kind is associated with the annulus wall boundary layer and the curvature of the blade camber $(2\omega_{n1}/2\rho WR_1)$. This secondary flow can be clearly seen from the distribution of the relative tangential velocity component near the core and shell housings in Figs. 8 and 9. This is marked S1 on the plots. The secondary flow of the second kind arises due to the blade boundary layer and the curvature of the core and shell housings $(2\omega_{n2}/2\rho WR_2)$. This secondary flow can be clearly seen from the distribution of the relative spanwise velocity component inside the boundary layers on the two blade surfaces. This is marked S2 on the plots. These two types of secondary flows are mainly confined to annulus wall regions and blade boundary layer regions.

The secondary flow of the third kind is marked S3 on the plots. It is evident from the numerical results (with and without rotation) that this type of secondary flow is caused by rotation $2\bar{\Omega} \times \bar{\omega}/\rho W^2 \cdot \bar{s}$. This secondary flow (S3) is dominant in the pump flow field. the absolute vorticity at the pump inlet is mainly due to velocity gradient in the spanwise direction (see Fig. 7). It is clockwise and dominant from 10 to 75 percent of the blade span (starting from the shell). According to Eq. (8), the induced secondary flow (S3) should be counter clockwise downstream of the inlet plane. The counter clockwise circulation at the mid-chord plane is confirmed by the numerical results.

The secondary flow field is reversed between the mid-chord and exit planes. This results was confirmed by the LDV velocity data of Gruver (1992). One possible cause is that $\bar{\omega}$ may change direction between the two planes.

Mass-Averaged Total Pressure Loss. The mass-averaged total pressure loss between $X = X_{1\infty}$ and any streamwise location X is

$$\bar{\zeta} = \frac{1}{\dot{Q}(0.5\rho U_{tip}^2)} \left\{ \int_{A_{1\infty}} P^*_{1\infty}(\bar{W} \cdot d\bar{A})_{1\infty} - \int_A P^*(\bar{W} \cdot d\bar{A}) \right\} \quad (9)$$

Equation (9) is used to calculate the mass-averaged total pressure loss as a function of the normalized meridional length. The predicted total pressure loss ($\bar{\zeta}$) for the measured inlet velocity profile case is shown in Fig. 10. The mass-averaged total pressure loss in the pump is about 6.3 percent of the dynamic pressure based on pump tip speed. From Fig. 5, the average C_p rise in the pump is only about 0.6 of the dynamic pressure. Therefore, the total pressure loss is about 10 percent of the pump pressure rise. This 10 percent loss is very significant, since it may be the biggest source of losses in the torque converter at $SR = 0.8$. The loss varies almost linearly from leading to the trailing edge. The loss downstream of the trailing edge (between X_2 and $X_{2\infty}$) is significant and it is due to wake mixing.

The predicted total pressure loss for the $\Omega_P = 0$ case is also shown in Fig. 10. It is about 3.7 percent of the dynamic pressure or 58 percent of the loss for the case with pump rotation. This result is expected, since the secondary flow field is significantly reduced for the $\Omega_P = 0$ case.

To further investigate causes of loss, an analysis is made for the case where inlet velocity profiles are uniform. The spanwise distribution of inlet velocity components (V_m, V_s and W_θ) is obtained from a one-dimensional performance model. The grid and all input parameters are identical except for the inlet velocity profiles. The predicted total pressure loss is compared to the other results in Fig. 10. The total loss for the uniform inlet velocity case is about 3.9 percent of the dynamic pressure; it is about 38 percent less than the loss for the measured inlet velocity profile case. This result is realistic, since there is no velocity gradient associated with the uniform inlet velocity case except for the no slip condition imposed on the blade surfaces and annulus walls. Therefore, the key to minimizing loss is to optimize inlet velocity profiles, such that velocity gradients in the spanwise and pitchwise directions are minimum.

Discussion. In spite of the shortcomings associated with the modeling assumptions and errors, computational fluid dynamics can play an important role in the analysis and design of torque converter components. Considering the complexity of the pump flow field, the predicted results are pretty good. A Navier-Stokes code can be used to predict: 1) the spanwise and pitchwise distributions of the through-flow velocity, 2) the development of secondary flow in the pump, 3) the mass-averaged total pressure loss in the blade passage, 4) the effects of inlet velocity profiles on the total pressure loss, and 5) the

effects of pump rotation on the secondary flow field and on the total pressure loss. Furthermore, a Navier-Stokes code can be used to perform parametric studies, such as the effects of blade spacing, inlet/exit blade angles, and torus shape. Similarly, a Navier-Stokes code can also be used to analyze the flows in the turbine and in the stator.

The most serious limitation is in turbulence modeling. In this investigation, the Reynolds number is only 5100 based on meridional blade length. For large passenger car applications, the Reynolds number can be an order of magnitude higher. It is well known that two-equation turbulence models are not effective in predicting flow fields with low Reynolds number. Further numerical investigations are needed to determine the effects of Reynolds number, rotation, and curvatures on the numerical results.

Conclusions

The INS3D Navier-Stokes code can be used to effectively predict the pump flow field. The code can fairly well predict the static pressure distribution, the distribution of the through-flow velocity, and the secondary flow field. In addition, it is found that: 1) the inlet velocity profile has a profound effect on the mass-averaged total pressure loss and 2) pump rotation has a major effect on the secondary flow field and the mass-averaged total pressure loss.

Acknowledgments

This work was a portion of the first author's dissertation and it was partially supported by the General Motors Corporation. The authors would like to express their gratitude to: Dr. Dochan Kwak of NASA Ames for providing the INS3D code; Tim Beach and Dr. John Adamczyk of NASA Lewis for providing the IGB grid code; Kevin Gruver, Klaus Brun and Prof. Ron Flack of the University of Virginia for providing the LDV velocity data; and John Mahoney for his continuous support and involvement.

References

Beach, T. A., 1989, "An Interactive Grid Generation Procedure for Axial and radial Flow Turbomachinery," NASA CSR-185167.

By, R. R. and Lakshminarayana, B., 1995, "Measurement and Analysis of Static Pressure Field in a Torque Converter Pump," ASME JOURNAL OF FLUIDS ENGINEERING, Vol. 117, March, pp. 109–115.

Chorin, A. J. 1967, "A Numerical Method for Solving Incompressible Viscous Flow Problems," *Journal of Computational Physics*, Vol. 2, pp. 12–26.

Coakley, T. J. 1983, "Turbulence Methods for the Compressible Navier-Stokes Equations," AIAA Paper #83-1693.

Gruver, J. K. 1992, "Laser Velocimetry Measurements in the Pump of an automative Torque Converter," Master thesis, Department of Mechanical and Aerospace Engineering, the University of Virginia.

Kwak, D., Chang, J. L. C., Shanks, S. P., and Chakravarthy, S. 1986, "A Three-Dimensional Incompressible Navier Stokes Flow Solver Using Primitive Variables," *AIAA Journal*, Vol. 24, No. 3, pp. 390–396.

Lakshminarayana, B. and Horlock, J. H. 1973, "Generalized Expressions for Secondary Vorticity using Intrinsic Coordinates," *Journal of Fluid Mechanics*, Vol. 59, pp. 97–115.

Rogers, S. E., Kwak, D. and Chang, J. L. C. 1987, "INS3D-An Incompressible Navier-Stokes Code in Generalized Three-Dimensional Coordinates," NASA TM-100012.

Centrifugal Pump Performance During Transient Operation

P. J. Lefebvre

W. P. Barker

Naval Undersea Warfare Center Division,
Newport, RI 02841

The effect of transient operation on the hydrodynamic performance of a centrifugal pump impeller was investigated experimentally. All experiments were conducted in the Naval Undersea Warfare Center's Impeller Test Facility (ITF), which was designed and built for transient and steady-state operation impeller research. The ITF provides transient operation through simultaneous control of both impeller rotational speed and flow rate over time. The impeller was accelerated from rest with peak angular accelerations up to 720 radians/s^2 and inlet flow mean accelerations up to 1.7 g, reaching a peak rotational speed of 2400 rpm and a flow rate of 416 l/s. The impeller was then decelerated to rest. Results showed substantial transient effects in overall impeller performance and demonstrated that the quasi-steady assumptions commonly used for the design of impellers that operate under high transient (accelerating or decelerating) conditions are not valid.

Introduction

Although pumps have been used for many years as prime movers in hydraulic systems, most of these applications required steady-state operation where pump performance at startup or shutdown was of no concern. Several applications in the Navy and industry, however, require controlled transient operation from startup to shutdown. One such Navy application is the pump used to launch weapons from submarines. This pump operates under highly transient conditions throughout the launch.

To date, weapon ejection pump impellers, along with those for other known transient applications, have been designed exclusively by applying quasi-steady analysis and techniques and ignoring any potential transient effects. This approach assumed that, at any instant in time during a transient, all flow conditions (and, hence, pump performance) were identical to those during steady-state operation while operating at the instantaneous pump speed and flow rate. This approach was taken because little was known about the physics of transient impeller operation.

Most transient flow studies, such as those reported in Saito (1982), Barrand et al. (1993), and Nguyen Duc et al. (1993), investigated the effect of transient operating conditions on the complete flow system without specifically concentrating on the pump, although some impeller related data were presented. Conversely, few studies have focused on the behavior of the impeller itself during transient operation such as those conducted by Tsukamoto et al. (1982) and (1986). The first Tsukamoto study was an experimental and numerical study that investigated pump performance during startup. The second study experimentally evaluated performance as the pump was decelerated to a stop. A conventional single-stage radial flow pump was used. Limited control over the startup transient was obtained by controlling pump rotational speed through the use of an electromagnetic clutch. Transient performance was obtained by measuring the instantaneous pressure rise across the pump.

The first study presented numerical results based on conformal mapping (rotational to linear cascade) inviscid calculations; the results agreed qualitatively with the experimental data. Both experimental and numerical results indicated an improvement in the transient performance over the quasi-steady performance at the start of the transient; the improvement was thought to be a result of impulsive pressure. This was followed by a period of reduced performance relative to the quasi-steady predictions and was thought to be due to lag in the formation of circulation and lift on the impeller blades.

The primary objective of the present study was to evaluate the quasi-steady assumption used to date by measuring the overall hydrodynamic performance of a centrifugal impeller while operating under both transient and steady-state conditions in the same facility. Follow-on studies have been initiated to investigate details of the transient flow field and cavitation.

This paper describes the test facility, instrumentation, test procedures, and test results obtained during the transient and steady-state hydrodynamic performance testing of the impeller. Four different transient profiles were evaluated. Each profile consisted of an initial duration of high acceleration followed by a relatively gradual deceleration.

Experimental Procedure

All experiments were conducted in the Naval Undersea Warfare Center's Impeller Test Facility (ITF). Unlike other standard pump test facilities that provide only steady-state operation, the ITF also allows transient operation. Control systems for

Contributed by the Fluids Engineering Division for publication in the JOURNAL OF FLUIDS ENGINEERING. Manuscript received by the Fluids Engineering Division October 2, 1993; revised manuscript received April 8, 1994. Associate Technical Editor: L. Nelik.

transient operation have been developed which operate simultaneously in order to produce user specified impeller rotational speed (N) and flow rate (Q) time histories. Simultaneous control of these variables provides a means of maintaining the desired time history for the parameter being modeled—the nondimensional flow coefficient C_q, which is defined as

$$C_q = \frac{V_x}{U} \alpha \frac{\frac{Q}{\pi(D^2 - d^2)/4}}{\frac{\pi N D}{60}}, \quad (1)$$

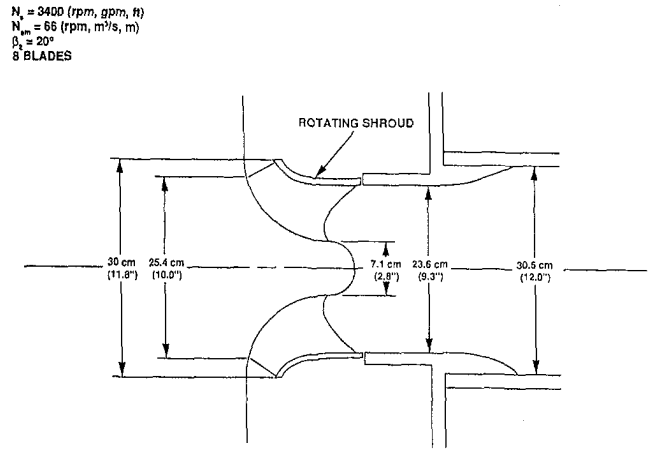

Fig. 1 Test Impeller

where D is the blade inlet tip diameter, d is the hub diameter, V_x is the annular inlet velocity, and U is the impeller tip speed at inlet and is proportional to $N \cdot D$.

The major dimensions and parameters of the impeller design are provided in Fig. 1. As shown, the impeller has eight blades and a design specific speed of 66 (rpm $*$ $\sqrt{m^3/s}/m^{0.75}$) or 3400 (rpm $*$ $\sqrt{gpm}/ft^{0.75}$).

The layout of the ITF (see Lefebvre and Barker, 1991) is shown in Fig. 2. The facility is a closed-loop recirculating system. The impeller under test is housed in the test section that was designed to simulate the near impeller flow field of an actual submarine impulse tank. The design of the impulse tank can accommodate a wide range of impellers and the addition of a diffuser or collector at the impeller discharge if required in the future. No diffuser was used during the present study.

Visual access for future flow visualization and laser Doppler velocimeter (LDV) measurements at the impeller discharge is obtained through 6-in.-diameter viewing ports on each side of the test section. The inlet flow to the impeller is through a 12-in.-diameter clear cast acrylic pipe that allows visual access to the leading edges of the blades.

The flow into the inlet pipe is conditioned by a 36-in. diameter settling tank and nozzle with 6-in.-long, 1/4-in.-cell size honeycomb sandwiched between each of the two flanges at the settling tank. The resulting flow at the inlet pipe entrance has a velocity profile uniform within 1.0 percent across its diameter and a turbulence intensity of less than 1.0 percent.

The flow in the facility is developed by the test impeller, which is powered by two General Electric, 200-hp, low-inertia, DC electric motors connected in series. The instantaneous rotational speed of the motors is controlled by a dedicated mi-

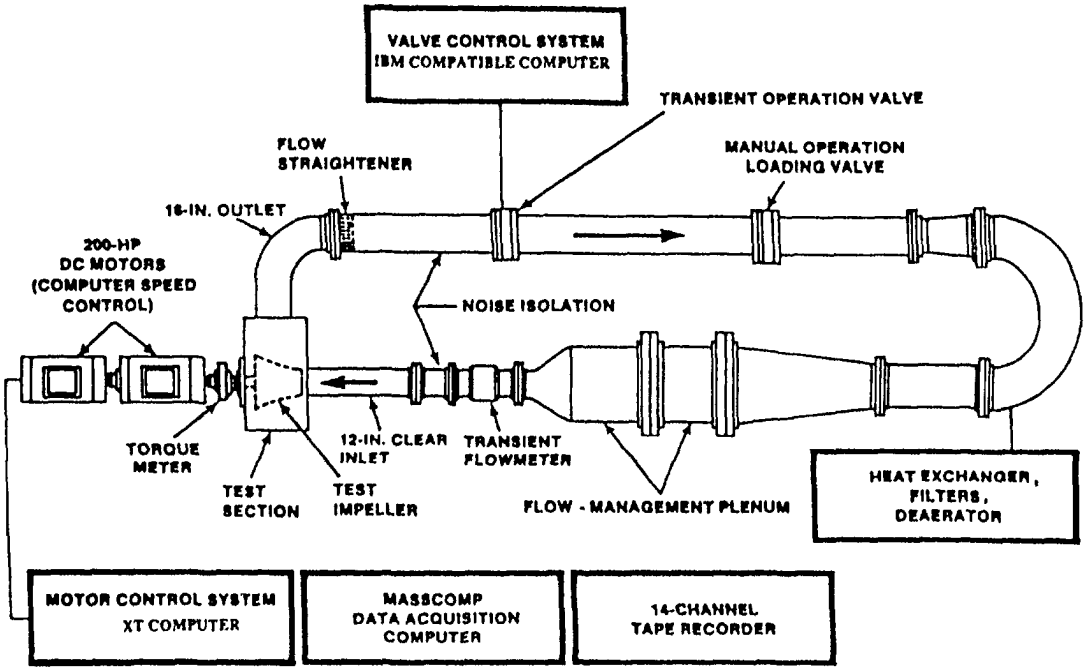

Fig. 2 Impeller test facility

Nomenclature

C_h = nondimensional static head coefficient
$C_{h_{qs}}$ = quasi-steady value of C_h
$C_{h_{tr}}$ = transient value of C_h
C_q = nondimensional flow coefficient
d = impeller hub inlet diameter
D = impeller blade inlet tip diameter
g = acceleration due to gravity
H = head developed by the pump
N = rotational speed
Q = flow rate
U = impeller inlet tip speed (α to $N \cdot D$)
V_x = annular inlet velocity
α = angular acceleration (rad/s^2)

croprocessor-based feedback control system, which has both steady-state and transient operating capabilities. The feedback signal is the rpm from a tachometer mounted on the motor shaft at the rear of the motors. The command signal, whether one constant value of rpm for steady-state operation or a file of rpm versus time for transient operation, is downloaded from an IBM-compatible PC to the microprocessor controller. The PC is used for all interfacing with the controller, including setting of all safety and operational parameters.

Flow rate is controlled by a second control system which governs the motion of the 16-inch-diameter control valve installed downstream of the test section. The feedback signal is the valve position as measured by a position indicator mounted on the valve stem. The command signal is generated by a second IBM-compatible PC. This control system operates in either steady-state mode or transient mode; for the latter, a transient valve position time history affords transient flow-rate control. This PC also controls initiation of all events, including gating of data acquisition hardware and triggering of the motor control system.

A second 16-in.-diameter valve is installed downstream of the control valve. This manually actuated valve is used to "load" or add additional hydrodynamic losses in the facility. In this way, the pressure drop required in the facility to control flow rate is accomplished across both the manual and the transient valve. This results in reduced noise and a lower susceptibility to cavitation at the valves relative to the case where the total pressure drop occurs over just one valve. This was desirable for planned future impeller noise and cavitation experiments requiring low facility noise. During a transient run, the manual valve is set to a stationary position chosen to provide the best distribution of pressure drop (low cavitation susceptibility) across each of the valves.

To reduce structural and fluid-borne noise, vibration and noise isolators are used where appropriate. The water in the facility is conditioned by use of a deaerator, a filter (1 to 25 microns), and a heat exchanger. Provision is included for conducting tests at facility pressures ranging from a slight vacuum up to a gauge pressure of 758,500 pascals (110 psig). In this study all tests, steady-state and transient, were conducted at facility pressures sufficiently high to preclude cavitation.

Pump hydrodynamic performance was obtained through measurements from the transient flowmeter, the high frequency response pressure sensors located in the inlet pipe and the test section, the torque meter located between the motor and impeller shafts, and the impeller rotational speed from the motor tachometer. Instantaneous flow rate was monitored to within ±1 percent of reading accuracy in either steady-state or transient operation by a transient, electromagnetic flowmeter (see Lefebvre and Durgin, 1990). Pressure transducers were installed at two locations in the test section. One sensor was on top, while the second one was in one of the side viewing ports. These sensors allowed for the identification of any asymmetry in the discharge flow field. A Masscomp 5500 Data Acquisition System was used to digitize and acquire the data.

Transient Profiles

Four different transient profiles were tested with the impeller accelerated from rest followed by a period of deceleration. One of the profiles was obtained solely by controlling motor rpm, i.e., "no flow control" (the control valve was held stationary at an open position). Peak N and Q for that profile were 2400 rpm and 416 l/s (6600 gpm), respectively. The purpose of the "no flow control" profile was to assess whether adjusting control valve position throughout the transient produced any anomalies regarding transient performance.

The remaining three profiles were obtained through simultaneous control of N and Q and were designated high-acceleration, half-acceleration, and low-acceleration. The half-acceleration profile was obtained by multiplying the time axis of the high-acceleration profile by a factor of two, thus halving the acceleration time history. The low-acceleration profile experienced the lowest acceleration of the three. Each experienced a peak flow rate of 315 l/sec (5000 gal/min) which resulted in a peak mean velocity in the inlet pipe of 4.3 m/s (14 ft/s). Depending on the profile, a peak rotational speed of either 2000 or 2400 rpm was reached within 0.4 to 0.8 second from the start of the transient. Once peak rotational speed was attained, impeller deceleration was immediately initiated. The complete transient, including deceleration, lasted from 1.5 to 3.5 seconds. A summary of the peak operating parameters for each of the four transient profiles are provided in Table 1.

Table 1 Summary of major operating parameters for the transient profiles

		MOTOR & FLOW CONTROL			NO FLOW CONTROL
		HIGH ACCEL.	HALF ACCEL.	LOW ACCEL.	
Q_{max}	l/sec (GPM)	315 (5000)	315 (5000)	315 (5000)	416 (6600)
$V_{inlet_{max}}$	m/sec (ft/sec)	4.3 (14)	4.3 (14)	4.3 (14)	5.7 (18.7)
$A_{inlet_{max}}$	g	0.9	0.6	0.5	1.7
N_{max}	RPM	2400	2400	2000	2400
α_{max}	rad/sec^2	720	390	266	720

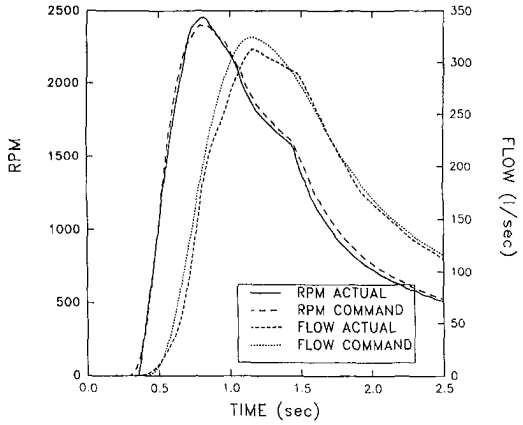

Fig. 3 Input profiles for high acceleration transient (uncertainty in N = ±1 percent, in Q = ±1 percent)

The input N and Q profiles for the high-acceleration time history are provided in Fig. 3. Both the user-specified command signal and the resulting transient are shown versus time for each variable. The successful transient performance of the facility is manifested in the close agreement between the curves of the command or input and those actually obtained in the facility for each of the control variables. Similar agreement was obtained for the other transient profiles which will be shown in later figures along with the resulting hydrodynamic performance data. For any given transient profile, the facility repeatability between runs was within ±0.5 percent.

The high level of acceleration in both N and Q during the early portion of the transient should be noted. For a considerable portion of the ramp-up, each variable experiences an approximately constant acceleration with values of 720 rad/s^2 and 0.9 g for N and Q, respectively. These values are also the maximum values for the complete transient as provided in Table 1. They were obtained by averaging the instantaneous acceleration values (calculated using a five point differencing method) of the Q or N curve up to a time just prior to that of peak Q or N. The resulting transient C_q versus time curve, shown in Fig. 4, is an indication of incidence angle at the blade leading edge and also its time rate of change.

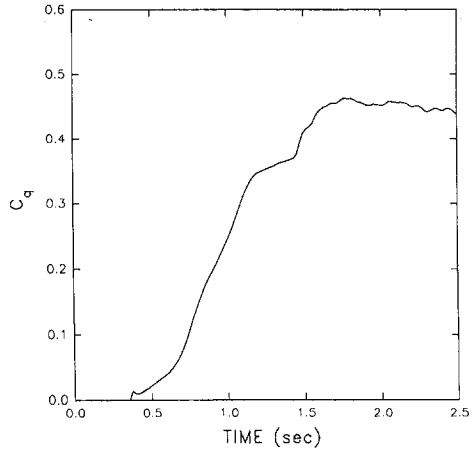

Fig. 4 C_q time history for high acceleration transient (uncertainty in C_q = ±4 percent, in time = ±60 ms)

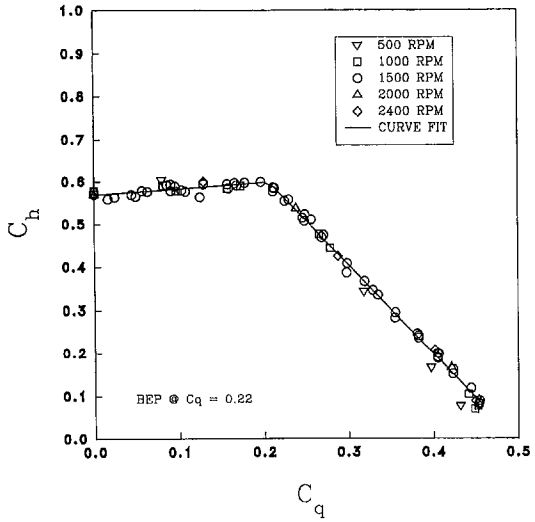

Fig. 5 Steady-state hydrodynamic performance (uncertainty in C_h = ±4 percent, in C_q = ±5 percent)

Results

Prior to transient testing, the impeller's steady-state hydrodynamic performance characteristics were determined in the ITF. These data formed the basis for the quasi-steady calculations to which the transient data were compared. Figure 5 shows the steady-state hydrodynamic performance of the impeller expressed as C_h versus C_q where C_h is the nondimensional head or pressure developed by the pump and is expressed as

$$C_h = \frac{gH}{(\pi ND/60)^2}, \tag{2}$$

where H is the head developed by the pump and g is the acceleration due to gravity. Data are presented for a range of impeller speeds and a least-squares curve fit of all the data is plotted as the solid line. The collapse of data onto a single curve for the different impeller speeds and the small amount of scatter provides confidence in the facility and associated instrumentation; it also indicates that speed scaling effects are negligible. The impeller's steady state best efficiency point (BEP) occurs at a C_q of approximately 0.22 with a corresponding C_h of 0.55.

In all of the following plots of transient performance data, the instantaneous value of pressure obtained from the upstream and downstream pressure sensors was used in calculating $C_{h_{tr}}$,

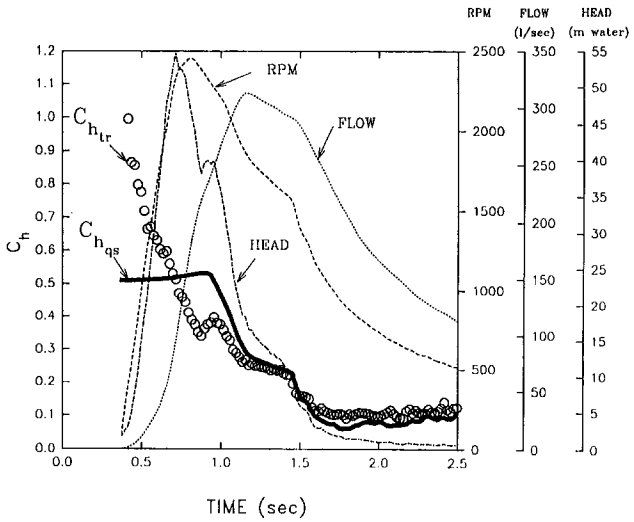

Fig. 6 Hydrodynamic performance during high acceleration transient (uncertainty in N = ±1 percent, in Q = ±1 percent, in H = ±2 percent, in C_h = ±4 percent, in time = ±60 ms)

as was done for the steady-state data. The pump actually develops an additional pressure rise during the transient, but this rise is not seen by the pressure sensors because it is used to accelerate the fluid mass within the impeller region. Ideally, this mass term should be added to the measured pressure rise. However, to calculate that term, instantaneous values of acceleration would have to be obtained by differentiating the transient flow-rate curve. This was done for several cases, and the additional pressure term was found to have a negligible effect, i.e., the acceleration term affected total pressure rise by no more than 2 percent and then only for several hundred milliseconds around peak acceleration. Because this term had less of an effect on $C_{h_{tr}}$ than the inaccuracy incurred from differentiating the flow-rate data, it was felt that a more accurate presentation of the data would result by omitting it.

All transient impeller performance data, expressed as transient head coefficient $C_{h_{tr}}$, were compared to the impeller's steady-state C_h values to evaluate the quasi-steady assumptions commonly used in transient impeller design. At each instant in time for which transient data were acquired, the instantaneous transient C_q value was calculated and subsequently applied to the steady-state least-squares curve fit to obtain the instantaneous quasi-steady value of $C_{h_{qs}}$.

The resulting transient hydrodynamic performance data, $C_{h_{tr}}$ versus time, for the high-acceleration input profile is presented in Figure 6 along with the quasi-steady equivalent, $C_{h_{qs}}$. Note that the actual transient begins at 0.38 second as a result of a triggering delay between the start of data acquisition and the transient. Also included in the figure for convenience and reference are the rpm, flow rate, and head curves.

As shown in the graph, acceleration has a profound effect on impeller operation. The apparent substantial and abrupt improvement in performance over the quasi-steady case at the start of the transient for times up to 0.7 second decays quickly and is most likely caused by impulsive pressure as the transient is initiated. Conversely, reduced performance is evident between 0.7 and 1.4 seconds, similar to that observed by Tsukamoto and Ohashi (1982) who attributed it to a time lag in the formation of circulation and subsequent lift force at the blades.

The reduced performance may be associated with the flow at the blades' leading edge where a high incidence angle exists during the beginning of the transient. It is likely that during transient operation, the extent of the blades' leading edge separation region differs from that during steady-state resulting

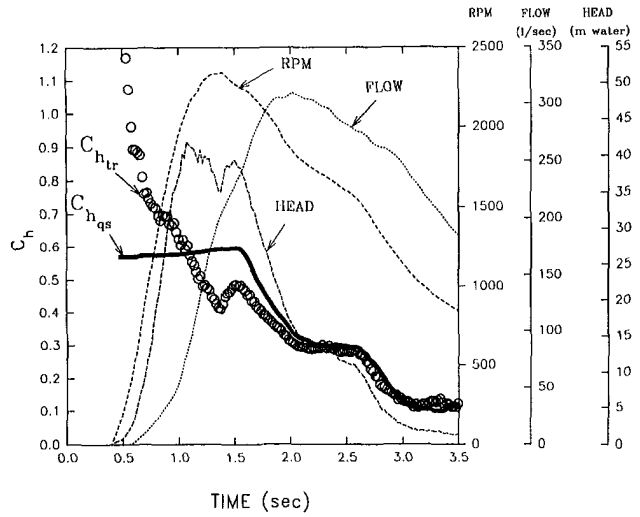

Fig. 7 Hydrodynamic performance during half-acceleration transient (uncertainty in $N = \pm 1$ percent, in $Q = \pm 1$ percent, in $H = \pm 2$ percent, in $C_h = \pm 4$ percent, in time = ± 60 ms)

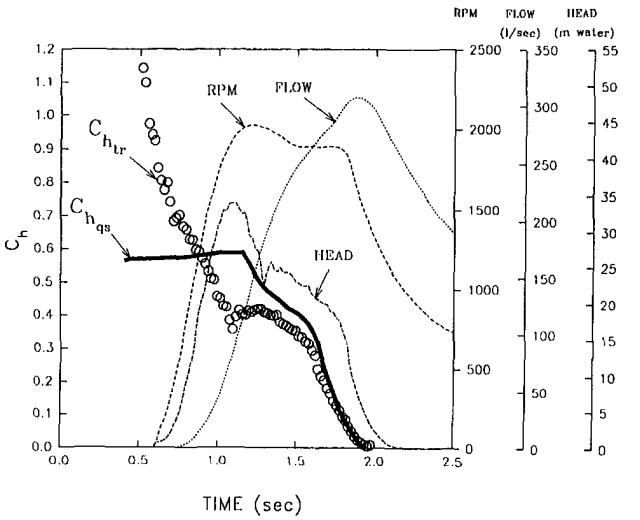

Fig. 8 Hydrodynamic performance during low acceleration transient (uncertainty in $N = \pm 1$ percent, in $Q = \pm 1$ percent, in $H = \pm 2$ percent, in $C_h = \pm 4$ percent, in time = ± 60 ms)

in a change in effective inlet area and, hence, performance. Additionally, the time scale of the transient is small relative to that of viscous diffusion which precludes or at least mitigates recirculation or backflow at and upstream of the impeller leading edge. Recirculation typically occurs during steady state operation at low C_q's (≤ 0.1) due to blade leading edge separation. This was at least partially confirmed through laser Doppler velocimetry measurements made through the clear inlet pipe at 30-cm (12 in.) upstream of the impeller. Significant recirculation was observed during the steady state and resulted in a turbulence intensity of about 20 percent of the local mean velocity; recirculation was not perceivable during the transient which exhibited a turbulence intensity of only 3 percent.

It is worth noting, that, deviations in leading edge effects between transient and quasi-steady were observed by many others including the early study of Farren (1935) on the simplified geometry of an airfoil initially at stall and undergoing a rapid decrease in incidence angle. Stall or leading edge separation persisted beyond the steady-state stall angle (to smaller angles). Throughout stall the transient lift force was significantly less than that in steady state indicating significant changes in the separated flow region.

One interesting point becomes apparent when comparing the rpm curve and the $C_{h_{tr}}$ curve of Fig. 6. An abrupt change in the sign of the slope of the $C_{h_{tr}}$ curve occurs approximately 0.07 second after the peak in rpm is reached or at a time of 0.87 second. After that time, the $C_{h_{tr}}$ curve tends to approach the quasi-steady values at a relatively fast rate. Because this change occurs very early in the deceleration phase of the motor rpm, it was at first felt that the deceleration and its effect on the flow field is responsible for the change of slope. However, data from the "no flow control" profile refute that supposition as will be discussed later.

The second bump in the $C_{h_{tr}}$ curve, where the sign of the slope changes again, occurs at approximately 0.9 second. This is near the C_q at which the slope also changes in the steady-state curve, Fig. 5, which is also near the time that the design C_q is reached. This indicates a potential similarity between steady-state and transient phenomena. This slope change, observable under both operating conditions, may be associated with the reduction in blade incidence angle as the design C_q is approached with the corresponding suppression of leading edge separation. The observation relative to the second bump was evident in all four profiles.

Figures 7 and 8 give the time histories for the half- and low-acceleration cases, respectively. The transient effect for both

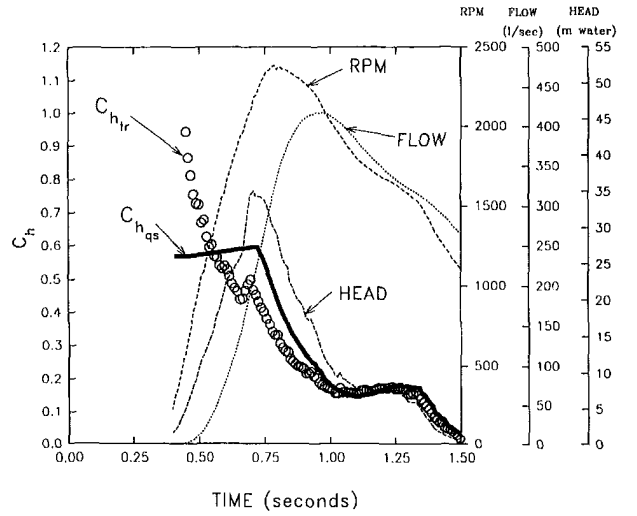

Fig. 9 Hydrodynamic performance during no flow control transient (uncertainty in $N = \pm 1$ percent, in $Q = \pm 1$ percent, in $H = \pm 2$ percent, in $C_h = \pm 4$ percent, in time = ± 60 ms)

cases is virtually identical to that of the high-acceleration case and all previous observations apply. For times after the effect of the impulsive pressure decays, the maximum deviation between the transient and the quasi-steady C_h occurs near the peak rpm at the first bump and is about 37 percent for the high-acceleration and low-acceleration cases. The half-acceleration case had a slightly reduced maximum deviation of approximately 32 percent.

The time history for the "no flow control" profile, shown in Fig. 9, has an rpm curve that is similar to that of the high-acceleration case, however, since Q was not controlled, its peak value reached 416 l/s rather than 315 l/s. Peak acceleration of Q was also considerably higher being 1.7 g's rather than 0.9 g's. The general trends for this case are similar to that of the other three transient cases, thus verifying that transient valve operation produced no anomalies. The maximum deviation between the transient and the quasi-steady C_h is lower than the other cases but still considerable at approximately 28 percent. Similar to the other profiles, the maximum deviation also occurs near the first bump in the curve. Unlike the other cases, this does not occur immediately after reaching peak RPM and during impeller deceleration; it occurs near the mid-

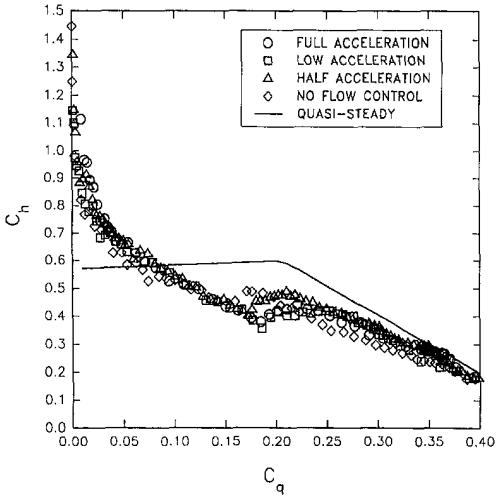

Fig. 10 Hydrodynamic performance for four transient cases (uncertainty in C_h = ±4 percent, in C_q = ±4 percent)

region of the linear rise in both rpm and Q. For all four profiles, however, this first slope change does occur fairly close to the location where the steady state curve changes slope and is likely related to the blade inlet incidence angle.

All four profiles also show that the developed head peaks and begins to decrease while the pump speed is still increasing. By viewing only the high, half and low acceleration cases (Figs. 6, 7, and 8, respectively) it appears that this occurs as the instantaneous value of $C_{h_{tr}}$ crosses below the quasi steady C_h curve. However, there is no apparent physical significance for any correlation between the transient and quasi-steady curves. Indeed, the "no flow control" profile, Fig. 9, shows the peak in developed head occurs significantly later than the cross over point and near the "knee" in the quasi-steady curve. Currently this phenomenon is being investigated further.

Figure 10 compares the transient performance for each of the four cases with the quasi-steady performance. This figure shows $C_{h_{tr}}$ data plotted against C_q rather than time. The data are shown for C_q from 0.0, which is the start of the transient, to 0.4. This range of C_q values includes the initial portion of the transient where C_q is increasing. The time during each transient that corresponds to a C_q of 0.4 is 1.5, 3.0, 1.7 and 1.0 seconds for the high-, half-, low-, and no flow control accelerations, respectively. The same discussion given for the $C_{h_{tr}}$ versus time data can be applied to Fig. 10. All transient curves virtually collapse onto a single curve with the transient effect very evident.

Conclusions

A new facility for transient and steady-state impeller research has been designed and built. The facility provides time-dependent control of C_q through user-defined, simultaneous, transient control of both impeller rotational speed and flow rate. This provides considerable flexibility when experimentally modeling pump performance in various piping systems.

A centrifugal impeller with a design specific speed of 66 (rpm * $\sqrt{m^3/s}/m^{0.75}$) or 3400 (rpm * $\sqrt{gpm}/ft^{0.75}$) was evaluated for hydrodynamic performance under steady state and transient operation in order to evaluate the quasi-steady assumption commonly used for the design of impellers operating under transient conditions. Four transient profiles were tested; each included a high acceleration at the outset of the transient followed by a relatively slow deceleration.

Results showed that transient effects are significant. At the start of the transient, non-dimensional head, $C_{h_{tr}}$, is considerably higher than the quasi-steady value; this difference has been tentatively assumed to be associated with an impulsive pressure rise. After the effects of this impulsive pressure decay, the situation reverses and the quasi-steady assumption overestimates the actual transient C_h values by as much as 37 percent. This reduced performance occurs over a significant portion of the transient. The mechanism(s) responsible for the reduced C_h values during the transient is unknown at this time but, hopefully, will become evident during planned future tests where details of the flow field will be investigated.

The substantial effects of transient operation on impeller hydrodynamic performance have demonstrated that the quasi-steady assumptions commonly used for the design of impellers that operate under transient (accelerating or decelerating) conditions are not valid for many applications. It should be noted that quasi-steady design methods may be applicable for other pump designs or less extreme transients. Transient effects must be incorporated in the design process to improve performance prediction capabilities and to optimize designs. That may prove difficult in application considering that, during a transient, the impeller operates most of the time far from the design point. This requires that a wide range of incidence angles at the blades leading edge must be accommodated.

Future plans include investigations of the cause of the transient effects by interrogating details of the flow field. Additional tasks include applying the knowledge gained from the experimental tasks to the development of a three-dimensional, incompressible, viscous-flow computer simulation of the transient flow field to extend the understanding of the physics and to make this simulation available as a design tool in the optimization of future impellers.

Acknowledgments

This project was supported by the Independent Research Program at the Naval Undersea Warfare Center Division, Newport, RI.

References

Barrand, J., Ghelici, N., Caignaert, G., 1993, "Unsteady Flow During the Fast Start-up of a Centrifugal Pump," ASME FED-Vol. 154, *Pumping Machinery*.

Farren, W. S., 1935, "The Reaction on a Wing Whose Angle of Incidence is Changing Rapidly," British ARC Report and Memorandum No. 1648.

Lefebvre, P. J., and Durgin, W. W., 1990, "A Transient Electromagnetic Flowmeter and Calibration Facility," ASME JOURNAL OF FLUIDS ENGINEERING, Vol. 112, No. 1.

Lefebvre, P. J., and Barker, W. P., 1991, "Evaluation of Transient Effects on 1/3-Scale-Model Submarine Launch Pump Impellers," Technical Report No. 7032, Naval Underwater Systems Center, Newport, RI.

Nguyen Duc, J., Von Kaenel, A., Danguy, F., 1993, "Transient Behavior of Liquid Hydrogen Pumps During Start-up and Shutdown of Rocket Engines," ASME FED-Vol. 154, *Pumping Machinery*.

Saito, S., 1982, "The Transient Characteristics of a Pump During Start Up," *Bulletin of the JSME*, Vol. 25, No. 201, Mar.

Tsukamoto, H., and Ohashi, H., 1982, "Transient Characteristics of a Centrifugal Pump During Starting Period," ASME JOURNAL OF FLUIDS ENGINEERING, Vol. 104.

Tsukamoto, H., et al., 1986, "Transient Characteristics of a Centrifugal Pump During Stopping Period," ASME JOURNAL OF FLUIDS ENGINEERING, Vol. 108.

G.R. Noghrehkar

M. Kawaji

Department of Chemical Engineering and Applied Chemistry, University of Toronto, Toronto, Ontario, Canada M5S 1A4

A.M.C. Chan

Ontario Hydro Technologies, Toronto, Ontario, Canada M8Z 5S4

H. Nakamura

Y. Kukita

Department of Safety Research, Japan Atomic Energy, Research Institute, Tokai-mura, Ibaraki 319-11, Japan

Investigation of Centrifugal Pump Performance Under Two-Phase Flow Conditions

A one-dimensional two-fluid model has been used to study the centrifugal pump head degradation phenomena and to analyze the gas-liquid interaction within the pump impeller under high pressure, steam-water two-phase flow conditions. The analytical model was used to predict the two-phase pump head data for the small-scale and full-scale nuclear reactor pumps and the predictions of the head degradation compared favorably with the test data for different suction void fractions. The physical mechanisms responsible for head degradation were also investigated.

1 Introduction

In loss-of-coolant accidents in nuclear reactors, which usually result from a break in the heat transport piping, the coolant may undergo rapid depressurization and form vapor-liquid two-phase flow. The reactor pumps continue to circulate the two-phase mixture for a while, however, the centrifugal pump head under two-phase flow conditions is known to degrade drastically compared to that for single-phase flow. The degree of pump head degradation is likely to depend on various physical, geometrical, and thermal conditions of the system, but the physical mechanisms responsible for the head degradation phenomena have not been well understood.

Because of the difficulties associated with the analytical modeling of two-phase flow performance of the centrifugal pump, most of the existing models or correlations for pump head degradation are empirical. The deficiencies in these empirical models have been discussed by Kim (1983) among others. The empirical correlations depend only on suction void fraction and have not considered the effects of slip velocity, pump geometry and specific speed, condensation and compressibility in determining the two-phase pump performance. For this reason, establishing a widely applicable empirical correlation valid for centrifugal pumps of all sizes and different impeller geometries is quite difficult and there is a clear need for an analytical model.

Hench and Johnston (1972) developed an analytical model for the calculation of two-phase flow in a stationary two-dimensional diffuser. In their study, the pressure recovery performance of straight-wall diffusers with the air/water mixtures was investigated. They used a one-dimensional control-volume method for solving the continuity and momentum equations for the gas and liquid phases. The flow was assumed to be steady-state and bubbly with no condensation taking place within the diffuser. Zakem (1980) applied the same method to straight-bladed impellers in a centrifugal pump. He developed an analytical description of the gas-liquid interaction that occurs in a rotating impeller in order to predict the slip ratio.

Furuya (1984) used the same method as that of Zakem and developed an analytical model which revealed several important features related to the basic mechanisms of two-phase pump head degradation. His analytical model incorporated pump impeller geometry, void fraction, flow slippage and flow regime into the continuity and momentum equations for gas and liquid flowing through the pump impeller. The compressibility and condensation effects were neglected in the first version, however, an improved version was developed by Furuya and Maekawa (1987), which fully took into account the condensation effects and compressibility of the vapor phase. One-dimensional control volume approach was used in their model, in which the mass conservation equations for each phase, the momentum equations for the two-phase mixture and the vapor phase, and the energy equation for the mixture were solved.

Minato and Yamanaouchi (1985) also developed an analytical model that solves the momentum equation for each phase within the pump without condensation taken into account. Their model predictions compared reasonably well with the steam/water test data obtained in three model pumps.

Some experiments have been conducted in the past to ex-

Contributed by the Fluids Engineering Division for publication in the JOURNAL OF FLUIDS ENGINEERING. Manuscript received by the Fluids Engineering Division March 4, 1993: revised manuscript received April 27, 1994. Associate Technical Editor: L. Nelik.

amine the nature of two-phase flow in small pump impeller passages and rotating ducts. Patel and Runstadler (1978) studied the effects of rotation on two-phase bubbly flow through a rotating square duct. Manzano-Ruiz and Wilson (1983) have reported observing bubbly and churn-turbulent flow regimes in an unshrouded impeller as more air was supplied to the water flowing through the pump. Minemura et al. (1993) recently measured void fraction distributions in a straight channel, which was rotated around an axis perpendicular to the channel. By circulating a bubbly air/water mixture through the 32 mm × 32 mm square channel, they reported significant variations in void fraction in both the axial as well as transverse directions.

In the present work, a one-dimensional two-fluid model, similar to that of Furuya and Maekawa (1987) has been used to predict the pump head and analyze the gas-liquid interaction within the pump impeller under steam-water, two-phase flow conditions. The model was used to predict the two-phase pump head data for small-scale and full-scale nuclear reactor pumps obtained recently at Ontario Hydro's Pump Test Facility under high temperature/pressure, two-phase flow conditions. In this paper the two-fluid model predictions are compared with the test data for different suction void fractions. The test facilities and procedure are first described briefly, followed by the model formulation and comparison of predictions with the data. Since the large-scale pumps have never been tested under two-phase flow conditions previously, a more detailed description of the full-scale pump tests and a complete set of experimental results will be presented in a separate paper (Chan et al., 1994).

Table 1 Pump specifications

	SMALL PUMP	LARGE PUMP
Pump Size	4" × 4" × 7-1/2"	20" × 20" × 24" × 32"
Pump Type	Vertical Centrifugal Single Suction	Centrifugal Double Volute Single Suction Double Discharge
Impeller Diameter	0.176 m	0.78 m
Rated Head	39.6 m	224.2 m
Rated Flow	0.06 m^3/s	3.1 m^3/s
Specific Speed (dimensionless)	0.168	0.164
Design Pressure	7.2 MPa	12.8 MPa
Design Temperature	280 °C	280 °C
Motor Power	29.8 kW	9400 kW
Motor rpm	3560	1793
Number of Blades	5	5

2 Test Facilities and Procedure

Two geometrically similar types of centrifugal pumps have been tested at Ontario Hydro. One was a low head (39.6 m) small-scale pump with a specific speed of 0.168, and the other was a high head (224.2 m) full-scale pump with a specific speed of 0.164 which is identical to those used in the Primary Heat Transport System of the CANDU nuclear reactors at Darlington Nuclear Generating Station. The specifications of the two pumps are shown in Table 1. The tests have been performed in the first quadrant of the head-flow diagram and at steady-state conditions.

2.1 Test Loop and Process Conditions. Two separate test loops with substantially different pipe sizes were used in the present tests. The description of the small-scale pump test loop can be found elsewhere (Chan et al., 1991). The test loop was fully instrumented to measure the flow conditions at the suction and discharge of the pump by a full complement of transducers covering pressure, temperature, pressure rise across the pump, single-phase liquid flow rate and motor parameters. Two single-beam, three-detector gamma densitometers and two arrays of five point Pitot probes were used at the suction and discharge of the pump to measure the local void fractions and the local velocity heads respectively.

The test loop configuration for the full-scale pump tests is shown in Fig. 1. The operating temperature and pressure of the test loop were varied from 110°C/0.15 MPa to 280°C/6.4 MPa. The initial single-phase flow rates at each temperature/pressure were set at 80, 100, and 130 percent of the pump's rated flow. The test loop was fully instrumented to monitor all the important parameters under two-phase flow conditions. They included flow rate, pump head, motor power, void fraction at the suction, and discharge of the pump as well as pressures and temperature around the loop. Similar instrumentation as the one used in the small-scale pump tests was used in this loop to measure the two-phase mass flow rate and void fractions at the suction and discharge of the pump. In particular, the suction void fraction was measured using a five-beam, five-detector gamma densitometer specially designed for a 24-in.

Nomenclature

A = cross-sectional area of the pump blade flow passage, m^2
C_d = drag coefficient
C_{vm} = virtual mass coefficient
e = total specific energy, J/kg
F_c = centrifugal force per unit axial length, N/m
g = gravitational constant, m/s^2
H = pump head, m
m = mass flow rate, kg/s
p = static pressure, Pa
R_b = gas bubble radius, m
r = radial distance measured from the center of rotation, m
u = relative velocity, m/s
v = absolute velocity, m/s
v_u = tangential component of v, m/s
x = quality
z = coordinate along the flow path
α = void fraction
β = geometrical angle of the z-coordinate made with the circle whose center is the center of rotation, rad
δ_w = rate of liquid vaporization per unit flow path length, kg/m · s
ΔZ = axial length of control volume, m
$\Delta H_{2\phi}$ = two-phase pump head increase, m
ΔH = single-phase pump head increase, m
ρ = density, kg/m^3
ω = angular velocity of the pump impeller, rad/s

Subscripts

b = bubble
c = centrifugal
d = drag
g = gas
l = liquid
R = rated
s = single-phase
sat = saturation
T = two-phase
vm = virtual mass
1 = inlet
2 = outlet
2ϕ = two-phase

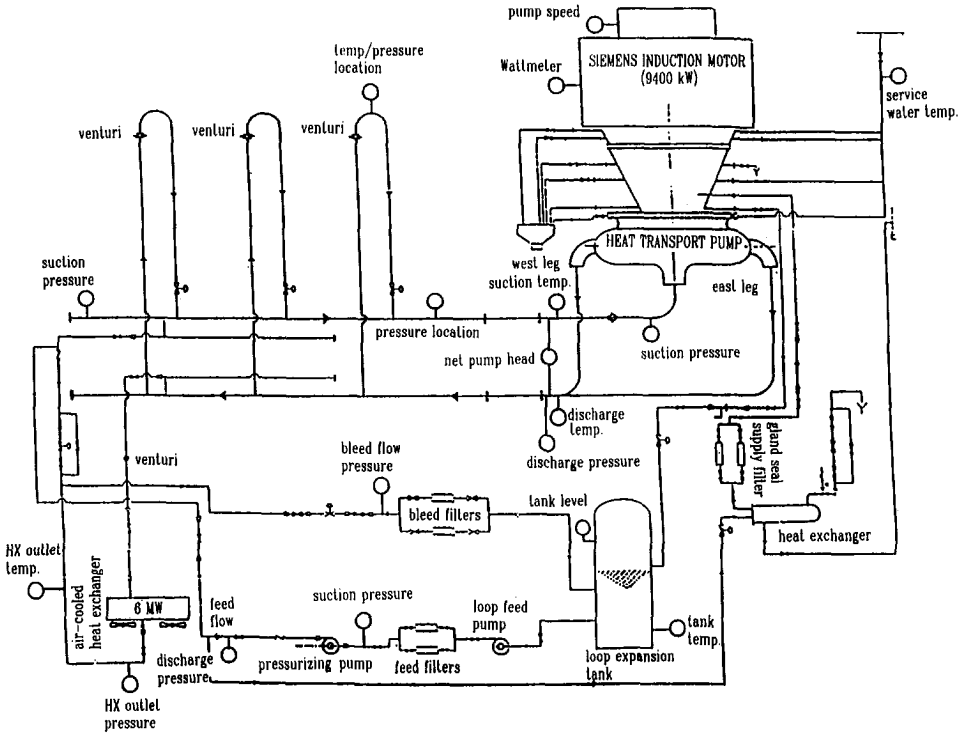

Fig. 1 Schematic of large-scale pump test facility

pipe. The design and calibration of the five-beam gamma densitometer have been described by Chan (1992).

2.2 Test Procedure and Data Reduction. In both tests, the test loop was first filled with de-aerated and de-ionized water and then pressurized and heated up to the desired temperature. After the loop was brought to the steady-state conditions, the water was bled from the loop in steps to create two-phase flow in the loop. The loop average void fraction could be determined by the amount of water drained from the loop. System voids of increasing magnitude were obtained by bleeding the loop in steps. When the loop conditions stabilized, the pump head and flow parameters such as pressure, mass flux and void fractions at suction and discharge of the pump were recorded. Separate tests were conducted at different loop temperatures. At each temperature, water was bled from the loop in small steps, so that the mass flow rate of the two-phase mixture decreased, and the average suction void as well as the loop average void fraction increased.

In reducing the two-phase pump head data, the water density, ρ_l, and steam density, ρ_g, were computed at the suction temperature of the pump under saturated conditions. The two-phase mixture density at the suction of the pump can be obtained from the following equation.

$$\rho_{2\phi} = \rho_g \alpha + (1 - \alpha)\rho_l \tag{1}$$

The two-phase pump head is calculated as the ratio of the static pressure difference across the pump to the two-phase mixture density obtained from Eq. (1).

$$H_T = \frac{p_2 - p_1}{\rho_{2\phi} g} \tag{2}$$

Normalized pump head is usually defined as the ratio of the pump head to the rated head, H_R. In the present study, in order to have a better comparison between the model predictions and experimental data, the normalized head is defined as the ratio of the two-phase pump head, H_T, to the single-phase pump head, H_s, at the same suction pressure/temperature.

2.3 Uncertainty Estimates. The estimated uncertainty in the suction void fraction data measured with the five-beam, five detector gamma densitometer is ±5 percent and that for the pressure rise across the pump is ±0.25 percent. The maximum uncertainty for the pump head under two-phase flow conditions was estimated to be ±5 percent.

3 Two-Fluid Model

3.1 Conservation Equations. The basic development of the present two-fluid model parallels the work done by Furuya and Maekawa (1987). The conservation equations derived for the present study include the continuity equations for the liquid and gas, momentum equations for the liquid, gas and two-phase mixture and an energy equation for the two-phase mixture. These equations were formulated assuming steady, one-dimensional, adiabatic flow of incompressible liquid and compressible gas through a pump impeller flow passage between neighboring blades. The liquid and gas were also assumed to be in thermodynamic equilibrium and viscous effects and other nonmechanical losses as well as gravitational effects were neglected.

A one-dimensional control volume, shown in Fig. 2, is defined by "z" denoting the arc length along the stream line which is parallel to the impeller blade profile, "A" denoting the cross-sectional area normal to the direction of "z," and radial distance from the shaft axis, "r." In the derivation of the governing equations, the product of the cross-sectional averages of the various quantities was assumed to be equal to the average of the products.

The continuity equations for the liquid and gas are given by,

$$\frac{d[\rho_l(1 - \alpha)u_l A]}{dz} = -\delta w \tag{3}$$

$$\frac{d[\rho_g \alpha u_g A]}{dz} = \delta w \tag{4}$$

where δw is the rate of vaporization/condensation per unit flow path length.

The momentum equations for the gas and liquid are given by,

$$\frac{d(\rho_g \alpha A u_g^2)}{dz} + C_{vm}\rho_l u_g \frac{d[(u_g - u_l)\alpha A]}{dz} = -\alpha A \frac{dp}{dz} + \rho_g r\omega^2 \alpha A \frac{dr}{dz} - \frac{3}{8}\rho_l \frac{C_d}{R_b}(u_g - u_l)|u_g - u_l|\alpha A \quad (5)$$

and

$$\frac{d[\rho_l(1-\alpha)Au_l^2]}{dz} - C_{vm}\rho_l u_g \frac{d[(u_g - u_l)\alpha A]}{dz} = -(1-\alpha)A\frac{dp}{dz} + \rho_l r\omega^2(1-\alpha)A\frac{dr}{dz} + \frac{3}{8}\rho_l \frac{C_d}{R_b}(u_g - u_l)|u_g - u_l|\alpha A \quad (6)$$

where the virtual mass force is considered using formulations by Drew et al. (1979) and Wallis (1969), and centrifugal force is also included.

Equations (5) and (6) can also be added to yield the momentum equation for the two-phase mixture,

$$\frac{d[\rho_g \alpha A u_g^2]}{dz} + \frac{d[\rho_l(1-\alpha)u_l^2]}{dz} = -A\frac{dp}{dz} + [\rho_g \alpha + \rho_l(1-\alpha)]r\omega^2 A\frac{dr}{dz} \quad (7)$$

Using the energy equation for the two-phase mixture as given by Furuya and Maekawa (1987) and the mechanical energy equations for the gas and liquid which can be obtained by multiplying Eqs. (5) and (6) by u_g and u_l, respectively, an expression for the vaporization/condensation rate, δw, can be derived as follows (Noghrehkar, 1992).

$$\delta w = -\frac{A}{h_g - h_l + \frac{1}{2}(u_l^2 - u_g^2)}\left\{\rho_g \alpha u_g \frac{dh_g}{dz} + \rho_l(1-\alpha)u_l\frac{dh_l}{dz} - \frac{1}{A}\left[u_g\frac{d(p\alpha A)}{dz} + u_l\frac{d[p(1-\alpha)A]}{dz}\right] - \frac{1}{A}\left[C_{vm}\rho_l u_g(u_g - u_l)\frac{d[(u_g - u_l)\alpha A]}{dz}\right] - \frac{3}{8}\frac{C_d}{R_b}\rho_l \alpha(u_g - u_l)^2|u_g - u_l|\right\} \quad (8)$$

The virtual mass term in the above equation contains the liquid density and is different from that given by Furuya and Maekawa (1987) containing the vapor density. From a physical view point, the present formulation is more appropriate for bubbly flows as it accounts for the acceleration of the liquid surrounding the vapor bubble, which is the virtual mass effect.

In the present model, Eqs. (3), (4), (5), and (7) were solved along with the condensation rate equation (Eq. (8)) and constitutive equations described below using the Runge-Kutta method to investigate the pump head degradation mechanism under steam-water two-phase flow conditions.

3.2 Flow Regimes and Constitutive Equations. Bubbly and churn-turbulent flow regimes were considered to be the main flow regimes occurring within the pump impeller flow channels under steam/water two-phase flow conditions. We could assume stratified flow pattern in the impeller passage, however, little work has been done on the flow pattern identification in centrifugal pumps at high pressure/temperature even in small-scale pumps and to the authors' knowledge, no reliable information is yet available on two-phase flow in full-scale centrifugal pumps.

In the present calculations, the bubbly flow regime was assumed to exist when the local void fraction is less than 0.25 and the ratio of drag coefficient to bubble radius, C_d/R_b, was taken to be 340.2 m^{-1} as originally used by Hench and Johnston (1968) for a flow in a diffuser. The value of the virtual mass coefficient, C_{vm}, for bubbly flow was set at 0.5.

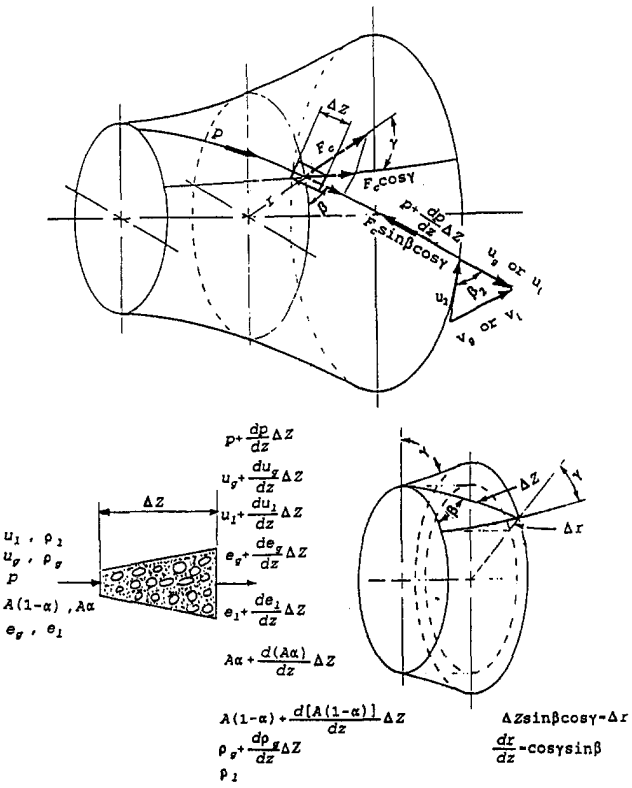

Fig. 2 Control volume method for rotating machines and force diagrams

If the local void fraction is greater than 0.35, the flow regime was assumed to be churn-turbulent and the value of C_{vm}, which applies only to discrete bubbles, was set to zero. For the ratio of drag coefficient to bubble radius, C_d/R_b, in churn-turbulent flow regime, Zuber and Hench (1962) suggested the following empirical correlation,

$$\frac{C_d}{R_b} = 110(1-\alpha)^3 \quad (9)$$

where C_d/R_b is given in m^{-1}.

For transition between the bubbly and churn-turbulent flow regimes, the values of C_d/R_b and C_{vm} were obtained by linear interpolation between their respective values at $\alpha = 0.25$ and $\alpha = 0.35$. Sensitivity of the model predictions to the particular values of C_d/R_b and C_{vm}, and the flow regime transition criteria used was also investigated and will be discussed in a later section.

The constitutive relations described above were used for both small and large scale pumps, although their applicability, especially to the larger flow passages in full-scale pumps, has not been fully established. The effect of scale is still an unresolved issue for two-phase flow even in straight pipes, as there are few data taken in such large channels. Thus, the approach taken here was to use the constitutive relations that would work for the smaller pump and see if there are any discrepancies between the predicted and measured results for the large-scale pump; if there are notable differences, then they could be attributed to the scale effect.

3.3 Two-Phase Pump Head Calculations. It is not easy to define a universally acceptable pump head for two-phase flow, because each phase has its own velocity and density. In various two-phase pump experiments conducted previously, only the static pressure difference between the suction and dis-

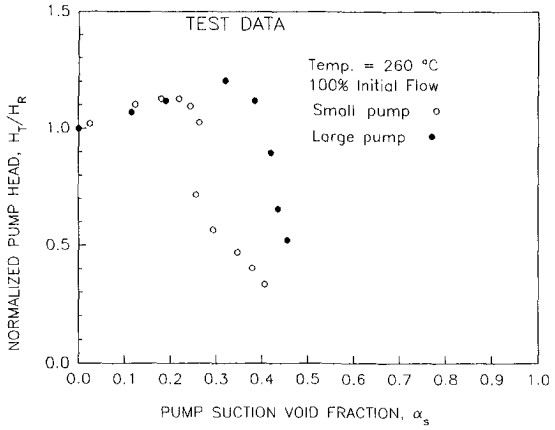

Fig. 3 Effect of pump geometry on threshold suction void fraction

charge of the pump was used and the dynamic heads at the inlet and outlet of the pump were neglected.

In the present analysis, the dynamic heads at the inlet and outlet of the pump impeller were considered to be significant, and it was decided to include this portion of energy for calculating the two-phase pump head as follows,

$$\Delta H_{2\phi} = \frac{p_2 - p_1}{(\rho_{2\phi})_1 g} + \frac{1}{2g}[v_{l2}^2(1 - x_2) - v_{l1}^2(1 - x_1)] + \frac{1}{2g}(v_{g2}^2 x_2 - v_{g1}^2 x_1) \quad (10)$$

where the subscripts 1 and 2 refer to the pump suction and discharge, respectively. The absolute gas and liquid velocities in Eq. (10) can be obtained from the velocity triangles at the inlet and outlet of the pump impeller (Fig. 2).

The values of p_2, α_2, u_{l2}, and u_{g2} obtained from the solution of the two-fluid model for a given set of initial conditions were used along with the qualities x_1 and x_2 corresponding to the void fractions α_1 and α_2. Since the inlet quality was not directly measured, it was estimated from the suction void fraction using a void fraction-quality correlation given by Smith (1970).

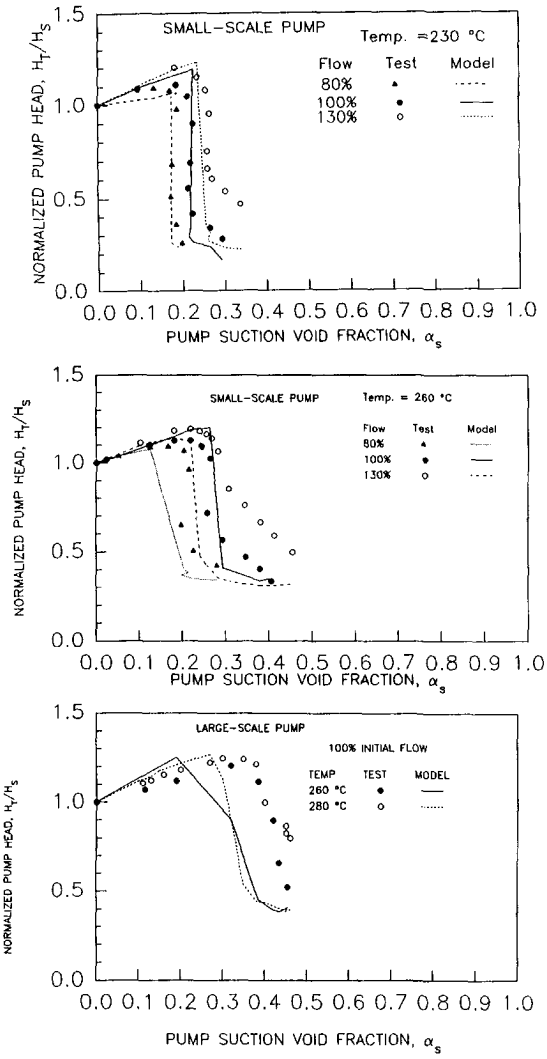

Fig. 4 Comparison of two-phase head between the theory and experimental data for small and large-scale pumps at different initial flow rates

4 Experimental Results and Comparison of Model Predictions

Two-phase pump head degradation data and head-flow characteristics for the small-scale pump have been previously discussed by Chan et al. (1991), so the present discussion will focus on the large pump data as much as possible.

The head degradation test data are plotted against suction void fraction for the small and large pumps in Fig. 3. Similar head degradation trends are observed for both pumps, however, the threshold suction void fraction, at which the pump head starts to degrade rapidly, is significantly higher for the large pump than the small pump. It was shown in Noghrehkar (1992) that under two-phase flow conditions, there exists a good agreement between the head-flow characteristics of the two pumps which have the same specific speed. Although the specific speeds, number of blades and exit blade angles of the pumps were nearly the same between the two pumps tested, the scale and the impeller blade profiles were quite different. As a result, the two-phase flow characteristics or flow regimes may have been different between the two pumps, which can lead to somewhat different head degradation characteristics between the two pumps as a function of suction void fraction.

The two-fluid model described earlier was used to predict the two-phase head degradation for the two geometrically similar centrifugal pumps operating under steam/water two-phase flow conditions. It should be noted that the present model was applied to the pump impeller flow passage only and did not calculate the flow through the pump volute between the impeller and discharge nozzle. In addition, calculation of the circulation loss for two-phase conditions is not well established, so that a direct comparison of the magnitudes of the predicted head or pressure increase between the inlet and outlet of the pump impeller, and the measured head between the suction and discharge of the pump which includes the circulation loss is not feasible. However, the model's validity can be checked by examining the head variation as a function of suction void and the threshold void fraction at which rapid degradation in head occurs.

Figure 4 shows the normalized pump head predicted by the present model compared with the data obtained at 230°C and 260°C for the small pump and at 260°C and 280°C for the large pump. The predicted and experimental results for pump head degradation are in good agreement, particularly for the small pump at the 100 percent initial flow rate. The trend in the measured variation in two-phase pump head as a function of suction void fraction is in general predicted reasonably well by the present analytical model, i.e., a slight increase in pump head at low suction void fractions, then a sudden drop at the threshold void fraction.

4.1 Two-Phase Flow and Heat Transfer Phenomena. From a detailed examination of the calculated variations

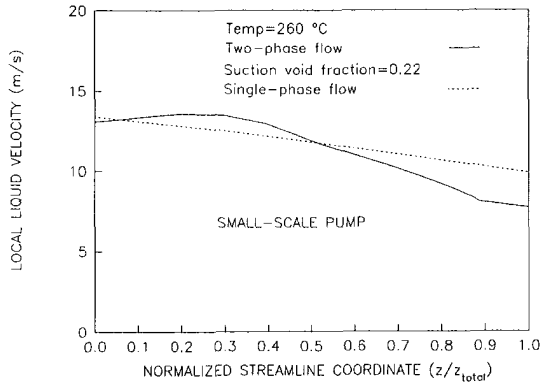

Fig. 5 Liquid velocity variations along the flow passage at 260°C and 22 percent suction void

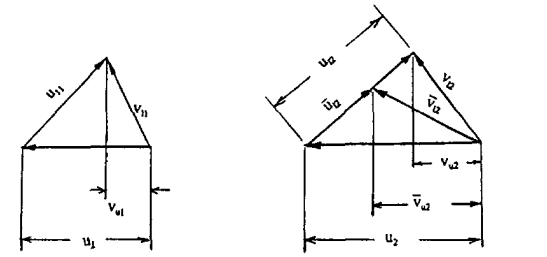

(a) Velocity triangle at impeller inlet

(b) Velocity triangle at impeller outlet

- : Overbar denotes two-phase

Fig. 6 Velocity triangles

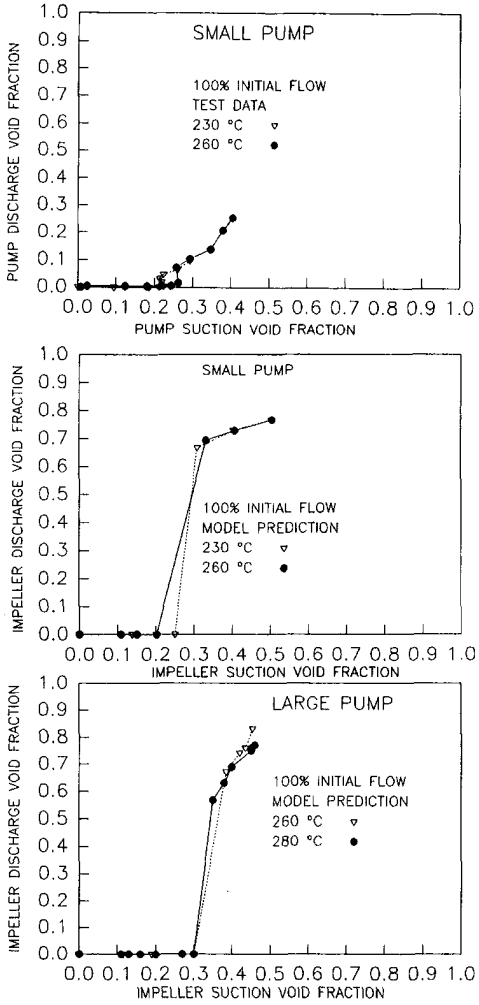

Fig. 7 Comparison of suction and discharge void fractions for small and large pumps at 100 percent initial flow rate and different temperatures

in void fraction, pressure, vapor and liquid velocities, and condensation rates along the flow path, one can obtain a better understanding of the two-phase flow and heat transfer taking place in the pump impeller, and also determine the physical mechanisms responsible for the two-phase head degradation phenomena. An initial increase in the two-phase pump head at low suction void fractions ($\alpha_s \leq 25$ percent) can be explained as follows: as the steam-water mixture flows through the impeller channel, the pressure increases and condensation will take place. The condensation of vapor within the pump impeller channel increases the effective flow area for the liquid phase and thus decreases the relative liquid velocity at the pump outlet compared to the single-phase liquid flow case. This is illustrated by the predicted variations in the liquid velocity along the impeller flow passage shown in Fig. 5 for the cases of two-phase flow at 22 percent suction void and single-phase liquid flow. The velocity triangle (Fig. 6) at the outlet of the pump shows that the reduced relative velocity of the liquid leads to an increase in the tangential component of the absolute velocity, thus generating a pump head even greater than the corresponding single-phase liquid flow (based on the Euler's pump head formula).

Figure 7 shows the measured discharge and predicted void fractions versus suction void fraction at 230°C and 260°C and at 100 percent initial flow rate for the small-scale pump. For suction void fractions less than 20 percent, it is seen that the measured pump discharge void fractions are less than 1 percent, due to condensation taking place along the flow passage. At the same conditions, the analytical results obtained from the present model for small-scale and full-scale pumps also show that for suction void fractions up to 25 percent, vapor is completely condensed even before reaching the exit of the pump impeller. Heidrick et al. (1978) have also shown experimentally that for suction void fractions less than 20 percent the vapor could be condensed totally to liquid and a single-phase liquid flow would be observed at the pump discharge. On the other hand, in two-component gas-liquid flow through the pump with no condensation, Furuya's (1984) calculations have shown that the local void fraction simply increases due to the two-phase slip effect and the head degrades without first increasing as the pump suction void increases. Thus, condensation of vapor is the key to explaining the head increase for suction void less than the threshold value.

For the pump suction void fractions greater than the threshold void fraction, condensation is no longer complete and a sudden pump head degradation can occur. This head degradation will be clearly understood by examining the local two-phase parameters obtained with the present two-fluid model. Figure 8 shows the variations in local void fraction and relative velocities of the gas and liquid along the impeller flow path at 280°C and 100 percent initial flow rate with the inlet void fraction, α_s, as a parameter. It can be seen from Fig. 8(a) that for an inlet void fraction, α_s, less than 30 percent the local void fraction along the flow passage increases slightly at first due to the slip between the phases, but subsequently decreases due to condensation taking place within the flow passage. This range of void fraction decrease corresponds to that for two-phase head increase. For suction void fractions larger than the threshold value ($\alpha_s \approx 25$ percent), the local void fraction rapidly increases along the flow channel (Fig. 8(a)) due to an assumption that the two-phase flow regime changes into churn turbulent flow and the interfacial drag term becomes much

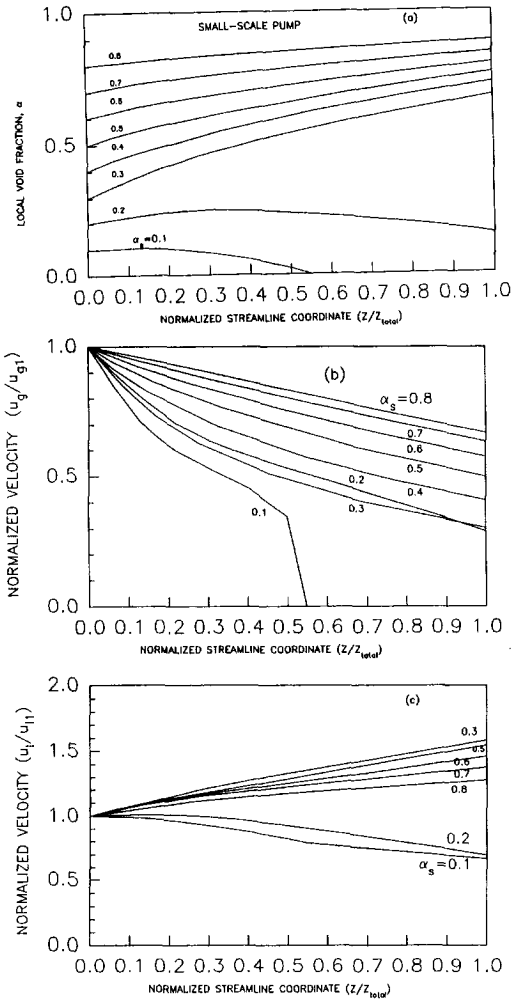

Fig. 8 Local void fraction and relative gas and liquid velocity variations along the flow passage for small pump at 280°C and 100 percent initial flow

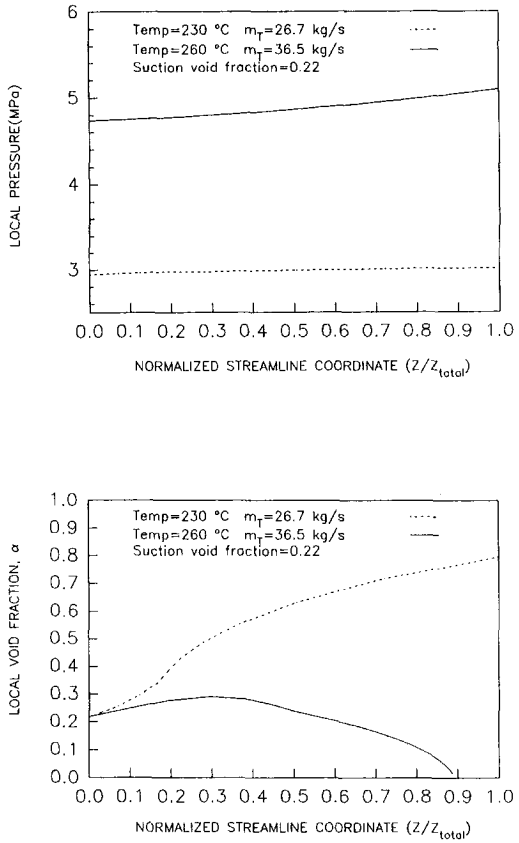

Fig. 9 Void fraction and static pressure variations along the flow passage for small-scale pump at 22 percent suction void and different temperatures

smaller than that for bubbly flow case. When the local void fraction increases, the gas velocity has to decrease (Fig. 8(*b*)) and the liquid phase has to accelerate (Fig. 8(*c*)) in order to maintain the total mass flow rate constant. The acceleration of the liquid phase at the pump outlet reduces the tangential component of the absolute velocity of the liquid (Fig. 6) and severely degrades the pump's two-phase head.

Furuya (1984) has also suggested that the major mechanism responsible for the two-phase pump head degradation is the acceleration of the liquid phase within the pump impeller channels compared to the single-phase liquid velocity. For non-condensible gas-liquid two-phase flow, the velocity of the liquid at the discharge of the pump is larger than that for a condensible two-phase system (for the same pump suction conditions). The increased velocity of the liquid due to a lack of condensation effect explains why the pump head degrades more severely in a non-condensible two-phase system than in a condensible system.

4.2 Temperature Effect on Head Degradation. The condensation effect can also explain why the pump head degrades much less and why the threshold void fraction is higher at higher system temperatures and pressures, as evident in Fig. 4. The figure displays the measured and calculated normalized pump head versus suction void fraction at 230°C/2.8 MPa and 260°C/4.7 MPa for the small pump and at 260°C/4.7 MPa and 280°C/6.4 MPa for the large pump. Both the experimental data and the analytical results obtained from the present model show that the two-phase pump head degrades less at higher system temperature/pressure. Kastner and Seeberger (1983) have also shown in their work that the pump head degrades much less at a higher two-phase system pressure/temperature. It is also seen in Fig. 4 that the measured and calculated threshold void fractions are both greater at a higher system temperature/pressure.

In order to understand why the threshold void fraction is higher at higher system temperatures, the local flow parameters obtained in the present calculations for the small pump were examined in detail. Figures 9 and 10 show the changes in local pressure, void fraction, vapor condensation rate, and relative velocities of gas and liquid at 230°C and 260°C for the same suction void fraction (α_s = 22 percent). The two-phase mass flow rates used in these calculations were taken from the actual test data at 100 percent initial flow rate.

Now, the local pressure and vapor condensation rate along the pump impeller channel at 260°C are greater than those at 230°C (see Figs. 9 and 10). At 230°C, the local void fraction (Fig. 9) and the liquid velocity (Fig. 10) rapidly increase while the velocity of the gas (Fig. 10) decreases along the pump impeller channel. This indicates that the pump head is degraded at this temperature for a suction void fraction of 22 percent. On the other hand, at 260°C the vapor condenses completely within the pump impeller before reaching the exit of the pump (Fig. 9) due to much higher vapor condensation rates experienced along the flow passage (Fig. 10). As a result, the velocities of the liquid and gas both decrease (Fig. 10), which means that the pump head increases compared to the single-phase liquid flow. Thus, the higher rate of vapor condensation at the higher system temperature/pressure gives rise to a greater threshold void fraction.

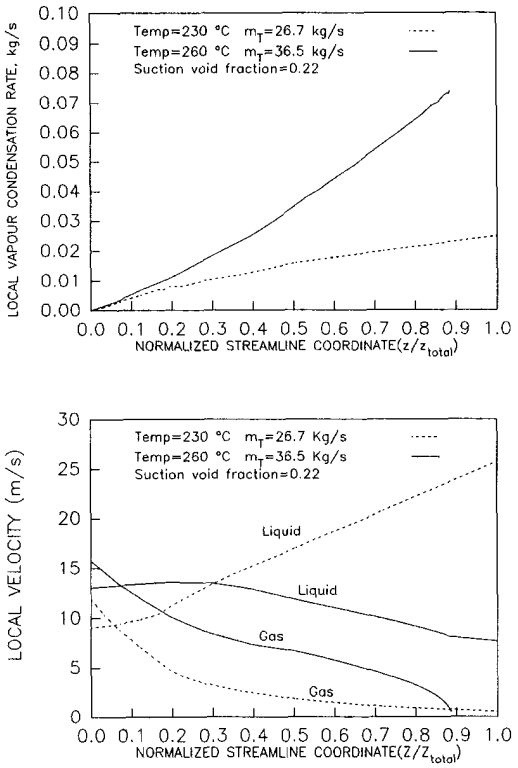

Fig. 10 Condensation rate and relative gas and liquid velocity variations along the flow passage for small-scale pump at 22 percent suction void and different temperatures

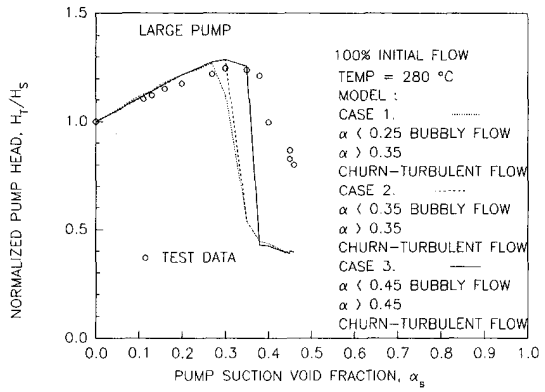

Fig. 11 Effect of flow regime transition criteria on head and threshold void fraction for large pump

4.3 Sensitivity Study. Hench and Johnston (1968) have shown that the pressure recovery in a diffuser is not sensitive to the bubble size and drag coefficient for bubbly flow. They have also shown that a significant error (of the order of ±50 percent) in the determination of bubble size or drag coefficient does not greatly affect the final results. Although not shown here, the sensitivity of the predicted two-phase pump head to bubble size and drag coefficient for bubbly flow regime was found to be quite small as well in the present work (Noghrehkar, 1992).

The effect of the virtual mass coefficient on the predictions of the present two-fluid model was also investigated. The value of the virtual mass coefficient, C_{vm}, used in the present model was 0.5, and this value was changed to 0.25 and then to 0, keeping the other parameters constant. The effect of C_{vm} on the predicted pump head degradation was seen to be insignificant (Noghrehkar, 1992).

It was also assumed that the bubbly and churn-turbulent flow regimes existed for $\alpha \leq 0.25$ and $\alpha \geq 0.35$, respectively. This assumption was acceptable for the small pump, as the predictions matched the experimental data quite well. However, the threshold void fractions were significantly underpredicted for the large-scale pump. In order to clarify the importance of the two-phase flow regimes, the effect of flow regime transition criteria on pump head and threshold void fraction for the large pump is shown in Fig. 11. The predicted threshold void fraction is seen to increase with a wider range of void fraction for the bubbly flow regime. Clearly, the constitutive relations that were seen to work well for the small-scale pump are inadequate for the large-scale pump in predicting the onset of two-phase head degradation. The flow passage between the impeller blades in the full-scale pump is much larger and the gas and the liquid phase distribution may be significantly different from that in the small-scale pump. The higher threshold void fractions measured in the large-scale pump tests suggest that the condensation rate remains high in the large pump even at those local void fractions (25 percent $< \alpha <$ 35 percent), at which the flow in the small pump would experience lower rates of condensation and acceleration of liquid that causes two-phase head degradation.

The present two-fluid model calculations assumed occurrence of bubbly and churn-turbulent flows instead of the stratified flow regime, in which vapor and liquid would flow as two separate streams sharing a smooth or wavy interface. While we cannot deny the possibility of stratification of the flow in the larger flow passage, the factors such as the persistence of high rates of condensation, large momentum coupling between the vapor and liquid so that the liquid does not accelerate, and continued increase in the head to higher values of suction and local void fractions in the large pump do not lend support to the stratified flow assumption. A recent experimental work by Minemura et al. (1993) using a horizontal, radially rotating 32 mm × 32 mm square duct has shown that the air/water two-phase flow in that flow channel displays significant nonuniformity in void fraction distributions in the transverse as well as in axial directions. This means that even if the local void fraction is substantially high at a given axial location in the impeller, we could have a high-void fraction flow regime such as churn-turbulent flow and low-void fraction bubbly flow coexisting at that location. If this is the case, the local condensation rate could remain high due to the presence of the bubbly flow regime and the head continue to increase even though the void fraction is well above that assumed for transition from a bubbly to churn-turbulent flow (α = 25–35 percent).

Although there should be some differences between the low-pressure air/water flow and high-pressure steam/water flow, it is reasonable to think that similar two-dimensional void fraction variations and simultaneous appearance of two different flow regimes at the same axial location could have existed in both small and large pumps tested in this work. Since this two-dimensional void distribution effect would be more profound in larger flow channels, the effect of pump scale or the impeller size may pose a more complicated problem to two-fluid modelling than simple changes in flow regime transition criteria. The assumption of one-dimensional flow and a given flow regime at any axial location may not be valid for modeling the two-phase flow in large flow channels such as the present full-scale pump. Clearly, more work is needed to better understand the two-phase flow phenomena in full-scale pumps.

5 Conclusions

Based on the experimental data and the predictions of the present two-fluid model, the centrifugal pump performance under high pressure steam-water, two-phase flow conditions and the gas-liquid interaction within the pump impeller have

been investigated. The predicted results for two-phase pump head degradation were seen to be in good agreement with the experimental data and the variations in the measured pump head as a function of suction void fraction were predicted reasonably well by the present analytical model, i.e., a slight increase in pump head at low suction void fractions, then a sudden drop at a threshold void fraction. The trends in the measured and predicted head degradation results were also the same for both the small and large-scale pumps, however, the threshold void fraction for the large pump ($\alpha \approx 35$–40 percent) was significantly higher than that of the small pump ($\alpha \approx 20$–25 percent).

Within the ranges of system temperature/pressure tested, both the analytical results and experimental data showed that for low suction void fractions below the threshold void fraction, the vapor phase is completely condensed inside the pump impeller and the head increases, while at higher suction void fractions, condensation is no longer complete and the pump head begins to rapidly decrease. The two-fluid model calculations further showed that the initial head increase at low suction void fractions is due to the deceleration of liquid as vapor is removed by condensation within the impeller, and that the head degradation phenomenon is related to the acceleration of the liquid phase due to rotation and void increase within the pump impeller. Thus, vapor condensation and liquid acceleration due to rotation compete with each other to determine the pump head variation in two-phase flow.

Finally, both the experiments and two-fluid model calculations have shown that the pump head degrades less at a higher system temperature/pressure for both small and large pumps, and the model attributed this phenomenon to greater condensation rates experienced inside the impeller at higher system temperature/pressure.

References

Chan, A. M. C., 1992, "Void Fraction Measurements in Large Diameter Pipes with Thick Metal Walls or Complex Internal Geometries," *ANS Proc. of National Heat Transfer Conf.*, Aug. 9–12, San Diego, pp. 236–244.

Chan, A. M. C., Barreca, S. L. and Hartlen, R. T., 1991, "An Experimental Study of Centrifugal Pump Performance Under Steam-Water Two-Phase Flow Conditions at Elevated Pressures," *Cavitation and Multiphase Flow Forum—1991*, ASME FED-Vol. 109, pp. 111–117.

Chan, A. M. C., Kawaji, M., Noghrehkar, G. R., Nakamura, H. and Kukita, Y., 1994, "Two-Phase Head Degradation in a Full-Scale Nuclear Reactor Pump," a paper to be submitted to the *ASME Journal of Fluids Engineering*.

Drew, D., Cheng, L. and Lahey, R. T. Jr., 1979, "The Analysis of Virtual Mass Effects in Two-Phase Flow", *International Journal of Multiphase Flow*, Vol. 5, pp. 233–242.

Furuya, O., 1984, "Development of an Analytic Model to Determine Pump Performance Under Two-Phase Flow Conditions," EPRI NP-3519, Electric Power Research Institute, May.

Furuya, O., and Maekawa, S., 1987, "An Analytical Method for Prediction of Pump Performance Operating Under Condensible Two-Phase Flows," *Proc. of 1987 JSME/ASME Thermal Engineering Joint Conference*, Honolulu, Hawaii, pp. 9–16.

Heidrick, T. R., Hancox, W. T., and Nguyen, D., 1978, "Centrifugal Pump Behavior in Steady and Transient Steam-Water Flows," *Polyphase Flow in Turbomachinery*, edited by C. Brennen et al., etc., ASME, Dec. pp. 139–156.

Hench, H. E., and Johnston, J. P., 1968, "Two-Dimensional Diffuser Performance With Subsonic Two-Phase Air-Water Flow," General Electric Report APED 5477, Atomic Power Equipment Department, San Jose, California.

Hench, J. E., and Johnston, J. P., 1972, "Two-Dimensional Diffusers Performance with Subsonic, Two-Phase, Air-Water Flow," ASME *Journal of Basic Engineering*, Mar., pp. 105–121.

Kastner, W. and Seeberger, G. J., 1983, "Pump Behavior and its Impact on a Loss-of-Coolant Accident in a Pressurized Water Reactor," *Nuclear Technology*, Vol. 60, pp. 268–277.

Kim, J. H., 1983, "Perspectives on Two-Phase Flow Pump Modeling for Nuclear Reactor Safety Analysis," *Cavitation and Multiphase Flow Forum-1983*, J. W. Hoyt, ed., ASME, June, pp. 29–33.

Minemura, K., Uchiyama, T., and Ishikawa, T., 1993, "Experimental Investigations on Bubbly Flows in a Straight Channel Rotated Around an Axis Perpendicular to the Channel," *International Journal of Multiphase Flow*, Vol. 19, No. 3, pp. 439–450.

Manzano-Ruiz, J. J., and Wilson, D. G., 1987, "Experimental Study of Two-Phase, Two-Component Flow in Centrifugal Pumps," *Proc. of 2nd International Topical Meeting on Nuclear Reactor Thermal-Hydraulics*, Jan., vol. II, pp. 956–964.

Noghrehkar, G. R., 1992, "Investigation of Centrifugal Pump Performance under Two-Phase Flow Conditions," M.A.Sc. thesis, Dept. of Chemical Engineering and Applied Chemistry, University of Toronto.

Patel, B. R., and Runstadler, P. W., 1978, "Investigations into the Two-Phase Flow Behavior of Centrifugal Pumps," *Proc. of Polyphase Flow in Turbomachinery*, ASME, New York, pp. 79–100.

Smith, S. L., 1970, "Void Fractions in Two-Phase Flow: a Correlation based upon an Equal Velocity Head Model," *Proceedings Instrumentation of Mechanical Engineers*, Vol. 184, No. 36, pp. 647–657.

Wallis, G. B., 1969, *One-Dimensional Two-Phase Flow*, McGraw-Hill, New York.

Zakem, S., 1980, "Analysis of Gas Accumulation and Slip Velocity in a Rotating Impeller," *Proceedings of a Cavitation and Polyphase Forum*, pp. 32–34.

Zuber, N., and Hench, J. E., 1962, "Steady State and Transient Void Fraction of Bubbling Systems and Their Operating Limits. Part I, Steady State Operation," General Electric Report No. 62GL100.

F. Bakhtar
School of Manufacturing and Mechanical Engineering, University of Birmingham, Birmingham, B15 2TT, England

M. R. Mahpeykar
Department of Mechanical Engineering, University of Mashhad, Iran, Formerly, University of Birmingham

K. K. Abbas
Formerly, University of Birmingham

An Investigation of Nucleating Flows of Steam in a Cascade of Turbine Blading-Theoretical Treatment

This paper describes the theoretical part of an investigation into nucleating flows of steam in a cascade turbine nozzle blading. The main flow field is regarded as inviscid and treated by the time-marching technique. The viscous effects are assumed to be concentrated in boundary layers which are treated by the integral method. The agreement obtained with the observed surface pressure distributions and overall efficiency measurements is very good.

Introduction

This paper describes the theoretical part of an investigation into nucleating flows of steam in a cascade of turbine blading. During the course of expansion of steam in turbines, the state path crosses the saturation line and the fluid first supercools and then nucleates to become a two phase mixture. The formation and subsequent behaviour of the liquid create problems which lead to losses of performance in the wet stages of turbines but the detailed mechanisms which give rise to these losses are insufficiently understood. Many investigations into the behavior of flowing wet steam in turbines have been reported, e.g., Moore and Sieverding (1976), Stastny (1979), Steltz, Lee and Lindsay (1981), Walters (1985), Kleitz, Laali and Courant (1988), Tanuma and Sakamoto (1991), Diebelius et al. (1987) and Haller et al. (1988). Nevertheless, the rule still quoted for estimating wetness losses is an empirical formula proposed by Baumann in 1921. A tangible wetness effect is erosion of blading but this is only one consequence of the presence of water in steam. More important are the local departures of the system from thermodynamic equilibrium, because the subsequent heat release resulting from return to equilibrium is accompanied by internal dissipation and affects the behavior of the parent vapor. The investigation being reported was undertaken as a contribution to a better understanding of these problems.

The development of nucleation theory has been of help to the study of wetness problems in steam turbines, but to examine two-phase flows in turbine blading the equations describing droplet formation and growth have to be combined with 2- and 3- dimensional field equations. A feature of flows in the low pressure wet stages of steam turbines is that they are generally transonic with appreciable supersonic zones while the speed of sound in two-phase mixtures is not explicit and depends on the local conditions and the form of the governing equations differ in sub- tran- and supersonic flows. Under these circumstances, although a solution using the streamline curvature method has been attempted (Yeoh and Young, 1982), the most suitable means of treating the equations is the time marching technique. The small number of solutions using the method reported demonstrate the promise of the technique. With the ultimate aim of the application of the treatment to three-dimensional flows in turbines, the necessary next step is the validation of two-dimensional solutions against direct measurements but experimental results suitable for the purpose are scarce.

Experimental investigation of condensing flows in turbines are hindered by the fact that at low and moderate pressures the supercooling associated with the first reversion of steam is substantial. To reproduce steam turbine nucleating and wet flow conditions realistically requires a supply of supercooled steam. The equipment constructed at Birmingham and used in the parallel experimental investigation achieves this under blowdown conditions. The present paper describes the application of the treatment to the first family of the measurements which have been carried out.

Outline of the Treatment

The approach used is the inviscid-viscous interaction procedure widely adopted in turbomachinery studies, e.g., Hansen, Serovy and Sokol (1979) and Calvert and Herbert (1980). The main flow field is regarded as inviscid and the viscous effects are assumed to be concentrated in the boundary layers. To treat the main flow field, the method of solution is a time-marching technique as developed by Denton (1982), modified to allow for two-phase effects. The boundary layer terms are calculated from the inviscid surface velocity distributions using the integral method.

To treat the main flow field, the governing equations are the conservation equations of mass, momentum and energy written for a two-phase mixture, which are then combined with equations describing droplet formation and interphase heat and mass transfer. In the present application, because of the

Contributed by the Fluids Engineering Division for publication in the JOURNAL OF FLUIDS ENGINEERING. Manuscript received by the Fluids Engineering Division October 19, 1993; revised manuscript received April 15, 1994. Associate Technical Editor: Jong J. Kim.

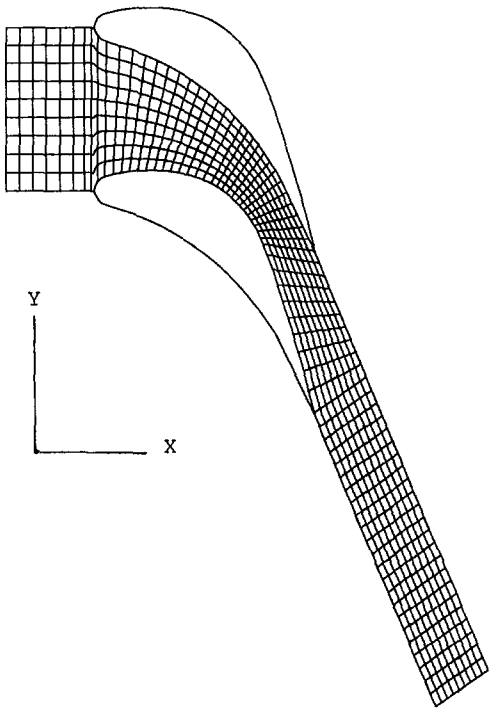

Fig. 1 General arrangement of mesh

smallness of the droplets, interphase slip is regarded as negligible. The method of treatment is essentially that described by Bakhtar and Mohammadi Tochai (1980) but its basic algorithm was subsequently modified in accordance with Denton's (1982) improved technique. The only limited previous comparison between solutions and actual experimental results was to the flow in a cascade of supersonic tip section blading (Bakhtar and So 1991). Although the general features of the flow were predicted reasonably well, the solutions were affected by shock smearing and the numerical errors associated with the procedure employed.

In the present investigation the above problems have been minimised by using a more orthogonal main grid. To achieve this, the numerical procedure was rearranged to deal with a more general mesh and a grid of the form shown in Fig. 1 but using 30 × 207 points was adopted. In addition, as already indicated to allow for viscous effects, a boundary layer routine described in the Appendix was added to the program. Furthermore, to speed up the calculation of droplet growth rates outside the condensation zone, an improved procedure was adopted.

Application to Experimental Results

The experimental investigation was carried out using the short duration cascade tunnel already described (Bakhtar et al., 1991). This equipment is uniquely capable of generating a supply of supercooled steam. The blade profile studied was based on a typical nozzle section of an operating turbine. The experimental observations carried out consist of surface pressure measurements, flow visualisations, velocity traverses downstream of the cascade and some tentative droplet measurements.

The surface pressure measurements carried out were extensive. It was observed that in nucleating tests the position and characteristics of the zone of rapid condensation were insensitive to the inlet supercooling over a relatively wide range (Bakhtar et al. 1993). Consequently, in the remainder of the investigation, comparisons were carried out between corresponding superheated and nucleating tests. The theoretical treatment has been applied to two sets of such measurements:

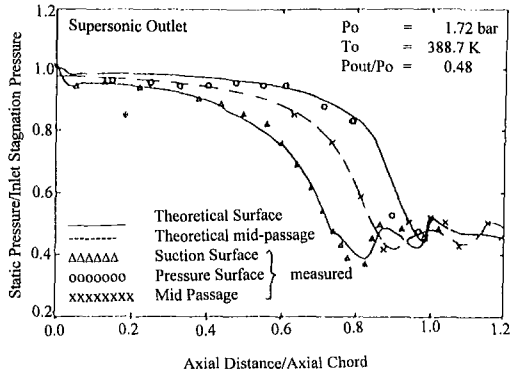

Fig. 2 Theoretical and experimental pressure distributions—superheated test

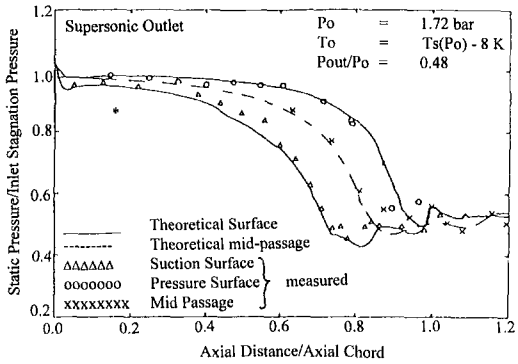

Fig. 3 Theoretical and experimental pressure distributions-nucleating test

one with supersonic and the other with subsonic outlets and the comparisons may be presented as follows.

Comparison With Surface Pressure Distributions in Tests With Supersonic Outlet. The theoretical and experimental surface pressure distributions for superheated and nucleating tests with supersonic outlet are compared in Figs. 2 and 3 respectively.

The theoretical solution plotted in Fig. 2 is one obtained as a preliminary to the nucleating solution. Although the inlet conditions adopted are those of supercooled steam, both the nucleation rate and wetness fraction have been set equal to zero in the theoretical solution, thus the behavior predicted would correspond with that of superheated vapor. It will be seen that both the measured and calculated results show an inflection in the pressure distribution on the suction surface at approximately 74% axial chord length. This corresponds with a change in the curvature of the suction surface which occurs just downstream of the throat. Downstream of this region, there are two further pressure rises on the suction surface. The first is due to the trailing edge shock wave on the pressure surface which has extended across the passage and is reflected from the suction surface, the second is the shock wave on the suction side of the trailing edge. All the flow features have been predicted satisfactorily by the solution.

In the case of the nucleating test, the measured pressure rise at 74% axial chord length on the suction surface is due to rapid condensation and occurs just downstream of the throat. This also corresponds in location with the change in the curvature of the suction surface. The location of the rapid condensation zone is predicted slightly late and there is some smearing of the pressure change in the theoretical solution but this is regarded as acceptable. It has already been described in connection with the experimental results that the position and characteristics of the rapid condensation zone, were insensitive to the inlet supercooling. Downstream of the rapid conden-

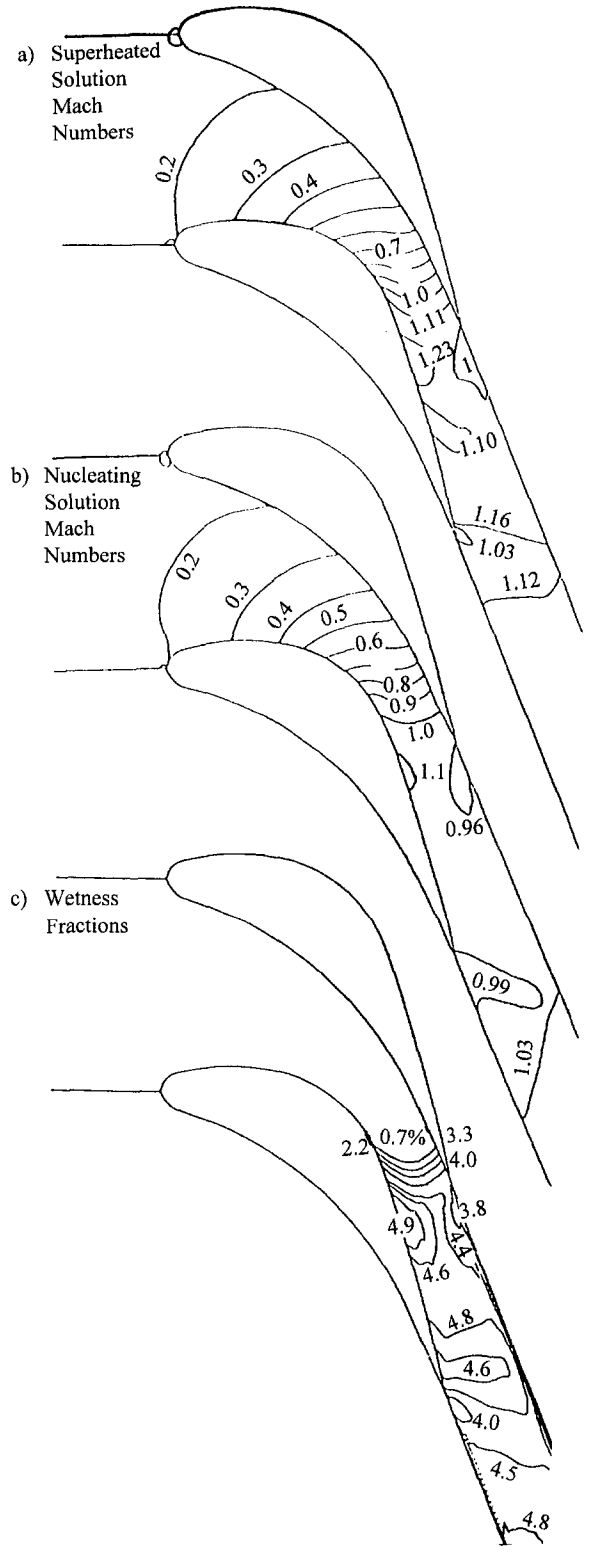

Fig. 4 Constant Mach number and wetness contours in theoretical solutions

sation zone the general features associated with trailing edge shock waves are similar except that, for similar pressure ratios, Mach numbers are lower in condensing flows.

Contours of constant Mach number for the superheated and nucleating solutions are presented in Figs. 4(*a*) and 4(*b*) respectively and contours of constant wetness fraction in the wet solution are given in Figs. 4(*c*). In the nucleating solution, the speed of sound used for calculating Mach numbers has been the frozen speed. In the region upstream of the throat the two

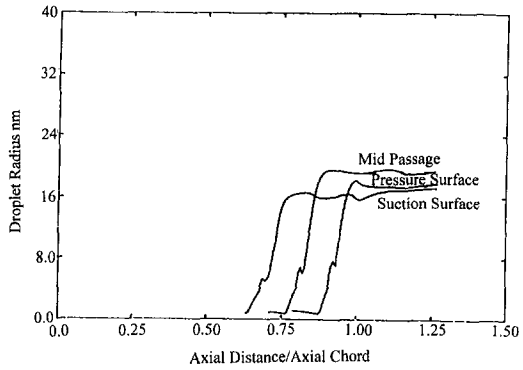

Fig. 5 Calculated droplet sizes

expansions are very similar. In the nucleating solution, the sonic line has shifted slightly downstream of the throat. The Mach number at the physical minimum area is below unity indicating that the flow has choked at a velocity below the frozen speed of round. Downstream of the throat, the detailed features of the nucleating solution differ from those of the superheated test mainly because of the lower Mach numbers in the condensing test.

Variations of mean droplet radius along the mesh lines corresponding with the suction surface, mid-passage and pressure surface are shown in Fig. 5. As expected, nucleation starts earlier on the suction surface. The steepness of rise in the droplet radius soon after nucleation is an indication of the extent of the rapid condensation zone. It will also be seen that surprisingly in the particular case examined, the variations of the droplet size across the passage is small.

Comparisons With Surface Pressure Distributions in Tests With Subsonic Outlet. Comparisons between the resulting theoretical and measured surface pressure distributions for the superheated and nucleating tests with subsonic outlet are given in Figs. 6 and 7 respectively. The theoretical solution plotted in Fig. 6 was obtained as a preliminary to the nucleating solution by setting the nucleation rate and wetness fraction equal to zero. Contours of constant Mach number from the superheated and nucleating solutions are plotted in Figs. 8(*a*) and 8(*b*) respectively and lines of constant wetness fraction from the nucleating solution are given as Fig. 8(*c*).

As already indicated, there is a change in the radius of curvature of the suction surface in the vicinity of the throat at 74% axial chord and the flow passage has a slightly divergent section downstream of this position. With reference to Fig. 6, there is a slight inflection in the pressure distribution on suction surface at this location in the dry test. With the overall pressure ratio selected, the flow becomes sonic at the throat and accelerates further for a short distance downstream. It then adjusts through a normal shock to attain the downstream pressure. These features are reflected in the measured pressure distributions and predicted satisfactorily by the solution.

With reference to Fig. 7, the flow accelerates until the throat in the nucleating test but does not choke it completely. There is an overexpansion region downstream of the throat on the suction surface. The flow accelerates beyond sonic velocity and rapid condensation occurs in the supersonic region. The actual location is very similar to those observed in tests with higher outlet Mach numbers. The subsequent diffusion downstream is affected by the heat release. In comparison with the superheated test, the pressure rise is more gradual and occurs over a longer distance.

The comparison between theoretical and experimental results presented in Figs. 6 and 7 include mid-passage pressure distributions. It will be noted that the agreement obtained is satisfactory.

Comparison With Measured Droplet Sizes. Variations of

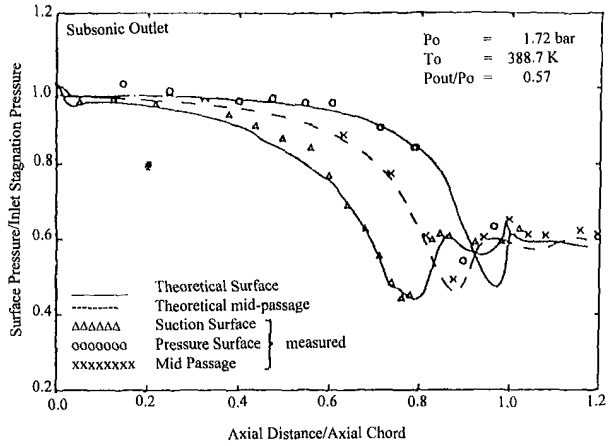

Fig. 6 Theoretical and experimental pressure distributions-superheated test

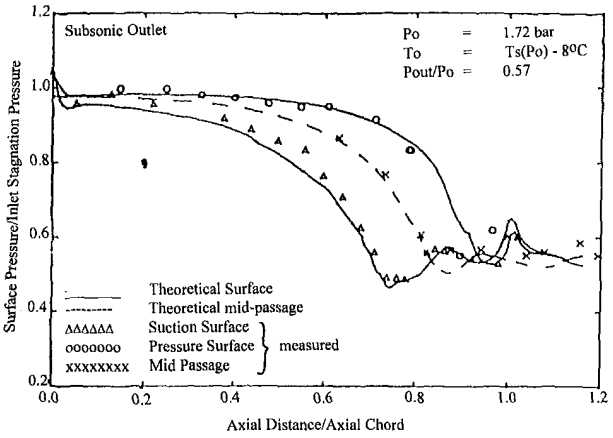

Fig. 7 theoretical and experimental pressure distributions-nucleating test

mean droplet radius along the mesh lines corresponding with the suction surface, mid-passage line and pressure surface in the above solution are shown in Fig. 9. The features are very similar to those of the previous solution.

Some tentative droplet measurements were carried out at flow conditions similar to the above using light extinction (Bakhtar et al. 1992). The measurements were carried out at a point at the intersection of the line joining the trailing edges of the blades and the mid-passage line.

Although the measurement of the attenuation of the intensity of light beams presented no particular difficulty, the deduction of droplet sizes from the intensity measurements depends on the uniformity of the droplet population. If the droplet population can be assumed monodispense the calculation of the mean droplet size and wetness fraction is straightforward, but examination of the results did not support this assumption. The alternative method is to estimate the wetness fraction from the pressure measurements and then still assuming a uniform droplet population, infer the mean droplet size from the extinction measurements. Using the second method, the inferred droplet radii for the tests with supersonic and subsonic outlets were 0.057 and 0.06 μm, respectively. The predicted droplet radii at the same locations are 0.019 and 0.02 μm, respectively.

The uncertainty in the droplet measurements arises from the bi-modal distribution of the droplet population. Any foreign particles present in the steam whether due to feed treatment or otherwise will act as condensation centres but their numbers will not be sufficient to maintain the flow close to equilibrium. The fluid then supercools sufficiently to nucleate to give two

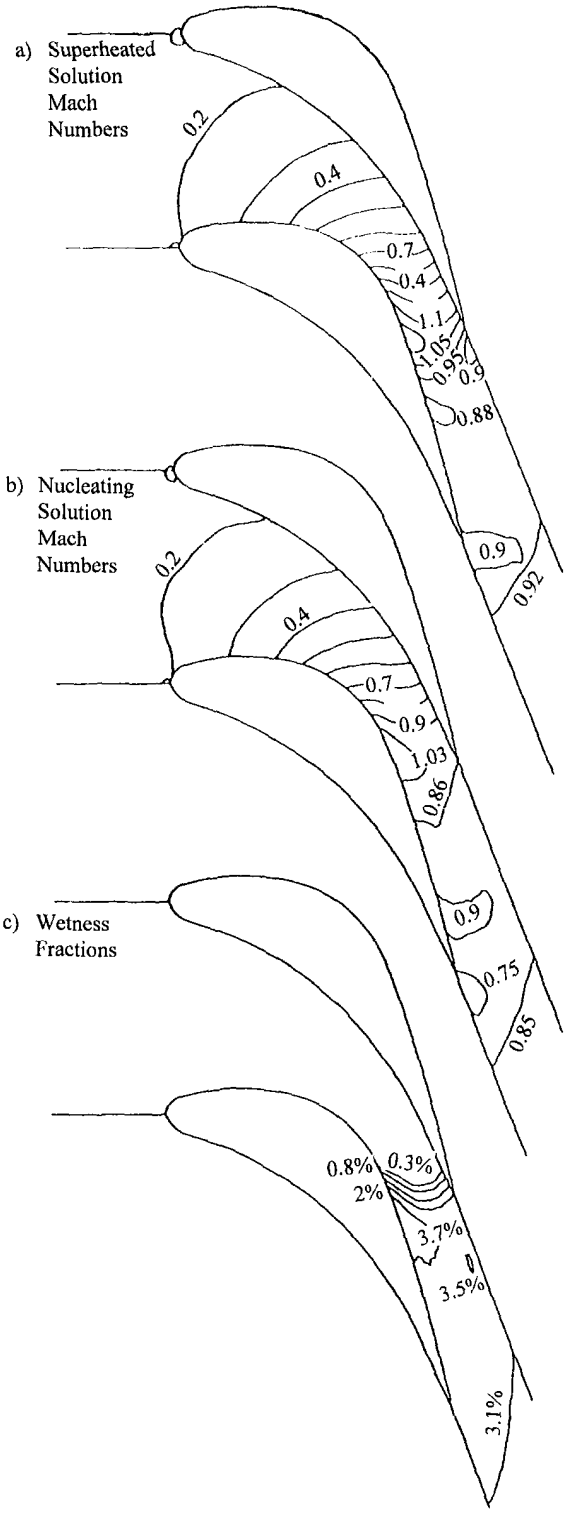

Fig. 8 Constant Mach number and wetness contours in theoretical solutions

populations of droplets within the flow. The procedure adopted in the measurements was to clear the foreign particles through a preliminary blow-down. Nevertheless their presence could not be avoided completely. The presence of this second family is a complicating factor in the droplet measurements. However, as these measurements were the first of their kind to be carried out on the equipment, the agreement should be regarded as promising and indicative of the need for further development of the measurement technique.

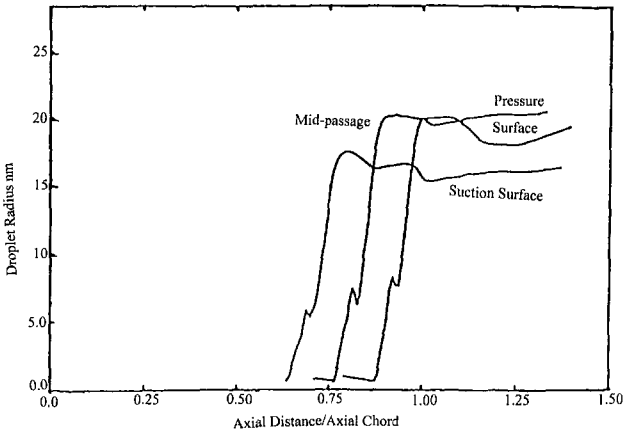

Fig. 9 Calculated droplet sizes

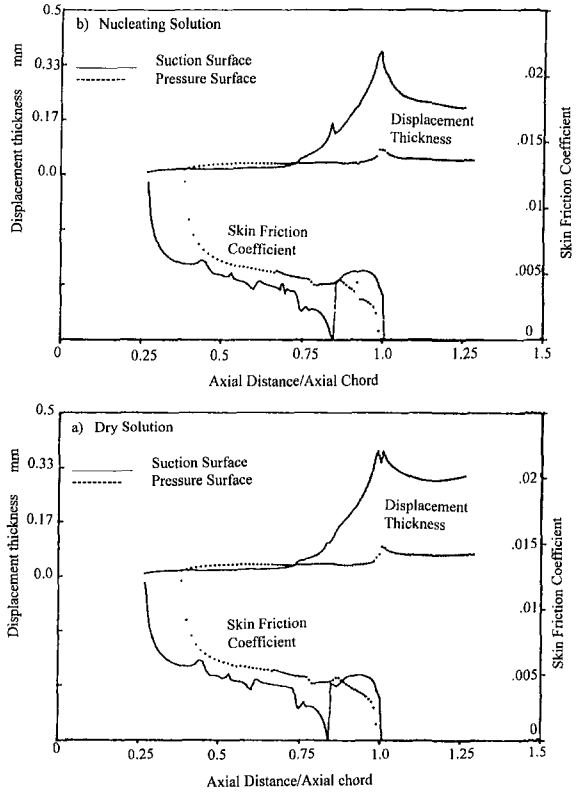

Fig. 10 Boundary layer parameters tests with subsonic outlet

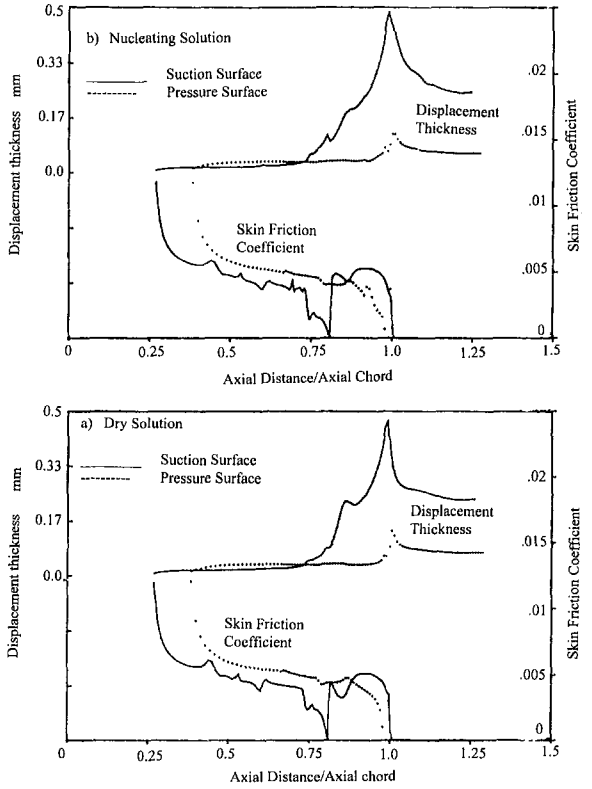

Fig. 11 Boundary layer parameters tests with supersonic outlet

Evaluation of the Losses

1 Calculation of Boundary Layer Parameters. To evaluate the influence of condensation on the aerodynamic losses, a boundary layer routine using the integral method was included in the treatment. It must, however, be stated that the empirical constants used in the relationships are those determined in air. No data to indicate their values in steam has been available. As the range of Mach numbers involved are not particularly high, it has been assumed that any modifications of these constants will have a small effect on the solutions.

Variations of the resulting displacement thickness and surface friction coefficients for the superheated and nucleating solutions with subsonic outlet are given in Figs. 10(*a*) and 10(*b*), respectively. Similar results for the solutions with supersonic outlet are given in Figs. 11(*a*) and 11(*b*).

It will be seen from the calculated variations of the momentum thickness for the superheated solutions shown in Figs. 10(*a*) and 11(*a*) that the boundary layers are extremely thin on the pressure surface in all the tests. They are also extremely thin on the suction surface until approximately 75 percent of axial chord, where there is some growth. Bubble separation occurs at approximately 85 percent axial chord due to encounter with the shock wave. It is assumed that transition occurs instantaneously and turbulent boundary layer is forced to start at the same position. A better impression of the location of transition may be obtained from the curves showing the variations of skin friction coefficient. There is a drop in the coefficient at 0.75 axial chord on the suction surface in both superheated solutions which is due to the inflection in the pressure distribution caused by the change in surface curvature.

The pattern is similar in the case of the nucleating tests. The zone of rapid condensation occurs very close to the location of change in the blade curvature. Comparison of the skin friction coefficient at 0.75 axial chord length on the suction surface in Figs. 10(*a*) and 10(*b*) shows that the drop in the friction coefficient is greater for the condensing tests. This is an indication of the effect of the pressure changes on boundary layer behaviour. Although in the present solution the heat release caused by condensation has not been sufficient to reduce the coefficient to zero and cause boundary layer transition, nevertheless it shows that transition to turbulent flow is more likely to occur earlier in condensing tests.

2 Aerodynamic Losses. The aerodynamic losses incurred by the flow arise from the following causes: boundary layers, base pressure losses, mixing downstream of the profile and shock waves.

With the boundary layer data evaluated, the corresponding losses were calculated at the trailing edge of the profile. The mixing losses were calculated approximately from the known velocity distribution at the trailing edge plane and assuming the process to occur at constant momentum. The shock losses were evaluated from the calculated changes in the Mach numbers from the theoretical solutions. No allowance for base pressure losses is included but the profile studied has a very

Table 1 Estimated losses percent of isentropic heat drop

Loss component	Value in subsonic test %		Value in supersonic test %	
	Dry	Nucleating	Dry	Nucleating
Boundary layer	3.2	3.7	2.4	2.6
mixing	0.5	0.2	0.6	0.6
shock	1.1	0.5	1.5	0.4
Thermodynamic	—	5.7	—	5.5
Total theory	4.8	10.1	4.5	9.1
Total measured	5.0	13.0	5.0	10.0

thin trailing edge. The estimated losses are summarised in Table 1.

3 Wetness Losses. In the nucleating tests studied slip is regarded as negligible because of the smallness of the droplets and the only additional losses incurred are the thermodynamic component caused by internal heat transfer within the fluid. When the flow is condensing, separation of the liquid is through the growth of the droplets present within the vapour. The condensing molecules give up latent heat to the droplets but the bulk of this energy has to be returned to the vapour. For this purpose a temperature difference will develop between the phases and flow of heat across it is irreversible. In cases of diffusion or encounter with a shock wave, there will have to be some evaporation from the droplets. For this purpose, they will have to receive heat from the vapor which will again occur irreversibly. The entropy increases were integrated along the droplet paths. The resulting estimates of these losses are also given in Table 1.

Comparison With the Efficiency Measurements. From the wake traverses, the efficiencies of the expansions and hence the total of the losses suffered by the flow were determined (Bakhtar et al., 1994). The results of these measurements are also given in Table 1.

The agreement between the total of the calculated losses and the measurements for the superheated tests is reasonable considering the assumption made. It can therefore be concluded that the magnitude of the different components of the aerodynamic losses incurred in the superheated tests are represented correctly by the treatment. A substantial proportion of the aerodynamic losses incurred by these flows are due to shock waves, some directly and a further proportion because of increased boundary layer losses after encounter with the shock waves.

The agreement between the total of calculated losses and the measurements is reasonable also for the nucleating test with supersonic outlet. The calculated boundary layer losses have been based on the predicted surface pressure distributions. The experimental measurements indicated a small rise in pressure at 0.74 axial chord length on the suction surface due to rapid condensations which was not predicted exactly by the solution and the position of the subsequent shock was also predicted a little downstream of the actual measurements. As both these differences will lead to thinner calculated boundary layers at the trailing edge, the associated losses would underestimate the true value.

The largest difference between the calculations and the measurements occurs in the nucleating test with subsonic outlet. If the calculated thermodynamic component of the loss suffered by the flow is accepted, 7.3% of the losses incurred by the flow must be attributed to aerodynamic causes which is substantially higher than the losses in the corresponding superheated test. A possible cause of the discrepancy between the calculated aerodynamic losses and the measurements might be the behavior of the boundary layer on the suction surface. The variations of the calculated skin friction coefficient shown in Fig. 10(*b*), indicate that, in the theoretical results, pressure rise associated with the rapid condensation zone at 0.75 axial chord is just insufficient to cause boundary layer transition. If in the actual flow the boundary layer undergoes bubble separation or transition at this position, it will grow further in the zone of diffusion increasing the losses.

Because of the uncertainty in the speed of sound in two-phase mixtures, the corresponding superheated and nucleating flows have been compared on the basis of similar overall pressure ratios. Consequently the Mach numbers have been lower in the nucleating tests leading to lower shock losses. If the frozen speed of sound in adopted as the basis of calculating Mach numbers in two phase flows, and comparisons carried out between tests with the same outlet Mach members, the shock losses would be expected to be higher in nucleating than dry flows but these would occur at different overall pressure ratios.

The largest single item of loss suffered by nucleating flows is the thermodynamic component. In the test with supersonic outlet, the sum of thermodynamic loss and reduced shock loss matches the difference between the measured efficiencies of the superheated and nucleating flows suggesting that the remainder of the aerodynamic losses in these tests are of similar magnitude. In contrast, the increased losses measured in the nucleating subsonic test must stem from aerodynamic causes.

Summary of Conclusions

Two dimensional blade-to-blade flows of nucleating steam can be treated satisfactorily by the time-marching method. The numerical errors resulting from the internal inconsistencies associated with some of the algorithms employed are a potential complication in the use of an otherwise powerful technique. By careful selection of a suitable grid the problems can be avoided.

The quality of agreement between the predicted and measured surface pressure distributions is good and those with the measured efficiencies are reasonable. The agreement with the measured droplet sizes is less satisfactory but the results are promising.

The most important characteristic of nucleating flows is the high degrees of supercooling initially attained by the fluid and the sudden release of latent heat as the system regains thermodynamic equilibrium. The resulting internal heat transfer is irreversible leading to unavoidable thermodynamic losses. But high degrees of supercooling need only be experienced once in a turbine expansion.

The release of heat caused by rapid condensation also affects the behavior of the flow. The measured aerodynamic losses resulting from this cause have been small in the test with supersonic outlet but significant in the particular case of the test with subsonic outlet. The consequential aerodynamic losses associated with condensing flows are not intrinsic to the process and can be avoided.

The experimental and theoretical results presented demonstrate that steam turbine two-phase flow conditions can be modeled. It is no longer necessary to rely on empirical rules proposed seventy year ago.

Acknowledgments

The investigations were carried out in the School of Manufacturing and Mechanical Engineering of the University of Birmingham and supported by grants from the Science and Engineering Research Council. The authors are also grateful for the assistance of Drs. R. A. Webb and M. H. Shojaee-Fard for the provision of the surface pressure measurements quoted.

References

Abu-Ghannam, B. J., and Shaw, R., 1980, "Natural Transition of Boundary Layer, the Effect of Turbulence, Pressure Gradient and Flow History," *Journal of Mechanical Engineering*, Vol. 22, No. 5, pp. 213–228.

Bakhtar, F., Ebrahimi, M. and Webb, R. A., 1994, "An Investigation of Nucleating Flows of Steam in a Cascade of Turbine Blading — Wake Traverses," ASME JOURNAL OF FLUIDS ENGINEERING, Vol. 16, pp. 121–127.

Bakhtar, F., and Mohammadi Tochai, M. T., 1980, "An Investigation of Two-Dimensional Flows of Nucleating Steam by the Time-Marching Method," *International Journal of Heat and Fluid Flow*, Vol. 2, No. 1, pp. 5–18.

Bakhtar, F., Shoejaee-Fard, M. H., and Savage, R. A., 1993b "An Investigation of Nucleating Flows of Steam in a Cascade of Turbine Blading—Effect of Overall Pressure Ratios," *Proc. Cavitation and Multiphase Flow Forum*, O. Furuya, ed., ASME Fluids Engineering Conference Washington June 20–24 FED 153, pp. 205–208.

Bakhtar, F., Siraj, M. A., Barmkole, B. O., Webb, R. A., and Ebrahimi, M., 1992, "A Study of Nucleating and Wet Steam Flows in a Cascade of Turbine Blading—Droplet Measurements," *Proc. Cavitation and Multiphase Flow Forum*, O. Furuya, ed., ASME Fluids Engineering Conference, Los Angeles, 21-26 June FED 135, pp. 167–170.

Bakhtar, F., and So, K. S., 1991, "A Study of Nucleating Flows of Steam in a Cascade of Supersonic Blading by the Time-Marching Method," *International Journal of Heat and Fluid Flow*, Vol. 12, No. 1, pp. 54–62.

Bakhtar, F., Webb, R. A., Shojaee-Fard, M. H., and Siraj, M. K., 1991, "An Experimental Facility for Studies of Nucleating and Wet Steam Flows in Turbine Blading," *Proc. Inst. Mech. Engrs., Conference, Turbomachinery Latest Developments in a Changing Scene*, Mechanical Engineering Publications, Paper C423/003, pp. 191–199.

Bakhtar, F., Webb, R. A., Shojaee-Fard, M. H., and Siraj, M. A., 1993, "An Investigation of Nucleating Flows of Steam in a Cascade of Blading," ASME JOURNAL OF FLUIDS ENGINEERING, Vol. 115, pp. 128–134.

Calvert, W. J., and Herbert, M. V., 1980, "An Inviscid-Viscous Interaction Method to Predict the Blade-to-Blade Performance of Axial Compressors," *Aeronautical Quarterly*, Vol. 31-32, pp. 173–196.

Cebeci, T., and Bradshaw, P., 1977, *Momentum Transfer in Boundary Layers*, Hemisphere Publishing.

Denton, J. D., 1982, "An Improved Time-Marching Method for Turbomachinery Flow Calculations," ASME Paper 82-GT-239.

Dibelius, G. H., Mertens, K., Pitt, R. U., and Strauf, E., 1987, "Investigation of Wet Stream Flow in Turbines" Proc. I. Mech. E. Conference "Turbomachinery—Efficiency Prediction and Improvement," 1987-6 Cambridge C 271/87, pp. 135–143.

Green, J. E., Weeks, D. J., and Brooman, J. W. F., 1973, "Prediction of Turbulent Boundary Layers and Wakes in Compressible Flow by a Lag-Entrainment Method," ARC R&M No 3791.

Haller, B. R., Unsworth, R. G., Walters, P. T., and Lord, M. J., 1988, "Wetness Measurements in a Model Multistage Low Pressure Steam Turbine," Proc. BNES/Mech. E. Conference, *Technology of Turbine Plant Operating with Wet Steam*, London, pp. 137–145.

Hansen, E. C., Serovy, G. K., and Sockol, P. M., 1979, "Axial—Flow Compressor Turning Angle and Loss by Inviscid-Viscous Interaction Blade-to-Blade Computation," ASME Paper 79-GT-5.

Horton, H. P., 1969, "A Semi-empirical Theory for the Growth and Bursting of Laminar Separation Bubbles," ARCCP No. 1073.

Kleitz, A., Laali, A. R., and Courant, J. J., 1988, "Fog Droplet Size Measurement and Calculation in Steam Turbines," Proc. BNES/IMechE. Conference, *Technology of Turbine Plant Operating with Wet Steam*, London, pp. 177–182.

Moore, M. J., and Sieverding, C. H., 1976, *Two-Phase Steam Flow in Turbines and Separators*, Hemisphere Publishing.

Stastny, M., 1979, "Structure of Secondary Phase Downstream of Moving Blades in L.P. Cylinder Stages of Steam Turbines," Proc. I. Mech. E. Conference, *Steam Turbines for the 1980s*, 1979-12 London, pp. 371–384.

Steltz, W. G., Lee, P. K., and Lindsay, W. T., 1981, "The Verification of Concentrated Impurities in Low Pressure Steam Turbines," *Aerothermodynamics of Steam Turbines* Steltz and Donaldson, eds., ASME Winter Annual Meeting, Washington D. C., pp. 73–82.

Tanuma, T., and Sakamoto, T., 1991, "The Removal of Water from Steam Turbine Stationary Blades by Section Slots," *Proc. Mech. E. Conference, Turbomachinery—Latest Developments in a Changing Scene*, 1991-3, London, C423/022, pp. 179–189.

Walters, P., 1985, "Wetness and Efficiency Measurements in L.P. Turbines With an Optical Probe as an Aid to Improving Performance," ASME paper 85-JPGC-GT-9.

Yoeh, C. C., and Young, J. B., 1982, "Non-equilibrium Streamline Curvature Throughflow Calculations in Wet Steam Turbines," ASME *Journal of Engineering for Power*, Vol. 104, pp. 489–496.

APPENDIX

Boundary Layer Treatment

The outlines of the approach used may be summarized as follows:

1. *Treatment of Laminar Layers.* The treatment used is that of Thwaites. The coefficients necessary for the calculation of the skin friction and displacement thickness were taken from Cebecci and Bradshaw (1977).

2. *Laminar—Turbulent Transition.* The method of Abu-Ghannam and Shaw (1980) has been adopted for the prediction of the start and end of transition and those of Horton (1969) for treating laminar separation bubbles. In the present study, transition was due to bubble separation but it occurred at the encounter with the shock wave and the length of the separation bubble was unrealistically long. Consequently, transition was assumed to occur instantaneously.

3. *Treatment of Turbulent Layers.* The treatment used is the lag-entrainment method as described by Green et al. (1973). The further auxiliary equations are also those given by the above authors. The system of equations was integrated by the Runge-Kutta technique.

4. *Treatment of Wakes.* The equations described above apply equally to the flow downstream of the trailing edge. The only change was that the skin friction coefficient was set to zero and the scaling factor allowing for the effect of the secondary influences on the turbulence dissipation length was halved.

The Inviscid—Viscous Procedure. The usual inviscid-viscous interaction procedure adopted is to find the inviscid free stream flow for the blade geometry and then to evaluate the boundary layer displacement thickness corresponding to the blade surface inviscid velocity distribution. The displacement thicknesses are then added in order to modify the blade geometry and the process is repeated until the results converge. In the present work, however, the magnitude of the displacement thickness was very small and the boundary layer routine was called only once at the end of the field calculation.

An Experimental Data Base for the Computational Fluid Dynamics of Reacting and Nonreacting Methanol Sprays

V. G. McDonell

G. S. Samuelsen

UCI Combustion Laboratory,
University of California,
Irvine, CA 92717-3550

The present data set consists of detailed measurements obtained within methanol sprays produced by a research atomizer which is operated with three atomizing air modes: none, non-swirling, and swirling. In addition, the cases with nonswirling and swirling atomizing air are characterized under reacting conditions. In each case, state-of-the-art diagnostics are applied. Measurements of the gas phase velocities in both the single and two-phase cases, droplet size distributions, and vapor concentration are obtained. The data are reported in a standardized format to ensure usefulness as modeling challenges. The results obtained reveal the presence of significant interaction between phases and significant changes in spray structure as a result of altering the atomizing air characteristics. Efforts have been directed toward delineation of errors and comparison with existing data sets where possible. The result is a comprehensive data base for vaporizing sprays under reacting and non-reacting conditions which permit a systematic variation in aerodynamic effects to be explored.

Introduction

In 1986, a NASA funded program for development of computational fluid dynamics codes for the prediction of complex aerothermochemical flows concluded that the development and verification of predictive codes was severely compromised by a lack of relevant and/or well documented experimental data (e.g., Mongia et al., 1986). One area in which data were found lacking is spray behavior. Recent developments in the area of spray characterization diagnostics are permitting information regarding spray behavior to be examined in great detail (e.g., McDonell and Samuelsen, 1990a). However, the goal of the majority of these studies has been to examine particular aspects of spray structure (e.g., droplet distribution means, droplet velocity). As a result of not measuring all aspects of the spray structure, these data sets have limited use for validation of computational fluid dynamic codes. Additionally, the majority of these data sets have *not* been made available in a format which provides the necessary information required for use in modeling challenges.

Recently, detailed data have been obtained in a series of evaporating sprays under both reacting as well as non-reacting conditions (McDonell and Samuelsen, 1993; McDonell et al., 1992; 1993a, b). These papers examine, in great detail, the structure of such sprays with the goal of providing insight not previously available. The present paper expands this data base and documents the results in a format (outlined in Appendix A) following that of Faeth and Samuelsen (1986).

The goal of the paper is to provide a collection of detailed data covering a range of fuel injector operation modes for model development, verification, and application.

Experiment

Fuel Injector. The fuel injector used for the present study is the Research Simplex Atomizer (RSA) which is manufactured by Parker Hannifin. Figure 1 presents details regarding the fuel injector geometry. A simplex injector tip is mounted centrally within a passage which allows air to be run through it. A swirler can be placed in the air passage to impart tangential momentum to the atomizing air. For the present data base, an additional concentric tube was placed over the end of the fixture shown to the left of Fig. 1, which brings the O.D. at the end of the inlet to 50.8 mm. Hence, the fuel injector assembly can be depicted as a round pipe 50.8 mm in diameter with a flat end and a hole 4.90 mm in diameter located at the center of the flat end.

The data base described features three modes of the injector operation: simplex (no atomizing air), nonswirling air-assist, swirling air-assist. The inlet geometry modifications required to obtain these modes are depicted in Fig. 2. In each case, the external geometry of the fuel injector remains the same. Hence, the only change made from a CFD standpoint is a modest change in inlet conditions.

Fuel. Methanol is employed for the testing. It is a single component fuel, so effects of variation in volatility with fuel

Contributed by the Fluids Engineering Division for publication in the JOURNAL OF FLUIDS ENGINEERING. Manuscript received by the Fluids Engineering Division May 6, 1993; revised manuscript received April 27, 1994. Associate Technical Editor: A. Prosperetti.

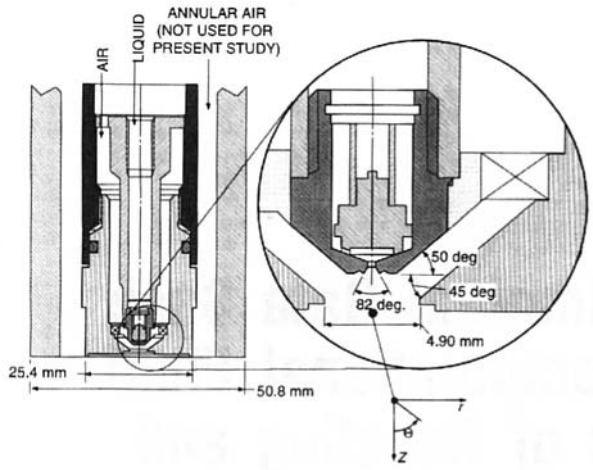

Fig. 1 Research simplex atomizer

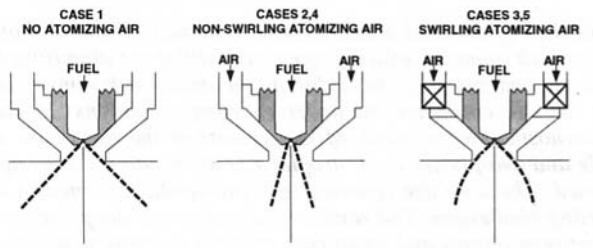

Fig. 2 Three modes of injection

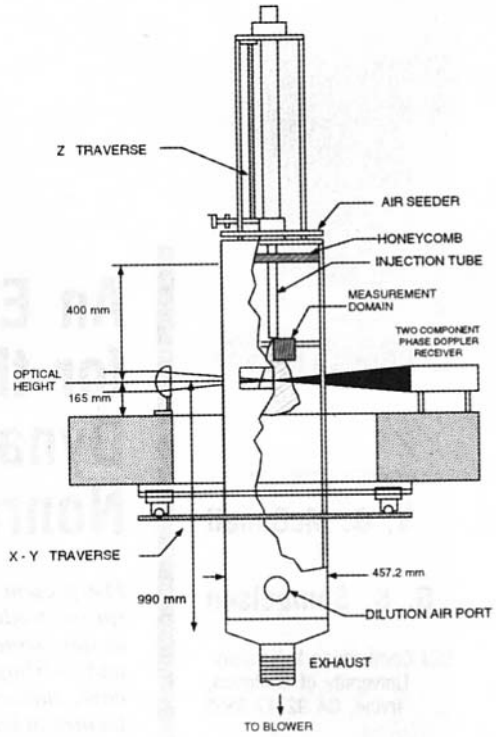

Fig. 3 Schematic of facility and measurement domain

composition are removed. For non-reacting conditions, the density of the methanol vapor is similar to that of air. Finally, for reacting conditions, the flame is relatively soot free which is attractive for characterization with non-intrusive diagnostics. As described below, the use of methanol also helps to reduce systematic errors associated with the optical diagnostic used.

Operating Conditions. The five cases included in the data base utilize methanol injected at a mass flow rate of 1.26 g/s (420 kPa pressure drop). When air is utilized (Cases 2–5), a mass flow rate of 1.32 g/s is injected. For the cases without swirl, this air flow results in a pressure drop of 3.73 and 3.48 kPa for conditions with and without spray, respectively. For cases with swirling atomizing air (Cases 3 and 5), the pressure drop is 13.79 kPa. Methanol and air are injected at 18–22 C.

Boundary Conditions. In each case, the sprays injected downwards from the center of a 495 × 495 mm square duct. Air is pulled through the top of the duct by a blower at a bulk velocity of 0.8 m/s. Measurements away from the centerline revealed that sufficient air is injected to enable a zero gradient boundary condition to be imposed near the wall of the duct (approximately 180 mm from the centerline). Measurements are obtained at axial locations, Z, of 15, 25, 35, 50, 75, 100, and 150 mm downstream of the injector. In addition, an "inlet" plane measurement is obtained near the injector. For the sprays considered, physical constraints (i.e., nonspherical drops) for the PDI permitted measurements to be obtained 7.5 mm downstream. For each case, this is taken as the "inlet" boundary. Figure 3 illustrates the overall geometry and indicates the relation of the measurement domain to the flow field.

Diagnostics. Phase Doppler-Interferometry (PDI) is the primary diagnostic tool employed. Additional details regarding the instrument as utilized for the present study are available elsewhere (McDonell and Samuelsen, 1990b, McDonell and Samuelsen, 1993). Note that the PDI system is used to measure the gas phase velocities in the presence of the spray. This is achieved by seeding all the air streams, optimizing the instrument to detect small particles, and then, via post-processing, isolating the velocity statistics associated with the small particles.

The vapor concentration measurement system (IRES) is also described in detail elsewhere (Adachi et al., 1991).

Results and Discussion

Global Structure. Figure 4 presents photographs of the five cases (Figs. 4 (a–e) correspond to Cases 1–5, respectively). The first three photos document the nonreacting sprays (Figs. 4(a–c)) and reveal the impact of the operating mode on the overall spray structure. The addition of non-swirling atomizing air collapses the spray and results in an apparent increase in concentration. Adding swirl to the air-assist results in a broadening of the spray compared to the case without swirl as well as an increase in the structure at the outer edges.

The reacting cases (Figs. 4(d–e)) reveal that the droplets are rapidly consumed downstream of the atomizer. In both cases, droplets at the centerline persist the farthest downstream. Note also that packets of isolated droplets appear in regions away from the centerline.

Gas Phase Behavior. To provide an overview of the gas phase behavior in the presence of the spray, Fig. 5 presents vectors of the velocity in the r-Z plane along with contours which depict the mean hydrocarbon concentration. Note that, in each non-reacting case, measurements of the single phase flow (absence of spray) are also available. These results are not included in detail here for brevity, but provide cases which eliminate, as a first step, the complexities of the two-phase interaction.

Figures 5(a–c) present results for the nonreacting cases. The gas phase velocities are strongly dependent upon the presence of atomizing air, as expected. In the case without atomizing air (Case 1: Fig. 5(a)), the gas phase mean velocities are generally less than 5 m/s. The results reveal the presence of entrainment associated with the injection of the spray. As the air

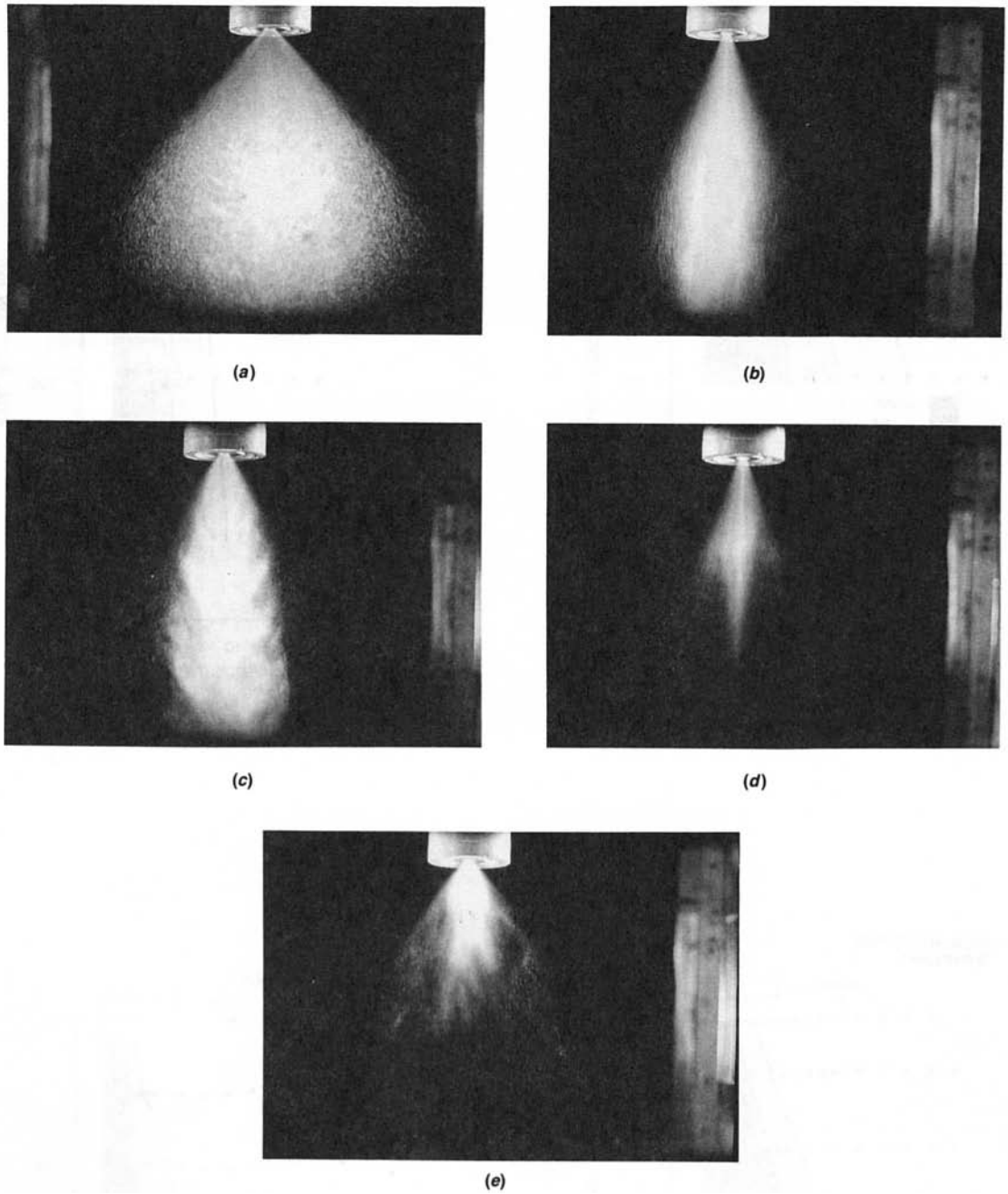

Fig. 4 Backlit photographs of the sprays for the five cases Fig. 4(*a*) Case 1 Fig. 4(*b*) Case 2 Fig. 4(*c*) Case 3 Fig. 4(*d*) Case 4 Fig. 4(*e*) Case 5

entrained reaches the area near the spray, it is accelerated by the spray and moves away from the centerline. By 75 mm downstream, the momentum exchange between phases is nearly completed and the gas moves nearly straight down. Note that, at regions away from the centerline, the air flow is essentially flowing in the axial direction.

The vapor concentration contours reflect, to a degree, the locations where the spray exists. The maximum concentrations exist at the centerline (3.8 percent by volume). This is attributed to (1) the presence of large numbers (McDonell and Samuelsen, 1990b) of small droplets in this region moving at low velocities (i.e., short vaporization time combined with long residence time) and (2) low dilution associated with entrainment air from outside the spray. Based on calculations and psychrometer experiments, the saturation temperature for methanol under the experimental conditions considered is between −8 and −4°C. If 3.8 percent vapor concentration is assumed to be a saturated condition, the gas temperature would be −3.7 to −1°C, suggesting that the conditions at the centerline of the CASE 1 spray are nearly saturated, precluding additional vaporization in this region. The vapor concentrations decrease with increased distance from the centerline due to entrainment of air surrounding the spray and a decrease in the total droplet concentration.

When non-swirling air-assist is added (Case 2: Fig. 5(*b*)), several changes in the Case 1 velocities are apparent. The velocities at the centerline are greatly enhanced (reaching 50 m/s). The spray width is reduced (Fig. 4(*a*)) which results in strong interaction with the gas phase in regions nearer to the centerline.

Like the Case 1 spray, the vapor concentrations in the Case 2 spray are highest at the centerline (2.4 percent). For Case 2, however, two sources of dilution exist, entrainment from the surrounding air and the atomizing air itself. As a result,

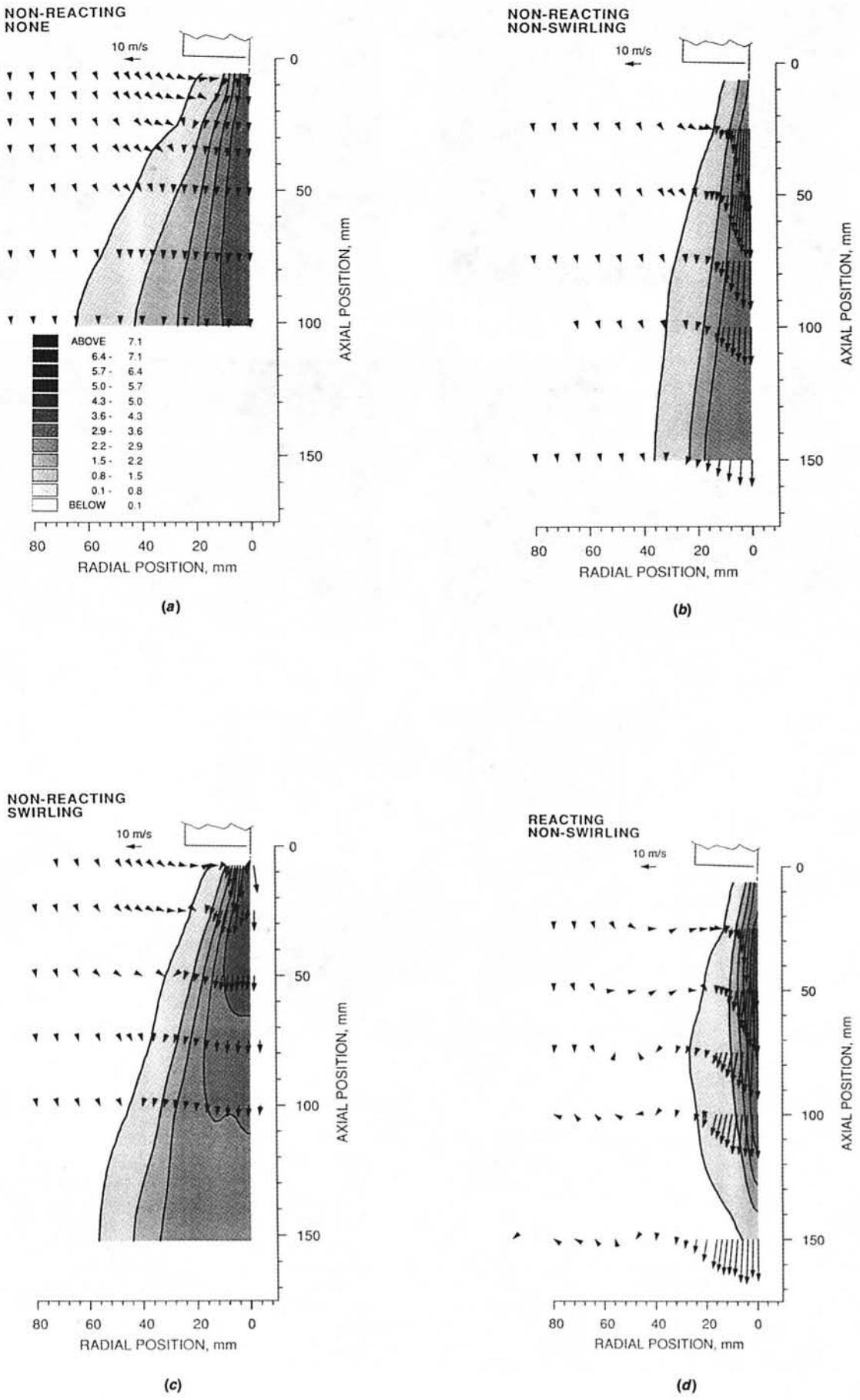

Fig. 5 Gas phase vectors in the *r-Z* plane and contours of hydrocarbon vapor percent by volume Fig. 5(*a*) Case 1 Fig. 5(*b*) Case 2 Fig. 5(*c*) Case 3 Fig. 5(*d*) Case 4 Fig. 5(*e*) Case 5

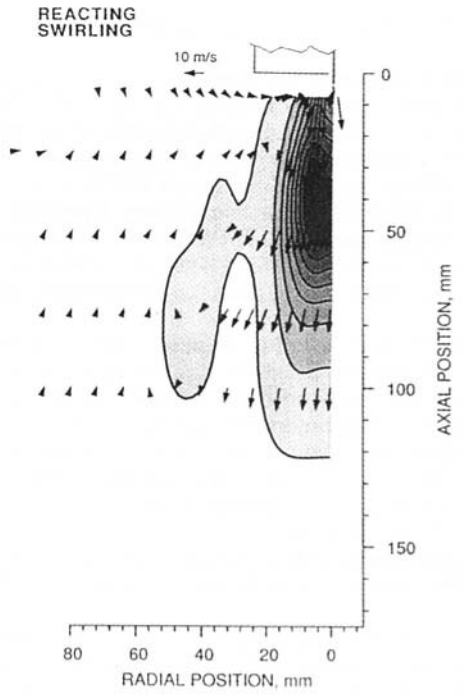

(e)

Fig. 5 Continued

the Case 2 spray may not be expected to reach saturation. However, convective effects may lower the temperature within the spray, resulting in lower concentrations at the saturated condition. Away from the centerline, entrainment of the surrounding air becomes significant enough to lower the vapor concentration.

When swirl is added to the atomizing air (Case 3: Fig. 5(*c*)), several features in the velocity change. In this case, a small recirculation zone is formed immediately downstream of the injector. This results in a local minimum in velocity at the centerline with increased distance from the injector. Compared to the Case 2 spray, an increase in the width is apparent (consistent with Figure 4a). The swirl reduces the maximum axial velocities.

The vapor concentrations in the Case 3 spray feature a local maximum at the centerline within a region extending about 65 mm downstream. The maximum concentrations in this region (3.6 percent) approach those in the Case 1 spray. In this case, the velocities are lower (increased residence time, decreased convective transfer), hence a saturation condition is more likely than in the Case 2 spray.

Figures 5(*d–e*) presents the same results for the reacting cases (Cases 4 and 5). The reacting case with nonswirling atomizing air (Fig. 5(*d*)) reveals features which are similar to those for the non-reacting case. The axial velocities retain the maximum values at the centerline. With increased distance downstream, the velocities increase compared to the non-reacting case due to the expansion of the gases. Note that, in the flow away from the spray, a region of reverse flow is present. This is due to buoyancy effects (recall that the experiment is downfired). In the Case 4 spray, this external recirculation zone helps to stabilize the reaction.

The vapor concentrations in the Case 4 spray still show a maximum at the centerline. In this case, the vapor is consumed as well as produced, so what is presented is really unburned hydrocarbons. The peak levels for the Case 4 spray (3.6 percent) suggest a lean reaction.

The velocities and vapor concentrations in reacting case with swirling atomizing air (Case 5: Fig. 5(*e*)) reflect the general

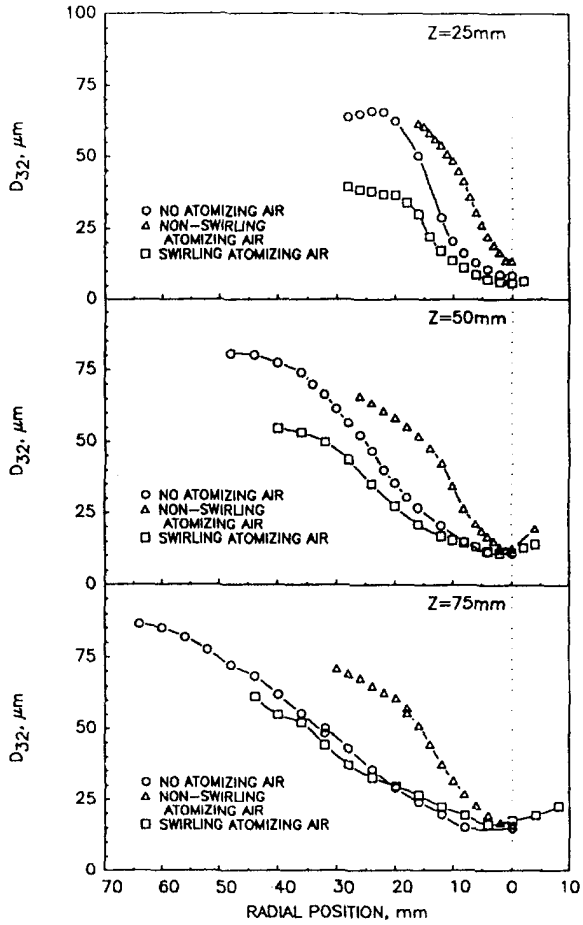

Fig. 6 Comparison of droplet size distribution sauter mean diameter for the nonreacting sprays

trends of the corresponding nonreacting case (3). Like Case 4, an external recirculation zone is formed which is due to buoyancy. In this case, more droplets are present in the region away from the centerline (recall Fig. 3(*b*)), and these droplets (local vapor sources) combined with the external recirculation zone lead to the "peninsula" of vapor away from the centerline.

Droplet Behavior. Figures 6 and 7 present comparisons of the droplet mean behavior in the non-reacting cases at three axial locations. Figure 6 compares the droplet size distribution Sauter mean diameter. In the absence of atomizing air, the radial profiles are typical of those from a hollow cone simplex spray, namely: minimum values at the centerline and maximum values at some radial location. This is due to isolation of drops according to momentum. Initially, the fuel is injected in an cone-annular sheet which, in this case, has an angle of 89 deg. As the sheet breaks up, small drops shed off both sides, with the larger drops maintaining a trajectory which is close to that of the original sheet. As the spray moves downstream, air entrained from the surroundings imparts a force radially inwards on the drops. This force results in more motion for small drops, and they are carried in towards the centerline. At axial locations close to the injector, the shedding of small drops off the outer and inner surface of the sheet leads to a local maximum in drop size at some radial distance from the centerline with smaller sizes found at radial locations beyond this distance. This effect disappears with increasing axial distance because the small drops on the outside of the sheet are carried back inside the trajectory of large drops.

When nonswirling atomizing air is added, the effect is primarily a collapse of the spray with only a small effect of the drop size. A concise statement of the droplet mean size is a

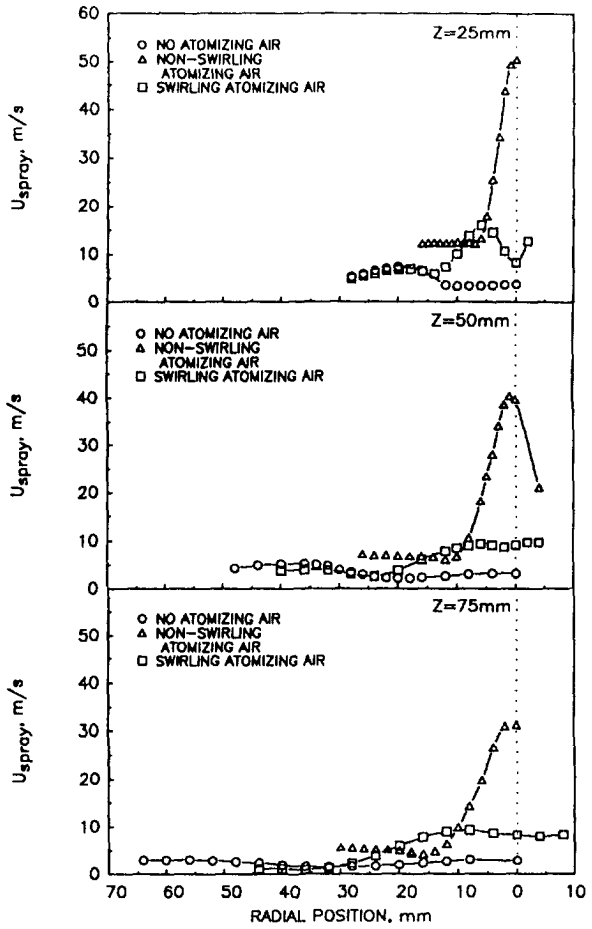

Fig. 7 Comparison of droplet mean axial velocity for the nonreacting sprays

line-averaged Sauter mean diameter. Using this as a quick indication of trends in drop size, at an axial location of 75 mm, the average drop size decreases from 35.3 μm to 31.5 μm when non-swirling atomizing air is added. This is somewhat surprising since the atomizing air impacts the cone-annular sheet at nearly normal angles. When swirl is added, the spray width is increased, and the average drop size is significantly reduced (from 31.5 μm to 17.4 μm).

Figure 7 presents the impact of the injection mode on the spray mean axial velocity. Note that this is the number weighted mean axial velocity for the entire spray. It does not account for size-velocity correlations. The trends in the droplet velocity are similar to those for the gas phase. The drop velocities for the spray with no atomizing air are generally less than 10 m/s. When non-swirling atomizing air is added, the droplet velocities are increased dramatically. Adding swirl to the atomizing air results in a reduction of this velocity, but to levels which are still greater than those found in the case without atomizing air.

These same types of results are available for the reacting cases as well (McDonell and Samuelsen, 1990b). Reaction does not change the general trends observed in the comparisons shown in Figs. 6 and 7. The primary effect of the reaction is to reduce the droplet size distribution means. However, it is also observed that the span of the distribution tends to increase with the presence of reaction. Also, the mean velocity measured at a given point increases. The interpretation of the drop velocity is challenging in the reacting case because the drop size is continually changing. This makes discrimination between momentum transfer between phases nearly impossible. In fact, a suitable predictive code could fill in the needed insight to better understand the role of vaporization and momentum transfer.

In order to determine the behavior of a particular size class, the mean velocity statistics can be calculated as a function of size class. Figure 8 presents radial profiles of the mean axial velocity as a function of droplet size for the non-reacting cases. The left column presents these results for the case without atomizing air (Case 01). Note that a strong dependency of drop velocity on drop size exists. For reference, the gas phase mean axial velocity is included. Significant slip velocities exist, indicating that strong momentum transfer between phases is occurring.

The middle portion of Fig. 8 presents the same type of results for the case with non-swirling atomizing air (Case 02). The trends are similar to those observed in the case without atomizing air. The primary differences are that the magnitude of the velocities are higher and, near the centerline, the velocity of gas phase exceeds that of the drops. This results in a situation where, at the centerline, momentum is transferred from the drops to the gas.

The right column of Fig. 8 presents the results for the case with swirling atomizing air (Case 03). Similar trends are observed.

Once again, the companion results for the reacting case are not presented for brevity, but are available as part of the data base (McDonell and Samuelsen, 1990b).

Quality Assurance Efforts. A primary challenge in applying state-of-the-art diagnostics to complex systems is the ensuring of accuracy. In the present data base, efforts were made, where possible, to ensure the quality and accuracy of the results. The following section delineates examples of the actions taken to ensure data quality.

Absolute Comparisons. Each instrument is subject to systematic errors associated with noise, optical alignment, etc. In the present data base, specific tests were carried out to better understand the fundamental limits in the measurement accuracy. The PDI instrument absolute accuracy suffers additionally from being dependent upon the spray measured. To this end, two studies were conducted in support of this data base as well as for general applications of the PDI instrument (McDonell and Samuelsen, 1990c; McDonell and Samuelsen, 1991). No short answer exists for determining the accuracy of the PDI measurements. The studies do indicate that the size and velocity of a single droplet can be measured with good accuracy (3 percent error in size, 1 percent error in velocity). Where the significant shortcomings arise are in the absolute counting of particles and the representation of the polydispersion. PDI is a single particle counter. If more than one particle enters the probe volume, either one or both particles will be invalidated (and hence quantities such as volume flux and concentration are subject to the largest errors). In addition, the dependency of the sample volume upon particle size must be somehow accounted for. The algorithms utilized suffer from inaccuracies and assumptions. As a result, the accuracy must be inferred from other tests (e.g., comparisons to other instruments, mass flux profile integrations).

The IRES measurement accuracy was evaluated for the sprays measured for the data base and are documented in Adachi et al., 1991. For the system used for in the present data base, the detectability limit is 0.1 percent. Maximum systematic errors of 7 percent and 15 percent are assigned to the nonreacting and reacting data, respectively.

A check which is often conducted for PDI measurements involves integration of a radial profile of volume flux. This integration should lead to the total liquid flow rate through the axial plane where measurements were obtained. In a vaporizing spray, some value which is less than the metered flow to the injector should be obtained. However, in the absence of quantification of the vaporization, this cannot give an ab-

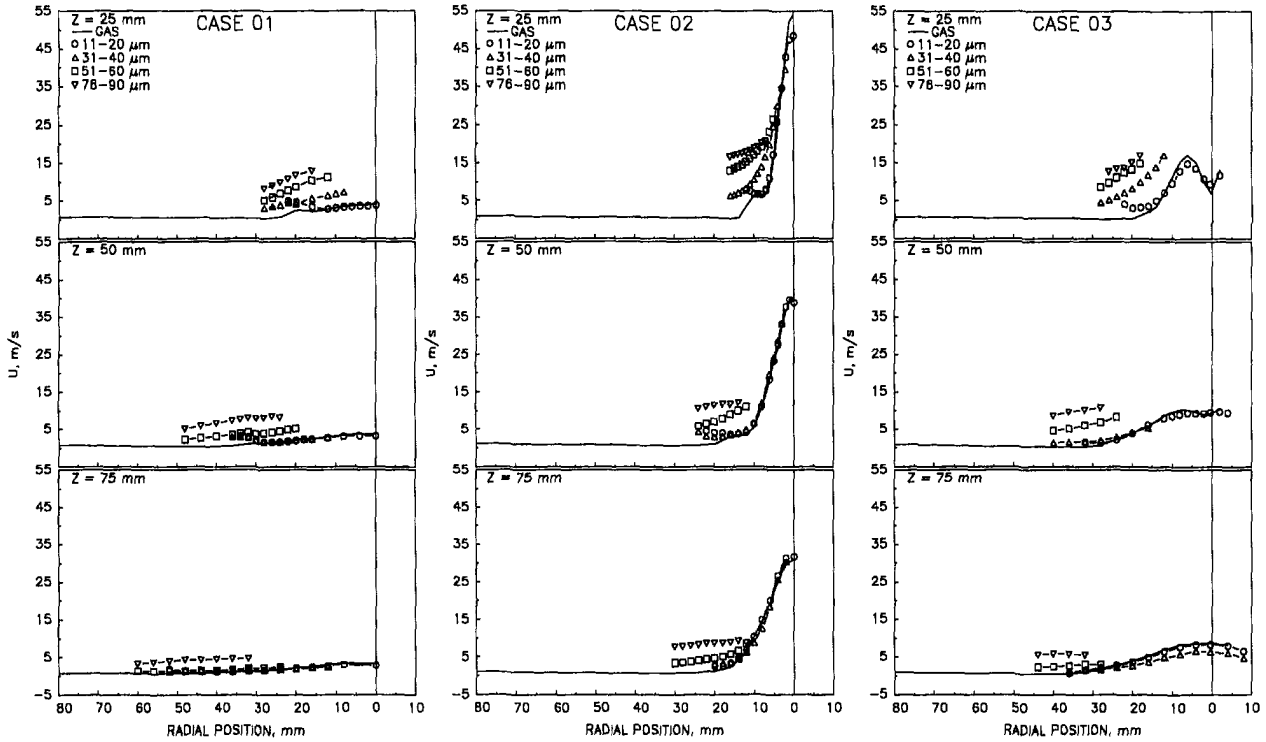

Fig. 8 Correlation between drop size and velocity for the nonreacting sprays

Table 1 Mass conservation in the nonreacting sprays

Case	Axial Plane	Liquid flow via PDI (g/s)[a]	Vapor flow via IRES (g/s)[b]	Total (g/s)	% Mass total[c]
1	25	0.914 ± 0.171	0.073 ± 0.007	0.987	78 ± 14
	75	1.130 ± 0.317	0.200 ± 0.020	1.330	106 ± 27
2	25	0.407 ± 0.048	0.075 ± 0.007	0.482	38 ± 5
	75	0.587 ± 0.226	0.185 ± 0.019	0.772	61 ± 19
3	25	0.299 ± 0.084	0.251 ± 0.025	0.550	44 ± 9
	75	0.434 ± 0.168	0.397 ± 0.056	0.831	66 ± 18

[a]Errors are established in this case by utilizing the ratio of samples attempted to samples validated at each radial location. The metered injected liquid mass flow rate is 1.26 g/s.
[b]A maximum systematic error of 7% was established for these sprays. Symmetry effects generally resulted in an additional 3% in uncertainty. At 75 mm for Case 3, asymmetries in the gas velocity (needed to compute vapor flux) are reflected as well.
[c]Assumes that errors in PDI and IRES are summed linearly and should reflect a "worst case" scenario.

solute comparison. In the present case, the IRES measurements can be combined with the PDI measurement of gas phase velocity to provide the total flow rate of vapor through each plane (McDonell and Samuelsen, 1992). The measurement of liquid flow (PDI) and vapor flow (IRES) permits accountability of all methanol injected. Table 1 summarizes these quantities at an axial locations of 25 and 75 mm.

At least two points are illustrated in Table 1: (1) mass conservation is worse at locations close to the injector, and (2) significant errors exist in the figures. In the cases where significant mass is not accounted for, yet errors are small (e.g., Case 3, Z = 25 mm), it is likely that many multi-drop occurrences are detected. Although initially disconcerting, the lack of mass conservation due to high concentrations does not likely invalidate distribution averages (Edwards and Marx, 1992). What is compromised in these cases are the measurement of total drop population (i.e., concentration), and volume flux. This must be considered when utilizing the present data for model comparison.

Symmetry Evaluation. For Cases 1 and 2, detailed symmetry assessments were carried out. This was accomplished by making PDI measurements for different injector orientations (in 45 deg increments). An example of the symmetry for the Case 2 spray is shown in Fig. 9. The results shown are the mean value from a given radial location with error bars which reflect the standard deviation about the mean. The Case 2 spray reveals excellent symmetry in terms of both gas phase velocities as well and distribution means. Case 1 shows similar

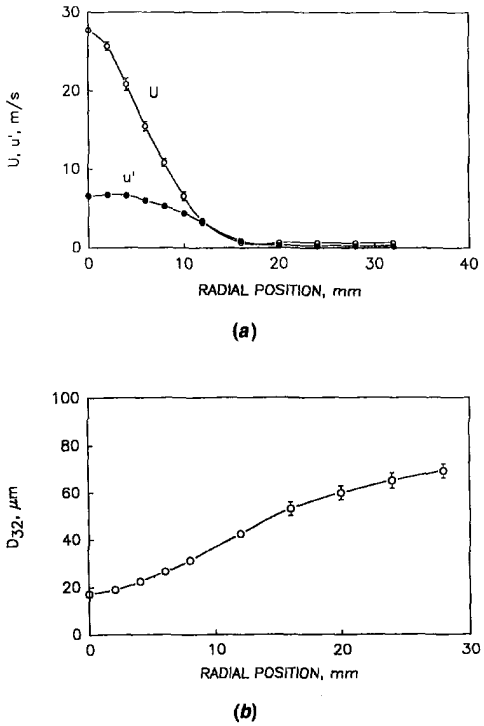

Fig. 9 Symmetry of the Case 2 spray

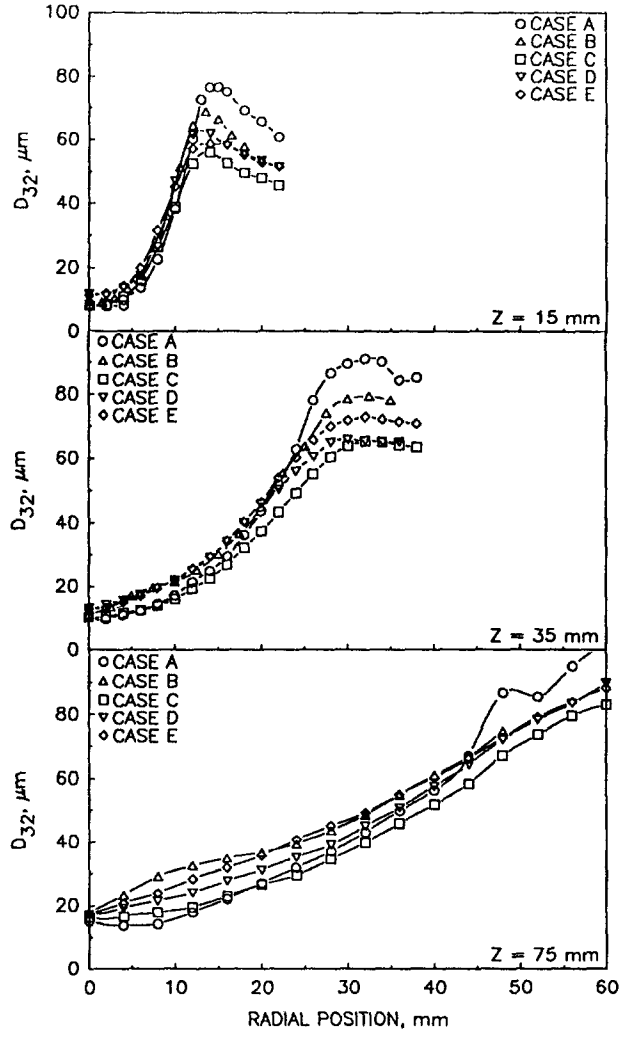

Fig. 10 Example of interlaboratory comparison for Case 1 spray (McDonell et al., 1994)

symmetry. The symmetry for Case 3 is not as good as for Case 1 and 2.

Repeatability. For Cases 1–3, at least two sets of PDI data were obtained. Generally, the mean quantities measured at a given point repeated to within 5 percent. In order to provide a more meaningful case for repeatability, the Case 1 spray has been characterized as part of an interlaboratory comparison (McDonell et al., 1994). Figure 10 presents an example of the comparison. In this study, five data sets (Cases A–E in Fig. 10) were obtained over a 27 month period of time on the same injector. The results show the degree to which measurements obtained in independent laboratories repeat.

Comparison to Existing Data. Unfortunately, spray characterization results are highly system specific. It is uncertain what level of agreement should be expected between detailed measurements obtained in general systems. In the current data base, some examples are available for the Case 1 spray where direct comparison can be made with existing data. In addition to the interlaboratory test carried out (McDonell et al., 1994), results previously obtained were also available (Dodge, 1986). An example of the comparison of the results from the present spray is shown in Fig. 11.

Summary and Conclusions

Detailed and well documented data sets, following the format prescribed in Appendix A, are available for the development and verification of computation codes proposed for spray behavior (McDonell and Samuelsen, 1990b). The data sets reveal that changes in the injection mode has profound effects on the spray behavior. In addition, the results provide cases in which momentum transfer occurs both to and from the droplets. Finally, the inclusion of vapor measurements within the sprays allows, for the first time, both diffusion and thermal gradient driven vaporization models to be evaluated.

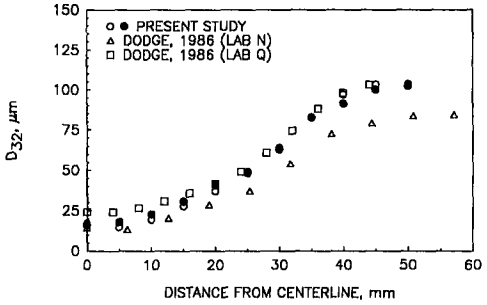

Fig. 11 Comparison of Case 1 spray measurements to data of Dodge (1986)

Acknowledgment

The continued support of Parker Hannifin for studies in the area of spray characterization is greatly appreciated.

References

Adachi, M., McDonell, V. G., and Samuelsen, G. S., 1991, "Non-Intrusive Measurement of Gaseous Species in Reacting and Non-Reacting Sprays," *Combustion Science and Technology*, Vol. 75, pp. 179–194.

Edwards, C. F. and Marx, K. D., 1992. "Analysis of the Ideal Phase-Doppler System: Limitations Imposed by the Single-Particle Constraint," *Atomization Sprays*, Vol. 2, pp. 319–366.

Dodge, L. G., 1986, "Comparison of Drop-Size Measurements for Similar Atomizer," Special Report, SwRI-8858/2, Southwest Research Institute, San Antonio, TX.

Faeth, G. M. and Samuelsen, G. S., 1986, "Fast-Reaction Nonpremixed Combustion," *Progress in Energy and Combustion Science*, Vol. 12, No. 4, pp. 305–372.

McDonell, V. G. and Samuelsen, G. S., 1990a, "Application of Laser Interferometry to the Study of Droplet/Gas Phase Interaction and Behavior in Liquid Spray Combustion Systems," *Combustion Science and Technology*, Vol. 74, pp. 343–359.

McDonell, V. G. and Samuelsen, G. S., 1990b, "Detailed Data Set: PDI and IRES Measurements in Methanol Sprays Under Reacting and Non-Reacting Conditions, Case A–C," UCI Combustion Laboratory Report UCI-ARTR-90-17A-C.

McDonell, V. G. and Samuelsen, G. S., 1990c, "Sensitivity Assessment of a Phase-Doppler Interferometer to User-Controlled Settings," *Liquid Particle Size Measurement Techniques: 2nd Volume, ASTM STP 1083*, E. Dan Hirleman, W. D. Bachalo, and Philip G. Felton, eds., ASTM, Philadelphia, pp. 170–189.

McDonell, V. G. and Samuelsen, G. S., 1991, Data Quality Control Evaluation of the Aerometrics Two-Component Phase Doppler Interferometer. UCI Combustion Laboratory Report UCI-ARTR-91-1.

McDonell, V. G. and Samuelsen, G. S., 1992, "Effect of Fuel Injection Mode on Fuel Vapor in Reacting and Non-Reacting Methanol Sprays," *24th Symposium (International) on Combustion*, The Combustion Institute, Pittsburgh, PA, pp. 1557–1564.

McDonell, V. G. and Samuelsen, G. S., 1993, "Structure of Vaporizing Pressure Atomized Sprays," *Atomization and Sprays*. Vol. 3, No. 3, pp. 321–364.

McDonell, V. G., Adachi, M., and Samuelsen, G. S., 1992, "Structure of Reacting and Non-Reacting Swirling Air-Assisted Sprays," *Combustion Science and Technology*, Vol. 82, pp. 225–248.

McDonell, V. G., Adachi, M., and Samuelsen, G. S., 1993a, "Structure of Reacting and Non-Reacting Non-Swirling Air-Assisted Sprays, Part I: Gas Phase Properties," *Atomization and Sprays*, Vol. 3, No. 4, pp. 389–410.

McDonell, V. G., Adachi, M., and Samuelsen, G. S., 1993b, "Structure of Reacting and Non-Reacting Non-Swirling Air-Assisted Sprays, Part II: Droplet Behavior," *Atomization and Sprays*, Vol. 3, No. 4, pp. 411–436.

McDonell, V. G., Samuelsen, G. S., Wang, M. R., Hong, C. H., and Lai, W. H., 1994, "Interlaboratory Comparison of Phase Doppler Measurements in a Research Simplex Atomizer Spray," *AIAA J. Propulsion and Power*, Vol. 10, No. 3, pp. 402–409.

Mongia, H. C., Reynolds, R. S., and Srinivasan, R., 1986, "Multidimensional Gas Turbine Combustor Modeling: Applications and Limitations," *AIAA Journal*, Vol. 24, No. 6, pp. 890–904.

APPENDIX A

Recommended Format for Data Base Documentation (Faeth and Samuelsen, 1986)

1 Experimental Facility
2 Experimental Configurations
3 Test Conditions
4 Inlet and Boundary Conditions
5 Quantities Measured
6 Diagnostics
7 Unusual Measurement Methods
8 Experimental Protocol
9 Quality Control
10 Error Analysis
11 Availability of the Data
12 References
13 Data

Dispersion of Ellipsoidal Particles in an Isotropic Pseudo-Turbulent Flow Field

Fa-Gung Fan

Goodarz Ahmadi

Department of Mechanical and Aeronautical Engineering, Clarkson University, Potsdam, NY 13699

Dispersion of ellipsoidal particles in a simulated isotropic pseudo-turbulent field is studied. A procedure using Euler's four parameters in describing the particle orientations is used, and the governing equations for the translational and rotational motions of particles are outlined. Turbulence fluctuation velocity field is simulated by a Gaussian random model. Motions of ellipsoidal particles of different sizes and lengths are analyzed. Ensemble and time averagings are used for evaluating various statistics of particle motion. Effects of size, shape, and density ratio on the mean-square particle velocities and the relative particle diffusivities are studied. By applying the orientation-averaging procedure, an analytical model for estimating the mean-square particle velocities and the relative diffusivities is developed. The predictions of the approximate model are compared with the simulation results and discussed.

Introduction

Understanding motions of small particles suspended in laminar and turbulent flows has received considerable attention due to its significance in numerous engineering applications. Reviews of the early works on turbulent dispersion were provided by Soo (1967) and Hinze (1975). Recently, Maxey (1987) analyzed the gravitational settling of aerosol particles in a random flow field. Ounis and Ahmadi (1989) simulated the motions of small suspended particles in a digitally generated three-dimensional Gaussian random field. Ounis and Ahmadi (1990), Wang (1990), and Mei et al. (1991) estimated the response statistics of spherical particles by using a spectral method. The effect of crossing trajectories on particle dispersion has been studied by Reeks (1977) and Wells and Stock (1983), among others.

These earlier works were almost exclusively concerned with idealized spherical particles. Thus, the effects of orientation of elongated particles and their rotational motions were ignored. It is well known that most natural dust and solid aerosol particles generated in industrial processes are nonspherical. Motions of nonspherical particles in shear fields are much more complicated than those of their spherical counterpart. For nonspherical particles, the orientation and the rotation can no longer be neglected. In the past decade, transport and deposition of nonspherical aerosol particles in laminar flows have received considerable attention. Gallily and Cohen (1979), Gradon et al. (1989), Schamberger et al. (1990), and Maxey (1990), among others, conducted several computer simulations of the motions of nonspherical particles in laminar flow conditions. In these works, Euler angles were used in describing the particle rotations. Studies of nonspherical particle motions in turbulent flows are, however, rather scarce compared with those for laminar ones. Recently, Fan and Ahmadi (1990) simulated the motions of nonspherical particles in an isotropic field. Knowledge on dispersion of these nonspherical particles in turbulent air streams is far less complete than their spherical counterpart.

In this study, a series of digital simulations for dispersion of ellipsoidal particles in an isotropic pseudo-turbulent field in the absence of gravity is carried out. The governing equations for the translational and rotational motions of particles are described. Here, unlike the simulation works existing in the current literatures, Euler's four parameters instead of Euler angles are used in describing the rotational motions of particles. (Use of Euler's parameters in simulations is superior to that of Euler angles because the latter involves a severe singularity.) The pseudo-turbulent flow field is generated by a Gaussian random model that was proposed by Kraichnan (1970). For different particle sizes, lengths, and densities, ensemble and time averagings are used to evaluate various statistics of particle motion. Effects of various parameters on the mean-square particle velocities and the relative particle diffusivities are studied. Based on an orientation-averaging procedure, approximate analytical expressions for the mean-square particle velocity and the relative diffusivity are developed. The analytical model predictions are compared with the simulation results and discussed.

Basic Equations

Figure 1 shows the schematic of an ellipsoidal particle moving in a general flow field and the corresponding inertia $[x, y, z]$ and particle $[\hat{x}, \hat{y}, \hat{z}]$ coordinate systems used. In this figure, a third coordinates system, $[\hat{\hat{x}}, \hat{\hat{y}}, \hat{\hat{z}}]$, with its origin coinciding with that of the particle frame and its axes being parallel to the corresponding axes of the inertia frame is also

Contributed by the Fluids Engineering Division for publication in the JOURNAL OF FLUIDS ENGINEERING. Manuscript received by the Fluids Engineering Division April 15, 1993; revised manuscript received August 9, 1994. Associate Technical Editor: A. Prosperetti.

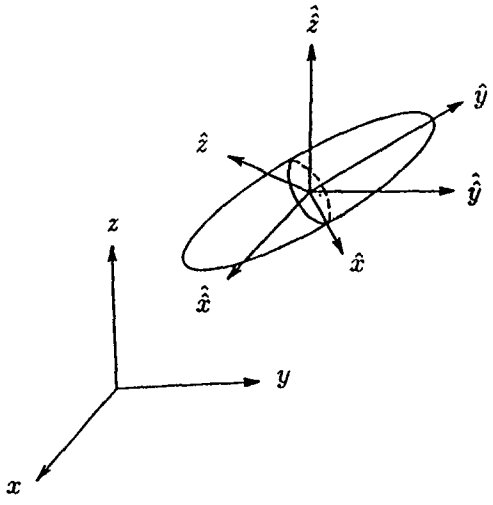

Fig. 1 Schematic diagram of the ellipsoidal particle and the corresponding coordinate systems

shown. This latter coordinate system will be called the co-moving frame for convenience. The equations of motion of an ellipsoidal particle moving in an arbitrary flow field, in the absence of Brownian and external effects is given as (Gallily and Cohen, 1979),

Translation Motion

$$m^p \frac{d\mathbf{v}}{dt} = \mathbf{f}^h, \tag{1}$$

Rotation Motion

$$I_{\hat{x}} \frac{d\omega_{\hat{x}}}{dt} - \omega_{\hat{y}}\omega_{\hat{z}}(I_{\hat{y}} - I_{\hat{z}}) = T^h_{\hat{x}}, \tag{2}$$

$$I_{\hat{y}} \frac{d\omega_{\hat{y}}}{dt} - \omega_{\hat{z}}\omega_{\hat{x}}(I_{\hat{z}} - I_{\hat{x}}) = T^h_{\hat{y}}, \tag{3}$$

$$I_{\hat{z}} \frac{d\omega_{\hat{z}}}{dt} - \omega_{\hat{x}}\omega_{\hat{y}}(I_{\hat{x}} - I_{\hat{y}}) = T^h_{\hat{z}}. \tag{4}$$

In these equations, m^p is the particle mass, t is the time, $\mathbf{v} = [v_x, v_y, v_z]$ is the translational velocity vector of the particle mass center, $\mathbf{f}^h = [f^h_x, f^h_y, f^h_z]$ is the hydrodynamic force acting on the particle, $[I_{\hat{x}}, I_{\hat{y}}, I_{\hat{z}}]$ is the moments of inertia of the particle with respect to the particle axes, $[\omega_{\hat{x}}, \omega_{\hat{y}}, \omega_{\hat{z}}]$ is the angular velocities of the particle with respect to the particle axes, and $[T^h_{\hat{x}}, T^h_{\hat{y}}, T^h_{\hat{z}}]$ is the hydrodynamic torque acting on the particle. It should be emphasized that, in Eqs. (1)–(4), the translation motions are expressed in an inertia frame, $[x, y, z]$, while the rotation motions are written in the particle frame, $[\hat{x}, \hat{y}, \hat{z}]$.

The particle position may be easily obtained from

$$\frac{d\mathbf{x}}{dt} = \mathbf{v}, \tag{5}$$

where $\mathbf{x} = [x, y, z]$ is the position vector. Evaluating particle orientation is, however, more complicated. The transformation between the co-moving and the particle frame coordinates is given by Goldstein (1980),

$$\hat{\mathbf{x}} = \mathbf{A} \cdot \hat{\hat{\mathbf{x}}}, \tag{6}$$

where $\hat{\mathbf{x}} = [\hat{x}, \hat{y}, \hat{z}]$, $\hat{\hat{\mathbf{x}}} = [\hat{\hat{x}}, \hat{\hat{y}}, \hat{\hat{z}}]$, and $\mathbf{A}$ is the transformation matrix. Euler angles $[\theta_1, \theta_2, \theta_3]$ are widely used for describing the rotational motions of rigid bodies. The transformation matrix, $\mathbf{A} = [a_{ij}]$, expressed in terms of these angles is given as

$$\mathbf{A} = \begin{bmatrix} c\theta_3 c\theta_1 - c\theta_2 s\theta_1 s\theta_3 & c\theta_3 s\theta_1 + c\theta_2 c\theta_1 s\theta_3 & s\theta_3 s\theta_2 \\ -s\theta_3 c\theta_1 - c\theta_2 s\theta_1 c\theta_3 & -s\theta_3 s\theta_1 + c\theta_2 c\theta_1 c\theta_3 & c\theta_3 s\theta_2 \\ s\theta_2 s\theta_1 & -s\theta_2 c\theta_1 & c\theta_2 \end{bmatrix}, \tag{7}$$

where $s\theta_1 = \sin\theta_1$, $c\theta_1 = \cos\theta_1$, etc. It should be mentioned that the x-convention definition of Euler angles as described by Goldstein (1980) is used here.

The time rates of changes of Euler angles are related to the angular velocities of the particle, i.e.,

$$\begin{bmatrix} \sin\theta_2 \sin\theta_3 & \cos\theta_3 & 0 \\ \sin\theta_2 \cos\theta_3 & -\sin\theta_3 & 0 \\ \cos\theta_2 & 0 & 1 \end{bmatrix} \begin{bmatrix} \dot{\theta}_1 \\ \dot{\theta}_2 \\ \dot{\theta}_3 \end{bmatrix} = \begin{bmatrix} \omega_{\hat{x}} \\ \omega_{\hat{y}} \\ \omega_{\hat{z}} \end{bmatrix}, \tag{8}$$

where a dot on top of a letter stands for a time derivative. There is, however, a complication in describing fully rotational motions by using Euler angles. The determinant of the coefficient matrix of Eq. (8) is $-\sin\theta_2$, which implies that the matrix becomes singular at $\theta_2 = 0$ and π. Thus, Eq. (8) cannot be inverted to solve for $\dot{\theta}_1$, $\dot{\theta}_2$, $\dot{\theta}_3$ near the singular values. Thus, while Euler angles are suitable for analyzing small to moderate rotations of rigid bodies, they are not convenient for describing the motions of particles which undergo full rotations.

To overcome the singularity difficulty, one can use Euler's four parameters $[\epsilon_1, \epsilon_2, \epsilon_3, \eta]$ instead of Euler angles $[\theta_1, \theta_2, \theta_3]$. Euler's four parameters, which are also known as quaternions, are defined by Hughes (1986) and Goldstein (1980). The most general rotation of a rigid body is a motion with only three degrees of freedom. The Euler's four parameters are therefore subject to a constraint given by $\epsilon_1^2 + \epsilon_2^2 + \epsilon_3^2 + \eta^2 = 1$. The transformation matrix $\mathbf{A}$ in Eq. (6) may be restated in terms of quaternions as (Hughes, 1986),

$$\mathbf{A} = \begin{bmatrix} 1 - 2(\epsilon_2^2 + \epsilon_3^2) & 2(\epsilon_1\epsilon_2 + \epsilon_3\eta) & 2(\epsilon_1\epsilon_3 - \epsilon_2\eta) \\ 2(\epsilon_2\epsilon_1 - \epsilon_3\eta) & 1 - 2(\epsilon_3^2 + \epsilon_1^2) & 2(\epsilon_2\epsilon_3 + \epsilon_1\eta) \\ 2(\epsilon_3\epsilon_1 + \epsilon_2\eta) & 2(\epsilon_3\epsilon_2 - \epsilon_1\eta) & 1 - 2(\epsilon_1^2 + \epsilon_2^2) \end{bmatrix}. \tag{9}$$

The time rates of changes of quaternions are given by

$$\begin{bmatrix} \dot{\epsilon}_1 \\ \dot{\epsilon}_2 \\ \dot{\epsilon}_3 \\ \dot{\eta} \end{bmatrix} = \frac{1}{2} \begin{bmatrix} \eta\omega_{\hat{x}} - \epsilon_3\omega_{\hat{y}} + \epsilon_2\omega_{\hat{z}} \\ \epsilon_3\omega_{\hat{x}} + \eta\omega_{\hat{y}} - \epsilon_1\omega_{\hat{z}} \\ -\epsilon_2\omega_{\hat{x}} + \epsilon_1\omega_{\hat{y}} + \eta\omega_{\hat{z}} \\ -\epsilon_1\omega_{\hat{x}} - \epsilon_2\omega_{\hat{y}} - \epsilon_3\omega_{\hat{z}} \end{bmatrix}. \tag{10}$$

At the initial stage, knowing the initial orientation of the particle (direction cosines, a_{ij}), the initial conditions for the quaternions are specified by using the following relations (Hughes, 1986). If $\eta \neq 0$,

$$\eta = \pm\frac{1}{2}(1 + a_{11} + a_{22} + a_{33})^{1/2},$$

$$\begin{bmatrix} \epsilon_1 \\ \epsilon_2 \\ \epsilon_3 \end{bmatrix} = \frac{1}{4\eta} \begin{bmatrix} a_{23} - a_{32} \\ a_{31} - a_{13} \\ a_{12} - a_{21} \end{bmatrix}. \tag{11}$$

If $\eta = 0$, then

$$\epsilon_1 = \pm\sqrt{\frac{1 + a_{11}}{2}}, \quad \epsilon_2 = \frac{a_{12}}{2\epsilon_1}, \quad \epsilon_3 = \frac{a_{23}}{2\epsilon_2}. \tag{12}$$

The nonuniqueness of the values as given by Eqs. (11) and (12) does not introduce any difficulty in the present study because they correspond to the same transformation matrix and result in identical particle trajectories.

Equation (10) shows that the time rates of changes of Euler's four parameters can always be evaluated and the singularity difficulty associated with using Euler angles is eliminated. When forces and torques that act on the particle are known, the trans-

lational and rotational motions of an ellipsoidal particle may be easily evaluated by using Eqs. (1)–(6) and (10)–(12).

Ellipsoids of Revolution

In this work, motions of particles which have the shape of an ellipsoid of revolution are studied. This class covers a wide range of particle geometries of practical interest, such as spherical, prolate spheroids, and needle shapes. Here, it is assumed that the $\hat{y}$-axis is along the particle major axis as shown in Fig. 1.

The hydrodynamic force acting on an ellipsoidal particle in an arbitrary flow field under Stokes flow condition was obtained by Brenner (1964) in the form of infinite series of flow velocity and its spatial derivatives. Unlike that of a spherical particle, the spatial derivatives higher than the second order also contribute to the hydrodynamic force. However, these higher-order corrections are proportional to higher-order powers of particle minor axis. Thus, these higher-order terms are negligible for small suspended particles. Retaining only the first two terms of the series, it follows

$$\mathbf{f}^h = \mu\hat{\hat{\mathbf{K}}}\cdot(\mathbf{u}-\mathbf{v}) + \frac{\mu}{6}\mathbf{A}^{-1}\cdot\hat{\mathbf{K}}\cdot D^2\hat{\mathbf{u}}, \tag{13}$$

where μ is the dynamic viscosity of fluid, and $\mathbf{u} = [u_x, u_y, u_z]$ is the fluid velocity vector at the particle centroid in the absence of particle. Here, a hat and a double hat denote a quantity expressed in the particle and the co-moving frames, respectively. In this equation, the translation matrix is given by,

$$\hat{\mathbf{K}} = \mathbf{A}^{-1}\cdot\hat{\mathbf{K}}\cdot\mathbf{A}, \tag{14}$$

and

$$D^2\hat{\mathbf{u}} = a^2\frac{\partial^2\hat{\mathbf{u}}}{\partial\hat{x}^2} + b^2\frac{\partial^2\hat{\mathbf{u}}}{\partial\hat{y}^2} + a^2\frac{\partial^2\hat{\mathbf{u}}}{\partial\hat{z}^2}, \tag{15}$$

for ellipsoids of revolution. As noted before, $\hat{\mathbf{u}} = [u_{\hat{x}}, u_{\hat{y}}, u_{\hat{z}}]$ is the fluid velocity vector with respect to the particle frame, and a and b are the semi-minor and the semi-major axes of the ellipsoid of revolution, respectively. The particle-frame translation matrix $\hat{\mathbf{K}}$ for an ellipsoid of revolution is a diagonal matrix with the diagonal elements given by

$$k_{\hat{x}\hat{x}} = k_{\hat{z}\hat{z}} = 16\pi a(\beta^2-1)\Big/\left[\frac{2\beta^2-3}{\sqrt{\beta^2-1}}\ln(\beta+\sqrt{\beta^2-1})+\beta\right], \tag{16}$$

$$k_{\hat{y}\hat{y}} = 8\pi a(\beta^2-1)\Big/\left[\frac{2\beta^2-1}{\sqrt{\beta^2-1}}\ln(\beta+\sqrt{\beta^2-1})-\beta\right], \tag{17}$$

where $\beta = b/a$ is the particle aspect ratio (ratio of the semi-major axis to the semi-minor axis). In the limit of spherical particles, the second term on the right-hand side of Eq. (13) reduces to the Faxen force (where the particle rotational motion is also ignored).

The components of hydrodynamic torque acting on an ellipsoid of revolution as obtained by Jeffery (1992) are given as,

$$T^h_{\hat{x}} = \frac{16\pi\mu a^3\beta}{3(\beta^2\beta_0+\gamma_0)}[(\beta^2-1)d_{\hat{y}\hat{y}} + (\beta^2+1)(w_{\hat{y}\hat{y}}-\omega_{\hat{x}})], \tag{18}$$

$$T^h_{\hat{y}} = \frac{32\pi\mu a^3\beta}{3(\gamma_0+\alpha_0)}(w_{\hat{x}\hat{z}}-\omega_{\hat{y}}), \tag{19}$$

$$T^h_{\hat{z}} = \frac{16\pi\mu a^3\beta}{3(\alpha_0+\beta^2\beta_0)}[(1-\beta^2)d_{\hat{y}\hat{x}} + (1+\beta^2)(w_{\hat{y}\hat{x}}-\omega_{\hat{z}})], \tag{20}$$

where

$$d_{\hat{m}\hat{n}} = \frac{1}{2}\left(\frac{\partial u_{\hat{m}}}{\partial x_{\hat{n}}}+\frac{\partial u_{\hat{n}}}{\partial x_{\hat{m}}}\right), \quad w_{\hat{m}\hat{n}} = \frac{1}{2}\left(\frac{\partial u_{\hat{m}}}{\partial x_{\hat{n}}}-\frac{\partial u_{\hat{n}}}{\partial x_{\hat{m}}}\right), \tag{21}$$

are elements of the deformation-rate and the spin tensors in the particle frame. Here, the subscript indices $\hat{m}$ and $\hat{n}$ run from 1 to 3 (corresponding to $\hat{x}$, $\hat{y}$, and $\hat{z}$) and $x_{\hat{m}} = \hat{\mathbf{x}} = [\hat{x}, \hat{y}, \hat{z}]$. The parameters, α_0, β_0, and γ_0 for an ellipsoid of revolution were given by Gallily and Cohen (1979) as

$$\alpha_0 = \gamma_0 = \frac{b^2}{b^2-a^2} + \frac{a^2b}{2(b^2-a^2)^{3/2}}\ln\left[\frac{b-\sqrt{b^2-a^2}}{b+\sqrt{b^2-a^2}}\right], \tag{22}$$

$$\beta_0 = -\frac{2a^2}{b^2-a^2} - \frac{a^2b}{(b^2-a^2)^{3/2}}\ln\left[\frac{b-\sqrt{b^2-a^2}}{b+\sqrt{b^2-a^2}}\right]. \tag{23}$$

It is noted that Eqs. (18)–(20) are valid for Stokes flow condition.

The velocity gradient in the particle frame needed in Eq. (21), may be obtained by using the transformation, $\hat{\mathbf{G}} = \mathbf{A}\cdot\hat{\mathbf{G}}\cdot\mathbf{A}^{-1}$, where $\hat{\mathbf{G}}$ and $\hat{\hat{\mathbf{G}}}$ stand for dyadics expressed in the particle and the co-moving frames, respectively. It should be noted here that these spatial derivatives of the velocity field are invariant in a change of frame from the inertial one to the co-moving frame.

Substituting Eq. (13) and Eqs. (18)–(20) into Eqs. (1)–(4) leads to the explicit equations of motion for an ellipsoid of revolution in an arbitrary fluid flow field. The mass of an ellipsoid of revolution is $m^p = (4/3)\pi a^3\beta\rho^p$ where ρ^p denotes the density of the particle. The moments of inertia for the particle are $I_{\hat{x}} = (1+\beta^2)a^2m^p/5$, $I_{\hat{y}} = 2a^2m^p/5$, and $I_{\hat{z}} = (1+\beta^2)a^2m^p/5$.

Motions of Ellipsoids in an Isotropic Turbulence

In this study, the Gaussian random field developed by Kraichnan (1970) is used to simulate the particle motion in a homogeneous and isotropic turbulence. This technique was used earlier by Maxey (1987) to study the gravitational settling of small particles and by Ounis and Ahmadi (1989) to study the turbulent diffusivity of spherical particles. The expression for the instantaneous velocity field is given by

$$\mathbf{u}^*(\mathbf{x}^*, t^*) = \sqrt{\frac{2}{N}}\left\{\sum_{n=1}^{N}\mathbf{p}(\mathbf{k}_n)\cos(\mathbf{k}_n\cdot\mathbf{x}^* + \omega_n t^*) + \sum_{n=1}^{N}\mathbf{q}(\mathbf{k}_n)\sin(\mathbf{k}_n\cdot\mathbf{x}^* + \omega_n t^*)\right\}, \tag{24}$$

with $\mathbf{p}(\mathbf{k}_n) = \zeta_n \times \mathbf{k}_n$, and $\mathbf{q}(\mathbf{k}_n) = \xi_n \times \mathbf{k}_n$. The components of vectors ζ and ξ and the frequency ω are independent zero-mean unit-variance Gaussian random variables, while each component of $\mathbf{k}$ is picked from a zero-mean Gaussian distribution with a standard deviation of $1/2$. Here, N is the number of terms considered in the series. It was shown by Ounis and Ahmadi (1989) that the velocity correlation of the digitally simulated field obtained with $N = 100$ is in good agreement with the theoretical values. Equation (24) is in nondimensionalized form with the dimensionless quantities given by,

$$\mathbf{x}^* = \frac{\mathbf{x}}{l_o}, \quad t^* = \frac{tv_o}{l_o}, \quad \mathbf{u}^* = \frac{\mathbf{u}}{v_o}, \tag{25}$$

where l_o and v_o denote the characteristic length and velocity scales of turbulence.

For pseudo-turbulent velocity field described by Eq. (24), the energy spectrum $E(k)$ and the Eulerian time correlation $Q(t^*)$ are given as

$$E(k) = 16(2/\pi)^{1/2}k^4e^{-2k^2}, \quad Q(t^*) = e^{-t^{*2}/2}, \tag{26}$$

where k is the wave number. It is clear that the velocity field

given by Eq. (24) does not satisfy the Navier-Stokes equation, and hence is not a genuine turbulent flow. Although it does not have the detail structures of turbulence, it exhibits similar random fluctuation characteristics.

Before the velocity field given by Eq. (24) can be used for dispersion analysis of ellipsoidal particles, it is convenient to nondimensionalize the equations of motion. By using the nondimensional quantities given by Eq. (25) and

$$\omega_l^* = \omega_l \frac{l_o}{v_o}, \quad \mathrm{Re}_l = \frac{v_o l_o}{\nu}, \quad S = \frac{\rho^p}{\rho^f}, \quad a^* = \frac{a}{l_o}, \quad \hat{\mathbf{K}}^* = \frac{\hat{\mathbf{K}}}{l_o}, \quad \hat{\mathbf{u}}^* = \frac{\hat{\mathbf{u}}}{v_o}, \tag{27}$$

the equations of motion (1)–(4) with hydrodynamic force and torque given by Eqs. (13) and (18)–(20) may be rewritten in nondimensional form as,

$$\frac{d\mathbf{v}^*}{dt^*} = \frac{3}{4\pi\beta S a^{*3}\,\mathrm{Re}_l}\left[\hat{\mathbf{K}}^* \cdot (\mathbf{u}^* - \mathbf{v}^*) + \frac{1}{6}\mathbf{A}^{-1} \cdot \hat{\mathbf{K}}^* \cdot D^{*2}\hat{\mathbf{u}}^*\right], \tag{28}$$

$$\frac{d\omega_x^*}{dt^*} = \omega_y^*\omega_z^*\left(\frac{2}{1+\beta^2} - 1\right) + \frac{20}{(\beta^2\beta_0 + \gamma_0)(1+\beta^2)S\,a^{*2}\,\mathrm{Re}_l}\left[(\beta^2 - 1)d_{zy}^* + (\beta^2 + 1)(w_{zy}^* - \omega_x^*)\right], \tag{29}$$

$$\frac{d\omega_y^*}{dt^*} = \frac{20}{(\gamma_0 + \alpha_0)S\,a^{*2}\,\mathrm{Re}_l}(w_{xz}^* - \omega_y^*), \tag{30}$$

$$\frac{d\omega_z^*}{dt^*} = \omega_x^*\omega_y^*\left(1 - \frac{2}{1+\beta^2}\right) + \frac{20}{(\alpha_0 + \beta^2\beta_0)(1+\beta^2)S\,a^{*2}\,\mathrm{Re}_l}\left[(1-\beta^2)\,d_{yx}^* + (1+\beta^2)(w_{yx}^* - \omega_z^*)\right] \tag{31}$$

In Eq. (27), $\nu = \mu/\rho^f$ is the kinematic viscosity of the fluid, and ρ^f is the fluid density. In Eqs. (28)–(31),

$$D^{*2}\hat{\mathbf{u}}^* = a^{*2}\frac{\partial^2\hat{\mathbf{u}}^*}{\partial\hat{x}^{*2}} + b^{*2}\frac{\partial^2\hat{\mathbf{u}}^*}{\partial\hat{y}^{*2}} + a^{*2}\frac{\partial^2\hat{\mathbf{u}}^*}{\partial\hat{z}^{*2}}, \tag{32}$$

$$d_{mn}^* = \frac{1}{2}\left(\frac{\partial u_m^*}{\partial x_n^*} + \frac{\partial u_n^*}{\partial x_m^*}\right), \quad w_{mn}^* = \frac{1}{2}\left(\frac{\partial u_m^*}{\partial x_n^*} - \frac{\partial u_n^*}{\partial x_m^*}\right), \tag{33}$$

where $[\hat{x}^*, \hat{y}^*, \hat{z}^*] = [\hat{x}, \hat{y}, \hat{z}]/l_0$.

When the dimensionless quantities for the physical properties of the ellipsoidal particle and the fluid Reynolds number Re_l are specified, Eqs. (5), (11), and (12), and (28)–(31) may be used for evaluating the particle translational and rotational motions. In the following numerical computations, a fourth-order Runge-Kutta scheme is used to evaluate the particle translational and rotational motions.

Figure 2 shows the xy-projection of a sample trajectory and orientation of the major axis of an ellipsoid of revolution with $a^* = 0.0015$, $\beta = 10$, $S = 1000$ and $\mathrm{Re}_l = 17$ as obtained from the digital simulation. This corresponds to a rigid fiber (ellipsoid) with a length of 17.4μm and a thickness of 1.74 μm moving in a turbulent air stream near the centerline of a 4 cm-diameter circular pipe with a mean velocity of 8 m/s.

The particle velocity autocorrelation tensor is given by,

$$\mathbf{R}_{\mathbf{v}^*\mathbf{v}^*}(t'^*) = \langle \mathbf{v}^*(t^*) \otimes \mathbf{v}^*(t^* + t'^*) \rangle, \tag{34}$$

where '$\otimes$' stands for a dyadic product, t' is the time lag, and the angular brackets '$\langle\ \rangle$' denotes the expected value (ensemble average). For an isotropic turbulence, the off-diagonal elements of the tensor vanish, and the diagonal elements are identical. At $t'^* = 0$, the diagonal elements of $\mathbf{R}_{\mathbf{v}^*\mathbf{v}^*}$ are the mean-square (MS) particle velocities.

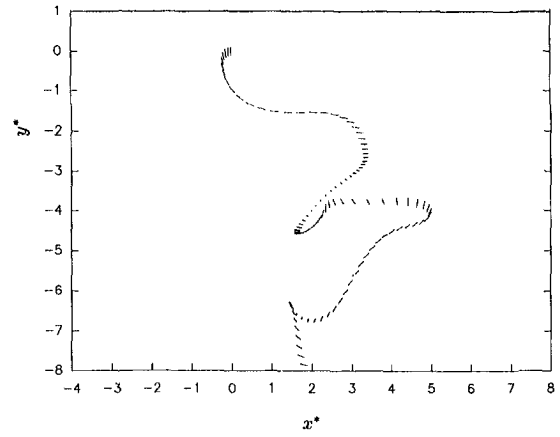

Fig. 2 A sample trajectory and the orientation for an ellipsoid of revolution with $a = 0.0015$, $\beta = 10$, and $S = 1000$ in a flow field of $\mathrm{Re}_l = 17$

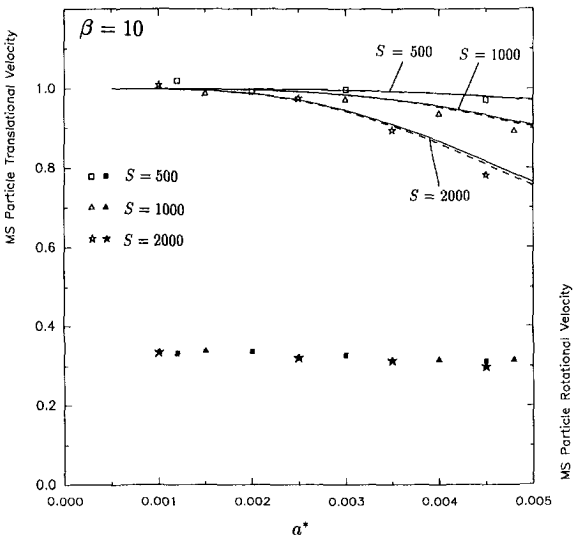

Fig. 3 Variations of MS particle translational and rotational velocities with particle size for various density ratios

For an isotropic field considered, the long-term particle diffusivity tensor is given as,

$$\mathbf{D}^p = \frac{\langle \mathbf{x}^* \otimes \mathbf{x}^* \rangle}{2t^*} = \int_0^\infty \mathbf{R}_{\mathbf{v}^*\mathbf{v}^*}(t'^*)\,dt'^*. \tag{35}$$

Like the velocity autocorrelation tensor, the diffusivity tensor is a diagonal matrix with identical diagonal elements. In Eq. (35), the diagonal elements of $\langle \mathbf{x}^* \otimes \mathbf{x}^* \rangle$ are the MS particle positions.

Results and Discussions

In this section, the results concerning the mean-square (MS) particle translational and rotational velocities and the relative mass diffusivity as obtained from the simulation studies are presented. A flow Reynolds number of $\mathrm{Re}_l = 17$ is assumed in these digital simulations. A simplified model based on spectral analysis for evaluating the MS particle translational velocities and the relative mass diffusivities is described in Appendix A. The model predictions and the simulation results are compared and discussed.

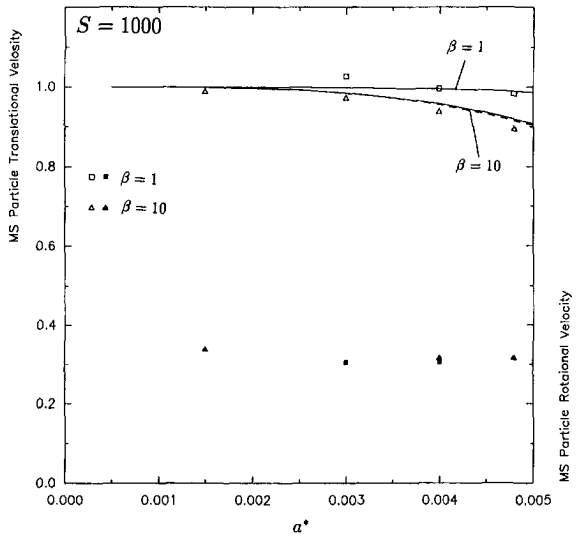

Fig. 4 Variations of MS particle translational and rotational velocities with particle size for various aspect ratios

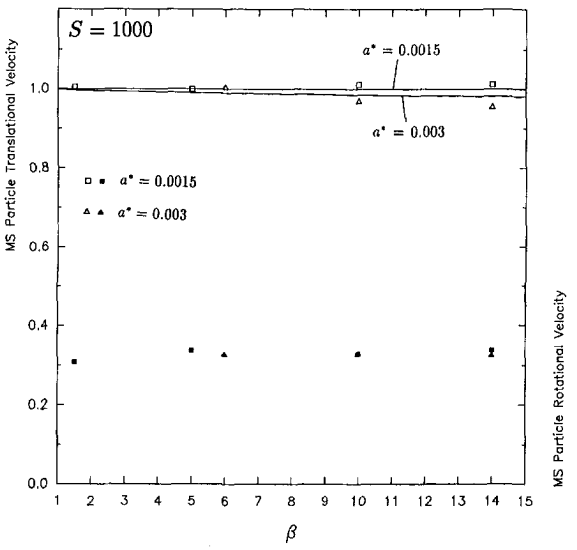

Fig. 5 Variation of MS particle translational and rotational velocities with aspect ratios

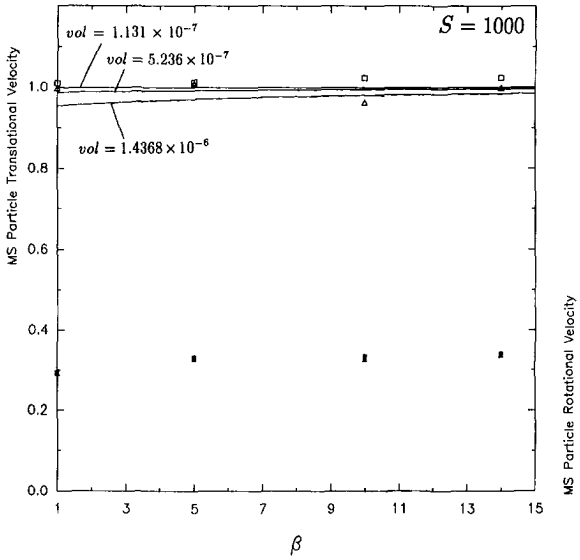

Fig. 6 Variations of MS particle translational and rotational velocities with aspect ratios for various particle volumes

Figures 3–6 show the MS particle translational and rotational velocities. In these simulations, the particle trajectories for a nondimensional time of $t^* = 15$ and five hundreds samples are used in the ensemble averagings. In addition to ensemble averaging, time averagings with durations of 6 to 11 nondimensional time units are performed for evaluating various statistics of particle motion.

Figures 3 and 4 display the variations of simulated MS particle translational and rotational velocities with a^* for various density and aspect ratios. The corresponding model predictions are also shown in these figures for comparison. In Fig. 3, the aspect ratio of particle is fixed at $\beta = 10$, while in Fig. 4 the density ratio is fixed at $S = 1000$. The simulated MS particle translational velocities for different conditions are shown by the various open symbols. The simulated MS particle rotational velocities displayed in these figures are the average of mean square angular velocities, $\langle\omega_x^2\rangle$, $\langle\omega_y^2\rangle$, $\langle\omega_z^2\rangle$. These values are shown by solid symbols corresponding to the open symbols for the translational velocities for various conditions. It is observed that as the particle size or density ratio increase, the MS particle translational velocities decrease. However, the MS particle angular velocities remain almost constant for the cases considered. The solid lines display the predictions of the simplified analytical model with the effective relaxation time, τ^*, as defined by Eq. (A.9). The dashed lines are the model predictions when Eq. (A.10) for τ^* is used. These figures show that the model predictions for the MS particle velocities are in good agreement with the digital simulation results. It is also observed that the resulting MS translational velocities are insensitive to the choice of the effective relaxation time used.

Figure 5 displays variations of the MS particle translational and rotational velocities with aspect ratio β for a fixed density ratio of $S = 1000$. The MS translational and rotational velocities as obtained from the digital simulations are displayed by the various open and solid symbols, respectively. The model predictions for τ^* given by Eq. (A.9) are displayed by the solid lines, while those obtained by using Eq. (A.10) are shown by the dashed lines. It is observed from this figure that the MS particle translational velocity decreases as the aspect ratio increases, while the MS rotational velocity remains constant. Figure 5 also shows that the simplified model predicts the MS translational velocities with a reasonable accuracy.

Figure 6 shows the variations of MS velocities with the aspect ratio for fixed particle volumes. While there are some scatter in the simulated MS translational velocities, the results indicate that both the MS translational and rotational velocities are roughly constant for the entire range of β considered. The simplified model predicts that, for a fixed particle volume, the MS particle translational velocity increases slightly with β. That is, among the particles with different aspect ratios but with the same mass, the elongated ones fluctuate somewhat more vigorously than spherical ones. The variation, however, is within the range of the statistical error of the simulations.

Figure 7 shows the simulated relative mass diffusivity as functions of a^*. For an ensemble of 1500 samples, the time evolution of $\langle \mathbf{x}^* \otimes \mathbf{x}^* \rangle$ for a duration of 15 time units is first evaluated. Equation (35) is then used to calculate the particle diffusivity tensor as a function of t^*. A time averaging (from $t^* = 5$ to 15) is employed to evaluate the long-term particle diffusivity tensor, $\mathbf{D}^p$. The mean particle diffusivity, D^p, which is the average of the three diagonal elements of $\mathbf{D}^p$ is then evaluated. To obtain the fluid diffusivity, ensemble of 1500 point particle trajectories are first generated. The fluid (point particle) counterpart of Eq. (35) and an averaging procedure identical to that for finite size particles are used for determining the long-term fluid diffusivity tensor $\mathbf{D}^f$. The mean fluid diffusivity D^f as given by $(1/3)tr\mathbf{D}^f$ is then computed. The

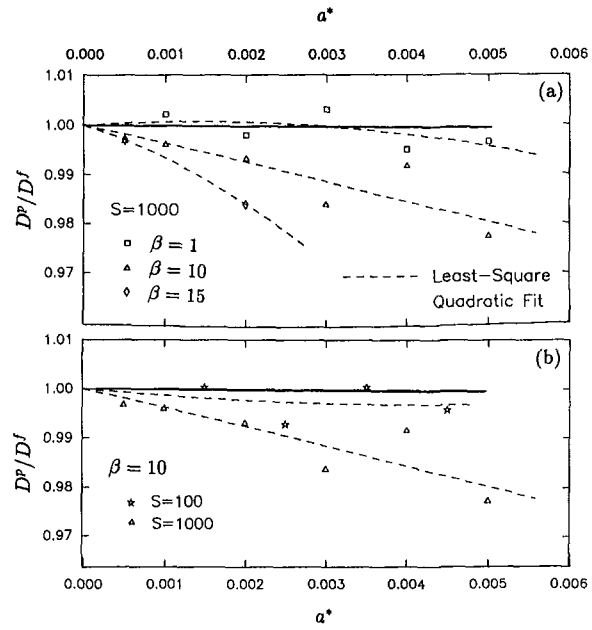

Fig. 7 Variations of relative diffusivity with a^* for various aspect and density ratios

relative diffusivity, D^p/D^f as obtained from the simulations for various conditions are displayed by different symbols in Fig. 7. The dashed lines shown in this figure are the least-mean-square quadratic fits (LSQF) to the simulation data.

The results for a particle-to-fluid density ratio of 1000 and various aspect ratios are shown in Fig. 7(*a*), whereas those for an aspect ratio of 10 and different density ratios are displayed in Fig. 7(*b*). Although there are some scatter in the simulation data, the trends of variations are clearly shown by the LSQF curves. It is observed that the finite size particles diffuse less than the fluid particles. For very small particles, the relative diffusivity approaches unity as is expected. Figure 7(*a*) shows, as the particle size increases (due to the increases in a^* or β), the relative diffusivity decreases. Figure 7(*b*) shows that particles with a larger density diffuse less than those with a smaller density. The reductions of D^p/D^f are only a few percents for the range of parameters considered. The solid lines in this figure correspond to the variations of relative diffusivity for particles with $S = 1000$ and $\beta = 10$ as predicted by the simplified model. Figure 7 shows that the simplified model underestimates the decrease in the relative diffusivities, although it provides reasonable predictions for the MS particle velocities as shown in Figs. 3–6. This is, in part, because the crossing trajectory effect is neglected in the simplified analytical model described in Appendix A. It is also observed that the model prediction actually fits to the simulation results for $S = 100$ better than those for $S = 1000$. For a large particle-to-fluid density ratio of 1000, the crossing trajectory due to particle inertia significantly affects the relative diffusivity. As the particle-to-fluid density ratio decreases, the crossing trajectory effects become less important. Thus, the model prediction agrees the simulation data for particles with a small density ratio.

Conclusions

In this work, the dispersion of ellipsoidal particles in an isotropic turbulent flow field in the absence of gravitational effects is studied. A pseudo-turbulent flow field is generated by a Gaussian model. The equations of motion for particles which are translating and rotating are integrated numerically. Use is made of Euler's four parameters for evaluating the particle orientation. This set of parameters is superior to the more commonly used Euler angles in that it avoids singularity. Ensembles of particle trajectory and orientation are generated and are used to estimate various particle response statistics. A simplified analytical model for evaluating the long-term particle response statistics is developed by using an orientation-averaging procedure. Based on the results presented in this study, the following conclusions may be drawn:

1. The simulation procedure described in this work which uses Euler's parameters for the rotational motions of ellipsoidal particles is effective and convenient.
2. The MS particle translational velocity decreases as particle size or density ratio increase, while the MS particle rotational velocity is insensitive to the variations in particle size and density ratio.
3. The effects of the Faxen-like force to the MS particle translational/rotational velocities and the relative diffusivity are small.
4. The relative diffusivity decreases with an increase in particle size and particle-to-fluid density ratio.
5. The simplified analytical model provides reasonably accurate estimates for the mean-square particle translational velocities. For large particle-to-fluid density ratios, however, the simplified model prediction for the relative diffusivity is inaccurate. This may be owing to the crossing trajectory effect is neglected in the simplified model.
6. For particles with a fixed volume and density ratio, the MS particle translational/rotational velocities and the relative diffusivity are insensitive to a variation in the aspect ratio.
7. For small ellipsoids with a relaxation time much smaller than turbulent time scale, the assumption of equality of the Eulerian spectrum with the Lagrangian one is reasonable.
8. The effective nondimensional particle relaxation time τ^* as defined in Eq. (A.9) or (A.10) provides a reasonable measure of particle response time scale for ellipsoidal particles.

Acknowledgments

Thanks are given to Raymond G. Bayer, Michael A. Gaynes, and Allen Smith of IBM-Endicott for many helpful discussions. Different stages of this study were supported by IBM-Endicott, the New York State Science and Technology Foundation (through the Center for Advanced Materials Processing, CAMP, of Clarkson University), and the Department of Energy (University Coal Research Program, PETC) under Grant DE-FG22-94PC-94213. The use of the supercomputer facility of the Cornell Theory Center is also gratefully acknowledged.

References

Brenner, H., 1964, "The Stokes Resistance of an Arbitrary Particle—IV Arbitrary Fields of Flow," *Chemical Engineering Science*, Vol. 19, pp. 703–727.

Brenner, H. and Condiff, D. W., 1972, "Transport Mechanics in Systems of Orientable Particles—III. Arbitrary Particles," *Journal of Colloid and Interface Science*, Vol. 41, pp. 228–274.

Fan, F.-G. and Ahmadi, G., 1990, "Dispersion of Nonspherical Particles in a Simulated Isotropic Turbulent Field," *Bulletin of the American Physical Society*, Vol. 35, No. 10, p. 2271.

Gallily, I. and Cohen, A.-H., 1979, "On the Orderly Nature of the Motion of Nonspherical Aerosol Particles II. Inertial Collision Between a Spherical Large Droplet and an Axially Symmetrical Elongated Particle." *Journal of Colloid and Interface Science*, Vol. 68, pp. 338–356.

Gradon, L., Grzybowski, P. and Pilacinski, W., 1989, "Analysis of Motion and Deposition of Fibrous Particles on a Single Filter Element," *Chemical Engineering Science*, Vol. 43, pp. 1253–1259.

Goldstein, H., 1980, *Classical Mechanics 2nd Ed.*, Addison-Wesley Publishing Co., Reading, MA.

Hinze, J. O., 1975, *Turbulence 2nd Ed.*, McGraw-Hill, New York.

Hughes, P. C., 1986, "Spacecraft Attitude Dynamics", John Wiley and Sons, New York, NY.

Jeffery, G. B., 1922, "The Motion of Ellipsoidal Particles Immersed in a Viscous Fluid", *Proceeding of Royal Society of London*, Series A, Vol. 102, pp. 161–179.

Kraichnan, R. H., 1970, "Diffusion by Random Velocity Field", Physics of Fluids, Vol. 11, pp. 22–31.

Lumley, J. L., 1957, "Some Problem Connected with the Motion of Small

Particles in Turbulent Fluid," Ph.D. Thesis, The Johns Hopkins University, Baltimore.

Lundgren, T. S., 1969, "Model Equation for Nonhomogeneous Turbulence," *Physics of Fluids*, Vol. 12, pp. 485–497.

Maxey, M. R. 1987, "The Gravitational Settling of Aerosol Particles in Homogeneous Turbulence and Random Flow Fields," *Journal of Fluid Mechanics*, Vol. 174, pp. 441–465.

Maxey, M. R. 1990, "On the Advection of Spherical and Non-Spherical Particles in a Non-uniform flow," *Philosophical Transaction of Royal Society of London*, Series A, Vol. 333, pp. 289–307.

Mei, R., Adrian, R. J., and Hanratty, T. J., 1991, "Particle Dispersion in Isotropic Turbulence under Stokes Drag and Basset Force with Gravitational Settling," *Journal of Fluid Mechanics*, Vol. 225, pp. 481–495.

Ounis, H. and Ahmadi, G., 1989, "Motions of Small Rigid Spheres in a Simulated Random Velocity Field," *ASCE Journal of Engineering Mechanics*, Vol. 115, pp. 2107–2121.

Ounis, H. and Ahmadi, G., 1990, "Analysis of Dispersion of Small Particles in a Random Field," ASME JOURNAL OF FLUIDS ENGINEERING, Vol. 112, pp. 114–120.

Reeks, M. W., 1977, "On Dispersion of Small Particles Suspended in an Isotropic Turbulent Field," *Journal of Fluid Mechanics*, Vol. 83, pp. 529–546.

Schamberger, M. R., Peters, J. E. and Leong, K. H., 1990, "Collection of Prolate Spheroidal Aerosol Particles by Charged Spherical Collectors," *Journal of Aerosol Science*, Vol. 21, pp. 539–554.

Snyder, W. H. and Lumley, J. L., 1971, "Some Measurements of Particle Velocity Autocorrelation Functions in a Turbulent Flow," *Journal of Fluid Mechanics*, Vol. 48, pp. 41–71.

Soo, S. L., 1967, *Fluid Dynamics of Multiphase Systems*, Blaisdell Publishing Co., Toronto.

Wells, M. R. and Stock, D. E., 1983, "The Effects of Crossing Trajectories on the Dispersion of Particles in a Turbulent Flow," *Journal of Fluid Mechanics*, Vol. 136, pp. 31–62.

Wang, L.-P., 1990, "On the Dispersion of Heavy Particles by Turbulent Motion," Ph.D. Thesis, Washington State University, Pullman, WA.

APPENDIX A

Simplified Model

In this Appendix, the crossing trajectory effect is neglected and a simplified model for analyzing the dispersion of ellipsoidal particles is formulated. Approximate analytical expressions for the mean-square fluctuation velocity, the velocity autocorrelation, and the relative diffusivities for ellipsoidal particles in an isotropic turbulence are derived. In order to develop the model, the $D^{*2}\hat{\mathbf{u}}^*$ term in Eq. (28), must first be estimated. It is assumed that

$$\frac{\partial^2 \hat{u}_i^*}{\partial \hat{x}_i^{*2}} = C_1 \hat{u}_i^* + C_2, \quad \text{(no sum on } i\text{)}. \tag{A.1}$$

The numerical coefficients were found to be $C_1 = -0.413$ and $C_2 = 0$ by the least mean square error estimate for an ensemble of simulated trajectories. Accordingly,

$$D^{*2}\hat{\mathbf{u}}^* = -0.413 a^{*2}(2 + \beta^2)\hat{\mathbf{u}}^*. \tag{A.2}$$

The estimate given by Eq. (A.1) was suggested by Lundgren (1969) in his closure of the probability density equation for fluid turbulence. This term corresponds to an extra drag which leads to an additional energy dissipation. The approximation used is consistent with the expected behavior.

Substituting Eq. (A.2) into Eq. (28) leads to,

$$\frac{d\mathbf{v}^*}{dt^*} = \frac{3}{4\pi\beta Sa^{*3}\mathrm{Re}_l}\hat{\mathbf{K}}^* \cdot [\mathbf{u}^* - \mathbf{v}^* - B\mathbf{u}^*], \tag{A.3}$$

where

$$B = 0.0688 a^{*2}(2 + \beta^2), \tag{A.4}$$

and the nondimensionalized form of Eq. (14), $\hat{\mathbf{K}}^* = \mathbf{A}^{-1} \cdot \hat{\mathbf{K}}^* \cdot \mathbf{A}$, is used.

For an isotropic turbulent flow field, it is expected that all orientations be equally probable. Since Euler angles are independent variables, the probability that the orientation of the ellipsoid lies between θ_1 and $\theta_1 + d\theta_1$, θ_2 and $\theta_2 + d\theta_2$, and θ_3 and $\theta_3 + d\theta_3$ is given as

$$p(\theta_1, \theta_2, \theta_3)d\theta_1 d\theta_2 d\theta_3 = \frac{1}{8\pi^2}\sin\theta_2 \, d\theta_1 d\theta_2 d\theta_3, \tag{A.5}$$

where $p(\theta_1, \theta_2, \theta_3)$ is the probability density function and the coefficient $1/8\pi^2$ is required by the normalization condition

$$\int_{\theta_3=0}^{2\pi}\int_{\theta_1=0}^{2\pi}\int_{\theta_2=0}^{\pi} p(\theta_1, \theta_2, \theta_3)d\theta_2 d\theta_1 d\theta_3 = 1. \tag{A.6}$$

An equivalent translation matrix $\mathbf{K}^*_{equ}$ may be defined as the expected value of the translation matrix $\hat{\mathbf{K}}^*$. Using Eq. (A.5), after some straightforward integrations, it follows that

$$\mathbf{K}^*_{equ} = \langle\hat{\mathbf{K}}^*\rangle = \frac{1}{3}(k^*_{\hat{x}\hat{x}} + k^*_{\hat{y}\hat{y}} + k^*_{\hat{z}\hat{z}})\mathbf{I}, \tag{A.7}$$

where $\mathbf{I}$ is the identity matrix, $k^*_{\hat{m}\hat{n}} = k_{\hat{m}\hat{n}}/l_0$, and a pair of angular brackets '$\langle\,\rangle$' stands for the expected value. Using the equivalent translation matrix $\mathbf{K}^*_{equ}$ in Eq. (A.3) to approximate the original translation matrix $\hat{\mathbf{K}}^*$, the translation equation of motion is given as

$$\frac{d\mathbf{v}^*}{dt^*} = \frac{1}{\tau^*}(\mathbf{u}^* - \mathbf{v}^* - B\mathbf{u}^*). \tag{A.8}$$

Here,

$$\tau^* = \frac{4\pi\beta Sa^{*3}\mathrm{Re}_l}{k^*_{\hat{x}\hat{x}} + k^*_{\hat{y}\hat{y}} + k^*_{\hat{z}\hat{z}}}, \tag{A.9}$$

is defined as the effective nondimensional particle relaxation time.

In their analysis of Brownian diffusion of nonspherical particles, Brenner and Condiff (1972) used the orientation-averaged mobility matrix instead of the translation matrix, i.e., $\mathbf{K}^*_{equ} = \langle\hat{\mathbf{M}}^*\rangle^{-1}$ where $\hat{\mathbf{M}}^*$ is the inverse of $\hat{\mathbf{K}}$. The corresponding effective nondimensional particle relaxation time then becomes

$$\tau^* = \frac{4}{9}\pi\beta Sa^{*3}\mathrm{Re}_l\left(\frac{1}{k^*_{\hat{x}\hat{x}}} + \frac{1}{k^*_{\hat{y}\hat{y}}} + \frac{1}{k^*_{\hat{z}\hat{z}}}\right). \tag{A.10}$$

The Fourier transform of Eq. (A.8) leads to,

$$\overline{\mathbf{v}^*} = \frac{(1 - B)}{1 + i\omega\tau^*}\overline{\mathbf{u}^*}, \tag{A.11}$$

where $i = \sqrt{-1}$ and a bar on the top of a letter denotes a Fourier transform. Equation (A.11) relates the particle velocity to the fluid velocity in the frequency domain. The power spectrum tensor of particle velocity is then given by,

$$\mathbf{S}_{\mathbf{v}^*\mathbf{v}^*}(\omega) = \frac{(1 - B)^2}{1 + \omega^2\tau^{*2}}\mathbf{S}_{\mathbf{u}^*\mathbf{u}^*}(\omega), \tag{A.12}$$

where $\mathbf{S}_{\mathbf{u}^*\mathbf{u}^*}(\omega)$ is the Lagrangian power spectrum tensor of fluid velocity as is seen by the particle.

The particle velocity autocorrelation function is given as,

$$\mathbf{R}_{\mathbf{v}^*\mathbf{v}^*}(t'^*) = \langle\mathbf{v}^*(t^*) \otimes \mathbf{v}^*(t^* + t'^*)\rangle = \int_0^\infty \mathbf{S}_{\mathbf{v}^*\mathbf{v}^*}(\omega)\cos\omega t'^* \, d\omega, \tag{A.13}$$

and the mean-square particle velocity is $\mathbf{R}_{\mathbf{v}^*\mathbf{v}^*}(0)$. The particle turbulent diffusivity tensor is defined by Eq. (35). Using the definition of Fourier transform and the eveness of autocorrelation function, Eq. (35) leads to,

$$\mathbf{D}^p = \frac{\pi}{2}\mathbf{S}_{\mathbf{v}^*\mathbf{v}^*}(0). \tag{A.14}$$

As mentioned before, $D^p_{\hat{x}\hat{x}} = D^p_{\hat{y}\hat{y}} = D^p_{\hat{z}\hat{z}} = D^p$ for an isotropic field, and other elements of the diffusivity tensor are identically zeros. Using Eq. (A.12) in Eq. (A.14), the relative par-

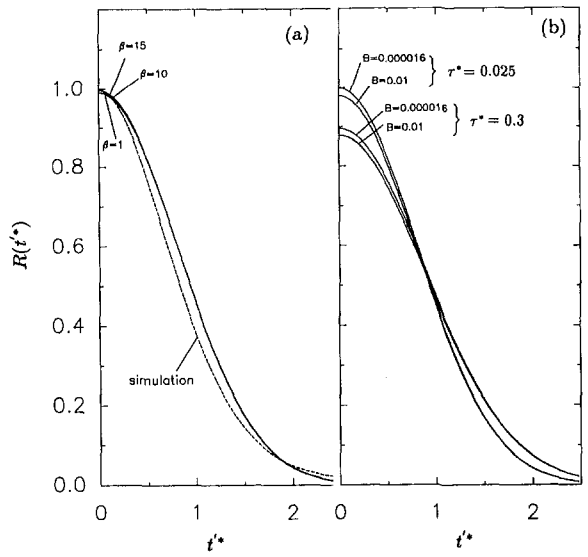

Fig. A1 Variations of particle velocity autocorrelations for various aspect ratios, relaxation times, and parameter *B*

ticle mass diffusivity becomes,

$$\frac{D^p}{D^f} = [1 - 0.0688a^{*2}(2 + \beta^2)]^2, \qquad (A.15)$$

where D^f stands for the diffusivity of fluid particles.

Although the Lagrangian and the Eulerian spectra are generally different, a completely satisfactory method for relating the two is not available (Lumley, 1957). Progress in estimating the Lagrangian spectra as seen by a relatively large spherical particle was recently reported by Wang (1990). However, even a rough estimate of the fluid Lagrangian spectra for ellipsoidal particles is not available. The data of Snyder and Lumley (1971) for small particles showed that the corresponding autocorrelations are indistinguishable within the experimental scatter. Here it is assumed that the particles are sufficiently small so that the Lagrangian fluid velocity spectrum as it is seen by the particles is approximately equal to the Eulerian spectrum. From Eq. (26), it follows that

$$\mathbf{S}_{u^*u^*}(\omega) = \frac{2}{\pi} e^{-\omega^2/\pi} \mathbf{I}. \qquad (A.16)$$

Equation (A.16) provides an approximate expression for the Lagrangian fluid velocity spectrum.

Simplified Model Prediction

In this section, the correlation functions as evaluated from the simplified model are presented. The effective particle relaxation time as given by Eq. (A.9) is used in these calculations.

For particles with a fixed nondimensional volume of 1.414×10^{-7} and different aspect ratios, the particle velocity autocorrelations as given by Eq. (A.13) are shown in Fig. A1(*a*). The corresponding simulated autocorrelation for $\beta = 10$ (also averaged for the three directions, $R(t'^*) = (1/3)[R_{xx}(t'^*) + R_{yy}(t'^*) + R_{zz}(t'^*)]$) as obtained from an ensemble of 500 samples is shown by the dashed line in this figure for comparison. It is observed that the aspect ratio β has no significant effect. It is also observed that the analytical model predicts the amplitude of the autocorrelation function near $t'^* = 0$ with a reasonable accuracy; however, it slightly overestimates the simulated autocorrelation function for $0.3 < t'^* < 2$.

Figure A1(*b*) compares the particle translational velocity autocorrelation functions for various particle relaxation time and different values of parameter B. It is observed that as the particle relaxation time increases, the mean-square particle velocity decreases, while the amplitude of $R(t'^*)$ for $t'^* > 1$ increases. Variations of parameter B has only a slight effect on the autocorrelation function.

Effect of Hydrofoil Planform on Tip Vortex Roll-Up and Cavitation

D. H. Fruman
Groupe Phénomènes d'Interface, ENSTA,
91120 Palaiseau,
France

P. Cerrutti

T. Pichon

Laboratoire d'Hydrodynamique,
Ecole Navale,
29240 Brest Naval,
France

P. Dupont
Institüt de Machines Hydrauliques et de
Mécanique des Fluides, EPFL,
CH-1007 Lausanne,
Switzerland

The effect of the planform of hydrofoils on tip vortex roll-up and cavitation has been investigated by testing three foils having the same NACA 16020 cross section but different shapes. One foil has an elliptical shape while the other two are shaped like quarters of ellipses; one with a straight leading edge and the other with a straight trailing edge. Experiments were conducted in the ENSTA, Ecole Navale and IMHEF cavitation tunnels with homologous foils of different sizes to investigate Reynolds number effects. Hydrodynamic forces as well as cavitation inception and desinence performance were measured as a function of Reynolds number and foil incidence angle. Laser Doppler measurements of the tangential and axial velocity profiles in the region immediately downstream of the tip were also performed. At equal incidence angle and Reynolds number, the three foils show different critical cavitation conditions and the maximum tangential velocity near the tip increases as the hydrofoil tip is moved from a forward to a rear position. However, the velocity profiles become more similar with increasing downstream distance, and at downstream distances greater than one chord aft of the tip, the differences between the foils disappear. The rate of tip vortex roll-up is much faster for the straight leading edge than for the straight trailing edge foil and, in the latter case, a significant portion of the roll-up occurs along the foil curved leading edge. The minimum of the pressure coefficient on the axis of the vortex was estimated from the velocity measurements and correlated with the desinent cavitation number for the largest free stream velocities. The correlation of data is very satisfactory. At the highest Reynolds number tested and at equal lift coefficients, the straight leading edge foil displays the most favorable cavitation desinent numbers.

Introduction

On a finite span wing, the pressure gradient in the region near the tip leads to a transverse flow which winds around the tip to form a vortex. Downstream of the tip, the vortex is continuously fed by the roll-up of the vortex sheet issued from the trailing edge of the wing. Depending on the roll-up process, the pressure on the vortex axis may decrease below the vapor pressure of the flowing liquid and cause cavitation to occur along the vortex path. Prediction of tip vortex cavitation (TVC) conditions has been the aim of numerous contributions, starting from the leading paper by McCormick (1962). A short review of recent investigations has been given by Fruman et al. (1992b) in the introduction of a paper devoted to analyze the effect of Reynolds number on cavitation occurrence. Recently, Pauchet et al. (1993) have shown that, at equal incidence angle and Reynolds number, a large change of the critical cavitation number is caused by the modification of the cross section of a wing with identical elliptical planforms. This finding is analogous to the one reported by Arndt and Dugúe (1992) for other cross sections of elliptical foils. The cause of the modification of the cavitation conditions are traced to viscous effects leading to a modification of the lift which affects the bound circulation at mid-span, the boundary layer thickness and the tip vortex core radius. The results of Pauchet et al. (1993) have demonstrated that, for the same foil planform, the modification of the cavitation conditions is only due to the change of the lift acting on the foil.

Much interest has been devoted to the investigation of the effect of the modification of the planform, and in particular of the tip local geometry, on the hydrodynamic characteristics of wings. For example, van Dam (1987) has been interested in the changes of the induced drag associated with shape changes of a family of wings of equal chord versus span distribution. Other works have concentrated on helicopter blade performance and tip vortex characteristics as a result of tip geometry changes (Spivey (1968)). Crimi (1970) was interested on the effect of modifying the sweep angle of a trapezoidal wing on attached cavitation, but no information concerning tip vortex cavitation is given.

It seems natural to think that the change of the planform will affect the initiation and development of the tip vortex and, thus, have a significant impact on the critical cavitation con-

Contributed by the Fluids Engineering Division for publication in the JOURNAL OF FLUIDS ENGINEERING. Manuscript received by the Fluids Engineering Division July 27, 1993; revised manuscript received May 11, 1994. Associate Technical Editor: M. Gharib.

ditions. McCormick (1962) investigated the tip vortex cavitation behaviour of elliptical and rectangular foils having the same area ratio and cross section. However, the local tip geometry is very different between an elliptical foil having a cross section of variable thickness, but constant relative thickness-to-chord ratio, and a rectangular foil with a constant thickness. In the latter case, the roll-up is very much affected by the geometry selected to join the lower and upper surfaces of the foil at the tip chord.

To contribute to the understanding of this complex problem, a research program involving several institutions has been recently conducted to investigate tip vortex roll-up characteristics and cavitation conditions of three untwisted foils having the same chord distribution along the span and the same cross section, NACA 16020, but different planforms. On potential flow grounds (lifting line theory), the load distribution and lift must remain identical for the three foils.

The rationale developed by Fruman et al. (1991, 1992a) and Pauchet et al. (1993) to investigate the effect of Reynolds number and cross section has been used in the present work. It comprises the measurement of the hydrodynamic forces acting on the foils and of the tangential velocity profiles at different stations along the vortex path and the determination of the critical cavitation conditions. Through the analysis of the velocity profiles, the local vortex intensity and the characteristic dimension of the viscous core region are estimated for positions along the vortex path and, in particular, in the very near region comprised between the tip and less than a maximum chord downstream. The local vortex intensity is then compared to the hydrofoil bound circulation at mid-span computed using the lift measurements and the viscous core dimension is compared to the thickness of the turbulent boundary layer on a flat plate of length equal to the maximum chord. Using these data and the tangential velocity distribution, the pressure coefficient on the vortex axis is estimated and its minimum compared to the desinent cavitation number. This procedure allows the critical cavitation conditions to be clearly related to the vortex roll-up.

Experimental Facilities

Experiments were conducted in three cavitation tunnels, whose geometry and operating conditions are given later, using three hydrofoils of area ratio 3.8, having the same chord distribution along the span and identical NACA 16020 cross section, but different shapes: one has an elliptical shape (E) and the other two are shaped like a quarter of an ellipse; one with a straight trailing edge (STE) and the other with a straight leading edge (SLE). Table 1 summarizes the size of the foils, scaled according to the test section dimensions of the tunnels, and the Reynolds number range, which extends from 10^5 to 2.4×10^6 and overlaps from one facility to the other.

The ENSTA cavitation tunnel (ECT) test section is 150 mm high and 80 mm wide. Lift and drag measurements were performed using a hydrodynamic balance. The LDV system operated in the back scatter mode using a 150 mW nominal laser, TSI fiber optics and an Intelligent Flow Analyser 550. For the optical arrangement chosen, the measuring volume was about 0.2 mm long. The displacement of the optics was controlled with step widths as small as 20 μm. The data rate was increased by seeding the water with Iriodine. The tangential velocity components of the tip vortex were measured for two incidence angles, 10.6 and 6 deg, and a Reynolds number, Re, of 3.6×10^5, at fourteen stations between the tip and 10 maximum chords downstream. Ten of these stations were between the tip and one maximum chord.

Table 1 Dimensions of the foils and Reynolds number range

Facility	Maximum chord [mm]	Half-span [mm]	Minimum Reynolds number	Maximum Reynolds number
ENSTA	40	60	10^5	5×10^5
EN	80	120	2.4×10^5	1.2×10^6
IMHEF	60	90	6×10^5	2.4×10^6

The Ecole Navale cavitation tunnel (ENCT) has a square test section 192 mm × 192 mm. Lift and drag forces were also measured using a hydrodynamic balance. A Dantec two-component LDV system, providing a measuring volume 0.5 mm long and coupled to two Dantec enhanced Burst Spectrum Analysers and Dantec Burstware software, was used to measure the axial and tangential components of the tip vortex velocity at eleven stations between the tip and one chord downstream, and several others farther downstream (up to 3.5 chords). The velocity profiles were obtained for 6 and 10 deg incidence angles and Reynolds numbers of 1.2×10^6 and 1.08×10^6, respectively.

The IMHEF cavitation tunnel (ICT) also has a square test section 150 mm × 150 mm. Hydrodynamic coefficients were measured using a strain gauge balance but no velocity profiles were performed in this facility.

Measurement Procedures

Tip vortex cavitation inception and desinence were obtained from direct visual observation. In all cavitation tunnels, visualization was improved using stroboscopic lighting. Tests were conducted using either a constant cavitation number or a constant angle procedure. In the first one, the free-stream velocity and test section pressure were kept constant while the incidence angle was varied until cavitation onset occurred. The incidence was then increased slightly to form a well-developed tip vortex cavity, in the shape of a continuous filament, and desinence conditions were obtained by reducing the angle. In the second procedure, specially adapted to investigate the effect of Reynolds number and susceptibility pressure in the tunnel, velocity and incidence angle were set and the pressure was varied until incipient and desinent conditions were reached.

The hydrodynamic zero incidence angle was defined as the zero lift position. This position was determined during the calibration of the balance and used as a reference afterwards.

The foils were mounted horizontally in the three cavitation tunnels. The spanwise direction coincides with the y axis and x is the streamwise direction. The origin of x is at the tip of

Nomenclature

a = distance from the vortex axis to the point of maximum tangential velocity
c_{max} = maximum chord
C_l = lift coefficient
C_P = pressure coefficient on the vortex axis
C_{Pmin} = minimum pressure coefficient on the vortex axis
P_∞ = pressure of the unperturbed flow
P_0 = pressure on the vortex axis
P_s = susceptibility pressure
P_v = vapor pressure
Re = Reynolds number based on maximum chord
y = distance from the vortex axis
V_∞ = free stream velocity
V_a = axial velocity
V_t = tangential velocity
α = incidence angle
δ = boundary layer thickness
Γ = tip vortex intensity
ν = liquid kinematic viscosity
ρ = liquid specific mass
σ_d = desinent cavitation number
σ_s = susceptibility cavitation number

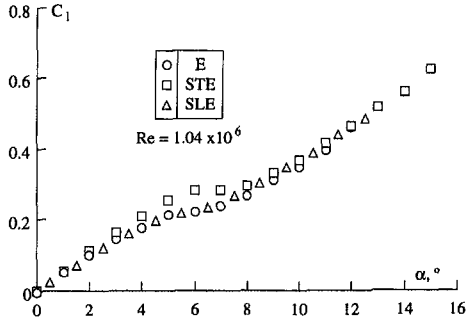

Fig. 1 Comparison of the lift coefficient versus incidence angle results for the three foils at Re = 1.04 × 10^6

the foil. The origin of y is at the vortex axis for each x position.

One of the major problems associated with the LDV measurements is to be sure that the measuring volume coincides with the centre of the vortex. This was done by making the point of crossing of the laser beams to coincide with the cavities convected in the vortex path for a cavitation number slightly below critical. Then, the vertical velocity component on a vertical axis (z direction) was determined for a short distance on both sides of this position in noncavitating conditions. The center of the extrema of the velocities corresponds, then, to the effective location of the vortex axis.

Results

Hydrodynamic Forces. Lift and drag results for the elliptical foil have been presented already by Fruman et al. (1992b). The lift coefficient increases linearly for incidence angles up to about 6 deg, reaches an intermediate (plateau) region with a lower slope, and then continues to grow with a slope close to the one for low incidence angles. This behavior is analogous to the one determined for a variety of two-dimensional NACA 16 foils tested at Reynolds numbers comprised between 0.85 and 2.0 × 10^6 by Lindsey et al. (1948). These authors also show that the slope at the origin decreases significantly and the extent of the plateau region increases when the thickness-to-chord ratio increases. For example, for a 21 percent thickness-to-chord ratio, the slope at the origin is only 4.63, 22 percent below the theoretical value of 2π achieved practically for a thickness-to-chord ratio of 9 percent. The slope at the origin for the elliptical foil of area ratio 3.8 is reported by Fruman et al. (1992b) to be a strong function of the Reynolds number, varying from 5.45 for Re = 2.5 × 10^5 to only 2.75 for Re = 1.2 × 10^6. These values are well below the one estimated from the lifting line theory and account for the significant effect of Reynolds numbers on the two-dimensional lift versus incidence angle slopes. The lift coefficient decreases more or less rapidly, depending on the angle of attack, when the Reynolds number increases and reaches a nearly constant value for Re > 1.5 × 10^6.

When the planform is altered without modifying the load distribution and the cross section, the lift coefficient follows the same general behavior but the absolute values are changed depending on the Reynolds number and the planform. For 10 deg incidence angle, for example, C_l decreases from 0.72 for the STE foil and 0.58 for the SLE foil at Re = 0.25 × 10^6 to nearly 0.38 for the two wings at Re = 2.1 × 10^6 (fully turbulent flow conditions). For Reynolds number larger than 0.5 × 10^6, however, there is no distinguishable difference between the three foils besides the plateau region comprised between 5 and 8 deg (see Fig. 1). Since the measurements demonstrated that the foils behave, to a good degree of accuracy, as symmetrical, all subsequent measurements were only limited to

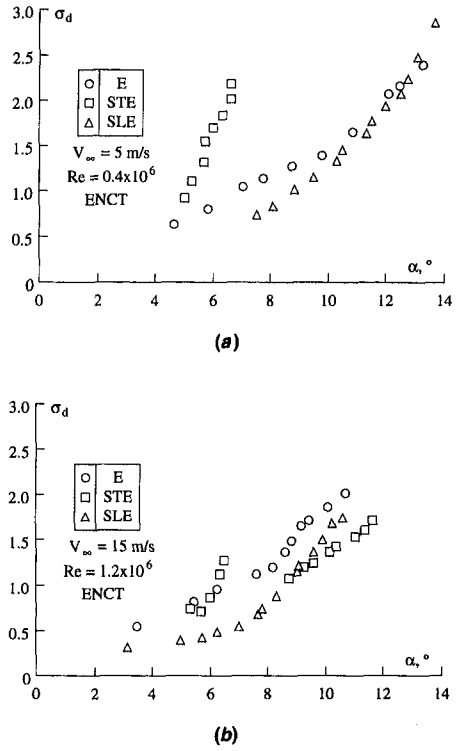

Fig. 2 Desinent cavitation number as a function of incidence angle for tests performed in the ENCT. (*a*) V_∞ = 5 m/s, Re = 0.4 × 10^6, (*b*) V_∞ = 15 m/s, Re = 1.2 × 10^6

positive incidence angles. The results obtained in the three cavitation tunnels are in general agreement.

Cavitation Numbers. The cavitation number is defined as usual by:

$$\sigma = \frac{P_\infty - P_v}{\frac{1}{2}\rho V_\infty^2}$$

where P_v is the vapor pressure and ρ the specific mass of the flowing water.

Figures 2(a) and 2(b) show, for tests conducted in the ENCT, the desinent cavitation number, σ_d, as a function of incidence angle for Re = 0.4 and 1.2 × 10^6. For the elliptical and straight leading edge foils, σ_d increases monotonically with incidence angle, and σ_d is larger for the E foil than for the SLE wing, especially for the highest Reynolds number. The behavior of the STE hydrofoil is completely different. For Re = 0.4 × 10^6, the σ_d increases more rapidly than for the two other foils but, and this is a rather unexpected behaviour, TVC occurs only over a very limited incidence angle range, comprised between 5 and 7 degrees. If the incidence angle increases, for constant velocity and pressure in the test section, there is no way of achieving TVC because a long leading edge sheet cavitation suddenly appears before TVC inception. Vapour bubbles shed by the leading edge cavity are captured within a very diffused vortex core. Therefore, when reducing the angle of attack to detect TVC desinence, there is no way to start from a well-defined vapor filament in the vortex core, as for the tests with the other planforms. These unusual results were repeated during the tests in the ECT for the same Reynolds number, Fig. 3.

For the STE foil at the larger Reynolds number, three distinct regions can be defined depending on the incidence angle. For 4.5 < α < 6.5 deg, the behaviour is analogous to the previous one; for α > 9 deg, the σ_d values are lower than for the other two foils, and for 6.5 < α < 9 deg, there is again

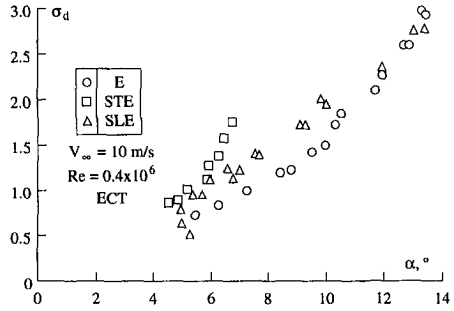

Fig. 3 Desinent cavitation number as a function of incidence angle for tests performed in the ECT (V_∞ = 10 m/s, Re = 0.4 × 10^6)

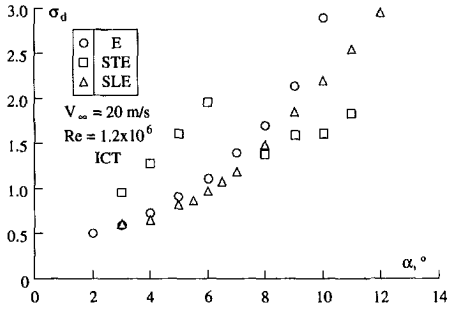

Fig. 4 Desinent cavitation number as a function of incidence angle for tests performed in the ICT (with nuclei injection) (V_∞ = 20 m/s, Re = 1.2 × 10^6)

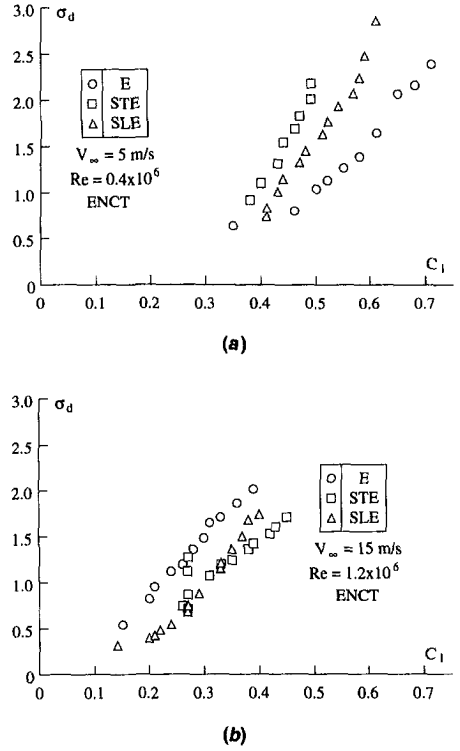

Fig. 5 Desinent cavitation number as a function of lift coefficient for tests performed in the ENCT. (*a*) V_∞ = 5 m/s, Re = 0.4 × 10^6, (*b*) V_∞ = 15 m/s, Re = 1.2 × 10^6

no way to achieve TVC. This complex behaviour is fully confirmed by the tests conducted in the ICT with nuclei injection at equal Reynolds numbers, Fig. 4, although the first region extends to lower angles and the σ_d values are significantly larger.

For incidence angles larger than 9 deg, visual observation of the inception and desinence process of the STE foil has shown a very short cavitating "bubble" situated on the suction side and slightly upstream of the tip that feeds the tip vortex. This is not a pure tip vortex cavitation process even if the disappearance of both the bubble and the fed vortex occur simultaneously. For incidence angles below 7 deg with the STE foil and for all incidence angles with the E and SLE foils, there is no difference in behaviour; cavitation always occurs first in the trailing vortex.

The σ_d values of Figs. 2(*a*) and 2(*b*) are plotted in Figs. 5(*a*) and 5(*b*) as a function of the lift coefficient. For the lowest velocity, at equal lift coefficient, cavitation occurs first for the STE foil, followed by the SLE and the *E* foil. For the largest velocity the trend is reversed. Cavitation occurs first for the *E* foil and then for the STE and the SLE foils, although the latter two are close together. The change in behaviour from low to high free stream velocity does not seem to be related to a Reynolds number effect but, as it will be discussed later, it can be associated to the water quality.

Velocity Measurements

Tangential Velocities. The tangential velocity profiles for elliptical foils have been thoroughly documented in previous papers, Fruman et al., (1991, 1992a, 1992b). The profiles measured at the tip of the foils have shown that a significant portion of the roll-up has already occurred and that the initiation of the viscous, solid body rotation region has taken place. Moving downstream, both the solid body rotation and the potential vortex regions extend radially on the outboard side while the wake effect, significant in the near region, fades away on the inboard side. Farther downstream (several mid-span chords) the profiles become symmetrical indicating the completion of the roll-up.

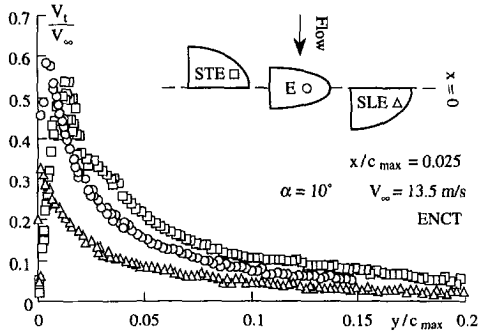

Fig. 6 Nondimensional tangential velocity as a function of the nondimensional distance to the vortex axis at x/c_{max} = 0.025 downstream the tip of the foils (ENCT)

The modification of the planform causes a strong modification of the tangential velocity profiles; in particular in the very near region (less than a maximum chord). Figure 6 shows the velocity profiles in the outboard region measured at x/c_{max} = 0.025, α = 10 deg, V_∞ = 13.5 m/s (Re = 1.08 × 10^6) in the ENCT. There is a very clear indication that the tangential velocities increase when the tip of the wing moves from a forward to an aft position. This is accompanied by an increase of the diameter of the viscous core.

However, for the STE foil the velocities are, near the maximum, smaller than expected from the ECT results. For an incidence angle of 6 deg, the maximum tangential velocities always increase when the tip moves from an aft to a rear position.

The STE foil offers, as opposed to the *E* and SLE foils, the possibility of determining the velocity distribution across the whole vortex starting from the tip. From this point of view, the results shown in Fig. 7 for tests conducted in the ECT with the STE foil at 10.6 and 6 deg incidence are rather unique and have not been presented before in the open literature. For both

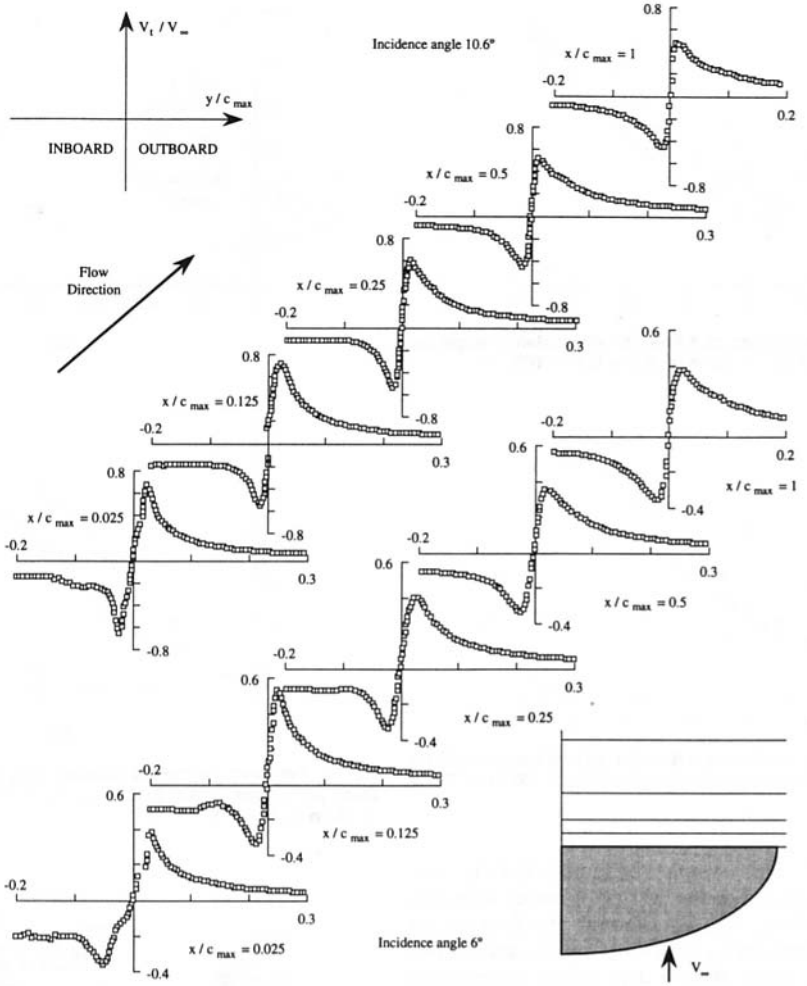

Fig. 7 Nondimensional tangential velocity as a function of distance to the vortex axis for different axial stations for the STE foil (ECT data for V_∞ = 9 m/s, α = 6 and 10.6 deg)

angles, the nondimensional tangential velocity has a maximum in the region very near the tip, at 0.125 mid-span chord, and decreases slowly with distance. At one chord downstream the velocity profiles are very much symmetrical regardless of the incidence angle. It should be noticed also that even for very short distance from the tip the absolute values of the maximum and minimum velocities are quite close. This result differs from those obtained with the elliptical (Fruman et al., 1992b) and with the straight leading edge foils. The reason can be traced to the fact that in these two foils there is a significant influence of the wing surface on the inboard velocities while for the STE foil this effect fades away more rapidly.

Axial Velocities. The axial velocity profiles show that the effect of the vortex is confined to a very limited region, of the size of and centered with the viscous core. Both a jet and a wake behaviour, already documented in the literature (Green and Acosta, 1991; Arndt and Keller, 1992; Fruman et al., 1992b; Pauchet et al., 1993), can exist depending on the wing shape and Reynolds number.

The major differences are limited to a very short distance since, for $x/c_{max} > 0.75$, all velocities tend to collapse into the free stream velocity, taking into account the scattering of the results. The E and SLE foils show a jet behaviour with a maximum velocity exceeding the free stream velocity by 30 percent. For the STE foil a very marked wake behaviour occurs with a velocity defect of up to 75 percent. It should be recalled that for the elliptical foil at high Reynolds numbers, $\approx 5 \times 10^6$, the jet behavior extends to very large distances downstream ($\approx 4c_{max}$) and shows excess velocities of up to 70 percent, (Fruman et al., 1992b). Pauchet et al. (1993) have shown that much larger peak velocities occur at the same Reynolds number if the cross section is a NACA 0020 instead of a NACA 16020.

Discussion

Desinent Cavitation Numbers. To take into account the influence of water quality, which Billet and Holl (1979) have mentioned to be an important factor in tip vortex cavitation, tests were performed in the ENCT with the elliptical foil at constant incidence angle and varying velocities and pressures to construct the results shown in Fig. 8. Because it is now rather well established (see Billet and Holl, 1979; Fruman et al., 1991, 1992a, 1992b, Arndt and Dugué, 1992) that the minimum pressure on the vortex axis, and hence the critical cavitation number, scales as the inverse of the square of the foil boundary layer thickness (not the inverse of the boundary layer thickness as in McCormick, 1962), the critical cavitation numbers should be proportional to the Reynolds number to the power 0.4 for fully turbulent boundary layers. Thus the reference, i.e., test section, pressure plotted as a function of $1/2\ \rho\ V_\infty^2\ \mathrm{Re}^{0.4}$ should be a straight line for each incidence angle and the intercept with the vertical axis should give an estimate of the susceptibility pressure, p_s, in the cavitation tunnel. The susceptibility pressure is larger than the vapor pressure since the mean of the three intercepts in Fig. 8 is equal to 7720 Pa.

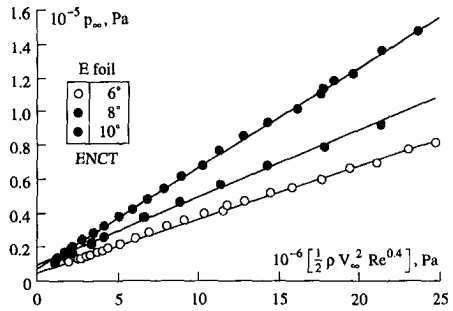

Fig. 8 Reference pressure for desinent cavitation as a function of the dynamic condition for the E foil. Tests in the ENCT

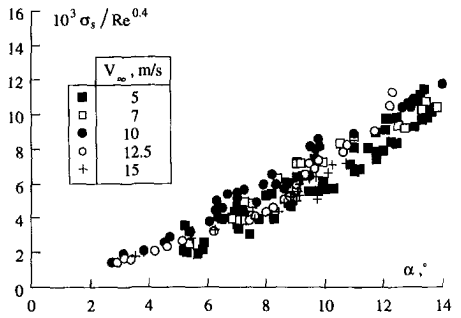

Fig. 9 Susceptibility cavitation number as a function of incidence angle for the E foil. Tests in the ENCT

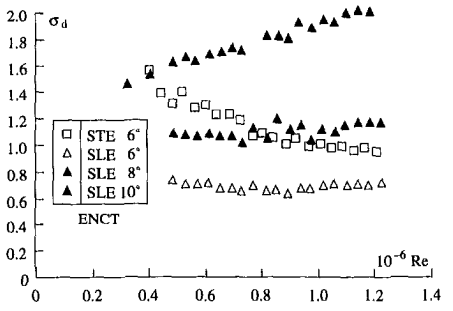

Fig. 10 Desinent cavitation number as a function of Reynolds number at constant incidence angle for tests performed in the ENCT

The slope of the straight lines in Fig. 8 is equal to $\sigma_s/Re^{0.4}$, where σ_s is a cavitation number computed using the susceptibility pressure instead of the vapor pressure. For the elliptical foil tested in the ENCT and for a very large range of free stream velocities and $0.4 \times 10^6 < Re < 1.2 \times 10^6$, the values of $\sigma_s/Re^{0.4}$, are plotted in Fig. 9 as a function of the incidence angle. As compared to a plot of $\sigma_d/Re^{0.4}$ the correlation of the data is slightly improved since a linear regression fit gives a correlation coefficient of 0,91 for σ_s instead of 0,88 for σ_d.

In Fig. 10, the σ_d results obtained in the ENCT are plotted for the STE foil at 6 deg incidence and for the SLE foil at 6, 8, and 10 deg incidence. For the STE foil, the ECT results are, at comparable Reynolds numbers smaller than in the ENCT. For increasing Reynolds number and constant incidence angle, 6 deg, the σ_d values do not change significantly for the SLE foil while they decrease substantially for the STE foil. But the STE results at equal angle of attack always remain much larger than those of the SLE.

For the STE foil at 6 deg incidence, the susceptibility pressure determined as above is 19500 Pa and the mean for the SLE foil is 7470 Pa. Using these values, the data for the STE and SLE foils obtained in the ENCT are plotted in the form of σ_s as a function of the Reynolds number in Fig. 11. The

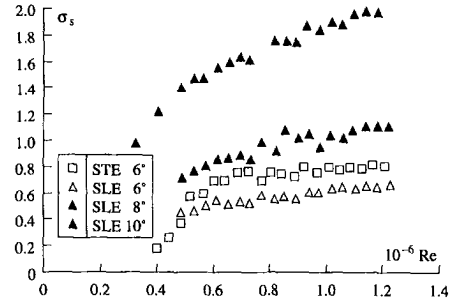

Fig. 11 Susceptibility cavitation number as a function of Reynolds number for the STE and SLE foils. Tests in the ENCT

somehow illogical results of Fig. 10 can be now interpreted. Indeed, there is no more decrease of σ_s with Re for the STE foil; at equal incidence angle, the STE foil gives σ_s larger than for the SLE foil as with σ_d, and, provided $Re > 0.5 \times 10^6$, the growth seems to be consistent with the already known behaviour for the E foil. It should be pointed out that for sufficiently large free stream velocities the contribution of the susceptibility pressure is negligible; then, the critical and the susceptibility cavitation numbers are nearly indistinguishable.

Tangential Velocities. There is no accepted procedure for estimating the local vortex intensity, Γ, from velocity measurements, especially in the very near region were roll-up is initiated and the tip vortex is highly three-dimensional. If a velocity vector plot is available in a plane normal to the free stream velocity it is possible to compute the circulation of the velocity vector on a closed path around the vortex center. However, depending on the size of the selected closed path, more or less of the vorticity shed by the wing will be accounted for as belonging to the tip vortex. This procedure requires the use of a three components LDV system or a Particle Displacement Velocimetry technique, Pogozelski et al. (1993), and has not been implemented as yet to investigate the roll-up in the very near region. Using the tangential velocities outboard of the foil on a line parallel to the span and passing through the vortex center, Fruman et al. (1991, 1992a, 1992b) had computed the angular momentum of the velocities, corrected for wall effects, and estimated the local intensity from the plateau reached outside the core. Comparison of the local intensity for the three different foils investigated in this work can be made since the same procedure was employed in the data reduction even if the absolute values are subject to caution because of the highly three-dimensional character of the vortex. Once the estimate of the local intensity is known, the local core radius, a, can be determined by fitting a Lamb velocity profile to the experimental velocity data outboard.

The local vortex intensity can be made non dimensional by using the mid-span bound circulation, Γ_0, computed from lift measurements,

$$\Gamma_0 = 1/2\, C_l\, V_\infty\, c_{max}$$

Figures 12(a) and 12(b) show the values obtained with the three planform hydrofoils as a function of the downstream distance to the tip for two incidence angles and Reynolds numbers. The order of magnitude of the vortex intensity and the growth rate with distance are consistent with previous results, Fruman et al. (1992a, 1992b), showing that the roll-up is only completed far from the foil tip, at a distance of about three chords downstream.

The vortex roll-up is, in all cases investigated, already well initiated at the tip as shown by the values of the local non-dimensional vortex intensity. For 10 deg incidence, the STE foil already shows 32 percent Γ_0 at the tip, while it decreases to 28 percent for the E foil and 15 percent for the SLE foil. The effect of sweep is even more pronounced in the ECT with

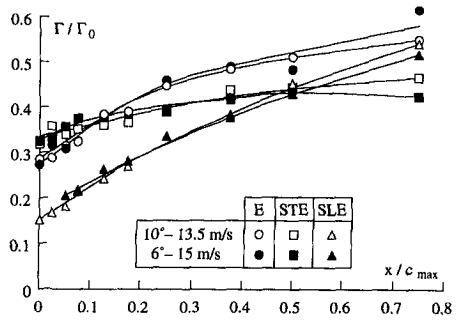

(a)

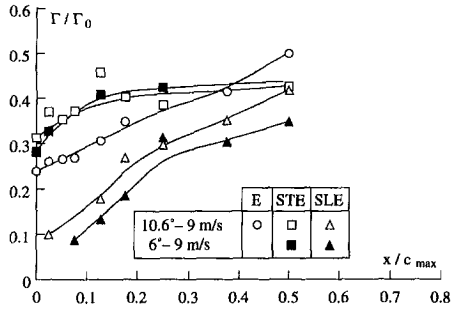

(b)

Fig. 12 Nondimensional local vortex intensity as a function of downstream distance in the ENCT (*a*) and ECT (*b*)

31, 24, and 10 percent at 10.6 deg incidence angle, respectively. Moving downstream, the local vortex intensity increases, as expected, by the continuation of the roll-up of the vortex sheet into the individualized and coherent tip vortex. The differences between vortices generated by different foil shapes shade away with distance to the tip.

It has been shown by Fruman et al. (1992a) that the thickness of the turbulent boundary layer of a flat plate of length equal to the maximum chord (Schlichting, 1979),

$$\delta = 0.37\, c_{\max}\left[\frac{\nu}{V_\infty c_{\max}}\right]^{0.2}$$

is an appropriate scale allowing to compare the dimension of the viscous core for a variety of foil sizes, free-stream velocities, and experimental facilities. A plot of a/δ for the present tests shows that the minimum of the core radius occurs at or in the immediate vicinity of the tip, depending on the planform of the foil. After the minimum, all the data but the one for the STE foil in the ENCT indicate the same growth tendency.

The evaluation of the pressure on the vortex axis by using the radial component of the momentum equation can only be conducted, as in most of the previous papers related to the subject (see Green 1991, Arndt et al., 1991, Stinebring et al. 1991), by neglecting the contribution of the radial velocity component. A recent paper (Pogozelski et al., 1993) has estimated the contribution of the radial and azimuthal gradient of the radial velocity to the total pressure drop at the core to be about 20 percent of all contributions, without specifying in what way the core pressure is altered. However, the axial gradient of the radial velocities, which can moderate the other contributions, has not been taken into account. We assume that, in spite of the three-dimensional tip vortex behavior in the near region and using the Lamb model, the pressure coefficient on the axis can be estimated by,

$$C_P = -0.044\left[\frac{\Gamma}{aV_\infty}\right]^2$$

Table 2 Comparison of the minimum pressure coefficient with desinent cavitation number

	E		STE		SLE	
	I	II	I	II	I	II
σ_d	0.83	1.6	1.03	1.36	0.48	1.6
$-C_{P\min}$	0.48	1.28	0.92	1.03	0.34	0.72

ENCT: (I) 6 deg and 15 m/s, (II) 10 deg and 13.5 m/s.

	E	STE		SLE	
	II	I	II	I	II
σ_d	1.8	1.27	—	1.05	1.95
$-C_{P\min}$	1.5	0.95	1.7	0.37	0.95

ECT: (I) 6 deg and 9 m/s, (II) 10.6 deg and 9 m/s.

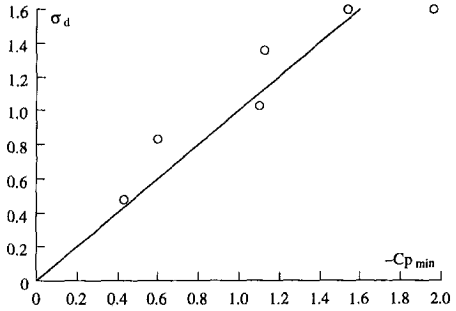

Fig. 13 Critical cavitation number as a function of the minimum pressure coefficient (with sign changed) computed by numerical integration of the values issued from the experimental tangential velocity profiles

or by numerically integrating the centrifugal contribution calculated with the experimental tangential velocities.

By replacing the values of Γ and a obtained experimentally, the minimum pressure coefficients on the axis are estimated. In Table 2, their values are compared with the measured desinent cavitation numbers for the same incidence angle and free stream velocity. As already mentioned, since the free stream velocities are large, comprised between 9 and 15 m/s, the contribution of the susceptibility pressure can be neglected.

The major differences are attached to the SLE foil. Indeed, if no account is taken of this foil, a linear regression of the six remaining data points gives a slope for σ_d versus $C_{P\min}$ of 1.17, a standard deviation of 0.10 and a correlation coefficient of 0.98. If the SLE foil is incorporated in the analysis, we obtain 1.11, 0.30 and 0.84, respectively. In any event, the previous findings by Fruman and co-workers leading to $\sigma_d \approx -C_{P\min}$ are fully confirmed. Taking into account the numerous manipulations necessary to obtain the estimates of $C_{P\min}$, the very varied experimental conditions and the accuracy of the velocity and cavitation results, the agreement between σ_d and $-C_{P\min}$ is truly remarkable. Indeed, the differences can be explained by the estimated contribution of the radial velocities to the radial momentum balance and/or the accuracy of the velocity measurements.

If the critical cavitation numbers obtained at the ENCT are now compared to the pressure coefficient obtained by numerically integrating the simplified radial equilibrium equation, the agreement is even better as it can be seen in Fig. 13. In any event, a 10 to 20 percent difference between the measured critical cavitation numbers and the estimated minimum pressure coefficients (with sign changed) is what can be expected from the data analysis procedure with no other extraneous contribution (i.e., axial velocity fluctuations) to the vortex core pressure.

Conclusion

An extensive investigation of the effect of hydrofoil planform on tip vortex roll-up and cavitation has been conducted

in three cavitation tunnels providing Reynolds numbers comprised between 2.5×10^5 and 2.4×10^6. The foils had the same cross section, NACA 16020; one has an elliptical planform and the others were like a quarter of an ellipse with a straight leading edge and a straight trailing edge. The cavitation test results show that:

(i) For large enough Reynolds numbers and moderate incidence angles, cavitation is slightly delayed for the straight leading edge foil as compared to the straight trailing edge and elliptical foils.
(ii) The cavitation behavior of the straight trailing edge foil is complex, showing the existence of three different regions; one, for very small incidence angles, where cavitation occurs much earlier than for the two other foils; one in which tip vortex cavitation cannot be achieved prior to extended leading edge cavitation and one where cavitation occurs first in a separation bubble on the upper surface of the foil slightly ahead of the tip.
(iii) For low Reynolds numbers (low test velocities), the correlation and the interpretation of the results is considerably improved if a susceptibility cavitation number, computed using a susceptibility pressure characterizing the nuclei population and air content, is used instead of the cavitation number based on vapour pressure.

The tangential velocity measurements in the near region, between the tip and a maximum chord downstream, show that:

(a) The evolution of the local vortex intensity and the local vortex core radius with distance along the vortex are comparable. However, the local vortex intensity at the tip increases when the tip moves from a forward to a rear position.
(b) The estimated minimum pressure coefficient at the vortex axis, computed numerically or analytically with the values of the local vortex intensity and the local vortex core radius (assuming an axisymmetric vortex in the near region), correlates very well with the desinent cavitation number of all foils but the straight leading edge.

As a general conclusion, it appears that a straight leading edge foil incurs a delay on the cavitation inception for the largest Reynolds numbers and moderate incidence angles. Tests conducted at much larger Reynolds numbers would demonstrate if forward sweep foils are of practical interest in marine applications where tip vortex cavitation is an important design parameter.

Experimental Uncertainties. The hydrodynamic balance is calibrated with standard weights which results in a precision of ± 0.5 percent on the lift force, issued from the average of 25 values for the same test condition, with an error of 2 minutes for the incidence angle. The free stream velocity uncertainty is in the range of ± 0.75 percent, hence the uncertainty associated with the lift coefficient is ± 2 percent maximum.

The uncertainty on the cavitation number results from the instrumental error on the measurement of the pressure (about ± 1.5 percent) and of the free stream velocity (± 0.75 percent). It can, thus, be estimated to be ± 3 percent. The accidental error is mainly associated with the visual appreciation of tip vortex cavitation inception and desinence. Measurements conducted by different manipulators in the ENCT at equal test conditions have shown a relative dispersion of ± 2.5 percent, lower than the estimated instrumental error.

The accuracy of the position of the LDV measuring volume is about 4 μm. The random uncertainty associated with the electronic and numerical traitement of the Doppler signal giving the instantaneous velocity is estimated to be less than ± 1.5 percent. For large enough samples, it can be expected that the error on the mean value is much less than 1.5 percent. The mean velocity values are based on 1000 to 2500 readings for each position. The uncertainty of the value of the pressure coefficient, computed by numerical integration of the simplified radial equilibrium equation, is about ± 4.5 percent due to uncertainty of the tangential velocity and of the free stream velocity. Moreover, the finite dimension of the measuring volume and the extent of the vortex wandering result on the underestimation of the tangential velocities, especially in the core region where curvature of the velocity profile is large. The additional effect of wandering and measuring volume size on the pressure coefficient has been estimated to be less than $+5$ percent (see Fruman et al., 1994).

Acknowledgments

The authors wish to express their deep appreciation for the continuous support of the Direction des Recherches, Etudes et Techniques (D.R.E.T.), Ministry of Defense, France, and, in particular, of Mrs Bourgeois-Gaffié, to the Action Concertée Cavitation (A.C.C.). The paper has benefitted from the comments and corrections of the reviewers and our colleague Scott Gowing. Our thanks go to Ms. J. Indeau for taking care of the illustrations.

References

Arndt, R. E. A., and Keller, A. P., 1991, Water Quality Effects on Cavitation Inception in a Trailing Vortex, *Cavitation 91*, ASME FED 116, pp. 1–8 and (1992). ASME JOURNAL OF FLUIDS ENGINEERING, 114, pp. 430–438.

Arndt, R. E. A., and Dugué, C., 1992, Recent Advances in Tip Vortex Cavitation Research, *International Symposium on Propulsors and Cavitation*, Hamburg, June.

Billet, M. L., and Holl, J. W., 1979, Scale Effects on Various Types of Limited Cavitation, *International Symposium on Cavitation Inception*, ASME Winter Annual Meeting, New York, pp. 11–23.

Crimi, 1970, Experimental Study of the Effects of Sweep on Hydrofoil Loading and Cavitation, *Journal of Hydronautics*, Vol. 4, pp. 3–9.

Fruman, D. H., Dugué, C., and Cerrutti, P., 1991, Tip Vortex Roll-Up and Cavitation, *Cavitation and Multiphase Flow Forum*, ASME FED 109, pp. 43–48.

Fruman, D. H., Dugué, C., and Cerrutti, P., 1992a, Enroulement et cavitation de tourbillon marginal, *Revue Scientifique et Technique de la Défense*, pp. 133–141.

Fruman, D. H., Dugué, C., Pauchet, A., Cerrutti, P., and Briançon-Marjollet, L., 1992b, Tip Vortex Roll-Up and Cavitation, *Nineteenth Symposium on Naval Hydrodynamics*, Aug. 24–28, Seoul.

Fruman, D. H., Castro, F., Pauchet, A., and Pichon, T., 1994, On Tip Vortex Turbulence, Wandering and Cavitation Occurrence, *Second International Symposium on Cavitation*, Tokyo, Japan, April.

Green, S. I., 1991, Correlating Single Phase Flow Measurements with Observations of Trailing Vortex Cavitation, ASME JOURNAL OF FLUIDS ENGINEERING, Vol. 113, pp. 125–129.

Green, S. I., and Acosta, A. J., 1991, Unsteady Flow in Trailing Vortices, *Journal of Fluid Mech.*, Vol. 227, pp. 107–134.

Lamb, H., 1945, *Hydrodynamics*, Cambridge University Press, London and New York.

Lindsey, W. F., Stevenson, D. B., and Daley, B. N., 1948, Aerodynamic Characteristics of 24 NACA 16-Series Airfoils at Mach Numbers Between 0.3 and 0.8, NACA Technical Report No. 1546.

McCormick, B. W., 1962, On Cavitation Produced by a Vortex Trailing from a Lifting Surface, ASME *Journal of Basic Engineering*, Sept., pp. 369–379.

Pauchet A., Briancon-Marjollet L., and Fruman D. H., 1993, Recent Results on the Effect of Cross Section on Hydrofoil Tip Vortex Cavitation Occurrence at High Reynolds Numbers, *Cavitation and Multiphase Flow Forum*, ASME FED 153, pp. 81–86.

Pogozelski, E. M., Shekarriz, A., Katz, J., and Huang, T. T., 1993, Three Dimensional Near Field Behaviour of a Tip Vortex Developing on an Elliptic Foil, 31st Aerospace Sciences Meeting and Exhibit, Reno, NV.

Schlichting, H., 1979, *Boundary Layer Theory*, Sixth Edition, McGraw-Hill, New York.

Spivey, R. F., 1968, Blade Tip Aerodynamics-Profile and Planform Effects, *24th Annual National Forum Proceedings*, Washington D.C., May 8–10.

Stinebring, D. R., Farrell, K. J., and Billet, M. L., 1991, The Structure of a Three-Dimensional Tip Vortex at High Reynolds Numbers, ASME JOURNAL OF FLUIDS ENGINEERING, Vol. 113, pp. 496–503.

van Dam, C. P., 1987, Induced Drag Characteristics of Crescent Moon Shaped Wings, *Journal of Aircraft*, Vol. 24, No. 2, pp. 115–119.

A Numerical Investigation of Laminar Flow Past Nonspherical Solids and Droplets

J.K. Comer

C. Kleinstreuer

Department of Mechanical and Aerospace Engineering, North Carolina State University, Raleigh, NC 27695

Steady laminar flow past solitary spheroids and nonspherical droplets has been numerically analyzed. Specifically, interfacial transport properties such as surface pressures, interfacial velocities, shear stresses and separation angles as well as the resulting drag coefficients are evaluated for specified aspect ratios ($0.2 \leq E = b/a \leq 1.0$) and intermediate gas stream Reynolds numbers ($40 \leq Re \leq 120$). For one case, it was determined that the use of the traditional spherical-droplet assumption would result in a 30 percent underprediction of the total drag coefficient.

Introduction

The analysis and prediction of the flow fields near solid particles and inside liquid droplets exposed to a steady laminar gas stream are a necessary component in the design of a wide range of engineering systems including atomizers, sprays, dryers, separators, gas turbines, medical devices, and so on. In most dispersed flow studies the solid or liquid particles are considered to be spherical. However, significant underprediction of, say, the drag coefficient for nonspherical droplets may result when the shape-dependence is ignored. Oblate spheroidal shapes of different aspect ratios are in many cases good approximations for actual solid or liquid particles in free streams of intermediate Reynolds numbers (cf. Dandy and Leal, 1989; and Clift et al., 1978).

Numerous theoretical and a few experimental contributions to the fluid mechanics, particle dynamics and heat transfer of *spherical* solids and droplets are available (cf. LeClair et al., 1972; Clift et al., 1978; Haywood et al., 1989; Raju and Sirignano, 1990; Chiang et al., 1992; Chiang and Kleinstreuer, 1991, 1992). Brief reviews of theoretical solutions to low-Reynolds-number flows past *nonspherical* axisymmetric solids are given in Happel and Brenner (1965) and Clift et al. (1978). Flow fields at intermediate Reynolds numbers have been investigated by Masliyah and Epstein (1970), Pitter et al. (1973) and more recently by Chuchottaworn and Asano (1986) and Dandy and Leal (1989). Masliyah and Epstein (1970) performed an extensive numerical study of the gas flow field around both oblate and prolate spheroids with principal axes ratios of 0.2 to 1.0 for Reynolds numbers up to 100. Pitter et al. (1973) studied experimentally and computationally gas flow past thin oblate spheroids with aspect ratios of 0.05 and 0.2 at intermediate Reynolds numbers. Chuchottaworn and Asano (1986) analyzed numerically transport phenomena associated with flow around prolate and oblate rigid spheroids, which they labeled "spheroidal droplets," over a wide range of aspect ratios. Dandy and Leal (1989) determined the steady-state or equilibrium shape of droplets as a function of Reynolds number, Weber number, density ratio, and viscosity ratio. Their numerical results indicate that for low Reynolds number flows the droplet shape varies from approximately spherical to a shape approaching a spherical cap as the Weber number is increased, while for intermediate Reynolds numbers the droplet shape becomes increasingly spheroidal as the Weber number is increased. All studies assume steady laminar axisymmetric flow past a solitary particle with a stationary wake. One exception is the 3-D flow investigation by Dwyer and Dandy (1989) who considered a solid ellipsoid under varying angles of attack.

The present study expands on previous contributions in providing a detailed analysis of the velocity field, surface pressure, separation angle, and drag coefficient as a function of the aspect ratio for rigid spheroids as well as spheroidal droplets. In addition, the effect of the viscosity ratio on the drag coefficient is analyzed.

Analysis

For the intermediate Reynolds number range of interest, i.e., $40 \leq \mathrm{Re} \leq 120$, vortex shedding can be neglected (cf. Clift et al., 1978), and the dimensionless equations for steady laminar axisymmetric flow past a solid or liquid particle are (cf. Fig. 1):

$$\nabla \cdot \boldsymbol{v}_i = 0 \qquad (1a,b)$$

and

$$(\boldsymbol{v}_i \cdot \nabla)\boldsymbol{v}_i = -\nabla p_i + \mathrm{Re}_i^{-1}\nabla^2 \boldsymbol{v}_i \qquad (2a,b)$$

where $i = g$ indicates the gas phase and $i = l$ represents the liquid phase in case of nonspherical droplets. Here,

$$\boldsymbol{v}_i = \boldsymbol{v}_i^*/u_\infty^*, \quad p_i = p_i^*/(\rho^* u_\infty^{*2}), \quad \nabla = \nabla^* d^*,$$

$$\text{and} \quad \mathrm{Re}_g = \frac{\rho_g^* u_\infty^* d^*}{\mu_g^*}$$

Contributed by the Fluids Engineering Division for publication in the JOURNAL OF FLUIDS ENGINEERING. Manuscript received by the Fluids Engineering Division October 7, 1993; revised manuscript received October 25, 1994. Associate Technical Editor: G. Karniadakis.

In addition to the gas phase Reynolds number Re_g, the aspect ratio $E = b/a$ and for the nonspherical droplet studies the density ratio $\zeta = \rho_l^*/\rho_g^*$ as well as the viscosity ratio $\lambda = \mu_l^*/\mu_g^*$ are the important system parameters considered. An additional droplet parameter of importance is the Weber number, $\mathrm{We} = u_\infty^{*2} d_e^* \rho_g^*/\gamma^*$. The Weber number indicates the degree to which droplets will dynamically deform. For this study, however, the droplet shapes are fixed thus the Weber number (i.e., the surface tension) does not appear in the problem statement. The liquid phase Reynolds number is a dependent dimensionless group, i.e., $\mathrm{Re}_l = (\zeta/\lambda)\mathrm{Re}_g$. The characteristic length d could be either the major principal axis for oblate spheroids (i.e., $d = d_a \equiv a$) or the spherical volume equivalent diameter (i.e., $d = d_e$). Thus, the gas-phase Reynolds numbers and the drag coefficients may be expressed as

$$\mathrm{Re}_{de} = \mathrm{Re}_{da} E^{1/3} \quad \text{and} \quad C_{D_{de}} = C_{D_{da}} E^{-2/3} \qquad (3a,b)$$

Considering a sufficiently large *cylindrical* computational domain for the continuous phase, the boundary conditions are (cf. Fig. 1):

$$\text{(inlet)} \quad u = 1 \quad \text{and} \quad v = 0 \qquad (4a,b)$$

$$\text{(outlet and top)} \quad \frac{\partial u}{\partial z} = \frac{\partial v}{\partial z} = 0 \quad \text{and} \quad \frac{\partial u}{\partial r} = \frac{\partial v}{\partial r} = 0 \qquad (5a\text{–}d)$$

$$\text{(centerline)} \quad \frac{\partial u}{\partial r} = 0 \quad \text{and} \quad v = 0 \qquad (6a,b)$$

The interfacial compatibility conditions are for the solid particles:

$$u = v = 0 \qquad (7a,b)$$

and for the droplets:

$$u_{n,g} = u_{n,l} = 0,\ u_{t,g} = u_{t,l} \quad \text{and} \quad \tau_{s,g} = \left(\frac{\rho_l}{\rho_g}\right) \tau_{s,l} \qquad (8a\text{–}d)$$

Solution Method

In the Galerkin finite element formation a system of nonlinear algebraic equations of the form (cf. Cuvelier et al., 1986)

$$[S]\mathbf{v} + [N(\mathbf{v})]\mathbf{v} + \epsilon^{-1}[L]^r[D]^{-1}[L]\mathbf{v} = \mathbf{F} \qquad (11)$$

appears. Linearization of (11) is obtained with the efficient quasi-Newton method if the radius of convergence is sufficient (cf. Cuvelier et al., 1986). Instead of solving the *global* system matrix, the gas phase quantities are obtained with a *segregated* solver algorithm using the "mixed" formulation where the pressure is directly computed (cf. Engleman, 1991). Hence, for large problems, creation of a huge global matrix is avoided in favor of a group of smaller submatrices which are solved in a sequential order.

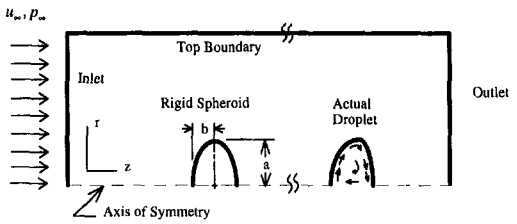

Fig. 1 System schematic

The dimensions of the computational domain depend primarily on the free stream velocity and the particle shape. The radial dimension is inversely related to the aspect ratio and the Reynolds number and the axial dimensions are directly related to the Reynolds number and inversely related to the aspect ratio. A variable-density meshing strategy is utilized where small elements are placed at the interface and smoothly transitioned to coarser elements at the boundaries. The nodal spacing on the interface is about 3.2 degrees for $E = 1$, i.e., a sphere. Nine-node isoparametric quadrilateral elements were used where the velocity was approximated by biquadratic shape functions and the pressure by linear shape functions (cf. Cuvelier et al., 1986). Meshes for spheroidal particles were generated by multiplying the sphere's streamwise axis by the aspect ratio. The mesh was refined and skewness of elements near the interface was reduced for the worst case, i.e., a spheroid with aspect ratio $E = 0.2$, until mesh-independence of the results was achieved. About 1020 to 1325 elements were needed for the gas-phase and 322 to 350 elements were necessary for the droplets.

The solutions of the gas and liquid flow fields were obtained as follows. Starting with Stoke's flow for the gas-phase as an initial guess, the interface is considered first to be rigid. Higher Reynolds number flows utilize the lower Reynolds number solution as their initial guess. The resulting shear stress at the interface is used as the boundary condition for the liquid phase. The stress-induced liquid-phase flow field is solved and the surface velocity is used as the interfacial boundary condition for the gas phase. The matching of the compatibility conditions required between nine and thirty iterations with an optimal under-relaxation coefficient of 0.65 and a maximum relative error bound of 10^{-3}.

Results and Discussion

A Model Validation. The numerical code was validated using benchmark data sets and correlations for rigid spheres, spherical droplets, and solid oblate spheroids (cf. Clift et al., 1978; LeClair et al., 1972; Masliyah and Epstein, 1970; and

Nomenclature

a = major principal axis of spheroid
b = minor principal axis of spheroid
C_D = drag coefficient
d = characteristic diameter of particle or droplet
D = pressure mass matrix
E = spheroid's aspect ratio, b/a
$\mathbf{F}$ = force vector
F_D = drag force
L = continuity matrix
n = normal coordinate
N = convective matrix
O = order of
p = pressure
r = radial coordinate
Re = Reynolds number, typically Re_g
S = diffusion matrix
u, v = velocity components in z and r directions
u_∞ = free-stream velocity
$\mathbf{v}$ = velocity vector
We = Weber number
z = axial cylindrical coordinate
γ = surface tension
θ_s = separation angle
λ = viscosity ratio
μ = dynamic viscosity
ν = kinematic viscosity
ρ = density
τ = shear stress
ζ = density ratio

Subscripts

a = principal axis
e = equivalent diameter
g = gas phase
i = fluid phase ($i = l$ or g)
l = liquid phase
n = normal
t = tangential
s = surface
∞ = free stream

Superscript

$*$ = dimensional quantities

Table 1 Comparison of data sets for rigid sphere

$Re_g = u_\infty d/\nu$		40	50	60	75	90	100	110	120
Separation angle, θ_s	Present model	143.9	138.9	135.3	131.4	128.4	126.6	125.2	123.8
	Clift et al. (1978)	144.4	139.3	135.5	131.4	128.2	126.5	125.0	123.7
Drag coefficient, C_D	Present model	1.80	1.58	1.43	1.27	1.15	1.09	1.04	1.00
	Clift et al. (1978)	1.79	1.57	1.42	1.26	1.14	1.09	1.04	0.99

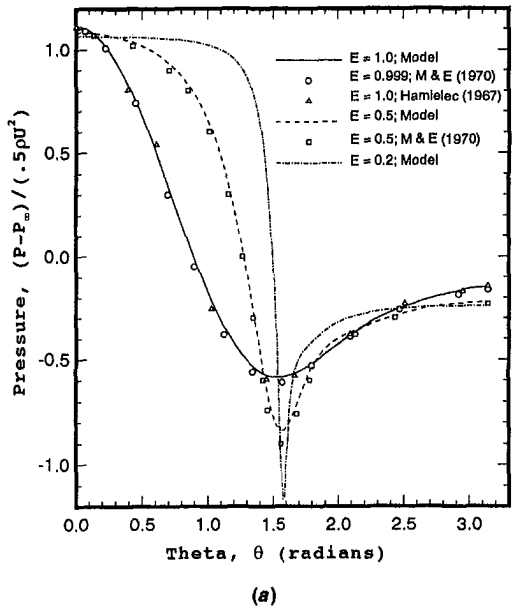

(*a*)

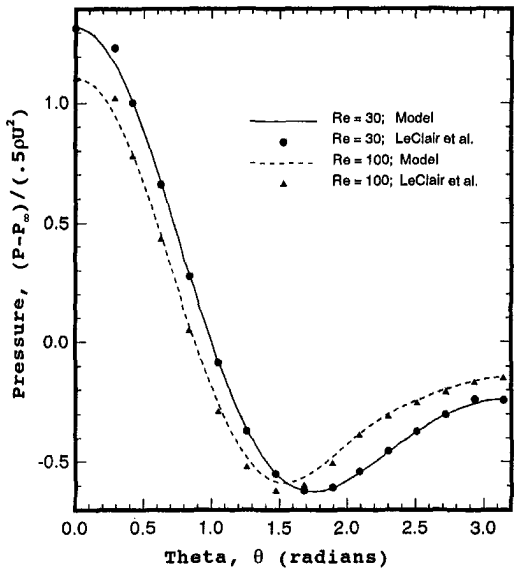

(*b*)

Fig. 2(*a*) Dimensionless pressure distribution over rigid spheroids at Re = 100 Fig. 2(*b*) Dimensionless pressure distribution over a liquid sphere at λ = 55 and ζ = 836 for Re = 30 and 100

Rivkind and Ryskin, 1976). Table 1 contains a matching comparison between model predictions and empirical correlations for the separation angle and the drag coefficient of a rigid sphere as a function of free-stream Reynolds number.

Figures 2(*a*) and 2(*b*) show detailed comparisons of the dimensionless surface pressure for solitary rigid particles with aspect ratios E = 1.0, 0.5 and 0.2 (cf. Masliyah and Epstein, 1970) and for a liquid sphere with a viscosity ratio λ = 55 and a density ratio ζ = 836 (cf. LeClair et al., 1972). As expected, spherical particles exhibit smoother pressure variations

Table 2 Comparison of data sets for liquid sphere

$Re_g = u_\infty d/\nu$		30	40	57	100	200
Drag coefficient, C_D	Present model	2.118	1.783	1.457	1.078	0.756
	LeClair et al. (1972)	2.10	1.78	1.51	1.08	0.76
	Rivkind and Ryskin (1976)	2.07	1.75	1.44	1.09	0.79

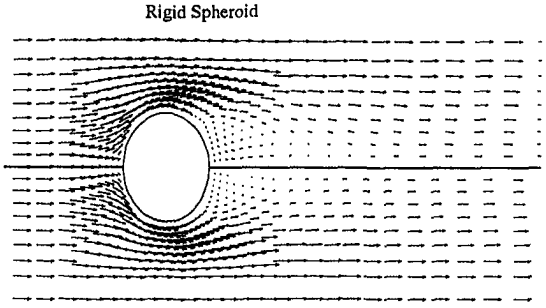

(*a*)

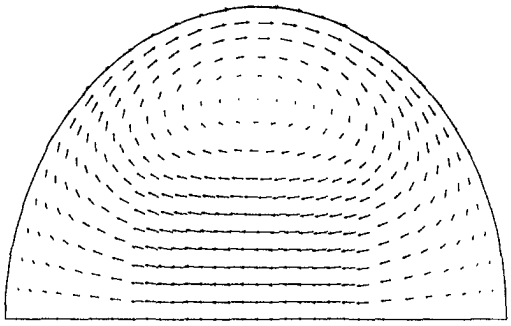

(*b*)

Fig. 3(*a*) Gas-phase velocity vector plot for a rigid spheroid (top) and a n-hexane spheroidal droplet (bottom) where λ = 4.12, ζ = 260.7, E = 0.8 and Re_{de} = 100 Fig. 3(*b*) Liquid-phase velocity vector plot for a n-hexane spheroidal droplet (λ = 4.12, ζ = 260.7, E = 0.8 and Re_{de} = 100)

while the oblate spheroids tend to have a somewhat flat profile over the front part with an increasingly abrupt pressure drop near flow separation as $E \rightarrow 0$. A swift but limited pressure recovery contributes, as form drag, a major part to the total drag of oblate spheroids. Table 2 shows good agreements between the current model and the results of LeClair et al. (1972) as well as the correlation of Rivkind and Ryskin (1976) for the drag coefficient of a liquid sphere (λ = 55 and ζ = 836). Additional validation results may be found in Comer (1993).

B Solid Particles. Figures 3(*a*) and 4(*a*) show the velocity vector plots for rigid spheroids and liquid spheroidal droplets of decreasing aspect ratio, i.e., E = 0.8 and 0.4. The upper halves of these figures depict the gas flow fields for rigid spheroids at Re = 100. As $E \rightarrow 0$, the front part of the flow field approaches stagnation point flow. When the Reynolds number is increased, the region of influence in the normal di-

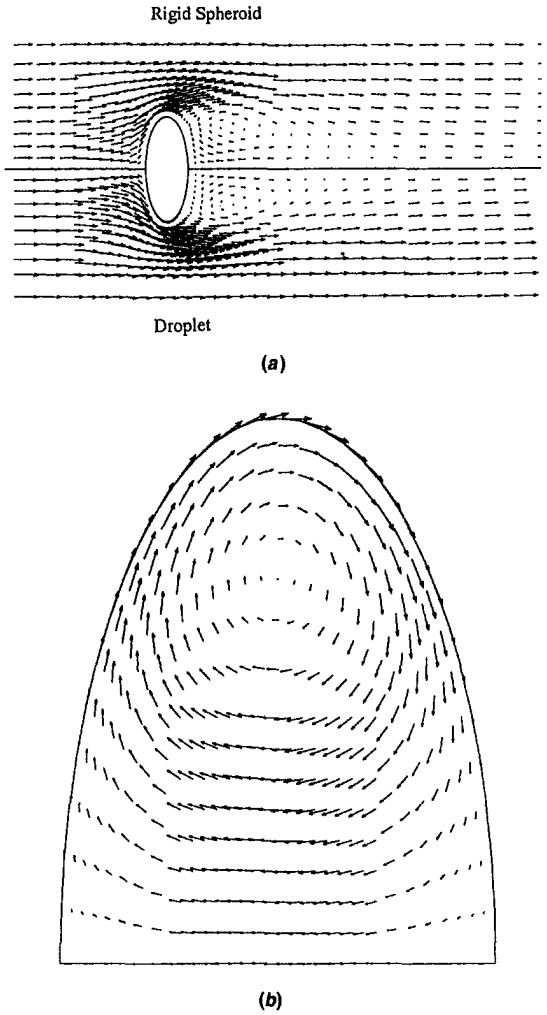

Fig. 4(*a*) Gas-phase velocity vector plot for a rigid spheroid (top) and a n-hexane spheroidal droplet (bottom) where $\lambda = 4.12$, $\zeta = 260.7$, $E = 0.4$ and $Re_{de} = 100$ Fig. 4(*b*) Liquid-phase velocity vector plot for a n-hexane spheroidal droplet ($\lambda = 4.12$, $\zeta = 260.7$, $E = 0.4$ and $Re_{de} = 100$)

rection decreases but the wakes vorticity and length increase. The intensity of the wake also increases when the spheroid's aspect ratio is reduced. These two system parameters (Re, E) influence the *local* flow fields (cf. Figs. 2, 3(a), 4(a)) which in turn determine global flow parameters such as the total drag coefficient discussed below as well as the Nusselt number for thermal flows (cf. Comer and Kleinstreuer, 1995).

Figure 5 indicates that spheroids with high aspect ratios have slightly higher drag coefficients at lower Reynolds numbers, whereas at larger Reynolds number the spheroids with higher aspect ratios generally have lower drag coefficients. This generates for C_D(Re, E) graphs "crossover points" with respect to the sphere's drag coefficient, i.e., C_D(Re, $E = 1.0$). The reason is that at low Reynolds numbers the contribution of $C_D(friction)$ to $C_D(total)$ is large, generating high C_D-values for, say, $E = 1.0$. However, as the Reynolds number increases, and the aspect ratio decreases the form drag, i.e., $C_D(pressure)$ becomes dominant. From Fig. 5 it can also be deduced that the total drag coefficient for $E = 0.2$ and $Re = 90$ is approximately equal to that for $E = 1.0$ at $Re = 75$. Noting that $d = d_a$ and ρ are constant, $C_{D_1} = C_{D_2}$ collapses by definition to

$$\frac{F_{\text{Drag},1}}{u_{\infty,1}^2} = \frac{F_{\text{Drag},2}}{u_{\infty,2}^2} \quad \text{or} \quad \frac{F_{D,1}}{F_{D,2}} = \left(\frac{u_{\infty,1}}{u_{\infty,2}}\right)^2$$

This implies that for the different free-stream Reynolds numbers, the two submerged bodies experience quite different forces although their drag coefficients are the same.

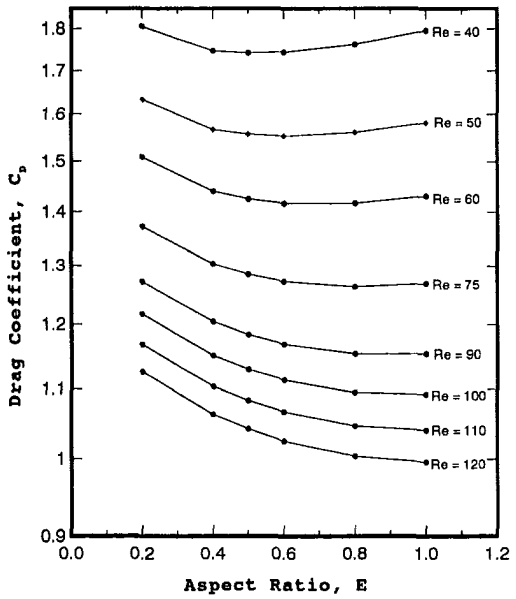

Fig. 5 Drag coefficients as a function of aspect ratio for rigid spheroids

C Nonspherical Droplets. In contrast to solid particles, droplets may deform in response to fluid dynamic forces and/or nonuniform heat transfer with phase change as in droplet condensation and vaporization. It is generally accepted that at intermediate Reynolds numbers droplets assume shapes which become increasingly spheroidal as the Weber number is increased (cf. Clift et al., 1978; Dandy, 1987; Dandy and Leal, 1989; and Wellek et al., 1966). Thus, it is realistic and computationally efficient to study fixed spheroidal droplet shapes in the range of $0.4 \leq E \leq 1.0$. Specifically, of interest are the effects of the droplet shape and the viscosity ratio on the local velocity field and the drag coefficient. Two viscosity and density ratios were used to represent typical liquids, i.e., $\lambda = 4.12$ and $\zeta = 260.7$ for water and $\lambda = 40.2$ and $\zeta = 845.6$ for n-hexane fuel.

The bottom halves of Figs. 3(a) and 4(a) show the gas-phase velocity fields for n-hexane spheroidal droplets at $E = 0.8$ and 0.4 for Re = 100 whereas Figs. 3(b) and 4(b) depict the corresponding internal circulation patterns. It can be seen that the liquid droplets have a smaller recirculation zone than the corresponding rigid spheroids. It is also evident that the smaller aspect ratio droplet, $E = 0.4$, has a slightly larger recirculation zone than the $E = 0.8$ droplet. However, care must be taken when comparing the velocity fields of the droplets since the characteristic diameter, and hence the Reynolds number, was based on the major principle axis. When the volume equivalent diameter is employed, the actual Reynolds number is less, i.e., $Re_{de} \approx 75$ for the case $E = 0.4$ (cf. Figs. 4(a, b)). Thus for the same volume equivalent Reynolds number the recirculation zone of the $E = 0.4$ droplet would be clearly larger than that of the $E = 0.8$. Typical internal droplet circulation is visualized in the velocity vector plots of Figs. 3(b) and 4(b) for spheroidal n-hexane droplets ($E = 0.8$ and 0.4). The strong primary vortex and the measurable surface velocity for 60 deg $\leq \theta \leq$ 120 deg are clearly visible.

The nonsphericity and viscosity effects on the total droplet drag coefficient are shown in Fig. 6. Because of the enhanced liquid-phase motion, n-hexane droplets exhibit lower drag coefficients than water droplets or solid particles (cf. Figs. 6, 7). Figures 7(a) and 7(b) indicate that for high viscosity ratio flows, such as water droplets in air, it may be possible to ignore the internal droplet circulation when determining the drag

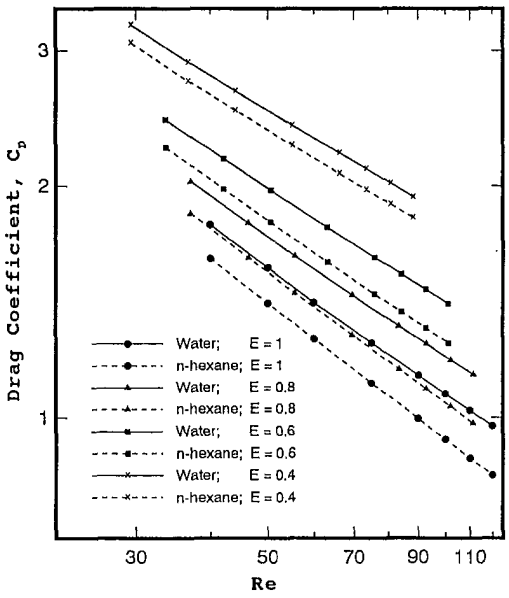

Fig. 6 Drag coefficients based on the volume equivalent diameter for a spheroidal water droplet (λ = 40.2 and ζ = 845.6) and a n-hexane droplet (λ = 4.12 and ζ = 260.7) at aspect ratios E = 1.0, 0.8, 0.6, and 0.4

coefficient, while for low viscosity ratio flows, such as light fuel droplets in air, the internal droplet circulation contributes significantly to the overall drag. From close examination of Fig. 7(*b*) it can be deduced that at the smallest aspect ratio, the viscosity ratio plays a diminished role in determining the drag because of the reduced internal droplet circulation.

In general, flow past droplets, especially those with low viscosity ratios, generates different interfacial quantities, leading to different separation angles, drag coefficients, etc., when compared with their rigid or high-viscosity counterparts because of the strong shear stress-induced internal circulation. Specifically, flow separation is delayed and the total drag decreases. Drag reduction is caused by lower velocity gradients at the moving interface (cf. $C_{D,\text{shear}}$) and by delayed flow separation generating smaller wakes (cf. $C_{D,\text{pressure}}$). It has to be noted that special care should be taken in: (i) determining the line of flow separation and (ii) choosing the reference length for data comparison. For high-viscosity-ratio flows a change in sign of the surface shear stress indicating separation is acceptable. However, for flows with $\lambda = O(1)$, such as light fuel droplets, the interfacial shear stress may change sign without any flow separation. What happens is that the surface velocity over the front of the droplet reaches a relatively large value, thus driving the internal droplet circulation. The gas-phase velocity over the rear of the droplet decreases, in correspondence to the pressure recovery of the gas stream, at a faster rate than the interfacial droplet velocity because of liquid-phase conservation of mass and momentum. Enhanced flow visualization is one possibility for recording this phenomenon. As given with Eq. (3*b*), the definition of the drag coefficient for spheroidal particles can be based on the volume-equivalent diameter or the major principle axis, both affecting the total drag differently. Thus, comparisons of integrated or global flow quantities based on the major principle axis are acceptable for different fluids in terms of λ and ζ but restricted to the same particle shapes. In contrast, comparisons of different particle shapes may be admissible when based on the volume-equivalent diameter.

Acknowledgment

This work was supported in part by the Computational Science Graduate Fellowship Program of the Office of Scientific Computing in the Department of Energy.

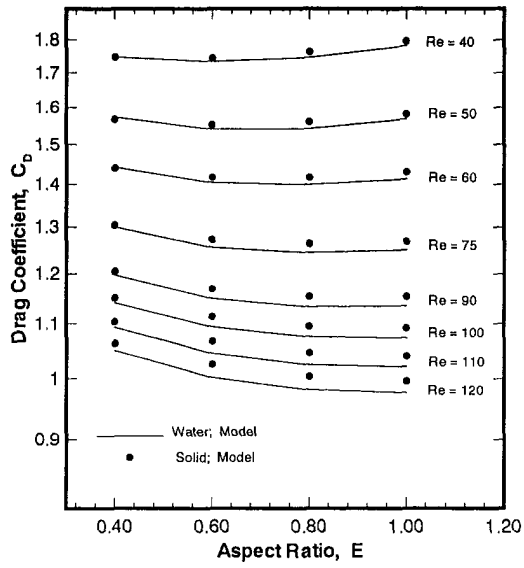

(*a*)

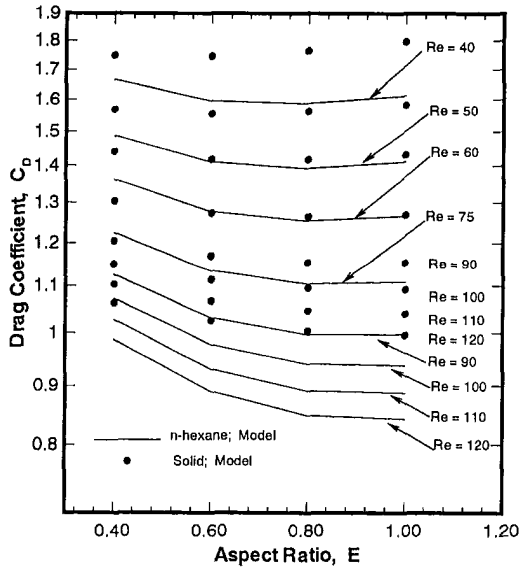

(*b*)

Fig. 7 (*a*) Drag coefficients based on principle axis for a spheroidal water droplet (λ = 40.2 and ζ = 845.6) and a rigid oblate spheroid at aspect ratios E = 1.0, 0.8, 0.6, and 0.4 Fig. 7(*b*) Drag coefficients based on principle axis for a spheroidal n-hexane droplet (λ = 4.12 and ζ = 260.7) and a rigid oblate spheroid at aspect ratios E = 1.0, 0.8, 0.6, and 0.4

References

Chiang, C. H., Raju, M. S., and Sirignano, W. A., 1992, "Numerical analysis of convecting vaporizing fuel droplet with variable properties," *International Journal of Heat and Mass Transfer*, Vol. 35, No. 5, pp. 1307–1324.

Chiang, H., and Kleinstreuer, C., 1991, "Laminar Flow Past Colinear Spheres With Fluid Injection," ASME JOURNAL OF FLUIDS ENGINEERING, Vol. 113, pp. 176–182.

Chiang, H., and Kleinstreuer, C., 1992, "Computational Analysis of Interacting Vaporizing Fuel Droplets on a One-dimensional Trajectory," *Combustion Science & Technology*, Vol. 86, pp. 289–309.

Chuchottaworn, P., and Asano, K., 1986, "Numerical Analysis of Drag Coefficients and the Heat and Mass Transfer of Spheroidal Drops," *Journal of Chemical Engineering of Japan*, Vol. 19, No. 3, pp. 208–213.

Clift, R., Grace, J. R. and Weber, M. E., 1978, *Bubbles, Drops and Particles*, Academic Press, New York.

Comer, J. K., 1993, "Computational Analysis of Thermal Flows Past Non-Spherical Solids and Drops," M.S. thesis, Department of Mechanical and Aerospace Engineering, North Carolina State University, Raleigh, NC.

Comer, J. K., and Kleinstreuer, C., 1995, "Computational Analysis of Convection Heat Transfer to Non-Spherical Particles," *International Journal of Heat and Mass Transfer* (in press).

Cuvelier, C., Segal, A, and Van Steenhoven, A. A., 1986, *Finite Element Methods and Navier-Stokes Equations*, D. Reidel Publishing Company, Dordrecht, Holland.

Dandy, D. S., 1987, "Intermediate Reynolds Number Free Stream Flows," Ph.D. thesis, California Institute of Technology, Pasadena, California.

Dandy, D. S., and Leal, L. G., 1989, "Buoyancy-driven Motion of a Deformable Drop through a Quiescent Liquid at Intermediate Reynolds Numbers," *Journal of Fluid Mechanics*, Vol. 208, pp. 161–192.

Dwyer, H. A., and Dandy, D. S., 1990, "Some Influences of Particle Shape on Drag and Heat Transfer," *Physics of Fluids A*, Vol. 2, No. 12, pp. 2110–2118.

Engleman, M. S., 1991, FIDAP *Manuals Volumes 1 to 4*, FDI, Evanston, Illinois.

Hamielec, A. E., Hoffman, T. W., and Ross, L. L., 1967, "Viscous Flow Around Circulating Spheres of Low Viscosity," *AIChE Journal*, Vol. 13, pg. 220.

Happel, J. and Brenner, H., 1965, *Low Reynolds Number Hydrodynamics*, Prentice-Hall, NJ.

Haywood, R. J., Nafziger, R., and Renksizbulut, M., 1989, "A Detailed Examination of Gas and Liquid Phase Ambient Processes in Convective Droplet Evaporation," ASME *Journal of Heat Transfer*, Vol. 111, pp. 495–502.

LeClair, B. P., Hamielec, A. E., Pruppacher, H. R., and Hall, W. D., 1972, "A Theoretical and Experimental Study of the Internal Circulation in Water Drops Falling at Terminal Velocity in Air," *Journal of The Atmospheric Sciences*, Vol. 29, No. 4, pp. 728–740.

Masliyah, J. H., and Epstein, N., 1970, "Numerical Study of Steady Flow Past Spheroids," *Journal of Fluid Mechanics*, Vol. 44, pp. 493–512.

Pitter, R. L., Pruppacher, H. R., and Hamielec, A. E., 1973, "A Numerical Study of Viscous Flow Past a Thin Oblate Spheroid at Low and Intermediate Reynolds Numbers," *Journal of The Atmospheric Sciences*, Vol. 30, pp. 125–134.

Raju, M. S., and Sirignano, W. A., 1990, "Interaction between two vaporizing droplets in an intermediate Reynolds number flow," *Physics of Fluids A*, Vol. 2, No. 10, pp. 1780–1796.

Rivkind, V. Y., and Ryskin, G. M., 1976, "Flow structure in motion of a spherical drop in a fluid medium at intermediate Reynolds numbers," *Fluid Dynamics*, Vol. 11, pp. 5–12.

Wellek, R. M., Agrawal, A. K., and Skelland, A. H. P., 1966, "Shape of Liquid Drops Moving in Liquid Media," *AIChE Journal*, Vol. 12, No. 5, pp. 854–862.

Malcolm S. Taylor

Csaba K. Zoltani

U.S. Army Research Laboratory,
Department of the Army,
Aberdeen Proving Ground, MD 21005-5066

Meta-Analysis of Gas Flow Resistance Measurements Through Packed Beds

Measurements of the resistance to flow through packed beds of inert spheres have been reported by a number of authors through relations expressing the coefficient of drag as a function of Reynolds number. A meta-analysis of the data using improved statistical methods is undertaken to aggregate the available experimental results. For Reynolds number in excess of 10^3 the relation log $F_v = 0.49 + 0.90$ log Re' is shown to be a highly effective representation of all available data.

1 Introduction

Experimental results are cumulative if in aggregate they unify and extend empirical relations and theoretical structures that may be obscured in individual investigations. Empirical cumulativeness, which Hedges (1987) describes as "... the degree of agreement among replicated experiments or the degree to which related experimental results fit into a simple pattern that makes conceptual sense," is the focus of this paper. Glass (1976) was among the first to recommend the use of quantitative procedures in integrative research reviews and to introduce the term "meta-analysis" to cover the collection of such procedures. Meta-analysis claims certain classical statistical procedures, as well as approaches developed specifically for research synthesis, and has found application in the social and biological sciences. The unification of experimental results obtained by different investigators operating independently with their own experimental protocol and sometimes using different methods of analysis, is the kernel of meta-analysis. A comprehensive treatment of this subject is given by Hedges and Olkin (1985).

Measurement in the physical sciences is generally regarded as highly accurate, and although some variability is inevitable, the variation itself is thought to be insignificant from a practical standpoint. Counterexamples to this notion are plentiful, even in carefully conducted experiments. Consider, for instance, the situation described by Touloukian (1975) involving two sets of measurements taken on the thermal conductivity of gadolinium. These data, shown in Fig. 1, ". . . are for the same sample, measured in the same laboratory two years apart in 1967 and 1969. The accuracy of curve 1 was stated as within 1 percent and that of curve 2 as 0.5 percent . . ." and yet, the curves differ by more than several hundred percent at higher values of temperature.

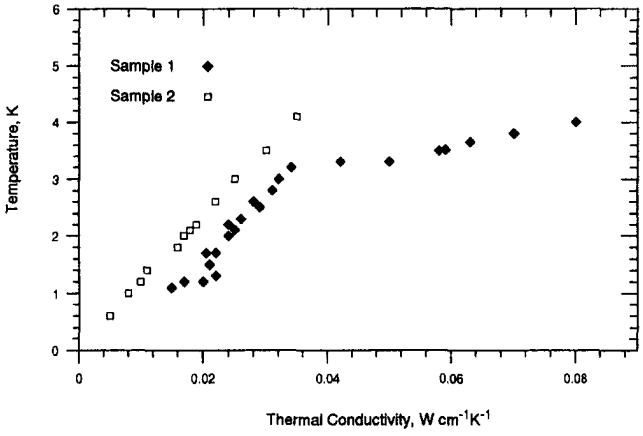

Fig. 1 Thermal conductivity of gadolinium

Physical scientists normally bring a careful qualitative analysis to their research studies. If prudently employed, interrogative statistics, which are part of meta-analysis, have a contribution to make in the physical sciences as well.

After data have been collected according to a carefully constructed experimental design (e.g., see Montgomery, 1991) the main reason for determining a correlation (a regression analysis) is to examine the effects that some variables exert, or appear to exert, on others. Even when no intuitive physical relationship is apparent, regression analysis may provide a convenient summary of the data. The summary can be accomplished in a number of ways and has been an active area of investigation since the time of A. M. Legendre (1752–1833), who published the first account of regression by least squares in 1805. Section 2 of this paper reviews the correlations that have been advanced for steady flow through inert spherically packed beds and some of the consequences of the attendant data analysis. In Section 3, a meta-analysis of the gas flow resistance measurements is undertaken. Section 4 contains a summary and main conclusions.

Contributed by the Fluids Engineering Division for publication in the JOURNAL OF FLUIDS ENGINEERING. Manuscript received by the Fluids Engineering Division September 15, 1993; revised manuscript received May 10, 1994. Associate Technical Editor: R. L. Panton.

2 Regression Analysis of Gas Flow Resistance Measurements

Ergun (1952), Kuo and Nydegger (1978), and Jones and Krier (1983) have proposed models relating coefficient of drag to Reynolds number for steady flow through packed beds of inert spheres. However, the correlations were developed under different experimental regimens. Robbins and Gough (1978) also investigated coefficient of drag at high Reynolds number but presented their results in terms of a friction factor $f_s' = F_v/[\mathrm{Re}/(1-\phi)]$, which is the ratio of coefficient of drag F_v, and Reynolds number Re scaled by a solids loading factor $(1-\phi)$.

In comparing Ergun's relation

$$F_v = 150 + 1.75\left(\frac{\mathrm{Re}}{1-\phi}\right), \tag{1}$$

to that of Kuo and Nydegger

$$F_v = 276.23 + 5.05\left(\frac{\mathrm{Re}}{1-\phi}\right)^{0.87}, \tag{2}$$

or of Jones and Krier

$$F_v = 150 + 3.89\left(\frac{\mathrm{Re}}{1-\phi}\right)^{0.87}, \tag{3}$$

a slight notational difference portends substantial complications. Equation (1) is a simple linear model. Equations (2) and (3) are nonlinear in the sense that one or more parameters appear nonlinearly. Nonlinearity complicates the statistical analysis of the data since determining appropriate choices for the parameters in Eqs. (2) and (3) becomes a computationally intensive optimization procedure, and inference about the resultant relation and parameters becomes much more tentative. The mathematical underpinnings of nonlinear regression will not support as much in the way of statistical inference or hypothesis testing as is available for linear regression. In general, nonlinear models should be avoided unless there is a compelling reason for their use. Draper and Smith (1981) discuss this issue in greater detail.

Standard regression procedures are developed under several assumptions. Fundamental among these is that the response (here, F_v) is measured with error but the predictor(s) (here, Re and ϕ) are measured without error. Jones and Krier provide estimates of error for F_v, Re, and ϕ, confirming that this assumption is not met, and call into question the efficacy of the resultant correlations. Sometimes an attempt to circumvent this requirement is undertaken by arguing that the error in predictor measurement is sufficiently small as to be ignored when compared to the range of the predictor variable. If this claim is invoked, reliance upon any resultant representation must be tempered accordingly.

Since a correlation provides a convenient representation of the available data, a direct attempt at evaluating the adequacy of a regression equation involves an examination of the differences between the measurements taken and the values predicted by the equation. These differences, $F_{v_i} - F'_{v_i}$, $i = 1, 2, \ldots, n$, are called residuals; F_{v_i} is an experimentally determined value of drag coefficient, and F'_{v_i} is the corresponding value predicted by the regression equation. A residual plot for Eq. (3) is shown in Fig. 2. These plots may serve as a diagnostic tool in addition to assessing the adequacy of a fitted regression model.

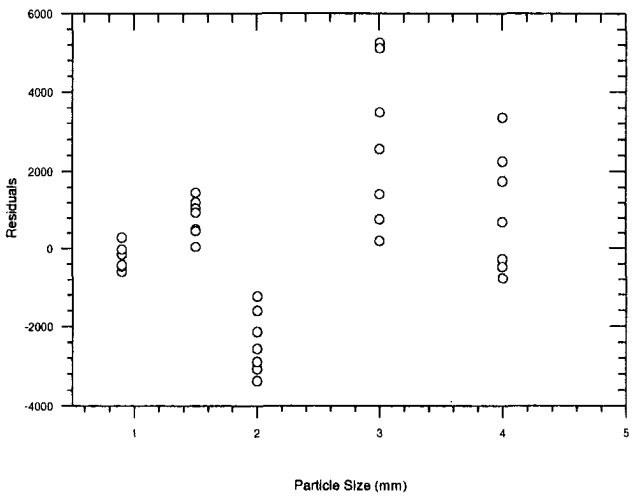

Fig. 2 Residuals versus particle diameter D_b; Jones and Krier data with 6-mm beads excluded

Figure 2 strongly suggests that another crucial regression assumption is not satisfied. The variance of the residuals does not appear constant over the range of $\mathrm{Re}' = \mathrm{Re}/(1-\phi)$; moreover, the departure from the fitted equation is systematic with bead diameter, D_b. Jones and Krier recommended reverting to the relation (Eq. (2)) proposed by Kuo and Nydegger to describe their own measurements taken for 6-mm beads. This recommendation is data specific and is difficult to justify in general. They conjecture that an interaction between bead size and tube diameter may be present, but this requires quantitative substantiation. In general, weighted least squares, or a transformation of the observations F_{v_i} before regression, are potential corrective procedures suggested by this residual pattern.

2.1 Regression Analysis Revisited. Nonlinear regression algorithms normally seek to minimize the sum of the squared residuals—as in ordinary linear regression—in attempting to determine the "best" choice of parameters to model the data. These procedures have previously been cited as computationally intensive. More specifically, they are iterative and may diverge or converge to local extrema, depending upon the choice of initial conditions. Through a systematic selection of initial conditions, it was determined that the equation

$$F_v = 61 + 2.7\left(\frac{\mathrm{Re}}{1-\phi}\right)^{0.91}, \tag{4}$$

provides an improved representation of the data reported by Jones and Krier.

Nomenclature

D_b = spherical particle (bead) diameter
D_c = test chamber diameter
f_s' = $F_v/[\mathrm{Re}/(1-\phi)]$, friction factor
F_v = $(\Delta P/L)(D_b^2/\mu\bar{u})[\phi/(1-\phi)]^2$, coefficient of drag
F_{v_i} = ith observed value of the drag coefficient
F'_{v_i} = predicted drag coefficient corresponding to the ith observed value
L = length scale
Re = $\mathrm{Re}_p\phi = \rho\bar{u}D_b\phi/\mu$, Reynolds number
Re′ = $\mathrm{Re}/(1-\phi)$
Re_p = Reynolds number based on particle size
$\bar{u}$ = average gas velocity
β_i, i = 0, 1, 2 = model coefficient
ΔP = change in pressure
ρ = density
ϕ = porosity of the packed bed
$(1-\phi)$ = solids loading
μ = gas viscosity

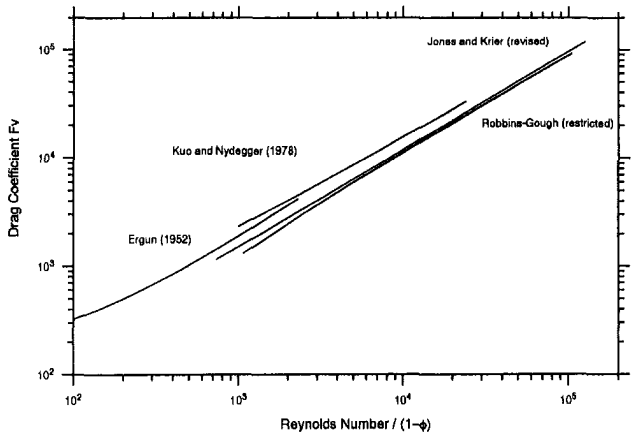

Fig. 3 Proposed models for relating coefficient of drag and Reynolds number

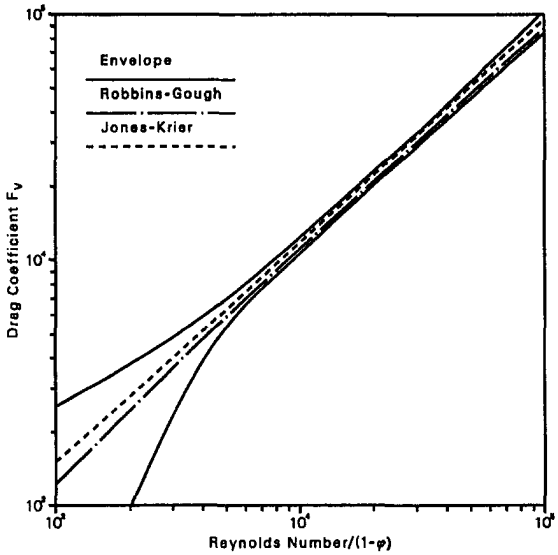

Fig. 4 Bootstrapped confidence envelopes for nonlinear regression based on Robbins and Gough data

The root mean square error (RMSE), an estimate of the standard deviation of the residuals and a commonly used measure for adequacy of fit, is reduced by 20 percent compared to that corresponding to Eq. (3). The measurements taken on the 6-mm beads, the chief contributor to heterogeneity of variance, have been excluded from the regression, making the comparison with Jones and Krier direct. A reduction of one-fifth in RMSE is not by itself a stunning improvement, but it does focus more sharply on the underlying physical process. The residual plot for Eq. (4) still exhibits the undesirable pattern of under(over) fitting categories of bead diameter but is an improvement compared to the display in Fig. 2.

The data collected by Robbins and Gough (1978, 1979), which "... correspond to several tests performed on several occasions" for beds of spheres, right circular cylinders, and multiperforated cylinders, may be transformed into units appropriate for comparison through the relationship $f_s' = F_v/[\mathrm{Re}/(1-\phi)]$. Restricting the analysis to data taken on 1.27-mm diameter lead shot and on 4.76-mm and 7.94-mm diameter steel spheres, the equation

$$F_v = -237 + 3.14\left(\frac{\mathrm{Re}}{1-\phi}\right)^{0.89}, \qquad (5)$$

was determined for representation of flow through spherically packed beds. Equations (4) and (5) are shown, along with the previously established correlations, Eqs. (1) and (2), in Fig. 3.

Transforming the variables (Re', F_v) by taking logarithms, which was suggested by the residual plot in Fig. 2, effectively linearizes the data. In regression analysis, a measure of precision of the regression line which is used in addition to RMSE, is given by a statistic denoted as R^2. R^2 assumes values in the unit interval [0, 1] and quantifies the amount of variation in the response accounted for by the regression line. Values close to 1.0 are highly desirable, indicating that the regression has effectively accounted for most of the variation in the response. The regression line determined after logarithmic transformation of the Jones and Krier data has $R^2 = 0.98$. The transformed Robbins and Gough data have $R^2 = 0.99$. These values are so close to 1.0 that pursuit of a nonlinear model is difficult to justify mathematically.

Comparison between linear models and nonlinear models is difficult. RMSE values cannot be compared across the transformation, and a well-defined R^2 statistic for nonlinear models does not exist.

3 Meta-Analysis of Gas Flow Resistance Measurements

Correlations that have been advanced for gas flow resistance measurements through spherically packed beds may be considered in aggregate. For the nonlinear models, a statistical resampling plan is applied, whose goal is to extract information from a set of data through repeated inspection. The procedure is called the "bootstrap," named to convey its self-help attributes, and it attempts to address an important problem in data reduction—after an estimate of a parameter is computed, what accuracy can be attached to the estimate? Accuracy here refers to the "± something" that often accompanies statistical estimates, and may be conveyed through such devices as variance, RMSE, or confidence interval. For the log-linear model, the available data are directly combined.

Full exploitation of a meta-analysis approach was hindered by an inability to obtain all the pertinent experimental data. It is unfortunate that experimental data are not routinely archived after collection; otherwise, additional information that it may hold is lost to extraction by subsequent investigations and by alternative statistical methods. The data of Jones and Krier and of Robbins and Gough, were accessible. With these data, this account proceeds as far as statistical prudence permits.

3.1 Bootstrapping Regression Correlations. Detailed descriptions of the bootstrap and accounts of its successful application are amply documented (e.g., Efron, 1979, 1982; Efron and Tibshirani, 1985; LePage and Billard, 1992). The computational contrivance that the bootstrap procedure exploits is the generation of perturbed data sets from a single set of data through sampling with replacement. Specific to this study, the set of paired observations taken on coefficient of drag and Reynolds number, $\{(F_{v_1}, \mathrm{Re}_1'), \ldots, (F_{v_n}, \mathrm{Re}_n')\}$, that is the basis for a reported correlation, is sampled with replacement to generate additional sets $\{(F_{v_1}^*, \mathrm{Re}_1'^*), \ldots, (F_{v_n}^*, \mathrm{Re}_n'^*)\}$, whose elements are copies (with duplication) of the original measurements. This set is called a bootstrapped data set. The process of sampling with replacement is repeated to generate a large number of bootstrapped data sets.

If a correlation is determined for each bootstrapped data set and its equation plotted, the sensitivity of the regression line to perturbation of the original data becomes apparent. In Figure 4, the results of 1,000 replications of this process are pictured. The outermost lines indicate boundaries within which the correlation (5) might be expected to lie if the original data set were simply perturbed. They were obtained from the max-

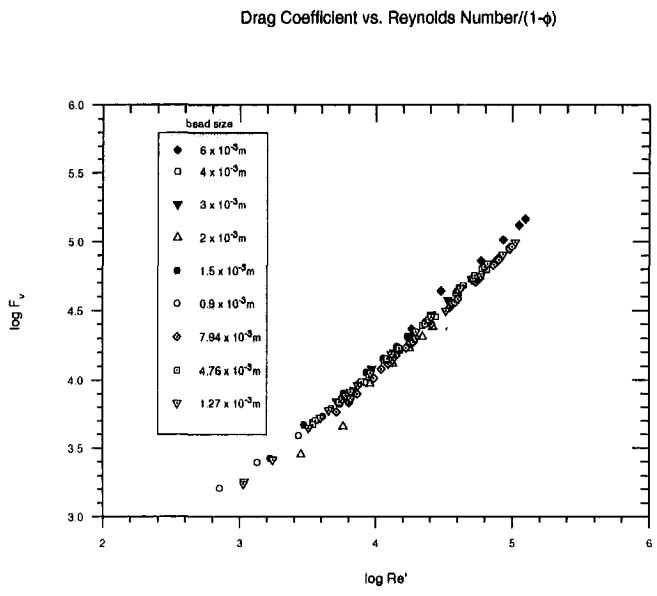

Fig. 5 Drag coefficients versus Reynolds number/(1 − ϕ); Jones and Krier, Robbins and Gough data combined

ima and minima of the drag coefficient predicted for particular values of Re′.[1]

The envelope constructed for correlation (5) contains correlation (4). This suggests that no significant difference between these empirical relations exists. Similar results are obtained if we begin with correlation (4); correlation (5) will lie within the corresponding confidence envelope. Consideration of perturbed data is highly appropriate here, since experimental results cannot be expected to be reproduced, even if the experiment is replicated under tightly controlled conditions. The theoretical justification for the use of bootstrapped data is given by Efron (1982).

The relationship of Kuo and Nydegger, for which the experimental data was not accessible, was determined for a single diameter bead, $D_b = 0.83$.

3.2 Log-Linear Regression. Figure 5 displays the logarithmic transformed data of Jones and Krier, and Robbins and Gough, combined. The fitted line for these data is

$$\log F_v = 0.49 + 0.90 \log \mathrm{Re}'; \tag{6}$$

included in the regression are the data taken on 6-mm beads, which was previously excluded.

Visually, the data appear linear after transformation. Statistically, the R^2-value for the regression is 0.99, making the fitted line a highly satisfactory representation of these data for all practical purposes.

A corresponding nonlinear expression may be established by applying the inverse log transformation to both sides of Eq. (6) to obtain

$$F_v = 3.09\,\mathrm{Re}'^{0.90}. \tag{7}$$

The coefficient 3.09 lies between the values determined for Eqs. (4) and (5), $2.7 < 3.09 < 3.14$; and the exponent 0.90 lies between the values determined for Eqs. (4) and (5), $0.89 < 0.90 < 0.91$. This is not unexpected, since Eq. (6) is intended to accommodate the data underlying both Eqs. (4) and (5). The absence of a constant term ($\beta_0 = 0$) is not especially meaningful, since the values of F_v over the range of Re′ for which Eqs. (4) and (5) are intended will dominate the constant term. The linear form Eq. (6) still holds the advantage of admitting additional statistical inference procedures that are denied the nonlinear model, Eq. (7).

[1] More precisely, the values represent extreme quantiles after all of the F_vs have been ranked; their values are not essentially different from maxima and minima.

4 Summary and Conclusions

For Reynolds number exceeding 10^3, a more effective representation and data analysis than presently available can be obtained after logarithmic transformation of the data. This linearizes the data and removes the necessity for nonlinear regression techniques. The equation

$$\log F_v = 0.49 + 0.90 \log \mathrm{Re}' \tag{8}$$

is an effective description of the available experimental data.

If a representation of the form

$$F_v = \beta_0 + \beta_1 (\mathrm{Re}/1-\phi)^{\beta_2} \tag{9}$$

is required, then Jones and Krier's results are more effectively reflected through the equation

$$F_v = 61 + 2.7\left(\frac{\mathrm{Re}}{1-\phi}\right)^{0.91}, \tag{10}$$

and Robbins and Gough's data restricted to spherically packed beds provide the relation

$$F_v = -237 + 3.14\left(\frac{\mathrm{Re}}{1-\phi}\right)^{0.89}, \tag{11}$$

but approximate confidence envelopes constructed with the aid of the bootstrap suggest that these relations may be combined without loss of underlying physical insight. The nonlinear analog of Eq. (8) was shown to be

$$F_v = 3.09\left(\frac{\mathrm{Re}}{1-\phi}\right)^{0.90}. \tag{12}$$

In total, the statistical analysis supports the combination of the various correlations, for the stated test conditions, into a single linear relationship.

While it is quite reasonable to suspect an interaction between the geometry of tube and packing, perhaps reflected through the ratio D_c/D_b, more extensive testing is required to establish this relation. Hopefully, this will be done in accordance with a formal statistical experimental design to minimize testing and maximize information gain.

Acknowledgments

Professor Herman Krier, University of Illinois, and Mr. F. W. Robbins, Army Research Laboratory, made available the raw data that were the basis of this meta-analysis. Mr. M. W. Coleman, Army Research Laboratory, performed the bootstrap computations. A referee emphasized the mathematical compatibility of these results with previous work and contributed to the cohesiveness of this paper.

References

Draper, N. R., and Smith, H., 1981, *Applied Regression Analysis*, 2nd ed., Wiley, New York, pp. 458-459.

Efron, B., 1979, "Computers and the Theory of Statistics: Thinking the Unthinkable," *SIAM Review*, Vol. 21, pp. 460-480.

Efron, B., 1982, *The Jackknife, the Bootstrap and Other Resampling Plans*, SIAM Monograph 38, Philadelphia.

Efron, B., and Tibshirani, R., 1985, "The Bootstrap Method for Assessing Statistical Accuracy," Department of Statistics Tech. Rept. No. 4, University of Toronto.

Ergun, S., 1952, "Fluid Flow Through Packed Columns," *Chemical Engineering Progress*, Vol. 48, No. 2, Feb., pp. 89-94.

Glass, G. V., 1976, "Primary, Secondary, and Meta-Analysis of Research," *Educational Researcher*, Vol. 5, pp. 3-8.

Hedges, L. V., 1987, "How Hard is Hard Science, How Soft is Soft Science? The Empirical Cumulativeness of Research," *American Psychologist*, Vol. 42, No. 2, pp. 443-455.

Hedges, L. V., and Olkin, I., 1985, *Statistical Methods for Meta-Analysis*, Academic Press, New York.

Jones, D. P., 1980, "Friction Factors for Packed Beds at Reynolds Numbers Greater than 10^3," Master's thesis, University of Illinois.

Jones, D. P., and Krier, H., 1983, "Gas Flow Resistance Measurements Through Packed Beds at High Reynolds Numbers," ASME JOURNAL OF FLUIDS ENGINEERING, Vol. 105, pp. 168-173.

Kuo, K. K., and Nydegger, C. C., 1978, "Flow Resistance Measurements and Correlation in a Packed Bed of WC 870 Ball Propellants," *Journal of Ballistics*, Vol. 2, No. 1, pp. 1-25.

LePage, R., and Billard, L., 1992, *Exploring the Limits of Bootstrap*, Wiley, New York.

Montgomery, D. C., 1991, *Design and Analysis of Experiments*, 3rd ed., Wiley, New York.

Robbins, F. W., and Gough, P. S., 1978, "Experimental Determination of Flow Resistance in Packed Beds of Gun Propellant," *Proceedings of the 15th JANNAF Combustion Meeting*, CPIA Pub. 297, Sept.

Robbins, F. W., and Gough, P. S., 1979, "Influence of Length and Diameter of Cylinders on Packed Bed Flow Resistance," *Proceedings of the 16th JANNAF Combustion Meeting*, CPIA Pub. 308, Dec.

Touloukian, Y. S., 1975, "Reference Data on Thermophysics," H. A. Skinner, ed., *International Review of Science—Physical Chemistry: Vol. 10, Thermochemistry and Thermodynamics*, Butterworth, London, pp. 119-146.

A Two-Temperature Model for Turbulent Flow and Heat Transfer in a Porous Layer

V. Travkin
Mem. ASME

I. Catton
Professor. Fellow ASME

Mechanical, Aerospace and Nuclear Engineering Department,
University of California,
Los Angeles, CA 90034-1597

A new model of turbulent flow and of two-temperature heat transfer in a highly porous medium is evaluated numerically for a layer of regular packed particles. The layer can have heat exchange from the defining surfaces. The commonly used models of variable morphology functions for porosity and specific surface were used to obtain comparisons with other works in a relatively high Reynolds number range. A few outstanding features of the closure models for additional integral terms in equations of flow and heat transfer are advanced. Closures were developed for capillary and globular medium morphology models. It is shown that the approach taken to close the integral resistance terms in the momentum equation for a regular structure can be obtained in a way that allows the second order terms for laminar and turbulent regimes to naturally occur. These terms are taken to be close to the Darcy term or Forchheimer terms for different flow velocities. The two-temperature model was compared with a one-temperature model using thermal diffusivity coefficients and effective coefficients from various authors. Calculated pressure drop along a layer showed very good agreement with experiment for a porous structure of spherical beads. A simplified model with constant coefficients was compared with analytical solutions.

1 Introduction

It is believed that the best results in porous media transport modeling are be achieved by following the most consistent and comprehensive methodology to take into consideration the assumed or assigned medium morphology. The problem, until recently, was in finding ways of developing mathematical statements which could describe not only common physical notions but rather the precise interconnection between porous medium morphology and its manifestation in the equation statements. Most researches have been made using convenient description of porous medium in "common" features.

Experimental investigation of heat transfer from a wall with the constant temperature in highly porous media $0.94 \leftarrow m_0 \leftarrow 0.97$, was performed by Hunt and Tien (1988a,b). Nield (1991) expressed some doubts about the terms in the final form of the averaged momentum equation. Slow laminar flow and heat transfer through a porous flat channel with isothermal boundaries were considered in the research of Kaviany (1985). The solution of the equations used by Kaviany, close to those used by Vafai and Tien (1981), showed the influence a porous medium morphology parameter $\gamma = (h^2 m_0/K)^{1/2}$. In the work by Vafai and Thiyagaraja (1987) the effects of flow and heat transfer near an interface region between two porous media, porous medium and fluid region and near solid wall were investigated employing the governing equations with constant porosities. Influence of three parameters on heat and laminar momentum transport in two-dimensional porous medium have been studied in the work by Vafai and Sozen (1990). Namely there were parameters of particle Reynolds number Re_p, Darcy number Da, and the ratio of the solid to vapor phase diffusivities. There was found that Da number is the most important factor in determining the assumption of local thermal equilibrium.

A few preliminary notions and comparisons regarding the increasingly detailed description of transport processes in porous media (see, for example, works by Hayes, 1990; Ward, 1964; Du Plessis and Masliyah, 1988) were made in papers by Travkin and Catton (1992a,c). There is a noticeable lack of experimental measurements of the real characteristics inside the porous medium. The absence of appropriate experimental methods has been the explanation. In an article recently published by Georgiadis et al. (1991) there were very interesting figures with the averaged structure, shown in small scale details, of porosity and velocity functions across a tube containing a packed bed. Unfortunately, the paper does not contain the needed details of the experiment such as the local Reynolds number, the distribution of specific surface, and descriptions of the porous medium inner channels, which could be, and most likely will be established by exploiting the experimental technique.

It is our view that more attention should be focused on the theoretical development needed to understand turbulent flow and heat and mass transfer exchange in the channels of complex configurations with various wall roughness, and conse-

Contributed by the Fluids Engineering Division for publication in the JOURNAL OF FLUIDS ENGINEERING. Manuscript received by the Fluids Engineering Division April 12, 1993; revised manuscript received October 5, 1994. Associate Technical Editor: O. C. Jones.

quently, on well described structures of porous media, since there are very few physically substantiated and fully developed theories.

2 Development of Turbulent Transport Models in Highly Porous Media

Let us assume that the obstacles in a globular porous medium structure and the channels between them are arranged randomly. A regular arrangement of obstacles is far more easily studied than a randomly nonhomogeneous one. The former has all of the merits of a canonical model which is suitable both for comparison with experiment and exact solutions as well as for treating conducting boundary transitions in the course of simulation of a process.

Derivation of the equations of turbulent flow and diffusion for a highly porous medium during the filtration mode is based on the theory of averaging over a certain REV (representative elementary volume) $\Delta\Omega$ (Whitaker, 1967) of the turbulent transfer equation in the fluid phase and the transfer equations in the solid phase of a heterogeneous medium (Primak et al. 1986; Scherban et al., 1986). Modeling of heterogeneous (two energy equation) non-Darcian flow for transient operation of a particle bed has not, thus far, been fully investigated. Experimental studies have revealed that at high Peclet numbers, transient operations in packed beds cannot be modeled correctly with a single energy equation for the medium. The tur-

Nomenclature

A_4 = morphology similarity number [−]
b = mean turbulent fluctuation energy [m^2/s^2] = $1/2\ \overline{u_i' u_i'}$
B_1 = similarity number in turbulent kinetic energy equation [−]
c_d = mean drag resistance coefficient in the REV [−]
c_{dm} = drag resistance scale and similarity number [−]
c_{dp} = mean form resistance coefficient in the REV [−]
c_{fL} = mean skin friction coefficient over the laminar region inside of the REV [−]
c_p = specific heat [J/(kg K)]
C_1 = constant coefficient in Kolmogorov turbulent exchange coefficient correlation [−]
Da = Darcy number [−] = K/H^2
d_{ch} = character pore size in the cross section [m]
d_p = particle diameter [m]
dS = interphase differential area in porous medium [m^2]
∂S_w = internal surface in the REV [m^2]
f = averaged over $\Delta\Omega_f$ value f
$\langle f \rangle_f$ = value f, averaged over $\Delta\Omega_f$ in a REV
$\hat{f}$ = value f morpho-fluctuation in a $\Delta\Omega_f$
H = width of the channel [m]
h = half-width of the channel [m]
h_r = pore scale microroughness layer thickness [m]
K = permeability [m^2]
K_b = turbulent kinetic energy exchange coefficient [m^2/s]
k_f = fluid thermal conductivity [W/(m K)]
$k_{f,e}$ = effective thermal conductivity of fluid [W/(m K)]
k_m = stagnant effective conductivity of porous medium [W/(m K)]
k_s = solid phase thermal conductivity [W/(m K)]
$\tilde{K}_m$ = averaged turbulent eddy viscosity [m^2/s]
K_{sT} = effective thermal conductivity of solid phase [W/(m K)]
K_T = turbulent eddy thermal conductivity [W/(m K)]
K_w = similarity number in eddy viscosity boundary condition [−]
l = turbulence mixing length [m]
L = scale [m]
m = porosity [−]
$\langle m \rangle$ = averaged porosity [−]
m_0 = mean porosity [−]
Nu_w = Nusselt number on the external wall [−]
Nu_f = Nusselt number across the porous layer [−]
p = pressure [Pa] and pitch in regular porous 2-D and 3-D medium [m]
Pe = local Peclet number [−]
Pr = Prandtl number [−]
Pr_T = turbulent Prandtl number [−] = K_m/K_T
Q_0 = outward heat flux [W/m^2]
Q_{w2} = similarity number in the boundary conditions for temperatures [−]
r_k = heat conductivity parameter [−]
Re_{ch} = Reynolds number of pore hydraulic diameter [−]
Re_p = particle Reynolds number [−] = $\tilde{u}\, d_p/\nu$
S_w = specific surface of a porous medium $\partial S_w/\Delta\Omega$ [1/m]
S_{wm} = characteristic scale for a specific surface [1/m]
S_{wp} = cross flow form specific surface [1/m]
S_{w0} = mean specific surface [1/m]
T = temperature [K]
T_a = characteristic temperature for given temperature range [K]
T_m = convective fluid temperature scale in the porous layer [K]
T_{fm} = mean convective fluid temperature across the porous layer [K]
T_s = averaged over $\Delta\Omega_s$ temperature [K]
T_w = wall temperature [K]
T_0 = reference temperature [K]
u = velocity in x-direction [m/s]
u_0 = mean velocity in the layer [m/s]
u_∞ = velocity outside of the momentum boundary layer (at the center of the porous layer) [m/s]
V_D = Darcy velocity [m/s]
w = velocity in z-direction [m/s]

Subscripts

e = effective
f = fluid phase
i = component of turbulent vector variable
k = component of turbulent variable that designates turbulent "microeffects" on a pore level
L = laminar
m = scale value
r = roughness
s = solid phase
T = turbulent

Superscripts

$\sim$ = value in fluid phase averaged over the REV
$-$ = mean turbulent quantity
$'$ = turbulent fluctuation value
$*$ = nondimensional value

Greek Letters

$\tilde{\alpha}_T$ = averaged heat transfer coefficient over ∂S_w [$W/(m^2K)$]
$\tilde{\alpha}_{T,m}$ = mean heat transfer coefficient across the layer [$W/(m^2K)$]
α_{Tm} = characteristic heat transfer coefficient scale [$W/(m^2K)$]
α_s = heat transfer parameter [$W/(m^2K)$]
α_w = heat transfer coefficient at the wall [$W/(m^2K)$]
$\Delta\Omega$ = representative elementary volume (REV) [m^3]
$\Delta\Omega_f$ = pore volume in a REV [m^3]
$\Delta\Omega_s$ = solid phase volume in a REV [m^3]
σ_b = turbulent coefficient exchange ratio $\tilde{K}_m/K_b$ [−]
σ_T = turbulent coefficient exchange ratio $\tilde{K}_m/\tilde{K}_T$[−]
μ = dynamic viscosity [Pa s]
ν = kinematic viscosity [m^2/s]
ρ = density [kg/m^3]

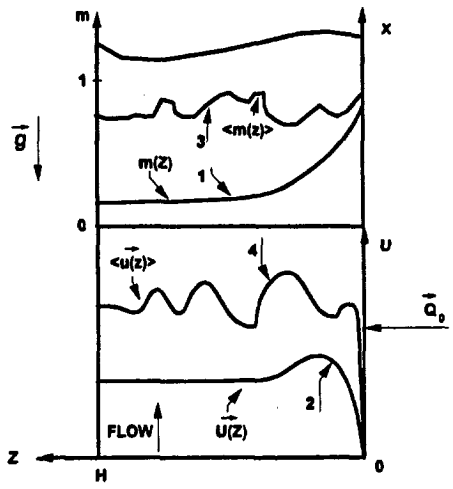

Fig. 1 Typical and actual flow and porosity properties in a porous layer: 1–2 typical profiles, 3–4 actual profiles

bulent transport statement set was considered here for the case of turbulent flow in a highly porous layer (Fig. 1) combined with a two energy equation model. The transfer equations for each of the phases are used with some simplification, determined by the turbulence order and medium regularness (Travkin and Catton, 1992b).

The REV in the porous layer is defined as the volume contained in a plane rectangular region parallel to the subsurface or a disk whose horizontal dimensions are far greater than characteristic dimensions of obstacles and infinite in one transverse direction. In the vertical direction perpendicular to the subsurface, the REV thickness is considerably smaller than that in the horizontal directions. The structure of selected REV forms is dictated by features of the highly porous layer medium and, specifically, by the length of its scales in different directions. Similar modeling assumptions about the macrovolume orthotropy, in the course of averaging, have been made (Whitaker 1967, Immich 1980) on the basis of specific features by posing the problems from a physical standpoint. The equations for turbulent boundary transfer in a porous layer under steady-state conditions and with penetration through an interface which were derived by Scherban et al. (1986) and augmented by Travkin and Catton (1992a,b,c) can be simplified to the following (see Appendix A)

$$\frac{\partial}{\partial x}(\langle m\rangle\tilde{\bar{u}}) + \frac{\partial}{\partial z}(\langle m\rangle\tilde{\bar{w}}) + \frac{1}{\Delta\Omega}\int_{\partial S_w}(\tilde{\bar{u}}_j + \hat{\bar{u}}_i)\cdot d\mathbf{S} = 0,$$

$$\langle m\rangle\tilde{\bar{u}}\frac{\partial\tilde{\bar{u}}}{\partial x}\langle m\rangle\tilde{\bar{w}}\frac{\partial\tilde{\bar{u}}}{\partial z} - \frac{\tilde{\bar{u}}}{\Delta\Omega}\int_{\partial S_w}(\tilde{\bar{u}}_l + \hat{\bar{u}}_i)\cdot d\mathbf{S} =$$

$$-\frac{1}{\rho}\frac{\partial}{\partial x}(\langle m\rangle\tilde{\bar{p}}) + \frac{\partial}{\partial z}[\langle m\rangle(\overline{-u_k'w_k'})] + \langle m\rangle\tilde{\bar{F}}_i -$$

$$\frac{\partial}{\partial z}(\langle\hat{\bar{u}}\hat{\bar{w}}\rangle_f) - \frac{1}{\Delta\Omega}\int_{\partial S_w}\bar{u}_j\bar{u}_i\cdot d\mathbf{S} - \frac{1}{\rho\Delta\Omega}\int_{\partial S_w}\bar{p}d\mathbf{S} -$$

$$\frac{1}{\Delta\Omega}\int_{\partial S_w}\overline{u_{jk}'u_i'}\cdot d\mathbf{S}, \quad j = 1, 3. \qquad (1)$$

The term with $\tilde{F}_i$ will specifically reflect the impact of microroughness and augment the previous level of the simulation hierarchy. The importance of this roughness has been shown by many authors. A one-dimensional model, under steady-state conditions and other simplifications, with no flow penetration through ∂S_w, for a homogeneous stream, described in the works by Travkin and Catton (1992b,c).

3 Development of Closure Models for Some Regular Capillary and Globular Kinds of Porous Media

There exist two main approaches to the development of closure models for non-Darcian or turbulent two-phase transport equations in highly porous media. It is implied that these equations are properly derived, yet they are now in doubt. The first approach is to develop an appropriate turbulence model. The second is to treat the numerous integrated and covariant terms in averaged transport equations.

To deal with uncertainties in determining and modelling effective coefficients in each phase, more fundamental developments are required. Among the problems that remain beyond the development of quantitative approaches, is, more importantly, the development of a general approach that can account for real differences between the structural and physical properties of each of the porous medium components. In most cases, researchers have not clearly described the simplifying assumptions they used to obtain the averaged equations and transport coefficient models. For example, models for transport coefficients are derived without any real consideration of the medium morphology or the introduction of a different averaging technique. According to a common and well-known approach, the simplest porous medium morphological models are the following

(A) Capillary (porous) models:
   1. A bundle of parallel tubes, all of the same diameter, d.
   2. A bundle of parallel slits, all of the same width, h, embedded in a solid, including numerous variations of the parallel tube and slit model.

(B) Globular morphology models:
   1. A set of one size beads (spheres) uniformly or nonuniformly placed in a fluid—this model is known as the "dusty-gas" model.
   2. A sets of parallel tubes, having definite distributions of diameter and spatial parameters.

All of the foregoing morphology simplifications have been exploited for laminar fluid flow (see, for example Kheifets and Neimark, 1982; Dullien, 1992 and other's successive works). Closure models have been achieved for turbulent flow in porous media and for diffusion models when fluctuations are ignored in the works by Travkin and Catton (1992a,c; 1993) and Gratton et al. (1993). The fundamental distinction between the resistance models presented in these works and those exploited before is the second power of velocity in all additive terms and for either laminar or turbulent regimes. The closure model is simple and presents a clear physical problem statement as well as incorporating three additional terms. The velocity power difference can be determined by another initial approach and consequently another initial set of equations along with the natural closure procedures considering a realistic assumption of the morphology structure of porous medium. In section 4, it will be shown that most experimental correlations can be related to the present work. Watanabe (1989) obtained a similar second power result for pressure drop dependence for granular packed beds when he used the drag force law for a single isolated sphere to derive the pressure drop formula for beds. It is an example of an attempt to accurately take into account the assumed morphology of a porous medium while evaluating it's numerical characteristics.

4 Transport Coefficients for Definite Kinds of Medium Morphology

In recent years, determination of effective transport coefficients has received considerable attention by researchers who are studying the transport of heat (or a conservative solute)

through fully-saturated porous media by advection and diffusion. Georgiadis and Catton (1986) showed that the Forchheimer-Brinkman extended model could explain the divergence of the Nusselt versus Rayleigh number data in terms of a new parameter which depends on the porous medium Prandtl number and the ratio d/L. The "effective" thermal conductivity of the medium was identified with its "stagnant" value obtained under no-flow conditions. In view of certain discrepancies between predicted and measured Nusselt number values for the porous Bénard problem, Georgiadis and Catton (1987) revised the constant conductivity model. They used a single energy equation with an "effective" thermal conductivity expressed as a linear function of the local Pe number

$$k = k_m + c\mathrm{Pe}. \tag{2}$$

Here it should be noted that linearly combining the second term with the stagnant mix thermal conductivity is an oversimplification of the physics.

In considering a porous medium canonically formed from tubes and slits, we will review some existing theoretical derivations and unify the various points of view and conclusions. One type of porous media will be considered with its various mathematical incarnations for the flat porous layer momentum equation. Momentum equation given by Vafai and Kim (1989),

$$\frac{\partial^2(\langle m\rangle\tilde{u})}{\langle m\rangle\,\partial z^2} = \frac{\langle m\rangle}{K}\tilde{u} + \frac{\langle m\rangle^3}{\nu}\frac{F}{K^{1/2}}\tilde{u}^2 + \frac{1}{\mu}\frac{d\tilde{p}}{dx}, \tag{3}$$

Poulikakos and Renken (1987)

$$\frac{\partial^2\tilde{u}}{\partial z^2} = \frac{1}{K(z)}\tilde{u} + \frac{A(z)}{\nu}\tilde{u}^2 + \frac{1}{\nu\rho_f}\frac{d\tilde{p}}{dx}, \tag{4}$$

and by this work

$$\frac{\partial}{\partial z}\left[\langle m\rangle\frac{\partial\tilde{u}}{\partial z}\right] = \frac{1}{2\nu}[c_{fL}S_w + c_{dp}S_{wp}]\tilde{u}^2 + \frac{1}{\nu\rho_f}\frac{d\langle p\rangle_f}{dx},$$
$$\langle p\rangle_f = \langle m\rangle\tilde{p}, \tag{5}$$

for the laminar regime momentum equation are considered. Further, drag resistance relationships derived from these equations for the middle part of the channel where the porosity is constant are, Vafai and Kim (1989) equation

$$-\frac{d\tilde{p}}{dx} = \frac{\mu}{K(z)}\langle m\rangle\tilde{u} + \rho_f\langle m(z)\rangle^3\frac{F}{K_{(z)}^{1/2}}\tilde{u}^2, \tag{6}$$

Poulikakos and Renken (1987) equation

$$-\frac{d\tilde{p}}{dx} = \frac{\mu}{K(z)}\tilde{u} + \rho_f A(z)\tilde{u}^2, \tag{7}$$

as well as the Ergun's (1952) relation

$$\frac{\Delta p}{L} = -\frac{d\tilde{p}}{dx} = \frac{\mu}{K(z)}\langle m(z)\rangle\tilde{u} + \rho_f A(z)\,\langle m(z)\rangle^2\tilde{u}^2, \tag{8}$$

and that obtained from this work for the laminar regime (turbulent or combined regime c_d should be calculated accordingly to the closure schemes)

$$-\frac{d\tilde{p}}{dx} = \left[c_{fL} + c_{dp}\frac{S_{wp}}{S_w}\right]\frac{S_w(z)}{\langle m(z)\rangle}\left(\frac{\rho_f\tilde{u}^2}{2}\right) = c_d\frac{S_w(z)}{\langle m(z)\rangle}\left(\frac{\rho_f\tilde{u}^2}{2}\right), \tag{9}$$

where

$$c_d = \left[c_{fL} + c_{dp}\frac{S_{wp}}{S_w}\right],$$

is drag resistance coefficient in a porous medium. These correlations of drag resistance can be evaluated for packed beds by noting that the last expression is the experimental relationship for pressure drop in packed beds

$$\frac{\Delta p}{L} = f\left(\frac{S_w}{\langle m\rangle}\right)\left(\frac{\rho_f\tilde{u}^2}{2}\right). \tag{10}$$

It can be seen that a good approximation for nearly-constant or large-scale nonuniform porosity is given by

$$c_d \cong f, \tag{11}$$

where f is taken from experimental correlations. It is easy to see that this approximation for resistance forces is restricted by variability of the morphology functions $m(x)$, S_w and others. Ergun's relation in terms of the previous formulae will be

$$\frac{\Delta p}{L} = f_{ER}\left(\frac{S_w}{\langle m\rangle}\right)\frac{\rho_f\tilde{u}^2}{2}, \tag{12}$$

where

$$f_{ER} = \frac{A}{\mathrm{Re}_{ch}} + B, \quad A = 33.33, \quad B = 0.583,$$

and for spherical particles

$$\mathrm{Re}_{ch} = \frac{2}{3}\frac{\langle m\rangle}{(1-\langle m\rangle)}\frac{\tilde{u}d_p}{\nu}.$$

These parameters are very close to those of the Klenov and Matros (1990) correlation with $A_{ch} = 36.3$ and $B_{ch} = 0.45$ for spherical particles and $A_{ch} = 37.6$ and $B_{ch} = 0.585$ for cylindrical particles. The formula for drag resistance of a spherical particle bed derived from Watanabe (1989) results in a drag resistance coefficient that corresponds to the present notation

$$f_w = c_{sph}\,25(1-\langle m\rangle)/12 = c_{d,w}, \tag{13}$$

where c_{sph} is the drag resistance coefficient of a single isolated bead of diameter d_p. The drag resistance coefficient derived from the correlations of Fand and Thinakaran (1990), for a large range of Reynolds numbers

$$10^{-5} < \mathrm{Re}_{sph} = d_p u/\nu < \approx 0(10^3),$$

is

$$c_{d,ft} = f_{ft} = 2A/(9\mathrm{Re}_{ch}) + B/3, \tag{14}$$

where A and B are given by Fand and Thinakaran (1990). The drag resistance coefficient for spherical particles in the Darcy regime is

$$c_{\mathrm{dar}} = f_{\mathrm{dar}} = 42.72/\mathrm{Re}_{ch}. \tag{15}$$

These relationships were used in the modeling procedures as well as the ideal parallel pores morphology model (see Travkin and Catton, 1992a,c) resistance coefficients for rough pores and rough flat surfaces developed by Taylor et al. (1985).

To evaluate the heat transfer coefficient using various known methods it is helpful to start with the analysis done in the review papers of, for example, Kaguei et al. (1983). Kokorev et al. (1987) established an interesting correlation between drag coefficient and heat transfer coefficient for turbulent flow in porous medium that contains only one empirical (apparently universal) constant. On the basis of this relationship, a concept of fluctuation speed scale of movement, is used to determine an expression for the heat transfer coefficient

$$\tilde{\alpha}_T = \frac{k_f}{d_p}(0.14\,(c_d\mathrm{Re}_{ch}^3)^{1/4}\mathrm{Pr}^{1/3}). \tag{16}$$

The many heat transfer expressions given in the *Heat Exchanger Design Handbook* (1983) and based on the use of a single sphere heat transfer coefficient for the porous medium, were used in this work as well. Direct simulation of variable morphology functions for regular spherical beads packing is explained in a paper by Gratton et al. (1993).

5 Numerical Method of Equation Solution

The governing equations (Travkin and Catton, 1992a) are cast into dimensionless form using the following scales

$$z_m = x_m = \frac{m_0}{S_{wm}}, \quad u_m = \left(-\frac{z_m}{\rho_f}\frac{d\tilde{p}}{dx}\right)^{1/2}, \quad b_m = u_m^2,$$

$$T_m = \frac{z_m Q_0}{K_{Tm}}, \quad K_{mm} = z_m u_m, K_{Tm} = K_{mm} c_{pf}\rho_f,$$

$$S_{wm} = \frac{6(1-m_0)}{d_p} \vee S_{w0}, m_0, \quad \alpha_{Tm} = \frac{K_{Tm}}{z_m}, \quad c_{dm} = \frac{2u_m^2}{u_0^2}. \tag{17}$$

The scaled governing equations are

$$\frac{\partial}{\partial z^*}\left[\langle m^*\rangle K_m^* \frac{\partial u^*}{\partial z^*}\right] = \frac{1}{2} c_{dm} c_d^* S_w^* u^{*2} - A_4, \tag{18}$$

where

$$A_4 = \frac{1}{m_0},$$

$$K_m^*\left(\frac{\partial u^*}{\partial z^*}\right)^2 + \frac{d}{dz^*}\left(K_b^*\frac{db^*}{dz^*}\right) + c_{dm}\left(\frac{c_d^* S_w^*}{\langle m^*\rangle}\right) u^{*3} - 2K_w\left(\frac{db^{*1/2}}{dz^*}\right)^2 - B_1 K_m^* \frac{\partial T_f^*}{\partial z^*} = C_1 \frac{b^{*2}}{K_m^*}, \tag{19}$$

where

$$K_w = \frac{\nu}{z_m u_m}, \quad B_1 = \frac{T_m z_m g}{u_m^2 T_a \sigma_T}, \quad K_b^* = \left(\frac{K_m^*}{\sigma_b} + \frac{\nu}{z_m u_m}\right),$$

$$K_m^* = C_1^{1/4} l(z^*) b^{*1/2}, \tag{20}$$

$$\langle m^*\rangle u^*(z^*)\frac{\partial T_f^*(x^*, z^*)}{\partial x^*} = = \frac{\partial}{\partial z^*}\left[K_T^* \langle m^*\rangle \frac{\partial T_f^*}{\partial z^*}\right] + \alpha_t^* S_w^*[T_s^*(x^*, z^*) - T_f^*(x^*, z^*)], \tag{21}$$

where

$$\langle m^*\rangle = \langle m^*(z^*)\rangle, \quad \alpha_T^* = \alpha_T^*(u^*, m^*, S_w^*), \quad S_w^* = S_w^*(z^*),$$

and

$$\frac{\partial}{\partial z^*}\left[(A_4 - \langle m^*\rangle) K_{ST}^* \frac{\partial T_z^*}{\partial z^*}\right] = \alpha_T^* S_w^* [T_s^* - T_f^*]. \tag{22}$$

The scaled boundary conditions are

$$z^* = 0: \quad u^* = 0, \quad K_m^*|_{z^*=+0} = K_w,$$

$$-K_T^*\left.\frac{\partial T^*}{\partial z^*}\right|_{z^*=+0} = -K_{ST}^*\left.\frac{\partial T_z^*}{\partial z^*}\right|_{z^*=+0} = Q_{w2}, \quad Q_{w2} = \frac{Q_0}{c_{pf}\rho_f u_m T_m},$$

$$z^* = h^*: \quad \frac{\partial u^*}{\partial z^*} = 0, \quad \frac{\partial b^*}{\partial z^*} = 0, \quad \frac{\partial T^*}{\partial z^*} = 0, \quad \frac{\partial T_z^*}{\partial z^*} = 0. \tag{23}$$

Both the scaling and the thermal transfer boundary conditions influence the general model equation structure. The same similarity number appears in the boundary conditions for the second temperature T_s^*. It is apparent that the main similarity numbers influencing the flow regime solution are the drag resistance similarity number C_{dm} and morphology number A_4. The value of the mixing length calculated using the porous medium "effective" pore scale was taken

$$l(z) = f_l\left(\frac{4\langle m(z)\rangle}{S_w(z)}\right), \quad z > l(z),$$

$$l(z) = f_w(z), \quad z \le \frac{4\langle m(z)\rangle}{S_w(z)}. \tag{24}$$

The set of governing equations consists of highly nonlinear second-order ordinary and partial parabolic differential equations. Solutions for the equation set were obtained mainly using finite difference methods described in papers by Travkin (1981, 1984, 1985). The finite difference schemes have incorporated a special local augmentation to deal with both numerical dissipation and diffusion. Solutions of the set of equations are sought using an uneven gridding and discontinuous coefficients. The last implementation is desirable because one can treat the highly variable or random coefficients in the equations. Most of the calculations were performed using 201 nodes across the layer. Comparisons of 200 node calculations with 401 and 501 nodes show local difference to be less then 1–3 percent. The Nusselt number at the wall is defined

$$\mathrm{Nu}_w = \left(-\left(\frac{\partial T}{\partial z}\right)\frac{h}{(T_w - T_{fm})}\right)\Bigg|_{z=+0}, \tag{25}$$

and inside of the porous medium

$$\mathrm{Nu}_z = \tilde{\alpha}_T(z) h/\tilde{K}_T(z), \quad 0 \le z \le h. \tag{26}$$

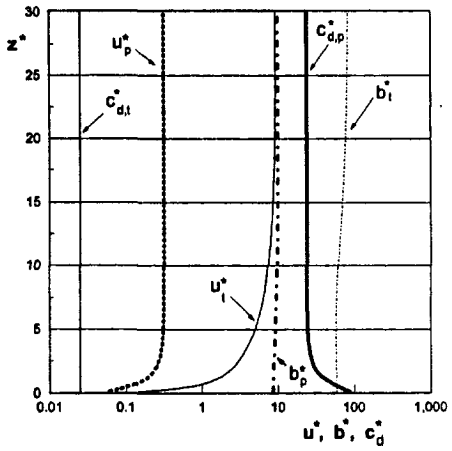

Fig. 2 Influence of porous medium morphology structure on the velocity u^*, kinetic energy b^*, and drag resistance c_d^*, in tube morphology model: $A_4 = 1.25$; $c_{dm} = 0.025$; $B_1 = 37.4$; $K_w = 0.0842$; spherical beads model: $c_{dm} = 279.5$; and the same other similarity numbers, indexes: t—tube model; p—spherical particles model

6 Results and Discussion

The thermophysical properties an air-steel porous media were chosen for numerical simulation with temperature boundary similarity number Q_{w2} scaled as 1. The regular and random porous structure of spherical packing were introduced by taking the coefficient correlations, while the mathematical statements in Eqs. (18)–(23) were developed with the respect of only regular particle locations. At the present time, there is little reliable data showing the difference between regular and random and regular (periodic) structure of the porous medium granules. For most of the calculated results the differences between the experimental pressure drop for spherical randomly located particles and the present work using experimental drag resistance correlations were less than 1–3 percent due to the overall bulk character of the experimental correlations. Figure 2 presents comparisons of some profiles for tube and nonstructured porous medium morphology models. It can be seen that it is inappropriate to use canonical morphology models as simple as regular straight tubes to represent a highly porous media morphology.

Figure 3 shows the profiles of drag resistance coefficient for different porous medium morphology. The difference in an admitted morphology structure resulted in four order change of magnitude of the resistance similarity number c_{dm} and consequently resulted in big differences in the temperature and Nusselt numbers. The Nusselt numbers as well as temperatures of the solid and fluid phases and other characteristics along the

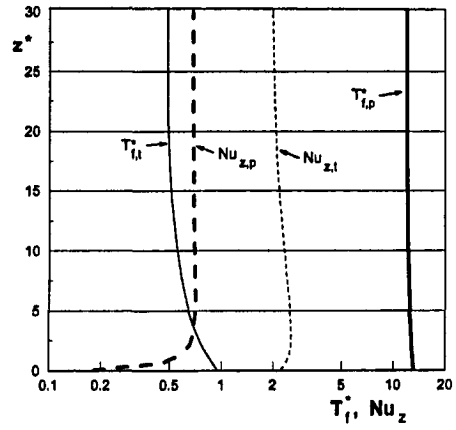

Fig. 3 Influence of porous medium morphology structure on the fluid temperature and local Nusselt number across the layer (see Fig. 2 for indexes)

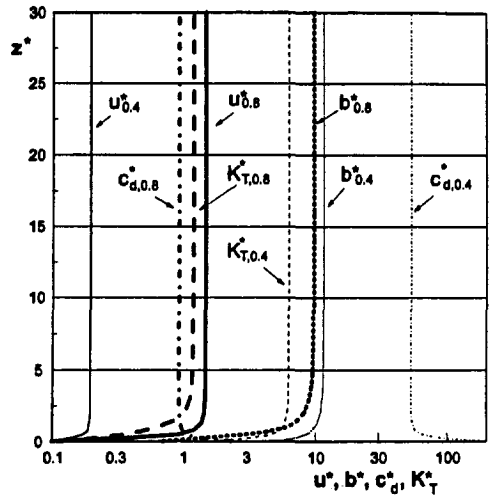

Fig. 5 Influence of porosity value on the characteristics of regular spherical beads porous medium morphology (see for indexes and similarity numbers Fig. 4)

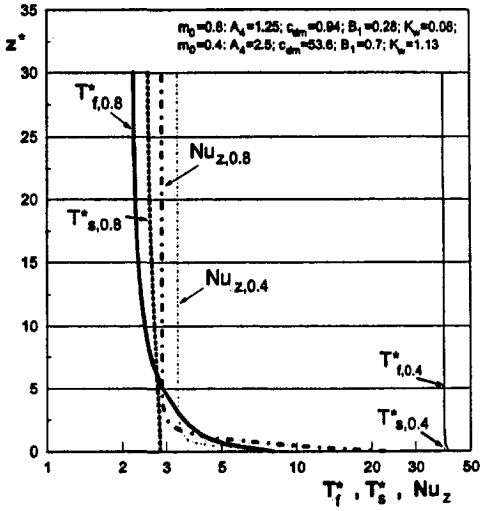

Fig. 4 Influence of porosity value on T^*_f, T^*_s, and Nu_z of regular spherical beads porous medium morphology, indexes: 0.4—porosity m_0 = 0.4; 0.8—m_0 = 0.8

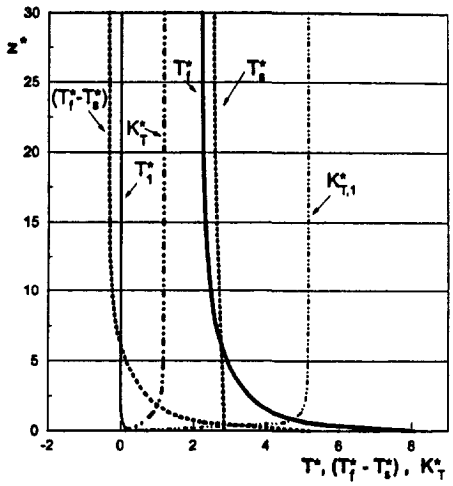

Fig. 6 Comparison of 2- and 1-temperature (T^*_f, $K^*_{T,1}$) models: m_0 = 0.8 (see Fig. 4 for similarity numbers)

channel are seen to depend strictly on the drag resistance, c_{dm}, and morphology, A_4, functions (see Figs. 4 and 5). These figures present the influence of varying the porosity value for regular spherical packing. Generalization of experimental measurements of the effective thermal conductivity of fluids in a porous medium are given by Aarov et al. (1979)

$$k_{f,e} = K_{ex}\rho_f c_{pf}\tilde{u}d_{ch}, \quad K_{ex} = 0.07 - 0.11. \tag{27}$$

The experiments by Kharitonov et al. (1987) showed that $K_{ex} = 0.075 \pm 0.009$ for water in the range $Re_{ch} = 11$–1500. The coefficient of effective thermal conductivity in a fluid, calculated as the coefficient of turbulent eddy thermal conductivity in this work,

$$k_{f,e} = m_0(\tilde{K}_T + k_f), \tag{28}$$

yielded values within ten to twenty percent without modification of any important constants C_1 nor the value of the mixing length. The initial value of the first was taken from boundary layer theory, whereas the second is the simple "effective" pore diameter in a regular spherical porous medium. There are three theoretical investigations, that are close to the present work mathematical statement for low velocity regime. All are analytical solutions. In the paper of Plakseev and Kharitonov (1988), a two-temperature model for a porous layer is solved for constant coefficients with an assigned heat flux on one wall, a restricted II-d kind boundary conditions on the other wall, and a constant value of velocity along the layer. In the work of Vafai and Kim (1989) (see also Vafai and Thiyagaraja, 1987) primary interest was paid to an approximate analytical solution of the momentum equation with constant coefficients. The analytical solution for the combined momentum equation of Vafai and Kim (1989) was compared to the mean values of velocity and gave the difference less than 3 percent for slow regimes.

Solution of the momentum part of the model statement, Eqs. (18)–(20), allows one to obtain an effective thermal conductivity of the fluid. It was incorporated into the weighted value of the effective 1-temperature thermal conductivity of a homogenized medium. In spite of large, and sometimes much larger effective thermal coefficients of conductivity in 1-temperature model, the values of the homogeneous temperature in a 1-temperature model were much smaller for the air-steel porous medium physical characteristics (Fig. 6). One should not be surprised by this result, because in models of the air-steel pair, analyzed in this work, the parameter

$$\alpha_s = (K_{ST}(1 - m_0)\,\tilde{\alpha}_{T,m}S_w)^{1/2}, \tag{29}$$

is the mean coefficient of heat transfer and the maximum capacity of the solid phase to extract energy to the fluid phase (Plakseev and Kharitonov, 1988), is much larger than the coef-

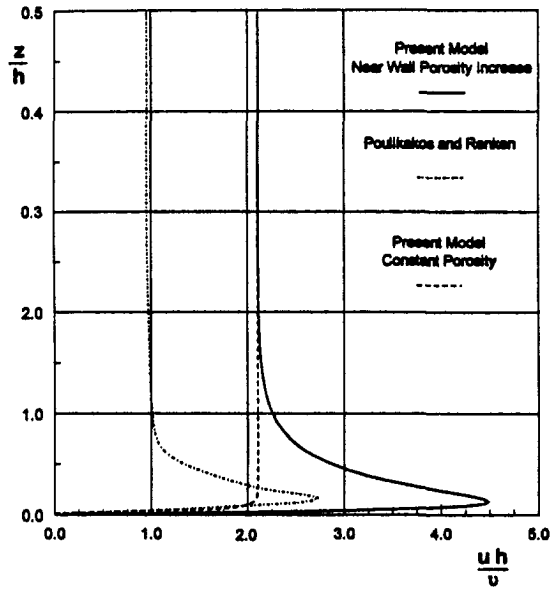

Fig. 7 Comparison of velocity profiles for two models, similarity numbers for present model: A_4 = 2.66; c_{dm} = 412; B_1 = 10.04; K_w = 3.99

ficient of heat transfer from the wall α_w. The latter was calculated independently from the numerical results of this work and from the correlations of Kokorev et al. (1987) and Aarov et al. (1979). The magnitude of α_s calculated in the present work for air-steel is $\alpha_s = 0(10^n)$, $n = 1 - 2$ and it means that almost all heat transfer from the wall is transferred by the solid phase. Also, according to Plakseev and Kharitonov (1988) the ratio $r_k = K_{ST}(1 - m_0)/k_{f,0} < 10$ denotes that most of heat is transmitted to the fluid by means of the heat exchange inside of the porous medium not at its boundaries. Similar result was obtained by Vafai and Sozen (1990) for heat transfer with constant wall temperature in a packed bed formed by the pair Freon-12-steel particles.

The sensitivity of the present model to the morphological characteristics of the porous medium is quite evident while providing the basis for the next numerical experiments. Calculations using the local porosity and specific surface distributions for a regular spherical cubic medium were compared to similar calculations where the only difference is calculation of the overall drag resistance coefficient. Calculations using a c_d model that depends on the local porosity distribution function were compared to the results of experimentally determined c_d values for a single spherical particle. In the latter model, c_d depends on the local particle Reynolds number over a wide range of Reynolds number dependent correlations. When used with the analytical local porosity and specific surface expressions, the model predicted oscillations in the main quantities, such as the drag coefficient and velocity distribution. The single spherical particle drag resistance model displayed both drag coefficient and velocity profile characteristics of beds with constant bulk morphology functions. It appears that while the first model uses the local morphology characteristic variation dependence, the second consists of dependence of the drag resistance only on the bead diameter. More results on variation dependencies of porous medium morphology are given in an article by Gratton et al. (1993).

The present results were compared with the numerical results of Poulikakos and Renken (1987) for flow and heat transfer with constant coefficients inside of a porous layer. The differences shown in Fig. 7 (where the variant of that by Poulikakos and Renken, 1987, is demonstrated with dimensionless parameters $B = -(h^3/(\rho\nu^2))(dp/dx) = 10^5$, dimensionless sphere diameter $d_* = d_p/h = 0.1$, $d_p = 0.005$m, $m_0 = 0.37$) are due to the differences of substantiation of the initial equations and particularly because of a rather contrary interpretation of resistance terms, as was shown in section 5 of this work. The mean characteristics of the comparison are relatively close, with differences being better observed in the boundary layer.

7 Summary

A nonlinear model for two-temperature heat and momentum turbulent transport is presented. All the coefficient models used and discussed in this work are strictly for assumed (or admitted) porous medium morphological models based on well described geometry. This approach shows that to model the morphology of a porous media, the coefficients in the equations, as well as the equation's forms itself must be consistent. The integral terms in the equations can be dropped or transformed depending on the porous medium structure, flow and heat transfer regimes. Developed closure approach allows one to obtain exact analytical closure dependencies for simple porous medium morphologies. Numerical analysis made with the help of parameters suggested by Plakseev and Kharitonov (1988) for heat exchange between wall-fluid, solid-fluid phases shows the impact of heat exchange correlations for α_s, α_w, r_k and reveals the combinations of similarity numbers that depict almost total heat removal from the wall by the solid phase for air-steel porous medium while an intense flow regime occurs.

Acknowledgment

This work was sponsored by the DOE Grant No. DE -FG03 -89ER14033 A002.

References

Aarov, M. A., Todes, O. M., and Narinsky, D. A., 1979, *Apparatuses with Stationary Granular Bed*, Chemistry, Leningrad.

Dullien, F. A. L., 1992, *Porous Media. Fluid Transport and Pore Structure*, Academic Press, New York.

Du Plessis, J. P., and Masliyah, J. H., 1988, "Mathematical Modelling of Flow Through Consolidated Isotropic Porous Media," *Transport in Porous Media*, Vol. 3, No. 2, pp. 145–161.

Ergun, S., 1952, "Fluid Flow Through Packed Columns," *Chemical Engineering Progress*, Vol. 48, pp. 89–94.

Fand, R. M., and Thinakaran, R., 1990, "The Influence of the Wall on Flow Through Pipes Packed with Spheres," ASME JOURNAL OF FLUIDS ENGINEERING, Vol. 112, No. 1, pp. 84–88.

Georgiadis, J. G., and Catton, I., 1986, "Prandtl Number Effect on Benard Convection in Porous Media," ASME *Journal of Heat Transfer*, Vol. 108, No. 2, pp. 284–290.

Georgiadis, J. G., and Catton, I., 1987, "Transport in Pipes Filled with Uniform, Non-Uniform and Random Porous Media," *Proceedings of the Second ASME/JSME Thermal Engineering Joint Conference*, Vol. 2, pp. 395–400.

Georgiadis, J., Behringer, R., Shattuck, M., and Johnson, G. A., 1991, "Interstitial Velocity and Temperature Fields in Fully-Saturated Porous Media," *Proceedings of the Ninth Symposium on Energy Engineering Sciences, Fluid and Dynamical Systems*, Argonne National Laboratory, Argonne, pp. 101–109.

Gratton, L., Travkin, V. S., and Catton, I., 1993, "Transport Coefficient Dependence upon Solid Phase Morphology for Single Phase Convective Transport in Porous Media," *Proceedings of the 29th National Heat Transfer Conference*, HTD-240, ASME, Atlanta, pp. 11–21.

Hayes, R. E., 1990, "Simulation of Mixed Convection Heat Transfer at the Wall of a Packed Bed," *Numerical Heat Transfer: Part A*, Vol. 17, No. 2, pp. 217–230.

Heat Exchanger Design Handbook, 1983, Spalding, B. D., Taborek, J., Armstrong, R. C. and et al., contribs., N.Y., Hemisphere Publishing Corporation, Vol. 1, 2.

Hunt, M. L., and Tien, C. L., 1988a, "Non-Darcian Convection in Cylindrical Packed Beds," ASME *Journal of Heat Transfer*, Vol. 110, No. 2, pp. 378–384.

Hunt, M. L., and Tien, C. L., 1988b, "Effects of Thermal Dispersion on Forced Convection in Fibrous Media," *International Journal of Heat and Mass Transfer*, Vol. 31, No. 2, pp. 301–309.

Immich, H., 1980, "Impulsive Motion of a Suspension: Effect of Anti-Symmetric Stresses and Particle Rotation," *International Journal of Multiphase Flow*, Vol. 6, pp. 441–471.

Kaguei, L., Tanisho, L., and Wakao, N., 1983, "Particle-to-Fluid Heat Transfer Coefficients at Low Flow Rates in Packed Beds—Approaching a Lim-

ited Value or Unlimited Decline?," *Third Pacific Chemical Engineering Congress*, Seoul, Korea, May 8–11, *Proceedings*, Vol. 2, pp. 7–12.

Kaviany, M., 1985, "Laminar Flow Through a Porous Channel Bounded by Isothermal Parallel Plates," *Intern. J. Heat Mass Transfer*, Vol. 28, No. 4, pp. 851–858.

Kharitonov, V. V., Plakseev, A. A., Fedoseev, V. N., and Voskoboinikov, V. V., 1987, "Fluid Flow Mixing Influence on the Heat Transfer in the Porous Insert Channels," *Teplopfizika Visokikh Temperatur*, Vol. 25, No. 5, pp. 954–961.

Kheifets, L. I., and Neimark, A. V., 1982, *Multiphase Processes in Porous Media*, Nedra, Moscow.

Klenov, O. P., and Matros, Yu, Sh., 1990, "Effect of Loading Conditions on the Porosity and Hydraulic Resistance of a Stationary Granular Bed," *Theoretical Foundations of Chemical Engineering*, Vol. 24, No. 2, pp. 206–210.

Kokorev, V. I., Subbotin, V. I., Fedoseev, V. N., Kharitonov, V. V., and Voskoboinikov, V. V., 1987, "On Interconnection of Hydraulic Resistance and Heat Transfer in Porous Media," *High Temperature*, Vol. 25, No. 1, pp. 82–87.

Nield, D. A., 1991, "The limitations of the Brinkman-Forchheimer equation in modeling flow in a saturated porous medium and at an interface," *International Journal of Heat and Fluid Flow*, Vol. 12, No. 3, pp. 269–272.

Plakseev, A. A., and Kharitonov, V. V., 1988, "Heat Transfer in Channels with Porous Inserts during Forced Fluid Flow," *Journal of Engineering Physics*, Vol. 56, No. 1, pp. 26–33.

Poulikakos, D., and Renken, K., 1987, "Forced Convection in a Channel Filled With Porous Medium, Including the Effects of Flow Inertia, Variable Porosity, and Brinkman Friction," ASME *Journal of Heat Transfer*, Vol. 109, No. 4, pp. 880–888.

Primak, A. V., Scherban, A. N., and Travkin, V. S., 1986, "Turbulent Transfer in Urban Agglomerations on the Basis of Experimental Statistical Models of Roughness Layer Morphological Properties," *Transactions World Meteorological Organization Conference on Air Pollution Modelling and its Application*, Geneva, Vol. 2, pp. 259–266.

Scherban, A. N., Primak, A. V., and Travkin, V. S., 1986, "Mathematical Models of Flow and Mass Transfer in Urban Roughness Layer," *Problemy Kontrolya i Zaschita Atmosfery ot Zagryazneniya*, No. 12, pp. 3–10.

Taylor, R. P., Coleman, H. W., and Hodge, B. K., 1985, "Prediction of Turbulent Rough-Wall Skin Friction Using a Discrete Element Approach," ASME JOURNAL OF FLUIDS ENGINEERING, Vol. 107, No. 2, pp. 251–257.

Travkin, V. S., 1981, "Steady Free Convection in the Cavity With Variable Wall Temperature," *Heat Exchange in Mono- and Biphase Media*, Naukova Dumka, Kiev, pp. 15–19.

Travkin, V. S., 1984, "Numerical Simulation of Heat and Mass Transfer in a Continuous-Casting Mold," *High Temperature*, Vol. 22, No. 2, pp. 251–258.

Travkin, V. S., 1985, "Numerical Integration of Free Convection Compressible Gas Equations in Enclosed Cylindrical Cavity on Conjugated Statement," *Numerical Methods of Continuous Medium Mechanics*, Vol. 16, No. 3, pp. 128–152.

Travkin, V., and Catton, I., 1992a, "Models of Turbulent Thermal Diffusivity and Transfer Coefficients for a Regular Packed Bed of Spheres," *Proceedings 28th National Heat Transfer Conf.*, ASME, HTD-Vol. 193, pp. 15–23.

Travkin, V., and Catton, I., 1992b, "Turbulent Forced Transport Governing Equations in High Permeability Medium," submitted to the *Physics of Fluids*.

Travkin, V., and Catton, I., 1992c, "The Numerics of Turbulent Processes in High Porosity Nonuniform Porous Media," *Proceedings of the SIAM 40th Anniversary Meeting*, Los Angeles, pp. A36.

Travkin, V. S., Catton, I., and Gratton, L., 1993, "Single Phase Turbulent Transport in Prescribed Non-Isotropic and Stochastic Porous Media," *Proceedings of the 29th National Heat Transfer Conference*, ASME, HTD-240, Atlanta, pp. 43–48.

Vafai, K., and Tien, C.L., 1981, "Boundary and Inertia Effects on Flow and Heat Transfer in Porous Media," *International Journal of Heat and Mass Transfer*, Vol. 24, pp. 195–203.

Vafai, K., and Thiyagaraja, R., 1987, "Analysis of Flow and Heat Transfer at the Interface Region of a Porous Medium," *Int. J. Heat Mass Transfer*, Vol. 30, No. 7, pp. 1391–1405.

Vafai, K., and Kim, S. J., 1989, "Forced Convection in a Channel Filled with a Porous Medium: An Exact Solution," ASME *Journal of Heat Transfer*, Vol. 111, No. 4, pp. 1103–1106.

Vafai, K., and Sozen, M., 1990, "Analysis of Energy and Momentum Transport for Fluid Flow Through a Porous Bed," ASME *Journal Heat Transfer*, Vol. 112, pp. 690–699.

Ward, J. C., 1964, "Turbulent Flow in Porous Media," *Journal of the Hydraulics Division, Proceedings of the ASCE*, Vol. 90, HY5, pp. 1–12.

Watanabe, H., 1989, "Drag Coefficient and Voidage Function on Fluid Flow through Granular Packed Beds," *International Journal of Engineering Fluid Mechanics*, Vol. 2, No. 1, pp. 93–108.

Whitaker, S., 1967, "Diffusion and Dispersion in Porous Media," *AIChE Journal*, Vol. 13, No. 3, pp. 420–427.

APPENDIX A

Turbulent transport equation set for the first level of hierarchy—in a pore was taken as next

$$\frac{\partial \bar{u}_i}{\partial x_i} = 0, \tag{A1}$$

$$\frac{\partial \bar{u}_i}{\partial t} + \bar{u}_j \frac{\partial \bar{u}_i}{\partial x_j} = -\frac{1}{\rho_f}\frac{\partial \bar{p}}{\partial x_i} + \frac{\partial}{\partial x_j}\left(\nu \frac{\partial \bar{u}_i}{\partial x_j} - \overline{u_i' u_j'}\right) + S_u, \tag{A2}$$

$$\frac{\partial \bar{T}}{\partial t} + \bar{U}_i \frac{\partial \bar{T}}{\partial x_i} = \frac{\partial}{\partial x_i}\left(\lambda(\mathbf{x}, \bar{T}, \bar{U}) \frac{\partial \bar{T}}{\partial x_i} - \overline{u_i' T'}\right) + S_T, \tag{A3}$$

where T represent any scalar field (temperature) that might be transported into either of the porous medium phases, and last terms on the right hand side of (A2) and (A3) are source terms.

This nonlinear set of equations has been averaged using developed nonlinear averaging technique (Primak et al., 1986; Scherban et al., 1986; Travkin and Catton, 1992b). Formalism of equation averaging in heterogeneous media differ from of the known ones in the account of different scale fluctuations, in the second averaging models and also in the differential operators averaging.

Turbulent quantities in the averaged equations are decomposed as follows:

$$U = \bar{U} + u' = \bar{U}_k + \bar{U}_r + u_k' + u_r',$$
$$\bar{U} = \tilde{\bar{U}} + \hat{\bar{u}}, \quad \hat{\bar{u}} = u_r', \tag{A4}$$

where the index "k" means for the turbulent components independent of nonhomogeneities of dimensions and properties of the multitude of porous media channels (pores), and "r" denotes the contributions due to the porous medium inhomogeneity. Turbulent kinetic energy Eq. (19) and averaged equation for mean eddy diffusivity (20) complement and close mathematical statement for 2-D (b-1) turbulent transport model in highly porous medium with regular morphology.

Journal of Fluids Engineering

Technical Briefs

Nonsteady Stagnation-Point Flows Over Permeable Surfaces: Explicit Solutions of the Navier-Stokes Equations

G. I. Burde[1]

Some new explicit solutions of the unsteady two-dimensional Navier-Stokes equations describing nonsteady stagnation-point flows with surface suction or injection are presented. The solutions have been obtained using a new approach for finding explicit similarity solutions of partial differential equations. As distinct from the common Birkhoff's similarity transformation, which permits only one form of an unsteady potential flow field and only one form of time dependence for suction (or blowing) velocity, the transforms obtained permit consideration of a variety of special solutions differing in the forms of time dependence.

1 Introduction

The solutions describing plane stagnation-point flows with surface suction or injection are of interest from both theoretical and technological points of views. Besides applications to the unsteady motion of bodies in fluids, which is important in many fields of aerodynamics and hydrodynamics, the significance of those solutions is enhanced by the fact that they satisfy the exact equations of viscous flow in two dimensions. The effects produced by withdrawing or expelling fluid through the body's surface also have numerous applications.

The problem is reduced to the dimensionless Navier-Stokes and continuity equations with corresponding boundary conditions, as follows

$$\frac{\partial u}{\partial t} + u\frac{\partial u}{\partial x} + v\frac{\partial u}{\partial y} = -\frac{\partial p}{\partial x} + \frac{\partial^2 u}{\partial x^2} + \frac{\partial^2 u}{\partial y^2} \tag{1.1}$$

$$\frac{\partial v}{\partial t} + u\frac{\partial v}{\partial x} + v\frac{\partial v}{\partial y} = -\frac{\partial p}{\partial y} + \frac{\partial^2 v}{\partial x^2} + \frac{\partial^2 v}{\partial y^2} \tag{1.2}$$

$$\frac{\partial u}{\partial x} + \frac{\partial v}{\partial y} = 0 \tag{1.3}$$

$$u = 0, \quad v = -C\varphi(t) \quad \text{at } y = 0 \tag{1.4}$$

$$u \to \beta(t)x, \quad v \to -\beta(t)\,y \quad \text{as } y \to \infty \tag{1.5}$$

where C is the suction parameter: $C > 0$ in the case of suction and $C < 0$ in the case of blowing. It is supposed that $\varphi(0) = 1$.

The solutions of the problem (1.1)–(1.5) corresponding to unsteady two-dimensional stagnation-point flows were studied by Yang (1958) and by Rajappa (1979) with the use of the similarity transformation established by Birkhoff (1960) on the basis of group theory. The extensions to axisymmetric and three-dimensional flows made by Williams (1968) and Cheng et al. (1971) are also based on Birkhoff's transform. Almost all of the existing exact similarity solutions of the unsteady Navier-Stokes equations (see review of Wang, 1989) are of the same form.

The solutions presented in this paper have been obtained with the help of a new approach for finding special explicit solutions of partial differential equations which was applied to the steady boundary layer equations in Burde (1994). The application of the approach to unsteady problems is more complicated as the additional independent variable appears. However, the problem of finding nonsteady solutions having stagnation-point form is simplified due to the fact that one of the space variables is detached. Thus, practically the same procedure as for the steady case is applicable. The method produces solutions having some special forms but, in return, it allows new similarity reductions containing arbitrary functions of time. Thus, each such solution can represent any one of a variety of solutions of specific problems differing in the forms of time dependence permitted for the external flow and suction velocity. Though particular cases include solutions of Birkhoff's form, in general, the solutions correspond to extended similarity reductions which can not be obtained either by dimensional analysis or by the Lie group method (see discussion in Burde, 1994).

2 Description of Method

The solutions of the problem (1.1)–(1.5) will be sought in the following form

$$u = \beta(t)x + x\beta(t)g'(\eta), \quad \eta = y/\gamma(t) \tag{2.1}$$

$$v = -\beta(t)y + \gamma(t)[q(t) - \beta(t)g(\eta)] \tag{2.2}$$

$$p = -(x^2/2)\,[\beta'(t) + \beta^2(t)] + R(\eta, t) \tag{2.3}$$

Here and in what follows primes denote derivatives with respect to t in the β, γ, and q functions and derivatives with respect to η in the g functions. The expressions (2.1) and (2.2) already satisfy the continuity Eq. (1.3). Substitution of (2.1)–(2.3) into (1.1) leads to the relation

$$(1/\gamma^2)g''' + (\beta)gg'' - (\beta)g'^2 + (\gamma'/\gamma + \beta)\eta g'' - (q)g'' - (\beta'/\beta + 2\beta)g' = 0 \tag{2.4}$$

which plays the main role in the subsequent analysis deter-

[1]Assistant Professor, Meteorology Unit, Ben-Gurion University, Blaustein Institute for Desert Research, Sede Boker Campus 84993 Israel.

Contributed by the Fluids Engineering Division of THE AMERICAN SOCIETY OF MECHANICAL ENGINEERS. Manuscript received by the Florida Engineering Division November 8, 1993; revised manuscript received August 9, 1994. Associate Technical Editor: R. W. Metcalfe.

mining the function $g(\eta)$ and possible forms of the functions $\beta(t)$, $\gamma(t)$, and $q(t)$. The relation obtained by substitution of (2.1)–(2.3) into (1.2) serves for determination of $R(\eta, t)$.

The usual analysis for possible similarity solutions requires, that (2.4) reduces to an ordinary differential equation for $g(\eta)$, and this requirement inevitably leads to Birkhoff's transformation. Below, a qualitatively different approach to the conversion of (2.4) into ordinary differential equations will be employed. The point of the approach may be outlined as follows. The relation (2.4) is satisfied by dividing it into two or more relations by combining different terms. Choosing the functions β, γ, and q in such a way that each of the relations obtained is reduced to an ordinary differential equation, one arrives at two or more equations for a single function g. If there exists a solution of such an overdetermined system, one can obtain a more general solution of the initial problem, since fewer restrictions are imposed on the functions β, γ, and q. In the following we will consider some of the variants of reducing (2.4) to overdetermined systems and examine one of the resulting solutions.

Restricting ourselves to the solutions for which

$$\beta = -\gamma'/\gamma \tag{2.5}$$

and assuming that

$$\beta = a_1\beta + b_1/\gamma^2 \tag{2.6}$$

$$-q = a_2\beta + b_2/\gamma^2 \tag{2.7}$$

$$-(\beta'/\beta + 2\beta) = a_3\beta + b_3/\gamma^2 \tag{2.8}$$

we arrive at a system of two ordinary differential equations for $g(\eta)$, namely,

$$-g'^2 + a_1 gg'' + a_2 g'' + a_3 g' = 0 \tag{2.9}$$

$$g''' + b_1 gg'' + b_2 g'' + b_3 g' = 0 \tag{2.10}$$

This overdetermined system is solved by the reduction $g' = S(g)$ beginning from the first equation. Different types of solutions can exist depending on the values of the constants a_i and b_i. We will consider only one of the solutions which has the form

$$g = -a_2 - a_3/B + D\exp(B\eta) \tag{2.11}$$

where the constants D, a_2, and a_3 are arbitrary and the following restrictions are imposed on the values of the other constants

$$a_1 = 1: b_1 = 0, b_3 = -b_2 B - B^2 \tag{2.12}$$

Then the solution of the initial equations (1.1)–(1.3) is given by the formulas (2.1), (2.2), (2.11), and (2.7) in which the functions β and γ are determined by the system of ordinary differential equations (2.8) and (2.5) and constants are specified by the boundary conditions.

This solution can be extended somewhat if one reduces the relation (2.4) to an overdetermined system of three differential equations. Assuming that the function $q(t)$ can be represented in the form

$$q = k_1\beta + k_2\beta'/\beta + k_3/\gamma^2 \tag{2.13}$$

where k_1, k_2, and k_3 are constants, one arrives at a system of three differential equations for a single function $g(\eta)$, namely,

$$-g'^2 + gg'' - 2g' - k_1 g'' = 0 \tag{2.14}$$

$$k_2 g'' + g' = 0 \tag{2.15}$$

$$g''' - k_3 g'' = 0 \tag{2.16}$$

The solution of this overdetermined system has the same form (2.11) (with other constants) but the corresponding solution of the initial equations (1.1)–(1.3) appears to be more general since the function $\beta(t)$ remains completely arbitrary (the constraints which were imposed on β by Eq. (2.8) are now absent). Substitution of the expressions for $g(\eta)$ and $q(t)$ into (2.1) and (2.2) after satisfying the boundary conditions gives the final expressions for u and v, as follows

$$u = x\beta(t)[1 - \exp(-m\eta)] \tag{2.17}$$

$$v = (\gamma/m)(\beta'/\beta + \beta) - (m/\gamma) - (\gamma/m)\beta[-1 + m\eta + \exp(-m\eta)] \tag{2.18}$$

$$\eta = y/\gamma(t),\ \gamma(t) = \exp\left(-\int_0^t \beta(\tau)d\tau\right) \tag{2.19}$$

where m is an arbitrary positive constant. The expression for the pressure obtained by substituting the expressions (2.17)–(2.19) and (2.3) into (1.2) has the form

$$p = p_0 - (x^2/2)(\beta' + \beta^2) + (\eta^2/2)\gamma(\beta\gamma)' + (\eta/m)\gamma^2[3\beta^2 + 2\beta' - (\beta'/\beta + \beta)' - (\beta\gamma)'/\gamma] + (\gamma^2\beta^2/2m^2)[8\exp(-m\eta) - \exp(-2m\eta) - 7] \tag{2.20}$$

3 Some Particular Cases

Consider some special cases of the formulae (2.17)–(2.20) corresponding to certain types of unsteady flows. First, we will take the function β (potential flow time dependence) in the form which is the same as that for solutions of Birkhoff's type. As distinct from Birkhoff's transformation, permitting only one form of similarity variable, the formulas (2.17)–(2.20) produce a set of solutions with different forms of the similarity variable, as follows

$$\beta = I(1 - \lambda t), \quad \gamma = (1 - \lambda t)^{I/\lambda} \tag{3.1}$$

where λ is the acceleration parameter and the parameter I determines the type of the stagnation point: $I = 1$ for forward stagnation-point flow and $I = -1$ for rear stagnation-point flow. The corresponding set of suction laws is given by

$$\varphi(t) = \mu(1 - \lambda t)^{-I/\lambda} - \frac{I + \lambda}{C^2\mu}(1 - \lambda t)^{(I/\lambda)-1} \tag{3.2}$$

where

$$\mu = 1/2 + [1/4 + (I + \lambda)/C^2]^{1/2} \tag{3.3}$$

Particular cases are easily obtained from these formulas, as, for example, the following: $\gamma = 1/(1 + It)$, $\varphi = 1 + It$ for $\lambda = -I$ and $\gamma = (1 - 2It)^{1/2}$, $\varphi = (1 - 2It)^{-1/2}$ for $\lambda = 2I$ (Birkhoff's case).

It is worth noting that the formulas (2.17)–(2.20) and (3.1)–(3.3) include as particular cases the exact solutions of the blowhard problem when the velocity component normal to the wall is an order of magnitude larger than that usually expected in a boundary layer with no blowing. Under such circumstances the boundary layer is blown off the body to form a shear layer containing the dividing streamline separating the outer potential flow region from the region of injected fluid near the wall. The problem of hard blowing for the unsteady oncoming flow of the stagnation-point type was treated approximately in the work of Rajappa (1979) where an asymptotic solution for $|C| \to \infty$ was sought. Our solutions are valid for any values of the parameter C and thus do not require separate treatment of the blowhard problem. Typical streamlines of the flow field corresponding to the particular case of the formulas (3.1)–(3.3) are shown in Fig. 1. The explicit form of solutions also allow us to obtain explicit formulae describing the behaviour of the distance of the dividing streamline from the body surface versus time and the suction parameter C for any particular case.

Let us consider another special case of the general solution (2.17)–(2.20) when the external potential flow is steady-state

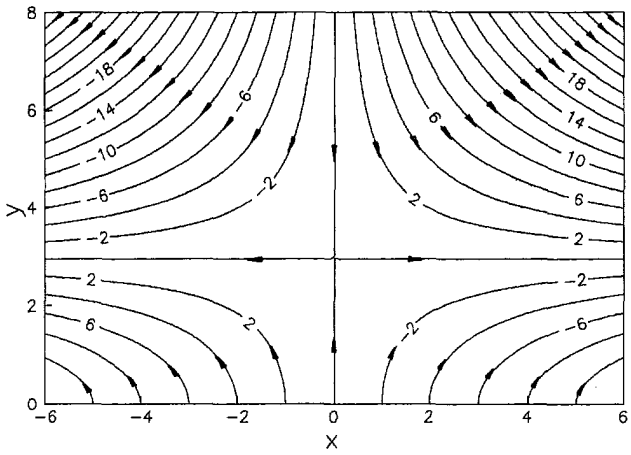

Fig. 1 Streamlines of the unsteady flow field at $t = 0$ for the solution given by (2.17)–(2.20) and (3.1)–(3.3) for $l = 1$, $\lambda = 2$ and $C = -2$

so that the flow near the surface is unsteady only due to a variable suction velocity. Such a solution obtained from (2.17)–(2.20) by setting $\beta = 1$ (forward stagnation point flow) corresponds to the suction law of the form

$$\varphi = (2/C)\sinh(t - t_*), \quad t_* = -\ln(m) \tag{3.4}$$

where

$$m = C/2 + (C^2/4 + 1) \tag{3.5}$$

The law of suction (3.4) implies that the solution describes the flow for which blowing with decreasing velocity is changed by suction with increasing velocity beginning from $t = t_*$. One can also obtain a rear stagnation-point counterpart of this solution.

References

Birkhoff, G., 1960, *Hydrodynamics, a Study in Logic, Fact and Similitude*, Revised Ed., Princeton University Press, pp. 137–139.

Burde, G. I., 1994, "The Construction of Special Explicit Solutions of the Boundary-Layer Equations. Steady Flows," *Quarterly Journal of Mechanics and Applied Mathematics*, Vol. 47, pp. 247–260.

Cheng, E. H. W., Ozisik, M. N., and Williams, J. C., 1971, "Nonsteady Three-Dimensional Stagnation-Point Flow," ASME *Journal of Applied Mechanics*, Vol. 38, pp. 282–287.

Rajappa, N. R., 1979, "Nonsteady Plane Stagnation Point Flow with Hard Blowing," *Zeitschrift fur Angewandte Mathematik und Mechanik*, Vol. 59, pp. 471–473.

Wang, C. Y., 1989, "Exact Solutions of the Unsteady Navier-Stokes equations," *Applied Mechanics Reviews*, Vol. 42, pp. S269–282.

Williams, J. C., 1968, "Nonsteady Stagnation-Point Flow," *AIAA Journal*, Vol. 6, pp. 2417–2419.

Yang, K. T., 1958, "Unsteady Laminar Boundary Layers in an Incompressible Stagnation Flow," ASME *Journal of Applied Mechanics*, Vol. 25, pp. 421–427.